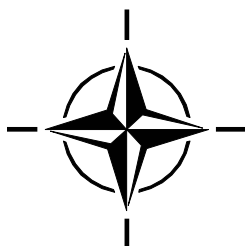# Internal Aerodynamics in Solid Rocket Propulsion

(L'aérodynamique interne de la propulsion
par moteurs-fusées à propergols solides)

The material in this publication was assembled to support a RTO/VKI Special
Course under the sponsorship of the Applied Vehicle Technology Panel (AVT)
and the von Kármán Institute for Fluid Dynamics (VKI) presented on
27-31 May 2002 in Rhode-Saint-Genèse, Belgium.

*Distribution and Availability on Back Cover*

AC/323(AVT-096)TP/70

www.rta.nato.int

**RTO EDUCATIONAL NOTES EN-023**                    **AVT-096**

# Internal Aerodynamics in
# Solid Rocket Propulsion

## (L'aérodynamique interne de la propulsion
## par moteurs-fusées à propergols solides)

The material in this publication was assembled to support a RTO/VKI Special

Course under the sponsorship of the Applied Vehicle Technology Panel (AVT)

and the von Kármán Institute for Fluid Dynamics (VKI) presented on

27-31 May 2002 in Rhode-Saint-Genèse, Belgium.

# The Research and Technology Organisation (RTO) of NATO

RTO is the single focus in NATO for Defence Research and Technology activities. Its mission is to conduct and promote co-operative research and information exchange. The objective is to support the development and effective use of national defence research and technology and to meet the military needs of the Alliance, to maintain a technological lead, and to provide advice to NATO and national decision makers. The RTO performs its mission with the support of an extensive network of national experts. It also ensures effective co-ordination with other NATO bodies involved in R&T activities.

RTO reports both to the Military Committee of NATO and to the Conference of National Armament Directors. It comprises a Research and Technology Board (RTB) as the highest level of national representation and the Research and Technology Agency (RTA), a dedicated staff with its headquarters in Neuilly, near Paris, France. In order to facilitate contacts with the military users and other NATO activities, a small part of the RTA staff is located in NATO Headquarters in Brussels. The Brussels staff also co-ordinates RTO's co-operation with nations in Middle and Eastern Europe, to which RTO attaches particular importance especially as working together in the field of research is one of the more promising areas of co-operation.

The total spectrum of R&T activities is covered by the following 7 bodies:

- AVT     Applied Vehicle Technology Panel
- HFM     Human Factors and Medicine Panel
- IST      Information Systems Technology Panel
- NMSG   NATO Modelling and Simulation Group
- SAS     Studies, Analysis and Simulation Panel
- SCI      Systems Concepts and Integration Panel
- SET      Sensors and Electronics Technology Panel

These bodies are made up of national representatives as well as generally recognised 'world class' scientists. They also provide a communication link to military users and other NATO bodies. RTO's scientific and technological work is carried out by Technical Teams, created for specific activities and with a specific duration. Such Technical Teams can organise workshops, symposia, field trials, lecture series and training courses. An important function of these Technical Teams is to ensure the continuity of the expert networks.

RTO builds upon earlier co-operation in defence research and technology as set-up under the Advisory Group for Aerospace Research and Development (AGARD) and the Defence Research Group (DRG). AGARD and the DRG share common roots in that they were both established at the initiative of Dr Theodore von Kármán, a leading aerospace scientist, who early on recognised the importance of scientific support for the Allied Armed Forces. RTO is capitalising on these common roots in order to provide the Alliance and the NATO nations with a strong scientific and technological basis that will guarantee a solid base for the future.

# Internal Aerodynamics in Solid Rocket Propulsion

## (RTO EN-023 / AVT-096)

# Executive Summary

Considerations of the optimal approaches to adapt space launchers to a changing market should lead to significant breakthroughs in solid rocket propulsion technology, mainly in the areas of reduced costs and improved performance characteristics. The goal of this NATO Research and Technology Organization (RTO) sponsored lecture series was to provide a forum for the review of various scientific and industrial aspects of solid rocket propulsion and an assessment of recent advances with emphasis on internal aerodynamics. The present lecture notes are intended as a natural follow-up to the AGARD-LS-180 "Combustion of Solid Propellants" organized in 1991.

These RTO-AVT / VKI Special Course notes provide the state of the art in internal aerodynamics in solid rocket propulsion, in a way accessible to attendees coming from both academic and industrial areas. Two families of solid motors can be identified: tactical rockets and large boosters for launch vehicles. The military rockets are subjected to combustion instabilities while vortex shedding drives the instabilities in the large boosters. After an overview of the motor internal flow dynamics, combustion of solid propellants and metal particulates were presented. Numerical modeling of internal flow aerodynamics, two-phase flow and flow/structural interactions were addressed, before focusing on the motor flow and combustion instabilities.

The main objective of these course notes is therefore to allow an information transfer between well-known scientists, leaders in the solid propulsion field, and demanding industries and laboratories. For these reasons, this proceeding appeals not only to experts already working in the domain, but also to newcomers to the field.

# L'aérodynamique interne de la propulsion par moteurs-fusées à propergols solides
## (RTO EN-023 / AVT-096)

# Synthèse

La considération des approches optimales de l'adaptation des lanceurs spatiaux à un marché en pleine évolution devrait conduire à des progrès décisifs dans le domaine des technologies de la propulsion par moteurs-fusées à propergols solides, principalement du point de vue de la diminution des coûts et de l'amélioration des caractéristiques de performance. Ce Cycle de conferences, organisé par l'Organisation OTAN pour la recherche et la technologie (RTO) a eu pour objectif de servir de forum pour l'examen de différents aspects scientifiques et techniques de la propulsion par moteurs-fusées à propergols solides, ainsi que pour l'évaluation des derniers progrès réalisés, en particulier en aérodynamique interne. L'actuel support de cours représente la suite naturelle du cycle de conférences AGARD-LS-180 sur « La combustion des propergols solides » organisé en 1991.

Ce support de cours spécial RTO-AVT/VKI présente l'état actuel des connaissances dans le domaine de l'aérodynamique interne de la propulsion par moteurs-fusées à propergols solides, de manière à rendre le sujet accessible à des participants venant aussi bien de l'industrie que des universités. Deux grandes familles de moteurs-fusées à propergols solides sont à distinguer : les fusées tactiques et les grandes fusées d'appoint pour lanceurs. Les fusées militaires sont sujettes à des instabilités de combustion, tandis que les instabilités des grandes fusées d'appoint sont occasionnées par le décollement des tourbillons. Suite à un aperçu de la dynamique des écoulements internes des moteurs, la combustion des propergols solides et des particules métalliques a été présentée. La modélisation numérique de l'aérodynamique des écoulements internes, ainsi que les interactions des écoulements bi-phase et des écoulements/structures ont été examinées, avant de considérer les flux internes des moteurs et les instabilités de combustion.

Ce support de cours a donc pour objectif de permettre un échange d'informations entre des scientifiques renommés, éminents dans le domaine de la propulsion par propergol solide, et les industries et les laboratoires qui s'intéressent à leur travail. Pour ces raisons, ces documents seront appréciés non seulement par les spécialistes du domaine, mais aussi par les néophytes.

# Table of Contents

---

† Paper not available at the time of publishing.

# List of Authors/Lecturers

## Special Course Directors

Assis. Prof. Jérôme Anthoine
Assistant Professor
von Kármán Institute for Fluid Dynamics
chaussée de Waterloo 72
1640 Rhode-Saint-Genèse
BELGIUM
email:  anthoine@vki.ac.be

Mr. Paul Kuentzmann
ONERA/DSG
BP 72
92322 Chatillon Cedex
FRANCE
email: ktz@onera.fr

## Lecturers

Mr. Grégoire Casalis
ONERA Toulouse
BP 4025
2 avenue E. Belin
BP 4025
31055 Toulouse Cedex
FRANCE
email: casalis@onecert.fr

Dr. J-F. Guéry
SNPE
BP 2
9171- Vert-le-Petit
FRANCE
email: j.guery@snpe.com

Mr. Guy Lengellé
ONERA Energetics
Centre de Palaiseau
Chemin de la Thumière
91120 Palaiseau Cedex
FRANCE
email: lengelle@onera.fr

Dr. F. Vuillot
ONERA
BP 72
93222 Chatillon Cedex
FRANCE
email: vuillo@onera.fr

Prof. Merill Beckstead
Brigham Young University
Dept of Chemical Engineering
Provo, UT 84062
USA
email: mwb@byu.edu

Prof. Fred E.C. Culick
Caltech
Mechanical Engineering and Jet Propulsion
1200 East California Blvd
Pasadena, California 91125
USA
email: fecfly@caltech.edu

Dr. John W. Murdock
The Aerospace Corporation
Vehicle Performance Subdivision
M4/964
PO Box 92957
Los Angeles, CA 90009-2957
USA
email:  john.w.murdoch@aero.org

Mr. M. Salita
TRW
875 S 2000 E
Clearfield, UT 84414
USA
email: mark.salita@trw.com

Prof. Vigor Yang
The Pennsylvania State University
Department of Mechanical Engineering
104 Research Building East
University Park, PA 16802
USA
email: vigor@psu.edu

# Introduction to Solid Rocket Propulsion

**P. Kuentzmann**
Office National d'Etudes et de Recherches Aérospatiales
29, avenue de la Division Leclerc – BP 72
92322 Châtillon Cedex
FRANCE

## SUMMARY

*The objectives of this introduction are to present the fundamentals of solid rocket motor (SRM), starting from the elementary analysis of rocket operation and then justifying the need of sophisticated computation of the internal flow. After a brief reminder of solid rocket history, a description of its main components is proposed. The elementary parameters controlling the operation are introduced and the basic formula predicting the steady-state operation pressure is established. The main issues faced by a SRM require an accurate description of internal aerodynamics, either to predict the pressure/thrust programs and the normal transient phases like ignition, or to study the motor stability. A short overview of the evolution of the codes devoted to SRM internal aerodynamics during the last thirty years is given in order to introduce the more specialized presentations; a discussion of the main limitations concerning these codes is also proposed. The prospects offered by SRM internal aerodynamics codes are finally described.*

## 1.0 GENERALITIES

### 1.1 History

The solid rocket motor belongs to the family of the rocket engine (thrust achieved by mass ejection) and its history can be considered both ancient and recent. It is possible to consider that the black powder is the precursor of modern solid propellants: composed of natural ingredients (sulfur, charcoal and salpetre), the black powder has been used from the $13^{th}$ century in Asia to propelled darts, certainly the first unguided stand-off weapons. A lot of work has been performed since this time to improve the solid propellant and to master its combustion but the main military application has been gun propellants up to the WW2. The WW2 has seen the first aeronautical applications (BACHEM Natter, JATO, RATO). The main developments for military (missiles) and space activities (launchers) started in 1945.

Regarding the space activities, the first flights were carried out by liquid propellant rockets, following the world's first successfully flown rocket on March 15, 1926 (R. Goddard, USA). The first satellites have been put into orbit by a liquid propellant launcher (R7 Semiorka, October 1957); the first successful US launch (Jupiter C, January 1958) used solid propellant rockets for the upper stages. The small US Scout has been the first all solid propellant launcher. Most of the first intercontinental missiles or intermediate range missiles used also liquid propellant engines, for their first generations.

The current situation is the following:

- Most of the modern strategic and tactical missiles use solid propellant propulsion. The only competitor for solid propulsion is ramjet propulsion for tactical missiles.

- Space launchers are in the western countries and in Japan based on an assembly of liquid and solid propelled stages; they remain all liquid propellant in Russia, Ukraine and China. This difference of design is clearly connected to economical considerations: development and

recurrent costs of a large solid propellant booster are lower than those of a large liquid propellant booster in the western countries, agreed that performance is better for liquid propellant propulsion. The orientation towards RLVs (Reusable Launch Vehicles) will favor of course liquid propulsion in the future.

## 1.2    The Basic Solid Rocket Motor

A solid propellant rocket is formed by four main components (fig. 1):

- A case containing the solid propellant and withstanding internal pressure when the rocket is operating.

- The solid propellant charge (or grain), which is usually bonded to the inner wall of the case, and occupies before ignition the greater part of its volume. When burning, the solid propellant is transformed into hot combustion products. The volume occupied by the combustion products is called combustion chamber.

- The nozzle channels the discharge of the combustion products and because of its shape accelerates them to supersonic velocity.

- The igniter, which can be a pyrotechnic device or a small rocket, starts the rocket operating when an electrical signal is received.



**Figure 1: Basic Solid Rocket Motor.**
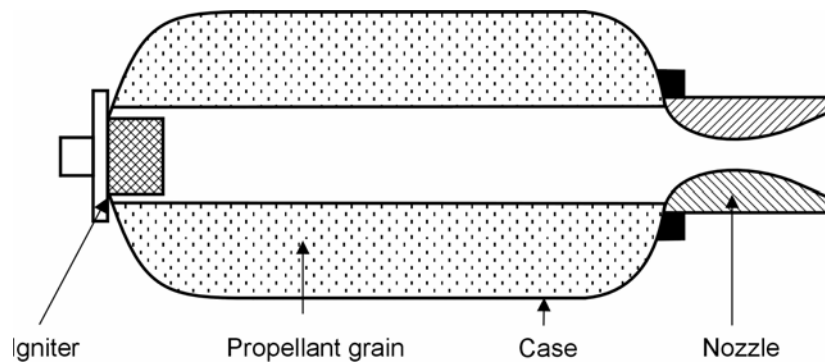
One can consider that the solid propellant after manufacturing is in a metastable state. It can remain inert when stored (in appropriate conditions) or it can support after ignition its continuous transformation into hot combustion products (self-combustion). The velocity of the transformation front is called *burning rate* (fig. 2).
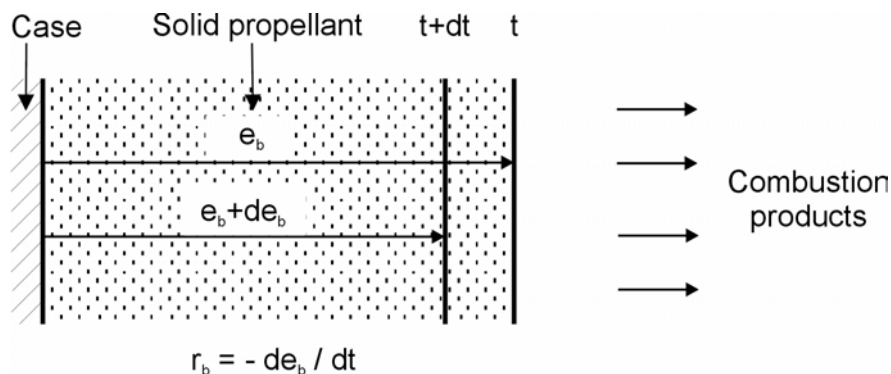


**Figure 2: Solid Propellant Rocket Motor.**

The solid rocket is therefore inherently simple and therefore can possess high intrinsic reliability. After ignition, a solid rocket motor normally operates in accordance with a preset thrust program until all the propellant is consumed. All the efforts should be directed to the accurate prediction of the thrust (and pressure) programs to get the benefit of solid rocket motor concept.

## 1.3 Definitions

Efficiency of a rocket if defined by specific impulse: $I_s = \dfrac{F}{\dot{m}g_o}$

where: $I_s$ is the specific impulse (in s),

$\dot{m}$ is the mass flow rate ejected by the rocket (in kg.s$^{-1}$),

$g_o$ is the reference gravity (9,806 m.s$^{-2}$).

This definition has been adopted because the second is a universal unit of measure. Specific impulse is used for all types of rocket (chemical, electric) and for ramjet/scramjet; specific impulse can be considered as the inverse of specific consumption. The higher is the specific impulse, the better is the rocket.

It should also be observed that specific impulse depends on the operation conditions of the solid rocket motor: pressure in the combustion chamber, rate of expansion in the nozzle, ambiant pressure. The theoretical specific impulse, for a given propellant and a fixed pressure, can be predicted by thermochemical computation. All countries in the world are using similar codes and, in the western countries, the same thermodynamic tables (JANAF). To avoid all the problems related to unit systems, standard conditions are adopted and comparisons can be performed:

- Pressure: 70 atm (close to 1000 psia).
- Expansion: 70 to 1 atm.
- Ambiant pressure: 1 atm (nozzle adaptation).

Under these reference conditions, the theoretical specific impulse of a conventional composite propellant (ammonium perchlorate, polybutadiene, aluminum) is around 265 s. In practice, the actual specific impulse is lower, due to specific impulse losses related to phenomena which cannot be taken into account in the thermochemical computation (multidimensional flow, two-phase effects, wall phenomena…). Specific impulse in vacuum is higher than $I_s$ at atmospheric pressure.

Another characteristic parameter, essentially defined for a chemical rocket equipped with a chocked convergent-divergent (de Laval) nozzle, is the *characteristic velocity*:

$$C^* = \frac{p_o A_c}{\dot{m}} (m.s^{-1})$$

- where $p_o$ is the pressure in the combustion chamber $(Pa)$,
- $A_c$ is the nozzle throat area $(m^2)$.

A simplified description of the flow in the nozzle (one-dimensional flow, ideal gas) gives a clear interpretation of $C*$:

$$C* = \frac{\sqrt{\frac{R}{M} T_o}}{\Gamma(\gamma)} ,$$

- where $R$ is the universal gas constant (8,3144 J.mol$^{-1}$.K$^{-1}$),

- $M$ is the molecular weight of the gas (kg/mole),

- $T_o$ is the gas temperature (K),

- $\gamma$ is the isentropic exponent ($C_p/C_v$),

- $\Gamma(\gamma)$ is the Vandenkerkhove's function: $\Gamma(\gamma) = \sqrt{\gamma} \left( \frac{2}{\gamma + 1} \right)^{\frac{\gamma+1}{2(\gamma-1)}}$

$C*$ characterizes obviously the combustion products and is totally independent of the expansion conditions and on the external pressure; nozzle chocking plays the role of an insulator between the combustion chamber and the external surrounding.

The third parameter, again defined for a chemical rocket and a chocked nozzle, is the thrust coefficient:

$$C_F = \frac{F}{p_o A_c} \quad \text{(non-dimensional)}$$

$C_F$ depends on the expansion rate and the external pressure. The simplified description of the nozzle flow gives: $C_F = C_F^{(A)} + \Delta C_F$ :

- where $C_F^{(A)}$ is the thrust coefficient for nozzle adaptation,

- $\Delta C_F$ is a correction of inadaptation.

It is possible to demonstrate that $C_F$ is limited when the expansion rate increases. A simple relationship between the different characteristic parameters can be written: $I_s = \frac{C* . C_F}{g_o}$

This relationship gives a clear interpretation of the respective contributions of combustion products and nozzle in the thrust production. Thermochemical computation gives $C*, C_F$ and $I_s$ by taking into account the actual thermodynamics of combustion products. For the conventional composite propellant previously mentioned:

$$C* \approx 1550 \ m.s^{-1}$$
$$C_F \approx 1,68 \qquad \text{(adapted nozzle)}$$

## 1.4 A First Approach of Motor Operation

A first approach of motor operation can be established by using the elementary *global* conservation laws. The main necessary assumptions are the following:

- Steady-state operation,

- Very low Mach number (M<<1) of the combustion products in the combustion chamber (that means that ratio of nozzle entrance section area to throat area is very large),

- The combustion products are totally generated on the combustion surface.

In these conditions, only two conservation principles for mass and energy should be satisfied:

- $\dot{m}_b = \dot{m}_T$, where $\dot{m}_b$ is the mass flow rate of combustion products entering the combustion chamber and $\dot{m}_T$ is the mass flow rate exhausted by the nozzle.

- $\dot{m}_b h_p = \dot{m}_T h$, where $h_p$ is the specific enthalpy of combustion products and $h$ is the specific enthalpy of the flow entering the nozzle.

Obviously $h_p = h$ and the stagnation temperature at nozzle entrance is the temperature of combustion products. Therefore it remains: $\dot{m}_b = \dot{m}_T$, where $\dot{m}_b = \rho_p r_b A_b$ ($\rho_p$: propergol density, $r_b$: burning rate, $A_b$: combustion area), $\dot{m}_T = \dfrac{p_o A_c}{C*}$, following the definition of $C*$.

A very simple relationship exists, expressing the mass conservation, between the different parameters:

$$\rho_p r_b A_b = \frac{p_o A_c}{C*}$$

It is more appropriate to write: $\dfrac{p_o}{\rho_p r_b C*} = \dfrac{A_b}{A_c}$.

The right hand expression is related to the *geometric* parameters of the rocket motor:

$$K_G = \frac{A_b}{A_c} \quad (K \text{ for the german world } Klemmung).$$

The left hand expression depends on the propellant characteristics ($\rho_p, r_b, C*$) and on the pressure ($p_o$). The (normal steady-state) burning rate is a function of pressure, *for a given propellant*:

$$K_p(p_o) = K_G$$

This equality between the parameters $K_p$, function of $p_o$, for a given propellant, and $K_G$, based on the rocket geometry, can be used in different ways:

- Determine $A_c$ si $A_b$ and $p_o$ are chosen,

- Predict $p_o$ si $A_b$, $A_c$ are fixed…

Finally, the first step of the design of a solid rocket propellant looks very simple. Unfortunately, is not sufficient to perform a complete motor design with the required high level of prediction and reliability, as explained later. However, the early solid propellant rocket motors have been developed on this basis.

## 1.5    Evolution of Parameters According to Time

A solid rocket motor has a variable internal geometry related to the continuous transformation of the solid propellant to combustion products. Change of the combustion area in time will result in change of pressure and thrust. A steady state view of operation can be adopted by considering different geometries separated by an increment of displacement of the combustion surface. An elementary analysis can justify this approach. One considers an elementary surface by assuming that the transformation of the solid propellant to combustion products occurs on the surface area and not in volume (fig. 3).
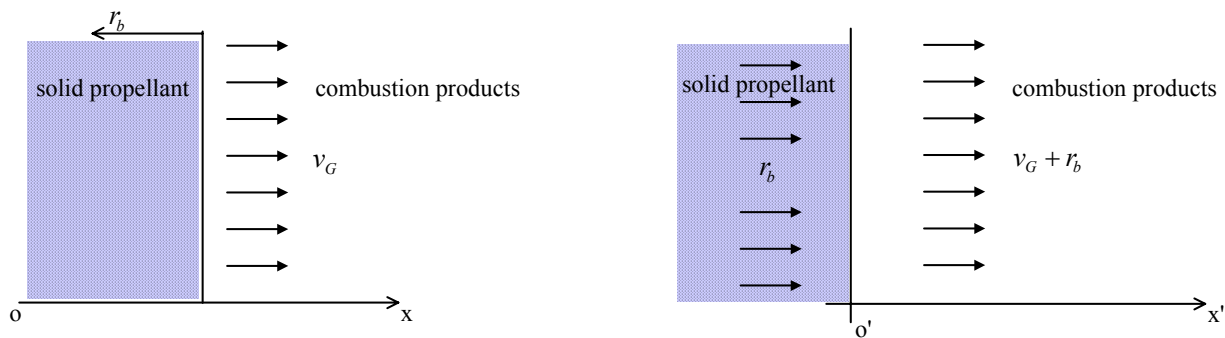


**Figure 3: Injection Conditions on the Combustion Surface.**

Mass conservation leads to:

$$\rho_G v_G \approx \rho_p r_b$$

If    $\rho_p = 1{,}78 g.cm^{-3}, r_b = 8 mm.s^{-1}, p = 70 atm,$

$T_o = 3494 K, \mathrm{M} \approx 28{,}46 g.mole^{-1},$ one finds:    $V_G \approx 2 m.s^{-1} >> r_b$

$$M_G \approx 1 \times 10^{-3}$$

Two consequences result from this elementary analysis:

- Velocity of the combustion products leaving the combustion surface is at least two order of magnitude higher than the burning rate; a reasonable approximation is to assume that the products are entering the combustion chamber from a fixed surface. This approximation justifies all the experiments performed by cold gas simulation (injection of a cold gas through a porous wall).

- Description of the flow in the entire motor implies Mach number from very low values (near the combustion surface) to very high values (nozzle exit) and then use of adapted numerical methods.

Conservation of momentum has also another consequence: the combustion products are emitted perpendicularly towards the combustion surface.

## 2.0   THE MAIN ISSUES OF SOLID PROPELLANT ROCKET MOTOR

Development of a solid rocket motor requires considerable technological investments in different domains. These investments are substantial given the severe conditions inside the motor: high pressure (around 5 MPa or 50 bar in the larger boosters), high temperature (around 3500 K for a composite metallized propellant), two phase flow (metallized propellant). The critical technologies concern the propellant itself, the propellant grain design, the thermal insulation, the nozzle design and the case. Besides, another well known difficulty is related to the near impossibility to perform detailed measurement inside the combustion chamber, due to the severe conditions prevailing there: the only usual measurement is the static pressure measurement through a pressure tube, generally at the motor front end. This difficulty can be considered as one of the main obstacles to the perfect validation of the prediction tools.

As this Short Course is devoted to aerodynamics, attention will now be focused on the particular aspects of design having an influence on aerodynamics and operation.

### 2.1   Burning Rate

Propellant burning rate plays a central role in motor operation. That is why perfect control of burning rate is absolutely mandatory. Fundamentals and recent developments regarding burning rate will be developed in another lecture. The discussion will here be limited to a classification of the different combustion regimes encountered during the whole motor operation.

### 2.1.1   Steady State Regimes

- Normal (regular) regime: burning rate is depending on only two parameters: pressure and initial temperature: $r_b = r_b(p_o; T_i)$. It is known that burning rate can change with the propellant temperature. Since only a very thin layer of the propellant is usually affected by the chemical transformation during the combustion process, a good assumption is that the initial grain temperature (considered as uniform) is an external parameter, without variation during operation. Sensitivity to pressure is related to the chemical reactions in gaseous phase (flames) above the combustion surface.

  Some parameters are defined to characterize locally the propellant sensitivity to pressure and temperature:

$$n = \left( \frac{\partial \ln r_b}{\partial \ln p_o} \right)_{T_i} = n(p_o; T_i)$$

$$\sigma_p = \left( \frac{\partial \ln r_b}{\partial T_i} \right)_{p_o} = \sigma_p(p_o; T_i), (K^{-1})$$

  It should be mentioned that the pressure exponent $n$ should be lower than 1 for a practical propellant; if not, the steady-state operation pressure is not stable; $n \approx 0.3$ for the more conventional composite propellants.

- Erosive burning regime: if the flow above the combustion surface is fast, it is possible to observe an increase in the burning rate for a given pressure (and, less frequently, a decrease in the burning rate for some double base propellants). A general accepted explanation of such an increase is linked to the enhancement of the convective thermal flux to the combustion surface due to the interaction between flow turbulence and flames. In this condition, burning rate is no longer pure feature of the propellant but a property mixing propellant and flow. Erosive burning can be responsible of a pressure overshoot at ignition. A simplified prediction can be obtained by characterizing the flow by the unit mass flow rate in the perforation (internal burning tube); erosive burning is then a threshold phenomenon.

### 2.1.2    Unsteady Regimes

When pressure or more generally the conditions above the combustion surface are changing very rapidly, direct dependence of burning rate on instantaneous parameters is no longer right; time is also involved. Several situations bring into play unsteady burning rate, essentially the transient phases (ignition and operation end) and the instability. The common approach is to make the distinction between linear burning rate and non-linear burning rate.

Linear burning rate corresponds to small perturbations of all the parameters around a steady state and it is typically the case for the low level instability. Response to the propellant burning rate to pressure (pressure coupling) has been proved (measured and explained); the response can be considered like a transfer function between pressure and burning rate:

$$R_{MP} = \frac{\tilde{r}_b / \bar{r}_b}{\tilde{p}_o / \bar{p}_o}$$

where, for instance, $\bar{p}$ is the steady state pressure and $\tilde{p}$ the amplitude of oscillation.

$R_{MP}$ is a complex parameter, function of the oscillation frequency. A temperature response $R_{TP}$ can be derived from $R_P$. At relatively low frequency, the pressure response is only linked to the thermal transfer in the solid propellant. $R_P$ plays an essential role in the combustion instabilities.

A response of the propellant burning to flow (velocity coupling) has been suspected but never really proved and measured.

Non-linear burning rate occurs either during ignition or during high level instabilities. If some analytical or computational tools are able to predict non linear burning rate, their validation by experiments is still very poor.

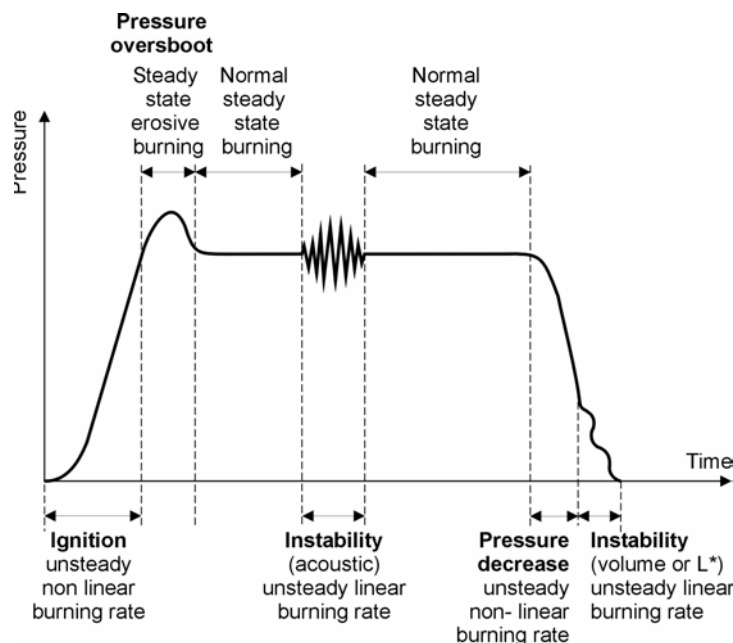The figure 4 summarizes the occurrence of the different burning rate regimes.



**Figure 4: The Different Operation Regimes.**

## 2.2    Grain Design

To achieve a better motor performance, an obvious objective is to integrate the maximum of propellant in a given case volume. The volumetric loading fraction can exceed 0.92 for a launcher upper stage. The thrust program should also be adapted to the motor mission: for the first stage of a space launcher, the thrust should be high at take-off then be reduced during the transonic flight and then can increase again; in the case of two large boosters attached to a central core (Titan 4, Ariane 5 for instance), attention should also be given to the synchronization of both thrust decreases before total extinguishment of the boosters. So a compromise should be found between different requirements. Art of the designer is to find the grain geometry leading to the better global performance, by satisfying a number of constraints at the same time.

Increasing the volumetric loading fraction leads to decrease the central bore and the area ratio at nozzle entrance, then with the direct consequence to increase the Mach number flow in the combustion chamber. This increase can produce erosive burning at the end of perforation and more generally generates differences of static pressure between the motor front end and the motor aft end; as the mechanical properties of a propellant are limited, particular care should be devoted to mechanical grain design to avoid any unexpected crack or dangerous grain deformation. Another consequence, more directly connected to aerodynamics, is that the simplified approach (§ 2.4) is not yet valid or accurate enough. Therefore refinement of flow description inside the combustion chamber is required.

## 3.0    IMPORTANCE AND NECESSITY OF SOPHISTICATED AERODYNAMIC PREDICTION

There are two main domains which need the development of the knowledge in internal aerodynamics: the steady-state operation and the transient unsteady regimes.

## 3.1    Steady-State Operation

Modern SRM design is characterized by a tridimensional geometry, generally associating axisymmetric and star-shaped patterns (for instance, finocyl grain). Grain grooves (French asymmetrical machined grains) or intersegments (segmented grains) generate noticeable pressure variation which cannot be predicted by too crude computation. Another trend is to use composite (filament winding) case, more deformable than a metallic one; the case deformation and the grain deformation should be taken into account in this situation and it is particularly important for the first phase of operation following ignition. So a natural trend is to couple the internal aerodynamics and the case/grain deformation, by taking into account the visco-elastic feature of the grain. Finally it appears that numerical computation can only provide an accurate prediction of the pressure field inside the combustion chamber, especially in the first part of the operation.

Currently, but with the exception of the CSAR program, prediction of steady operation is made by a set of computations at different fixed geometries, which are computed by another code. The principle is the following (fig. 5):

- Aerodynamics at $t$ : aerodynamic computation for a known geometry giving the pressure field on the combustion surface and then the field of burning rate on the combustion surface.

- Geometry at $t + \delta t$ : geometrical computation of the new geometry by using the field of burning rate on the combustion surface at $t$ .

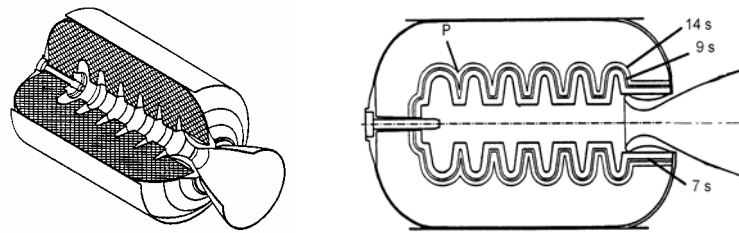- Aerodynamics at $t + \delta t$ : new aerodynamic computation...

**Figure 5: Grain Geometry Evolution.**

A totally coupled computation of aerodynamics and geometry evolution requires use of variable meshes in the combustion chamber and in the grain and is very expensive in terms of computation time. In the classical approach previously mentioned, where accuracy is, *a priori*, of first order, $\delta t$ can be chosen to maintain the computation time in a reasonable range.

It should be also mentioned that the modern codes do not distinguish the flow zones at low velocity and the flow zones at high velocity. The whole flow from the combustion surface to the nozzle exit is described and computed with the same compressible equations and the same numerical methods. This way of computing avoids difficult and unsolved issues of matching between domains (combustion chamber, nozzle).

## 3.2    Unsteady Regimes

The main issues are connected to the ignition phase and to the prediction of the stability (or of the instability level).

If certain characteristic times can be predicted by simple analytical calculations, using an unsteady variant of the global conservation laws, this type of approach is totally insufficient for a total mastery of the ignition phase. In fact, transient ignition phase should be described by taking into account a lot of phenomena: igniter operation, thermal convective and radiative transfer from the igniter combustion products to the inert grain combustion surface, propellant surface temperature increasing and propellant ignition, unsteady propellant combustion, flame propagation. In detail and for realistic igniter, grain and propellants, the complete problem is rather difficult to solve because of the propagation of various waves inside the motor, the difficulty to predict accurately the thermal transfer for igniter two phase combustion products and in the recirculation zones, and of the unsteady combustion. However some modern validated codes (unsteady two phase flow), are able to solve the problem.

More difficult is the prediction of stability or level instability. Instability is a natural phenomenon observed for a long time on all the engines, from the pressure recording: instead of being stable (with a little random component due to the noise), pressure exhibits an oscillation well organized around a frequency, or possibly around several frequencies to form a non-harmonic unsteady signal. That is the appearance of an instability. This phenomenon, called combustion instability or operation instability, is rather frequent and a lot of solid rocket motors are flying with a low level of instability during certain phases of their operation; but an instability can become very dangerous if its level increases: in this case the mean burning rate tends to be erratic, the pressure uncontrolled and the thermal insulation consumption drastically augmented.

Different classes of instability have been determined fifty years ago. The simplest one to understand is the volume instability or $L^*$ instability; it is clearly a combustion instability, i.e. that the propellant pressure coupling is needed to drive the instability. The $L^*$ instability occurs generally at low pressure and low frequency and is not dangerous. The most critical and scientifically interesting instabilities are acoustic:

that means that the unsteady pressure distribution inside the combustion has a certain relationship with the unsteady pressure distribution corresponding to a pure acoustic mode in the cavity which is defined by the combustion surface and a closure in the nozzle entrance plan. This type of instability is known as a combustion instability because propellant pressure response is conditioning stability in the classical analytical approach (acoustic balance). It is not the case in reality for the first longitudinal modes in the larger booster, the propellant pressure response seeming not to be the primary driving phenomenon; the term of operation instability is then, maybe, more appropriate. Stability should be assessed at each operation time, that is to say for different grain geometries (fig. 5).

Prediction of steady-state operation and unsteady regimes clearly requires a detailed description of the flow inside the combustion chamber. Evolution of the computation method (and of the computer capacities) has allowed a substantial progress during the last thirty years, even if this evolution does not yet solve all the problems.

# 4.0 APPROACH OF INTERNAL AERODYNAMICS IN SOLID ROCKET PROPULSION BY COMPUTATION

Approach of steady state operation by using the global conservation laws is under the dependency of different assumptions and finds rapidly its limits, either because of the difficulty to find explicit analytical solutions (case of ignition for instance) or because of the physics which needs a more local and refined flow description. Concerning this second point, an academic example can be mentioned, the one concerning the nozzleless motor (fig. 6). For a sufficient length to perforation diameter ratio and a rather high propellant burning rate, flow inside the perforation is naturally chocked; the explanation is the formation of a multiple fluid nozzles in the flow due to the lateral injection.
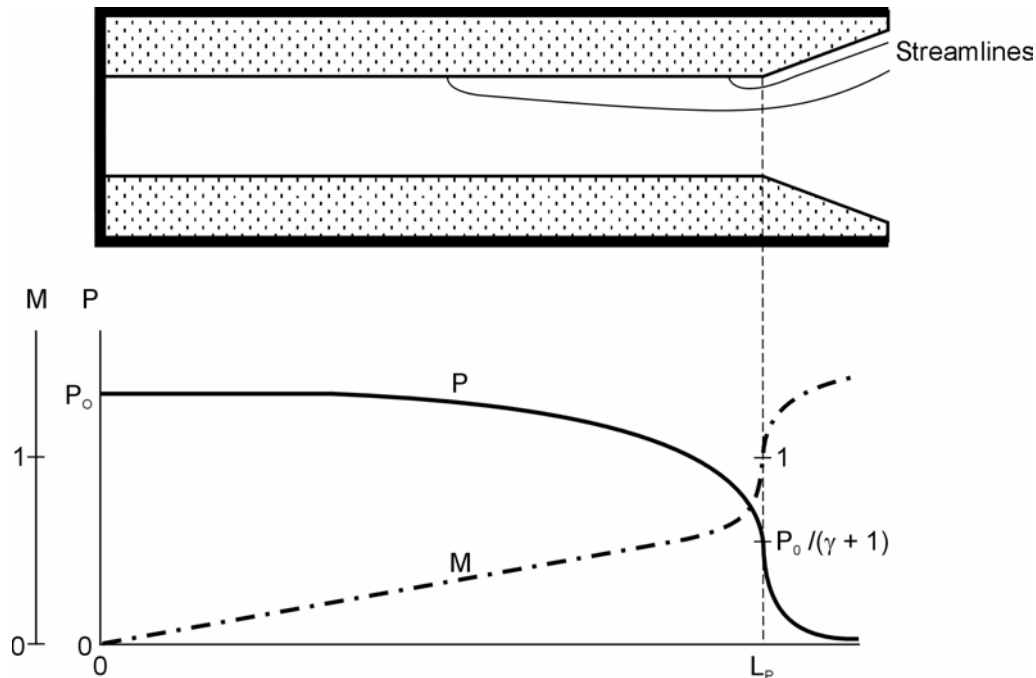


**Figure 6: The Nozzleless SRM.**

By using some simplifications (constant burning rate and constant diameter along the combustion surface, ideal gas), it is possible to determine the pressure at the front end (here $p_o$) and the distribution of

pressure and Mach number (1D description) in the perforation. It has been demonstrated that $p_o$ can be calculated by the relation:

$$\frac{p_o}{\rho_p r_b(p_o)C*} = 2\left(\frac{2}{\gamma+1}\right)^{\frac{1}{\gamma-1}} \frac{2L}{R}$$

or, under another form:

$$K_p(p_o) = 2\left(\frac{2}{\gamma+1}\right)^{\frac{1}{\gamma-1}} K_G,$$

where $K_G$ is the ratio of the combustion area to the passage area $A_p$. The relation obtained is very similar to those previously given for a conventional motor with a large nozzle entrance ratio, except for the factor $2(2/(\gamma+1))^{\frac{1}{\gamma-1}}$. This difference is the direct consequence of the organization of the flow, the Mach number of which being 1 at the end of the cylindrical perforation. This example proves that aerodynamics can be essential for pressure prediction. There is total continuity between the conventional rocket operation and the nozzleless motor operation; it is possible to propose a generalization of the relation between $K_p(p_o)$ and $K_G$ (always with some simplifications): $K_p(p_o) = kK_G$, where $k$ can be calculated as the solution of a transcendental equation: $k(K_2, \gamma)$ where: $K_2 = A_p / A_c$

$$k \to 1 \text{ if } K_2 \to \infty$$

$$k = 2(2/(\gamma+1))^{1/(\gamma-1)} \text{ if } K_2 = 1$$

Real computation of the steady flow began at the beginning of the 70's for a one dimensional flow description, it was extended to a 2D flow description in the 80's, then to a 3D flow description in the 90's. The first computation codes have described the combustion products as an ideal gas (one-phase aerodynamics); extensions have been made but not always integrated in the code to take into account the actual thermodynamics (thermodynamic equilibrium or frozen composition) and to the two-phase flow aspects (combustion of aluminium droplets, alumina droplets). Use of the most advanced codes is still facing three main difficulties:

- Long computation time.

- Lack of accuracy of certain input data, especially for the condensed phases.

- Uncertainties on some phenomena: flow turbulence, interactions between droplets for instance.

Concerning the transient phenomena (ignition phase), some derivatives have been made from the previous codes without too many difficulties for the flow phenomena. The main issues have been rather connected to the heat transfer and the propagation of the flame on the combustion surface. However, some validations have been made by using a special small scale model with a dedicated instrumentation and the results are rather promising. Besides, the physical time to simulate is rather small and computation time affordable. Coupling between aerodynamics and grain/case deformation should be improved.

Prediction of the level of instability requires in essence a non-linear approach. Extension of the acoustic balance and coupling of modes, by the averaging method, constitutes a first possibility and presents the advantage of a clear physical understanding. In parallel, a numerical approach can be used and certain improvements have been made for the past ten years; some of them will be presented in lectures by F. Vuillot, G. Casalis and J.F. Guery. Without claiming to be the ideal solution, computation allows a

certain level of prediction in certain situations. The most current computations are two-dimensional, when that is allowed by the grain geometry, even if there is no intrinsic difficulty for 3D computations, but only some problems of computation time.

The main difficulties to face for instability level prediction are the same as those mentioned for the steady-state computation: lack of accuracy of certain input data (condensed phases…), uncertainties regarding the description of fundamental phenomena (flow turbulence, interaction between droplets…) but physics is here more complicated since unsteady. In fact, the situation can be summarized as follows:

   •   Rather good level of prediction at low scale for a non metallized propellant and sometimes simplified geometries, when the unsteady phenomena driving phenomena are well identified.

   •   Relative uncertainties at large scale, for a metallized propellant and complicated geometries; large sensitivity to input data.

## 5.0   PHYSICAL OBSTACLES

If computation is more and more used by industry, some physical obstacles remain to be overcome, in order to achieve a better prediction on actual motors and for all the regimes. Unsteady flow description can be considered today as the general needed approach, the steady state operation being viewed as the limit of an unsteady operation. The numerical methods should be adapted to correctly deal with the propagation of the different waves (acoustic, entropic, vorticity). In some specific situations, it has been proved that vortex shedding plays a central role in combustion instability but in other situations, it appears that other phenomena will prevail. Instability of tactical motors, especially for tangential modes, certainly gives more importance to pressure coupling and acoustic streaming.

The basic phenomena, whose description should be greatly improved, can be classified in three categories:

   •   Flow phenomena: turbulence in one-phase flow and two-phase flow. Turbulence generated by combustion is very poorly known. Two-phase phenomena are suspected to have an influence in some conditions (distributed aluminium combustion, wave damping by alumina droplets) but the data remains uncertain.

   •   Propellant combustion: unsteady combustion of the propellant remains a challenge, especially for a metallized propellant; for this type of propellant, it is not clear, for instance, if the usual definition of the linear response is totally valid.

   •   Fluid-"structure" coupling: structure is understood here as the assembly of all the solid parts of the motor: restrictors, grain, case, nozzle. Participation of restrictor vibration has been suspected for instability driving in some large segmented SRMs. But the problem is more general and invites to couple aerodynamics and solid mechanics.

The well known difficulty to improve the knowledge of this different phenomena is linked to the nearly impossibility to carry out detailed measurements inside an actual motor, even at a low scale and for a non-metallized propellant. The phenomena should be isolated and studied on skilled set-ups, for which the main issue remains to be their representativity.

## 6.0   PROSPECTS

This introduction has attempted to throw a bridge between the apparent simplicity of the rocket motors and the difficulty to perfectly master its operation; internal aerodynamics forms the pile of this bridge and cannot be bypassed.

Development of a large SRM needs a very large investment. For instance, development of the Ariane 5 has required around 2ε billion (including the propellant factory and the test bench in Kourou). Each ground test costs around 20ε million. Cost reduction is presently a leitmotiv for the civil and military industry. A general trend is therefore to develop reliable tools to reduce the number of tests during development and qualification. Tools are also needed to explain abnormal operation.

Since 1990, some important national programs have been initiated and have produced new results:

- In France, the ASSM program, with the sponsorship of CNES, under the scientific responsibility of ONERA and with the participation of several CNRS and universities laboratories (and of the VKI), for the Ariane 5 MPS P230 (SRM). Mainly focused on instability level prediction, this program allowed to develop numerical tools, to improve the flow description and… to measure the limits of the available knowledge. A new program is currently being prepared between France and Italy (SPADA program).

- In the USA, among the different known programs, the MURI program and the CSAR program. This last one, funded by the DoE is focusing on very high level computation, is more ambitious and more general than the programme ASSM and has started producing some initial encouraging results.

It is still a long way to solve all the issues regarding SRM aerodynamics. According to the author's opinion, a good balance should be maintained between computational improvement and improvement of the knowledge regarding the basic phenomena.

This short course provides a unique opportunity to bring together the specialists deeply involved in Europe and in the USA in SRM aerodynamics. All the important aspects of aerodynamics and SRM operation mentioned in this introduction are covered and will give to the attendees an updated state of the art.

## 7.0   SELECTED REFERENCES

### Fundamentals

[1]   *The Pocket Rocket Reader*, J.M. Vogel, United Technologies/Chemical Systems, 1980.

[2]   *Fundamental Aspects of Solid Propellant Rockets*, AGARDograph 116, Oct. 1969.

[3]   *Progress in Astronautics and Aeronautics*, Vol. 90, AIAA, 1984 (*Experimental Observations of Combustion Instability*, E.W. Price, Ch. 13).

### Instabilities

[4]   *Publications* of Pr. F.E.C. Culick.

[5]   *Publications* of Pr. V. Yang.

[6]   *Combustion Instability in Solid Propellant Rocket Motors*, J. Swithenbank, Report n° HIC 100, University of Sheffield, Oct. 1969.

[7]   *Combustion Instability in Solid Propellant Rockets*, E.W. Price, G.A. Flandro, AFOSR TR 89-0460, March 21, 1989.

[8]   *Combustion Instabilities*, AGARD LS n° 180, Sept. 1991.

[9] *Solid Rocket Motor Combustion Instability Workshop*, AIAA/SAE/ASME/ASEE, 31st Joint Propulsion Conference and Exhibit, San Diego, CA, July 12, 1995.

## ASSM/POP Program

[10] *Fonctionnement des moteurs à propergol solide segmentés pour lanceurs spatiaux*, Colloque CNES/ONERA, Châtillon, FR, Dec. 8-9, 1992.

[11] *Fonctionnement des moteurs à propergol solide segmentés pour lanceurs spatiaux,* Journées R et T CNES, Paris, FR, June 26-28, 1995.

[12] *Colloque écoulements propulsifs dans les systèmes de transport spatial*, Bordeaux, FR, Sept. 11-15, 1995 (*Some Basic Problems and Control of Combustion Instabilities*, F.E.C. Culick).

[13] *Ecoulements internes en propulsion solide*, 3ème Colloque R et T CNES, Poitiers, FR, March 25-27, 1998.

[14] *Réunion de synthèse ASSM-POP*, CNES Evry, FR, March 21, 2001.
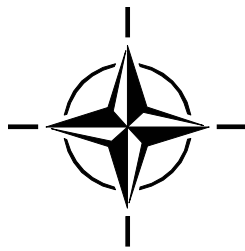
# Flow-Structural Interaction in Solid Rocket Motors

**John W. Murdock and William A. Johnston**
Distinguished Engineer and Senior Project Engineer
The Aerospace Corporation
P. O. Box 92957 – M4-964
Los Angeles, CA 90009-2957
USA

## SUMMARY

*This article reviews and summarizes recent work on flow-structural interaction in solid motors. This interaction is important because it can lead to rocket motor failure. In the first part of the document, an idealized model of the failure mechanism is developed to illustrate in simple terms how such an event can occur. In the second part of this article recently published numerical modeling work, which models flow-structural interactions in some detail, is summarized. The static test failure of the Titan solid rocket motor upgrade (SRMU) that occurred on 1 April 1991 demonstrated the importance of flow-structural modeling in the design of large solid rocket motors.*

## INTRODUCTION

The first discussion, known to us, of the possibility that an interaction between the propellant grain and the motor flow field could cause motor failure is in Wimpress (1950). He shows various curves with a critical value of the elastic modulus, E, below which, "there is no finite equilibrium pressure…and the motor blows up."

Bartley and Mills (1959) also discuss grain instability in tubular, internal solid motors. Their model also shows that for the grain geometry considered, there is a critical propellant modulus, below which the motor fails.

Glick, Cavney, and Thurman (1967) modeled a bore constriction failure of the Castor II motor that occurred at a propellant slot. They point out that the stability of the propellant can be significantly enhanced if the propellant downstream of the slot has a radius. They state that H. W. Ritchey first suggested the use of such a radius and they term it a Ritchey radius.

There was a flurry of activity in the area of flow-structural interaction subsequent to the Titan SRMU test failure. The initial efforts were aimed at understanding the failure and analyzing the new Titan design to make sure the problem was fixed (Johnston and Murdock [1995], Chang, Patel, and Yang [1994], Cosstephens [1995], Johnson and Lauterbach [1992]). This work was followed by analyses of other existing or new motors, to make sure that they were designed with an adequate safety margin (Johnston [1996], Wang, Yang, Than, and Ndefo [1994]). This work is reviewed in some detail in the latter part of this document.

An important goal of this article is to assure that the possibility of flow-structural interaction leading to a motor failure is not forgotten or overlooked – as it seems to have been in the period between 1967 and 1991.

## A SIMPLE PHYSICAL MODEL OF GRAIN INSTABILITY

We are interested in the interaction of the propellant grain and the motor flow that can produce a catastrophic motor failure. How can such a thing occur? Examination of known failures shows that they have been initiated by events occurring either at transverse slots in the grain or at the location of joints of multi-segment motors.

The flow past one such slot is shown in Fig. 1. The flow impinges on the upstream-facing propellant and raises the pressure on that face. The flow also expands around the corner of the grain and reduces the pressure on the interior of the bore. The combination of these two forces causes the flow area to constrict, as shown in Fig. 1. If the elastic modulus of the propellant grain is too low or the local bore flow rate is too high, then unconstrained deflection of the grain can occur. This will fracture the propellant grain and/or block the motor bore. Either of these events will be catastrophic for the motor.
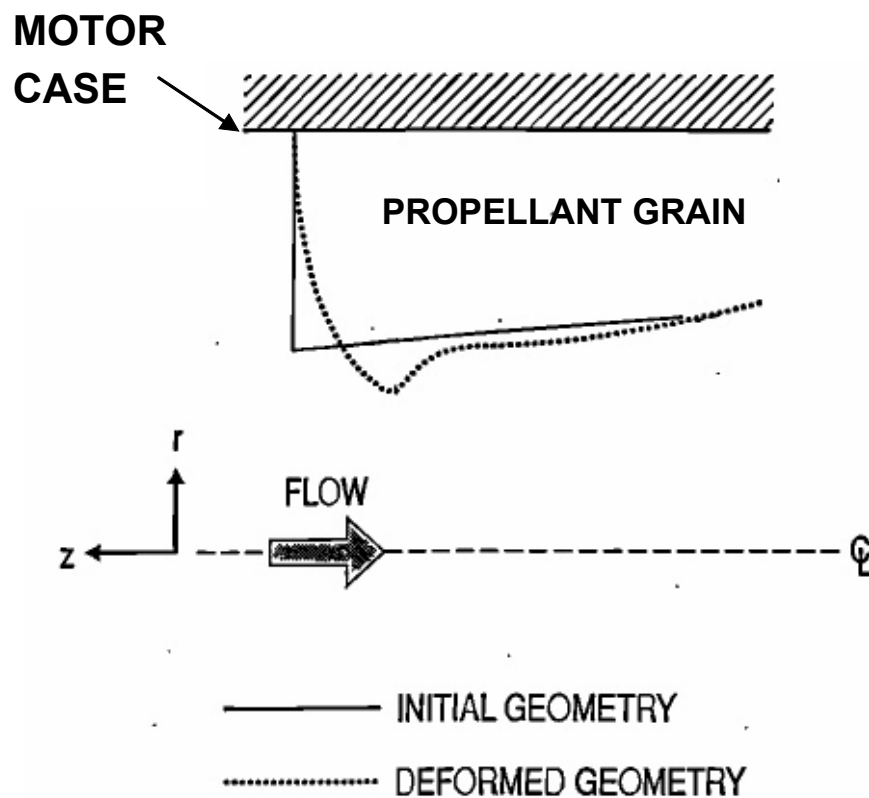


**Figure 1: Schematic of Failure Mechanism.**

In order to give a simple physical picture of the flow-structural instability that can lead to grain and motor failure, a very simple, analytical model is constructed to illustrate how such a failure occurs. With this in mind, the emphasis will be on simplicity rather than fidelity with the real physical situation.

In accord with this approach, we model the flow through the constriction in Fig. 1 as a choked, perfect gas flow. This gives the simple expression

$$W = KPA \qquad (1)$$

where $W$ is the mass flow rate past the bore constriction, $P$ is the stagnation pressure upstream of the constriction, $A$ is the area of the bore constriction, and $K$ is a constant that is easily obtained from gas-dynamic theory. [See, for example, Shapiro (1953).] We note here that a well-designed motor bore would never have locally sonic flow, so that eq. (1) is an approximation. The main justification for its use is the simplicity; eq. (1) could be replaced with the orifice equation for subsonic-flow, but the subsequent analytical solutions would have to be replaced with less obvious numerical solutions. Also, observe that if a bore-constriction failure does occur, the flow is likely to choke during that process.

It is convenient to use a dimensionless version of eq. (1) and normalize the mass flow rate and pressure with their nominal values that would be obtained with an undeformed grain area $A_0$.

$$w = \frac{W}{W_0} \tag{2}$$

$$p = \frac{P}{P_0} \tag{3}$$

$$a = \frac{A}{A_0} \tag{4}$$

With this normalization, eq. (1) becomes

$$w = pa \tag{5}$$

and the constant in eq. (1) is related to the normalization constants by

$$K = \frac{W_0}{P_0 A_0} \tag{6}$$

The second half of the model relates the bore area to the pressure. In keeping with maximum simplicity, a linear relation between the area and pressure is used. (Letting the bore radius decrease linearly with pressure results in a somewhat more complicated mathematical model with some improvements to the physical model. Predictions made with both models are compared with Titan SRMU data in the following section.)

$$A = A_0 - CP \tag{7}$$

In eq. (7), $C$ is a constant of proportionality that varies as the reciprocal of the elastic modulus of the propellant.

Putting eq. (7) in dimensionless form, gives the result

$$a = 1 - \left( \frac{CP_0}{A_0} \right) p = 1 - cp \tag{8}$$

where the dimensionless version of the constant $C$ is implicitly defined by eq. (8).

Equations (5) and (8) can be combined and either the pressure or the bore area eliminated. Elimination of the area, results in a quadratic equation with solutions

$$p = \frac{1 \pm \sqrt{1 - 4cw}}{2c}$$

(9)

Equation (9) has real solutions only for

$$w \leq \frac{1}{4c}$$

(10)

The solutions to eq. (9) are plotted in Fig. 2 as a function of the reciprocal stiffness parameter of the propellant, $c$. The dimensionless mass flow rate produced by the propellant has been taken to be constant, with a value of unity; this approximation implies that the propellant grain is a flow source. The flow from the propellant grain is actually a weak function of pressure – so this is a reasonable approximation.
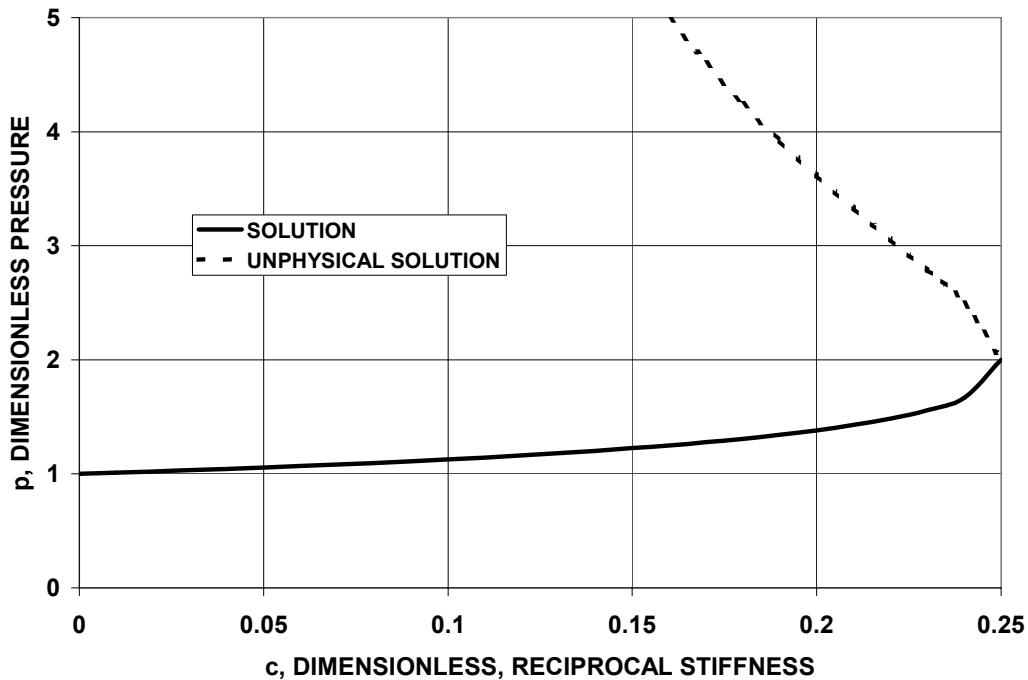


**Figure 2: Model Problem with** $w = 1$.

The two solutions to eq. (9) are shown in Fig. 2. The lower locus of solutions has positive slope and can occur physically; the solutions on the upper curve are physically unrealizable. (If one were somehow able to start out on the upper curve, the flow state would immediately jump to the other, lower-energy curve.) The two solutions are connected at the point at which the product of $w$ and $c$ is a maximum (or in the case of Fig. 2, maximum $c$). This critical value occurs when the equality in eq. (10) is satisfied. The models of Wimpress (1950) and Bartley and Mills (1959) also show double-valued solution curves, only one of which is physically realizable. As both these articles point out, attempts to operate beyond the critical point will cause the motor to blow up.

In summary, the very simple model developed here shows that at low flow rates or high propellant modulus, there are two solutions to the model equations. Only one of these solutions has physical significance. These two solutions join and terminate at a critical flow rate given in dimensionless terms by the equality in eq. (10) and in dimensional terms by

$$W_{crit} = \frac{KA_0^2}{4C}$$

(11)

The motor has no operating point for flows exceeding the critical one defined by eq. (11). This model illustrates how the grain and the flow can couple and result in an unstable motor. Furthermore, the physics of this simple model is the same as in the large-scale numerical models used previously to study this phenomenon and discussed subsequently.

## APPLICATION OF SIMPLE MODEL TO TITAN SRMU

It is interesting to apply the simple model developed in the previous section to the Titan failure to assess its validity, since the critical flow rate only depends on three parameters.

The first parameter in eq. (11) is simply the constant relating pressure, flow rate, and area for choked flow. This constant can easily be obtained from the known motor pressure, motor flow rate, and nozzle flow area. Table 1 gives the relevant Titan SRMU constants and the value of $K$ computed from the values in the first three lines of the table.

**Table 1: Selected Titan SRMU Parameters**

| | | |
|---|---|---|
| Motor mass flow rate, Mg/s | $W*$ | 18.8 |
| Motor chamber pressure, MPa | $P_c$ | 7.45 |
| Nozzle throat area, m$^2$ | $A*$ | 0.535 |
| Choked flow constant, ms/m | $K$ | 4.72 |
| Specific heat ratio | $\gamma$ | 1.13 |
| Sonic pressure ratio | $P*/P_c$ | 0.578 |
| Mass flow from forward two segments, Mg/s | $W_{12}$ | 13.2 |
| Propellant elastic modulus (at failure), MPa | $E$ | 8.2 |

The other two parameters can be obtained from Fig. 3, which is obtained from Johnston and Murdock (1995). (This paper will be discussed in more detail, subsequently. For now we are only concerned with Fig. 3.)
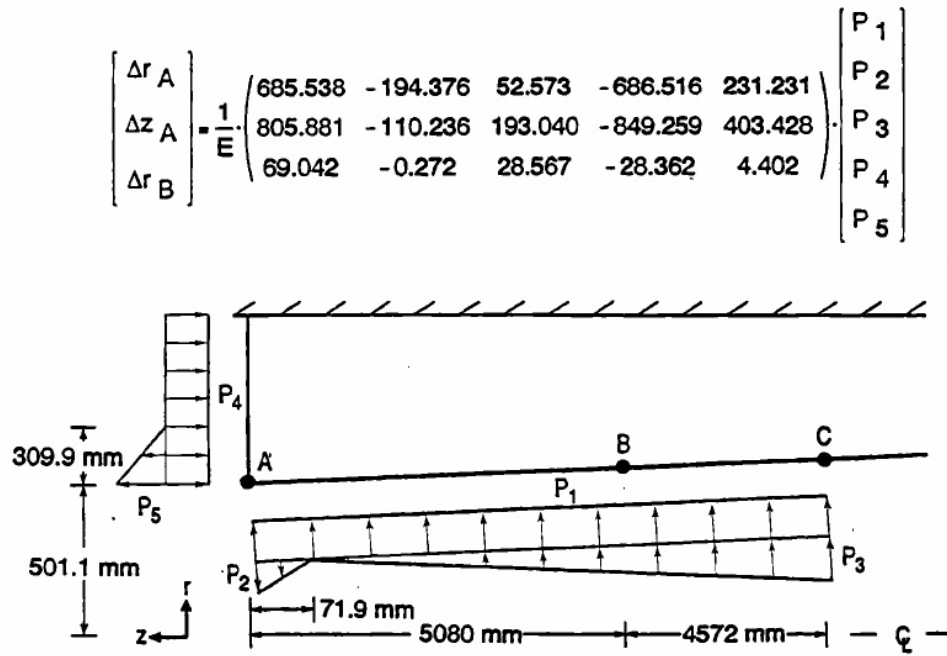
$$\begin{bmatrix} \Delta r_A \\ \Delta z_A \\ \Delta r_B \end{bmatrix} = \frac{1}{E} \cdot \begin{pmatrix} 685.538 & -194.376 & 52.573 & -686.516 & 231.231 \\ 805.881 & -110.236 & 193.040 & -849.259 & 403.428 \\ 69.042 & -0.272 & 28.567 & -28.362 & 4.402 \end{pmatrix} \cdot \begin{bmatrix} P_1 \\ P_2 \\ P_3 \\ P_4 \\ P_5 \end{bmatrix}$$



**Figure 3: Structural Influence Coefficients for the Aft Propellant Segment, Titan SRMU.**

The figure shows the initial diameter of the grain at point A. This is the forward corner of the aft propellant segment and is the known location of the grain collapse. The radius of 501 mm gives a value of $A_0$ of 0.789 m².

The matrix operator in Fig. 3 also shows the structural influence coefficients of the aft propellant section. These coefficients were obtained from a series of grain structural analyses carried out using the ABAQUS (1989) code. The grain deformations can be obtained by multiplying the coefficient matrix by the indicated pressure loads. The quantity $E$ is the propellant modulus (MPa); $P_1$, $P_2$, $P_3$, $P_4$, and $P_5$ are the values of the depicted pressure loads (MPa); $\Delta r_A$, $\Delta z_A$, and $\Delta r_B$ are the radial and axial displacements (mm) of points $A$, $B$, which are at the corner and midpoint of the segment.

The first row of the matrix in Fig. 3 can be used to compute the rate of change in bore radius with pressure. This can be related to the constant $C$ in the simple model by differentiating eq. (7)

$$C = -\frac{dA}{dP} = -2\pi r \frac{dr}{dP}$$

(12)

It is now necessary to relate the single, stagnation pressure in the model to the five pressure loads in Fig. 3. Only the pressures acting at the point $A$ are of interest, so $P_3$ which does not act at that location is neglected. Two distributed pressure forces act on the left-hand face in Fig. 3, $P_4$ and $P_5$. The algebraic sum of these ($P_4 - P_5$ according to the sign convention of Fig. 3) is equated to the variable $P$ used in the present model.

We arbitrarily partition half the pressure to each component. These assumptions give

$$P_4 = P/2 \tag{13}$$

$$P_5 = -P/2 \tag{14}$$

It assumed that the radial pressure acting on point $A$ is the sonic throat pressure, which according to Table 1 is 0.578 times the stagnation pressure. In a similar manner we assume that the algebraic sum of $P_1$ and $P_2$ equals the sonic pressure and the partitioning is again equal. This gives

$$P_1 = 0.578P/2 \tag{15}$$

$$P_2 = -0.578P/2 \tag{16}$$

The matrix equation in Fig. 3 can now be used to determine $dr/dP$, using the approximate propellant modulus at failure, taken from Johnston and Murdock (1995) and replicated in Table 1. Combining this value with eqs. (12) and (11) gives

$$W_{crit} = 9.33 \, \text{Mg/s} \tag{17}$$

Comparing this with the flow from the two forward segments, given in Table 1, we see that the simple prediction indicates that a 30 percent lower motor flow than the actual one would have caused a grain with this modulus to collapse. (The model and the present discussion neglect the weak variation of motor flow rate with pressure.)

$$\frac{W_{crit}}{W_{12}} = 0.71 \tag{18}$$

An alternative interpretation is that at the motor flow rate, even if the modulus had been 30 percent higher, the motor would still have failed. Stated still another way, the simple model is conservative by 30 percent compared to the large-scale numerical model.

It was briefly mentioned previously that the simple model could be improved by replacing the linear pressure-area relation, eq. (7), with a linear pressure-radius model. Such a model may be written as

$$R = R_0 - C_R P \tag{19}$$

Combining this equation, rather than eq. (7), with eq. (1) gives a cubic rather than a quadratic equation. Analytical solutions are still possible, but the algebra is more complicated. Skipping the details, an equation for the critical mass flow rate, similar to eq. (11) can be obtained in this case. It is

$$W_{crit} = \frac{4\pi K R_0^3}{27 C_R} \tag{20}$$

Substitution of numerical values into eq. (20), gives

$$W_{crit} = 11.1 \, \text{Mg/s} \tag{17}$$

This value is 16 percent lower than the flow from the two forward segments. Thus, this model is conservative by about half as much as the linear pressure-area model.

To summarize, a quite simple model of the grain collapse has been developed to illustrate the physics of this interaction. This model has been applied to the Titan SRMU failure and found to produce reasonable and conservative predictions of the failure. However, we have used in this model the numerically generated influence coefficients for the grain displacement. Thus, the actual application of the model used a combination of fluid mechanical approximations and numerical stress analysis. Even so, this model is significantly simpler than the coupled, unsteady flow-structural interaction calculations discussed subsequently in this document.

It is surprising that this model works as well as it does. As noted, it was developed primarily for illustrative purposes, rather than predictive purposes. Also it has only been compared against a single data point. Any application of this model to new designs should keep these limitations in mind.

## COMPLETE MOTOR MODEL

During the ignition transient period of solid rocket motor (SRM) operation, several complex, time-dependent coupled processes occur. In a large segmented SRM, the hot gas from the igniter travels down the bore and heats the propellant surface to ignition; once ignition occurs, the propellant surface becomes a site of gas generation. Since the convective and radiative heat transfer that lead to propellant ignition are dependent on the developing flowfield, and since the development of the internal flowfield is dependent on the rate at which the flame spreads down the motor, the time-dependent flow and surface temperature are coupled. Furthermore, the surface pressure load on the propellant grain causes deformation, which in turn alters the flowfield. This results in additional coupling of the internal flowfield with the propellant geometry. This flow-structural coupling is particularly important in segmented SRMs, in which the propellant segments have forward corners (see Fig. 1) that jut out into the bore at intersegment slots (e.g., Titan 7 segment SRM, Space Shuttle SRM, Titan SRMU, Ariane 5 MPS). When axial flow impinges on a protruding corner, the surface pressure deforms the corner out into the bore and further constricts the flow, which then raises the upstream pressure and exacerbates the pressure loading on the corner. If this feedback loop proves to be unstable, then the corner will continue to deform and the motor to pressurize, until either the grain and/or the motor case fails.

Johnston and Murdock (1995) developed the first, multidimensional, coupled numerical procedure for analysis of the flow-structural interaction. Their computer code simultaneously modeled the developing flowfield and the associated propellant grain deformation during the ignition transient period of SRM operation. It is during this initial period of motor operation, when the propellant surface has receded only a little through burning and erosion, that the pressure differential across propellant segment corners typically is at a maximum and the bore radius at a minimum. It is at this time that the interaction between the grain and the flowfield, and the associated danger of grain and motor case failure, is greatest. The following elements were coupled together to create a code, designed to provide a model of the time-dependent, fluid-solid interaction inside an SRM:

1) An ignition transient flow code (Johnston [1991]), which provides a detailed picture of the time-dependent flowfield and flame spreading inside the motor. The ignition transient flow code is itself created by coupling together an unsteady internal- flow code (Ton, Wang, and Widhopf [1990]) with an unsteady heat conduction solution for the propellant surface temperature.

2) A set of structural influence coefficients, that allows the major features of the grain deformation that result from a given surface pressure distribution to be calculated (Patel and Yang [1991]).

3) A grid-generation code, which generates a grid mesh for the internal-flow passages, based on the deformed shape of the propellant grain. This grid mesh then is used in the ignition transient flow code.

These three elements are needed for any flow-structural interaction code. Further details of these three elements as assembled by Johnston and Murdock (1995) are given in the remainder of this section.

## Ignition Transient Flow Solution

Johnston (1991) developed the numerical calculation procedure for treating the ignition transient flowfield. The ignition transient flow solution is a composite calculation. It combines an unsteady, axisymmetric solution of the equations of inviscid fluid motion with semi-empirical models for the convective and radiative heat transfer to the propellant surface during the run-up to ignition. The inviscid, single-phase, single-component flow solution is obtained from a time-marching, finite-volume numerical solution of the Euler equations. This numerical solution, which is spatially second-order accurate and employs the total variation diminishing (TVD) methodology of Harten (1983), is described by Wang and Widhopf (1989) and has been implemented for segmented SRMs by Ton, Wang, and Widhopf (1990). An unsteady, one-dimensional, heat conduction solution for the propellant grain is coupled to this flow solution in order to calculate the propellant surface temperature. Together with a surface temperature ignition criterion, this determines the ignition delay and flame-spreading rate.

## Grain Shape Calculation

In the Johnston and Murdock (1995) approach, the grain deformation component in the flow-structural interactive calculation procedure is employed periodically at constant intervals throughout the time-marching process. An interval of 100 time steps between geometry updates was found by experience to provide sufficient time accuracy and to be economically feasible. Since the typical flow solution time step was limited by numerical stability to the order of $10^{-5}$ s, it follows that the grain shape was recalculated about every millisecond.

The grain deformation calculation itself consists of multiplying (for each propellant segment under consideration) a pressure loads vector by a structural influence coefficient matrix to get the resultant displacements at a few key points, which define the shape of the grain. This procedure was illustrated for the aft segment of the SRMU in Fig. 3 and the details of its implementation were discussed in a previous section.

Note that although the coefficient matrices used therein were relatively small, there is no fundamental limitation on size.

## Grid Geometry

The final element needed in the flow-structural interaction calculation is a grid generation package. Many excellent grid generation codes are available today, so that most of the approximations made in some of the earlier work would not be necessary today.

One exception is the treatment of star grains, which are treated with an axisymmetric model to avoid a full three-dimensional computer code. The propellant in the forward closure of the Titan SRMU has a star-grain cross-section with axial grooves. To account for this three-dimensional feature in the axisymmetric model, the axial grooves were omitted, resulting in an annular propellant cross section. The inner radius of this annulus was set so that the void volume in the actual forward segment and the computational forward segment

were matched. Then the burning rate in the forward closure was adjusted upward to account for the discrepancy in the burning area.

Another consideration is the procedure for mapping the numerical solution for the old grid onto the new grid geometry. Johnston and Murdock (1995) used a grid generation code in which the number of flowfield cells did not change nor did the relative position within the mesh change as that mesh undergoes distortion. As a consequence, when a geometry update was carried out, the shape and position of the cells changed only slightly. For this reason, the cell values of pressure, density, temperature, and velocity during the geometry update process were simply carried over.

Although the prior approach gave satisfactory results, a more rigorous approach is to derive the moving boundary finite difference equations for the flow model, as has been done by Wang (1992), and use these equations when the grid is updated. Wang, Yang, Than, and Ndefo (1994) used this approach when they did flow structural calculation for the Titan 7-segment rocket motor. However, one drawback to this more rigorous approach is the requirement to deform the grid and remesh each time step.

## LARGE MOTOR SOLUTIONS

There were two consequences of the failure of the Titan SRMU. The first was an extensive effort to model and understand the failure, so that a recurrence could be prevented. Subsequent to this, other large motors were analyzed to make sure there was no chance of a grain failure. Some of these analyses were done before the motors were flown, as in the case of the Ariane V, and some were carried out for motors already flying successfully, such as the Titan 7-segment SRM. The results of these efforts are summarized here.

### Titan SRMU Solutions

Johnston and Murdock (1995) carried out several numerical stimulations using the time-dependent, flow-structural interactive procedure described herein in order to simulate the static firing of the Titan SRMU, which occurred on April 1, 1991, at Edwards Air Force Base, California. At about 1.6 s into this static test, the motor case failed due to excessive internal pressure. Chamber pressure measurements obtained just prior to the failure showed the head-end chamber pressure increasing rapidly and the aft-end pressure dropping. This divergence of the head-end and aft-end chamber pressures implies a bore constriction, and strain gauge measurements from various axial locations placed this critical constriction at the aft slot. The probable cause of this bore constriction was judged to be the uncontrolled deformation, or collapse, of the forward corner of the aft propellant segment under the applied pressure load.

Due to the uncertainty in the value of the propellant modulus, and the crucial role that this property plays in the success or failure of the motor, numerical static firing simulations were performed for a range of propellant moduli. Simulations were produced with the modulus represented as a decreasing function of time and with constant modulus. The first type of behavior was intended to model change in effective modulus as the propellant undergoes pressurization. The assumed modulus functions for the four cases considered here are shown in Fig. 4. Also shown in Fig. 4 are the cases in which a grain collapse was or was not predicted.
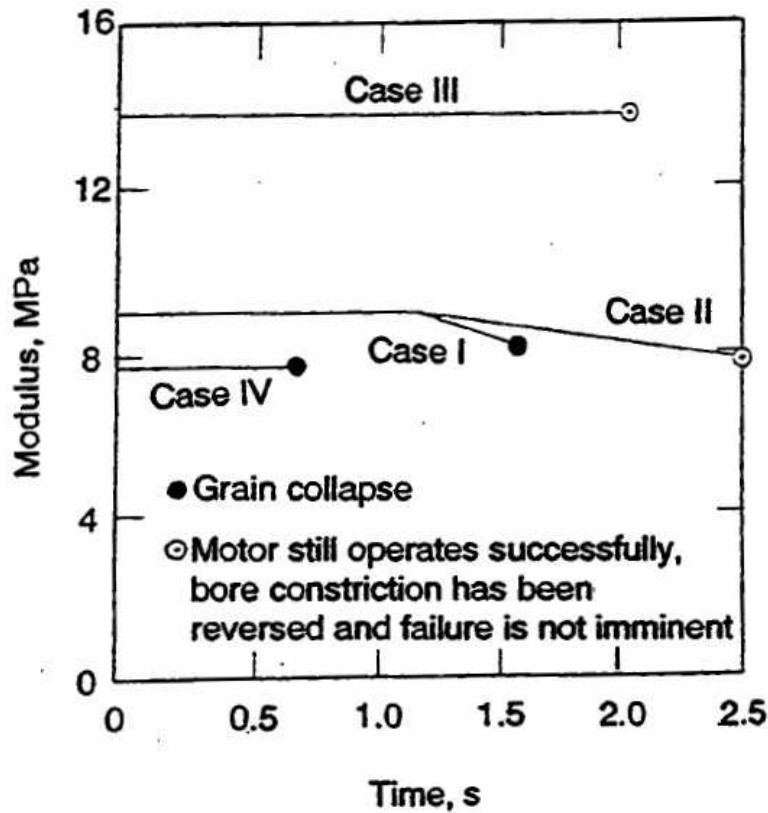
**Figure 4: Modulus Functions for Titan SRMU Simulations.**

The numerical solution using the modulus shown in Fig. 4 as Case I gave best agreement with the static firing data and is the only result shown herein. The modulus in this case is defined by

$$E = 9.0 \; ; \; t \leq 1.1$$

$$E = 9.0 - 1.7(t - 1.1) \; ; \; t > 1.1 \tag{18}$$

where $E$ is in MPa and $t$ in seconds.

The predictions for Case I are shown in Figs. 5 and 6. The computed bore radii at the forward and aft corners of the center and aft propellant segments are given in Fig. 5. Figure 5 shows that the forward corner of the aft segment is deflected slowly inward for about the first 1.5 s. It then very suddenly collapses to essentially zero, when the motor fails. A comparison of the pressure data at the fore and aft ends of the motor with predictions for the same locations is shown in Fig. 6. The agreement is quite good, except that the run up to failure is slower in the actual case than in the prediction. This disagreement is most probably associated with the approximations made in modeling the propellant modulus by eq. (18).
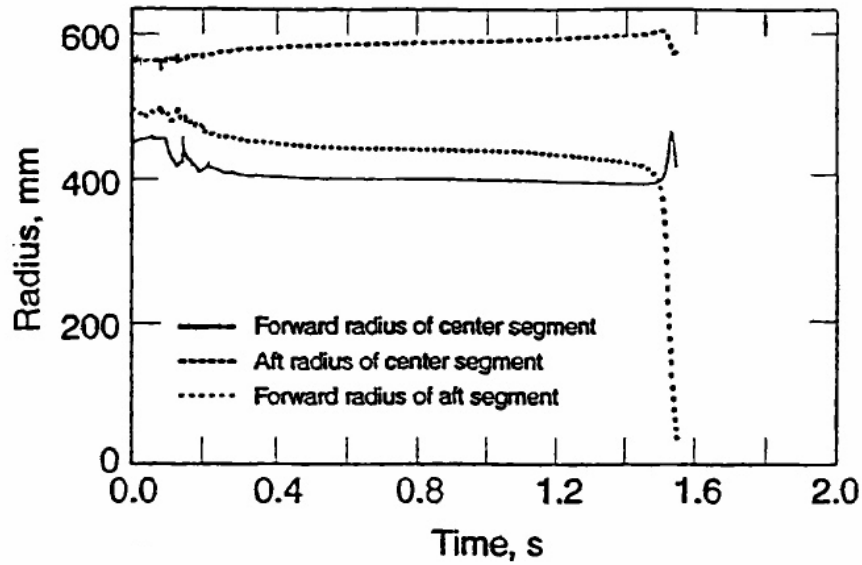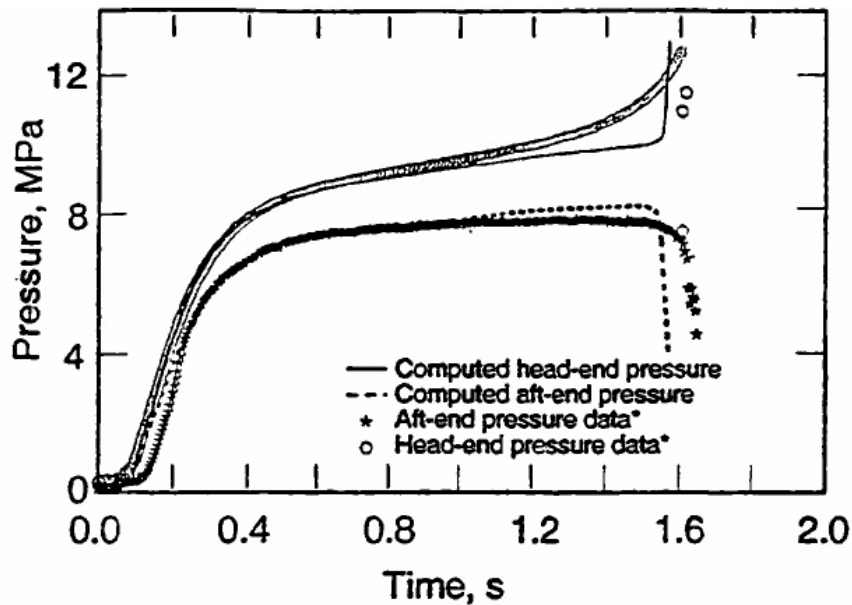
**Figure 5: Computed Bore Radii (Case I), Titan SRMU.**



\* Data supplied by Hercules Corp. to The Aerospace Corp.

**Figure 6: Comparison of Computed (Case I) and Measured
Head- and Aft-End Pressures, Titan SRMU.**

Since a catastrophic bore constriction arises when forward corners of propellant segments jut out into the bore flow, designs that remove or mitigate this feature will produce a better motor design. The obvious way to do this is to chamfer (i.e., either chop off or round) the forward corners of the segments as shown in Fig. 7.
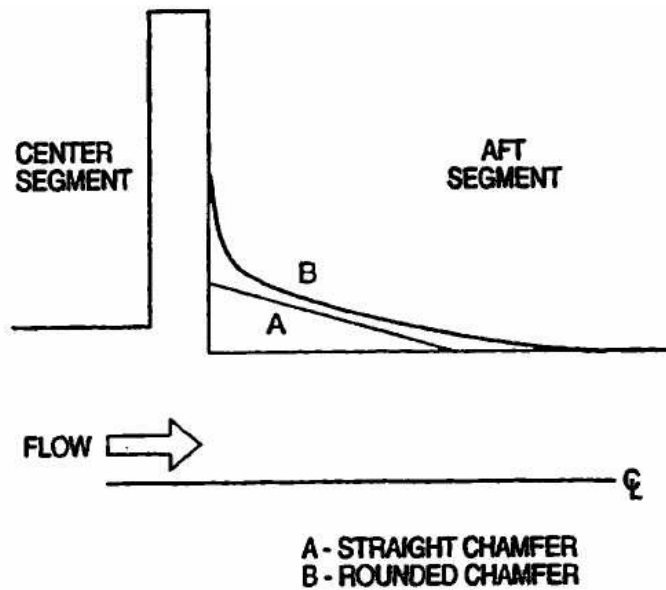
**Figure 7: Chamfering Concepts.**

Johnston and Murdock (1995) carried out a flow-structural simulation for an SRMU with a straight chamfer at the forward corner of the aft segment, but with the center segment unchanged. This chamfer, which removes a triangular cross-sectional piece from the corner, is shown as A in Fig. 7. The modulus was lowered until the motor failed; the results from this numerical solution may be found in Figs. 8 and 9. This failure was interesting, because in this case the catastrophic bore constriction occurred at the forward corner of the center segment (see Fig. 8). The grain deformation of the aft segment was diminished considerably by the chamfer, and the numerical results indicated that a failure originating at the aft segment would not be possible for this motor.
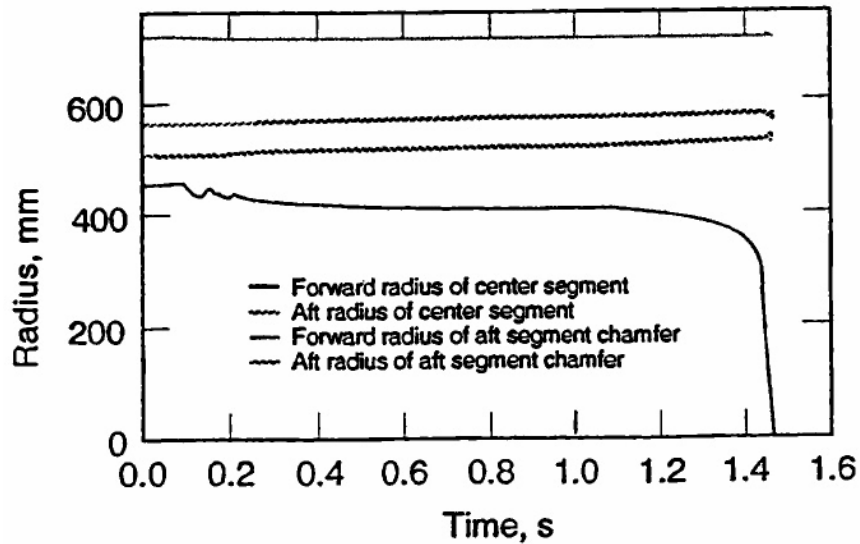


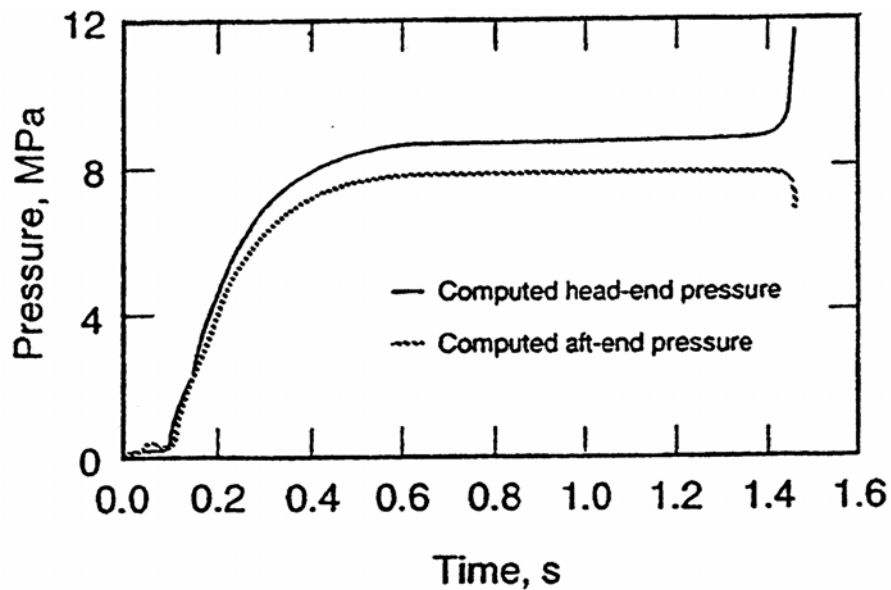**Figure 8: Computed Bore Radii, Titan SRMU, Straight Chamfer on Aft Segment.**

**Figure 9: Computed Head- and Aft-End Pressures, Titan SRMU, Straight Chamfer on Aft Segment.**

The model developed in the first section of this article shows that, because the flow rate is larger there, the preferred failure site for a motor is the forward corner of the aft-most segment. However, the numerical simulations for the Titan SRMU shown in Figs. 8 and 9 show the forward corner of the center segment can also experience failure. These results suggest that a successful design may require chamfering most or all of the segments in a multi-segment motor.

## Ariane 5 MPS Solutions

Johnston (1996) analyzed the Ariane 5 MPS. Despite the fact that this motor has chamfered leading edges of both the center and aft segments, it is susceptible to a grain collapse if the modulus is small enough. (The internal grain geometry and finite difference mesh used to analyze the flow are shown in Fig. 10.)
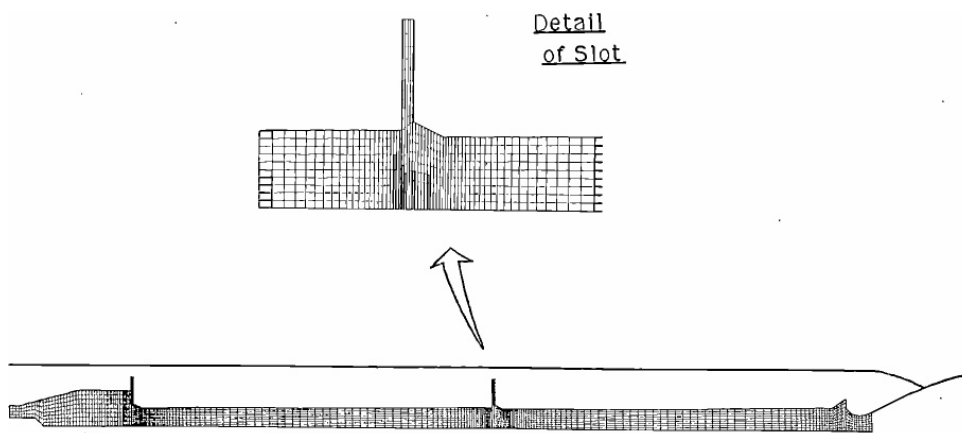


**Figure 10: Initial Geometry and Cell Mesh for the Ariane 5 Internal Flowfield.**

Johnston found that if the modulus exceeded 500 psi (3.4 MPa) then the grain is stable. However, when he analyzed the case with a propellant modulus of 400 psi (2.8 MPa) he found a grain collapse. These results are shown in Figs. 11 and 12. Figure 11 shows the bore radii and the two corners of the chamfered grain, with the collapse occurring after 0.3 s. The grain oscillations at about 0.1 s are deemed to be non-physical and associated with the fact that the propellant mass and damping are neglected. Since these oscillations damp out before the collapse they are not a concern.
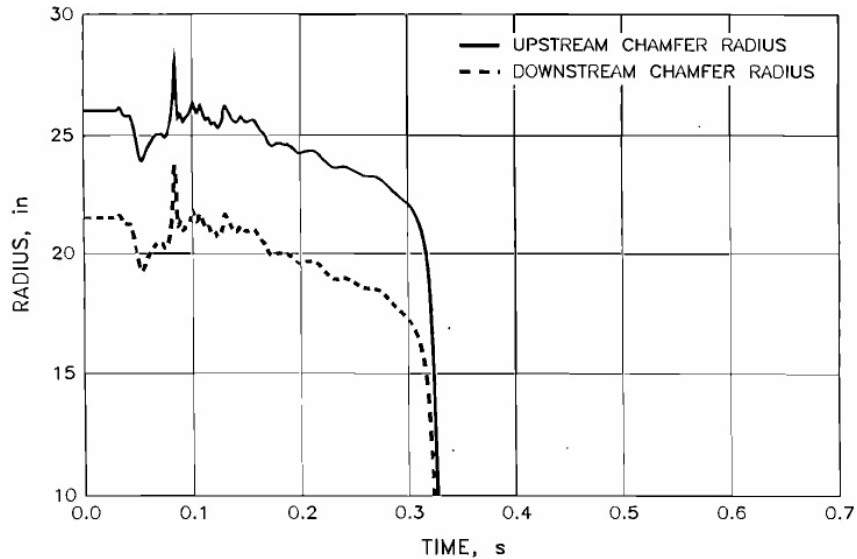


**Figure 11: Computed Bore Radii at the Upstream and Downsteam Corners of the Aft Segment Chamfer, Ariane 5 MPS (E = 2.8 MPa).**

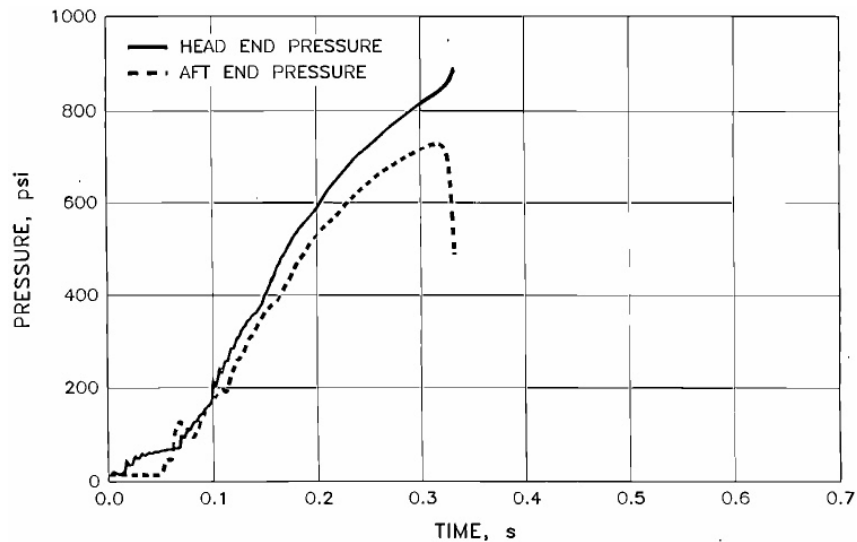The divergence of the head- and aft-end pressures at the time of the collapse is shown in Fig. 12.



**Figure 12: Computed Head- and Aft-End Pressures, Ariane 5 MPS (E = 2.8 MPa).**

## Titan 7-Segment Solutions

Wang, Yang, Than, and Ndefo (1994) carried out a flow-structural analysis for the Titan IV 7-segment motor. As noted previously, these calculations make fewer grid generation approximations than the earlier models but may expend more computer time. It is again found that if the modulus of the propellant is low enough, a grain collapse will occur. For this motor, the authors found that the Titan 7-segment motor will fail at the corner of the $7^{th}$ segment if the modulus is 600 psi (4.1 MPa) or less. As expected the failure occurs at the forward end of the last segment, where the flow rate is largest.

## CONCLUDING REMARKS

Flow-structural interaction of the bore flow and the propellant grain has caused occasional rocket motor failures. The most notable and recent one is the Titan SRMU. With modern computer methods, this failure mechanism can be modeled and steps, such as chamfering, taken to eliminate it if it is found to be possible.

Even though motor failures of this class had occurred prior to the first test of the Titan SRMU and their cause documented, the possibility of a grain collapse on this motor was overlooked. A possible cause of this oversight is that this failure involves two disciplines, fluid and structural mechanics. Hopefully, this article can help to prevent such a lapse in the future.

## REFERENCES

ABAQUS, 1989, *Version 4.8, User's Manual,* Hibbit, Karlson, and Sorensen, Inc., Palo Alto, CA.

Bartley, C.E., and Mills, M.M., 1959, "Solid Propellant Rockets," *Jet Propulsion Engines, Vol. XII, High Speed Aerodynamics and Jet Propulsion,* Ed. O.E. Lancaster, pp. 541-544, Princeton University Press, Princeton.

Chang, I-S., Patel, N.R., and Yang, S., 1994, "Titan IV SRMU Anomaly and Redesign Analyses," AIAA Paper 94-3284.

Cosstephens, S.D., "An Efficient Model for Coupling Solid Rocket Internal Flows with Grain Deformation," AIAA Paper 95-2875.

Glick, R.L., Cavney, L.H., and Thurman, J.L., 1967, "Internal Ballistics of Slotted-Tube, Solid-Propellant Rocket Motors," *Journal of Spacecraft and Rockets*, Vol. 4, No. 4, pp. 525-530.

Harten. A., 1983, "High Resolution Schemes for Hyperbolic Conservation Laws," *Journal of Computational Physics*, Vol. 49, No. 3, pp. 357-393.

Johnson, D.H., and Lauterbach, D.D., 1992, "Coupled Flow-Structural Analysis of the Redesigned Titan IV SRMU," AIAA Paper 92-3825.

Johnston, W.A., 1991, "A Numerical Procedure for the Analysis of the Internal Flow in a Solid Rocket Motor During the Ignition Transient Period," AIAA Paper 91-1655.

Johnston, W.A., 1996, "Flow-Structural Analysis of the Ariane 5 Solid Rocket Motor During Ignition Transient," AIAA Paper 96-0653.

Johnston, W.A., and Murdock, J.W., 1995, "Flow-Structural Interaction Inside a Solid Rocket Motor during Ignition Transient," *Journal of Propulsion and Power*, Vol. 11, No. 5, pp. 998-1005.

Patel, N.R., and Yang, S.H., 1991, Personal Communication, The Aerospace Corp., Los Angeles, CA.

Shapiro, A.H., (1953), *The Dynamics and Thermodynamics of Compressible Fluid Flow,* p. 85, Ronald Press, New York.

Ton, V.T., Wang, J.C.T., and Widhopf, G.F., 1990, "Segmented Solid Rocket Motor Internal Flow Simulations," AIAA Paper 90-0683.

Wang, J.C.T., 1992, "A Full Conservation Finite Volume TVD Algorithm for Initial-Boundary Value Problems with Moving Boundary," *Advances in Computer Methods for Partial Differential Equations – VII,* Ed. V. Vichnevetsky, D. Knight, and G. Richter, pp. 782-787, IMACS, New Brunswick, NJ.

Wang, J.C.T., Yang, S.H., Than, P.T., and Ndefo, E.D., 1994, "Coupled Transient Flowfield and Propellant Deformation Analyses for the Titan IV 7-Segment Solid Rocket Motor," AIAA Paper 94-3285.

Wang, J.C.T., and Widhopf, G.F., 1989, "A High-Resolution TVD Finite Volume Scheme for the Euler Equations in Conservation Form," *Journal of Computational Physics*, Vol. 84, No. 1, pp. 145-173.

Wimpress, R.N., 1950, *Internal Ballistics of Solid-Fuel Rockets,* p. 79, McGraw-Hill, New York.
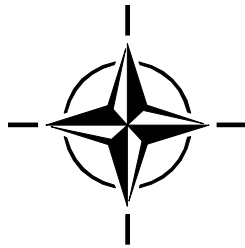
# Combustion of Solid Propellants

**G. Lengellé, J. Duterque, J.F. Trubert**
Research Scientists, Energetics Department
Office national d'études et de recherches aérospatiales (ONERA)
29 avenue de la Division Leclerc
BP 72 – 92322 Châtillon Cedex
FRANCE

## ABSTRACT

*A review of **the understanding of the combustion mechanisms** of solid propellants that the authors have built from their work and from the literature is presented. Such an understanding is an important part of the process carried out to master the behavior of solid propellants and to obtain desired characteristics (with respect to energetic level, burning rate level, sensitivity to pressure and initial temperature, nature of emitted combustion products, vulnerability to various aggressions...).*

***The propellants and propellant components considered** are:*

- *double-base propellants, based on nitrocellulose and nitroglycerin,*

- *active binder, based on an inert polymer (or energetic such as PAG) and a liquid nitrate ester,*

- *inert binders, such as polybutadiene,*

- *ammonium perchlorate,*

- *nitramines, such as HMX, RDX and CL20 (HNIW),*

- *composite ammonium perchlorate-inert binder propellants,*

- *composite propellants based on a nitramine and an active binder,*

- *aluminum, with respect to the two previous types of propellants,*

- *additives, when appropriate.*

***The features of the combustion zone described** are:*

- *In the condensed phase, the thickness of the temperature profile and of the decomposition zone, the kinetics of the decomposition, the energy released, the nature of the gases evolved, the surface temperature;*

- *In the gas phase, the type of flame structure (diffusion or kinetically controlled), the possibility of staging (such as in double-base propellants), the kinetics of the reaction(s), the energy released, the flame temperature (primary and final, when applicable).*

*It is concluded that a fairly proper knowledge of the combustion of the various components and propellants has been acquired (being now extended to new ingredients, oxidizers or binders). Furthermore, based on this knowledge, a first approach modeling description can be achieved. Such a description is necessary in accompanying the elaboration of new propellants and in preparing the investigation of more complicated regimes such as those of erosive burning and of non-stationary response.*

## INTRODUCTION

Much work has been devoted in various countries to investigating the combustion mechanisms of solid propellants. It is timely to bring together the information obtained by the authors and compared to that of the literature on the combustion of the individual components as well as of their combination into propellants. This review is about the existing components and propellants: double-base propellants and active binders, inert binders, ammonium perchlorate, HMX, RDX and CL20 and the corresponding composite propellants, ammonium perchlorate – inert binder (plus possibly aluminum), HMX (or RDX or CL20) – active binder.

The viewpoint adopted here is that of the understanding of the combustion behavior of propellants. Therefore as much information as possible is presented about the fundamentals of the processes (thermal properties, kinetics in the condensed phase and in the gas phase...), whereas no attempt is made to establish a complete catalog of practical results on various propellants with different particle sizes, catalysts, variations on the percentage of ingredients. The aim is to give a clear, as conclusive as possible picture. This will then be non compatible with a complete discussion of the various, sometimes contradictory, mechanisms proposed in the literature. Also precluding such a discussion is the will to compare the different components and the corresponding propellants.

Some space is taken up by physico-chemical modeling. The aim is not so much to give the elements of mathematical descriptions which could be used for a priori computations of burning characteristics of propellants (to the extent that such computations are possible). The point is more to put to test the hypotheses made on the mechanisms of combustion by incorporating them in reasonable models and confronting the results thus obtained to experimental data.

These descriptions can also be viewed, along-side with the data given for each component or propellant, as useful for mastering the regimes of combustion which go beyond stationary combustion: that is erosive burning and unsteady (under pressure excursions or pressure oscillations) combustion responses.

Table 1 gives information about the various types of propellants of actual use.

**Table 1: Performances/Characteristics of Various Propellants**

| PROPELLANT | COMPOSITION (main ingredients) | $\rho_p$ g/cm$^3$ | $I_s$(70/1) theoretical. (losses) | APPLICATIONS /CHARACTERISTICS |
|---|---|---|---|---|
| Extruded DB | Nitrocellulose Nitroglycerin | ≤ 1.66 | ≤ 230 s (≈ - 10 s) | - Anti-tank rockets and missiles<br>- AS rockets<br>- Some tactical missiles (SA) Minimum smoke |
| Powder cast DB | Nitrocellulose Nitroglycerin | ≤ 1.66 | ≤ 225 s (≈ - 10 s) | - Anti-tank missiles<br>- Some tactical missiles (AS) Minimum smoke |
| AP composite | Ex: 88 % AP - 12 % HTPB | 1.72 | ≈250 s (≈ - 10s) | - Some AS rockets<br>- Some tactical missiles Reduced smoke (HCl-H$_2$O) |
| AP composite with aluminum | Ex: 68 AP - 20 al. - 12 HTPB | ≈1.82 | 265 s (≈ - 20 s) | - AA tactical missiles<br>- Anti-ship missiles (booster)<br>- Tactical ballistic missiles<br>- Strategic ballistic missiles<br>- Apogee motors<br>- Boosters for space launchers (Titan III, IV, V, Space Shuttle, Ariane V, H2A...) Smoky (Al$_2$O$_3$) |
| HMX (RDX) composite | HMX or RDX - XLDB binder | < 1.75 | < 255 s (≈ - 15 s) | - Anti-ship missiles (cruise)<br>- SA missiles Minimum smoke (without AP) |
| HMX composite with aluminum | HMX + AP+ Al XLDB binder | 1.87 | 273 s | - Strategic ballistic missiles (upper stages) (Trident, MX...) Smoky (Al$_2$O$_3$) |

Sources:     Air et Cosmos n° 1000, May 1984.
              Annales des Mines, Jan-Feb. 1986.
              Aéronautique et Astronautique, n° 138, 1989.

*Double-base propellants* (made by the extrusion or powder casting techniques) are used in anti-tank rockets or missiles and in some tactical missiles. Their main advantage is that they produce a minimum amount of smoke (only from a small amount of additives).

*Composite propellants, based on ammonium perchlorate (AP)* without aluminum, generate reduced smoke, HCl and H$_2$O vapor will precipitate into droplets in the plume under given temperature and humidity conditions. They are used for various tactical missiles. With aluminum, they are widely used in missiles and space launchers. They produce alumina smoke, which, in the case of space launchers, could be considered in the future to be undesirable (along with HCl).

*Composite propellants based on nitramines and an "active" binder* (cross linked polymer with nitroglycerin or other liquid nitrate esters) are used more and more. Without aluminum, they are in the minimum smoke category and they replace DB propellants. With aluminum, they reach the highest specific impulse and density and are used so far for upper stages of strategic missiles.

The combustion of the components and then of the various propellants will be seen in the next chapters.

A few general references about chemical propulsion, solid propellants and combustion can be found at the end of the main text, ahead of more specialized references introduced progressively in the following chapters.

## COMBUSTION OF DOUBLE-BASE PROPELLANTS AND ACTIVE BINDERS

### 1.0    Introduction

It seems appropriate to consider double-base propellant combustion mechanisms in the first place because they correspond to relatively simpler premixed processes which lend themselves to a better understanding and because they have been investigated for a long time (starting in the 1950's) in the US, the then USSR, the UK, Japan and France in particular. General background on the combustion of double-base propellants can be found in references [1-6].

As will be seen, the mechanisms involved in the combustion of double-base propellants will apply as well to the active binders ( ≈1/3 polymer, ≈ 2/3 nitroglycerin, or other liquid nitrate esters).

Double-base propellants are made in a number of ways. When they are rolled or extruded, the components are nitrocellulose and nitroglycerin, to which some stabilizers such as centralite and plasticizers are added. When they are cast, a casting powder (made of nitrocellulose, some nitroglycerin, and the various additives) is swelled within the mold by a liquid mixture of nitroglycerin and triacetin. The grain thus obtained is then inhibited and used free standing in the motor. The propellant ingredients can also be mixed, cast, cross-linked, and the grain case bonded.

Depending on the relative amounts of nitrocellulose and nitroglycerin, Figure 1, the energetic level of the propellant can be increased or, in the usual terminology, its "heat of explosion" or "calorimetric value", that is, the heat evolved in a calorimetric bomb by combustion under an inert atmosphere. One can then talk about "cool" and "hot" compositions.
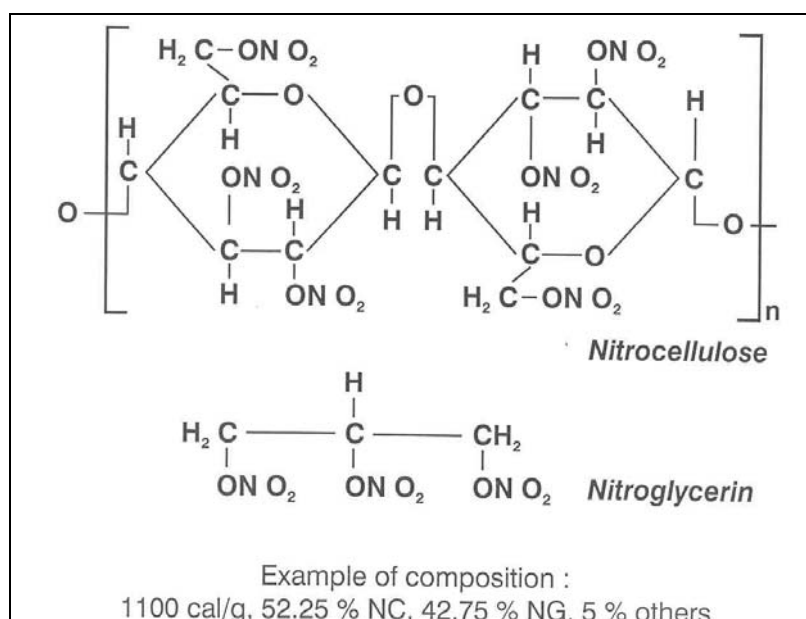


**Figure 1: Components of Double Base Propellants.**

Double-base propellants are used in small and medium sized rockets and thus exposed to varying ambient temperatures. The sensitivity of the motor operation to temperature depends upon the propellant burning rate sensitivity to both the temperature and the pressure. As can be seen on Fig. 2, the pressure exponent, in the usual empirical law $v_b \sim p^n$, is around 0.7 and increases to nearly 1 at high pressure. Super-rate effects (Fig. 3) are created by the use of additives, most often lead and copper salts combined with carbon black. At the end of the super-rate zone, the burning rate falls back to that of the control propellant, with the occurrence of a nearly zero pressure exponent zone, a "plateau" effect, or a negative exponent zone, a "mesa" effect. These terms are used by analogy with topographical features. A fairly complete set of results can be found in reference [6]. It is only in these reduced pressure exponent zones that the propellant is used to minimize the motor operation sensitivity to ambient temperature. Due to this fact, the study of the combustion of propellants without additives should be conceived only as a first step leading to an understanding of modified (that is, with additives) propellants.
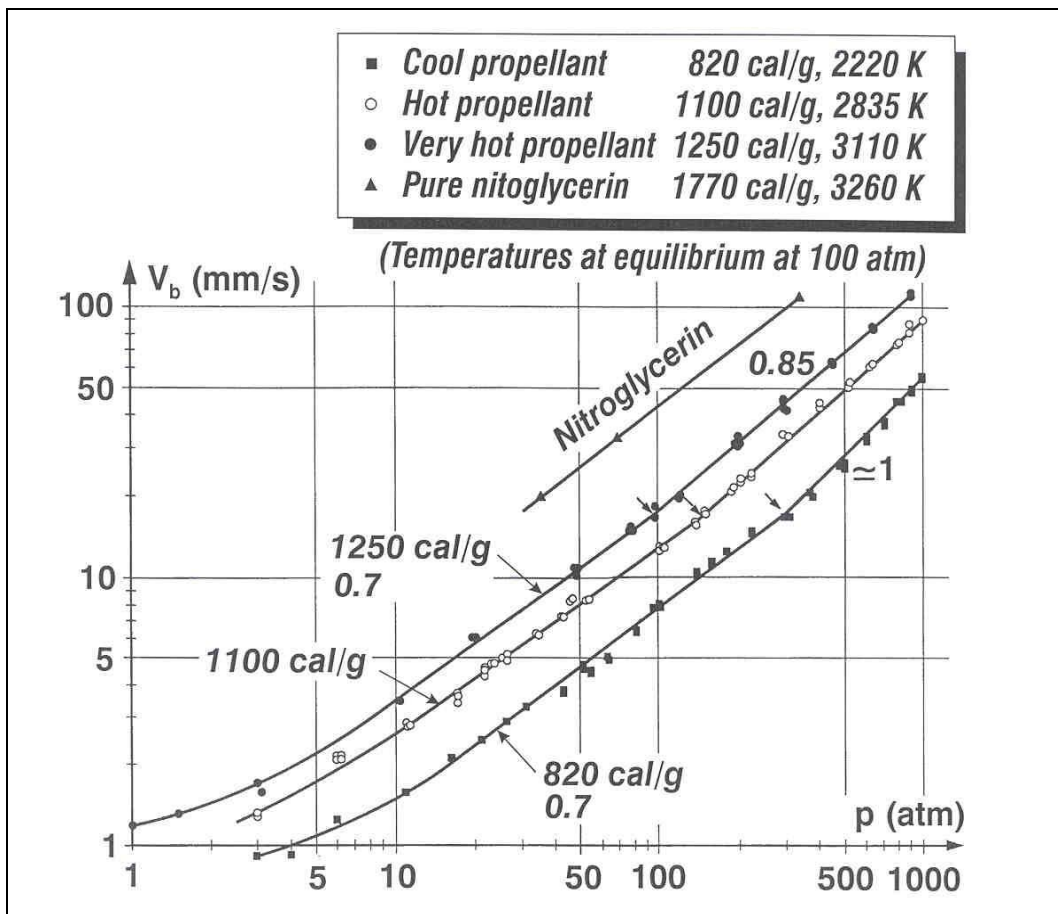


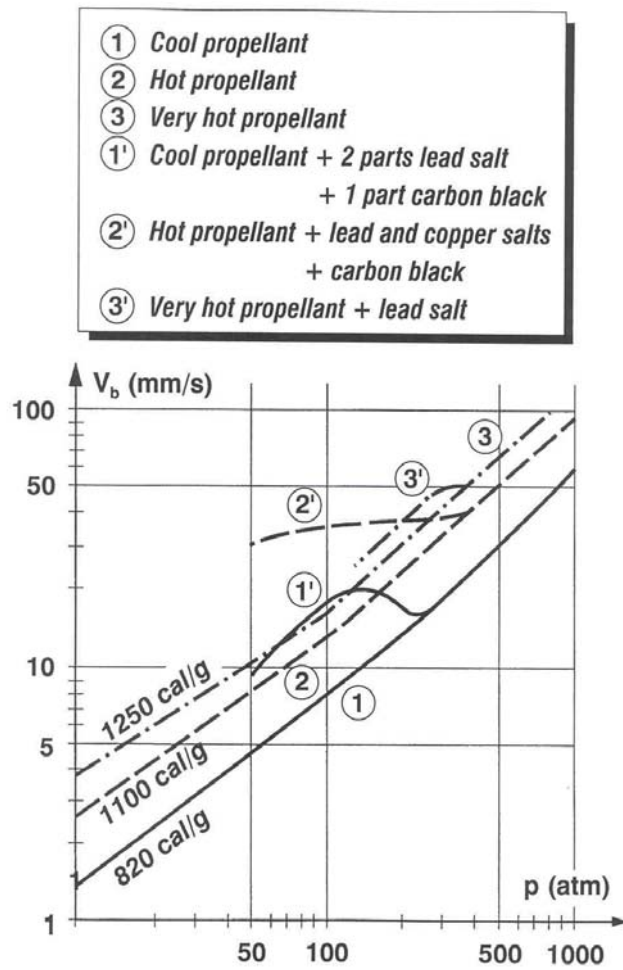**Figure 2: Burning Rate vs Pressure.**
**(Double Base Propellants)**

**Figure 3: Super-Rate Effects.**
**(Double Base Propellants)**

## 2.0    Flame Structure

From the works mentioned previously it is possible to describe the combustion wave structure of double-base propellants, in particular its chemical processes, see Figs. 4 and 5. The various data will be discussed and justified later. Gas analysis results are from reference [7]; they refer to mass fractions.
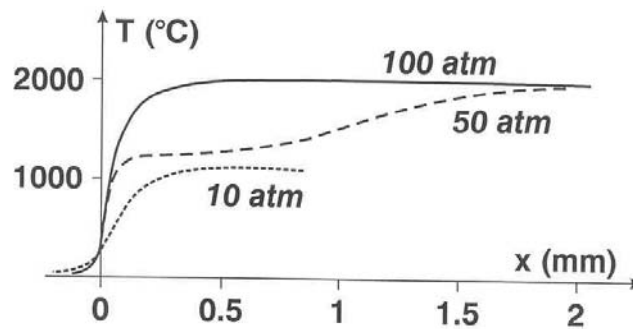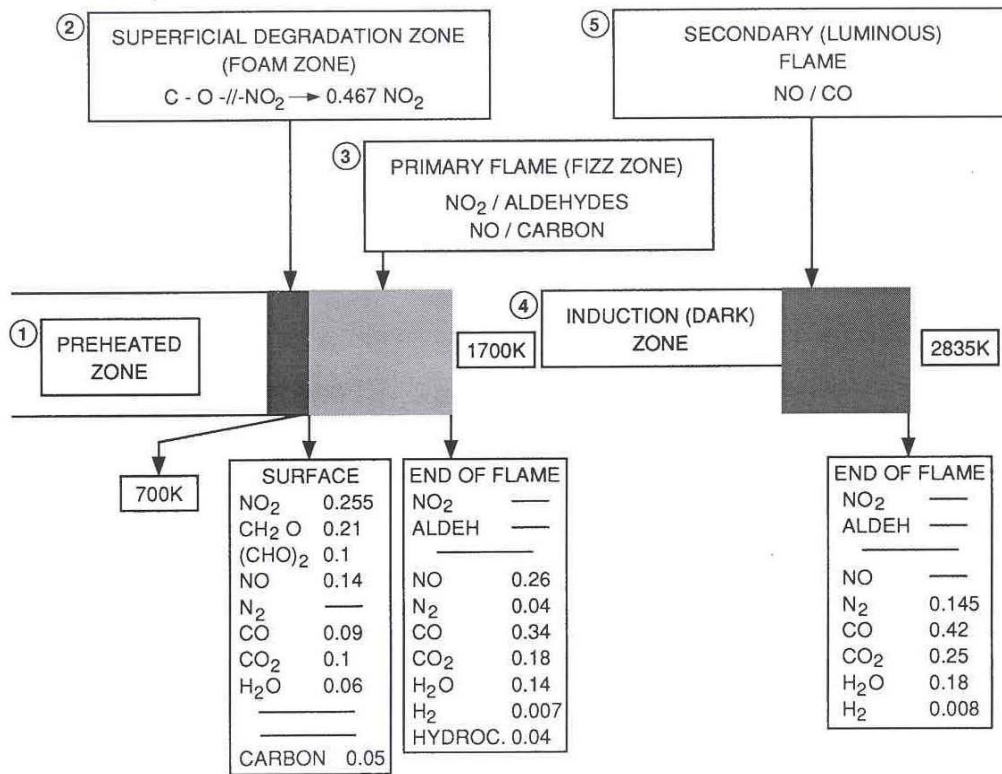


**Figure 4: Temperature Profiles.**
**(Double Base Propellant)**

Figures for an 1100 cal/g propellant. Surface and primary flame (at 11 atm) mass fractions from gas analysis
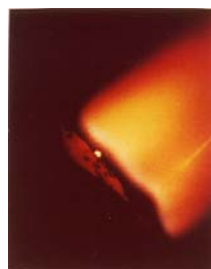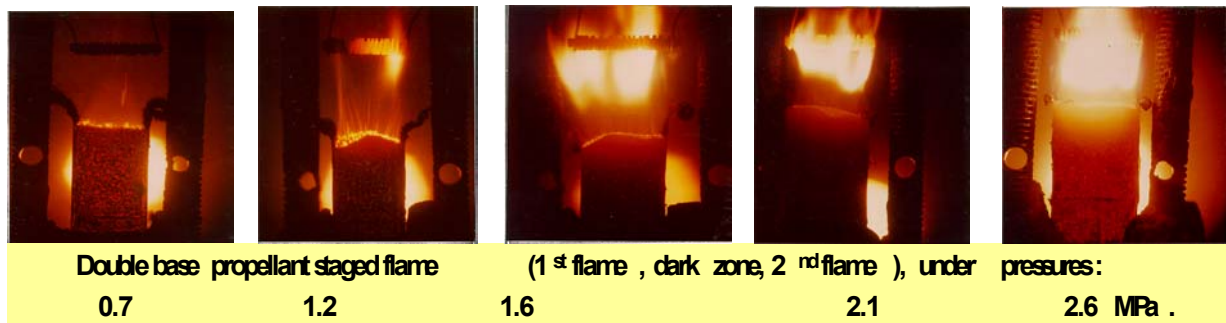
**Figure 5: Various Zones of the Combustion of a Double Base Propellant.**

The propellant components pass unaffected through a preheated zone of a few tens of micrometers in a few milliseconds and reach a superficial degradation zone (or "foam" zone in the early literature) where the temperature becomes high enough for the molecular degradation to take place, initiated by the rupture of the $C-O-//-NO_2$ bond. Simultaneous recombination occurs so that a mixture of $NO_2$, aldehydes, but also NO emerges from the surface and so that the net energy balance of the degradation is exothermic. At pressures under about 100 atm, a clearly separated primary flame ("fizz" zone) and a secondary flame ("luminous" flame) are observed, the first involving $NO_2$-aldehydes reactions and the second probably NO-CO reactions. In this pressure range the secondary flame is too far away to have any effect on the surface or even to induce a temperature gradient into the primary flame. The burning rate is then entirely under the influence of the latter. This corresponds to a burning rate/pressure law with a 0.7 pressure exponent (Fig. 1). As the pressure increases, the secondary flame enhances and then merges into the primary flame and a transition is observed to a zone with a pressure exponent close to 1. When the secondary flame is fully developed, even at pressures for which it does not yet influence the burning rate, the final products ($N_2$, CO, $CO_2$, $H_2O$ and $H_2$) and the final temperature (2100-3100 K, depending on the heat of explosion) are attained.

Table 2 gives data relative to the various zones of the combustion wave.

**Table 2: Characteristics of the Combustion Zones (Measured Results from Zenin)**

| Pressure atm. | 10 | 50 | 100 |
|---|---|---|---|
| $v_b$ mm/s | 1.9 | 6.7 | 10.6 |
| $T_s$, K | 610 | 662 | 685 |
| Preheated zone, µm (measured/computed) | 140/194 | 50/55 | 45/35 |
| Residence time in preheated zone, ms | 100 | 8 | 3 |
| Superficial degradation zone µm | 11 | 3 | 2 |
| Residence time in superficial zone, ms | 6 | 0,5 | 0,2 |
| Flame thickness, µm (measured) | 200 | 75 | 110 (secondary flame) |



**Double base propellant staged flame (1st flame, dark zone, 2nd flame), under pressures:**
**0.7          1.2          1.6                    2.1                    2.6 MPa.**



**HMX, under 0.15 MPa**

**Visualizations with high speed camera, for a double base propellant, showing the secondary flame moving closer to the surface, and a comparative picture for HMX which will be evoked further on.**

## 3.0 Condensed Phase Processes

*The preheated zone* of a regressing propellant is described by the conservation of energy in a coordinate (x > 0 in the gas phase) regressing with the surface:

$$\rho_p \, v_b \, c_p \, dT / dx = d( \lambda_p \, dT / dx ) / dx \tag{1}$$

in such a way that a temperature profile

$$( T - T_0 ) / ( T_s - T_0 ) = \exp( x \, v_b / d_p ), \; d_p \equiv \lambda_p / \rho_p \, c_p \tag{2}$$

will progress with the surface into the propellant. From measurements up to 100°C and from ignition experiments, representative average values are taken as indicated in Table 3.

**Table 3: Values of the Condensed Phase Properties (Double-Base Propellants)**

> $\rho_p = 1.6$ g/cm$^3$, $c_p = 0.4$ cal/g K,
> $\lambda_p = 5.1 \; 10^{-4}$ cal/s cm K
> $d_p = 0.8 \; 10^{-3}$ cm$^2$/s

The thickness $e_{cond.}$ of the conduction zone can be taken conventionally as

$$T( \text{end of cond. zone} ) - T_0 = 10^{-2} ( T_s - T_o )$$

$$e_{cond.} = ( d_p / v_b ) \ln 10^2 \tag{3}$$

As an example, for $v_b = 10$ mm/s

$e_{cond.} = 37\mu m$, a thickness through which the temperature rises from 293 K to about 700 K. The residence time through this conduction zone is:

$$\tau_{cond.} = ( d_p / v_b^2 ) \ln 10^2 \tag{4}$$

about 4 ms in this example; a very short time for a temperature increase of 400 K.

The *superficial degradation zone* has its thickness ruled by the conservation of the non degraded propellant mass fraction $Y_p$:

$$\rho_p \, v_b \, dY_p / dx = - \rho_p \, A_c \exp( - E_c / R \, T ), \tag{5}$$

with the decomposition represented by an Arrhenius law. Numerous investigations by thermogravimetry, differential scanning calorimetry, on nitrocellulose, nitroglycerin and other nitrate esters, as well as on double base propellants, and ignition studies [5] result in:

**Table 4: Values for the Condensed Phase Degradation Kinetics (Double-Base Propellants)**

> Decomposition order 0, $A_c = 1 \; 10^{17}$ s$^{-1}$, $E_c = 40$ kcal/mole

The thickness of the degradation layer is related to the fast drop in the degradation rate. When this rate is $10^{-2}$ that at the surface temperature, the lower limit of the reaction layer is conventionally reached:

$$\exp[ - \xi_c / ( 1 - \Delta T / T_s )] = 10^{-2} \exp( - \xi_c ), \qquad \xi_c \equiv E_c / R T_s$$

the temperature drop is then

$$\Delta T / T_s = 1 / ( 1 + \xi_c / \ln 10^2 ) \qquad (6)$$

$\Delta T \simeq 100$ K for $T_s = 700$ K. Such a temperature drop inserted in Eq. (2) gives an estimation of the reaction layer thickness

$$e_{reaction} = - ( d_p / v_b ) \ln[ 1 - \Delta T / ( T_s - T_o ) ]$$

or taking into account the magnitude of the reduced activation energy ( $\xi_c \approx 30$ ).

$$e_{reaction} \approx e_{cond.} T_s / \xi_c ( T_s - T_o ) \qquad (7)$$

For the values taken above, at $v_b = 10$ mm/s, $e_{react} \approx 2$ μm, with an associated residence time $\tau_{react}$ of 0.2 ms.

The summation of Eq. (5) through the degradation layer results in:

$$\rho_p v_b ( Y_{p,s} - Y_{p,0} ) = - \int \rho_p A_c \exp( - E_c / R T ) \, dx \qquad (8)$$

$$v_b \sim A_c \exp( - E_c / R T_s ) e_{reaction} = A_c \exp( - \xi_c ) ( d_p / v_b ) \ln 10^2 ( 1 / \xi_c ) [ T_s / ( T_s - T_0 ) ]$$

A more rigorous approach [8] (which is almost identical to a numerical computation [9]) gives, for a zero order reaction:

$$v_b^2 = ( d_p / \xi_c ) A_c \exp( - \xi_c ) / ( 1 - T_0 / T_s - Q_s / 2 c_p T_s ) \qquad (9)$$

This equation indicates a relation between surface temperature and burning rate: the mass flow rate $\rho_p v_b$ emitted from the surface is the result of the decomposition of the propellant into gases throughout the superficial degradation layer, Eq. (8). The higher the burning rate $v_b$, the smaller the residence time $\tau_{react.} \sim 1 / v_b^2$, and the higher is the surface temperature reached to allow for the complete degradation of the propellant.

Traverses with micro-thermocouples (as seen previously the thickness of the combustion wave is of the order of tens of μm) allow to obtain measurements of the surface temperature [2,3,4,5]. One example is given on Fig. 6. The results from various sources are collected (see [5] for references), as burning rate versus $1 / T_s$, on Fig. 7. Also indicated is the correlation obtained from Eq. (9). Due to the thinness of the conduction zone, a few tens of micrometers, fairly large errors and scatter should be expected in the measurements of the surface temperature. Nevertheless, some conclusions can be reached (see also Refs. [3,10]). The initial degradation of the propellant components is controlled by the breaking of the -C-O-//-NO$_2$ bond (characterized by the 40 kcal/mole activation energy). This is considered to be a temperature sensitive only process, irreversible (therefore not influenced by the pressure level). It is noteworthy that the kinetics of the degradation is the same from thermal decomposition (by TG and DSC) at about 400 K, to ignition from 400 to 500 K [5] and combustion at temperatures up to 700 K. Also important is the conclusion, if one looks at the details of Fig. 7, that the presence of super rate producing additives does not affect the condensed phase kinetics.

*The energetics of the reaction layer* is now to be considered. The initial degradation of the propellant, taking into account the assumed decomposition of nitroglycerin into $3 NO_2$, $2 CH_2O$ and $0.5 (CHO)_2$, is thought to give (for the example of the 1100 cal/g propellant) the mass balance

$$1 \text{ propellant} \rightarrow 0.467 \, NO_2 + 0.364 \, CH_2O + 0.1 \, (CHO)_2 + 0.06 \text{ hydrocarbons} \tag{10}$$
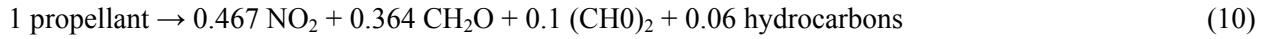
with a corresponding endothermic heat of degradation

$Q_d = -135$ cal/g of propellant.

It is thought [5,9,10] that within the superficial layer the exothermic reaction between $NO_2$ and aldehydes can start. A plausible mole balance (in order to match various results, in particular the analysis [7] of the gases emitted from the surface of regressing propellants) is

$$NO_2 + CH_2O \rightarrow NO + 1/2 \, CO + 1/2 \, CO_2 + 1/2 \, H_2O + 1/2 \, H_2 \tag{11}$$
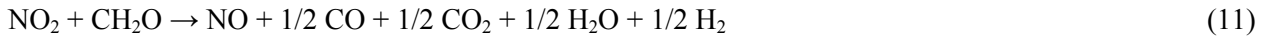
with a corresponding exothermic heat of reaction

$Q_{NO2} = 1040$ cal/g of $NO_2$.

Conservation of the species $NO_2$ (in terms of mass fraction Y) is written (no diffusion is taken into account)

$$\rho_p \, v_b \, dY_{NO2} / dx = Y_{NO2,i} \, \rho_p \, A_c \exp( - E_c / R \, T ) - A_{NO2} ( p \, M / R \, T ) \, Y_{NO2} \exp( - E_{NO2} / R \, T ) \tag{12}$$

if a first order reaction with respect to the molar concentration of $NO_2$ is assumed (it will be seen that this is probably the case).

The conservation of energy is written

$$\rho_p \, v_b \, c \, dT / dx - d( \lambda \, dT / dx ) / dx = - Q_d \, \omega_p - Q_{NO2} \, \omega_{NO2} \tag{13}$$

with $\omega_p$ the rate of reaction of the propellant, as in Eq. (5), and $\omega_{NO2}$ that of $NO_2$ as in the second term of Eq. (12). The summation of Eqs. (5,12,13) through the condensed phase to the surface leads to:

$$\lambda \, dT / dx|_s = \rho_p \, v_b \, ( c_g \, T_s - c_p \, T_o - Q_s ) \equiv \rho_p \, v_b \, Q_c \tag{14}$$

$$Q_s \equiv Q_d + Q_{NO2} ( Y_{NO2,i} - Y_{NO2,s} ) \tag{15}$$

The first equation is the heat balance at the surface, it means that the heat flux from the flame in the gas phase allows the heating and pyrolysis of the propellant. The net heat of decomposition of the propellant $Q_s$ is exothermic to the extent that some $NO_2$ already reacts exothermically in the condensed phase.

From thermocouple traverses such as that of Fig. 6 and the balance of Eq. (14), the net heat $Q_s$ can be estimated (again scatter should be expected). The results from various sources are given on Fig. 8. The net heat of decomposition is seen to be exothermic and increasing with burning rate (due to an increase in pressure). Summation of Eq. (12) yields (with Eq. (5) taken into account)
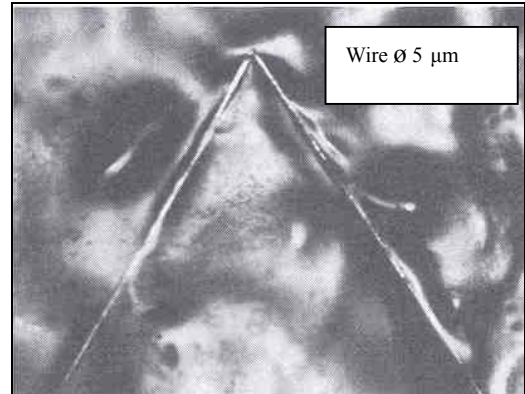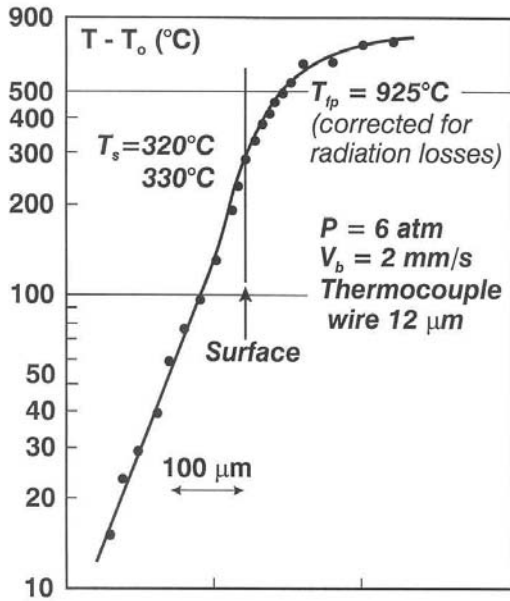
$$\rho_p \, v_b \, ( Y_{NO2,i} - Y_{NO2,s} ) = A_{NO2} \int (p \, M / R \, T ) \, Y_{NO2} \exp( - E_{NO2} / R \, T ) \, dx$$

$$\approx A_{NO2} ( p \, M / R \, T_s ) \, Y_{NO2} \exp( - E_{NO2} / R \, T_s ) \, e_{react.}$$

and with Eq. (8)

$$Y_{NO2,i} - Y_{NO2,s} \sim ( p \, M / R \, T_s ) \exp( - E_{NO2} / R \, T_S ) / \exp( - E_c / R \, T_s )$$

Figure 6: Temperature Profile in the Condensed Phase.
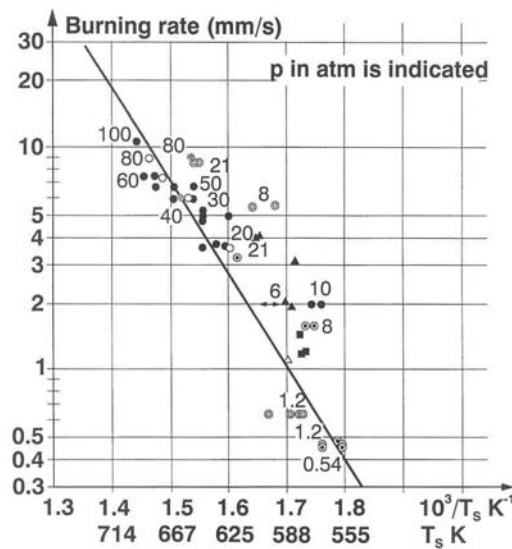(Double Base Propellant)



Figure 7: Pyrolysis Law.
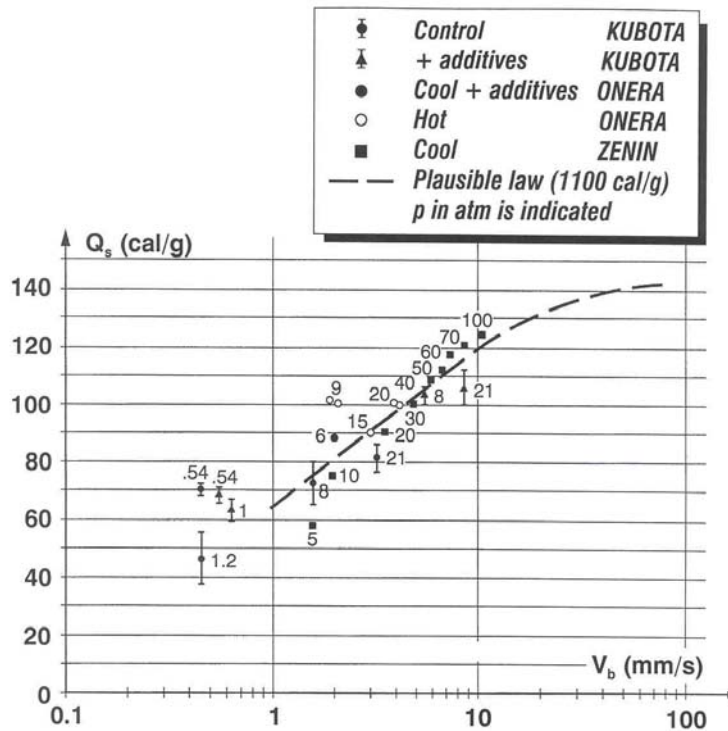(Double Base Propellants)

**Figure 8: Heat Evolved in the Condensed Phase.**
**(Double Base Propellants)**

This relation indicates that the amount of $NO_2$ reacting in the condensed phase will increase with pressure, and thus $Q_s$ will increase, if the reaction rate for $NO_2$ catches up with the decreasing residence time in the degradation layer,

$$\tau_{react.} \sim 1 / v_b^2 \sim 1 / \exp( - E_c / R \, T_s )$$

(due to Eq. (9)). A plausible law is obtained for a first order $NO_2$ reaction with an activation energy $E_{NO2}$ of about 15 kcal/mole.

It should be observed that the heat evolved in the condensed phase $Q_s$ has to be affected by the amount of $NO_2$ present in the propellant, that is by the heat of explosion.

One important feature of Fig. 8 is that the heat evolved in the condensed phase is not affected by the presence of additives.

## 4.0    Flame Zone

As seen above, the reaction between $NO_2$ and aldehyde starts in the condensed phase in such a way that the surface gas composition [7] indicated on Fig. 5 is obtained, with $NO_2$ being significantly less (0.255) as compared to what results from the initial degradation of the propellant (0.467, in the case of an 1100 cal/g propellant) and with NO already present (0.14). The mole balance of Eq. (11) allows to match as well the gas analysis at the end of the primary flame ([7], measurements at 11 atm)

$$NO_2 + CH_2O \rightarrow NO + 1/2 \, CO + 1/2 \, CO_2 + 1/2 \, H_2O + 1/2 \, H_2 \tag{11}$$
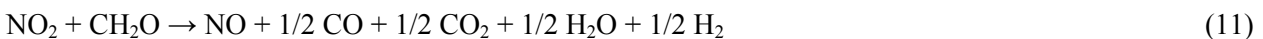
$Q_{NO2} = 1040$ cal/g of $NO_2$.

It is likely that aldehyde-aldehyde reactions also occur following (again to match the gas analysis results):

$$CH_2O + CH_2O \rightarrow CO + 1/2 \, C_2H_4 + H_2O \,, \quad Q_{ald.1} = 389 \text{ cal/g of } CH_2O \tag{16}$$

$$(CHO)_2 + (CHO)_2 \rightarrow 4 \, CO + 2 \, H_2 \,, \quad Q_{ald.2} = -533 \text{ cal/g of } (CHO)_2 \tag{17}$$
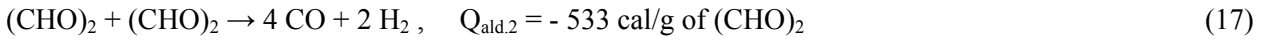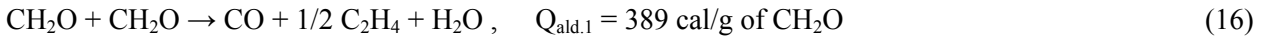
At low pressure when probably only the reaction of (11) can take place, an energy balance between initial temperature and end of the primary flame yield:

$$c_g \, T_{fp} - c_p \, T_0 = Q_d + Q_{NO2} \, Y_{NO2,i}, \, p \leq 1 \text{ atm} \tag{18}$$

since the initial $NO_2$ is totally consumed in the condensed phase and the primary flame. An evaluation of $T_{fp} = 1340$ K results. It is seen on Fig. 9 that measurements with small thermocouples indicate a large increase with pressure of the primary flame temperature from this value. The aldehyde reactions of Eqs. (16,17) do not produce energy in significant amount. It is assumed [5] that the NO already present at the surface as well as that produced from the $NO_2$-aldehyde reaction react with the layer of carbon residue, attached to the surface, which is observed by direct visualization under combustion and after extinction by scanning electron microscopy.
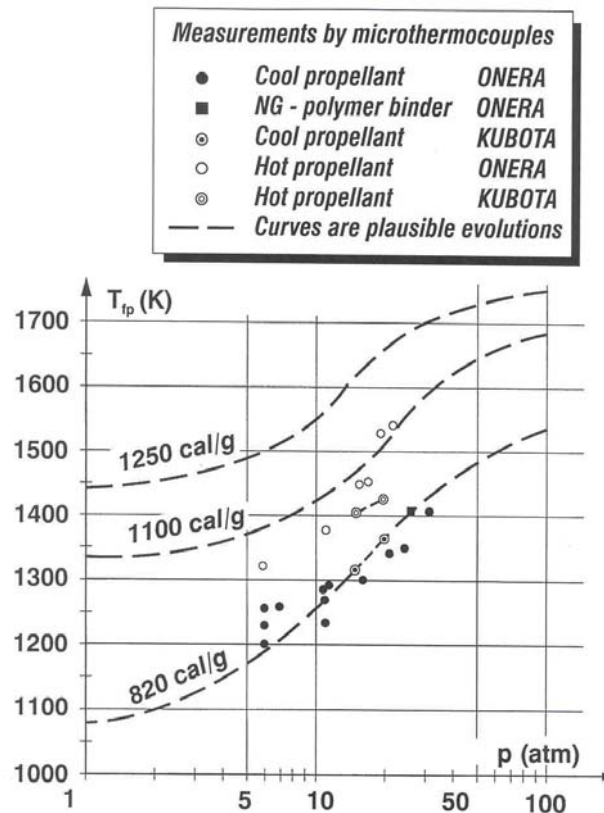


**Figure 9: Primary Flame Temperature of Double Base Propellants.**

The NO/carbon reaction had been investigated in [11]. If one makes use of the results obtained, the conservation of the species carbon can be written as (knowing that the carbon layer regresses with the surface)

$$v_b \, d\rho_c / dx = (M_c / M_{NO}) \, \omega_{NO} \tag{19}$$

$\omega_{NO} = - A_{NO/C} \exp( - E_{NO/C} / R \, T ) \, \rho_c \, S_{s,c} \, Y_{NO} \, p \, M$ , in $g/cm^3 s$

(this form resulting from the way the data of [11] is cast), the reaction balance being assumed to be:

$NO + C \rightarrow 1/2 \, N_2 + CO$ , $Q_{NO/C} = 1600$ cal/g of NO             (20)

and $S_{s,c}$ being the specific surface area of the carbon (at most $10^6$ $cm^2$ /g). Reference [11] produces (after rounding $E_{NO/C}$)

$A_{NO/C} = 2 \; 10^{-3}$ mole/s $cm^2$ atm, $E_{NO/C} = 30$ kcal/mole

A rough estimate of the amount of $N_2$ produced by reaction (20) through the primary flame is given by (with $m \equiv \rho_p \, v_b$ the mass flow rate)

$m \, Y_{N2,fp} = - ( 1 / 2 ) ( M_c / M_{NO} ) <\omega_{NO}> x_f$

$<\omega_{NO}>$ being evaluated at average values through the flame. With $p = 11$ atm, $v_b = 0.28$ cm/s, $<Y_{NO}> = 0.2$, $<\rho_c> = 0.5$ $g/cm^3$, $<T_f> = 1400$ K and $x_f = 400$ $\mu$m (from thermocouple measurements) it is obtained

$Y_{N2,fp} \approx 0.06$

a reasonable value (with respect to the result of Fig. 5). This tends to indicate that the NO/carbon reaction has a kinetics indeed fast enough with respect to the residence time allowed in the primary flame.

An energy balance taking into account the NO/carbon reaction is written:

$c_g \, T_{fp} - c_p \, T_0 = Q_d + Q_{NO2} \, Y_{NO2,i} + Y_{NO,cons.} \, Q_{NO/C} + Q_{ald} \, Y_{ald,cons.}$        (21)

(the consideration of the aldehyde reaction cools the flame by about 80 K). In this balance $Y_{NO,cons.}$ is the amount of NO consumed in the primary flame:

$Y_{NO,cons.} = Y_{NO2,i} ( M_{NO} / M_{NO2} ) - Y_{NO,fp}$

in the case of the example of Fig. 5 and taking into account the uncertainty on the measurements: $Y_{NO,cons.} = 0.035$ to $0.047$ and Eq. (21) results in $T_{fp} = 1420$ to $1475$ K, an admissible value when compared to the results of Fig. 9.

The temperature profile in *the primary flame* is controlled by the conservation of energy [5].

$m \, c_g \, dT / dx - d(\lambda_g \, dT / dx) / dx = - Q_{NO2} \, \omega_{NO2} - Q_{NO/C} \, \omega_{NO} - Q_{ald} . \omega_{ald.}$        (22)

**Table 5: Values Considered as Representative for the Gas Phase (Double-Base Propellants)**

$$c_g = 0.35 \text{ cal/g K,}$$

$$\lambda_g = 1.25 \; 10^{-4}( \, T / 700 \, )^{0.7} \text{ cal/cm s K}$$

$$M = 30 \text{ g/mole}$$

The evaluation of the heat flux received at the surface, which will then control the burning rate according to Eq. (14), results from the summation of Eq. (22) through the flame zone. Only a true numerical evaluation of the temperature and species profiles will give the proper heat flux. However conclusions can be drawn from approximate relations. The activation energies of the reactions of Eq. (22) being moderate, the flame is distributed and an approximation of the temperature profile is written as:

$$( T_f - T ) / ( T_f - T_s ) = \exp( - 3\, x / x_f ) \tag{23}$$

which will produce a shape such as that of Fig. 6. The coefficient of 3 is such that, when $x = x_f$, $T_f - T$ is 5 % of $T_f - T_s$, that is close enough to the final temperature.

With Eq. (14)

$$\lambda_{g,s}\, dT / dx|_s \equiv q_s = m\, Q_c \equiv \rho_p\, v_b\, (c_g\, T_s - c_p\, T_0 - Q_s) \tag{14}$$

Eq. (23) yields

$$q_s = 3\, \lambda_{g,s}\, ( T_f - T_s ) / x_f\,, \qquad x_f = 3\, \lambda_{g,s}\, ( T_f - T_s ) / m\, Q_c \tag{24}$$

The summation of Eq. (22) through the flame results in

$$m\, c_g\, ( T_f - T_s ) + q_s = 3\, Q_g <\omega_g>\, x_f \quad (<\omega_g> \text{ positive is the average rate})$$

or with Eqs. (14,24), and taking into account an overall equation for conservation of energy

$$c_g\, ( T_f - T_s ) = Q_g - Q_c,$$

$$m = [3 <\omega_g>\, \lambda_{g,s}\, ( T_f - T_s ) / Q_c]^{1/2} \tag{25}$$

At very low pressure, $\approx 1$ atm, when only the $NO_2$ reaction probably takes place, the burning rate follows pressure according to, see Eq. (12),

$$m \equiv \rho_p\, v_b \sim ( <\omega_{NO2}> )^{1/2} \sim p^{1/2} \exp( - E_{NO2} / 2\, R\, T_{fp} ) \tag{26}$$

a pressure exponent which is indeed observed, see Fig. 2. As the pressure increases the NO/carbon reaction takes on more importance and, referring to Eq. (19),

$$m \equiv \rho_p\, v_b \sim [ p \exp( - E_{NO2} / R\, T_{fp} ) + \sim p \exp( - E_{NO/C} / R\, T_{fp} ) ]^{1/2}, \tag{27}$$

which, with the increase of the flame temperature with pressure, see Fig. 9, accounts for the pressure exponent of 0.7.

At higher pressures, above about 150 atm for the 1100 cal/g propellant for example, a change in the pressure sensitivity, Fig. 2 is observed. This tends to indicate that *the secondary flame*, probably characterized by a second order, with respect to pressure, reaction for NO, comes into the primary flame and progressively dominates it, with a pressure exponent, according to Eq. (25), increasing to close to 1.

Referring to Fig. 10, for the 1250 cal/g propellant, the temperature sensitivity is indicated:

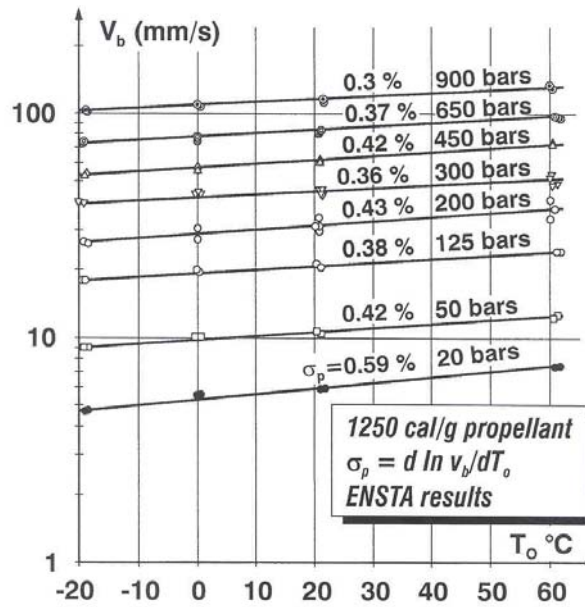$$\sigma_p = ( d\, lnv_b / dT_o ) \text{ at p given} \tag{28}$$

**Figure 10: Temperature Sensitivity of a Double Base Propellant.**

According to Eq. (27) the burning rate is under the influence (noting that the condensed phase energy balance also contains the effect of $T_0$ see Eq. (14)) of a premixed flame heat flux and therefore very sensitive to changes in the primary flame temperature, in the pressure domain when the two flames are separated. From Eq. (21), any change in initial temperature will affect the primary flame temperature and therefore induce a change in burning rate. As the pressure rises the primary flame temperature increases (up to 1800 K) and then for higher pressures the burning rate comes under the influence of the final flame (with a temperature reaching 3110 K for the 1250 cal/g propellant). It is seen from Eq. (27) that a given change in $T_0$ and therefore in $T_f$ has a smaller impact on the burning rate for higher flame temperatures, that is for higher pressures, a tendency observed on Fig. 10.

## 5.0    Active Binders

Various types of active binders, based on nitrocellulose or an inert binder and nitroglycerin or less energetic liquid nitrates, can be used, see reference [10] for a complete description. The cross-linked double-base binders (XLDB) will be considered here, in which the polymer is cured with an isocyanate after mixing with NG.

**Table 6: Values for a XLDB Binder**

Composition: $\approx$ 2/3 NG, 1/3 polyethylene glycol.

Heat of explosion: 850 cal/g.

$T_{ff}$ = 2000 K. $\rho_p$ = 1.42 g/cm$^3$.

$c_p$ = 0.46 cal/g K.

$\lambda_p$ = 3.9 10$^{-4}$ cal/cm s K. $d_p$ = 0.6 10$^{-3}$ cm$^2$/s

$Y_{NO2,i}$ = 0.421. $Q_d$ = - 150 cal/g

Although the burning rates of the different active binders can be, for a given heat of explosion, somewhat different at low pressures [10], above 10 atm the differences become small , see Fig. 11. In the case of a double-base propellant and of a XLDB binder (that of the above table), with nearly the same heat of explosion, the burning rates for a large range of pressure are very close, Fig. 12.
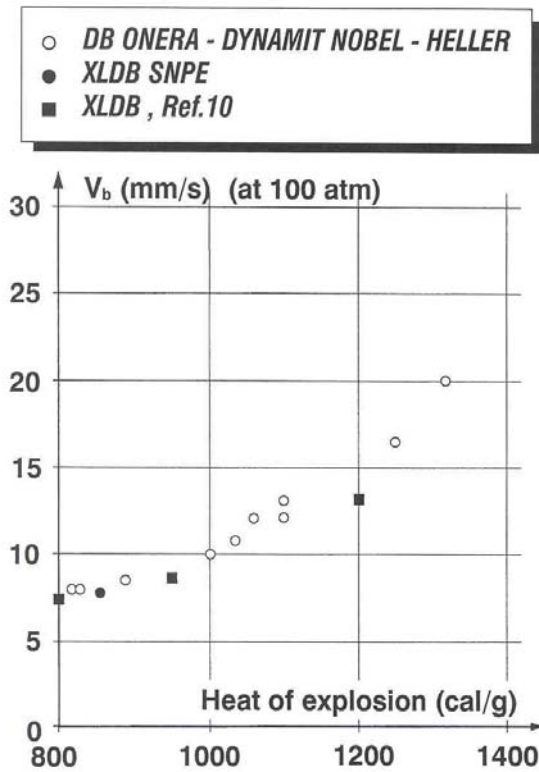


**Figure 11: Burning Rate vs Heat of Explosion.
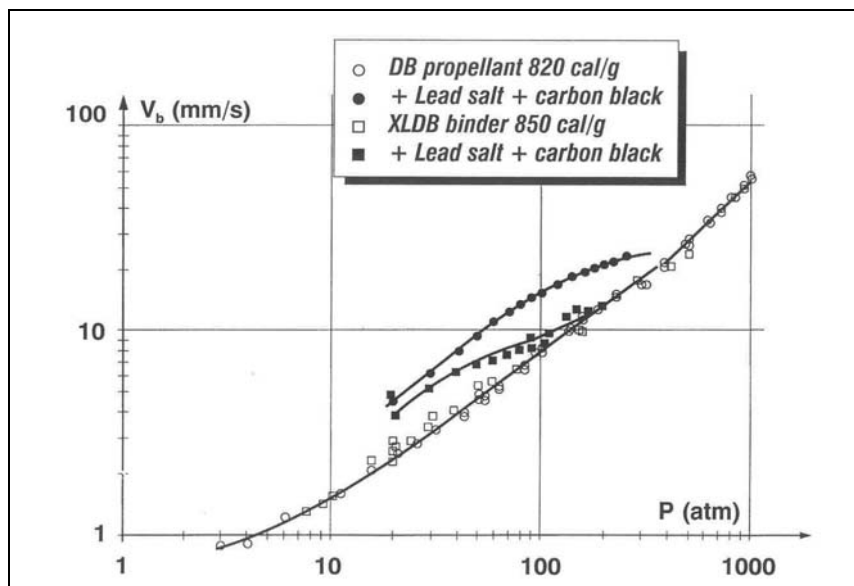(Double Base Propellants and XLDB Binders)**



**Figure 12: Double Base Propellants and Active Binder Burning Rates.**

Measurements for XLDB binders of the degradation kinetics, of the surface temperature, of the heat evolved in the condensed phase, as in Fig. 8, and of the primary flame temperature, Fig. 9, show that these characteristics are very close to those of DB propellants.

**Table 7: Gases Evolved from the Surface, Mass Fractions. XLDB Binder [7]**

| $NO_2$ | $CH_2O$ | $(CHO)_2$ | NO | CO | $CO_2$ | $H_2O$ | HC |
|--------|---------|-----------|------|------|--------|--------|------|
| 0.31 | 0.37 | 0.08 | 0.07 | 0.03 | 0.04 | 0.02 | 0.08 |

Gas analysis at the surface gives results which are qualitatively comparable to those of DB propellants, Fig. 5.

It can then be stated that the combustion mechanisms of the various types of double-base propellants and of the active binders are very similar.

## 6.0 Mechanisms of Action of Additives

The incorporation of a few per-cents of lead (and copper) salts and carbon black enables to obtain super-rate effects followed by mesa or plateau effects in the burning rate versus pressure laws of double-base propellants, Fig. 3, as well as of active binders, Fig. 12, although in the latter case these effects are much less pronounced.

What is thought to be the mechanism of action of the additives has been presented in references [5,6] by the authors and in reference [12].

It has been found that the active part of the lead salt is the oxide of lead which accumulates above the propellant surface, after the salt has been trapped in the carbon residue layer which can be observed, immersed in the primary flame (the decomposition kinetics of the salt is slower than that of the propellant components and it thus emerges from the surface unchanged). If the propellant (when its heat of explosion increases) or the active binder naturally produces less carbon residue, then the lead salt particles are in large part ejected from the surface and cannot act. This is the case probably when the amount of nitrocellulose is reduced (hot double-base propellants) or almost absent (XLDB binders). In the latter case however the inert polymer leaves some carbonaceous residue. Addition of carbon black is probably favorable because it accumulates on the surface in the naturally produced carbon layer.

It has been found by the authors that PbO reacts preferentially with aldehydes to form carbon and $CO_2$. It has been observed systematically [6] that there is a relation between the amount of carbon residue and the importance of the super-rate observed (for example, depending on the fabrication process: solventless extrusion, powder casting, mixing). It was seen that the primary flame is due to an $NO_2$-aldehyde reaction. But NO starts to react with carbon as well close to the surface, leading to the increase in primary flame temperature of Fig. 9. It is believed that the extra carbon produced in the presence of additives enhances the NO/C reaction (see ref. [12] for more results on this reaction), depositing extra energy in the primary flame (an increase in primary flame temperature is observed in the presence of additives [5]) and resulting in a higher heat flux to the surface, and thus a higher burning rate.

Figure 13 shows surface structures of a cool propellant with a strong super-rate and a corresponding thick carbon residue. In this case, visualization shows that a physical effect occurs in which the secondary luminous flame attaches in streaks to the carbon layer and deposits its high temperature ($\approx 2200$ K as compared to the $\approx 1400$ K of the primary flame) closer to the surface. The abrupt end of the super-rate,

the mesa effect, is believed to be due to the too thick carbon residue being expelled from the surface. At the end of the mesa effect the surface is almost clean of carbon.
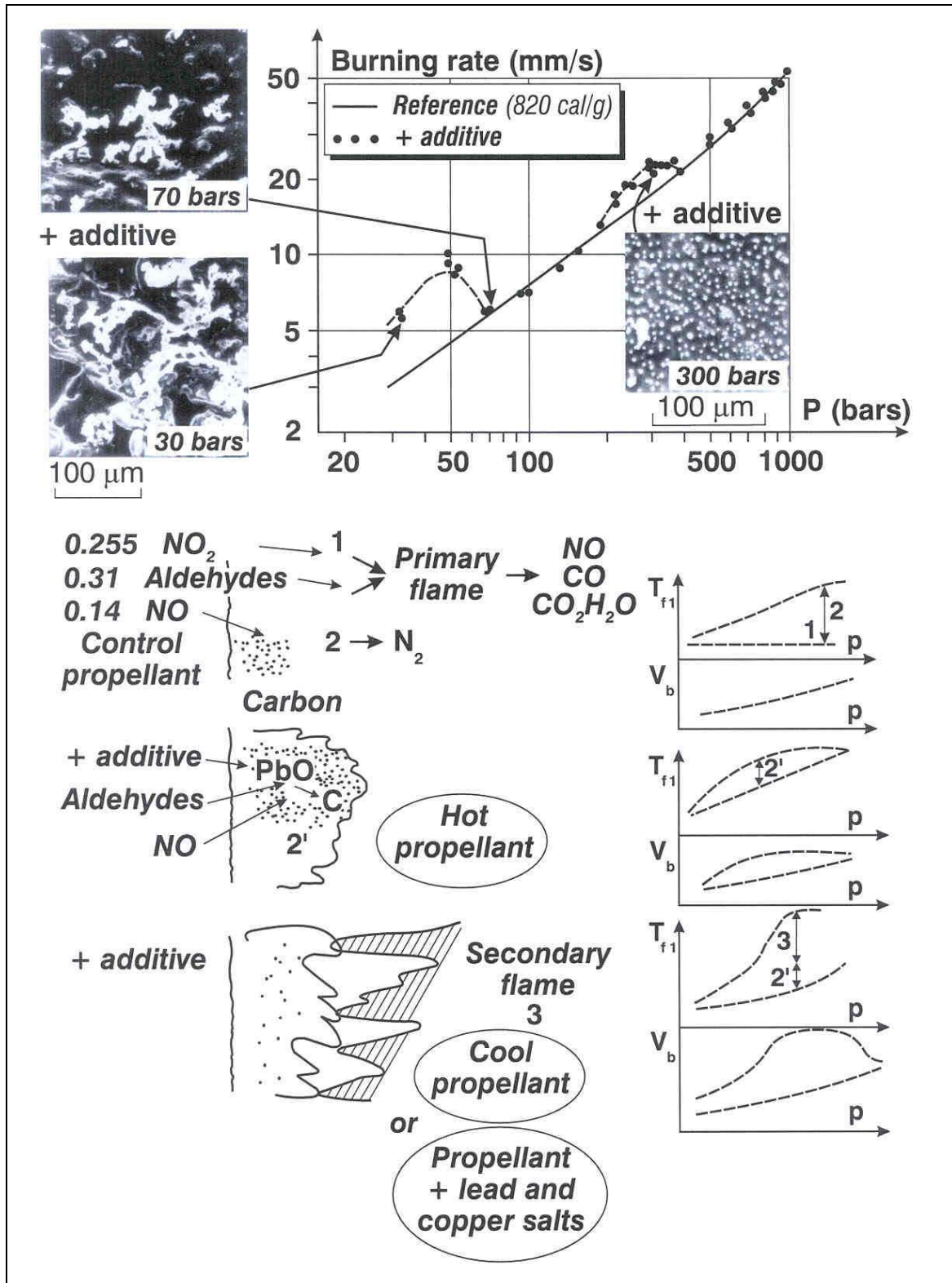


**Figure 13: Super Rate Effects in Double Base Propellants.**

In the case of hot propellants, Fig. 3, the super-rate is probably due only to the chemical effect of the enhanced NO/C reaction. As the pressure increases the secondary flame, where NO will react anyway, merges into the primary flame and progressively the modified propellant is caught up by the reference propellant, a plateau effect thus resulting.

In the high pressure domain when the flame system has reduced to one overall flame, a second super-rate occurs (when only lead salt or oxide is added), see Fig. 13 for the cool propellant and Fig. 3 for a 1250 cal/g propellant. This effect seems to be purely physical, related to the presence of lead oxide particles accumulating and imbedding into the surface, Fig. 13, with for example an enhancement of the thermal conductivity of the flame zone or more probably a flame holding effect (the protruding particles perturb the flow from the surface). At higher pressures and burning rates the thickness of the condensed phase heated zone and reaction layer and flame zone becomes so small that the particles will not attach to the surface or will be too large to perturb the combustion process.

## PYROLYSIS OF INERT BINDERS

A number of books and works has been devoted to the behavior of polymers, whether or not usable as binders, under thermal loads, references [13-17] are examples. Much work has been carried out with thermogravimetric analysis (TGA) or differential scanning calorimetry (DSC), with heating rates at most of the order of 1°C/s. Under linear pyrolysis (for a binder within a solid propellant) the rate of temperature increase is of the order of $10^5$ °C/s. It is far from obvious a priori that the degradation kinetics will remain the same. In Ref. [8] it was attempted to establish that this is indeed the case for a number of polymers.

Although it is hardly a propellant binder, Teflon is an interesting reference polymer. Its degradation kinetics (obtained by TGA) and thermal properties [8] ( $\lambda_p = 6.34 \ 10^{-4}$ cal/cm K s, $\rho_p = 2.1$ g/cm$^3$, $c_p = 0.25$ cal/g K) are indicated on Fig. 14. In order to extrapolate these characteristics to the regime of linear pyrolysis (obtained experimentally by pressing the sample on a hot plate) the procedure of reference [8], also explained in the condensed phase paragraph of the double-base propellants chapter, is applied. In the case of a first order (with respect to the non degraded polymer) reaction, the relation between regression rate and surface temperature is (again, numerical computation shows this relation to be accurate to about 1 %)

$$v_r^2 = ( d_p / \xi_c ) A_c \exp( - \xi_c ) /[ ( - \ln Y_{p,s} ) ( 1 - T_0 / T_s - Q_s / c_p T_s ) + Q_s / c_p T_s ] \qquad (1)$$

$$\xi_c \equiv E_c / R T_s$$

In this relation $Q_s$ is the heat evolved in the condensed phase, in this case endothermic and equal to - 340 cal/g ( $Y_{p,s}$ mass fraction of the remaining polymer at the surface can be set at 0.01 ). It is seen on Fig. 14 that there is a good match between extrapolated law and measurements. These measurements are obtained under various atmospheres, showing no influence of this factor. The conclusion is then reached that the pyrolysis of such a polymer is an irreversible thermal mechanism.
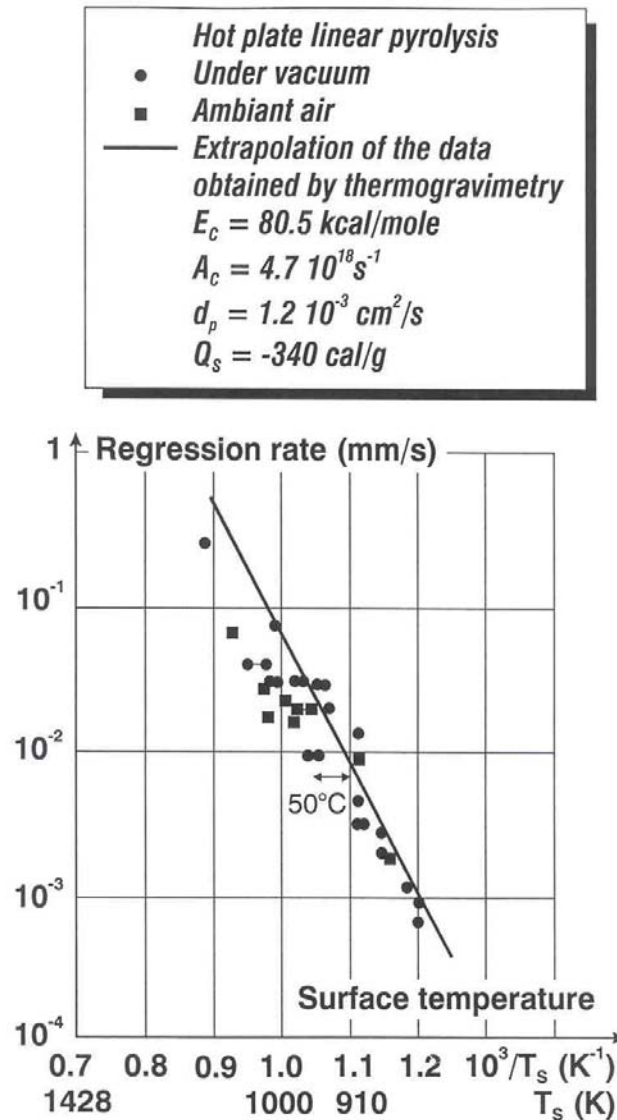
**Figure 14: Linear Pyrolysis and Extrapolation of Thermogravimetric Results (Example of Teflon).**

In the case of an actual, widely used, propellant binder such as hydroxyl terminated polybutadiene (HTPB) the same extrapolation can be made, Fig. 15 (the thermal properties used: $\lambda_p = 3.6 \ 10^{-4}$ cal/cm K s, $\rho_p = 0.92$ g/cm$^3$, $c_p = 0.39$ cal/g K), and compared to the results of Ref. [15], obtained in a hybrid motor, gaseous oxygen upon HTPB, with the surface temperature being measured by infra-red pyrometry (with some dispersion). A measurement obtained by the authors with $CO_2$ laser heating and IR pyrometer is also indicated. The agreement, considering the extent of the extrapolation, is very satisfactory. Further on, the pyrolysis law based on the TGA and DSC kinetics will be considered to apply.
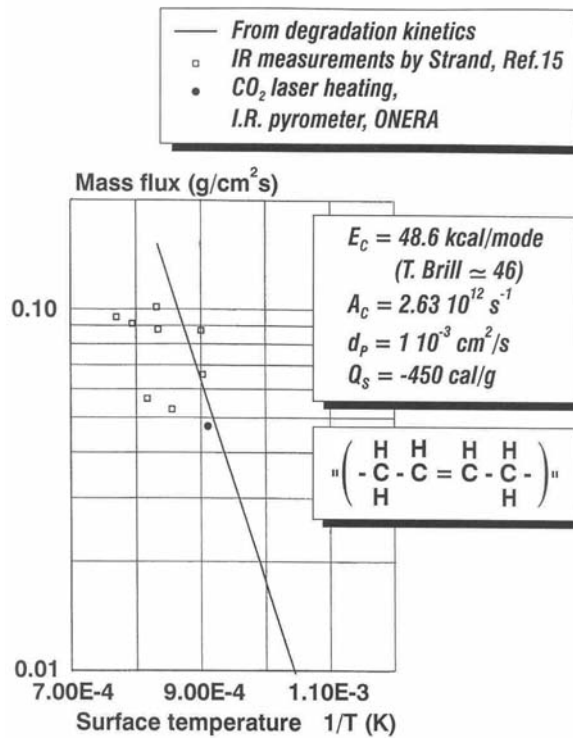
**Figure 15: Pyrolysis Law for HTPB.**

Equation (1) and Fig. 15 indicate how the surface temperature adjusts itself to allow the polymer to degrade into gases when the regression rate changes. Further considerations to better know the binder behavior are the nature of the gases resulting from the pyrolysis and the corresponding heat of degradation.

The heat of ablation of HTPB was measured in Ref. [16] by relating the mass ablated to the radiation heat flux received by a sample. For a regression rate of 0.4 mm/s (and from Fig. 15 $T_s \approx 1060$ K) it is obtained:

$$h_{abl} = c_p ( T_s - T_0 ) - Q_s = 750 \text{ cal/g}$$

$$Q_s = -450 \text{ cal/g}$$

It is found that this value is compatible with the production of mostly $C_4H_6$ as pyrolysis gas. Gas analysis at low temperature [13] reveals a complex set of gases ($\approx 45$ % in mass butadiene, ethylene, propene…) resulting from the degradation of HTPB. If one evaluates the difference in heats of formation between the initial material and butadiene it is found:

$$\Delta h = h^\circ (C_4 H_6 ) - h^\circ (HTPB) = 496 \text{ cal/g} - 5 \text{ cal/g} \approx 490 \text{ cal/g}$$

close to the measured heat of degradation. At high heating rates butadiene is probably the major degradation gas.

## COMBUSTION OF AMMONIUM PERCHLORATE

Ammonium perchlorate (AP), $NH_4 ClO_4$, is a widely used oxidizer and as such has been the object of numerous investigations. References [18 to 22] are a sampling, with [22] giving a detailed list. A view of

the combustion of AP is presented herein attempting to make use as much as possible of the various experimental data available. Due to the large number of works on AP combustion, somewhat contradictory interpretations and corresponding models have been produced. A simplified model is presented, which is considered to represent reasonably the combustion mechanism of AP, although it will not be in agreement with all of the above mentioned interpretations.

## 1.0 Condensed Phase Behavior

The considerations presented previously for the condensed phase of a pyrolysing monopropellant apply to AP. The conduction zone has a thickness

$$e_{cond.} = ( d_p / v_b ) \ln 10^2$$

(with the thermal diffusivity [21] $d_p \approx 1.2 \ 10^{-3} \ cm^2/s$ at an average temperature in the heat wave), thus equal to $\approx 55 \ \mu m$, for a burning rate of 10 mm/s.

**Table 8: Condensed Phase Values for AP [19,21]**

$c_p = 0.31$ cal/g K (orthorhombic phase < 513 K) = 0.365 cal/g K (cubic phase)

$\rho_p = 1.95$ g/cm$^3$ , $d_p = 2.5 \ 10^{-3}$ - $4.55 \ 10^{-6}$ T(°C)cm$^2$/s

Based on observations by scanning electron microscopy after extinction, the idea has been advanced that the self-deflagration of AP, possible only above 20 atm, requires that a large amount of exothermic reaction already takes place in the condensed phase in a thin liquid layer (above a melting temperature estimated at 835 K) [19,20,21,22].

## 2.0 Energetics of the AP Combustion

The model of Ref. [19] is subscribed to in order to describe the combustion of AP alone. The AP undergoes a phase transition at 513 K, melts around 830 K and, in the thin (a few microns) superficial liquid layer thus created, an exothermic reaction, affecting 70 % of the AP, takes place and creates the final combustion gases, $O_2$ in particular. The remaining 30 % of the AP sublime into $NH_3$ and $HClO_4$ which react exothermically in a premixed flame very close to the surface (a few microns), Fig. 16.
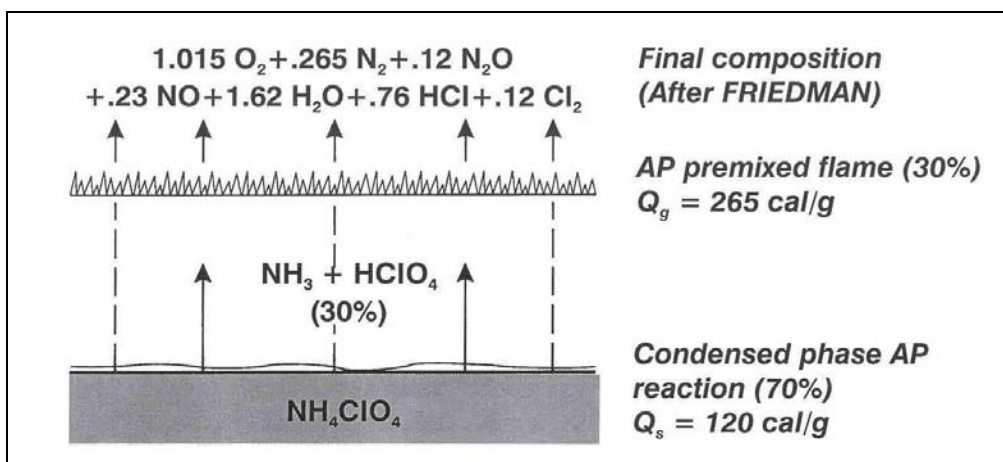


**Figure 16: Autonomous Combustion of Ammonium Perchlorate.**

From the data collected in [19] the change of enthalpy per gram of AP required to heat up the AP to its surface temperature, $T_{S,AP}$, is estimated as

$\Delta h_{H,AP} = 0.31 ( 513 - 293 ) + 21 + 0.365 ( 835 - 513 ) + 60 + 0.328 ( T_{S,AP} - 830 )$,

$= 266 + 0.328 ( T_{S,AP} - 835 )$ cal/g           (1)

where the heat of transition and the heat of liquefaction appear. The exothermic condensed phase degradation involves an enthalpy change of [19]

$\Delta h_{D,AP} \approx - 380$ cal/gram of reacting AP.           (2)

The heat of sublimation is 58 $\forall$ 2 kcal/mole or

$\Delta h_{S,AP} = 476$ to $510$ cal/gram of subliming AP.          (3)

The adiabatic flame temperature for the combustion of AP alone has been estimated in [18] to be $T_{f,AP}^{ad} = 1205$ K, corresponding to the reaction

$NH_4 ClO_4 \rightarrow 0.265 N_2 + 0.12 N_2O + 0.23 NO + 1.62 H_2O + 0.76 HCl + 0.12 Cl_2 + 1.015 O_2$   (4)
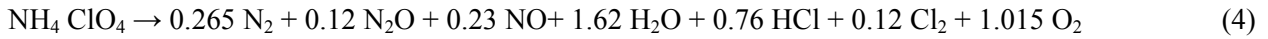
The change of enthalpy, $\Delta h_{C,AP}$, corresponding to the combustion of the sublimed $NH_3$ and $HClO_4$ (to give the combustion products of (4)) is obtained from the equation expressing the conservation of enthalpy between the unreacted AP at initial temperature and the combustion products downstream of the flame:

$0.3 \Delta h_{C,AP} + c_g ( T_{f,AP}^{ad} - T_{S,AP} ) + 0.3 \Delta h_{S,AP} + 0.7 \Delta h_{D,AP} + \Delta h_{H,AP} = 0$     (5)

For $c_g \approx 0.3$, value taken in [19], it is found

$\Delta h_{C,AP} = - 850$ to $- 885$ cal/gram of reacting AP,          (6)

depending on the value adopted for the heat of sublimation, 476 or 510 cal/g, and independently of the value of $T_{S,AP}$ in the range found in [19].

It should be noticed that the value given here for the transformation of the AP into gases (that is $NH_3$ and $HClO_4$ for the subliming 30 % and the combustion gases of (4) for the 70 % reacting in the condensed phase), namely

$- Q_s = 0.3 ( 476$ to $510 ) + 0.7 ( - 380 ) = - 123$ to $- 113$ cal/g of AP,     (7)

is also found in [20], where a model for the combustion of AP similar to that of [19] is adopted. The heat evolved in the condensed phase $Q_s$ ( $> 0$ if exothermic) will be set equal to 120 cal/g.

One last check of consistency can be performed: with the enthalpy of formation of AP at $h^0_{AP} = - 602$ cal/g and that of the combustion products of (4) $h^0_{CP} = - 877$ cal/g, an overall energy balance between initial AP and combustion products is:

$c_g T_{f,AP}^{ad} + h^0_{CP} = c_{ortho} T_0 + h^0_{AP}$           (8)

resulting in $T_{f,AP}^{ad} = 1215$ K, close enough to the previous value.

## 3.0 Surface Pyrolysis of AP

Attempts to measure the surface temperature give values between 670 and 973 K. These results, obtained either by using thermocouples imbedded in the AP pellet, or by measuring the radiation emitted by the surface, are always associated with some uncertainty due to the operating methods. In effect, the large size of the thermocouples, in relation to the temperature gradients encountered, favors errors; further, the measurement represents an averaging of surrounding conditions. The temperatures thus obtained are therefore probably somewhat lower than in reality. In the case of experiments using an optical technique, the temperature is deduced from measuring the radiation emitted by the surface and transmitted through the gaseous layer. The disturbance caused by the radiation of the gases and the screening action of the flame limits the application of this method to 60 atm. That is why the original technique suggested by Seleznev [23], carried out by using a sapphire light guide inserted in the solid substance and by reading the infra-red emission in the direction of the condensed phase, has the considerable advantage of providing a direct measurement of the radiation emitted by the surface, without any hot gases and the reaction of the flame being interposed. Its application can therefore be extended to high pressures and the measurements appear to be more convincing. These results enable to determine the AP pyrolysis law.

Further, estimates of the AP melting temperature are mentioned by a number of authors; the values suggested vary from 715 to 865 ± 20 K and are useful in interpreting the extinction phenomenon at low pressure.

The pyrolysis law of the AP is written as:

$$m_{AP} = \rho_{AP}\, v_{b,AP} = A_{S,AP} \exp( - E_{S,AP} / R\, T_{S,AP} ) \qquad (9)$$

The parameters characterizing the pyrolysis law are determined so as to obtain a good agreement between the rates and the surface temperatures measured by Seleznev [23] (Fig. 17). The activation energy obtained is 20 kcal/mole, a figure compatible with the various estimates encountered. The measurement of the surface temperature made at 40 atm is the only one which deviates from that computed by the pyrolysis law used. On the other hand, for the critical rate of 0.27 cm/s obtained at 20 atm (AP combustion pressure limit), this law allows for a surface temperature of 830 K, corresponding to the assumed AP melting temperature [19].
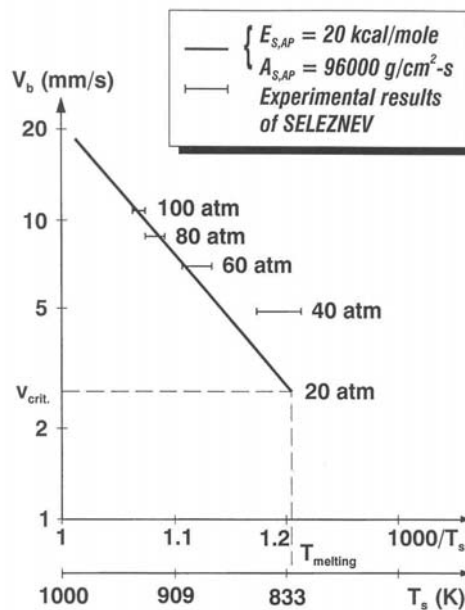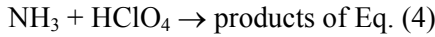


**Figure 17: Pyrolysis Law for Ammonium Perchlorate.**

## 4.0    Flame Structure of the AP Combustion

The approach of [19] considers 14 different reactions to describe the flame zone of the AP, involving 30 % of the material sublimed into $NH_3$ and $HClO_4$. An overall second order reaction is then obtained

$NH_3 + HClO_4 \rightarrow$ products of Eq. (4)

with an activation energy of $E_{g,AP}$ = 15 kcal/mole.

A simplified model is constructed like the one used in the chapter on the double base flame. The temperature profile is approximated as

$$( T_{f,AP}{}^{ad} - T ) / ( T_{f,AP}{}^{ad} - T_{S,AP} ) = \exp( - 3 x / x_f ) \tag{10}$$

with the boundary condition

$$q_s \equiv \lambda_{g.s} \, dT / dx|_s = m_{AP} \, Q_c \tag{11}$$

$$Q_c = \Delta h_{H,AP} - Q_s$$

$Q_c$ is the heat required to bring the AP from $T_0$ to gases at the surface, see Eqs. (1) and (7).

Combining (10) and (11) results in

$$m_{AP} = 3 \, \lambda_{g,s} \, ( T_{f,AP}{}^{ad} - T_{S,AP} ) / x_f \, Q_c \tag{12}$$

Summation of the energy equation from $T_{s,AP}$, x = o, to $x_f$ yields, after using Eqs. (11) and (12) and Eq. (5) written as

$$Q_g + c_g ( T_{f,AP}{}^{ad} - T_{S,AP} ) + Q_c = 0$$

$$m_{AP} = [ \, 3 <\omega_g> \lambda_{g,s} \, ( T_{f,AP}{}^{ad} - T_{S,AP} ) / Q_c \, ]^{1/2} \tag{13}$$

In this equation the average reaction rate is written as

$$3 <\omega_g> = p^2 \, A_{g,AP} \exp( - E_{g,AP} / R \, T_{f,AP}{}^{ad} ) \tag{14}$$

expressing a second order overall rate. The burning rate is then found to follow pressure with an exponent close to 1. Table 9 indicates various values for AP combustion.

**Table 9: Values Considered as Representative for the AP Flame Zone**

| | |
|---|---|
| $\rho_{AP}$ | = 1.95 g/cm$^3$ |
| $E_{S,AP}$ | = 20 kcal/mole |
| $A_{S,AP}$ | = 96000 g/cm$^2$ s |
| $E_{g,AP}$ | = 15 kcal/mole |
| $A_{g,AP}$ | = 700 g/cm$^3$ s atm$^2$ |
| $\gamma$ | = 30 % |
| $c_g$ | = 0.3 cal/g K |
| $\lambda_g$ | = 1.9 10$^{-4}$ cal/cm s K |

Taking into account the various values given, it is obtained for $v_b$ = 10 mm/s ( $T_{S,AP} \approx 925$ K ) the flame stand-off distance, Eq. (12), ( $Q_c$ = 175 cal/g ), $x_f \approx 5$ μm, the height to reach $T_f$ within 5 %.

The only input data which is not defined from outside considerations is the pre-exponential factor $A_{g,AP}$ used as a floating parameter for the model. Various numerical values associated with the input parameters of the model are brought together in the above table. Just by the choice of the prefactor $A_{g,AP}$ adjusted at 700 g/cm$^3$ s atm$^2$, the model satisfactorily reproduces variations in the AP burning rate due to pressure as well as due to the change in the initial temperature of the product. Figure 18 provides a comparison of computed rate curves with experimental points [21].
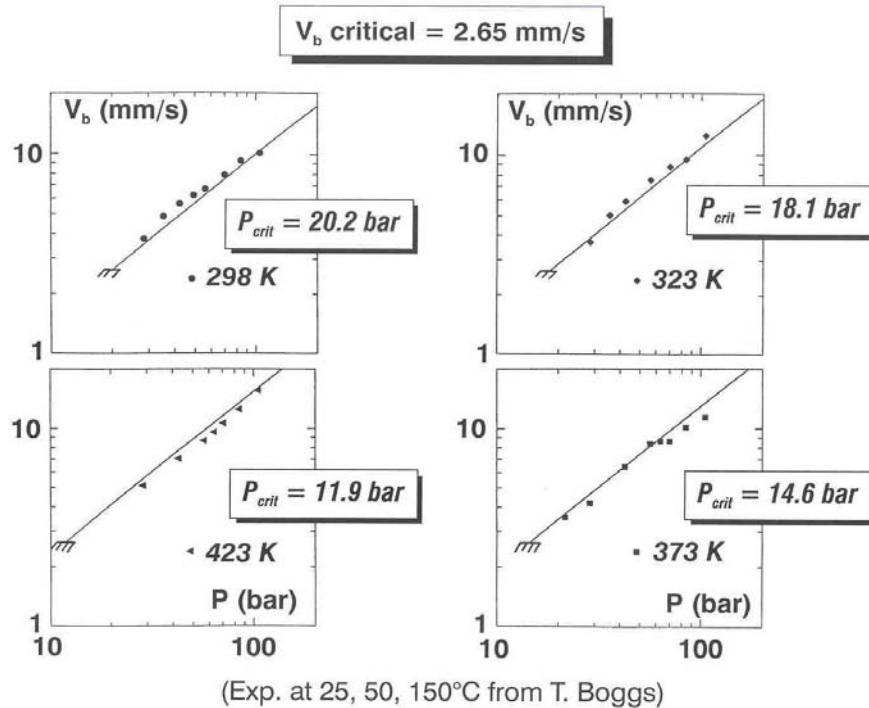


**Figure 18: Burning Rate of Ammonium Perchlorate at Different Initial Temperatures.**

At sufficiently high pressures, the energy transmitted from the flame toward the surface, to which must be added the effect of the superficial exothermic reactions, maintains the surface temperature above the AP melting point. When the pressure falls, the premixed flame moves away and the surface temperature can then drop below the limiting value, thus causing the disappearance of the liquid surface layer which was enabling the exothermic reactions to occur. The energy from the flame is then much too small to maintain a pyrolysis which has become strongly endothermic and AP no longer burns. This minimum pressure, beyond which the combustion cannot propagate itself, sets the pressure limit for AP self-degradation.

On the basis of this hypothesis, the combustion pressure limit is reached when the surface temperature is equal to the AP melting temperature. It is interesting to use the model in order to follow the variation of the computed limiting pressure with the initial temperature. At atmospheric temperature, the combustion limit is 20 atm, in agreement with experimental results. The critical rate of 0.27 cm/s and the surface temperature of 830 K, representing the AP melting temperature, corresponds to it. The computation method consists, for the initial temperature varying between 0 and 200°C, in finding for what pressure the surface temperature is equal to 830 K. A comparison between the computed and experimental pressure limits is very good, Fig. 19, and confirms the soundness of the hypothesis following which AP only burns if the surface temperature exceeds its melting temperature.
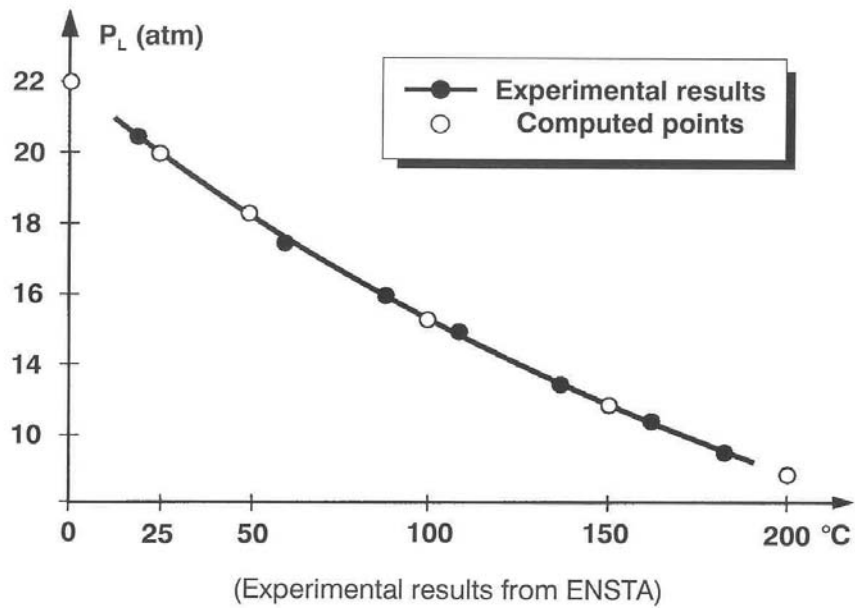
**Figure 19: Limiting Pressure for Combustion of Ammonium Perchlorate.**

One further set of results is presented. Questions have been raised about the combustion of AP at high pressures, above about 100 atm, with many conflicting results. Measurements of burning rates on carefully inhibited samples are presented on Fig. 20. It is concluded that no strong change of combustion regime is observed. The model based on the above presented hypothesis seem to follow quite well the results to high pressures.
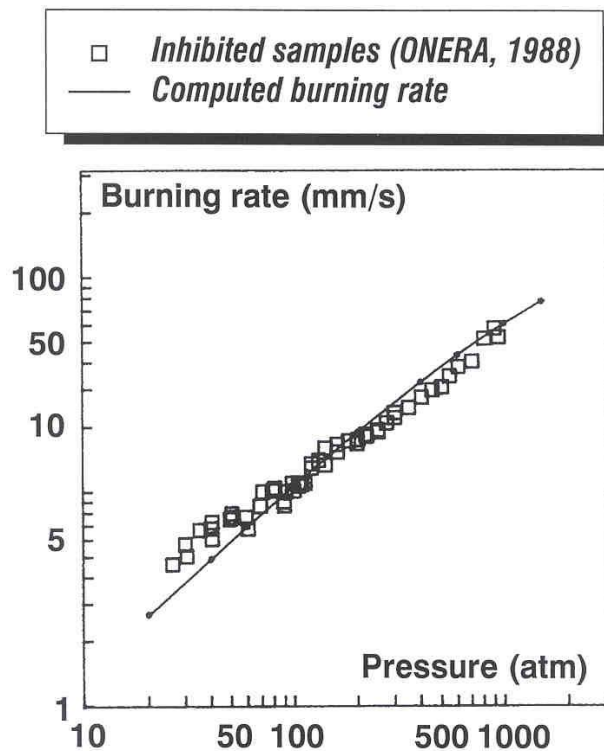


**Figure 20: Burning Rate of Ammonium Perchlorate at High Pressures.**

## COMBUSTION OF HMX

The combustion of HMX, which has balanced oxidizing and combustible elements (to reach CO, $H_2O$ and $N_2$) and a combustion temperature of 3280 K, is controlled by processes in the condensed phase as well as in the flame zone. Information about these processes is to be found in references [24 to 31] (also [21]).
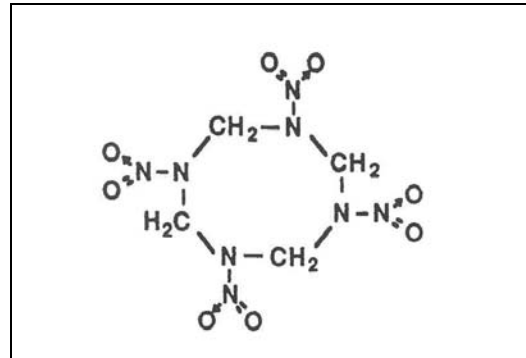
**Figure 21: Chemical Structure of HMX.**

### 1.0     Condensed Phase Processes

The kinetics of the decomposition of HMX can be obtained by differential thermal analysis [24,29]. A fairly extensive review is given in Ref. [25]. Results obtained around the (assumed) melting temperature of 556 K are indicated on Fig. 22, with the kinetics extracted for a reaction order of 1 (refer to [29] for the method utilized). The condensed phase properties considered to be representative are indicated below.
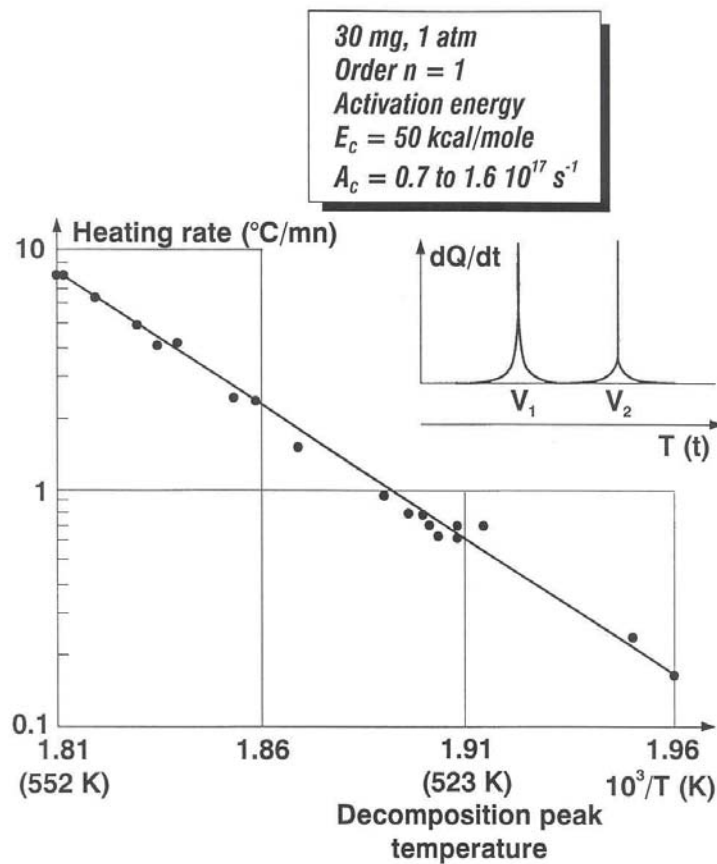
**Figure 22: Differential Thermal Analysis of HMX Decomposition.**

**Table 10: Condensed Phase Properties (Average in the Thermal Wave) for HMX [31]**

$\rho_p = 1.9$ g/cm$^3$, $c_p = 0.33$ cal/g K

$d_p / \lambda_p / \rho_p c_p = 1 \ 10^{-3}$ cm$^2$/s
(also found from thermocouple traverses)

$\lambda_p = 6.3 \ 10^{-4}$ cal/cm s K

Another technique to obtain the decomposition kinetics, at somewhat higher temperatures, is through ignition tests, by exposing the sample to a given surface heat flux and detecting the delay for the first exothermic ignition reaction (rapid deviation of the surface temperature from that of an inert material). The results are seen on Fig. 23 and confirm those obtained by DTA (the first method gives a good estimate of the activation energy, whereas the ignition experiments are better for estimating the prefactor). All these results correspond to an irreversible thermal decomposition of the HMX bonds with no influence of the pressure.
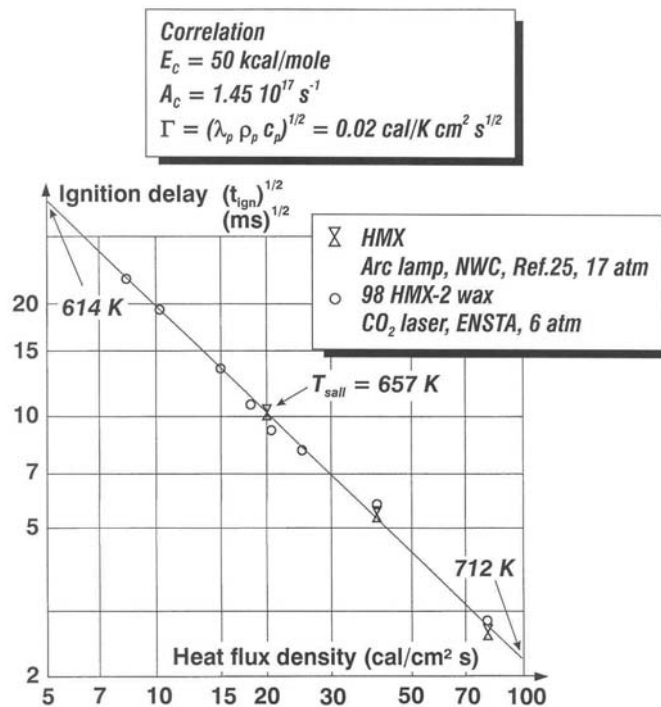


**Figure 23: Ignition of HMX.**

Finally, the investigation of the condensed phase processes under combustion is carried out by determining the temperature profile through the combustion wave by use of micro-thermocouples. As was seen on several occasions the thermal wave thickness is:

$$e_{cond.} = \ln 10^2 \ d_p / v_b \qquad (1)$$

that is, in the case of Fig. 24, $e_{cond.} \approx 220$ μm. The thermocouple junction has to be very small, in the present case 5 μm platinum wires are welded end to end by electric discharge with the junction at about this size. A measurement of the thermal diffusivity is also obtained, close to that indicated in Table 10.

The relationship between the surface temperature (obtained from measurements such as that of Fig. 24) and the burning rate is displayed on Fig. 25. Scatter of the measurements is hard to avoid (about 50 K). Also indicated are thermocouple results from reference [28]. The pyrolysis law is also established from the decomposition kinetics obtained by DTA and by ignition experiments, making use of the approach mentioned for double-base propellants as well as for inert binders, according to which [8], for a first order reaction,

$$v_b{}^2 = ( d_p / \xi_c ) \, A_c \exp( - \xi_c ) / [( - \ln Y_{p,s} ) ( 1 - T_0 / T_s - Q_s / c_p T_s ) + Q_s / c_p T_s ] \tag{2}$$

$\xi_c \equiv E_c / R \, T_s$ and $Q_s$ is the heat evolved in the superficial reaction layer of the HMX; its value will be seen next. The amount of HMX at the surface $Y_{p,s}$ is set at 0.01. It is seen that there is continuity between the decomposition (thermal breaking of the chemical bonds, with probably no participation of the vaporization of the HMX) under DTA conditions, $\approx 550$ K, for ignition, from 600 to 700 K, and under combustion, up to 900 K. This conclusion on such a continuity, which is not a priori guaranteed, was also reached for double-base propellants (as well as for various binders).
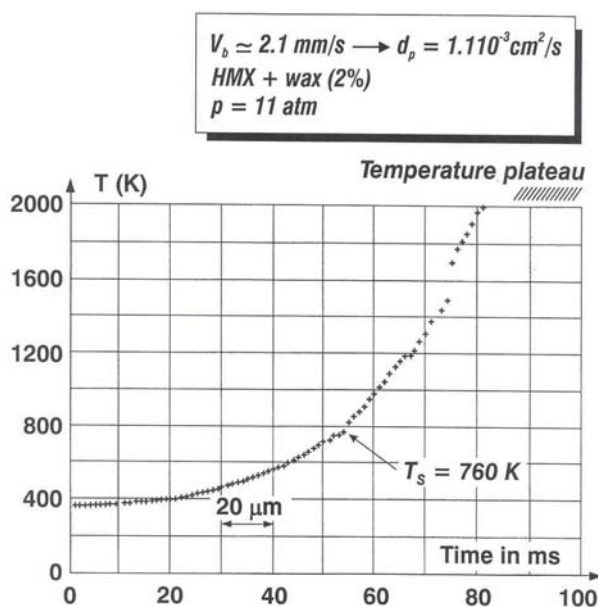


**Figure 24: Temperature Profile, Under Combustion, in HMX by Thermocouple.**
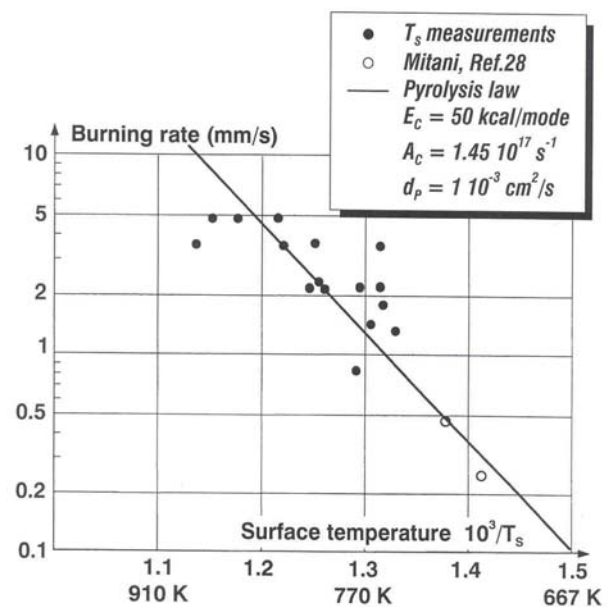


**Figure 25: Pyrolysis Law for HMX.**

From the temperature profiles, as on Fig. 24, the heat evolved in the condensed phase can be evaluated by use of the relation:

$$\lambda_g \, dT / dx|_s = \rho_p v_b [ c_g T_s - c_p T_o - Q_s ] \tag{3}$$

with $Q_s > 0$ if exothermic. The results of Fig. 26 show that indeed the transformation of HMX into gases is exothermic. The energy absorbed by the breaking of the HMX bonds is more than compensated by exothermic reactions taking place in the superficial degradation layer, probably between $NO_2$ and HCHO (see further for the identification of these gases). This mechanism was already observed for double-base propellants.
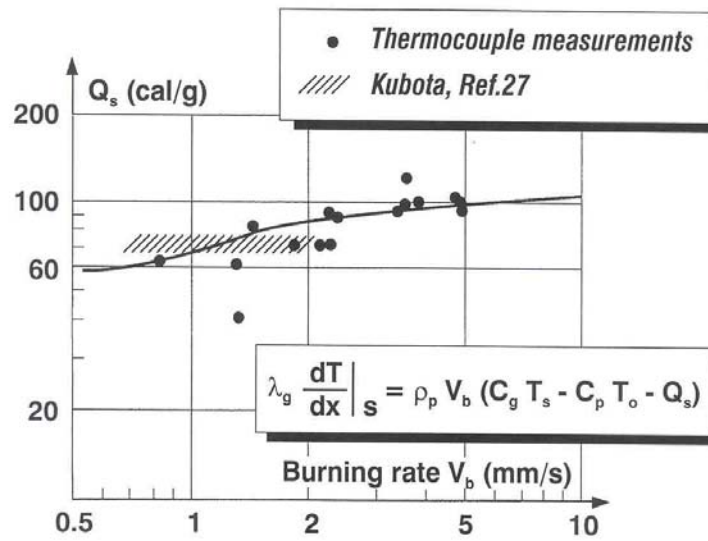
**Figure 26: Heat Evolved in the Condensed Phase of HMX.**

Experiments have been performed [7] by maintaining the linear regression (at about 1 mm/s) of HMX samples with an external heat flux (radiation or contact with a heated plate), under vacuum so as to avoid any gas flame. The sampled gases are then analyzed by mass spectrometry. The following table indicates the results.

**Table 11: Gases Evolved from the Surface of HMX (Mass Fractions [7])**

| $NO_2$ | NO | $N_2O$ | $N_2$ | $CO_2$ | CO | $H_2O$ | $H_2$ | HCHO | HCN |
|---|---|---|---|---|---|---|---|---|---|
| 22.2 | 17.5 | 19.1 | 3 | 1.4 | 1.6 | 3.7 | 0.1 | 14.1 | 16.8 |
| $\approx 59\ \%$ | | | $\approx 10\ \%$ | | | | $\approx 31\ \%$ | | |

It is seen that the initial degradation produces probably $NO_2$ and $N_2O$ in similar amounts and HCHO and HCN. See also for such conclusions reference [32]. Exothermic reactions involving $NO_2$ occur in the superficial degradation layer to give a large amount of NO. Results in rough agreement with those of the above table have also been obtained in Ref. [33] with an infra-red analysis technique.

## 2.0   Gas Phase Behavior

The production from the condensed phase of HMX of several oxidizing gases, $NO_2$, $N_2O$ and NO, can create a two-stage flame. This was seen to be the case for double-base propellants for which $NO_2$ and NO are created in the condensed phase: the primary flame involves $NO_2$ and the secondary flame NO; above $\approx 200$ atm the two flames merge into one. In the case of HMX, observation at pressures around 1 atm reveals the existence of a dark induction zone and a detached luminous flame, similar to those of double-base propellants. Also the micro-thermocouple traverses below about 10 atm, such as in Fig. 24, show a plateau in the temperature profile at about 2000 K, much below the final temperature of 3280 K.

The burning rate of HMX, as single crystals or as pressed samples, obtained in Ref. [25] is shown on Fig. 27. The evolution of this burning rate with pressure shows that around 20 atm a pressure exponent of

about 1 is attained, revealing that the staged flame has collapsed into one (as in the case of double-base propellants above about 200 atm).
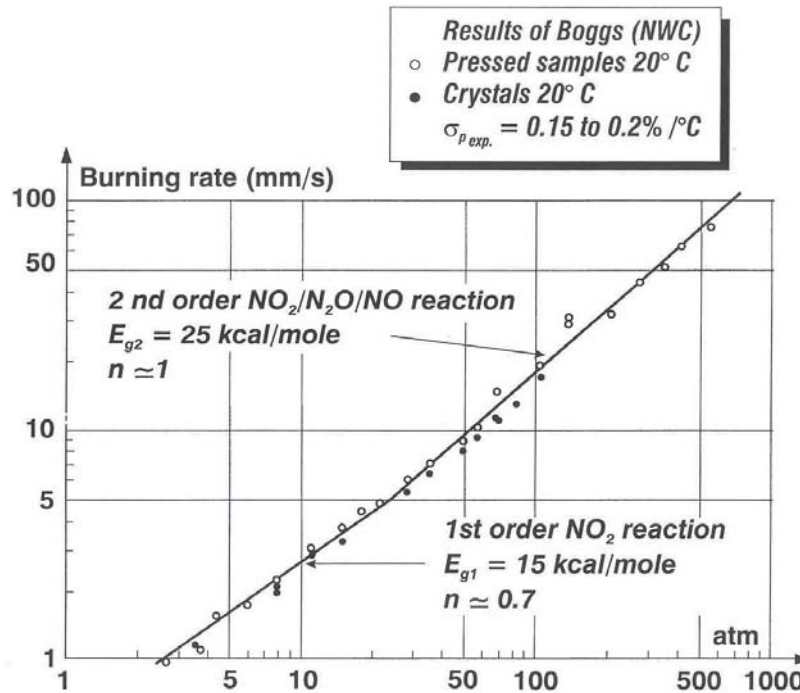


**Figure 27: Burning Rate of HMX.**

It was seen in the chapter on double-base propellants that in the case of a distributed flame an approximation for the temperature profile is:

$$( T_f - T ) / ( T_f - T_s ) = \exp( - 3 \, x / x_f ) , \qquad x_f = 3 \, \lambda_{g,s} ( T_f - T_s ) / m \, Q_c , \qquad Q_c = c_g \, T_s - c_p \, T_0 - Q_s \qquad (4)$$

(at $v_b$ = 10 mm/s this will give $x_f$ = 48 μm, the height to reach $T_f$ within 5 %) and the burning rate becomes:

$$m = \rho_p \, v_b = [ \, 3 <\omega_g> \lambda_{g,s} ( T_f - T_s ) / Q_c \, ]^{1/2} \qquad (5)$$

With $<\omega_g>$ the summed reaction rate through the flame zone. More complete descriptions of the flame zone can be found in references [29,30], the conclusions of which are essentially those which can be extracted from the above simplified approach.

**Table 12: Values Considered to be Representative of the Gas Phase of HMX**

$$c_g = 0.35 \text{ cal/g K}, \quad \lambda_g = 1.25 \; 10^{-4} \; ( \, T \, / \, 700 \, )^{0.7} \text{ cal/cm s K}$$

At low pressures the primary flame, involving $NO_2$ in a first order reaction, controls the burning rate, with, according to Eq. (5), a pressure exponent around 0.5. At higher pressures the collapsed flame is probably dominated by a second order reaction involving NO and $N_2O$, with a pressure exponent close to 1.

# COMBUSTION OF RDX

RDX has a structure similar to that of HMX. The present authors have not considered this component very much, as opposed to HMX. The information comes mostly from the work of Ref. [34].
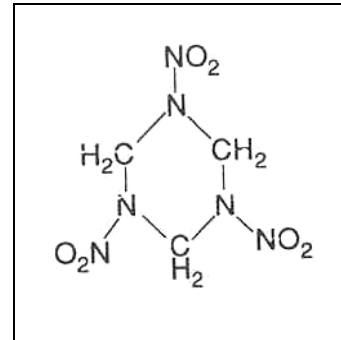


**Figure 28: Chemical Structure of RDX.**

It has been seen that HMX has a behavior somewhat similar to that of a DB propellant, due to the fact that it creates gases which can produce primary and secondary flames, see Table 11. In this case, a very simplified model, based on overall kinetics, shows that the secondary flame dominates the burning rate as soon as 20 to 30 atm (for DB propellants this occurs above 100 atm), in such a way that there is no possibility of creating a super-rate effect (and the accompanying plateau). A much more elaborate model, see Fig. 30, has been presented by Yang et al [34] for RDX. This model takes into account the two condensed phase decomposition paths suggested by Brill, but also incorporates a large amount of evaporation of the RDX (it has to be noted that in the case of HMX, referring to Figs. 22 to 25, the conclusion is reached that the condensed phase process under combustion corresponds to complete decomposition, as observed under DSC-DTA conditions, and thus with no contribution of evaporation). In the melt layer of the RDX (melting temperature supposed at about 470 K) the products of the first decomposition start reacting, much as was seen for double base propellants and for HMX, this being manifested by the gas composition obtained at the surface, see Fig. 30. At the surface, with a temperature depicted on Fig. 29, an important void fraction is computed, corresponding to the amount of RDX which has decomposed in the condensed phase.
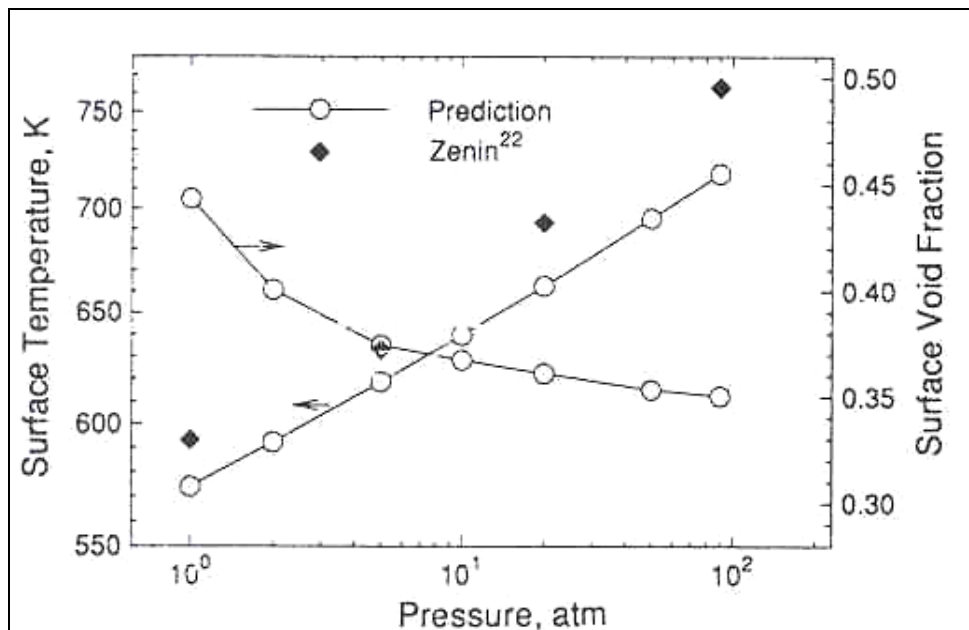


**Figure 29: Conditions at the Surface of RDX [34].**

From T. Brill

$$RDX_{(c)} \xrightarrow{k_1} 3CH_2O + 3N_2O \qquad (R1)$$

$$RDX_{(c)} \xrightarrow{k_2} 3HCN + \tfrac{3}{2}NO + \tfrac{3}{2}NO_2 + \tfrac{3}{2}H_2O \qquad (R2)$$
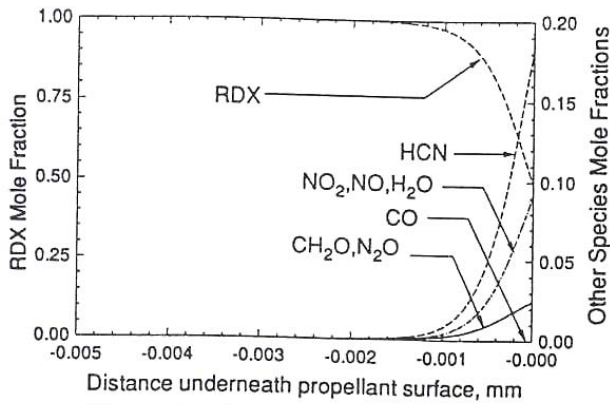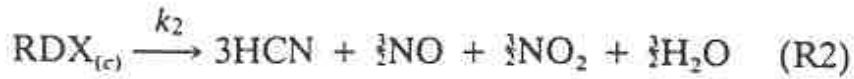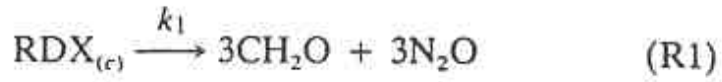
Close-up view of temperature and species-concentration profiles in subsurface region at 90 atm.
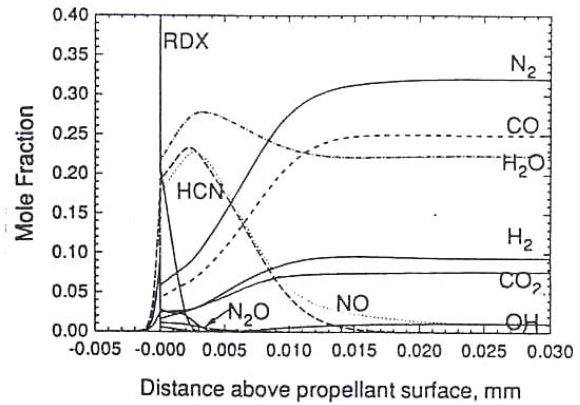
Distributions of temperature and major species concentrations of self-sustained RDX combustion at 90 atm.
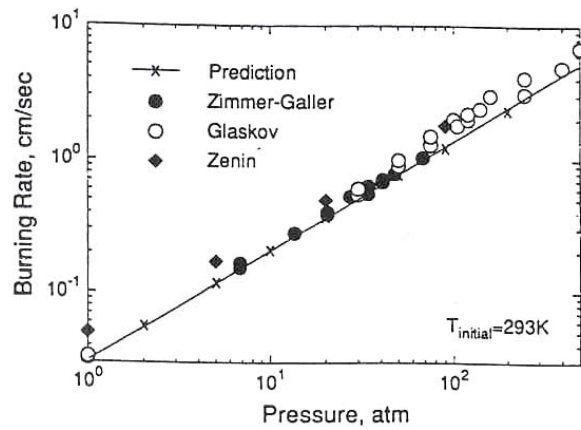
Effect of pressure on strand burning rate of RDX monopropellant.

**Figure 30: Modeling of RDX Combustion [34].**

# COMBUSTION OF CL20 (HNIW)

A new caged nitramine called either CL20 or HNIW (hexaaza hexanitro isowurtzitane) has appeared in the last few years (1987). Because of its high energy content it is envisioned that when combined to an energetic binder, as compared to HMX or RDX compositions, it will be better performing in terms of impulsion and level of burning rate, with smokeless properties maintained and similar safety behavior, Ref. [35].
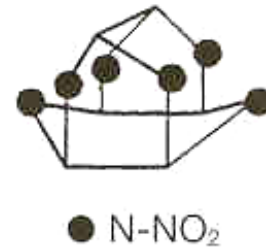


**Figure 31: Chemical Structure of HNIW.**

Differential scanning calorimetry (DSC) and thermogravimetry (TG) contribute to the thermal knowledge of the components to get specific heat, degradation steps and kinetic constants of the material. Helium pycnometry and a thermal diffusivity set-up, at ambient temperature and atmospheric pressure, give the other physical properties. Table 13 brings together the results obtained by these methods. See Ref. [36] for full details.

**Table 13: Thermal and Physical Properties of HNIW**

| Properties | Symbols | SI units | HNIW |
|---|---|---|---|
| Specific heat | $c_p$ | $[J.kg^{-1}K^{-1}]$ | 1004 ($\pm$ 13 %) |
| Specific mass (density) | $\rho$ | $[kg.m^{-3}]$ | 1980 ($\pm$ 1 %) |
| Thermal diffusivity | $d_{th}$ | $[m^2.s^{-1}]$ | $0.457*10^{-7}$ ($\pm$ 6 %) |
| Thermal conductivity | $\lambda=\rho*c_p*d_{th}$ | $[J.m^{-1}K^{-1}s^{-1}]$ | 0.068 |
| Activation energy | $E_A$ | $[J.mole^{-1}]$ | 224000 ($\pm$ 4.5 %) |
| Frequency factor | $k_0$ or A | $[s^{-1}]$ | If n*=1 $\Rightarrow$ $5*10^{+19}$ |

*n is the reaction order.

The gases evolved from the condensed phase are obtained, as was done for the double base propellants and HMX, with the linear pyrolysis technique under vacuum so as to avoid the gas flame, the regression rate is about 0.5 mm/s.
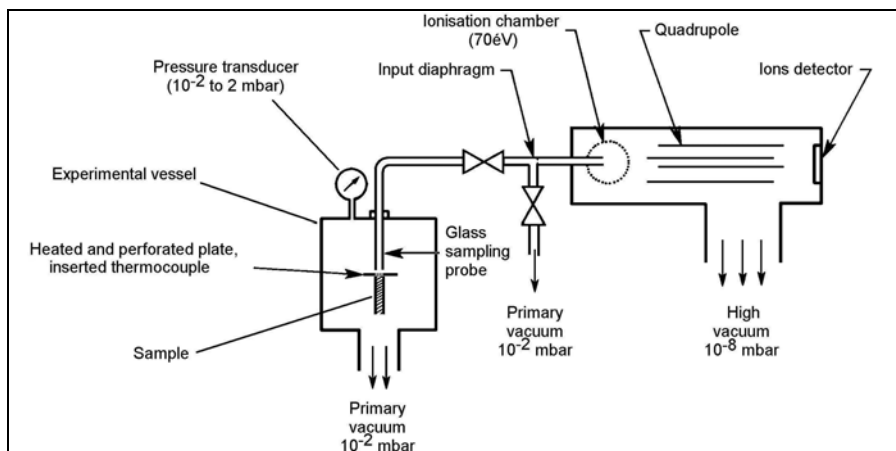


**Figure 32: Set-Up for the Linear Pyrolysis.**

Table 14 shows the results. $NO_2$ and NO are present in large amount, as for HMX, $N_2O$ is in much smaller amount. This gas composition should lead in principle to a staged flame, but due to the high temperature reached at the end of the primary flame, which involves a high mass fraction of $NO_2$, it is likely that the two flames will collapse into one even faster than for HMX.

**Table 14: Molar and Mass Fractions of the Products from HNIW Linear Pyrolysis**

| Species | $NO_2$ | $CO_2$ | $N_2O$ | HNCO | HCHO | NO | HCN | $H_2O$ | CO | $N_2$ | Solid residue 1 | Solid residue 2 |
|---|---|---|---|---|---|---|---|---|---|---|---|---|
| Molar fraction | 0.61 | 0.017 | 0.024 | 0.010 | 0.017 | 0.142 | 0.046 | 0.049 | 0.044 | 0.029 | | |
| Mass fraction | 0.71 | 0.018 | 0.027 | 0.011 | 0.013 | 0.107 | 0.031 | 0.022 | 0.031 | 0.020 | | |
| Mass fraction Gas +Res. | 0.59 | 0.015 | 0.023 | 0.009 | 0.0109 | 0.0899 | 0.026 | 0.0185 | 0.0259 | 0.017 | 0.11 | 0.05 |

Figure 33 gives burning rate measurements for HNIW, on a "strand burner", but it has been now given up in favor of a closed autopressurizable bomb with an ultrasonic measurement technique. This has the advantage of giving the evolution of the burning rate versus pressure with a very low number of experiments, by excursion of a pressure shift during the experiment. Results on ADN, ammonium dinitramide, $NH_4$-N-$(NO_2)_2$, another new oxidizer of interest, is also indicated. These results are in good agreement with most of the literature.
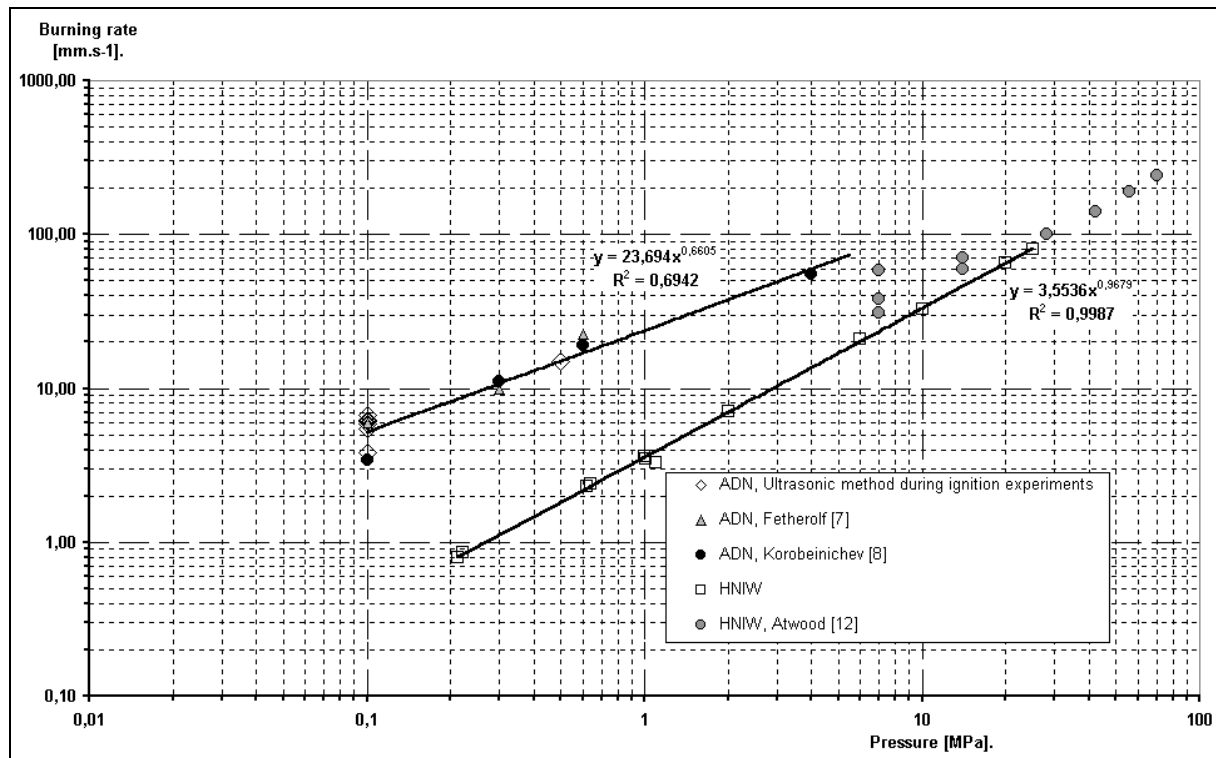


**Figure 33: Burning Rate of HNIW (and ADN).**

Small thermocouples imbedded in the burning sample allow to measure the temperature profile, Fig. 34, the surface temperature, in the vicinity of 800 K, Fig. 36, and from the heat balance at the surface an evaluation of the heat evolved in the condensed phase is obtained, Fig. 35, it is exothermic around 400 kJ / kg, about 100 cal/g similar to the value observed for HMX.
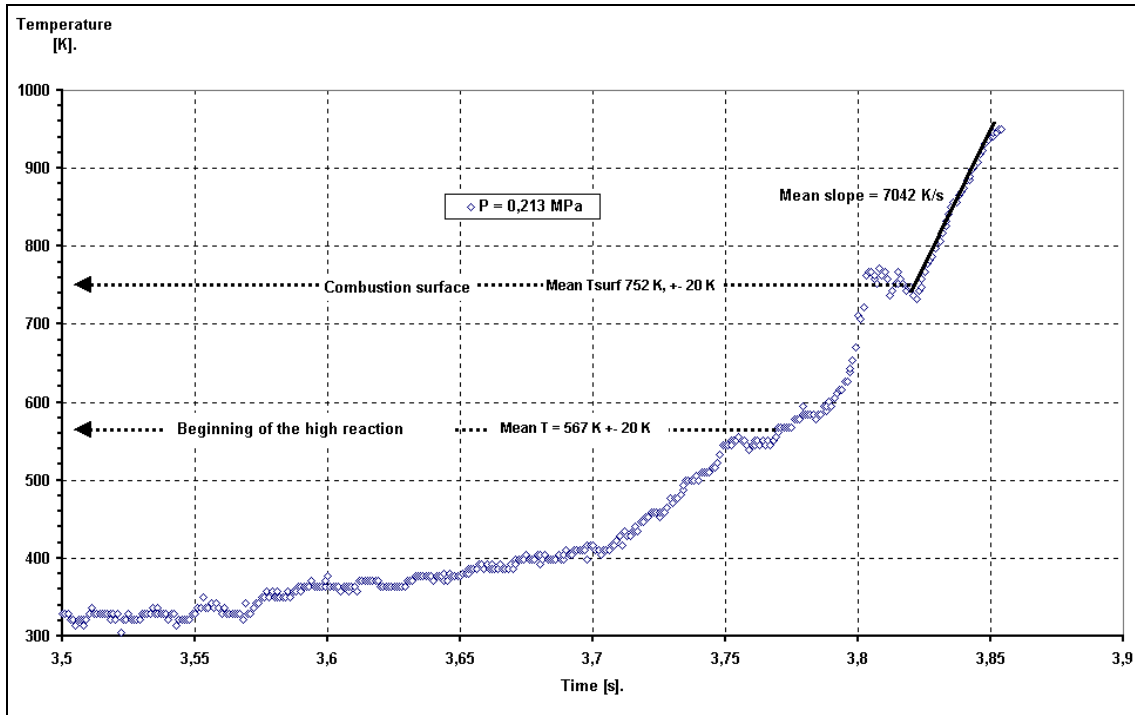


**Figure 34: Temperature Profile in Burning HNIW.**
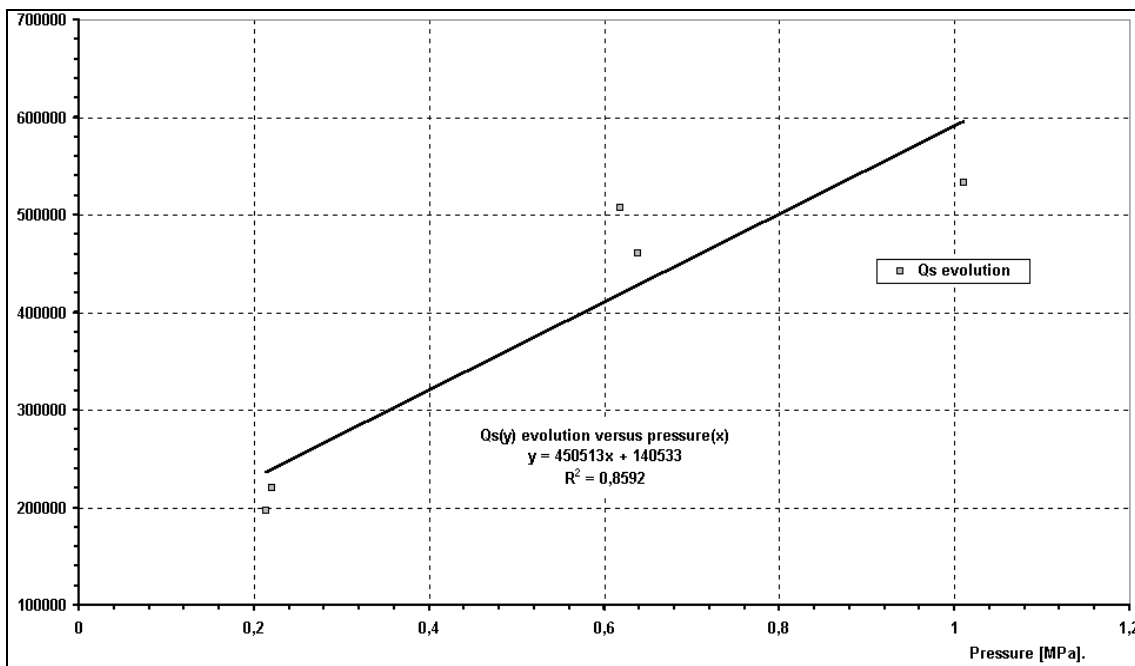


**Figure 35: Energy Released in the Condensed Phase of HNIW, J / kg.**
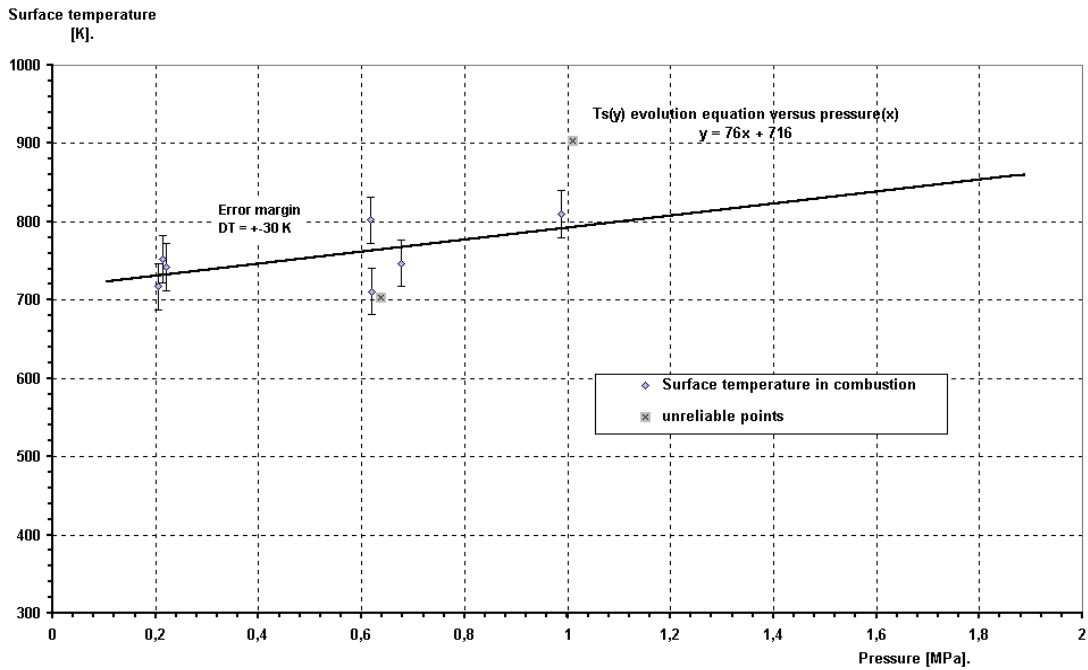
**Figure 36: Surface Temperature of HNIW.**

Figure 37 compares measured surface temperatures and the correlation obtained from the extrapolation (according to the method exposed for HMX) of the condensed phase decomposition kinetics. Taking into account a large uncertainty related to the size of the thermocouple, the agreement is appropriate and found to mean that the decomposition of the HNIW into gases is a purely thermal phenomenon, as measured by DSC, not affected by pressure and with no evaporation entering in the process.
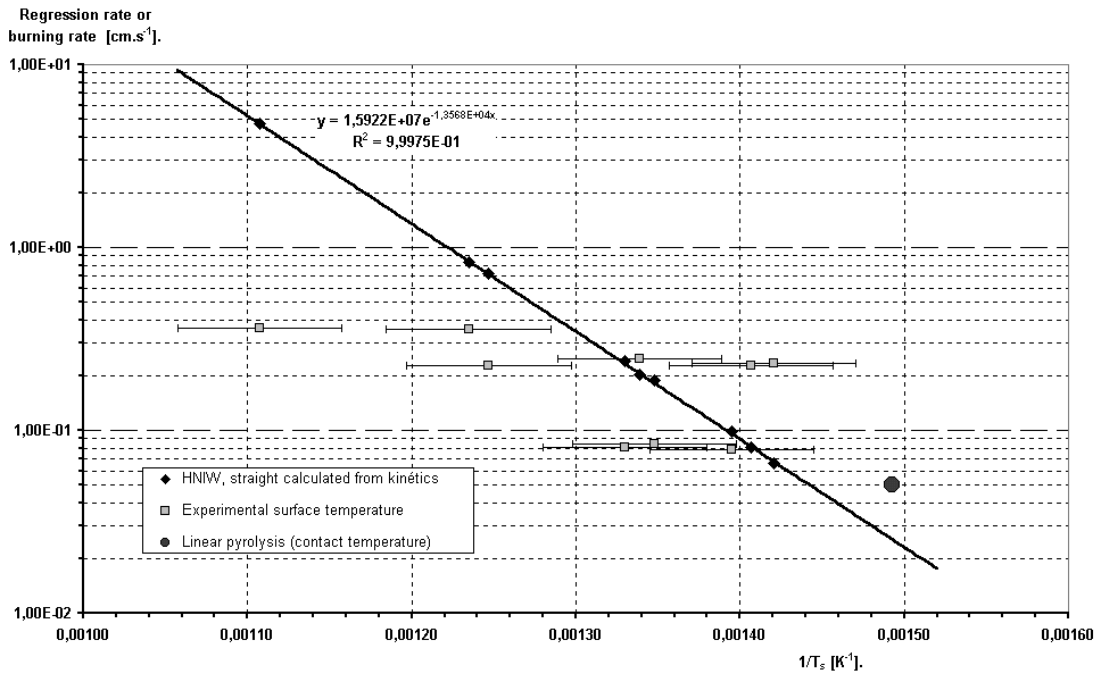


**Figure 37: Surface Temperature vs Regression Rate Correlation.**

# COMBUSTION OF COMPOSITE PROPELLANTS

This chapter is devoted to the description of propellants made of an oxidizer, ammonium perchlorate or HMX, RDX, HNIW, and a binder, inert such as polybutadiene or active, a mixture of a liquid nitrate and a polymer. For the sake of clarity only these two categories will be considered, the main point being, as was said in the introduction, to attempt to improve the understanding of the combustion of propellants rather than to present an extensive catalog of results.

## 1.0    Comparative Picture of Composite Propellants Combustion

Drawing from the results presented previously for the various components, the comparative picture of AP-inert binder and HMX or another nitramine -active binder is found on Fig. 38.



**Burning rate of 10 mm/s. Positive heats are exothermic**
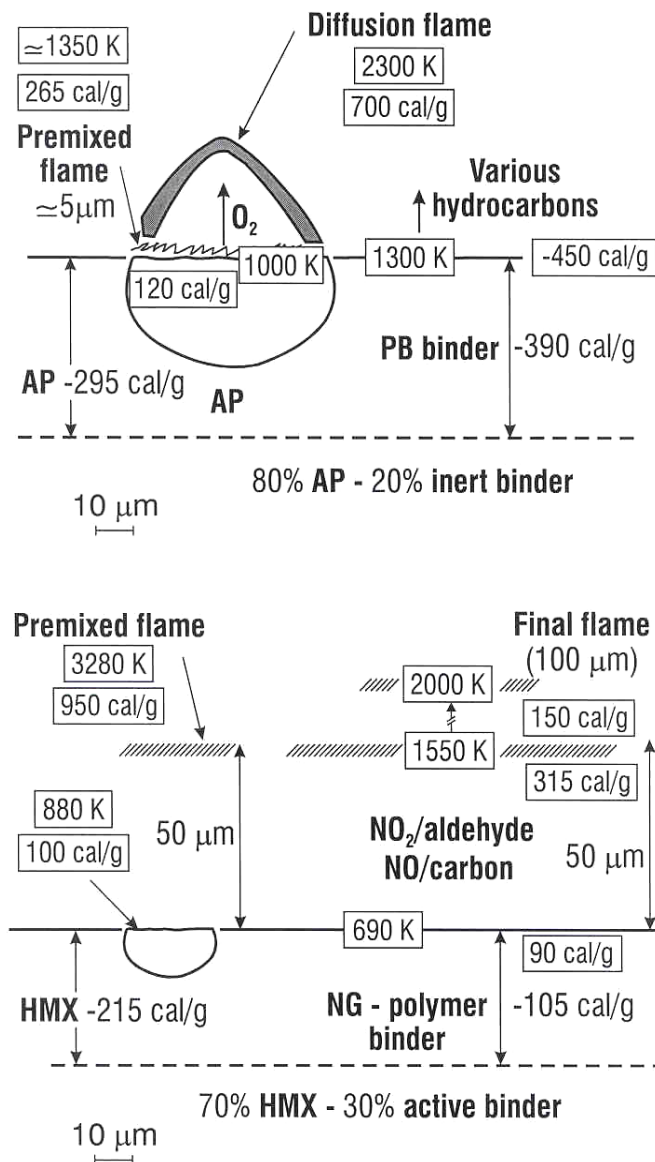
Figure 38: Comparative Picture of AP-Inert Binder and HMX-Active Binder.

The *combustion of AP* results in a premixed flame at about 5 μm from the surface at ≈ 1300 K or higher. From this flame 1 mole of $O_2$ comes out for each initial AP mole. From the binder surface at nearly the same temperature, combustible gases are ejected, which, after diffusion, react with $O_2$. As will be seen further on, the diffusion flame height is directly related to the AP particle size. The smaller the particle size the closer is the flame and the higher the heat flux to the surface and therefore the burning rate of the propellant. The pyrolysis of the inert binder is purely endothermic (heat required to bring the temperature to 1300 K and heat to decompose it into gases). In the case of particles of a few tens of μm, the burning of the AP being close to adiabatic (its flame receives some heat flux from the final flame, but computation results show that there is only a moderate deviation from adiabatic conditions), the heat flux from the final flame serves primarily to keep the binder regressing.

*The combustion of HMX or another nitramine* is also through a premixed flame, about 50 μm from the surface, reaching the final stage of 3280 K (for HMX). The gases emitted from this flame cannot sustain any further combustion. The active binder goes through its own combustion, with a primary flame reaching ≈ 1550 K some 50 μm from the surface. The final flame somewhat further away reaches about 2000K. There is no direct interaction between the two components of the propellant. The burning of the propellant is then an average of the individual burning rates. There exist however an indirect interaction of the active binder on the HMX particles. As was seen, the thermal properties of HMX and the active binder are close and the HMX particles are immersed in the temperature profile of the binder. Upon reaching the surface the top of the particle is at about 700 K, the surface temperature of the binder. This so happens to be very much the temperature for first ignition of HMX (see Fig. 23). There will be however a transition delay of the HMX particle to full combustion for which its surface temperature is about 900 K. This will be dealt with in more details further on.

In the case of AP, the ignition temperature is around 650 K and the surface temperature for full combustion is around 900 to 1000 K. Immersed in the inert binder with a surface temperature of ≈ 1300 K, the AP should reach combustion as soon as it is uncovered with no transition delay.

## 2.0    Propellant Burning Rate Resulting from Component Rates

Various approaches have been presented in the literature to build the propellant burning rate from the components' own burning rates. One of the first comprehensive models for composite propellant combustion modeling, Ref. [37], had a picture of AP and binder burning in parallel with a partitioning of the surface between the two ingredients and a surface averaged propellant burning rate. This view is also found in Refs. [38,39], with Ref. [40] being a complete review for AP-inert binder propellants, including references preceding the work of [37]. A view of a sequential burning mechanism, in which a given path goes through oxidizer particles separated by layers of binder, Fig. 39, with as a consequence a time averaged propellant burning rate, was first presented in Ref. [42].
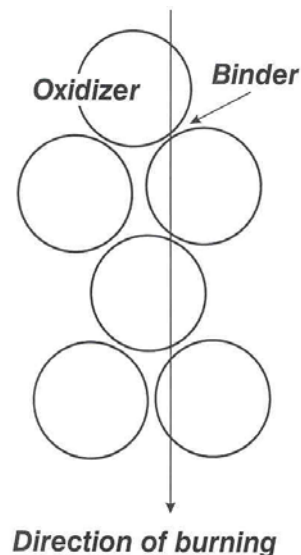


**Figure 39: Time Averaged Propellant Combustion.**

This viewpoint is subscribed to in the present work, as was done in Ref. [43], although the details have since then evolved into the option presented herein (which seems to be coherent with the latest view of

M. Beckstead [45]. Averaging of the components' burning rates, HMX and active binder, in Ref. [41] into the propellant burning rate is obtained by assuming that the components melt and mix at the surface and then form an average premixed gas flame. Due to the very small thickness of the melt (to the extent that melting occurs) layers (of the order of μm) and very short residence times in these layers (tenths of ms), it is believed that such premixing of the components should not take place. This is also the conclusion of [45].

Finally, in the recent work of Ref. [44], a surface average is operated for AP-binder interactions whereas a time average HMX-binder approach is adopted within the same mixed oxidizers propellant.

*In a randomly packed arrangement of oxidizer spheres* of diameter $D_{ox}$, with the average height through the sphere from a given direction (perpendicular to the surface) $h_{ox}$, and for a volume of 1 cm$^2$ on the surface by 1 cm in depth, the number of particles intercepted along 1 cm of length being N, one has:

$$N h_{ox} \, 1 \, cm^2 / N h_b \, 1 \, cm^2 = \xi_{ox} / ( 1 - \xi_{ox} ) \tag{1}$$

with $h_b$ the average binder height between particles and $\xi_{ox}$ the volume fraction loading in oxidizer. Then it comes:

$$h_b = h_{ox} ( 1 - \xi_{ox} ) / \xi_{ox} \tag{2}$$

and due to

$$N ( h_{ox} + h_b ) = 1 \, cm, \quad N = \xi_{ox} / h_{ox} \tag{3}$$

For a propellant burning rate $v_{b,p}$, the time to run through 1 cm of depth is

$$t = 1 / v_{b,p} = t_{ox} + t_b = N \, h_{ox} / v_{b,ox} + N \, \Delta t_{ox} + N \, h_b / v_{b,b} \tag{4}$$

$\Delta t_{ox}$ being the (possible) transition delay to full combustion after the top of the oxidizer particle has reached the surface. Then the propellant burning rate, as expressed with the component burning rates, is, with Eq. (3) taken into account,

$$1 / v_{b,p} = \xi_{ox} / v_{b,ox} + \xi_{ox} \, \Delta t_{ox} / h_{ox} + ( 1 - \xi_{ox} ) / v_{b,b} \tag{5}$$

Consideration of a sphere being traversed randomly along a given direction leads after some computation to $h_{ox} = D_{ox} ( \pi / 4 )^2$.

In the *case of AP- inert binder propellants with no transition delay*, the propellant burning rate is

$$1 / v_{b,p} = \xi_{ox} / v_{b,AP} + ( 1 - \xi_{ox} ) / v_{b,b} \tag{6}$$

The relation ship between volume fraction loading $\xi$ and mass fraction loading $\alpha$ being

$$\alpha_i = \xi_i \, \rho_i / \rho_p \tag{7}$$

$$\sum \xi_i = 1 \, , \quad 1 / \rho_p = \alpha_{ox} / \rho_{AP} + ( 1 - \alpha_{ox} ) / \rho_b \tag{8}$$

that is for example for an 88 % AP - 12 % PB binder $\rho_p = 1.72$ g/cm$^3$.

The mass burning rate of the propellant is

$$m_p = \rho_p \, v_{b,p}$$

and Eq. (6) yields

$$1 / m_p = \alpha_{ox} / m_{AP} + ( 1 - \alpha_{ox} ) / m_b \qquad\qquad (9)$$

In the *case of a propellant loaded with aluminum*, it is known that the aluminum particles are ejected from the surface [46,47] (Ref. [47] being an extensive review of the processes of aluminum combustion) and burn at several hundreds of μm from the surface. The view of the combustion of aluminum is summarized here, see Figs. 40,41,42.
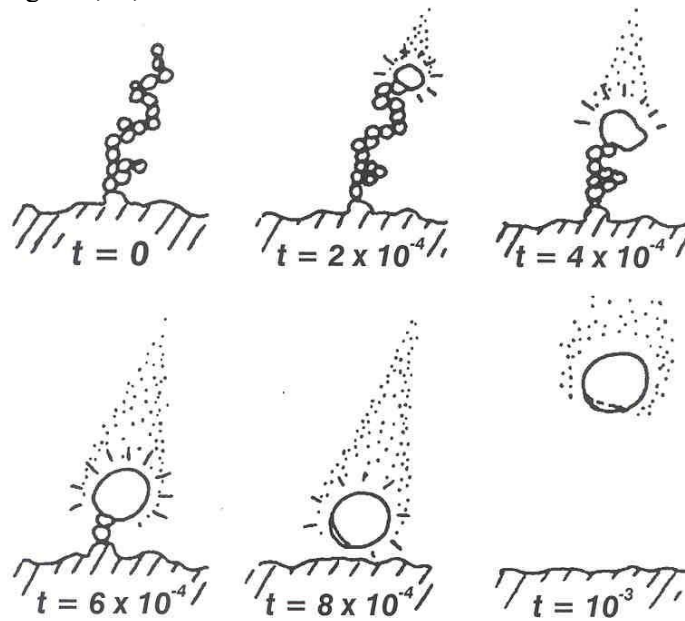


**Figure 40: Visualization of Aluminum Behavior (From Ref. [47]).**
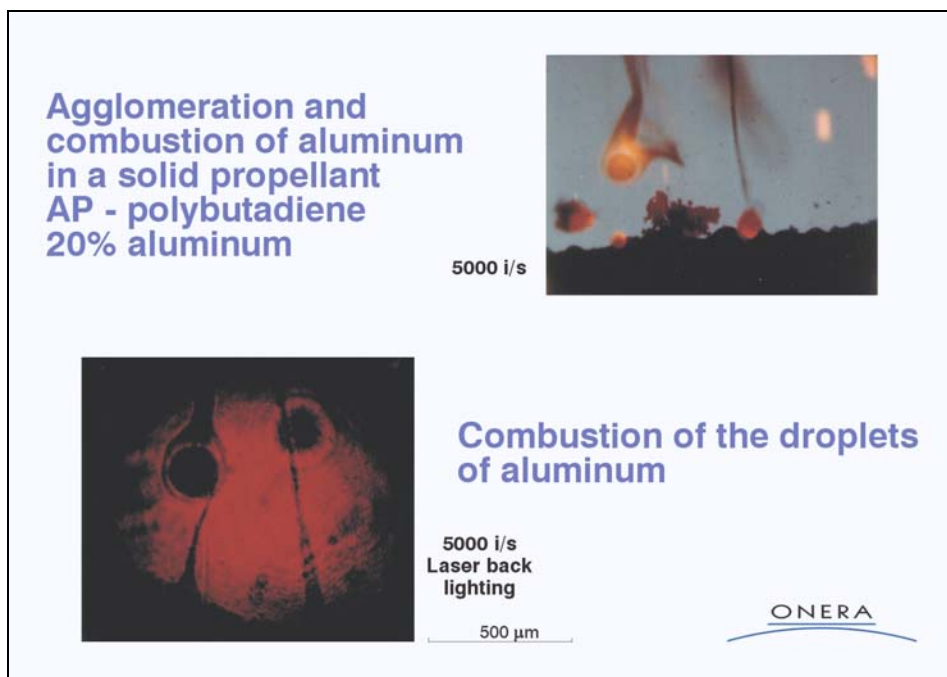


**Figure 41: Aluminum Combustion.**
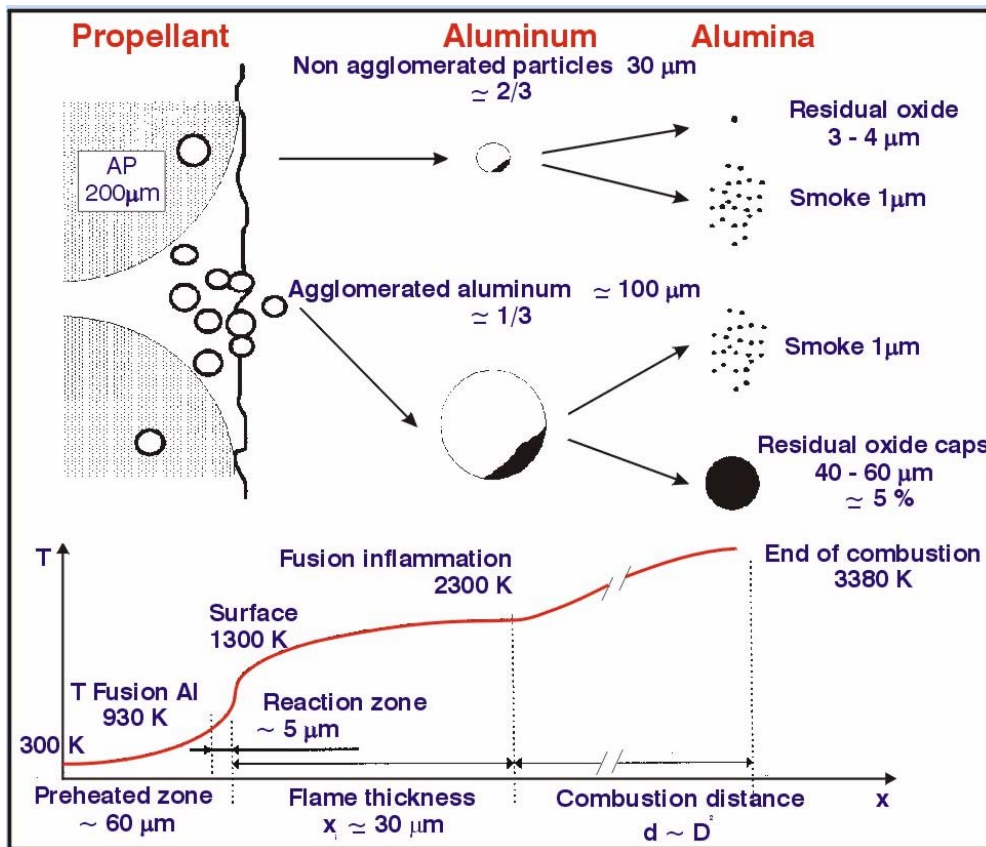
**Figure 42: Behavior of Aluminum (18 %) in a Composite Propellant.**

- Aluminum melts at 930 K (inert binder reaches about 1300 K) (active binder reaches about 700 K) and individual particles aggregate in part into clusters.

- Sketches of selected frames of high speed motion pictures, Fig. 40, illustrate a protracted (because the protective $Al_2O_3$ coating melts at 2300 K) ignition-agglomeration event in which the hottest portion of the accumulate inflames and precipitates the complete inflammation-agglomeration of the (already hot) accumulate.

- The $Al_2O_3$ protective coating collapses into cap, exposing the Al globule (typically $\approx$ 100 µm).

- Aluminum vaporizes at $\approx$ 3300 K and reacts in nearly-spherical flame with $CO_2$ and $H_2O$ from AP-binder flame.

- The caps give $Al_2O_3$ particles of a few tens µm, the spherical flames give $Al_2O_3$ smoke of $\approx$ 1µm.

- Not all aluminum particles go into accumulates (packs of original particles sticking together) from pockets within large AP particles. About 2/3 of the original particles escape individually from the surface, giving as combustion product essentially 1 µm smoke [48].

The volume fractions being

$\xi_{ox}$ , $\xi_b$ , $\xi_{al}$

Eq. (8) becomes

$$1 / \rho_p = \alpha_{ox} / \rho_{ox} + \alpha_b / \rho_b + \alpha_{al} / \rho_{al} \tag{10}$$

that is, for example, for a 70 % AP, 20 % aluminum ($\rho_{al}$ = 2.7 g/cm$^3$), 10 % PB binder ($\rho_b$ = 0.92/cm$^3$), $\rho_p$ = 1.84 g/cm$^3$.

With respect to the burning rate of the propellant loaded with aluminum it is obtained:

$$1 / v_{b,p} = \xi_{ox} / v_{b,ox} + N_{al} h_{al} / v_{b,al} + N_{al} \Delta t_{al} + \xi_b / v_{b,b} \tag{11}$$

The "burning" rate of aluminum can be considered as infinite since it is ejected from the surface, whereas its "transition delay" is the time for the binder to regress through the particle height:

$$\Delta t_{al} = h_{al} / v_{b,b}$$

Also, for each component N h = $\xi$ its volume fraction loading. The propellant burning rate becomes

$$1 / v_{b,p} = \xi_{ox} / v_{b,ox} + \xi_b / v_{b,b} + \xi_{al} / v_{b,b} = \xi_{ox} / v_{b,ox} + ( 1 - \xi_{ox} ) / v_{b,b} \tag{12}$$

that is the relation which would be obtained for a corresponding propellant with no aluminum, with the binder filling in for it.

From an energetics point of view the modeling of the combustion of aluminized propellants should include at the surface the heat of fusion of aluminum ≈ 95 cal/g of Al. One can see Ref. [49] for such an approach.

## 3.0    HMX (or RDX) (or HNIW) – Active Binder Propellants

Both HMX and the active binder have independent burning rates. The resulting propellant burning rate is given by Eq. (5), where the transition delay has to be evaluated.

The emerging HMX particle offers to the external heat flux the surface area of the sphere cap which has been exposed by the binder regressing at $v_{b,b}$ after the time t from first appearance has evolved:

$$S = \pi D_{ox} ( v_{b,b} t )$$

With $\alpha$ being the part of the sphere which is heated by the superficial flux $\Phi$ , the temperature rise is

$$\alpha ( \rho_p c_p )_{ox} dT / dt ( 4 \pi / 3 ) ( D_{ox} / 2 )^3 = \Phi \pi D_{ox} v_{b,b} t \tag{13}$$

The heat flux received is that of the binder flame when the particle first emerges and it transitions to that of the HMX flame when the particle has reached full combustion, a transition formula being assumed to be

$$\Phi = \Phi_b + [ ( T_s(t) - T_{s,b} ) / ( T_{s,ox} - T_{s,b} ) ] ( \Phi_{ox} - \Phi_b )$$

with

$$\Phi_{ox,b} = \rho_p v_b ( c_g T_s - c_p T_o - Q_s )|_{ox,b}$$

The fraction of the sphere heated by the flux is taken to be, with K finally adjusted at 0.1,

$$\alpha = \exp( - K D_{ox} / e_p* )$$

$e_p*$ is the thermal wave thickness for which the temperature is at 90 % of its surface value, that is, sufficiently close to it,

$$( T - T_o )/( T_s - T_o ) = 0.9 = \exp( - e_p^* \, v_{b,b} / d_p )$$ (14)

When $D_{ox} / e_p^* \rightarrow 0$ the particle is vanishingly small with respect to the thickness of the layer at about the surface temperature, $\alpha \rightarrow 1$ and the particle is heated in its entirety by the heat flux. If $D_{ox} /e_p^* \rightarrow \infty$ the particle is very large compared to the surface layer, $\alpha \rightarrow 0$, it is heated on a vanishingly small part. When $D_{ox} = e_p^*$ , $\alpha = 0,9$, the particle is immersed in the binder layer at $T \approx T_{s,b}$ and it is almost totally heated by the external flux. The transition delay from Eq. (13) is then

$$\Delta t_{ox}^2 = \alpha \, ( \rho_p \, c_p )_{ox} \, ( D_{ox}^2 / 3 \, v_{b,b} ) \, [ \, ( T_{s,ox} - T_{s,b} ) \, ] / ( \, \Phi_{ox} - \Phi_b \, )] \ln( \Phi_{ox} / \Phi_b )$$ (15)

One noteworthy feature of this relation is that the transition delay is proportional to the particle size $D_{ox}$, in such a way that inserted in Eq. (5) it renders the burning rate insensitive to $D_{ox}$, a fact which is observed experimentally for HMX-energetic binder propellants [43].

Figures 43 and 44 show two examples of propellant burning rate laws with the corresponding component rates. It is seen that the propellant burning rate is intermediate between those of HMX and of the binder (its being close to that of the binder at pressures under 100 atm is coincidental).
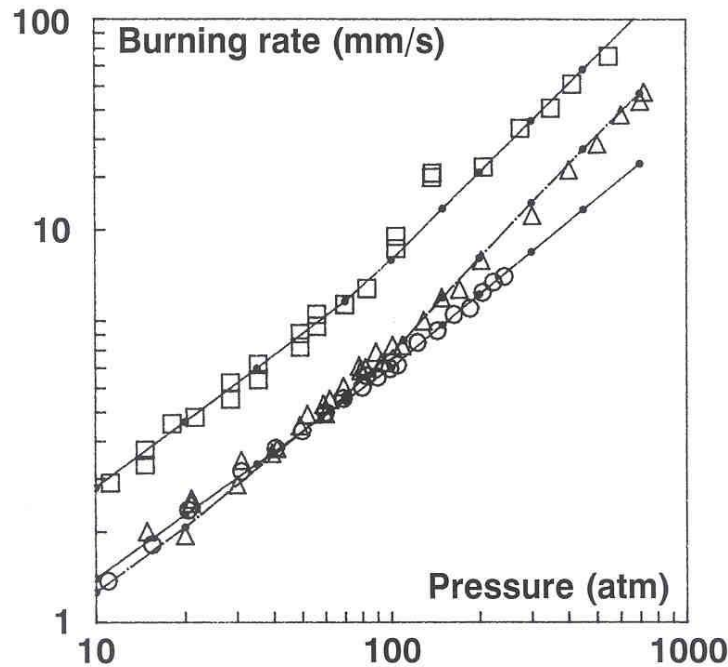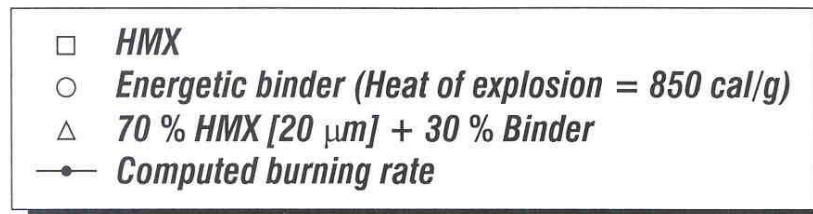


**Figure 43: Experimental and Computed Burning Rate of a Nitramine Based Propellant.**
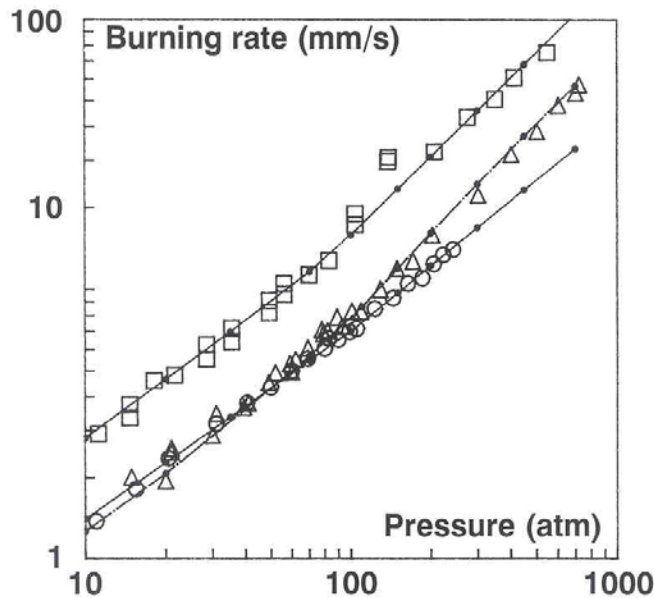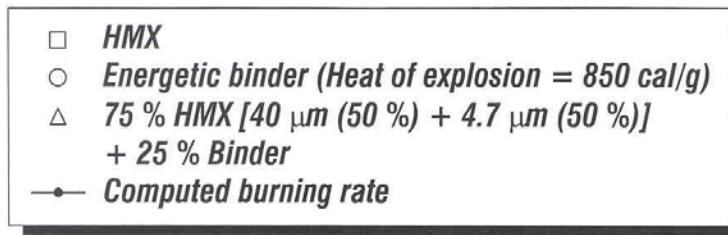
**Figure 44: Experimental and Computed Burning Rate of a Nitramine Based Propellant.**

The model presented above, and, what is important, the mechanisms it takes into account (that is the absence of diffusional interaction between the components and the importance of a transition delay for the HMX particles), is quite representative of the experimental results. Some of the details of the making of the burning rate are given in Table 15.

**Table 15: Elements for the Evaluation of the Burning Rate (70 % HMX – 30 % Active Binder)**

| PRESSURE | 20 atm | 100 atm | 250 atm |
|---|---|---|---|
| $v_{b,b}$ | 2,4 mm/s | 7,1 | 14,5 |
| $T_{s,b}$ | 622K | 667 | 698 |
| $v_{b,ox}$ | 4,5 mm/s | 17 | 37,5 |
| $T_{s,ox}$ | 828K | 907 | 962 |
| % of burning time due to delay | 32 % | 16 % | 4 % |
| $v_{b,p}$ | 2,3 mm/s | 9,4 | 22,7 |

It is seen that at low pressures the transition delay has a strong impact and the burning rate of the propellant happens to fall close to that of the binder. At high pressure the propellant burning rate is nearly the time average of the component rates (without delay the average at 250 atm is 24 mm/s).

It is observed that, for a given HMX-energetic binder composition, the burning rate law is locked and that there is no way to tailor it (as can be done in AP-inert binder compositions by acting upon the particle size). Furthermore the pressure exponent is too high to be acceptable for the motor operation. Attempts to act upon the HMX burning rate by the use of additives have not been successful. One possibility of action however is with additives specific to double-base propellants, lead and copper salts and carbon black, incorporated in the active binder. It has been found on Fig. 12 that a moderate super rate effect can be obtained. It is seen on Fig. 45 that such a modified binder associated with HMX, and after optimization of the amount and of the size of the additives, yields a burning rate law with moderate pressure exponent and initial temperature sensitivity.
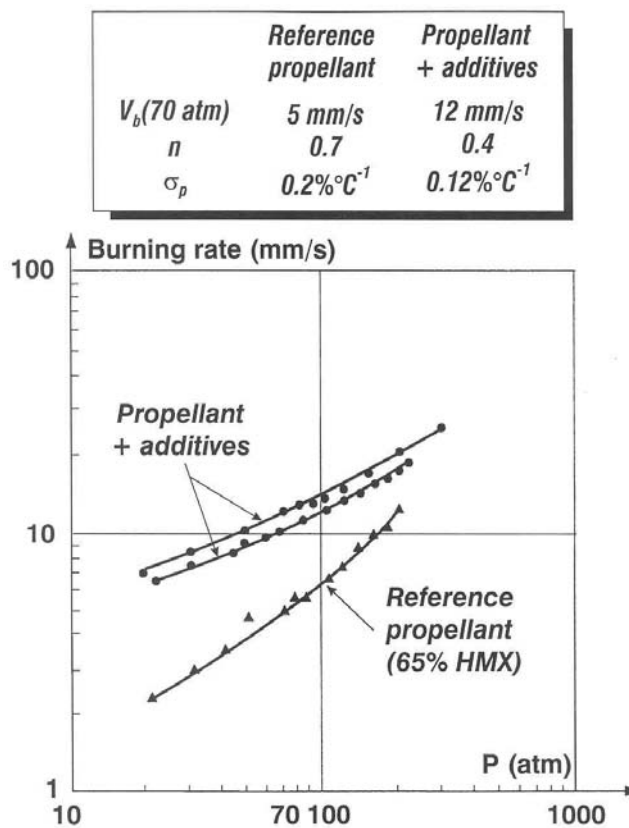


**Figure 45: HMX – Active Binder Propellant with Additives.**

Propellants based on the new oxidizer HNIW and binders made from GAP (glycidyl azide polymer) have been considered. GAP has been studied in Refs. [50,51] with the techniques employed for the double base propellants, in particular its surface temperature under combustion is similar, around 800 K. In the actual binder GAP is associated to a liquid nitrate ester, see Ref. [35], the behavior of which is very close to a cool active binder. The modelization has been applied to these propellants (in particular assuming no interaction, other than the transition delay for the full burning of the oxidizer), it can be seen to give a proper account of the resulting burning rate, Fig. 46. As opposed to HMX or RDX which are balanced to give CO, $H_2O$ and $N_2$, HNIW is over oxygenated to give

$$C_6H_6N_{12}O_{12} \rightarrow 6\,CO + 3\,H_2O + 6\,N_2 + 3/2\,O_2$$
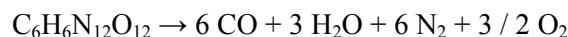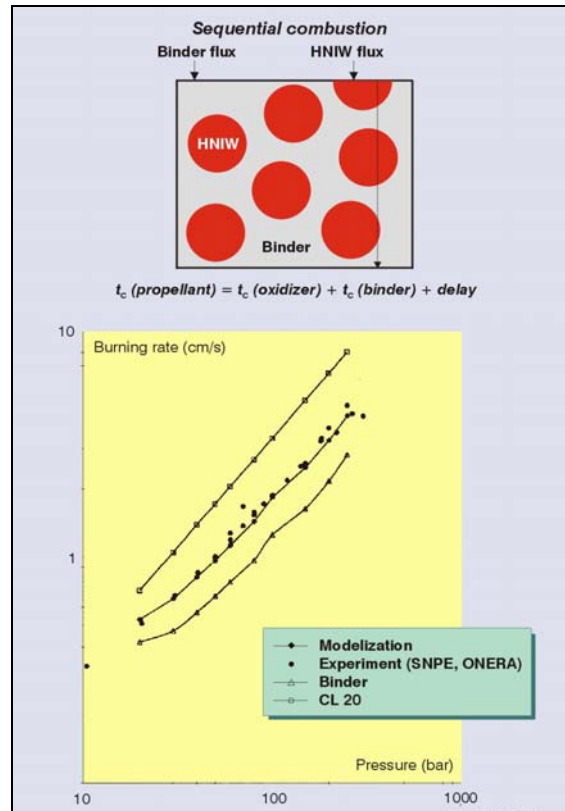
**Figure 46: HNIW (60 %) – Binder GAP + Nitrate Ester.**

A possible recombustion with the gases from the flame of the active binder could be conceivable, this implying an influence of the oxidizer particle size and a possibility of regulating the burning rate as in AP composite propellants. The modelization does not confirm this possibility. Comparing propellants with different particle sizes would clarify this point.

## 4.0    AP-Inert Binder Propellants

The burning rate of a propellant based on AP and an inert binder such as HTPB is thought to be described by the averaging rule of Eq. (9) from the burning rates of the components. In this case the binder has of course no autonomous burning rate. Its regression rate is due to the heat flux from the diffusion flame, as depicted on Fig. 38, between $O_2$ from the AP flame and the hydrocarbons from the pyrolysis of the binder. A description of such a flame is given here.

A column of $O_2$ containing gases is ejected from a particle with an efficient diameter $D_{ox}*$ proportional to $D_{ox}$ at a velocity $v_g$, such that $m_p = \rho_g v_g$. This column is consumed by a *lateral diffusion* characterized by a diffusion velocity

$$v_{diff} = A_d \text{Đ} / ( D / 2 ) \tag{16}$$

D being the local diameter of the column, $A_d$ some constant of order 1 and Đ the diffusion coefficient in $cm^2/s$. The variation of the column diameter is then given by

$$dD = - 2 v_{diff} dt , dx = v_g dt$$

$$D \, dD = - 4 A_d \text{Đ} \, dx / v_g$$

Resulting in

$$D_{ox}^{*2} = 8 A_d Ð x_{fd} / v_g, \quad x_{fd} = D_{ox}^{*2} m_p / 8 A_d \rho Ð \tag{17}$$

In this relation $D_{ox}^{*}$ is the average diameter of a sphere cut randomly by a plane

$$D_{ox}^{*} = 2 D_{ox} / \sqrt{6}$$

When the lateral diffusion of $O_2$ and hydrocarbon gases into each others is purely laminar the diffusion coefficient is expressed as:

$$Ð = Ð_0 T^{\alpha} / p \,, \quad \rho Ð = Ð_0 T^{\alpha - 1} M / R$$

(with the equation for perfect gases $p / \rho = R T / M$ being used) and the flame stand-off distance

$$x_{fd} = D_{ox}^{*2} m_p ( R / M ) / 8 A_d Ð_0 T^{\alpha - 1} \tag{18}$$

does not depend explicitly upon the pressure. In this limiting case and due to the fact that

$$m_p \sim 1 / x_f \,,$$

it is obtained

$$m_p \sim 1 / D_{ox}$$

independent of the pressure level and directly dependent on the particle size.

As will be seen later, it has been found that the diffusion flame process might become turbulent at high pressures when large differences exist between the mass flow rates emitted from the AP and from the binder. This conclusion is also mentioned in reference [40]. A general expression for a turbulent transport coefficient is

$$\rho Ð \sim \rho u' \ell$$

with u' the magnitude of the fluctuating gas velocity and $\ell$ its scale. It is then assumed

$$\ell \sim D_{ox} / 2 \,, \quad \rho u' \sim ( m_{ox} - m_b )$$

that is the turbulent enhancement is related to the difference between the mass flow rates within the $O_2$ containing column and in the surrounding gases. Then Eq. (17) becomes

$$x_{fd} = D_{ox}^{*2} m_p / 8 A_d ( \rho Ð )_{eff} \tag{19}$$

$$( \rho Ð )_{eff} = Ð_0 T^{\alpha - 1} M / R + K ( D_{ox} / 2 ) ( m_{ox} - m_b ) \tag{20}$$

where K should be of the order of 0.1.

An extra *flame thickness related to the chemical time* for the completion of the $O_2$-hydrocarbons reaction should be taken into account. It is obtained

$$x_{fr} \, (\sim v_g \, \tau_{ch} \sim m \, \tau_{ch}/\rho \sim m/\omega) = m_p / A_r p^2 A_{g,f} \exp ( - E_{g,f} / R T_f ) \tag{21}$$

the characteristics being related to the final $O_2$ - hydrocarbons flame.

The stages of the combustion of an AP propellant are shown on Fig. 47, which is to be seen side by side with Fig. 38 for the corresponding values. The temperature profiles are approximated as

$$( T_f - T ) / ( T_f - T_s ) = \exp( - 3 \, x / x_f ) \tag{22}$$

with

$$q_s = 3 \, \lambda_{g,s} \, ( T_f - T_s )/ x_f \tag{23}$$
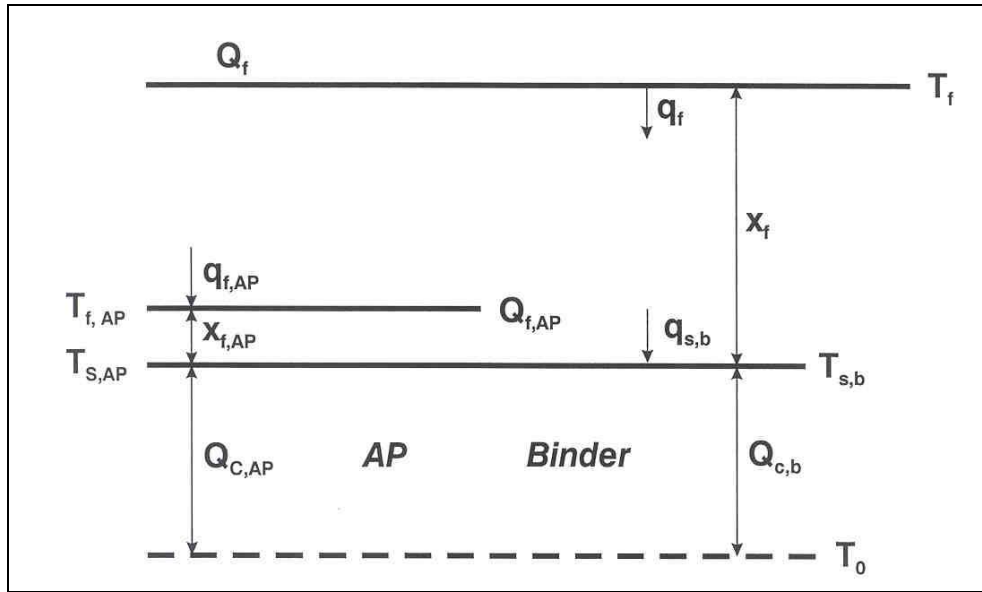


**Figure 47: Stages of an AP – Inert Binder Propellant.**

The *mass regression rate of the binder* is then given by

$$m_b \, Q_{c,b} = q_{s,b} = 3 \, \lambda_{gs} \, ( T_f - T_{s,b} ) / x_f \tag{24}$$

where the constituting elements of this relation have been seen in the chapter on inert binders. It should be noticed that, to simplify the description, a uniform mass flow rate $m_p$ is taken in the gas phase above the binder and the AP flame. The flame height $x_f$ is then the sum of Eqs. (19 and 21).

*The mass burning rate of the AP*, see Eq. (13) of the corresponding chapter,

$$m_{AP} = [ \, 3 <\omega_{AP}> \lambda_{g,s} \, ( T_{f,AP} - T_{s,AP} ) / Q_{c,AP} \, ]^{1/2} \tag{25}$$

$$3 <\omega_{AP}> = p^2 \, A_{g,AP} \, \exp[ \, - E_{g,AP} / R \, T_{f,AP} \, ]$$

Now, due to the fact that the AP flame receives a heat flux from the final flame, the flame temperature is no longer the adiabatic temperature ( $T_{f,AP}{}^{ad} = 1205$ K ). It is given by

$$m_{AP} \, c_g \, ( T_{f,AP} - T_{s,AP} ) + m_{AP} \, Q_{c,AP} = m_{AP} \, Q_{g,AP} + q_{f,AP} \tag{26}$$

with, from Eq. (22), applied between $x_{f,AP}$ and $x_f$ the heat flux from the main flame into the AP flame

$$q_{f,AP} = 3 \, \lambda_g \, ( T_f - T_{f,AP} ) / ( \, x_f - x_{f,AP} \, ) \tag{27}$$

Results for the burning rate of AP-HTPB propellants are indicated on Fig. 48, where is seen a strong influence of the AP particle size. The model described above, and what is important the mechanisms it contains, gives a satisfactory account of these results.
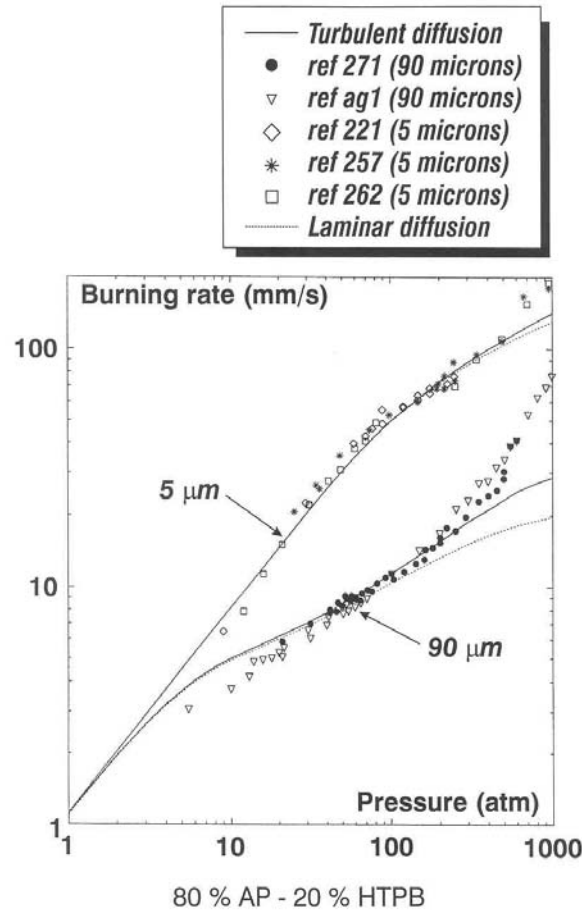


**Figure 48: Computed Burning Rates Compared to Experiments.**

For the *very small AP particle sizes* the final flame is mostly dominated by the chemical process, very sensitive to pressure, as is the AP flame. This results in a variation of the burning with a pressure exponent close to 1.

For *large particle sizes* the final flame is dominated by the diffusion process, which is insensitive to pressure. This, combined with the pressure dependent flame of the AP, see Fig. 38, gives rise to a propellant burning rate which is moderately sensitive to pressure. It is found in the modeling that the contribution of the turbulent diffusion, see Eq. (20), becomes important above about 100 atm. However above 300 to 400 atm the burning rate of the propellant undergoes a sharp exponent break that the model cannot follow. In some references this exponent break has been assumed to be due to the burning rate of the AP which would also increase sharply. It has been seen on Fig. 20 that, when the samples are carefully inhibited, this is not the case.

The strong influence of the AP particle size upon the propellant burning rate, as expressed by the modeling, is also shown on Fig. 49. It is seen that at about 1 μm there is no further gain in the burning rate. This is due to the fact that there will always exist a non vanishing flame stand-off distance related to the chemical time for the $O_2$-hydrocarbons reaction.
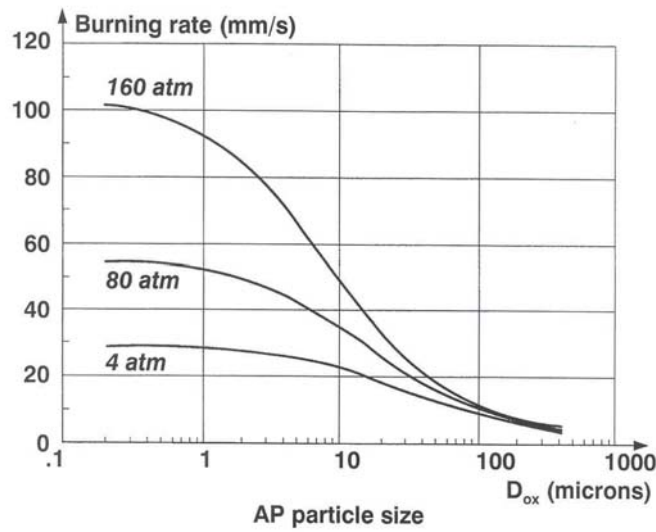
**Figure 49: Computed Burning Rate vs AP Particle Size (80 % AP – HTPB).**

On Fig. 50 the burning rate computed from the mechanisms modeled as described above is compared to results from the literature [38, 39] for mixed AP particle sizes. The agreement is adequate for the larger particle sizes and approximate for the small ones (Now, how representative are the particle sizes indicated?). This reveals that the physico-chemical features incorporated in the model of the AP-inert binder propellant are probably sound. However, once a model has been "tuned" to represent a set of experimental results, as on Fig. 48, it cannot be expected that it will "predict" very accurately other results for different values of the parameters.
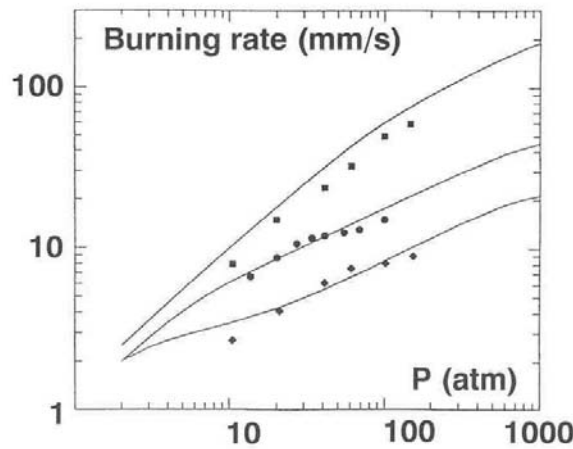


**Figure 50: Multi-Modal AP Propellants.**

It has been seen that by acting upon the AP particle size it is possible to tailor the burning rate of the propellant, but that there exist a limiting size below which the effect will be non existent, Fig. 49. It is possible to gain further by incorporating *metallic additives*, Fig. 51, such as of the ferrocenic type (which during processing will dissolve into the not yet cross-linked binder for a proper mixing). There also exist a polybutadiene binder which incorporates within its chemical structure the ferrocenic pattern (to avoid migration problems). Various results, and in particular the similarity of action of a silicon binder which produces on the propellant surface a fine structure of $SiO_2$ residue, to which it can hardly be attributed a catalytic efficiency, indicate that the mode of action of the additive is probably physical (rather than catalytic, in the sense of enhancing some chemical reactions). The layer of residue deposited on the surface has probably a flame-holding effect, the gases flowing in tortuous paths through this residue will react closer to the surface, with the final temperature not being modified, in such a way that an enhanced heat flux will act on the surface. This is taken into account in the model by decreasing the diffusion flame height, see Eq. (18), by a given factor throughout the pressure range.
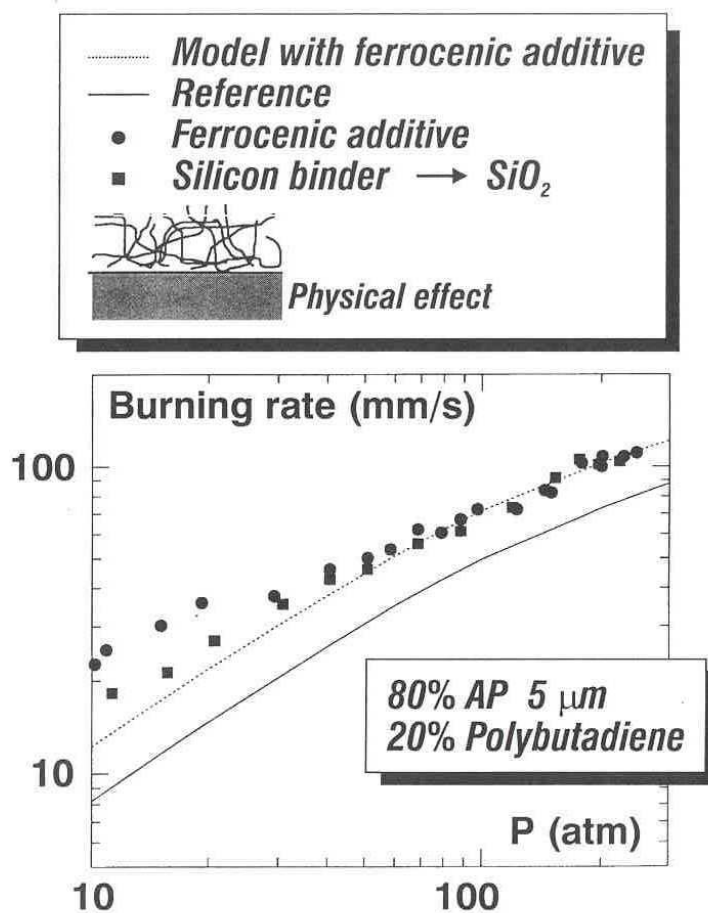


**Figure 51: Additive Modified Propellant.**

Finally, the procedure to describe the combustion of AP composite propellants is applied to a practical propellant containing two AP particle sizes and aluminum. It is observed on Fig. 52 that the presence of aluminum, which has been seen to burn far away from the surface in such a manner that no significant conductive heat flux from its flame zone goes back to the propellant surface, should be taken into account by adding a radiative heat flux as measured in Ref. [52] for propellants very close to the ones considered here. It is found then that the experimental burning rate law is followed quite well.
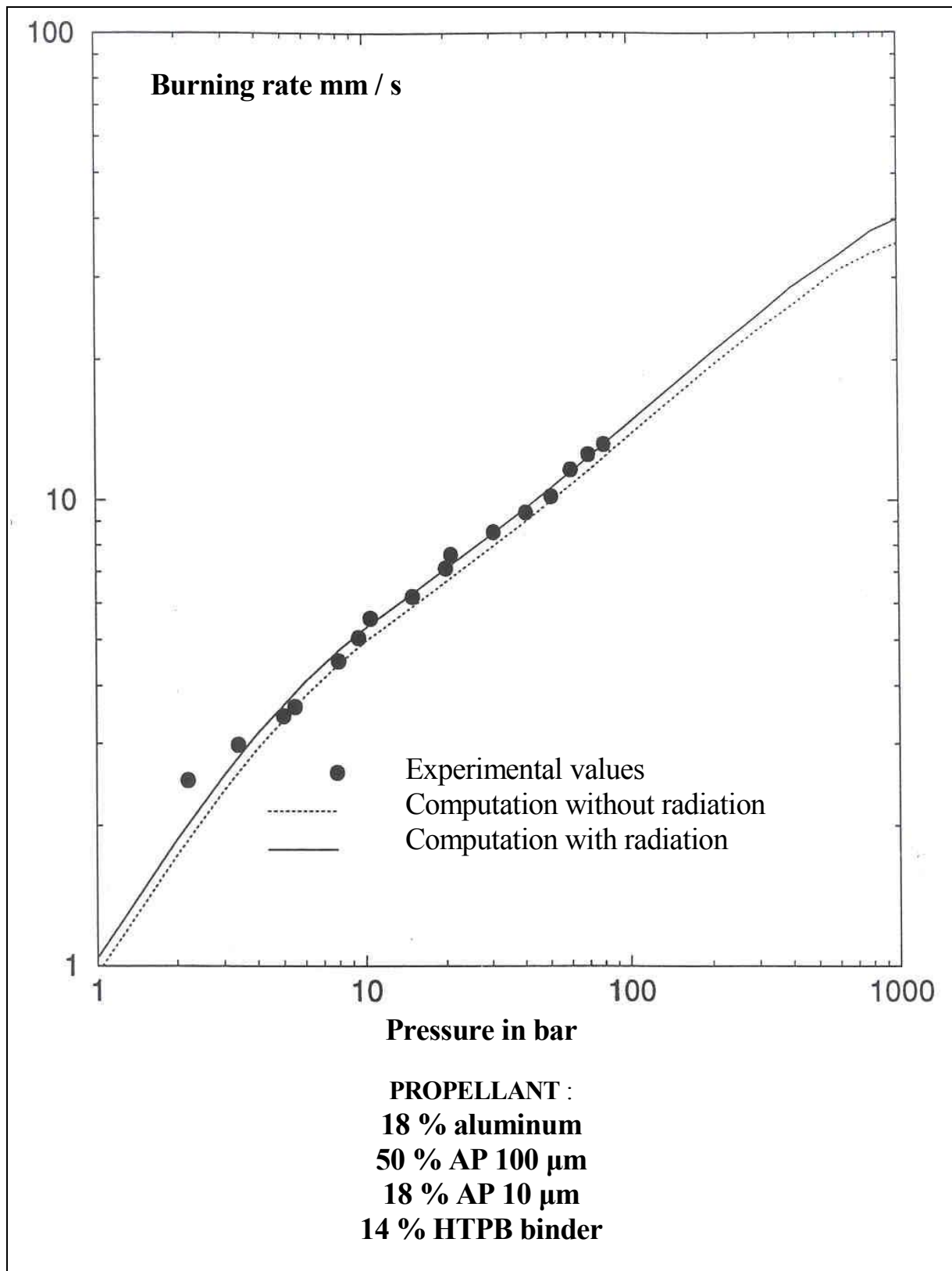
**Figure 52: Burning Rate of an Industrial Propellant.**

# CONCLUSIONS

A review has been presented of the viewpoint of the authors on the combustion mechanisms of components and of solid propellants. Some noteworthy points are stressed here.

*Double-Base Propellants and Active Binders:*

A fairly good knowledge of the processes in the condensed and gas phases has been acquired. The main point is the presence of a two-flame system, involving $NO_2 \rightarrow NO \rightarrow N_2$, collapsing into one flame above 200 to 300 atm. Specific additives (lead and copper salts and carbon black) have a true chemical interaction, that is the enhancement of the NO-carbon reaction, bringing some of the energy normally evolved in the second flame closer to the surface. This knowledge carries over to the active binders, which are however less prone to super-rate effects because they produce less structured carbon residue.

*Inert Binders:*

Not so many reliable pyrolysis measurements have been performed on actual binders. It has been shown (from comparisons for a number of materials) that the pyrolysis characteristics obtained at low heating rate (by thermogravimetric analysis or differential scanning calorimetry) should extrapolate and apply under combustion conditions. The mechanism of pyrolysis is a thermal breaking ( not influenced by pressure) of the cross-links and of the polymer, not affected by additives.

*Ammonium Perchlorate:*

It is believed that the mechanism of combustion is properly known. A large amount, about 70 %, of the AP exothermically decomposes in a thin ($\approx$ 1 µm) condensed phase superficial layer, the remaining 30 % sublimes into $NH_3$ and $HClO_4$ which react in a flame very close (a few µm) to the surface. Due to the thickness, and the very short residence time associated, of these zones, additives have no true catalytic (i.e. chemical) action.

*HMX, RDX and HNIW:*

The combustion of HMX (or RDX) is qualitatively comparable to that of a DB propellant, with the occurrence of two flames, involving $NO_2$ and $N_2O/NO$. However above 20 atm these flames collapse into one and therefore it is not possible to induce super-rate effects with specific additives, as was the case for DB propellants. Also, additives which were hoped to accelerate the melting-decomposition of HMX fail to act under combustion characteristics. The burning of HNIW, the new caged nitramine, seems to be of the same nature, with a condensed phase decomposition due to thermal degradation and probably no evaporation phenomenon; also the gas flame is probably very quickly collapsed into a single overall flame, with therefore no possibility of additive effect of the double base type.

*AP or HMX Inert or Active Binder (Aluminum) Propellants:*

The approach believed to describe adequately the combustion of composite propellants is a sequential one. When following a path through the propellant, it meets successively the combustion of the oxidizer particles and of the binder layers.

In the case of *AP-inert binder propellants*, the propellant burning rate is an average of the components' rates. However an interaction flame between $O_2$ from AP and hydrocarbons from the binder enhances the rate of AP and allows the pyrolysis of the binder. The burning rate of the propellant can be quite widely tailored by reducing the AP particle size and further by adding metallic compounds which leave an oxide residue layer, the action of which is likely to be a flame holding effect, i.e. a physical action. Aluminum

incorporated in such propellants of course increases the final temperature by as much as 1000 K, but its combustion is so far from the surface that it does not influence much the regression rate of the propellant.

In the case of *HMX – RDX – or HNIW - active binder propellants*, both components have autonomous burning rates. The resulting propellant burning rate is the average of the two rates, with a further slowing down due to the fact that the HMX, or other nitramine, particles, upon reaching the surface, have to undergo a transition to full combustion. This delay is of importance up to roughly 150 atm; above it tends to become negligible. No additives have been found to act on HMX and additives of the DB type act only moderately on the active binder. The tailorability of HMX, or other nitramine, - active binder propellants is therefore more limited than for AP propellants.

*Further trends on new ingredients* are related in the first place to the need to reduce the vulnerability to various aggressions of missile motors employing solid propellants: "cook off" due to fires, bullet or fragment impact, "sympathetic detonation". Another emerging concern is that of the pollution caused by the large boosters of space launchers, using AP - inert binder - aluminum propellants, with production of HCl and $Al_2O_3$ smoke.

These considerations have led to reconsidering ingredients such as ammonium nitrate, $NH_4NO_3$, discarded previously as being insufficiently energetic, reconsidered and seemingly not considered any longer, and to introducing energetic binders such as GAP, glycidyl azide polymer (containing the $N_3$ group, inducing an exothermic decomposition), briefly mentioned in the text, or oxidizers containing the $N-NO_2$ group while being less sensitive than HMX or RDX, such as ADN ($NH_4-N-(NO_2)_2$).

Also considered are caged nitramines, such as CL20 (also called HNIW), which maintains the energetic level with a lesser amount of oxidizer, thus reducing the vulnerability, or which allows a higher energetic level. A number of new results on this component has been presented in the text.

It is hoped that the large amount of information gathered and the understanding acquired about the already used propellants ingredients will allow an efficient approach to the mastering of the behavior of the new ingredients and the corresponding propellants.

## ACKNOWLEDGEMENTS

## REFERENCES

This document is very much extracted from:

- G. Lengellé: "Recent Developments and Challenges in Ignition and Combustion of Solid Propellants". Invited plenary conference, 4th International Symposium in Chemical Propulsion,

Stockholm, May 1996. Publication in 1997 "Challenges in Propellants and Combustion", Begell House, New York.

- G. Lengellé, J. Duterque and J.F. Trubert: "Physico-Chemical Mechanisms of Solid Propellant Combustion". Contribution to "Solid Propellant Chemistry, Combustion and Motor Interior Ballistics", Volume 185, Progress in Astronautics and Aeronautics, AIAA, 2000.

## General References (Combustion, Chemical Propulsion, Solid Propellants)

- Williams F.A., *Combustion Theory* (Second Edition), Benjamin/Cummings Publishing Co, Menlo Park, 1985.

- Kuo K.K., *Principles of Combustion*, John Wiley and Sons, New York, 1986.

- Williams F.A., Barrère M. and Huang N.C., *Fundamental Aspects of Solid Propellant Rockets*, AGARD 116, 1969.

- Timnat Y.M., *Advanced Chemical Rocket Propulsion*, Academic Press, London, 1987.

- Kuo K.K. and Summerfield M. (Eds), *Fundamentals of Solid Propellant Combustion*, Volume 90 of Progress in Astronautics and Aeronautics, 1984.

- Yang V. and Zarko V.E. (Eds), "Solid Propellant Motor Interior Ballistics and Combustion of Energetic Materials", Special issue of Journal of Propulsion and Power, Vol. 11, n° 4, July-August 1995.

- Yang V., Brill T.B. and Ren W.Z., *Solid Propellant Chemistry, Combustion and Motor Interior Ballistic*, Volume 185 of Progress in Astronautics and Aeronautics, 2000.

## Double-Base Propellants and Active Binders References

[1] Heller C.A. and Gordon A.S., "Structure of the Gas Phase Combustion Region of a Solid Double-Base Propellant", The Journal of Physical Chemistry, Vol. 59, n° 8, pp. 773-777, 1955.

[2] Zenin A.A., "Structure of Temperature Distribution in Steady-State Burning of a Ballistite Powder", Combustion, Explosion and Shock Waves, Vol. 2, n° 3, pp. 67-76, 1966.

[3] Kubota N., Ohlemiller J.J., Caveny L.H. and Summerfield M., "The Mechanism of Super-Rate Burning of Catalyzed Double-Base Propellants", 15th Symposium (International) on Combustion, pp. 529-537, The Combustion Institute, 1975.

[4] Kubota N. and Ishihara A., "Analysis of the Temperature Sensitivity of Double-Base Propellants", 20th Symposium (International) on Combustion, pp. 2035-2041, The Combustion Institute, 1984.

[5] Lengellé G., Bizot A., Duterque J. and Trubert J.F., "Steady-State Burning of Homogeneous Propellants", in Fundamentals of Solid-Propellant Combustion (Ed. K.K. Kuo and M. Summerfield), Vol. 90 of Progress in Astronautics and Aeronautics, 1984.

[6] Duterque J., Hommel J. and Lengellé G., "Experimental Study of Double-Base Propellants Combustion Mechanisms", Propellants, Explosives, Pyrotechnics, Vol. 10, pp. 18-25, 1985.

[7] Trubert J.F., "Analysis of the Condensed Phase Degradation Gases of Energetic Binders", La Recherche Aérospatiale, 1989, n° 2 (March-April), pp. 69-79; AGARD/PEP Specialists Meeting on Smokeless Propellants, Florence, September 1985, AGARD C.P. n° 391.

[8]     Lengellé G., "Thermal Degradation Kinetics and Surface Pyrolysis of Polymers", AIAA Journal, Vol. 8, n° 11, pp. 1989-1996, 1970.

[9]     Bizot A. and Beckstead M.W., "A Model for Double-Base Propellant Combustion", 22nd Symposium (International) on Combustion, pp. 1827-1834, The Combustion Institute, 1988.

[10]    Cohen N.S. and Lo G.A., "Combustion Chemistry of Nitrate Ester-Based Propellants", AIAA Paper 83-1198, June 1983; 20th JANNAF Combustion Meeting, October 1983.

[11]    Song Y.H., Beer J.M. and Sarofim A.F. "Reduction of Nitric Oxide by Coal Char at Temperatures of 1250-1750 K", Combustion Science and Technology, Vol. 25, pp. 237-240, 1981.

[12]    Youfang C., "Combustion Mechanism of Double-Base Propellants with Lead Burning Rate Catalysts", Propellants, Explosives, Pyrotechnics, Vol. 12, pp. 209-214, 1987.

## Inert Binders References

[13]    Madorsky S.L., *Thermal Degradation of Organic Polymers*, Interscience Publishers, New York, 1964.

[14]    Jellinek H.H.G., *Aspect of Degradation and Stabilization of Polymers*, Elsevier Scientific Publishing Co, New York, 1978.

[15]    Strand L.D., Jones M.D. and Ray R.L., "Characterization of the Hybrid Rocket Internal Flux and HTPB Fuel Pyrolysis". AIAA Paper 94-2876, 30th Joint Propulsion Conference, Indianapolis, June 1994.

[16]    Cohen N.S., Fleming R.W. and Derr R.L., "Role of Binders in Solid Propellant Combustion", AIAA Journal, Vol. 12, n° 2, pp. 212-218, 1974.

[17]    Beck W.H., "Pyrolysis Studies of Polymeric Materials Used as Binders in Composite Propellants: A Review", Combustion and Flame, Vol. 70, pp. 171-190, 1987.

## Ammonium Perchlorate References

[18]    Levy J.B. and Friedman R., "Further Studies of Pure Ammonium Perchlorate Deflagration", 8th Symposium (International) on Combustion, pp. 663-672, The Combuston Institute, 1962.

[19]    Guirao C. and Williams F.A., "A Model for Ammonium Perchlorate Deflagration between 20 and 100 atm", AIAA Journal, Vol. 9, n° 7, pp. 1345-1356, 1971.

[20]    Beckstead M.W., Derr R.L. and Price C.F., "The Combustion of Solid Monopropellants and Composite Propellants", 13th Symposium (International) on Combustion, pp. 1047-1056, The Combustion Institute, 1971.

[21]    Price C.F., Boggs T.L. and Derr R.L., "The Steady State Combustion Behavior of Ammonium Perchlorate and HMX", AIAA paper n° 79-0164, 17th Aerospace Sciences Meeting, 1979.

[22]    Godon J.C., "Model of Ammonium Perchlorate Self-Deflagration", La Recherche Aérospatiale, 1982-2, pp. 43-50.

[23]    Seleznev V.A., "An Optical Method of Measuring the Burning Surface Temperature of Condensed Systems", Combustion and Flame, Vol. 13, n° 2, 1969.

**HMX, RDX, HNIW References**

[24] Rogers R.N., "DSC Determination of the Kinetics Constants of Systems that Melt with Decomposition", Thermochemica Acta, Vol. 3, pp. 437-447, 1972.

[25] Boggs T.L., "The Thermal Behavior of RDX and HMX", in Fundamentals of Solid-Propellant Combustion (Ed. K.K. Kuo and M. Summerfield), Vol. 90 of Progress in Astronautics and Aeronautics, 1984.

[26] Cohen N.S., Lo G.A. and Crowley J.C., "Model and Chemistry of HMX Combustion", AIAA Journal, Vol. 23, n° 2, p. 276, 1985.

[27] Kubota N. and Sakamoto S., "Combustion Mechanism of HMX", 19th International Annual Conference of ICT, Karlsruhe, June 1988.

[28] Mitani T. and Williams F.A., "A Model for the Deflagration of Nitramines", 21st Symposium (International) on Combustion, pp. 1965-1974, The Combustion Institute, 1986. Also, Sandia Report 86-8230, December 1986.

[29] Lengellé G. and Duterque J., "Combustion of Propellants Based on HMX", AGARD/PEP Specialists' Meeting on Smokeless Propellants, AGARD CP n° 391, Florence, September 1985.

[30] Bizot A. and Beckstead M.W., "A Model for HMX Combustion", International Seminar on Flame Structure, Alma-Ata (Former USSR), September 1989.

[31] Shoemaker R.L. et al, "Thermophysical Properties of Propellants", Thermal Conductivity, Vol. 18, pp. 199-211, 1985.

[32] Hatch R.L., "Chemical Kinetics of HMX Combustion", 24th JANNAF Combustion Meeting, Monterey, Cal., October 1987.

[33] Brill T.B., "Heat Flow / Chemistry Interface in the Condensed phase (HMX)", ONR Workshop on Energetic Material Initiation Fundamentals, Livermore, Cal., December 1988.

[34] Liau Y.C. and Yang V., "Analysis of RDX Monopropellant Combustion with Two-Phase Subsurface Reactions", Journal of Propulsion and Power, Vol. 11, July 1995, p. 729.

[35] Longevialle Y., Golfier M. and Graindorge H., "New Generation of Propellants for High Performances Solid Rocket Motors", RTO / AVT Symposium Small Rocket Motors, 1999.

[36] Trubert J.F. and Hommel J., "Study of the Condensed Phase Degradation and Combustion of Two New Energetic Charges for Low Polluting and Smokeless Propellants: HNIW and ADN", ICT Annual Conference, June 2002.

**Composite Propellants References**

[37] Beckstead M.W., Derr R.L. and Price C.F., "A Model of Composite Solid-Propellant Combustion Based on Multiple Flames", AIAA Journal, Vol. 8, n° 12, pp. 2200-2207, 1970.

[38] Cohen N.S., "Review of Composite Propellant Burn Rate Modeling", AIAA Journal, Vol. 18, n° 3, pp. 277-293, 1980.

[39] Cohen N.S. and Strand L.D., "An Improved Model for the Combustion of AP Composite Propellants", AIAA paper n° 81-1553, 17th Propulsion Conference, 1981.

[40] Ramohalli K.N.R., "Steady State Burning of Composite Propellants", in Fundamentals of Solid-Propellant Combustion (Ed. K.K. KUO and M. Summerfield), Vol. 90 of Progress in Astronautics and Aeronautics, 1984.

[41] Cohen N.S., Crowley J.C. and Lo G.A., "Effects of HMX Addition on the Combustion of Energetic Binders", 21st JANNAF Combustion Meeting, October 1984.

[42] Beckstead M.W. and McCarty K.P., "Modeling Calculations for HMX Composite Propellants", AIAA Journal, Vol. 20, n° 1, pp. 106-115, 1982.

[43] Duterque J. and Lengellé G., "Combustion Mechanisms of Nitramine Based Propellants with Additives", AIAA paper n° 88-3253, 24th Propulsion Conference, 1988. Journal of Propulsion and Power, Vol. 6, n° 6, pp. 718-726, December 1990.

[44] Blomshield F. and Osborn J., "Nitramine Composite Solid Propellant Modeling", AIAA paper n° 90-2311, 26th Propulsion Conference, 1990.

[45] Beckstead M.W., "A Model for Composite Modified Double-Base Propellant Combustion", 26th JANNAF Combustion Meeting, October 1989.

[46] Cohen N.S., "A Pocket Model for Aluminum Agglomeration in Composite Propellants", AIAA Journal, Vol. 21, n° 5, pp. 720-725, 1983.

[47] Price E.W., "Combustion of Metalized Propellants", in Fundamentals of Solid-Propellants Combustion (Ed. K.K. Kuo and M. Summerfield), Vol. 90 of Progress in Astronautics and Aeronautics, 1984.

[48] Duterque J., "Experimental Studies of Aluminium Agglomeration in Solid Rocket Motors", 4th International Symposium on Special Topics in Chemical Propulsion, Stockholm (Sweden), 1996, Begell House Inc. Publisher.

[49] Renie J.P. and Osborn J.R., "Combustion Modeling of Aluminized Propellants", AIAA paper n° 79-1131, 15th Propulsion Conference, 1979.

[50] Lengellé G., Fourest B., Godon J.C. and Guin C., "Condensed Phase Behavior and Ablation Rate of Fuels for Hybrid Propulsion", AIAA paper n° 93-2413, 29th Propulsion Conference, 1993.

[51] Trubert J.F., Duterque J. and Lengellé G., "Study of the Condensed Phase Degradation and Combustion of Glycidyl Azide Polymer", ICT Annual Conference, June 1999.

[52] Ishihara A., Brewster M.Q., Sheridan T.A. and Krier H., "The Influence of Radiative Heat Feedback on Burning Rate in Aluminized Propellants", Combustion and Flame Vol. 84, pp. 141-153, 1991.

# A Summary of Aluminum Combustion[*]

M.W. Beckstead

Brigham Young University

Provo, Utah, USA

## Abstract

The combustion characteristics of aluminum combustion are summarised in an overview of the subject, focusing on the burning time of individual particles. The fundamental concepts that control aluminum combustion are discussed starting with a discussion of the "$D^n$" law. Combustion data from over ten different sources with almost 400 datum points have been cataloged and correlated. Available models have also been used to evaluate combustion trends with key environmental parameters. The exponent is shown to be less than two, with nominal values of ~1.5 to 1.8 being typical. The effect of oxidizer is pronounced with oxygen being twice as effective as water and about five times more effective than carbon dioxide. The observed effect of pressure and initial temperature is minimal.

In the second part of the paper a two-dimensional unsteady state kinetic-diffusion-vaporization controlled numerical model for aluminum particle combustion is presented. The model solves the conservation equations, while accounting for the species generation and destruction with a 15 reaction kinetic mechanism. Two of the major phenomena that differentiate aluminum combustion from hydrocarbon droplet combustion, namely the condensation of the aluminum oxide product and the subsequent deposition of part of the condensed oxide, are accounted for in detail with a sub-model for each phenomenon. The effect of the oxide cap in the distortion of the profiles around the particle has been included in the model. The results obtained from the model, which include two-dimensional species and temperature profiles, are analyzed and compared with experimental data. The combustion process is found to approach a diffusion controlled process for the oxidizers and conditions treated. The flame zone location and thickness is found to vary with oxidizer. The result shows that the exponent of the particle diameter dependence of burning time is not a constant and changes from about 1.2 for larger diameter particles to 1.9 for smaller diameter particles. Due to the deposition of the aluminum oxide on the particle surface, particle velocity oscillates. The effect of pressure is analyzed for a few oxidizers.

## Introduction

Aluminum has been added to propellants for many years as an extra energy source for the propellant. Thus, research on the combustion mechanism of burning aluminum has been an ongoing effort. A very significant effort was expended in the 1960's and 1970's shortly after the effects of aluminum were first conceived. In an early study Glassman[1,2] recognized that metal combustion would be analogous to droplet combustion, and that the $D^2$ law ought to apply, and that ignition and combustion ought to depend on the melting and boiling points of the metal and the oxide. He speculated that ignition would not occur until the oxide shell melted at its melting point and that subsequent combustion would achieve a steady state condition with the aluminum at its boiling point. These basic concepts have provided a general framework for interpreting aluminum combustion.

---

A question that has often been asked, is whether laboratory data in air at ambient pressure and temperature can be related to motor conditions at high temperature, high pressure and in propellant products that do not contain oxygen. One of the purposes of this study was to develop sufficient understanding of aluminum combustion based on laboratory data, simulated motor data and actual motor data, to answer that question. Other questions can be asked about the effect of aluminum on combustion efficiency, slag formation, effects of agglomeration, and the potential effect of aluminum on a propellant's burning rate. These questions will not be addressed in this paper, although the understanding gained here should be applicable to some of the questions.

In the 70's and early 80's several survey papers and reports were written, summarizing the work up to that time. Some of the most useful are the works of Pokhil, et al[3], Frolov, et al[4], Micheli and Schmidt[5], Glassman, et al[6], and Price, et al[7,8]. This paper will focus on the burning time of aluminum and the effect of various parameters on that burning time. Extensive research has been performed in Russia (then, the Soviet Union) and brief summary of that work is included. Following that, data from those sources that were available to the author, evaluating the effects of particle diameter, oxidizing species, pressure, and temperature on aluminum combustion.

Aluminum combustion in air[1] suggests that it burns as a vapor and the combustion is controlled by the diffusion of the fuel and oxidizer. However, aluminum combustion cannot be analyzed with a simple hydrocarbon droplet combustion model. This is due to some complications with aluminum combustion. First, in aluminum combustion, the gas phase combustion products condense to liquid aluminum oxide. This condensation dominates the combustion process and contributes considerably to the amount of heat released during combustion. Second, condensed aluminum oxide can deposit on the particle surface to form an oxide cap, which distorts the distribution of gasification velocity, temperature and other quantities around the particle. Also, the oxide cap cam cause jetting and fragmentation of the particle. Third, the dissociation of the condensed product maintains the flame temperature fairly constant at the gasification temperature of the aluminum oxide. Hence, hydrocarbon droplet combustion models cannot be extended directly to model aluminum combustion.

The second part of this paper focuses on modeling the basic combustion process of a burning aluminum particle. Aluminum combustion models have been developed since the 1960's. Brzustowski and Glassman[2] were among the first to suggest that aluminum burns in the vapor phase. They stated that a metal would burn in the vapor phase if its boiling point temperature were lower than that of its oxide. Their model included many of the same assumptions as in hydrocarbon droplet combustion models. Law[3] was the first to acknowledge some of the effects of the oxide condensation in a model. Law's analytical model has been upgraded by Turns[4], Brooks[5,6] and Bhatia[7] by relaxing certain assumptions in Law's model. Many of the earlier models[2,3] have focused on calculating the burning time and flame temperature, but could not predict the distributions of physical quantities nor processes such as condensation and deposition. The postulated combustion mechanisms were much simplified, using global kinetics. Many of the models[2,3,8] have not accounted for the effects of the oxide cap in the distortion of the symmetrical flame. Many of the models have assumed quasi-steady state[3,8,9]. Many of the models have concentrated on aluminum combustion in air, while one of the main uses of aluminum is in rocket motors, where the oxidizers mainly consists of $CO_2$ and $H_2O$.

## Aluminum Combustion Research in Russia

Overviews and surveys of Russian work on aluminum combustion or metal combustion in general has been performed by Pressley[9] in the US, as well as the Pokhil[3], and Frolov[4], papers previously referenced. The reader is referred to these reports for discussions on the work prior to that time.

In 1968 Belyaev, et al[10] published a classic paper on aluminum combustion, which has been referenced by most subsequent papers in the Russian literature. They incorporated aluminum into propellants at 0.01% so they were measuring the burning rates of individual particles, avoiding agglomeration effects.

They varied the effective $CO_2$ and $H_2O$ concentrations in the gas, (i.e. $a_K$), diameter and pressure, and developed an expression for particle burning time as:

$$= 0.67 \, D^{1.5}/a_K^{0.9} \tag{1}$$

where D is the particle diameter in µm, $a_K$ is the relative concentration of $CO_2$ and $H_2O$ in the gas, and is the burning time in msec. CO was not considered an active oxidizer because the energy to break down the CO molecule is double that of either $CO_2$ or $H_2O$. Below pressures of ~25-30 atm, they observed burning time decreasing ~10-12%, but at greater pressures they did not observe a change with pressure. They varied the propellant formulation so that $a_K$ was varied from 0.3 to 0.7, and particle diameters were varied from 70 to 140 µm, determining the exponent of 0.9, and the coefficient of 0.67 in the equation. They also observed that burning time decreases with increasing ambient temperature up to ~2000K. They examined the ignition time of the particles, concluding that it is proportional to $D^2$ with an activation energy of ~32 kcal/mol. Equation (1) is the expression used in most Russian papers to describe the burning time of aluminum up to the current time.

Boreisho, et al[11] reported that the photographically determined flame sizes around a burning particle could be 1.5 up to 4 times larger than actual. Arkhipov, et al[12] measured flame distances by dropping burning particles onto glass slides observing flame distances of ~ $3D_o$. Dreizen and Trunov[13] have recently reported similar experiments.

A number of papers have focused on the ignition process of metals, aluminum in particular. Merzhanov, et al[14] postulated that the ignition temperature coincides with the melting point of $AL_2O_3$, 2300 K, and estimated an activation energy of 17 (Belyaev reported a value of 32). Breiter, et al[15] published an extensive summary of the ignition of metals considering thirteen different metals and six alloys based on Glassman's work in this country. They classified the ignition characteristics of the metals according to the relative densities of the metal versus that of the oxide and the melting point of the oxide. Thus, the impervious character of aluminum oxide inhibits ignition up to the temperature, at which it melts, which then results in ignition and combustion. Ermakov, et al[16] embedded a thermocouple into an aluminum particle, and measured ignition temperatures of ~2000-2100 K, concluding that ignition occurs due to the failure of the oxide shell integrity, but not necessarily due to melting. Lokenbakh, et al[17] contend that mechanical cracking of the oxide shell can occur under varying heating and ambient conditions, leading to ignition and/or enhanced agglomeration at temperatures as low as 1000 to 1300 K. Boiko, et al[18] examined ignition of several metals in a reflected shock wave, also concluding that ignition can occur due to fracturing of the oxide shell when subjected to mechanical stresses. Rozenband and Vaganova[19] also propose ignition by fracture of the oxide shell due to mechanical stresses caused by thermal expansion and density differences during rapid heating. Rozenband, et al[20] also claim that $CrCl_3$ can react with the oxide shell reducing the ignition temperature to ~900K.

The characteristics of the oxide particles formed from the combustion of a metal are very important relative to performance (i.e. combustion efficiency) and acoustic particle damping. Fedorov, et al[21] measured a bimodal distribution of $Al_2O_3$ in the exhaust from small motors, observing most of the oxide as smoke ~1.5 to 2 µm, but with a second larger fraction of particles ~6 µm. They also observed that the percentage of fines increased at higher pressures. Arkhipov et al[12] measured oxide particles of ~1-2 µm at one atm pressure in a laboratory experiment.

There are a large number of papers discussing models that describe the ignition process leading to metal combustion. For example, Gostintev et al[22], Gremyachkin[23], Arutyunyan, et al[24], etc., all developed models describing the ignition of metals, usually aluminum. Gurevich, et al[25], Gremyachkin[23], Gostintev[22], Bezprozvannykh, et al[26], Rozenband and Vaganova[19] and Kovalev[27] all developed models allowing for the growth of protective oxide on the surface, comparing that to another aspect of the

ignition process (e.g. strength of the oxide layer, transient heating, etc.). Both Gremyachkin and Rozenband and Vaganova showed that ignition could occur well below the oxide melting point. Kovalev[27] showed that the ignition time should be proportional to $D^2$. Medvedev, Fedorov and Fomin[28] conclude that Mg ignites by thermal explosion while Al ignites by a critical ignition temperature (the oxide melting temperature).  There is obviously a diversity of opinion, but also the different authors developed their models for different ignition conditions, some considering slow heating, others considering very rapid heating, etc.

Kudryavtsev, et al[29], Gremyachkin, et al.[30,31], etc all developed models for describing the rate of combustion of metals, usually aluminum.  Babuk, et al[32] have studied the effect of metal oxide formation on the combustion.  Gremyachkin, et al[31] developed a model for the combustion of aluminum particles (droplets) including oxidizer diffusion to the surface and heterogeneous reaction there.  They also contend that aluminum can react with the oxide on the surface forming $Al_2O$ which has a high vapor pressure.  They account for the effects of $O_2$, $H_2O$ and $CO_2$ as oxidizers, concluding that the burning times for $CO_2$ are twice as long as for water, and that the burning times for water are 1.5 times as long as for oxygen. Kudryavtsev, et al[29] developed a model including the reaction of aluminum and water.  Their model shows burning times constant above ~350 psi, but varying at lower pressure (in agreement with experimental data).  They say that the low pressure variation is due to the diffusion process being inhibited by the oxide cloud.

### Experimental Investigations into Aluminum Particle Combustion

As part of this study, as much data as possible has been accumulated, documented and assembled in a common format. The various sources are listed in Table I, along with a brief summary of the range of test conditions for which they performed their experiments.  Only sources have been used where variations in the data were sufficient to show a trend.  Many other sources where data have been obtained at a single set of conditions have not been included.   A data base of approximately 400 datum points have been compiled and analyzed to evaluate the dependencies of the various parameters on the aluminum burning time.  The results of those studies are presented below.

This brief summary is not necessarily comprehensive, but is intended to identify major research contributions, particularly where burning time data were available that could be correlated with other researchers.  A brief description of their technique is included along with a discussion of their results and conclusions.  For simplicity, research has been separated by the technique used to ignite the aluminum particle: propellant, gas burner, laser, flash, and shock.

Propellant Ignited Aluminum Particles

Using propellant to ignite aluminum particles is obviously advantageous since conditions similar to that of a rocket motor are created. Yet the high temperature, high pressure, and corrosive environment of propellant combustion is difficult to control experimentally.

Table I - Sources of Aluminum Combustion Data

| Author | Date | Do (µm) | Ambient T To (K) | P(atm) | Gas Concentrations (%) H2O | O2 | CO2 | CO | N2 | Ar | HCl |
|---|---|---|---|---|---|---|---|---|---|---|---|
| Friedman & Macek[33,34] | 1962-3 | 15-67 | 2510 | 1 | 17 to 18 | 5 to 6 | 12 to 14 | 0 | 63 to 65 | 0 | 0 |
| Davis[35] | 1963 | 60-96 | 2200-3200 | 1-204 | .5 to 50 | 0 to 27 | 9 to 50 | 9 to 41 | 9 to 41 | 0 | 0 -21 |
| Macek[36] | 1967 | 32-49 | 2500 | 1 | 0 to 17 | 8 to 16 | 13 to 43 | 0 | 40 to 58 | 0 | 0 |
| Hartman[37] | 1971 | 23-94 | 3000-3189 | 25.5 | 27 to 34 | 0 to 4 | 17 to 23 | 9 to 30 | 13 to 20 | 0 | 0 - 8 |
| Wilson & Williams[38] | 1971 | 24-74 | 298 | 2 - 5 | 0 | 10 to 30 | 0 | 0 | 70 to 90 | 90 | 0 |
| Prentice[39] | 1974 | 250-400 | 298 | 1 | 0 to 3 | 15 to 75 | 0 to 50 | 0 | 0 to 80 | 0 - 85 | 0 |
| Turns and Wong[40,41] | 1987 | 300-760 | 1809-1827 | 1 | 29 to 31 | 10 to 25 | 27 to 30 | 15 to 49 | 46 to 64 | 0 | 0 |
| Roberts, et al[42] | 1993 | 20 | 2225-2775 | 85.-34 | | 99 | | | 1 | | |
| Marion[43,44] | 1995 | 35-40 | 298 | 1 - 39 | 0 | 21 | 0 | 0 | 79 | 0 | 0 |
| Olsen & Beckstead[45] | 1996 | 40-70 | 3000 | 1 | 66 to 89 | 11 to 16 | 0 to 18 | 0 | 0 | 0 | 0 |
| Melcher, et al[46] | 1999 | 106 | 2300 | 13-22 | 41 to 38 | 0 to 11 | 12 to 16 | 9 to 2 | 10 | 0 | 18 |
| Dreizin[47,48] | 1999 | 90,200 | 298 | 1 | | 5-100 | | | 5-90 | 0-95 | ** |
| Zenin[49,50] | 2000 | 185-500 | 298 | 1 - 40 | 0 | 0 to 20 | 0 to 100 | 0 | 0 to 80 | 0 - 80 | 0 |

Davis[35] prepared ammonium perchlorate and paraformaldehyde propellants with less than 1% aluminum by mass. These propellant samples were ignited in a 'bomb' apparatus with pressures ranging up to 200 atm. Particle combustion was captured with high-speed cinematography through windows. Using aluminum particles with initial diameters ranging from 53 to 103 µm, Davis found that an exponent of 1.8 for Equation 3.1 fit the data well. Davis also noted that the burning rate increased while the pressure climbed from 20 to 70 atm, but the rate was constant thereafter. Similar to Davis, Friedman and Macek[33] and Macek[36] also created aluminized propellant samples which burned with pressures ranging up to 135 atm. Friedman and Macek noted that hollow oxide spheres were produced when the apparatus was operated at atmospheric pressure.

Hartman[37] performed similar experiments using composite modified, double base propellant which contained three oxidizers: ammonium perchlorate, nitrocellulose, and nitroglycerin. Varying the formulation of this propellant provided a wider range of oxidizer environments in which aluminum particles could burn. Hartman chose particle distributions with mean diameters of 23, 54, and 94 µm and did testing at pressures of 19, 26, and 50 atm. He found a dependence on pressure and oxidizer environment similar to that seen by Davis. Hartman reported his data by using Equation 3.1, but observed a dependence on pressure raised to the 0.4 power.

Krier (Burton, et al[51] and Melcher, et al[52]) has tried two approaches to investigate aluminum particle combustion with an AP/HTPB propellant as an ignition source. Similar to the research just reviewed, Krier aluminized his propellant sample for one approach. Additional oxygen could be introduced into the propellant exhaust products via an injector to increase the oxygen concentration up to 10%. The burning rate was only slightly dependent on the oxygen concentration, but this conclusion may be in error due to poor mixing of the oxygen with the propellant exhaust. Pressure was varied from 13 to 22 atm and the burning rate increased linearly with pressure over this range. For a second approach, an injector delivered a mono-disperse aluminum particle stream to the exhaust products of a non-aluminized AP/HTPB propellant. Using strobed photographic techniques, burning times were 10±2 ms for nominally 68 µm particles which is in general agreement with other published research.

Gas Burner Ignited Aluminum Particles

In experiments where gas burners are used, the aluminum particles are passed through a gaseous flame hot enough to achieve ignition. Propane, carbon monoxide, methane, hydrogen, and cyanogen are some fuels that have been used. Oxygen is the typical oxidizer with nitrogen used as a dilutant. After an aluminum particle ignites, it burns in the exhaust products of the gaseous flame, which includes both water and carbon dioxide as oxidizer species, in addition to any available diatomic oxygen. These studies create an atmosphere that is similar to that in a solid propellant, but allowing the experimentalist greater control over what could be achieved with actual propellants. With a few exceptions, most studies using gas burners to ignite aluminum particles have been performed at atmospheric pressure since controlling a gaseous flame at high pressures is challenging.[45] Strobe photography and high-speed cinematography are typical tools used to measure particle burning times.

Friedman and Macek[33,34] and Macek[36] provide some of the first reported burning time data for aluminum particle combustion. They ignited small particles (30 to 50 µm) in propane or carbon monoxide flat flame burners. Little difference in burning times was found using either fuel. In both burners, a fine oxide smoke and porous or hollow oxide spheres were formed. These oxide 'bubbles' were more numerous in the exhaust environments containing water. They also saw consistent fragmentation during the vigorous combustion of aluminum particles in oxygen rich environments. Their data suggested an exponent of 1.2 to 1.5 for Equation 3.1.

Bartlett, et al[53] used a methane flame to ignite several different aluminum particle distributions with mean diameters ranging from 15 to 32µm. Hollow oxide spheres were found after particle burnout which were close to the size of the original aluminum particle. The spheres were crushed and examined under a microscope. A porous structure was observed with small specks of metal.

Davis[35] used a carbon monoxide flame to ignite his aluminum particles that were between 53 and 66 µm. In Davis' photographs he was able to discern that the particle's flame front was several diameters larger than the particle and thus had evidence for vapor-phase combustion. Davis also observed porous oxide spheres in the residue collected after combustion. He noted increasing particle fragmentation for any oxygen concentration over 32% by volume. He suggested that the particle burning time was inversely proportional to the oxygen partial pressure. He also concluded that the ambient oxygen concentration was more important to the particle combustion rate than the ambient temperature.

Drew, et al[54,55], Prentice[39] and Price, et al[56] performed a number of aluminum particle combustion experiments, many of them qualitative, but some were quantitative. Their burners used hydrogen, carbon monoxide and cyanogen combined with oxygen. Particles ranged in size from 30 to 400µm. Burning

times were determined using photographic techniques, and combustion morphology was investigated by using microscopes to examine particles quenched during combustion.

Particle spinning, metal vapor jetting, and violent fragmentation were observed in both the hydrogen and carbon monoxide flames. With a hydrogen flame, a smaller flame diameter was observed, possibly due to the higher diffusivity of water as opposed to carbon monoxide. Also large numbers of hollow oxide spheres were formed. In the carbon monoxide flame, few hollow oxide spheres were present, and a noticeable amount of unburned aluminum was present in the exhaust residue. If just 5% hydrogen were added to the carbon monoxide flame, results were similar to the pure hydrogen and oxygen flame. Particles ignited in the cyanogen flame exhibited behavior similar to that seen with a carbon monoxide flame.

Wong and Turns[40,41] added aluminum powder to jet fuel (JP-10) to create slurry droplets with diameters ranging from 500 to 1100 µm. These droplets were suspended on silicon carbide fibers and then suddenly exposed to the hot exhaust gases of a carbon monoxide or methane flame. Upon burnout of the jet fuel, the aluminum would agglomerate forming an aluminum particle with a diameter ranging from 300 to 800 µm. Using high-speed cinematography, they observed that the vapor-phase flame front was smaller for the methane flame, where water would be present, when compared to the 'dry' environment of the carbon monoxide flame. Also eruptions and fragmentation were noted for the 'wet' environment. They found that burning times decreased when the flames were operated fuel lean such that there was excess oxygen in the flame exhaust.

Olsen and Beckstead[45] used a carbon monoxide/hydrogen diffusion flame to ignite aluminum particles one at a time. A photomultiplier tube was used to record the combustion event. Particles, ranging in size from 40 to 80 µm, were meticulously chosen individually under a microscope. Olsen interrupted the combustion of some particles by quenching. Using scanning electron microscopy and X-ray analysis, he was able to examine the combustion morphology of the particles and the formation of porous oxide spheres that were prevalent. Olsen found that his oxidizer concentration ($H_2O$, $CO_2$, or $O_2$) had a strong effect on the particle burning rate. He concluded that the difference in the burning rate exponent among different researchers was as much due to the varied data reduction techniques used as it was due to the diverse physical conditions of each experiment. Olsen also postulated that the burning rate exponent probably changed during the combustion history of a particle—ranging from approximately two at ignition and decreasing towards one at particle burnout. He suggested this burning rate decrease would occur because of the increasing fraction of aluminum oxide covering the molten aluminum sphere.

Foelsche, et al[57] recently used photodiodes to measure the burning time of a small cloud of aluminum powder (approximate diameter of 22 µm) inside a combustion bomb with pressures ranging from 38 to 145 atm. The aluminum particles were injected into the bomb shortly after the ignition of a $H_2/O_2/N_2$ mixture generated high temperatures and pressures. Foelsche found his data compared favorably with that of Davis, but showed a greater pressure dependency.

Laser, Flash, and Shock Ignited Aluminum Particles

By using lasers, flash tubes, or shock waves some researchers have ignited aluminum particles and observed their behavior. Since this ignition method is independent of the ambient environment, the temperature, pressure, oxidizers, and inert species can be varied widely. Wilson and Williams[38] ignited single aluminum particles with a laser in an oxygen/argon atmosphere. They found that dilute amounts of argon suppressed oxide cap formation and particle fragmentation. Without an oxide cap, the particles appeared to burn in accordance with the vapor-phase model suggested by Brzustowski and Glassman[58].

High-speed photography captured the combustion history of the nominally 50 µm particles in a chamber with pressures ranging to 5 atm.

Drew, et al[59] and Prentice, et al[39,60] used lasers to ignite individual particles. In addition, a xenon flash tube was used to ignite small aluminum foil discs. The molten discs formed particles approximately 250 to 400 µm in diameter. These particles were burned in room temperature combinations of $CO_2/O_2$, $N_2/O_2$, and $Ar/O_2$. For some tests, the atmosphere was made 'wet' by introducing water vapor as a second oxidizer. All experiments were performed at atmospheric pressure. Particle combustion history was recorded with high-speed cameras, while the combustion morphology of quenched samples was examined using scanning electron microscopy.

Oxide caps did not form when the environment was argon and oxygen, similar to the observations of Wilson and Williams. When water was introduced, caps did form. At ambient temperature, the particles would extinguish in the carbon dioxide environment before all the aluminum metal was consumed. With an $N_2/O_2$ atmosphere, the particles would consistently fragment irrespective of the amount of water vapor present. Once again, hollow oxide spheres were observed for many test cases.

Roberts, et al[42] used a shock tube to ignite aluminum, magnesium, and aluminum/magnesium alloy particles at pressures up to 34 atm in almost pure oxygen. Several thousand particles with a nominal diameter of 20 µm were placed on a knife blade near the reflecting wall of the shock tube. The passing shock knocked the particles into free fall and ignited them where a photodiode recorded the light emitted during combustion. The researchers concluded that the burning time for the aluminum particles was not a strong function of pressure although a slight decrease in burning time was noted for increasing pressure.

Bucher, et al[61,62,63] used a 150 W laser to ignite aluminum particles nominally 230 µm in pure $N_2O$, pure $CO_2$, and in mixtures of $O_2$, $N_2$, Ar, and He. In-situ temperature and species distributions around individual burning particles were made using planar laser-induced fluorescence. Quenched particles were investigated with electron probe microanalysis. Bucher found that the flame diameter around a particle decreased with varying environment gas mixture in the following order: $O_2/Ar$, $O_2/N_2$, $CO_2$, and $N_2O$. AlO was found to be an intermediate species in the combustion reaction while for the first time the presence of aluminum-oxy-nitrides was established. Measurements confirmed the idea that the aluminum oxide's boiling point limits the flame temperature.

Marion, et al[43,44] measured the burning time of 40 micron aluminum at 1 to 40 atm in air, using a laser for ignition. Burning times were observed to decrease slightly with pressure increasing from 1 to 4 MPa. They also report calculated burning times for a modified Law model[64] (very similar to the Brooks[65] model). In calculating the decreasing size of the aluminum particle, they predicted a residual oxide particle approximately 70% of the size of the original aluminum particle, and increasing slightly with increasing pressure. Their predicted burning times are slightly greater than experimentally observed burning times, and they attribute that to the uncertainty in the density-diffusivity product which they used in their model.

Dreizien and Trunov[13] burned 150 µm Al droplets in air at room temperature and 1 atm, similar to Prentice's work. They saw a region of spherically symmetric burning, followed by two regions of oscillating burning with the particles giving off smoke jets and spiraling.. Subsequently Dreizien[47,48] tested 90 and 250 µm particles in $N_2/O_2$, $Ar/O_2$, $He/O_2$ and pure $O_2$ varying concentrations. He saw spinning and periodic brightness oscillations mainly in the $N_2/O_2$ case but also in $He/O_2$. The size of observed oxide caps are much smaller with $Ar/O_2$ and $He/O_2$ than in air. He reports burning time data for

the mixtures at varying concentrations, showing a significant decrease in burning time with increasing oxygen concentration. Rates in argon, nitrogen and helium fall virtually on top of each other He assumes this is due to the fact that the density-diffusivity product is approximately constant. He has also examined the aluminum flame structure both with and without gravity, using photomultiplier tubes.

<div align="center">

**Summary of Experimental Combustion Data**

</div>

The burning time data from as many of these sources as could be readily determined from their papers are presented in Figure 1. The data scatter is readily apparent. Several of the investigators only used a single particle size, varying the test conditions. For example, Dreizin[47,48] did extensive testing varying gas concentrations, but with only two particle sizes. Melcher[46] and Roberts[42] both did their testing with a single particle size, and much of Prentice's work[39] was done with a single particle size. The differing test conditions lead to different burning times, introducing what appears as "data scatter" in Figure 1. The following sections discuss various other sources of data scatter. It is curious that the optimum fit of the data results in a $D^2$ correlation. The following sections will also address the potential value of the burning time exponent.
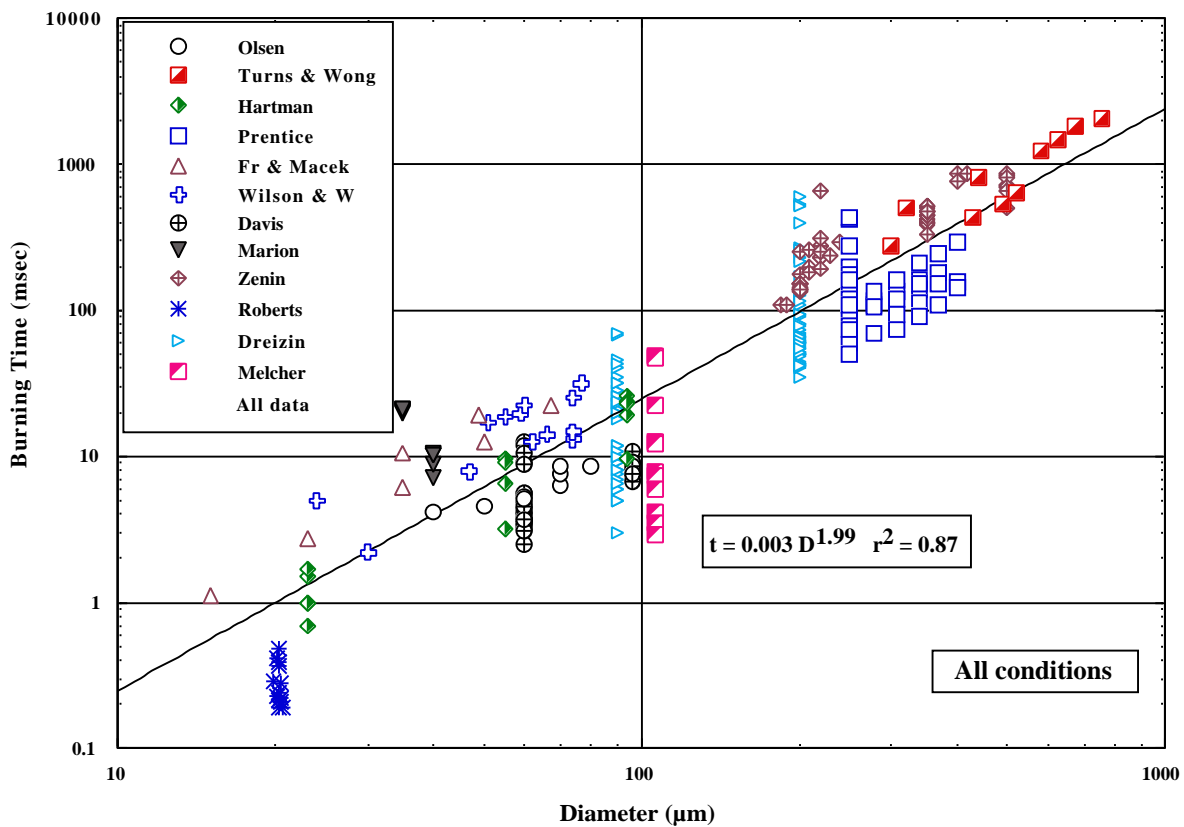


Figure 1. Aluminum burning time measurements from eleven different sources, measured under a wide variety of conditions and test techniques.

<div align="center">

**The "$D^2$" Law in Aluminum Combustion**

</div>

The geometrical aspect of particle or droplet combustion can be described by a simple mass balance. Assuming that the droplet is spherical and regresses uniformly, the mass burning rate will be

$$\dot{m} = -\frac{d}{dt}\left(\text{volume} \times \text{density}\right) = -\frac{d}{dt}\left(\frac{4}{3}\pi r^3\right) = -4\pi r^2 \frac{dr}{dt} \qquad (2)$$

or, in terms of diameter

$$= -\pi D^2 \frac{d(D/2)}{dt} = -\frac{\pi D}{4}\frac{dD^2}{dt} \qquad (3)$$

Solving for the rate of change of the diameter gives

$$\frac{dD^2}{dt} = -\frac{4\dot{m}}{\pi D} = \text{constant} \qquad D^2 = D_o^2 - \beta t \quad \text{where} \quad \beta = \frac{4\dot{m}}{\pi D} \qquad (4)$$

Solving for time

$$t = \frac{D_o^2 - D^2}{\beta} \qquad \text{at burn out, } D \to 0 \qquad t = \frac{D_o^2}{\beta} \qquad (5)$$

This is the $D^2$ law. The question is how well it applies to the combustion of aluminum. First, it should be noted that the inherent assumption is that the spherical droplet is regressing uniformly. Many of the papers discussed above have noted that an oxide lobe develops on the burning aluminum. Thus, the droplet is NOT regressing uniformly. If one accounts for this, the complete spherical surface area is not available for combustion, leading to a reduced exponent in the $D^n$ law. Second, it is assumed that the particle burns out to a diameter of zero. This is not consistent with experimental observations either. Many researchers have observed fragmentation of burning aluminum, indicating that towards the end of burning the residual aluminum/oxide cap can break up in a violent manner, resulting in more than one resultant particle. In addition, even when fragmentation does not occur, the residual oxide particle is often very large, due to porosity. The fact that the particle does not burn to a diameter of zero will also lead to a reduced exponent (less than two). Marion, et al[44] recently used a model to calculate the burning time of aluminum. Within their model they calculate the size of the residual oxide, with fractional values of 0.6 to 0.7 compared to the original aluminum particle.

The conclusion of these observations (including those of many of the above researchers) is that few would expect the exponent to have a value of two. A value of 1.5 to 1.8 is much more likely.

Some of these observations are reinforced by a recent paper by Olsen and Beckstead[45]. A series of tests were performed interrupting the burning process with a glass slide, and then taking SEM photographs of the residual particles. Particles were hand selected to be as close to the same size (70μm) as possible and then were interrupted at increasing distances from their ignition source. Figure 2 is an example. An interesting aspect of this SEM is that the right hand side of the figure is the Al2O3, while the much smaller lobe of the sample is the aluminum. This was determined from the smoke halo on the left and by X-Ray analysis, showing that the oxide cap can be larger than the original aluminum later in burning.

The right hand lobe of the particle is oxide and the left hand, donut shaped part of the particle is aluminum.

As part of the tests, a photodiode was used to register the light intensity from the burning particles. Figure 3 contains the photodiode traces for five different particles quenched at different distances. The particle in Figure 2 was the second trace in Figure 3. It is apparent (see also the full paper by Olsen) that if one uses the entire photodiode trace to determine the burning time of a particle, the majority of that time will represent the combustion of a small fraction of the aluminum. The majority of the aluminum is burned very quickly, but a photodiode will continue to register light, just from the hot, radiating oxide particle, with a very small fraction of aluminum still burning. From examining each of

the five particles, it is evident that a large fraction of the aluminum was burned by the time the first particle was quenched, representing a burning time of ~1.5 msec. If one were to take the entire trace as the burning time a value of 6.5 msec would be recorded. The potential variability in choosing a "burning time" by different researchers can introduce a significant amount of data scatter when comparing data from different sources.
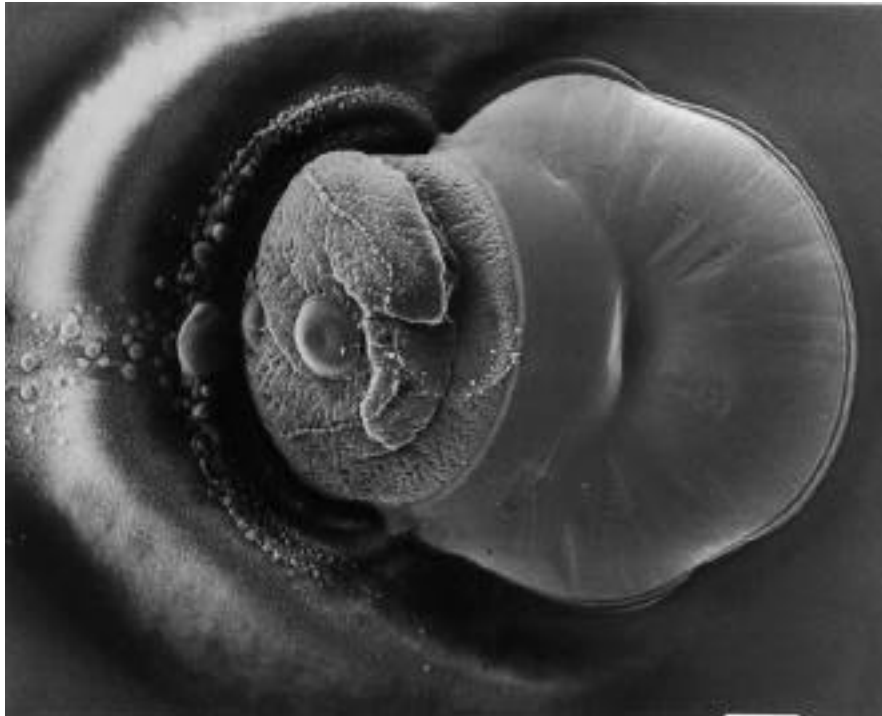


Figure 2.  SEM micrograph of a 70 µm aluminum particle quenched 2.5 to 3 msec after ignition.
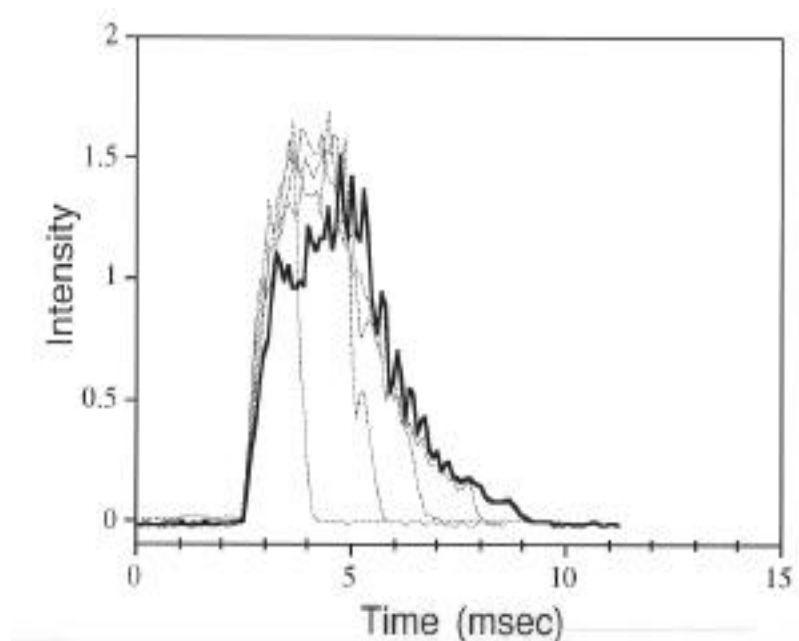


Figure 3. Photodiode emission traces of five different 70 µm aluminum particles quenched on glass slides at varying distances from the ignition point.

   In an analytical modeling study[65], the relative amounts of aluminum and oxide were estimated as part of the calculated burning time.   Those results are shown in Figure 4 for a 35 µm particle burning in a simulated propellant atmosphere at one atmosphere.  Two calculations are reported; one accounting for oxide accumulation on the particle and the other neglecting oxide buildup.  The calculation ignoring oxide buildup gives a burning time the correlates with $D^2$, while the calculation allowing for oxide accumulation gives a $D^{1.5}$ relationship.  These results are consistent with those of Marion, previously referenced, and represent another argument that the diameter exponent must be less than two.

   In most experimental investigations, the measured aluminum particle combustion has varied from the simple $D^2$ model.  For example, Pokhil, et al[3], Law[66], Prentice[39], King[67], Kuo[68], Brooks[65] and Melcher, et al[46] have all suggested a lower value of the exponent, varying from 2.0 to as small as 1.2.  The statistical analysis that has been performed as part of this study indicates that an n of ~1.8 appears to correlate the data best.
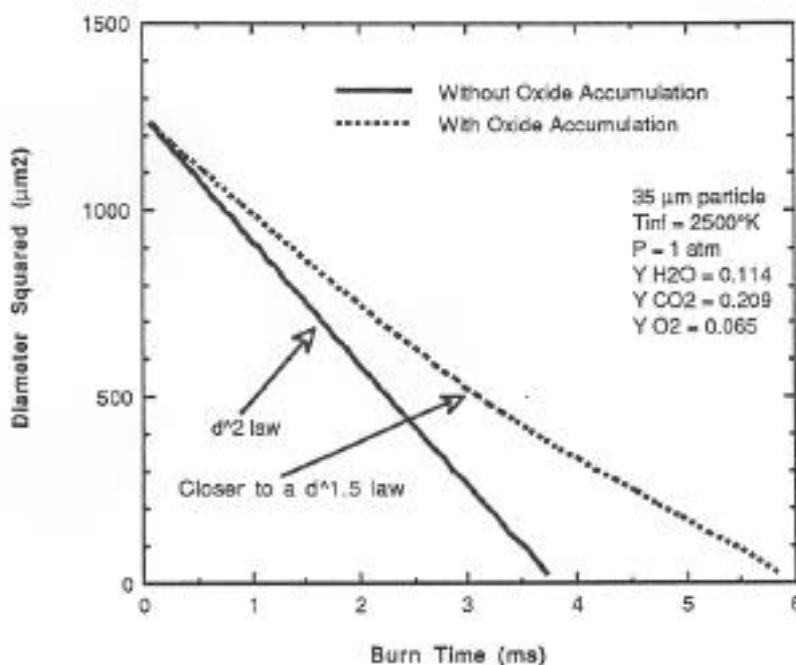


   Figure 4.  Calculated effect of oxide accumulation on the surface of a burning particle, using the Brooks model[65].

**Effects of Oxidizing Atmosphere**

The Effect of Oxygen

Referring to the data scatter in Figure 1, it is apparent that much of the scatter is due to the different oxidizing (and inert) gases used in the different tests.  Several investigators focused on the effect of the different environmental gases.  Prentice performed experiments varying the oxygen content with the other gas being nitrogen or argon.  These tests were done at one atmosphere with 250 µm particles.  His results are presented in Figure 5. The results show a very pronounced effect of oxygen concentration; the higher the concentration, the shorter the burning time.  This is to be expected, because in a diffusion

flame the concentration gradient is the principle driving force for the flame, and higher concentrations should result in shorter burning times.

Prentice also varying the particle diameter along with varying the oxygen concentration. Those results are presented in Figure 6, plotted as burning time versus diameter. The data of Turns and Wong and of Zenin are included for reference, and the overall correlation curve is included also. These results show the same effect as that of Figure 5, but within the context of the usual burning time curve.
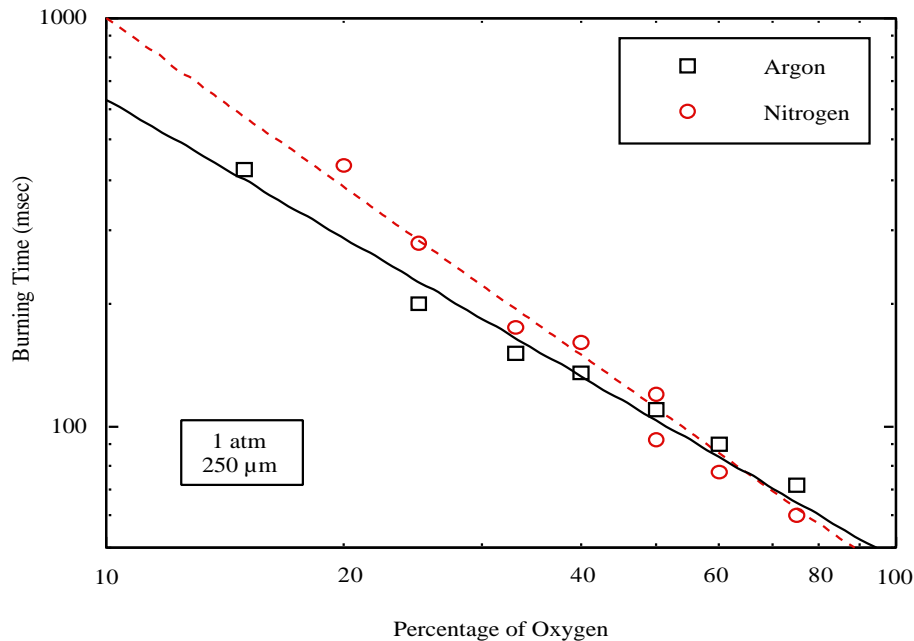


Figure 5. Prentice[39] data for 250 µm particle burning in oxygen/nitrogen and oxygen/argon.

The Effect of Diffusivity

More recently Dreizin[47] has reproduced data very similar to Prentice's, varying the oxygen concentration with inert gases of nitrogen, argon and helium. His results substantiate Prentice's results in a very quantitative manner. Using helium adds another dimension to the data. The differential equation describing diffusion contains the product of diffusivity times density both multiplying the concentration gradient. Thus it is important to consider the potential effect of diffusivity in the combustion process. In general, the diffusivity is proportional to temperature to the 1.65 power and inversely proportional to the pressure. Thus, the product of the density times the diffusivity should be approximately independent of pressure, but slightly dependent on the ambient temperature (approximately the 0.65 power). Helium has a higher diffusivity than nitrogen or argon, but it has a much lower molecular weight (which enters in to the product of density times diffusivity). Thus, the low molecular weight can compensate for a high diffusivity.

Dreizin's data (for 200µm particles) are plotted in Figure 7, comparing them to Prentice's 250 µm data. The data show that the burning time decreases, going from nitrogen to argon to helium, for low concentrations of oxygen. The molecular weight is not in the same order, i.e argon is 40, nitrogen is 28 and helium is four. A similar effect was postulated by Widener[69] in the correlation that he developed. He included the effect of diffusivity, particularly that of hydrogen. He did see a consistent effect,

dependent on the amount of hydrogen produced from the water/aluminum reaction.  This observation warrants further invstigation.
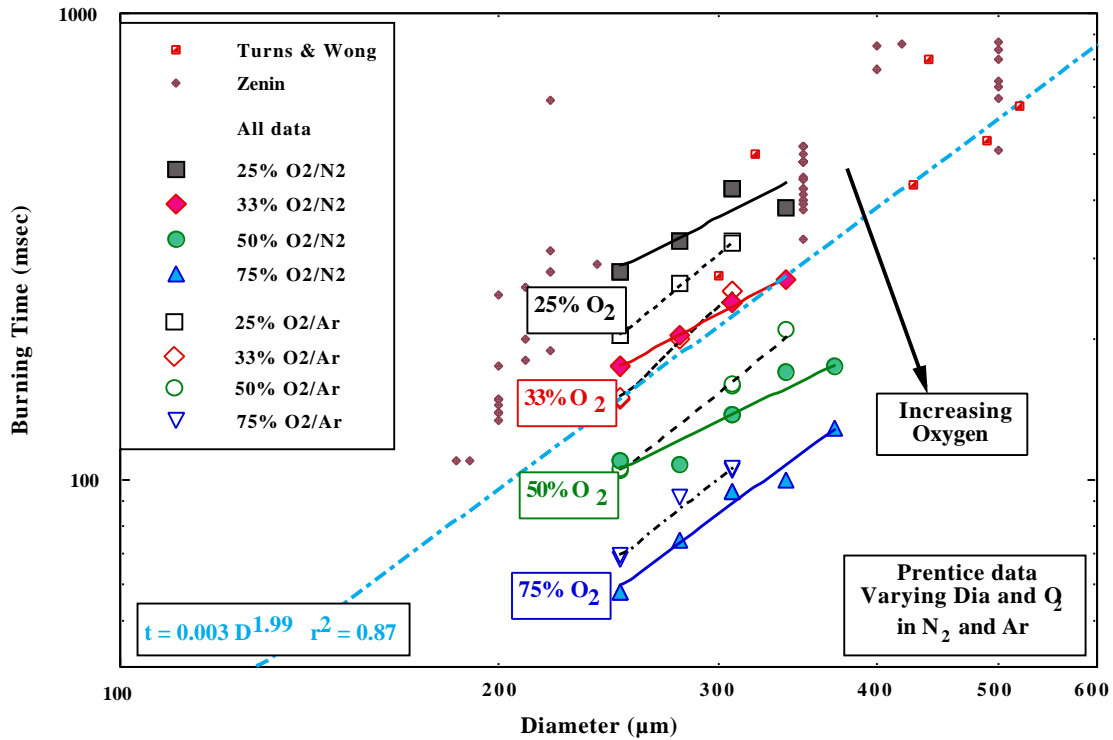


Figure 6.  Prentice[39] data varying particle size and  burning in oxygen/nitrogen and oxygen/argon.
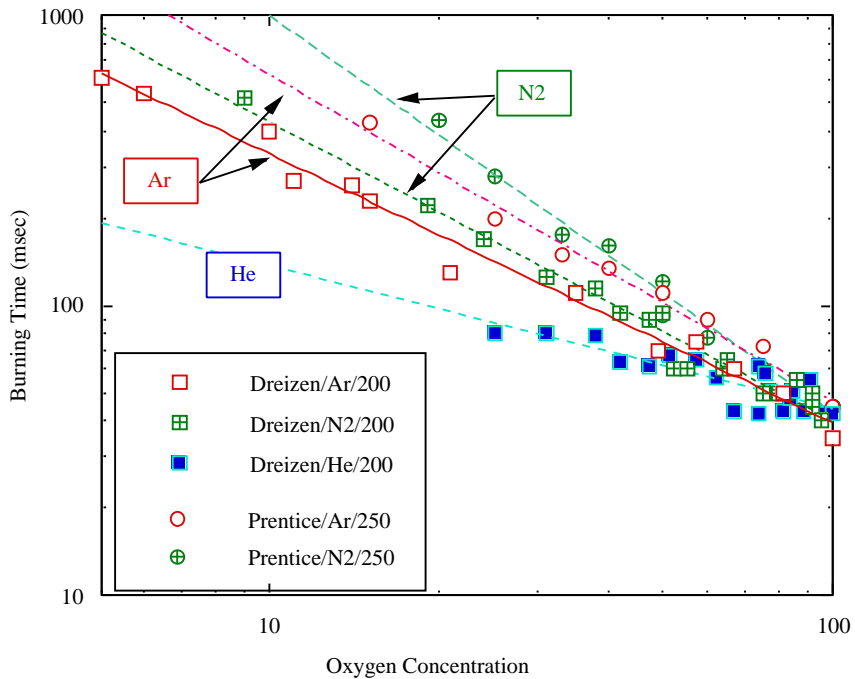


Figure 7.  Data from Prentice[39] and Dreizin[47] varying oxygen concentration in nitrogen, argon and helium.

The Effect of CO$_2$ and Water

Determining the effect of CO$_2$ and water on the burning time has proven somewhat elusive. It is difficult to create laboratory tests where one can systematically vary the concentrations of CO$_2$ or water. Most of the data the involve CO$_2$ and water come from tests involving either propellant or a gaseous flame. Olsen varied the amount of water in his experiments by utilizing a hydrogen flame, giving a greater amount of water than normal. Unfortunately, it was still difficult to make systematic variations in the water content. Thus, the available data are much less definitive than the oxygen data discussed above. In Widener's previous correlation he arrived at relative values for oxygen water and CO$_2$ of 1:0.58:0.25.

Recently Zenin[49,50] has burned aluminum in air and in CO$_2$, giving an excellent set of data for determining the influence of CO$_2$. He also burned the same size particles in mixtures of oxygen/nitrogen and oxygen/argon, similar to Dreizin and Prentice, but not over a range of concentrations. Figure 8 contains his data for 220 and 350 µm particles in 20% oxygen and both nitrogen and argon. He then burned the same size particles in 100% CO$_2$. The burning times in 100% CO$_2$ were essentially the same as in 20% O$_2$. The conclusion is that CO$_2$ is only ~20% as effective an oxidizer as O$_2$. The averaged data from Prentice for his 250 µm particles in O$_2$/argon and Dreizin's 200 µm particles also in O$_2$/argon are included for reference.
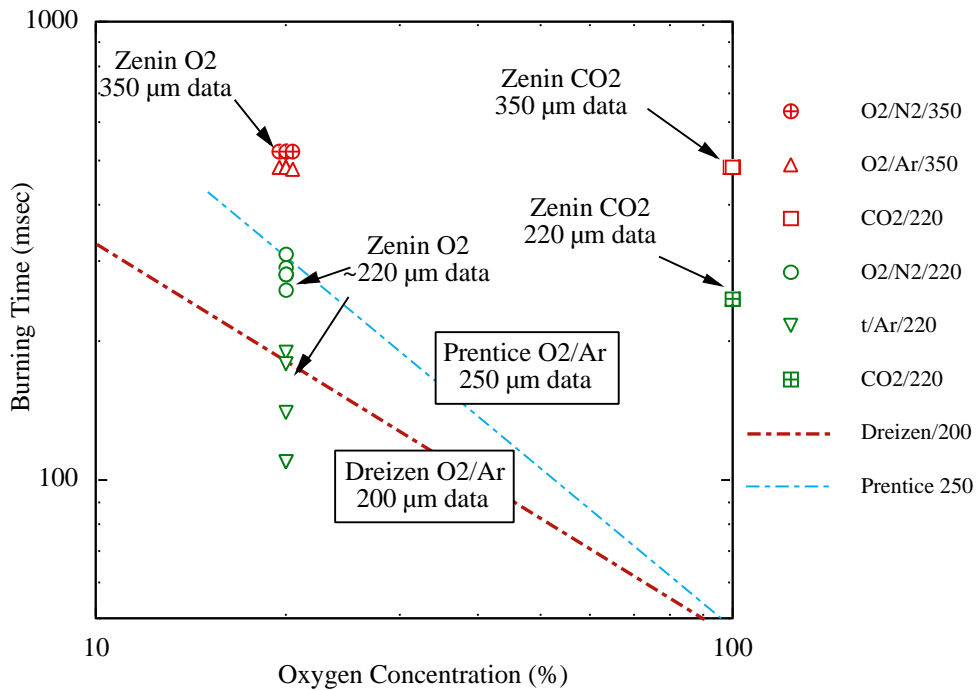


Figure 8. Zenin's data[49] comparing rates for O$_2$ and CO$_2$ as oxiziders. Data from Prentice and Dreizin are included for reference (see Figure 7).

From the available data there were no studies that provided data on the effect of water that were conclusive. Brooks[65] suggested defining an effective oxidizer, weighting the relative effects of oxygen, water and CO$_2$.

$$Xeff = C_{O2} + a_{H2O} \, C_{H2O} + a_{CO2} \, C_{CO2}$$

Using his model calculations in his original publication, he arrived at coefficients of 1:0.533:0.135. The results from various studies are summarised in Table II. Based on the current study, the $CO_2$ coefficient would appear to be ~0.22. Several different ways of analyzing the data have all led to the same value. This is apparently due to Zenin's data. Because he measured burning times in 100% $CO_2$, that large percentage apparently weights the data significantly, yielding the coefficient of 0.22. As mentioned above, data varying the concentration of water are very difficult to achieve, and the results there are some what inconclusive. The current study indicates that a value on the order of 0.5 to 0.6 yields relatively consistent results. It is interesting to note that the agreement between the different studies is surprisingly consistent.

Table II - Relative Oxidizer Coefficients for Water and $CO_2$

|  | Year | $O_2$ | $H_2O$ | $CO_2$ | Source |
|---|---|---|---|---|---|
| Belyaev[10] | 1968 | - | 1 | 1 | Data? |
| Kudryavtsev[29] | 1979 | 1 | 0.667 | 0.333 | Model |
| Brooks[65] | 1995 | 1 | 0.533 | 0.135 | Model |
| Widener[69] | 1998 | 1 | 0.67 | 0.33 | Model |
| This study | 2000 | 1 | 0.5-0.6 | 0.22 | Data |

**Effects of Pressure and Ambient Temperature**

Studies on the effect of pressure have also been rather inconclusive. In the early Russian work, it was proposed that the pressure has a small effect at low pressure, but no effect above ~20 atm. This may be a reasonable approximation. The recent work by Marion concludes essentially the same as the early Russian work. Using the effective oxidizer definition with the values noted in the previous section, all of the available data where pressure was a variable were plotted as $t \cdot Xeff/D^n$ versus pressure to determine if there were a trend. The data scatter is still very large, but using a pressure exponent of -0.1, as Belyaev and Marion did, yields the best results. Using the diameter exponent of 1.8 produced a slightly reduced scatter in the data relative to using an exponent of 1.5.

Studies on the effect of initial temperature have also been somewhat inconclusive. Virtually no data exist where some one has systematically varied the initial temperature. The statistical analysis of the entire data set gave a minimum error with the initial temperature exponent of -0.2. Using the diameter exponent of 1.8 produced a slightly increased scatter in the data relative to using an exponent of 1.5.

**Summary Correlation of the Data**

Based on the analysis of the entire set of data, the following equation is proposed to estimate burning times of aluminum particles:

$$t_b = \frac{a\,D^n}{Xeff\;P^{0.1}\,T_o^{0.2}} \tag{6}$$

where $\quad$ Xeff $= C_{O2} + 0.6\, C_{H2O} + 0.22\, C_{CO2}$

$\quad$ a = 0.0244 for n = 1.5 and

$\quad$ a = 0.00735 for n = 1.8

and pressure is in atmospheres, temperature in K, diameter in μm, and time in msec.

The results are shown in Figure 9, where the modified ordinate is $\,t_b\, X_{eff}\, P^{0.1}\, T_o^{\,0.2}$.

The raw data from Figure 1 are also re-plotted in Figure 9 to provide a basis of comparison. A regression analysis for the modified data gives an $r^2$ value of 0.964 while the corresponding regression of the raw data gives an $r^2$ of 0.87. The reduced data scatter between the correlation and the raw data is readily apparent. The most significant effect contributing to the reduced scatter is the utilization of the effective oxidizer definition. In spite of the reduced scatter, it is somewhat discouraging to see the relatively large data scatter that still exists. This is apparently due to the diversity of methods used to obtain the data, and the different methods of reducing the data, i.e. defining particle burn-out.
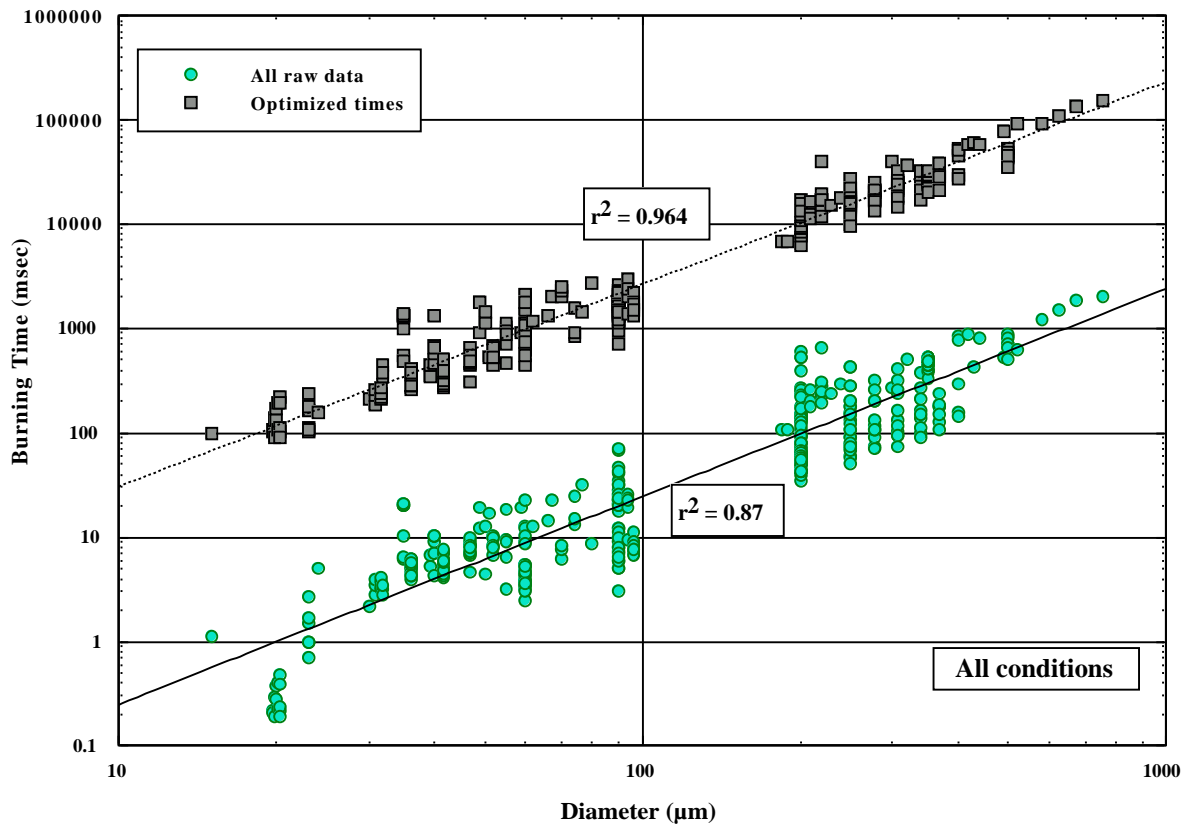


Figure 9. A comparison of aluminum burning time measurements with the proposed correlation of burning times, multiplied by the effective oxidizer and initial temperature and pressure raised to a power.

## Modeling Aluminum Combustion

This section of the paper summarizes the modeling work by Liang and Beckstead[69,70,71,72,73,74] simulating aluminum particle combustion at both laboratory and rocket motor conditions.

## Background

The adiabatic flame temperature for aluminum combustion is typically greater than the boiling point of aluminum. For example, in the case of aluminum combustion in oxygen at 1 atm, aluminum has a boiling point of 2791˚K, which is below the flame temperature of 4000˚K[1]. The heat feed back from the flame causes the aluminum at the particle surface to vaporize and the vapor proceeds to burn homogeneously in the gas phase with the oxidizer at some distance from the particle surface. There are a few exceptions however, as in the case of aluminum combustion in CO where aluminum burns heterogeneously.[61] Aluminum sub-oxides are the main initial products at the flame zone. The aluminum sub-oxides condense to form liquid aluminum oxide. In the flame zone, the heat release, if sufficient, is used to dissociate the main combustion product, liquid aluminum oxide. Due to the dissociation, the maximum temperature is maintained at the dissociation temperature of the oxide until all the oxide is dissociated. The flame zone position and thickness are both functions of the oxidizer and pressure.

During solid propellants combustion under rocket motor conditions, the embedded aluminum particle is in the molten state on the solid propellant surface due to the heat from combustion of other solid propellant ingredients. Agglomeration of the aluminum particles occurs on the surface of the regressing solid propellant. The agglomerated molten particles at the propellant surface lift off from the propellant surface due to the force of the gases from the propellant surface. The aluminum particles then undergo homogeneous combustion until they reach the nozzle of the rocket motor.

The major product of aluminum combustion is liquid aluminum oxide, which is formed from the condensation of aluminum sub-oxides. A fraction of the oxide diffuses back and deposits on the particle surface and is termed as the 'oxide cap'. The oxide cap tends to accumulate on the lower end of the falling particle. The accumulation of the oxide on the particle surface and the porosity of the oxide cap result in a final oxide cap size of the order of the initial particle size. The other fraction of the oxide is transported outwards and is termed as the 'oxide smoke'. The oxide smoke can be seen as a trail of white smoke behind the particle. The oxide smoke dampens the acoustic instabilities in a rocket motor and hence the quantity of smoke formed is important in a rocket motor.

The oxide cap results in fragmentation and jetting. The burn time is proportional to the initial diameter raised to the power of the order of 1 to 2, which is in contrast to the exponent on the diameter being exactly 2 for hydrocarbon droplet combustion[1]. This is apparently due to the formation of the oxide cap, which increases the burn time. The oxide cap effect on the burning time depends on the initial size of the particle too.

## Liang and Beckstead's Model

The model by Liang and Beckstead is a 2-dimensional, unsteady state, evaporation-diffusion-kinetics controlled numerical model. The physical interpretation of the model is depicted in Figure.10. The model simulates the combustion of a single aluminum particle, after ignition, free falling in an atmosphere containing the oxidizer. The model has been developed to describe aluminum combustion in rocket motors. The ignition temperature is typically in the range of 1700˚-2200˚K. In rocket motors, the aluminum particle usually ignites near the propellant surface. Hence in this model, ignition has been assumed to have occurred initially and the model concentrates on the combustion after the ignition.
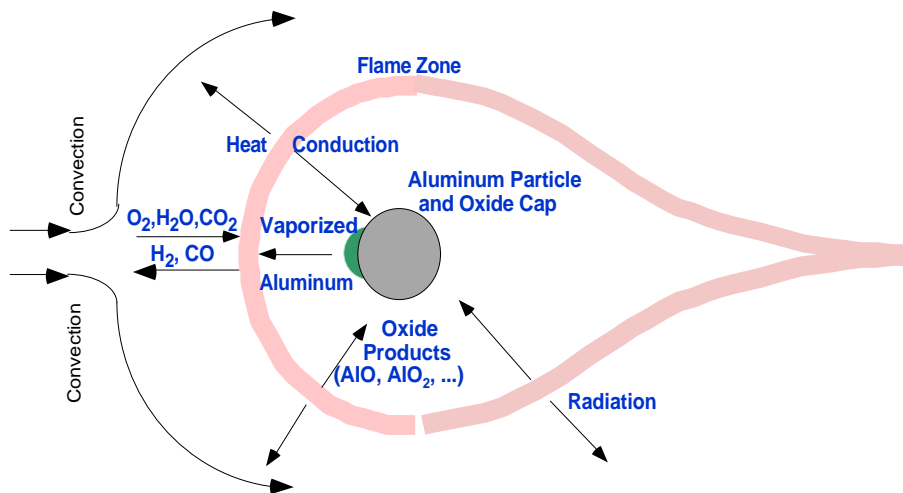
Figure 10.  Conceptual schematic of the combustion process surrounding an aluminum particle

For the sake of convenience, gravity is taken to act in the horizontal direction from the right to left direction. The particle falls with some acceleration, after being released from an initial velocity. The acceleration has been taken to be due to gravity for the calculations presented in this paper. Deceleration has been taken to occur due to the drag and the effect of the large flux of aluminum due to evaporation from the particle surface. Since ignition is taken to have occurred, the initial particle surface temperature is taken to be the boiling point of aluminum at the prevailing pressure. A flux of the oxidizer from the surroundings towards the aluminum particle and a flux of aluminum from the particle surface outwards results in the fuel and oxidizer reacting homogeneously to form aluminum sub-oxides and other products in accord with some kinetic mechanisms. The aluminum sub-oxides undergo a reaction followed by homogeneous condensation to form liquid aluminum oxide. Diffusion and convection results in a portion of the condensed aluminum oxide depositing on the particle surface to form an oxide cap. The oxide cap blocks the evaporation of the aluminum from under the region it covers and thus causes a modification in the species and temperature profiles. The oxide cap also provides heat to the evaporation of the aluminum due to the higher temperature of the oxide cap than the particle surface. The heat required for the vaporization of aluminum is provided by the heat feed back from the flame which includes the radiation heat from the flame, heat conduction from gases surrounding the particle and the heat due to the deposition of the oxide cap. The particle radius changes with time due to the vaporization of aluminum and the deposition of oxide cap. The model considers the r and   directions (in spherical coordinates) and solves the continuity, r and    momentum, energy and species continuity equations simultaneously to obtain the species and temperature profiles and the burn time. There seems to be no accepted method in the literature for calculating the burn times for aluminum particle combustion. This model estimates the burn time as the time required for the particle to be 95% consumed.

Although experimental results have indicated that the flame zone is within a distance of 10 particle radii, the calculation domain for this model covers 60 particle radii to ensure that the input conditions are totally unaffected by the combustion. Due to convection, all the input of oxidizers from the surroundings to the calculation domain is taken as from the left half of Figure.10 and all the output of gases, including inert and product gases, to the surroundings is taken as from the right half. The symmetricity of the flame is affected by the convection and the oxide cap.

The model is capable of handling different oxidizers, pressures, input enthalpies and accelerations. The transport and thermodynamic properties are calculated using the CHEMKIN transport and thermodynamic package[75], thus relaxing the common assumption of constant physical properties[41,66,67,76]. The transport and thermodynamic properties are calculated for every node for each time step for the various species. The fragmentation and jetting processes have not been considered, since no concrete rationale has been established to describe these processes. By using a numerical model, many of the simplifications required for an analytical model[66,41,76] have been relaxed.

The assumptions made in the model are:

       1) The particle is spherical

       2) Flow around the particle is laminar

       3) The local homogenous flow (LHF) model is applicable to the liquid aluminum oxide smoke.

The flow around an aluminum particle is usually laminar in rocket motor conditions, due to the small size of the particle (typically diameter is less than 200μm). The model had been used initially for investigating air and $O_2$-Ar at atmospheric pressure, since most of the available experimental data are for those conditions. These data served to validate the model. However, as has been mentioned previously, the typical oxidizer in a rocket motor is $CO_2$ and $H_2O$. Hence, the investigation of aluminum combustion with the $CO_2$-Ar and $H_2O$-Ar oxidizers, both at atmospheric pressure and higher pressures has been made. It may be noted that the oxidizer in a rocket motor for aluminum combustion consists of a high percentage of CO, but aluminum combustion in CO has not been considered. This is because aluminum burns heterogeneously in CO due to thermodynamic considerations, and since surface reactions are involved, it can be expected that the reaction rate will be slow when compared with the homogeneous gas phase reactions with the other constituents like $CO_2$ and $H_2O$. The atmospheric case investigation has been done for the $CO_2$ and $H_2O$ oxidizers to compare the results with some experimental data pertaining to species and temperature profiles. This has been followed with a study of high pressure combustion in a mixture of gases that resemble the oxidizer in a rocket motor.

## Aluminum Combustion Mechanism

Many of the previous models have assumed infinite kinetics.[2,64,65] There has been some question as to whether aluminum combustion is purely diffusion controlled or if kinetics can have an influence.[67,69] Experiments have also shown that the flame zone thickness, which is also an indicator of the pace of the kinetics, varies with each oxidizer.[62,63] In the case of CO as the oxidizer, it has been suggested from experimental data that the combustion could be heterogeneous,[63] which might lead to a kinetically controlled process as surface reactions are expected to be slower than gas phase reactions. Gremyachkin[31] had suggested in his modeling work that for small particles, the reaction could be kinetics controlled. One main disadvantage of the diffusion controlled combustion assumption is that the precise species and temperature profiles cannot be calculated. The approach taken was to include the full kinetics and examine the limiting factors in the combustion process. In this paper, four oxidizer mixtures, namely, $O_2$-Ar, $O_2$-$N_2$, $CO_2$-Ar, $H_2O$-Ar are considered.

The kinetic mechanism in the model consists of surface reactions and gas phase reactions for the formation of the aluminum sub-oxides. The aluminum sub-oxides later react and condense to form liquid aluminum oxide. The path to condensation consists of two steps; a homogeneous gas phase reaction, followed by homogeneous condensation. The combustion mechanism accounts for the first kinetic step of the two-step process, while the second step is described with the condensation model in the next subsection.

Unfortunately, the kinetic data in the literature for all the required aluminum reactions is not very accurate for the temperature regime considered. Reliable kinetic data for the Al-$O_2$ reactions has been published only recently.[63] As for the Al-$CO_2$ reaction, even though the data have been obtained only for the temperature range of 300°-1900° K, the lack of other kinetic data has forced the extrapolation of the available data to higher temperature ranges.[77] These data had been used by King[67] for his modeling work. The kinetic data for the Al-$H_2O$ reaction has been obtained only for the 298°-1174° K temperature range, but as in the Al-$CO_2$ reaction, the lack of data has forced the extrapolation of the available data to

the 2000°-4000° K temperature range.[77] There has been little investigation done into the probable condensation paths for the aluminum oxide formation when the oxidizers are $CO_2$ or $H_2O$. Hence, the condensation paths in the presence of $CO_2$ and $H_2O$ oxidizers are taken to be the same as the pure $O_2$ oxidizer case.[77]

Surface reactions:

$$Al_{(l)} \quad\quad Al_{(g)} \tag{R1}$$

$$Al_{(l)} + AlO_{(g)} \quad^{k_2} \quad Al_2O_{(g)} \tag{R2}$$

Gas phase reactions:

$$Al_{(g)} + O_2 \quad^{k3} \quad AlO + O \tag{R3}$$

$$k_3 = 9.76 \times 10^{13} \exp(-80/T) \; cm^3 mol^{-1}s^{-1}$$

$$AlO + O_2 \quad^{k4} \quad AlO_2 + O \tag{R4}$$

$$k_4 = 4.63 \times 10^{14} \exp(-10008/T) \; cm^3 mol^{-1}s^{-1}$$

$$Al + CO_2 \quad^{k5} \quad AlO + CO \tag{R5}$$

$$k_5 = 2.5 \times 10^{-13} T^{0.5} \exp(-1030/T) + 1.4 \times 10^{-9} T^{0.5} \exp(-14000/T)$$

$$Al + H_2O \quad^{k6} \quad AlO + H_2 \tag{R6}$$

$$k_6 = (1.9 \pm 1.5) \times 10^{-12} \exp(-(442.87 \pm 221.44)/T) + (1.6 \pm 0.7) \times 10^{-10} \exp(-(2868.6 \pm 452.94)/T)$$

$$O + O + M \quad^{k7} \quad O_2 + M \tag{R7}$$

$$k_7 = 6.17 \times 10^{15} \times T^{-0.5} \exp(0/T)$$

$$O + N_2 \quad^{k8} \quad NO + N \tag{R8}$$
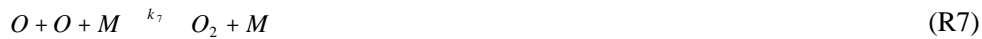
$$k_8 = 1.80 \times 10^{12} \exp(-38345.14/T)$$

$$N + O_2 \quad^{k9} \quad NO + O \tag{R9}$$

$$k_9 = 6.40 \times 10^{09} \exp(-3125.26/T)$$

Dissociation reaction:

$$Al_2O_{3(l)} \quad^{k10} \quad 2AlO + \frac{1}{2}O_2 \tag{R10}$$

Condensation:

$$2AlO + \frac{1}{2}O_2 \quad^{k11} \quad Al_2O_{3(l)} \tag{R11}$$

$$2AlO + CO_2 \quad^{k12} \quad Al_2O_{3(l)} + CO \tag{R12}$$

$$2AlO + H_2O \quad^{k13} \quad Al_2O_{3(l)} + H_2 \tag{R13}$$

$$Al_2O + O_2 \quad^{k14} \quad Al_2O_{3(l)} \tag{R14}$$

$$Al_2O + 2CO_2 \quad^{k15} \quad Al_2O_{3(l)} + 2CO \tag{R15}$$

$$Al_2O + 2H_2O \quad^{k16} \quad Al_2O_{3(l)} + 2H_2 \tag{R16}$$

$$AlO_2 + AlO_2 \quad^{k17} \quad Al_2O_{3(l)} + \frac{1}{2}O_2 \tag{R17}$$

The rate of the first reaction, which represents the rate of vaporization of the molten aluminum, is given by the boundary condition (Equation 34, see below). While the rate of vaporization depends on the surface temperature (i.e., boiling point of the aluminum metal), the boiling point depends on the pressure of the system. The vast majority of earlier models have assumed that the temperature of the aluminum particle is fixed at the boiling point of aluminum at atmospheric pressure. The relation between the boiling point and the vapor pressure of the aluminum vapor has been expressed in this model as

$$T_{\text{boil}} = (P/7.6673 \times 10^{-43})^{1/12.266} \tag{7}$$

The dissociation temperature is a function of the pressure of the system too. It is expressed as a function of the partial pressure of the aluminum sub-oxides and aluminum oxides using the Clausius-Clapeyron equation. The relation between the dissociation temperature, which is the upper limit of the flame temperature, and the vapor pressure of aluminum oxide is

$$T_{\text{flame}} = 1/(0.000250501 - 14.132 \times 10^{-6} \times \ln(P)) \tag{8}$$

The second reaction is assumed to be a diffusion controlled surface reaction. Gaseous $Al_2O$ gets transported away from the particle after the reaction. All the gas phase reactions except (R5) and (R6) have been represented by fundamental reactions. As explained previously, the lack of sufficient reliable kinetic data has been a limiting factor in the number of equations considered. Reaction (R10) is not represented by a rate expression, instead the dissociation reaction keeps dissociation temperature of aluminum oxide as the upper limit of the flame temperature. The following equation is solved to determine $\dot{}_{dAlO}$ to keep $T_{ij} = T_{\text{flame}}$.

$$f_{ij}(T_{ij}, \dot{}_{dAlO}) - T_{flame} = 0 \tag{9}$$

The reactions (R11)-(R17) are the first step of the condensation. It is assumed that

$$k_{11} = k_{12} = k_{13} = k_{14} = k_{15} = k_{16} = k_{17} = \dot{}_{cond}. \tag{10}$$

## Condensation Model

Experimental studies have shown the presence of aluminum sub-oxides near the particle surface[63] during the combustion process and the main end product to be liquid aluminum oxide. The aluminum sub-oxides must thus be consumed in the production of liquid aluminum oxide. A simple kinetic mechanism alone cannot be considered for the production of aluminum oxide from aluminum sub-oxides due to the thermodynamics. Thermodynamically, the heat of the reaction of aluminum sub-oxides to form liquid aluminum oxide is sufficient to cause the dissociation of the newly formed liquid aluminum oxide. Hence, there must be a mechanism beyond a simple kinetic mechanism to form the liquid aluminum oxide. This is simulated in the Liang & Beckstead condensation model. The condensation model consists of a two-step process as shown below.

$$aC_m + bC_n \xrightarrow{k_r} Al_2O_{3(g)} \xrightarrow{r_{con}} Al_2O_{3(l)} \tag{R18}$$

The first step is a chemical reaction that gives gaseous aluminum oxide (R11-R17). It can be described by an Arrhenius expression. The second step is a condensation process of gaseous aluminum oxide to liquid aluminum oxide. It may be noted here that gaseous aluminum oxide has not been observed experimentally and that liquid aluminum oxide would be expected to dissociate before vaporizing. However, from calculations, it has been observed that the rate of the condensation step is far greater than that of the kinetic step. The gaseous aluminum oxide can thus be considered as an intermediate product with a very short life time. The intermediate product nature of gaseous aluminum oxide, combined with the complexity of the combustion process, warrants some assumptions and the condensation model seems to be reasonable. The number of reactions considered for the first step have been limited by the kinetic data availability in the literature.

Homogeneous condensation is assumed to occur for the second step. Homogeneous condensation refers to condensation processes where the nuclei formation for condensation occurs randomly due to interactions between the constituents in the vapor phase and is not catalyzed by surfaces, ions or impurity molecules. Homogeneous nucleation can occur only in supersaturated vapors.[78] It can be described by classical homogeneous nucleation theory.[78] A nuclei can grow into a droplet if it can attain a size greater than a critical radius. The critical radius is calculated as the radius for which the G is a maximum for a given supersaturation.[78]

For the first reaction step, the rate expression is

$$\dot{\omega}_1 = k_r C_m^a C_n^b \tag{11}$$

For the second condensation step, the rate expression is

$$\dot{\omega}_2 = C_c r_{con} \tag{12}$$

where $r_{con}$ is the nucleation rate. The rate of the nucleation is calculated as the rate of sticking of molecules impinging upon the nuclei with critical radius. From homogeneous nucleation theory,[78]

$$r_{con} = (\frac{n_i^* P}{kT})(2\sigma/m)^{\frac{1}{2}}(\nu m/\sigma)n_1 \exp\left[-\frac{16\pi\sigma^3\nu^2}{3k^3T^3(\ln S)^2}\right] \tag{13}$$

where m is the mass of a molecule, $\rho$ is the liquid density, $n_i^*$ is the number of critical size clusters per unit volume, $\nu$ is the volume per molecule in the liquid state.

The total rate for the two-step condensation process is

$$\dot{\omega}_{cond} = \frac{1}{\frac{1}{\dot{\omega}_1}+\frac{1}{\dot{\omega}_2}} = \frac{C_c k_r r_{con} C_m^a C_n^b}{k_r C_m^a C_n^b + C_c r_{con}} = \frac{r_{con} C_m^a C_n^b}{\frac{C_m^a C_n^b}{C_c}+\frac{r_{con}}{k_r}} \tag{14}$$

Next it is assumed in the model that the denominator in Equation (14) does not change significantly during the condensation. So the equation reduces to

$$\dot{\omega}_{cond} = K r_{con} C_m^a C_n^b \tag{15}$$

where $K$ becomes an empirical constant.

In Equation (14) the supersaturation S of the vapor phase has a large effect on the condensation process. It has been experimentally observed[78] that in homogeneous nucleation, for nuclei to start forming, the supersaturation should exceed a critical level and that the condensation rate increases more than proportionally with an increase in supersaturation. For a typical condensation process

$$S = \frac{p}{p^*} \tag{16}$$

where p is the partial pressure of the vapor in system and $p^*$ is the vapor pressure of the condensed phase.

In the aluminum combustion process, p is zero since aluminum oxide dissociates before it vaporizes. So Equation (16) cannot be used in Equation (15). Instead Equation (17) has been used to determine S.

$$S = 1 + \frac{\sum_i p_i}{p_{Al}} \tag{17}$$

where $p_i$ is the partial pressure of species i, and i= $AlO$, $AlO_2$, $Al_2O$. The partial pressure term in (16) is thus substituted for by the sum of the partial pressures of the aluminum sub-oxides and aluminum, the

components of aluminum oxide dissociation. It is difficult to define a vapor pressure for aluminum oxide, due to the dissociation processes. The vapor pressure term in (16) is taken to be the partial pressure of aluminum in (8). In the condensation process, liquid aluminum oxide is formed from aluminum sub-oxides, which in turn are formed from aluminum. Hence, the more the partial pressure of aluminum, the lesser is the concentration of aluminum sub-oxides, and in turn the lesser is the concentration of liquid aluminum oxide, which should imply a lesser supersaturation according to (13). The assumption for vapor pressure of aluminum oxide in (17) can thus be explained qualitatively. Many of the previous models have assumed condensation to take place in an infinitely thin zone[2,31] or on the particle surface.[41,79] This model has relaxed that assumption and the condensation depends on factors such as species concentration, supersaturation, temperature, and hence on the position.

It has been assumed that the oxide deposits uniformly on the particle surface and migrates to the downstream side to coalesce into an oxide cap. It has been observed experimentally that the oxide does not dissolve in the metal, but rather stays on the surface.[45] The coalescence has been observed experimentally[45] and has been explained by the difference in the surface tension of the molten metal and oxide. The hollow nature of oxide caps is not accounted for in the model. Whether any reactions occur between the oxide cap and the metal on the particle surface has not been established clearly experimentally. Hence, that possibility has not been considered here.
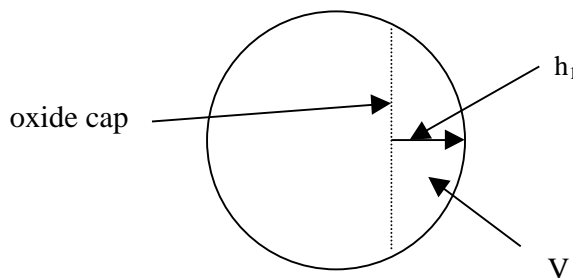


Figure 11. Model of oxide deposition on the aluminum particle surface.

The deposition height $h_1$ shown in Figure 11, can be described by the equation

$$h_1^3 - 3Rh_1^2 + \frac{3V}{} = 0 \tag{18}$$

where V is the volume of the cap calculated from the $Al_2O_{3(l)}$ diffusion to the particle surface. It may be noted that the radius and mass of the particle changes with time due to the aluminum vaporization and due to the aluminum oxide deposition, thus causing a change in $u$, the particle velocity with time. According to the model, the oxide cap inhibits aluminum vaporization from the portion of the sphere it covers. This is because the oxide has almost twice the density of the metal and so the metal cannot diffuse through the oxide. The particle surface temperature does not exceed the dissociation temperature of the oxide but is above the melting point of the oxide. So the oxide exists in a molten state throughout. The model does not account for any physical processes that may be involved in the initial bonding of the diffusing oxide to the particle surface. Also, the time required for the diffusion of the oxide to the particle surface is assumed to be the limiting factor in the deposition. In other words, the deposition is assumed to be diffusion controlled.

## General Mathematical Model

The general form of the governing equation can be written as

$$\frac{}{t} + \ (\ V\ ) = \ (\qquad) + S \tag{19}$$

In spherical coordinates,

$$(\ V\ ) = \frac{1}{r^2}\frac{}{r}(\ r^2 u_r\ ) + \frac{1}{r\sin}\frac{}{}(\ u\ \sin\ ) \tag{20}$$

$$(\qquad) = \frac{1}{r^2}\frac{}{r}\left(\ r^2\frac{}{r}\ \right) + \frac{1}{r^2}\frac{1}{\sin}\frac{}{}\left(\ \sin\frac{}{}\right) \tag{21}$$

For the continuity equation,

$$=1, \quad =0 \text{ and } S\ =0 \tag{22}$$

For the r-direction momentum equation,

$$=\ u_r, \quad =\mu \text{ and}$$

$$S\ = -\frac{p}{r} + \frac{u^2}{r} + \frac{1}{r^2}\frac{}{r}\left(\ r^2\mu\frac{u_r}{r}\ \right) + \frac{1}{\sin}\frac{}{}\left(\ \mu\sin\frac{}{r}\frac{u}{r}\ \right) -$$

$$\mu\ \frac{2}{r^2}\frac{u}{} + \frac{4u_r}{r^2} + \frac{2u\ \cot}{r^2} + \frac{4}{3r}\mu\left(\ \vec{V}\right) - \frac{2}{3r^2}\frac{}{r}\left[r^2\mu\left(\ \vec{V}\right)\right] \tag{23}$$

For the -direction momentum equation,

$$=\ u\ , \quad =\mu \text{ and}$$

$$S\ = -\frac{1}{r}\frac{p}{} + \frac{u_r u}{r} + \frac{1}{r^2\sin}\frac{}{}\left(\ \mu\sin\frac{u}{}\right) + \frac{1}{r^2\sin}\frac{}{}\left(2\mu u_r\sin\ \right) -$$

$$\frac{1}{r^2}\frac{}{r}\left(r\mu u\ \right) + \frac{1}{r^2}\frac{}{r}\left(\ r\mu\frac{u_r}{}\ \right) - \frac{1}{r\sin}\frac{}{}\ \frac{2}{3}\mu\sin\ \left(\ \vec{V}\right) + \mu\frac{}{r}\frac{u}{r}$$

$$+ \frac{\mu}{r^2}\frac{u_r}{} - \frac{\mu\cot}{r}\ 2\ \frac{u_r}{r} + \frac{u\ \cot}{r}\ -\frac{2}{3}\left(\ \vec{V}\right) \tag{24}$$

For the species conservation equations,

$$=\ Y_i, \quad =\ D_i\ (i\quad Al_2O_{3(l)}), \quad _{Al_2O_{3(l)}} = \frac{}{_A} \text{ and } S\ =\ \dot{}_i \tag{25}$$

where $Y_i$ is the mass fraction of species i, $_A$ is the Schmidt number (with $_A=0.5$)

and i$= Al, AlO, Al_2O, AlO_2, O_2, O, Al_2O_{3(l)}, Y_{N_2} = 1 - \sum_{i\ N_2} Y_i$

To ensure a balance of the mass, the calculated diffusion velocities, $\bar{V}_i = -\frac{D_i}{Y_i}\ Y_i$, are corrected by a uniform velocity vector to keep

$$Y_i\bar{V}_i = 0 \tag{26}$$

For the energy equation,

$$=T, \quad (\qquad) = \frac{1}{C_{pm}}\ (k\ T) \text{ and}$$

$$S\ = \frac{1}{C_{pm}}\left[\frac{Dp}{Dt} - \sum_i^N h_i\ \dot{}_i - \sum_i^N Y_i\bar{V}_i\ (C_{pi}\ T) + \sum_i^N (\ Y_i\bar{V}_i\ \bar{f}_i)\right] \tag{27}$$

where $\bar{f}_i$ is the body force of unit mass of species i.

Introducing non-dimensional quantities, the non-dimensional form of equation (19) is

$$\frac{\partial(R^*\Phi^*)}{\partial t^*} + \nabla \cdot (\Phi^* V^*) = \frac{1}{R\ u_{ref}R_o}\nabla \cdot (\Gamma \nabla \Phi) + \frac{RR_o}{u_{ref}}S_\Phi + \frac{(r^* \Phi^*)}{r^*}\frac{dR}{dt} \tag{28}$$

## Boundary Conditions

(1) Inlet condition:

The model considers the particle falling downward under the effect of gravity after being released from an initial position. The particle thus encounters the oxidizer at a velocity $u_\infty(t)$ in a coordinate system that considers the particle to be stationary. The inlet conditions are the conditions at a distance of 60 particle radii from the center of the particle. the inlet conditions are not affected by the combustion process.

$$u_\theta^* = \sin\theta \ , \ u_r^* = -\cos\theta \ , T^* = 1, \ u = u_\infty(t) \tag{29}$$

For $O_2$-$N_2$ oxidizer, $Y_{0_2} = 0.233$, $Y_{N_2} = 0.767$ $Y_i = 0.(i \neq O_2, N_2)$

For $O_2$-Ar oxidizer, $Y_{0_2} = 0.233$, $Y_{Ar} = 0.767$ $Y_i = 0.(i \neq O_2, Ar)$

For $CO_2$-Ar oxidizer, $Y_{C0_2} = 0.233$, $Y_{Ar} = 0.767$ $Y_i = 0.(i \neq CO_2, Ar)$

For $H_2O$-Ar oxidizer, $Y_{H_20} = 0.233$, $Y_{Ar} = 0.767$ $Y_i = 0.(i \neq H_2O, Ar)$

The inlet velocity $u_\infty(t)$ is governed by

$$m_p\frac{du_\infty}{dt} = m_p g - C_D\frac{\rho}{2}u_\infty^2 A - \int_s \rho u_r^2 \bar{n} \cdot \bar{i} \ ds \tag{30}$$

The first term on the right hand side represents the gravity term; the second term represents the drag term, where $C_D = 24/R_e$. Creeping flow around the particle is assumed, since the Reynolds number is low due to the small size of the particle. The last term on the right hand side is integration on the particle surface to consider the contribution of the evaporation to the particle movement.

(2) Outlet condition:

$$\frac{\partial\Phi^*}{\partial r} = 0 \tag{31}$$

(3) Symmetrical condition:

$$\frac{\partial\Phi^*}{\partial\theta} = 0, \ u_\theta = 0, (\theta = 0, \pi) \tag{32}$$

The symmetrical condition has been assumed for simplicity.

(4) Particle surface interface condition:

Energy balance*:*

$$k_g\frac{\partial T_g}{\partial r}\bigg|_s - Q_2\dot{m}_{AlO}\big|_s + Q_{dep} + Q_{rad} = \dot{m}_{vap}\ h_{vap} \tag{33}$$

The physical interpretation of this equation is that the heat required for the evaporation of the droplet and the reaction (R2) is provided by the heat feed back from conduction of heat from gases near the particle surface, radiation heat flux from the flame and the heat due to deposition of condensed aluminum oxide. The radiation term consists of the difference between the radiation flux to the particle and the radiation flux from the particle. The shape factors are not considered. There is no evaporation in the area covered by the oxide cap. The oxide cap is at a temperature far greater than the particle surface. This causes energy $Q_{dep}$ to be transferred to the particle for evaporation from the depositing oxide cap. The temperature of the particle surface has an upper limit of the boiling point of aluminum, at which point the evaporation starts to occur. The Stefan flow is assumed not to affect the heat transfer to the particle surface.

$$\dot{m}_{vap} + \dot{m}_{AlO}\big|_s \, \frac{M_{Al,O}}{M_{AlO}} = \ _s u_{r_s} \tag{34}$$

According to (34), the bulk flow from the particle outwards is due to the flow of Al and $Al_2O$. It may be noted that the two surface reactions (R1) and (R2) result only in the products Al and $Al_2O$, which leave the surface and move outwards as they are both gases. It is interesting to analyze the direction of bulk velocity away from the surface. While the direction of the bulk velocity away from the surface is determined from the conservation equations and boundary conditions, it may be noted that one of the main factors influencing the bulk velocity, apart from the inlet velocity of the oxidizer is the velocity of the products. In a typical metal combustion, the volumetric rate of the products is lesser than that of the reactants. Even though the formation of an oxide cap in aluminum combustion results in diffusion of the products towards the particle, in a combustion experiment with a stationary aluminum particle, the bulk velocity in the infinity- flame front zone may be expected to be towards the particle, while the bulk velocity in the flame front- particle zone may be expected to be towards the flame front. The presence of an input velocity may change the direction of the bulk velocity, but the surface condition remains the same and (34) still holds.

*Species balance*:

$$Y_{AlO} = 0 \tag{35}$$

This relation is because reaction (R2) is assumed to be diffusion controlled so that no AlO should be found at the particle surface.

$$Y_{Al(g)} = \frac{p_{Al}}{p} \frac{M_{Al}}{\overline{M}} \tag{36}$$

This relation assumes the ideal gas law, which is valid at such high temperatures.

$$D_{Al_2O} \frac{Y_{Al,O}}{r}\bigg|_s + \dot{m}_{AlO}\big|_s \frac{M_{Al,O}}{M_{AlO}} = \ u_r \, Y_{Al_2O}\big|_s \tag{37}$$

Equation (3728) implies that the net rate of $Al_2O$ transport, which is equal to the rate of $Al_2O$ diffusing outwards, is equal to the rate of production of $Al_2O$. Any other flux of $Al_2O$ diffusing will be countered by the bulk flow at the surface. In other words, there is no accumulation of $Al_2O$ on the surface and whatever $Al_2O$ is produced on the surface is transported from the surface, which is to be expected since $Al_2O$ is a gas.

$$D_i \frac{Y_i}{r}\bigg|_s = \ u_r Y_i\big|_s \qquad i \quad Al, Al_2O, Al_2O_3 \tag{38}$$

Equation (38) implies that the net flux of all the other species other than $Al_2O$, $Al_2O_3$ and Al at the surface is zero, or in other words there is no accumulation of the other species on the surface, which is to be expected since all those species are gaseous.

$$T = 34860 \Big/ [12.537 - \ln(p_{Al})] \qquad \text{(King}[67]) \tag{39}$$

This relation is used to determine the partial pressure of aluminum at the surface, from the particle surface temperature.
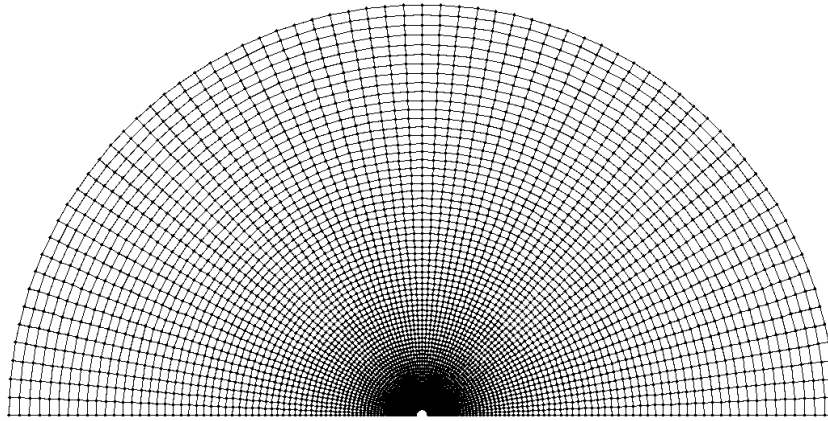


Figure 12 Computation domain for the numerical method.

The fully implicit SIMPLER[80] algorithm is used to solve the partial differential equations in which QUICK scheme is used. A staggered grid system is used where the velocities are defined at the control volume surface and scalar quantities are defined at the center of the control volume. The grid is uniform in the direction with 71 nodes. Non-uniform grids are used in the r-direction in order to improve the accuracy. There are 80 nodes in the r-direction extending upto 60 times the particle radius. The smallest distance between grids in the r-direction is near the particle surface and is about $0.0001\ r_o$. The gas phase grid used in this study is shown in Figure 12.

The role in constructing a non-uniform grid QUICK scheme is to always use two upwind nodes and one downwind node as shown in Figures 13 and 14. For example, consider the control volume i below

when $u_e > 0$,



Figure 13. Construction of QUICK scheme when $u_e > 0$

and
$$\phi_e = \phi_i + \left[ -\frac{(x_1 - x_2)^2}{4 x_1 x_2} \phi_{i-1} + \frac{x_2 - 3x_1}{4 x_1} \phi_i + \frac{x_1 + x_2}{4 x_2} \phi_{i+1} \right] \quad (40)$$

when $u_e < 0$,



Figure 14. Construction of QUICK scheme when $u_e < 0$

and
$$e = {}_{i+1} + \left[ -\frac{x_1(2x_2 - x_1)}{4x_1x_2} \right]_i + \left[ \frac{2x_2 - 3x_1}{4(x_1 - x_2)} \right]_{i+1} + \left[ \frac{x_1^2}{4x_2(x_1 - x_2)} \right]_{i+2} \tag{41}$$

## Modeling Results and Discussion

To check the validity of the unsteady simulation, an unsteady flow passing a sphere was simulated, calculating the wake development as a function of time. The results were very reasonable, and the final wake length is in good agreement with available experimental data.[81]

Model calculations have been made for a variety of conditions, to help validate the model and to explore the effects of different gases and conditions. An analysis of the temperature profiles in Figure 15 shows that the flame temperature for the three oxidizers, $O_2$, $H_2O$ and $CO_2$ are different, which is to be expected when thermodynamics are considered. The flame temperature of $CO_2$ is lesser than the dissociation temperature of aluminum oxide, because the enthalpy of the reaction and hence the heat released is not sufficient to raise the flame temperature to the dissociation temperature.[62] The flame temperature is equal to the dissociation temperature for both the cases of the $O_2$ and $H_2O$, which implies that some of the product liquid aluminum oxide gets dissociated to limit the flame temperature.
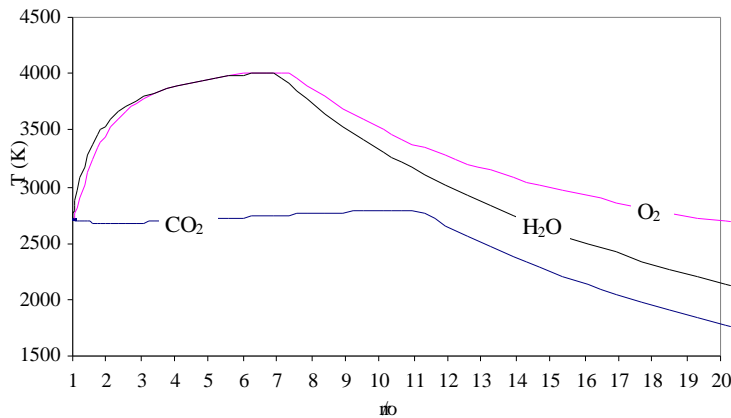


Figure 15  Temperature profiles for 21% $O_2$/Ar, 21% $CO_2$/Ar, and 21% $H_2O$/Ar cases, $T_{amb}$=300 K, P=1 atm.

Figures 16-18 show the 2-dimensional view of the calculated temperature profile around a burning particle for the three environments corresponding to the results in Figure 7.
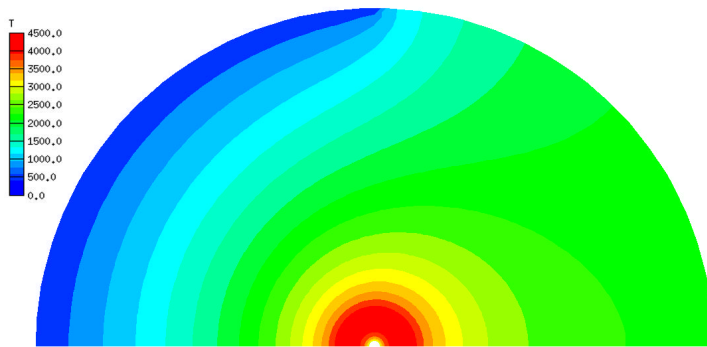
Figure 16. Predicted temperature distribution for aluminum particle combustion in 21%$O_2$/Ar, $T_{amb}$=300K, P= 1 atm, d=230 microns.
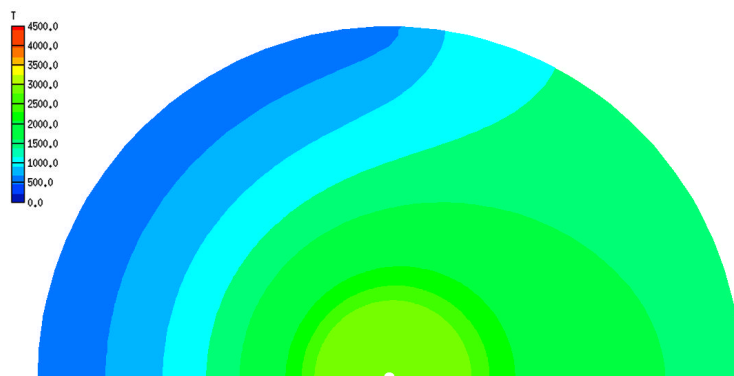


Figure 17. Predicted temperature distribution for aluminum particle combustion in 21%$CO_2$/Ar, $T_{amb}$=300K, P=1 atm, d=230 microns.
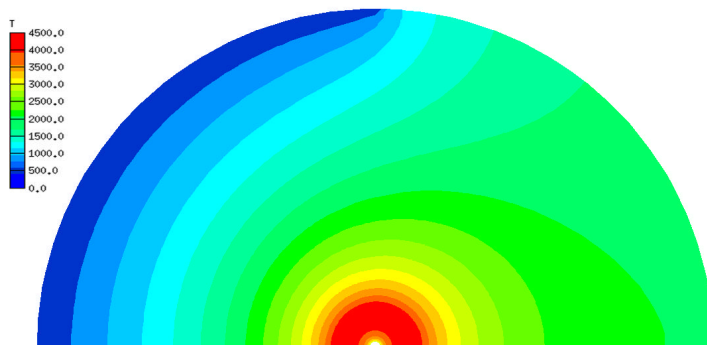


Figure 18 Predicted temperature distribution for aluminum particle combustion in 21%$H_2O$/Ar, $T_{amb}$=300K, P=1 atm, d=230 microns.

The flame zone for aluminum combustion includes the reaction zone and the condensation zone, both of which release a large amount of energy. The flame zone can be discerned from the plateau in the temperature profile, wherein the temperature is maintained at the dissociation temperature of the aluminum oxide. The flame zone location has been predicted to be farthest from the particle for the case of the $CO_2$ oxidizer, and closest to the particle in the case of the $H_2O$ oxidizer. Turns et al observed in their experiments that the flame zone was closer to the particle surface in the presence of $H_2O$ than without $H_2O$. One of the reasons attributable to this behavior is the value of the diffusivities. While $H_2O$ has the highest diffusivity in Ar, $CO_2$ has the lowest diffusivity of the three oxidizers in Ar. The higher diffusivity results in the oxidizer diffusing relatively faster towards the particle than the aluminum diffusing outwards. In all the three cases, the aluminum diffuses through an almost similar mixture, dominated by argon. However, this argument holds good only when the convection is comparable to the diffusion, which is true for the present case, wherein the velocity has been assumed to be at a steady at 0.001m/sec. Another effect to be considered would be the evaporation rate of aluminum. In the case of $CO_2$-Ar, since the flame temperature is comparatively low, the evaporation rate should be lesser and hence the stoichiometric amount of fuel and oxidizer should be obtained at a relatively closer distance to the particle surface due to this effect. It may be noted that for diffusion flames, the flame zone is the region where the fuel and oxidizer are in stoichiometric amounts.

It may be seen from Figures 19-24 that the combustion resembles a diffusion flame for the considered cases, since the region in which the reactants coexist is very small. The fuel and the oxidizer are seen to coexist at the edge of the flame zone in all the cases. This implies that the condensation tends to concentrate in a region closer to the particle surface than the reaction zone, and the condensation results in a large flame zone. Many of the models have assumed infinite kinetics[2,66,65] and hence a diffusion controlled model. The predictions of this model, namely the little coexistence of the aluminum and oxidizer for the oxidizers $O_2$, $CO_2$, $H_2O$, gives validity to that assumption. The conclusion drawn above assumes that the kinetics are well represented in the model. An observation can be made, about the assumption of condensation occurring in the reaction zone in some models, from the flame zone predicted in the model. As stated earlier, condensation tends to concentrate in a region a little bit closer to the particle surface than the reaction zone. Hence, based on the predictions of this model for the oxidizers and conditions studied, it can be concluded that the models that assumed the condensation to occur in the reaction zone were more accurate than the models that took the condensation to occur on the particle surface.

The 2-dimensional pictures are a view of the upper half of the particle shown in Figure.10. The 2-dimensional pictures show the effect of the oxide cap and convection on the distortion of the temperature profiles. The low temperature on the left side of the figures is a combined effect of the convection, which makes the gases flow from left to right, and the oxide cap, which accumulates on the left side. An interesting observation is that on the upper side of the falling particle, the temperature is around 1000° - 1250°K at a distance of 60 radii from the particle. The oxidizer concentration is also not equal to the ambient concentration even at a distance of 20 $r_o$. This tends to point to the need for group combustion studies. In a rocket motor, there is a good chance of particle spacing in the order of 60 $r_0$.

The main combustion product is seen to be $Al_2O_3$. It can be seen that some of the oxide diffuses outwards, which is the oxide smoke. This model does not attempt to determine the size of the oxide smoke, which is expected to be a function of the condensation. The concentration of the aluminum sub-oxides is negligible at distances far from the particle surface, which is to be expected considering their fast condensation and other kinetic reactions. AlO is seen to be main aluminum sub-oxide produced in the flame zone. The concentration of the argon at the particle surface is non-zero, as the argon passes through the flame zone without any reaction. Although any possible reaction between some of the products like $H_2$, CO & oxide cap with the aluminum has not been considered in this model due to the constraint of kinetic data availability, those reactions could have a role in the fragmentation and jetting of aluminum particles, which has been observed experimentally.[47,82]

Figure 19.        Major species mass fraction for 21% $O_2$/Ar, $T_{amb}$=300 K, P= 1 atm.



Figure 20.        Major species mass fraction for 21% $CO_2$/Ar, $T_{amb}$=300 K, P= 1 atm.
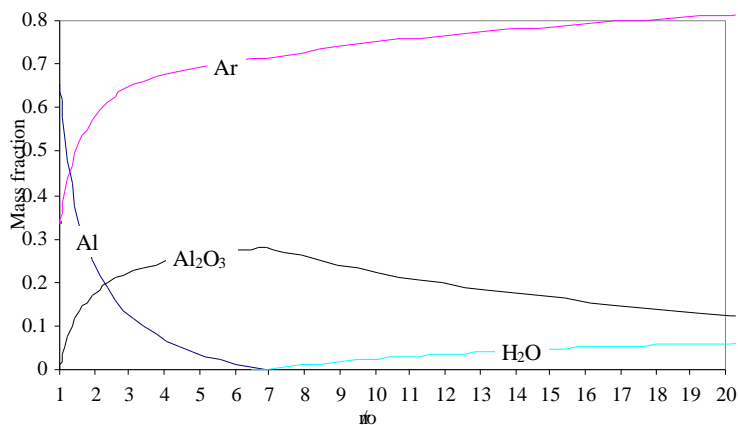


Figure 21.        Major species mass fraction for 21% $H_2O$/Ar, $T_{amb}$=300K, P=1 atm.
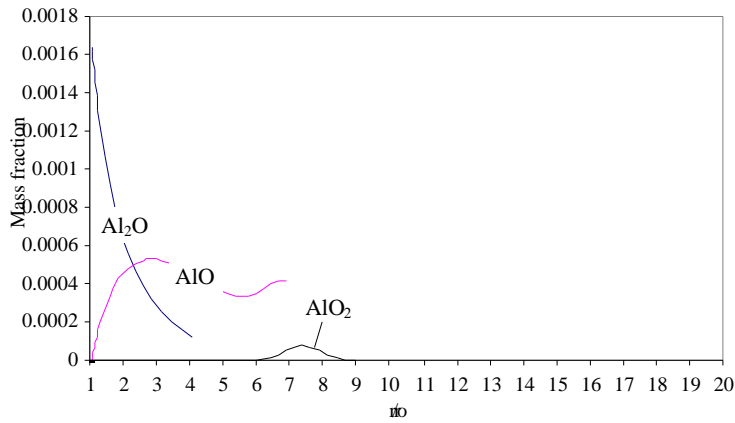
Figure 22.  Minor species mass fraction for 21% $O_2$/Ar, $T_{amb}$=300 K, P= 1 atm.
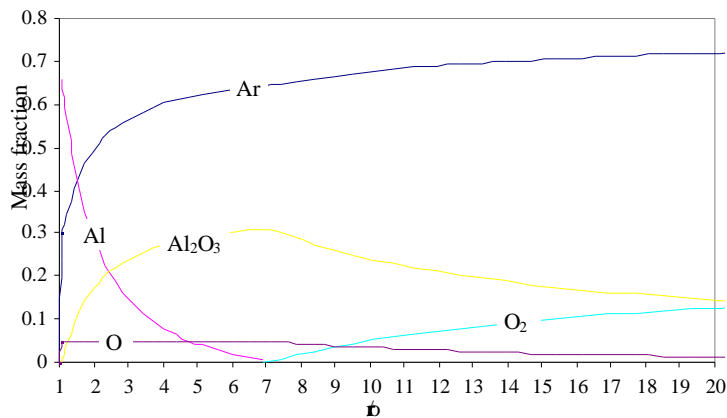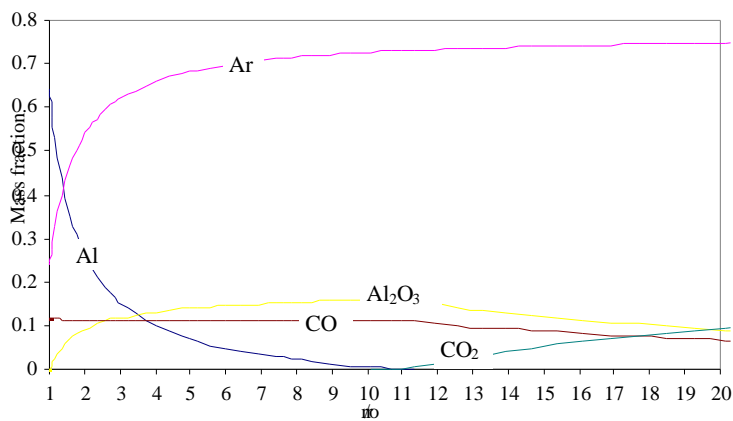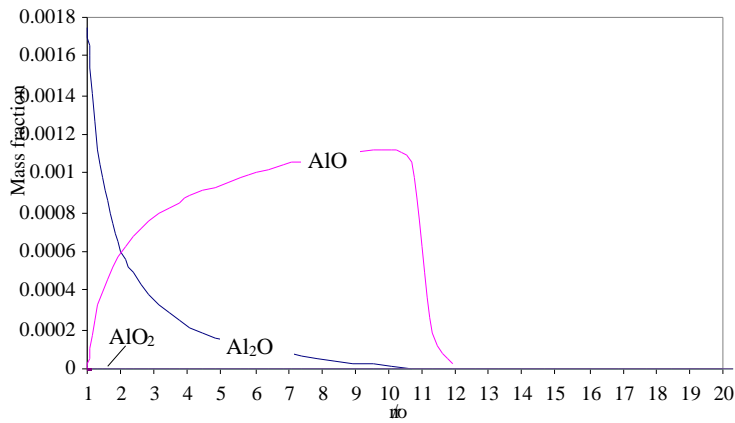


Figure 23.  Minor species mass fraction for 21% $CO_2$/Ar, $T_{amb}$=300 K, P= 1 atm.
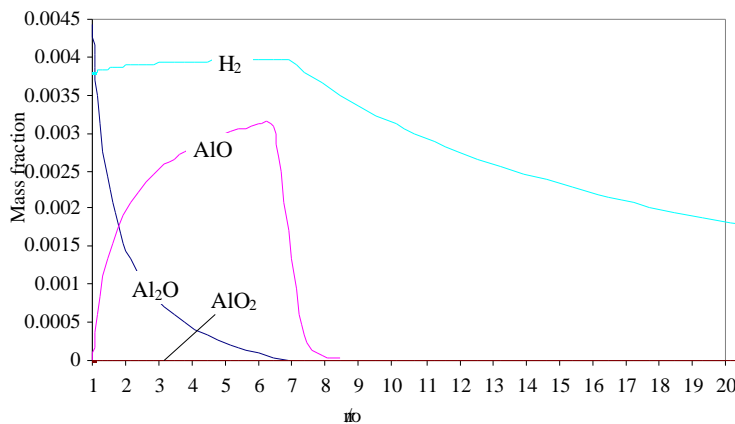


Figure 24.  Minor species mass fraction for 21% $H_2O$/Ar, $T_{amb}$=300K, P=1 atm.

The effect of pressure on aluminum combustion, which has not been addressed in a lot of experimental and modeling efforts, needs to be given priority considering the rocket motor conditions. Figures 25 and 18 show the calculated temperature distributions for a particle burning at 1 atm and 65 atm pressure respectively. The gas composition used in the calculations was the same as that by Davis[35], so that the results of the model could be compared with the experimental data. The first observation which can be made is the difference in overall temperatures. The surface and flame temperatures are higher for the high pressure case than for the low pressure case. The flame temperature is ~400K higher at 65 atm. This is reasonable because the aluminum and aluminum oxide boiling (dissociation for aluminum oxide) points have increased with ambient pressure. This increase in flame temperature is a very important concept which has not been treated by most investigators. The second observation which may be drawn from these figures is that the flame zone was calculated to be more narrow and closer to the surface at high pressure than at low pressure. Brzustowski and Glassman[2] showed experimentally that in metal combustion an increase in pressure is accompanied by an approach of the flame front toward the particle surface. This agrees with the calculations illustrated in Figures 17 and 18.
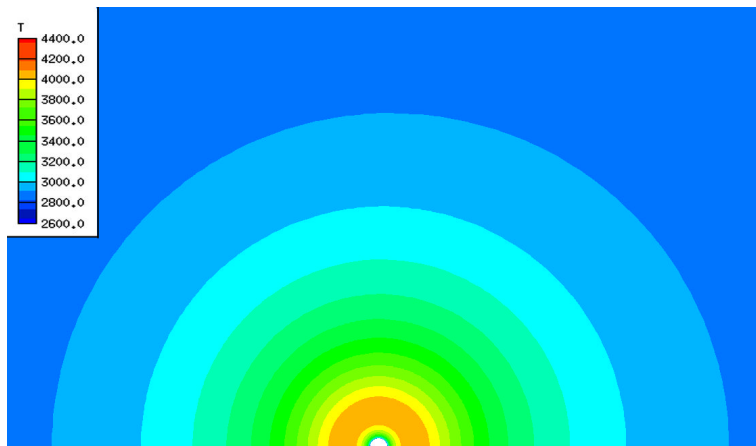


Figure 25. Predicted T(K) distribution in 44.4% $H_2O$, 11.4% $O_2$, 13.9% $CO_2$, 10.1% $N_2$, 20.2% HCl, $T_{amb}$=2600 K, and P= 1 atm.
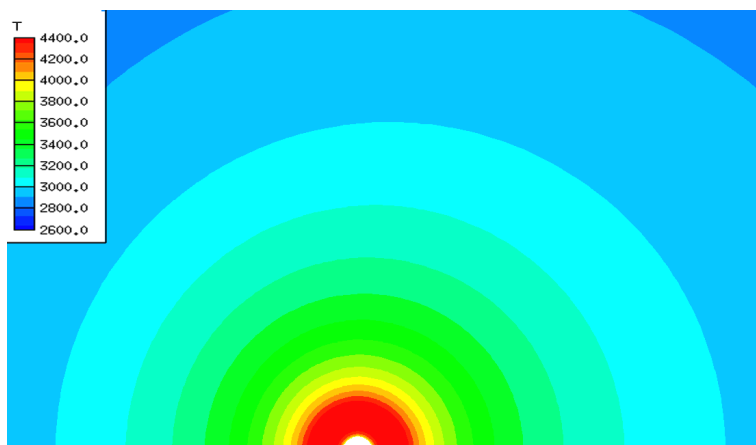


Figure 26. Predicted T(K) distribution in 44.4% $H_2O$, 11.4% $O_2$, 13.9% $CO_2$, 10.1% $N_2$, 20.2% HCl, $T_{amb}$=2600 K, and P= 65 atm.
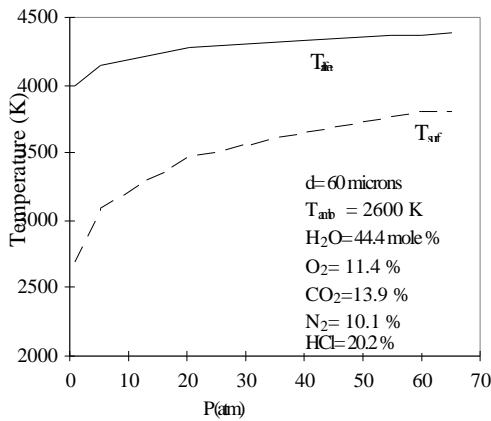
Figure 27. Predicted particle surface temperatures as pressure is varied.
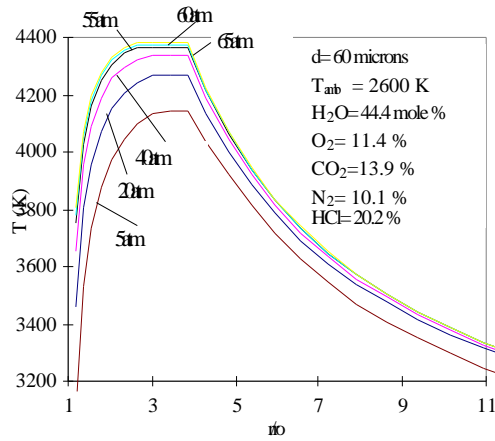


Figure 28. Predicted temperature profiles vs. flame non-dimensional radius for various pressures.

Figure 27 shows the predicted dependence of surface temperature and flame temperature on pressure. Notice that there is a gradual increase in surface and flame temperatures as the pressure is increased. The case of one atm and 65 atm has been demonstrated already in Figures 25 and 26. Figures 27 and 28, however, show the trend over the entire pressure range studied. Figure 28 puts this into a spacial perspective, showing the distribution of the calculated temperatures from the surface outward. In Figure 28, the predicted temperature profiles vs. non-dimensional radius are shown for the same range of pressures as in Figure 27. It can be seen that the temperature profile of the flame zone is increasing in height as the pressure increases.

It is interesting to compare some of the results from Liang's modified model with recent experimental data. Some of the latest and best experimental measurements of temperature and species distributions around a burning aluminum particle have been performed by Bucher et al.[61,62,63] at Princeton. In one of their experiments, they burned aluminum particles in an $O_2$/Ar atmosphere and measured the temperature profile extending outward from the particle surface in very small increments. Figure 29 shows a comparison of Bucher's data with the temperature profile calculated by the modified Liang model.[69] Excellent agreement between predictions and measurements was achieved.
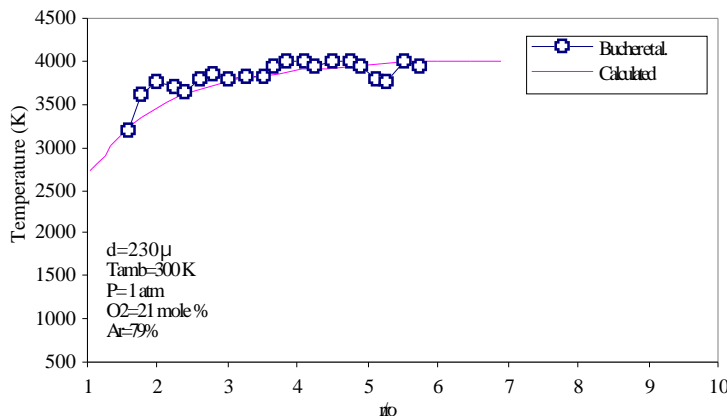


Figure 29. Calculated temperature (K) profile vs. non-dimensional radius compared with experimental data from Bucher et al.

Figure 30 shows the calculated relative AlO concentration profile compared with data from the same experiment. It can be seen that the profiles are very similar, although Bucher et al. observed a peak in AlO concentration at around $r/r_o$= 2.2, and the calculated peak value is at ~ 3.0. Figure 31 shows a comparison of Bucher's data with a calculated temperature profile for an $N_2/O_2$ atmosphere, similar to the $Ar/O_2$ case shown in Figure 29. It must be noted that the dissociation of $N_2$ was not included earlier in these calculations, hence the disagreement between the earlier calculated values and experiment. However, very recent calculations, which take into account the $N_2$ dissociation, result in much better agreement between the two as shown in Figure 31. This is a very logical outcome since heat is required to dissociate $N_2$, thus lowering the calculated temperature of the system. In addition to looking at temperature and species profiles, the burn times calculated by this model were compared against experimental data, as well as against calculated values from the Brooks model.[65] Figure 32 shows several burn times predicted by the modified Liang model, along with calculated burn times from the modified Brooks (analytical) model,[69] as well as experimental data from Hartman[37] and Davis[35] Only a limited number of calculations were performed because of the time required for each calculation (about 12 cpu hours).
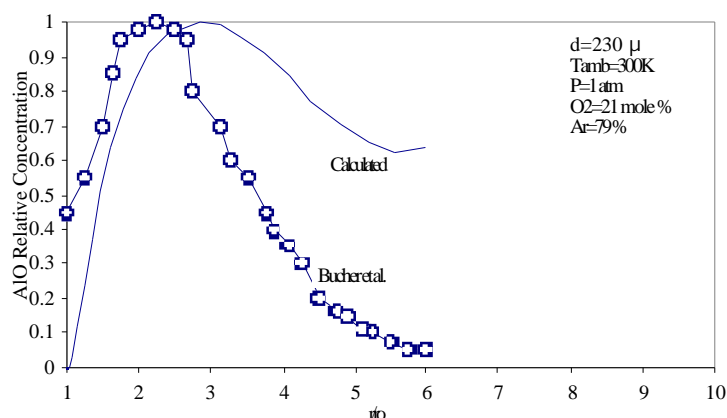


Figure 30.  Calculated relative AlO concentration vs. non-dimensional radius compared with experimental data from Bucher et al.
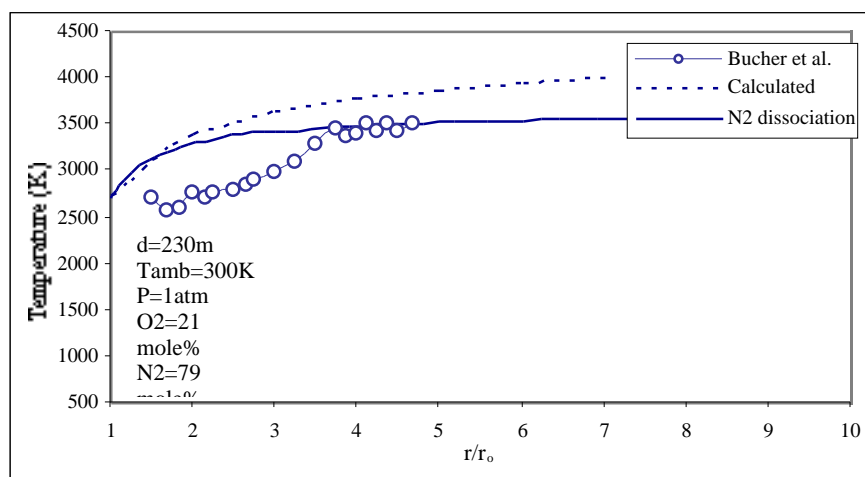


Figure 31.  Calculated temperature profile versus non-dimension radius compared with experimental data from Bucher, et al, with $N_2$ replacing Ar as the inert gas.
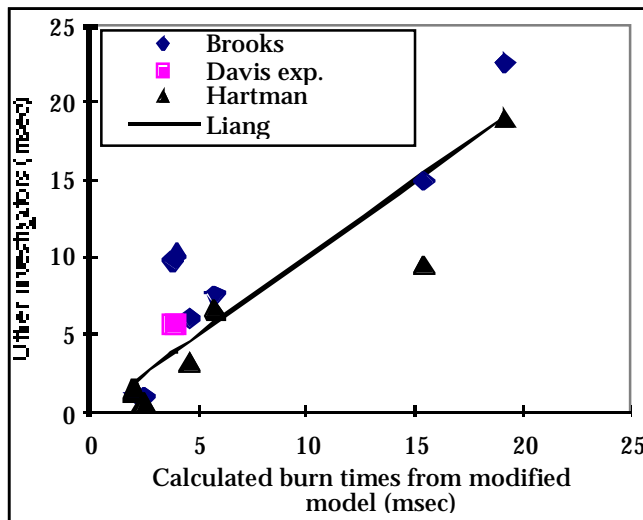
Figure 32. Comparison of burn times calculated by the modified Liang model with calculations from the modified Brooks (analytical) model, and with experimental data from Hartman[37] and Davis. [35]

Since Liang's model is a steady-state calculation, a particle burn time had to be approximated from the calculated steady-state evaporation rate of aluminum.  To do this, it was assumed that the steady-state evaporation rate represented the initial rate, and that thereafter the evaporation rate was proportional to the fraction of original aluminum remaining.  In addition, when 95 percent of the original aluminum was evaporated, the particle combustion was assumed complete.  In this manner, particle burn times were approximated from the steady state calculations, and are shown in Figure 32.  As can be seen from this figure, there seems to be reasonable agreement between the calculations of the modified Liang model, the modified Brooks (analytical) model, and experiment

For the analysis of the condensation, dissociation rates and the reaction rates of some of the reactions, the case of aluminum combustion in air has been analyzed. Figure 33 shows the dissociation rate of aluminum oxide. It can be seen that the dissociation occurs exactly in the region where there is a temperature plateau.

The condensation rate of liquid aluminum oxide is shown in Figure 34. We can see the condensation determines the location of the flame and the temperature distribution and occurs very rapidly in a narrow region. Figure 35 shows a plot of the reaction rates of some species in the aluminum combustion process in air. The reaction of aluminum with oxygen is observed to occur only in the narrow flame zone. Between the particle surface and the flame zone the most important species is AlO. AlO is produced in the flame zone and diffuses back to the particle surface reacting with the liquid aluminum to form $Al_2O$. In the flame zone there are two reactions of species AlO.  One is to form $AlO_2$ and another is the condensation reaction. Figure 35 shows that the formation of $AlO_2$ is the dominant process. Because of these two reactions, the concentration of AlO at the outer edge of flame goes to zero.
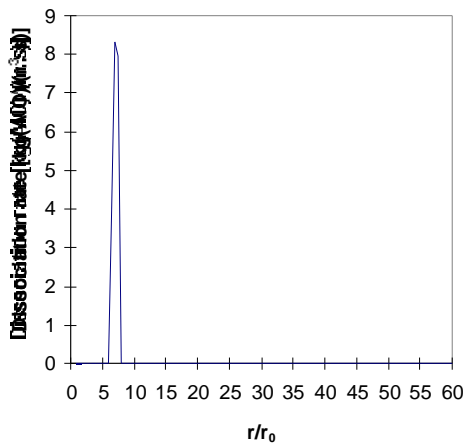
Figure. 33 Dissociation rate of aluminum oxide vs. radial non-dimensional distance
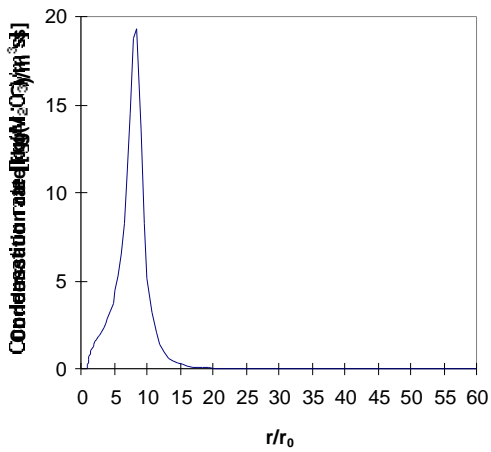


Figure. 34 Condensation rate vs. radial non-dimensional distance
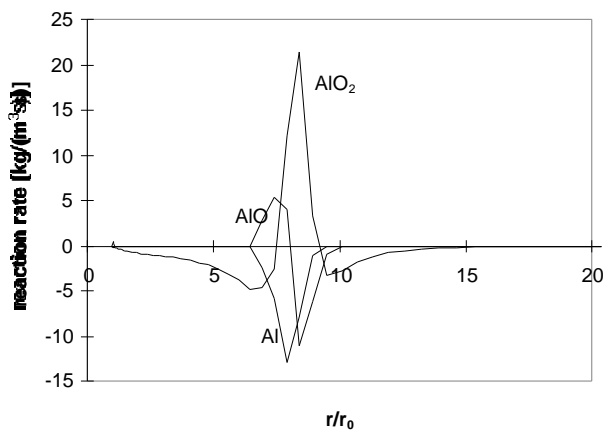


Figure 35.  Reaction rate vs. radial non-dimensional distance

The condensation reaction[18] $AlO_2 + AlO \qquad Al_2O_{3(l)}$ cannot occur at that location which will let a lot of $AlO_2$ exist in the final combustion product. Therefore, we assume $AlO_2$ condenses through reaction (R17) and $AlO_2$ will be finally condensed. Species $Al_2O_{3(l)}$ is mainly produced in the flame zone and diffuses to the particle surface and deposits on the particle surface. From the results we can see that next to the condensation rate the most important quantity to influence the condensation is the $O_2$ concentration which is different from the classical condensation process.

For hydrocarbon droplet combustion, the burn time is proportional to the initial diameter raised to the power of 2. For aluminum combustion, the model predicts the burn time to be proportional to the initial diameter raised to the power of 1.2 for small diameters to 1.88 for large diameters. The reason the exponent is lesser than 2 is due to the oxide cap and the convection, which cause the evaporation rate of aluminum to decrease and thus cause the burning time to increase. The oxide cap has another effect of providing energy to the particle surface during deposition, which cancels off some of the effect due to the blockage of the aluminum evaporation due to the oxide cap.

## Summary and Conclusions

The combustion characteristics of aluminum combustion have been summarised in an overview of the subject, focusing on the burning time of individual particles. The fundamental concepts that control aluminum combustion are discussed starting with a discussion of the "$D^n$" law. Combustion data from over ten different sources with almost 400 datum points have been cataloged and correlated. The wide variety of experimental techniques and a lack of standard definitions of the burning time, contribute to the large data scatter observed between different investigators. A thorough evaluation of the data indicates that an exponent on the order of 1.5 to 1.8 correlates the data best, with the value of 1.8 slightly better than 1.5.

There is a rich body of data varying the environmental gases. These data have bee systematically analyzed showing that oxygen is a more powerful oxidizer than water or $CO_2$. Zenin's data shows that $CO_2$ is only 20% as efficient as oxygen. Although the data were not conclusive about the precise effect of water, it appears that water is probably about half as effective as oxygen. And about half as effective as $CO_2$. Interesting studies have been performed using various inert gases while varying the oxygen concentration. There appears to be an effect of the gaseous diffusivity, with the product of the density times the diffusivity. The inference being that smaller gaseous molecules will tend to reduce the burning time. The observed effect of pressure and initial temperature is minimal. Early Russian investigators proposed that pressure has a small effect at low pressure, but no effect above ~20 atm. More recent work seems to verify that trend. The effect of initial temperature is also relatively small with an exponent of -0.2 resulting in a minimization of error.

A proposed equation that can be used to estimate burning times of aluminum particles is (Eqn. 6)

$$t_b = \frac{aD^n}{Xeff \; P^{0.1} T_o^{0.2}}$$

where $\qquad Xeff = C_{O2} + 0.6 \, C_{H2O} + 0.22 \, C_{CO2}$

$a = 0.0244$ for $n = 1.5$ and

$a = 0.00735$ for $n = 1.8$

and pressure is in atmospheres, temperature in K, diameter in μm, and time in msec.

A two-dimensional, unsteady state kinetic-diffusion-vaporization controlled numerical model for aluminum particle combustion is presented. The model solves the conservation equations, while accounting for species generation and destruction with a 15 reaction kinetic mechanism. Two of the major phenomena that differentiate aluminum combustion from hydrocarbon droplet combustion, namely the condensation of the aluminum oxide product and the subsequent deposition of part of the condensed oxide, are accounted for in detail with a sub-model for each phenomenon. The effect of the oxide cap in the distortion of the profiles around the particle has been included in the model.

Parametric calculations were made to examine the flame structure for oxygen, water and carbon dioxide flames. Each of the three calculations was made for a mixture of 21% of the oxidizer mixed with 79% argon, all at one atm. The results show a dramatic difference for the $CO_2$ case. The flame temperature for the $CO_2$ case as~2700 K while for both $O_2$ and water the temperature is ~4000 K. These correspond to the thermodynamic equilibrium for the three oxidizers. There is much less energy in the $CO_2$ flame. The calculations also indicate that the flame for the CO2 extends further from the surface than either O2 or H2O. The calculated species profiles indicate that the flame corresponds to a diffusion flame as virtually none of the oxidizer penetrates beyond the flame.

The calculated temperature profiles have been compared with recent experimental data by Bucher, et al, showing good agreement between the model and the available data. The modeling results also show that the exponent of the particle diameter dependence of burning time is not a constant and changes from about 1.2 for larger diameter particles to 1.9 for smaller diameter particles. The calculations also indicate that due to the deposition of the aluminum oxide on the particle surface, particle velocity oscillates.

Calculations indicate that both the flame temperature and surface temperature increase with increasing pressure. Between 5 and 60 atm the flame temperature is calculated to increase by approximately 400 K. Calculations were also made for conditions corresponding to what might occur in a solid propellant rocket motor where little oxygen is present, and the principal oxidizers are water and $CO_2$.

## Nomenclature

| | | | | |
|---|---|---|---|---|
| | density | | $\dot{}$ | mass flux of 'species produced' |
| u | velocity | | h | latent heat |
| p | pressure | | h | enthalpy |
| D | diffusivity | | R | particle radius |
| Y | mass fraction | | V | velocity vector |
| T | temperature | | $C_p$ | specific heat |
| M | molecular weight | | $R_p$ | instantaneous particle radius |
| $\dot{m}$ | flux | | S | supersaturation |
| k | thermal conductivity | | | surface tension of a flat liquid surface |
| m | mass | | $\overset{*}{i}$ | condensation coefficient |
| Q | heat flux | | | |

**Non-Dimensional variables**

$$u_r^* = \frac{u_r}{u}$$ \qquad non-dimensional radial velocity

$u^* = \dfrac{u}{u}$     non-dimensional tangential velocity

$t^* = \dfrac{tu}{R_0}$     non-dimensional time

$r^* = \dfrac{r}{R_0}$     non-dimensional radial distance

$^* = \text{———}$     non-dimensional density

$\mu^* = \dfrac{\mu}{\mu}$     non-dimensional viscosity

$D_i^* = \dfrac{D_i}{D}$     non-dimensional diffusivity

$T^* = \dfrac{T}{T}$     non-dimensional temperature

$p^* = \dfrac{p}{u^2}$     non-dimensional pressure

## Subscripts

| | | | |
|---|---|---|---|
| r | radial direction | vap | vaporization |
| | tangential direction | dep | deposition |
| | infinity conditions | 0 | initial condition |
| p | particle | i | species |
| g | gas | m | mean |
| s | surface | | |

## References
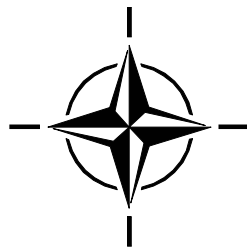
[1] Glassman, I., "Metal Combustion Processes", American Rocket Society Preprint 938-59, New York, 1959.

[2] Brzustowski, T. A. and Glassman I., "Spectroscopic Investigation of Metal Combustion", Heterogeneous Combustion, Academic Press, New York, 1964, pp 41-74.

[3] Pokhil, P. F., Belyayev A. F., Frolov Yu. V, Logachev V. S. and Korotkov A. I., "Combustion of Powdered Metals in Active Media", Nauka, FTD-MT-24-551-73 (English translation), 1972.

[4] Frolov, Yu. V., Pokhil P. F. and Logachev V. S., "Ignition and Combustion of Powdered Aluminum in High-Temperature Gaseous Media and in a Composition of Heterogenous Condensed Systems", *Combustion, Explosion & Shock Waves*, Vol. 8, No. 2, 1972, pp. 168-187

[5] Micheli, P. L. and Schmidt W. G., "Behavior of Aluminum in Solid Rocket Motors", *AFRPL-TR-77-29*, Vol II, Aerojet Solid Propulsion Co., 1977.

[6] Glassman, I., Mellor A. M., Sullivan H. F. and Laurendeau N. M., "A Review of Metal Ignition and Flame Models", AGARD Conference Proceedings No. 52, 1970, pp. 19-1 - 19-30.

[7] Price, E. W., Kraeutle K. J., Prentice J. L., Boggs T. L., Crump J. E. and Zurn D. E., "Behavior of Aluminum in Solid Propellant Combustion", *NWC TP 6120*, Naval Weapons Center, 1982,

[8] Price, E. W., "Combustion of Metalized Propellants", *Fundamentals of Solid-Propellant Combustion*, Volume 90, Progress in Astronautics and Aeronautics, Chapter 14, 1984, pp. 479-514

[9] Pressley, H. M., "Survey of Soviet Work in Aluminum Combustion", *14th JANNAF Combustion Meeting*, III, 1977, pp. 85-104.

[10] Belyaev, A. F., Frolov Yu. V. and Korotkov A. I., "Combustion and Ignition of Particles of Finely Dispersed Aluminum", *Combustion, Explosion & Shock Waves*, Vol. 4, No. 3, 1968, pp. 323-329.

[11] Boreisho, A. S., Ivashchenko A. V. and Shelukhin G. G., "Problem of Determining the Sizes of Burning Metal Particles", *Combustion, Explosion & Shock Waves*, Vol. 11, No. 4, 1975, pp. 659-660.

[12] Arkhipov, V. A., Ermakov, V. A., and Razdobreev, A. A., "Dispersity of Condensed Products of Combustion of an Aluminum Drop," *Combustion, Explosions, & Shock Waves*, Vol. 18, No. 2, pp. 16-19, 1982.

[13] Dreizin, W. L. and Trunov M. A., "Surface Phenomena in Aluminum Combustion", *Combustion and Flame*, Vol. 101, No. 3, 1995, pp. 378-382.

[14] Merzhanov, A. G., Grigorjev Yu. M. and Gal'chenko Yu. A., "Aluminum Ignition", *Combustion and Flame*, Vol. 29, 1977, pp. 1-14.

[15] Breiter, A. L., Mal'tsev V. M. and Popov E. I., "Models of Metal Ignition", *Combustion, Explosion and Shock Waves*, Vol. 13, No. 4, 1977, pp. pp 475-484.

[16] Ermakov, V. A., Razdobreev A. A., Skorik A. I., Pozdeev V. V. and Smolyakov S. S., "Temperature of Aluminum Particles at the Time of Ignition and Combustion", *Combustion, Explosion and Shock Waves*, Vol. 18, No. 2, 1982, pp. pp 256-257.

[17] Lokenbakh, A. K., Zaporina N. A., Knipele A. Z., Strod V. V. and Lepin L. K., "Effects of Heating Conditions on the Agglomeration of Aluminum Powder in Air", *Combustion, Explosion & Shock Waves*, Vol. 21, No. 1, 1985, pp. 73-82.

[18] Boiko, V. M., Lotov V. V. and Papyrin A. N., "Ignition of Gas Suspensions of Metallic Powders in Reflected Shock Waves", *Combustion, Explosion & Shock Waves*, Vol. 25, No. 2, 1989, pp. 67-74.

[19] Rozenband, V. I. and Vaganova N. I., "A Strength Model of Heterogeneous Ignition of Metal Particles", *Combustion and Flame*, 88, 1992, pp. 113-118.

[20] Rozenband, V. I., Afanas'eva L. F., Lebedeva V. A. and Chernenko E. V., "Activation of Ignition of Aluminum and its Mixtures with Oxides by Chromium Chloride", *Combustion, Explosions and Shock Waves*, 26, No. 5, 1990, pp. 13-15.

[21] Fedorov, B. N., Plechov Yu. L. and Timokhin E. M., "Particle Size of Aluminum Oxide Particles in the Combustion Products of Condensed Substances", *Combustion, Explosion & Shock Waves*, Vol. 18, No. 1, 1982, pp. 22-27.

[22] Gostintev, Yu. A., Lazarev V. V. and Frolov Yu. V., "Calculation of Critical Combustion Conditions for Metal with High-Velocity Heating by a Stream of Oxidizing Agent", *Combustion, Explosion & Shock Waves*, Vol. 22, No. 3, 1986, pp. 10-14.

[23] Gremyachkin V.M., "Theory of Ignition of Metallic Particles", *Combustion, Explosion & Shock Waves*, Vol. 19, No 3, 1983, pp. 259-262.

[24] Arutyunyan, A. B., Kharatyan S. L. and Merzhanov A. G., "Theory of Metal Particle Ignition I. Ignition of Metal Particles in the Formation of Solid Solutions", *Combustion, Explosion & Shock Waves*, Vol. 15, No. 3, 1979, pp. 16-22.

[25] Gurevich, M. A., Ozerov E. S. and Yurinov A. A., "Effect of an Oxide Film on the Inflammation Characteristics of Aluminum", *Combustion, Explosion & Shock Waves*, Vol. 14, No. 4, 1978, pp. 448-451.

[26] Bezprozvannykh, V. A., Ermakov V. A. and Razdobreev A. A., "Induction Period for the Heating of Metal Particles by Continuous Laser Radiation", *Combustion, Explosion & Shock Waves*, 28, 6, 1992, pp. 60-63.

[27] Kovalev, O. B., "Adiabatic Method in the Thermal Theory of Ignition of Metal Particles in Gases", *Combustion, Explosions and Shock Waves*, Vol. 30, No. 5, 1994, pp. 29-33.

[28] Medvedev, A. E., Fedorov A. V. and Fomin V. M., "Mathematical Modeling of Metal Particle Ignition in the High-Temperature Flow Behind a Shock", *Combustion, Explosion & Shock Waves*, Vol. 18, No. 3, 1982, pp. 261-265.

[29] Kudryavtsev, V. M., Sukhov A. V., Voronetskii A. V. and Shapara A. P., "High-Pressure Combustion of Metals (Three-Zone Model)", *Combustion, Explosion & Shock Waves*, Vol. 15, No. 6, 1979, pp. 731-737.

[30] Gremyachkin, V. M., Istratov A. G. and Leipunskii O. I., "Effect of Immersion in a Flow on Metal-Drop Combustion", *Combustion, Explosion & Shock Waves*, Vol. 15, No. 1, 1979, pp. 32-36.

[31] Gremyachkin, V. M., Istratov A. G. and Leipunskii O. I., "Model for the Combustion of Metal Droplets", *Combustion, Explosion & Shock Waves*, Vol. 11, No. 3, 1975, pp. 313-318.

[32] Babuk, V. A., Belov V. P. and Shelukhin G. G., "Combustion of Aluminum Particles in Composite Condensed Systems Under Low and High Pressures", *Combustion, Explosion & Shock Waves*, Vol. 17, No. 3, 1981, pp. 26-31.

[33] Friedman, R. and Macek A., "Combustion Studies of Single Aluminum Particles", *Ninth Symposium (International) on Combustion*, 1963, pp. 703-709.

[34] Friedman, R. and Macek A., "Ignition and Combustion of Aluminum Particles in Hot Ambient Gases", *Combustion and Flame*, 6, 1962, pp. 9-19.

[35] Davis, A., "Solid Propellants: The Combustion of Particles of Metal Ingredients", *Combustion and Flame*, Vol. 7, 1963, pp. pp 359-367.

[36] Macek, A., "Fundamentals of Combustion of Single Aluminum and Beryllium Particles", *Eleventh Symposium (International) on Combustion*, 1967, pp. 203-217.

[37] Hartman, K. O., "Ignition and Combustion of Aluminum Particles in Propellant Flame Gases", *8th JANNAF Combustion Mtg.*, Vol. 1, 1971, pp. pp 1-24.

[38] Wilson, R. P. and Williams F. A., "Experimental Study of the Combustion of Single Aluminum Particles in $O_2$/Ar", *Thirteenth Symposium (International) on Combustion*, The Combustion Institute, Pittsburgh, PA, 1971, pp. 833-845.

[39] Prentice, J. L., "Combustion of Laser-Ignited Aluminum Droplets in Wet and Dry Oxidizers", AIAA 12th Aerospace Sciences Meeting, AIAA Paper No. 74-146; see also "Aluminum Droplet Combustion: Rates and Mechanisms in Wet and Dry Oxidizers", NWC TP 5569, 1974.

[40] Wong, S. C. and Turns S. R., "Ignition of Aluminum Slurry Droplets", *Combust. Sci. and Tech.*, 52, 1987, pp..221-242.

[41] Turns, S. R., Wong S. C. and Ryba E., "Combustion of Aluminum-Based Slurry Agglomerates", *Combust. Sci. and Tech.*, Vol. 54, 1987, pp. pp 299-318

[42] Roberts, T. A., Burton R. L. and Krier H., "Ignition and Combustion of Aluminum/Magnesium Alloy Particles in $O_2$ at High Pressures", *Combustion and Flame*, 92, 1993, pp. 125-143.

[43] Marion, M. Chauveau C. and Gokalp I., "Studies on the Ignition and Burning of Aluminum Particles", *AIAA 95-2861*, 1995,

[44] Marion, M., Chauveau C. and Gokalp I., "Studies on the Ignition and Burning of Aluminum Particles", *Combustion Sci. & Technology*, Vol. 116, 1996, pp. 369-390.

[45] Olsen, S. E. and Beckstead M. W., "Burn Time Measurements of Single Aluminum Particles in Steam and Carbon Dioxide Mixtures", *J. of Propulsion & Power*, Vol. 12, No. 4, 1996, pp. 662-671.

[46] Melcher, J. C., Burton R. L. and Krier H., "Combustion of Aluminum Particles in in Solid Rocket Motor Flows", *36th JANNAF Combustion Meeting*, Vol. I, CPIA # 691, 1999, pp. 249-258.

[47] Dreizin, E. L., "On the Mechanism of Asymmetric Aluminum Particle Combustion", *Combustion & Flame*, Vol. 117, 1999, pp. 841-850.

[48] Dreizin, E. L., "Experimental Study of Aluminum Particle Flame Evolution in Normal and Micro-Gravity", *Combustion & Flame*, Vol. 116, 1999, pp. 323-333.

[49] Zenin, A. A., Kusnezov G. and Kolesnikov V. and Zenin, A. A. Kusnezov G. and Kolesnikov V., "Physics of Aluminum Particle Combustion at Zero-Gravity", AIAA-99-0696, 1999.

[50] Zenin, A. A., Kusnezov G. and Kolesnikov V., "Physics of Aluminum Particle Combustion at Convection", AIAA-2000-0849, 2000.

[51] Burton, R. L., Schneider, D. S., and Krier, H., "Aluminum Particle Combustion in a Pressurized Flow Reactor", *Thirty-Fourth JANNAF Combustion Meeting*, Vol. II, CPIA Pub. No. 662, Laurel, MD, 1997, pp. 287-294.

[52] Melcher, J. C., Burton R. L. and Krier H., "Combustion of Aluminum Particles in in Solid Rocket Motor Flows", *Solid Propellant Chemistry, Combustion and Motor Interior Ballistics*, AIAA Progress in Astronautics and Aeronautics, Vol. 185, 2000.

[53] Bartlett, R. W., Ong J. N., Fassell W. M. and Papp C. A., "Estimating Aluminum Particle Combustion Kinetics", *Combustion and Flame*, Vol. 7, 1963, pp. pp 227-234.

[54] Drew, C. M., Gordon, A. S., and Knipe, R. H., "Study of Quenched Aluminum Particle Combustion," *Heterogeneous Combustion,* AIAA, Progress in Astronautics and Aeronautics Series, Vol. 15, Academic Press, New York, NY, 1964, pp. 17-39.

[55] Gordon, A. S. Drew C. M. Prentice J. L. and Knipe R. H., "Techniques for the Study of the Combustion of Metals", *AIAA Journal*, 6, 4, 1968, pp. 577.

[56] Price, E. W., Christensen, H. C., Knipe, R. H., Drew, C. M., Prentice, J. L., and Gordon, A. S., "Aluminum Particle Combustion Progress Report," NOTS-TP-3916, Naval Ordnance Test Station, China Lake, CA 1966.

[57] Foelsche, R. O., Burton, R. L., and Krier, H., "Ignition and Combustion of Aluminum Particles in $H_2/O_2/N_2$ Combustion Products," *J. of Propulsion and Power*, Vol. 14, No. 6, 1998, pp. 1001-1008.

[58] Brzustowski, T. A. and Glassman, I., "Spectroscopic Investigation of Metal Combustion," pp. 41-73 and "Vapor-Phase Diffusion Flames in the Combustion of Magnesium and Aluminum," *Heterogeneous Combustion*, AIAA, Progress in Astronautics and Aeronautics Series, Vol. 15, Academic Press, New York, 1964,. pp. 75-115,

[59] Drew, C. M., Gordon, A. S., and Knipe, R. H., Kraeutle, K. J., Prentice, J. L., and Price, E. W., "Metal Particle Combustion Progress Report," NWC-TP-4435, Naval Weapons Center, China Lake, CA, 1968.

[60] Prentice, J. L. and Krauetle, K. J., "Metal Particle Combustion Progress Report," NWC-TP-4658, Naval Weapons Center, China Lake, CA, 1969.

[61] Bucher, P., Yetter, R. A., Dryer, F. L., Vicenzi, E. P., Parr, T. P., and Hanson-Parr, D. M., "Observations on Aluminum Particles Burning in Various Oxidizers", *33rd JANNAF Combustion Meeting*, Vol. II, CPIA Pub. No. 653, Laurel, MD, 1996, pp. 449-458

[62] Bucher, P., Yetter, R. A., Dryer, F. L., Parr, T. P., and Hanson-Parr, D. M., "Aluminum Particle Gas-Phase Flame Structure", *34th JANNAF Combustion Meeting*, Vol. II, CPIA Pub. No. 662, 1997, Laurel, MD, pp. 295-305.

[63] Bucher, P., Yetter, R. A., Dryer, F. L., Parr, T. P., and Hanson-Parr, D. M., "PLIF Species and Ratiometric Temperature Measurements of Aluminum Particle Combustion in $O_2$, $CO_2$, and $N_2O$ Oxidizers, and Comparison with Model Calculations," *27th Symposium (International) on Combustion*, The Combustion Institute, Pittsburgh, PA, 1998, pp. 2421-2429.

[64] Law, C. K., "A Simplified Theoretical Model for the Vapor-Phase Combustion of Metal Particles, " *Combustion Science and Technology*, Vol. 7, 1973, pp. 197-212.

[65] Brooks, K. P. and Beckstead, M. W., "Dynamics of Aluminum Combustion," *Journal of Propulsion and Power*, Vol. 11, No. 4, 1995, pp. 769-780.

[66] Law, C. K., "A Simplified Theoretical Model for the Vapor-Phase Combustion of Metal Particles, " *Combustion Science and Technology*, Vol. 7, 1973, pp. 197-212.

[67] King, M. K., "Modeling of Single Particle Aluminum Combustion in $CO_2/N_2$ Atmospheres," *17th (International) on Combustion*, The Combustion Institute, Pittsburgh, PA, 1977, pp. 1317-1328.

[68] Kuo, K. K., *Principles of Combustion*, John-Wiley & Sons, Inc., New York, NY, 1986, pp. 383-385.

[69] Widener, J. F. and Beckstead M. W., "Aluminum Combustion Modeling in Solid Propellant Combustion Products", AIAA 98-3824, 1998.

[70] Liang, Y. and Beckstead, M.W. "Numerical Simulation of Quasi-Steady, Single Aluminum Particle Combustion in Air," AIAA 98-0254, 1998.

[71] Liang, Y., and Beckstead, M.W. "Numerical Simulation of Single Aluminum Particle Combustion in Air," *34th JANNAF Meeting*, 1997, CPIA No. 662, Vol. IV, pp. 197-208.

[72] Liang, Y., and Beckstead, M.W. "Numerical Simulation Of Unsteady, Single Aluminum Particle Combustion In Air", AIAA 98-3825, Cleveland, OH, July 1998

[73] Widener, J.F., Liang, Y and Beckstead, M.W. "Aluminum Combustion Modeling In Solid Propellant Environments", AIAA-98-0449, Los Angeles, CA, June 1999.

[74] Widener, J.F., Liang, Y and Beckstead, M.W. "Aluminum Combustion Modeling In Solid Propellant Environments", *35th JANNAF Combustion Meeting*, 1998, CPIA No 680, Vol I, pp. 577-592.

[75] Kee, R. J., Dixon-lewis, G., Warnatz, J., Coltrin, M. E. and Miller, J. A., "A fortran computer code package for the evaluation of gas-phase multicomponent transport properties", SAND86-8246, 1992.

[76] Bhatia,R. and Sirignano, W.A., "Metal Particle Combustion With Oxide Condensation", Submitted *to Combustion Science & Technology,* 1993.

[77] Widener, J.F. "Computer Modeling Of Aluminum Particle Heat-Up And Combustion Under Rocket Motor Conditions", MS Thesis, Dept. of Chemical Engineering, Brigham Young University, Provo, Utah, 1998.

[78] Zettlemoyer, A. C., *Nucleation,* Marcel Dekker Inc. New York, 1969.

[79] Brooks, K. "Characterization of the Flame and Aluminum Particles in a Rijke Burner", MS Thesis, Dept. of Chemical Engineering, Brigham Young University, Provo, Utah, 1992.

[80] Patankar, S. V., *Numerical Heat Transfer and Fluid Flow,* Hemisphere Publishing Corporation, 1980.

[81] Kalra, T.R. and Uhlherr, P. H. T., Aust. Conf. Hydraul. Fluid Mech. 4th, Melbourne, 1971.

[82] Prentice, J. L. and Nelson,L.S. "Differences between the combustion of Aluminum particles in air and Oxygen-Argon mixtures", *Journal of Electrochemical Society,* Vol.115, 1968, p.809-812.

# Motor Flow Instabilities – Part 1

### F. Vuillot, G. Casalis

ONERA

BP 72

92322 Châtillon Cedex

FRANCE

## INTRODUCTION

This paper will be given in two separate talks, a first one presenting the general problem and applications to actual motors and a second talk dealing more specifically with stability theory.

Solid propellant rocket motor instability has been the subject of many research works for more than 40 years and valuable reviews can be found in references [1, 2]. First concerns were to understand the sometimes violent instabilities that occurred during motor firings that could lead to motor failure or destruction. The combustion mechanisms were among the first to be studied since most of the energy released in the motor chamber is due to chemical reactions linked to propellant combustion. Indeed, only a very small fraction of this energy could, if directed to few instability modes, results in abnormal strains that could lead to propellant or case failure and then to motor destruction (see [2]). Instability modes can be of several types and had been classified into volume modes and acoustic modes (see [1]). Only the latter will be considered here since they appeared to be the most unpredictable. In such situations, the instabilities organize themselves around chamber acoustic modes and produce acoustic resonances,

much like an organ pipe. The fact that motor combustion chamber consists of a closed cavity (except for the nozzle, but we will see that it may be assimilated to an acoustically closed end) favors that interpretation. The so-called acoustic balance methods belong to that vision. Expressions for gains and losses to given chamber acoustic modes are looked for from knowledge of propellant combustion and mean flow organization incorporated into a linearized analysis. The objective is to identify modes that could be linearly unstable, that is to say that would grow to infinite amplitudes from infinitely small perturbations. In that acoustic view and in order to obtain tractable expressions, the flow field had to be idealized and was viewed as a perturbation of acoustic equations. However in the last 20 years it became evident that the complexity of the chamber internal flows could produce flow instabilities that could alone drive the resonance. Interestingly enough, the musical paradigm was shifted to the flute, where the role of air motion is more evident than in an organ pipe (although the physical mechanisms are very much the same). In that process, most of the simplified hypotheses of the acoustic balance approach had to be questioned and the resulting vision was much more general and embraced the entire internal flow (including combustion) and the instabilities were non longer solely combustion instabilities but flow instabilities.

Before we go into the details of that paper, few remarks must be made, relative to time and length scales. Although solid propellant motors have the particularity of having a combustion chamber whose geometry continuously varies with time (due to propellant combustion) analysis of time scales permits to consider a succession of fixed geometries. Indeed the propellant regression rate (< 1 cm/s) is at least two order of magnitude smaller than flow velocity (few m/s) which is itself at least two order of magnitude smaller than the speed of sound (1000 m/s) that governs the propagation of acoustic waves. As a result, one can considers that the geometry is fixed during the time one looks at vortices development and displacement into the chamber or the time one looks at the amplification of an acoustic wave during few cycles. Only analysis of long time behaviors or hysteresis phenomenons would require the consideration of propellant surface regression. A similar analysis can be performed for the length scales. Indeed, propellant gaseous combustion occurs in few tens of microns above the propellant surface, while the vortices or acoustic length scales are often close to the cm or m. Again, one can consider the combustion of gaseous species to be assimilated to the boundary conditions of the instability problem. Only the case of condensed phase combustion (typically aluminum combustion) which has length scale of cm, could impact the instability analysis. This will be discussed later on.

Another remark must be made at this stage. A quick view of motor operating pressures (in the range of several $10^6$ Pa) and temperatures (from 2600 to 3600 K) indicates that measurements inside the motor is a challenging task (not mentioning the vibrations, the presence of combustion products in condensed phase and the difficulty of drilling holes for probe access in a lightweight pressurized vessel). It is thus an evidence that measurements in a production motor is scarce and that only research motors can be equipped with the needed transducers to acquire a satisfactory knowledge of what is going on inside. Most often, investigators must rely on a limited number of pressure transducers, only some of them being rated for the necessary unsteady measurements. To compensate these intrinsic difficulties, researchers have developed several means of simulating rocket motor operating conditions. These rank from cold flow simulators, where air, or nitrogen, is injected through porous surfaces that simulate the motor geometry at chosen time points during the burn and, more recently, to numerical simulations of chamber internal flows, again at chosen time points during the burn. These simulations permit to access to the details of the internal flow which complement the pressure measurements obtained from actual motor firings.

## MOTOR STABILITY

### General Overview

Motor stability discussion will be limited to the case of acoustic instabilities, where the fluctuating field is organized around the chamber standing acoustic modes. The case of longitudinal modes is the most

documented case and will be used throughout this paper. Extensions to transverse modes (radial or tangential modes), although important, will not be directly addressed nor can it be either easily deduced from the presented materials. The interested reader is let to work out his way in that matter by his own.

Analysis of motor stability relies on the following simple decomposition: $P(\mathbf{r}, t) = \overline{P}(\mathbf{r}) + p'(\mathbf{r}, t)$, where overbar indicates mean values, prime indicates fluctuating values, $\mathbf{r}$ is the position vector and t is the time variable. This decomposition is general and no assumptions are made at this point.

The figure below presents a schematic of physical processes that take place inside a solid propellant rocket motor.



1) Heterogeneous combustion
2) Convection et radiation of acoustic waves through the nozzle
3) Acoustic boundary layers (forced vortical waves)
4) Reactive condensed phase
5) Vortex-shedding (free vortical waves)
6) Turbulence
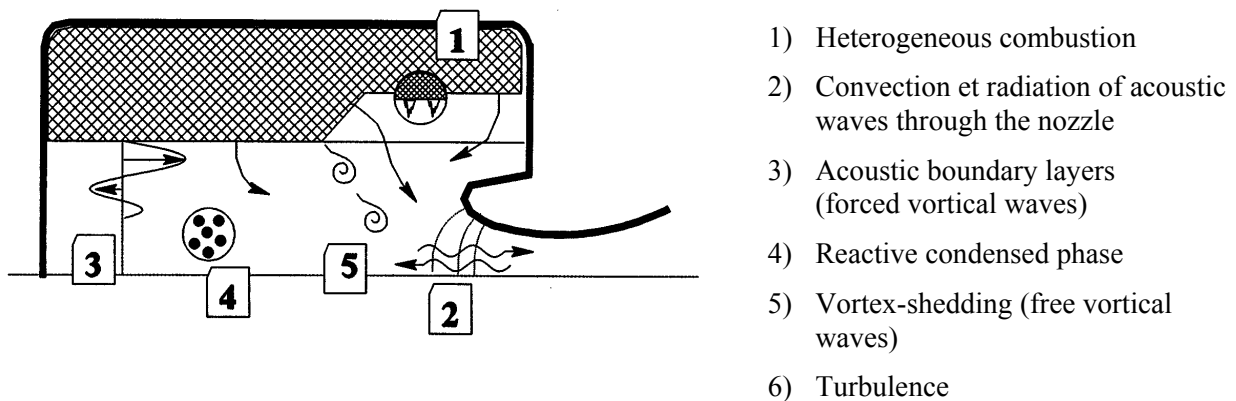
**Figure 1: Physical Phenomenons in a SRM.**

Not all these phenomenons are directly taken care of in usual approaches of motor instabilities. Approximations are common place, due to the lack of knowledge and/or the complexity of the mechanisms. For instance, the heterogeneous nature of the combustion of solid propellant is rarely given a full treatment, most often, it is averaged and treated as an equivalent homogeneous process, such as burning rate laws ($ap^n$) or response functions to fluctuating pressure. Nozzle treatment relies on numerous analyses and is quite satisfactory, at least for the most classical case of longitunal modes and axial nozzles. Acoustic boundary layers is a particular topic which corresponds to attempts to introduce the vortical nature of the unsteady flow into acoustic treatments. We will see that this question largely overpasses the simple acoustic treatment since the notion of unsteady vorticity fiercely opposes the acoustic point of view. For the present time, it suffices to say that unsteady vortical waves are naturally generated when an acoustic wave sweeps above the burning propellant surface, where the velocity is forced to be perpendicular to the surface (no slip condition). The role of viscosity in that process has been misunderstood (as essential in stating the no-slip condition while this condition can be simply, in an inviscid view, linked to mass and momentum balances at the propellant surface) and finally may appear to be of secondary importance. However, the impact of this process on the acoustic balance is important and the fact that it is not yet fully understood does not diminish its role. Quite often the condensed phase is considered as inert (e.g. alumina droplets) and composed of a limited number of sizes, although it is known that aluminum burns in a complex (and not yet perfectly known) manner, generating a continuum of droplet sizes, from the microns to the tenths of millimeter sizes. This matter constitutes one of the presently active research issues relative to motor stability and will be discussed later on. Vortex-shedding will also be discussed in some details later on, since the research is much more advanced on that subject. Its merit is to introduce the flow field as an actor to its own destabilization. Indeed periodic vortex-shedding can be viewed as a path for energy to be transferred from the mean flow to the fluctuating field. The fact that vortex-shedding can occur at discrete frequencies, some of them being capable of matching acoustic frequencies, differentiates this mechanism from the next one, turbulence, which rather implies a

continuum of frequencies. Although turbulence is also an energy path between the mean flow and the fluctuating field, the lack of distinguished frequencies makes this path much less effective in producing instabilities. Indeed, the gained experience shows that large turbulent levels inhibit motor instabilities which are built on a delicate balance of resonant mechanisms. However, it must not be forgotten that turbulence, when limited to usual levels, is also a very effective seed to local instabilities that can then feed the overall instability mechanisms.

It is useful to consider the equation for a simple oscillator of state variable p, where dot indicates time derivative, $\alpha$ the linear damping coefficient, $\omega$ the angular frequency and F(t) a forcing function:

$$\ddot{p} \;+\; 2\alpha\dot{p} \;+\; \omega^2 p \;=\; F(t)$$

$$\alpha \;<\; 0 \quad \text{unstable}$$
$$\alpha \;>\; 0 \quad \text{stable}$$

This apparently linear equation can bear some form of non-linearities that can show up in the form of dependencies of the coefficients on the state variable, p, such as $\alpha(p)$ or $F(p, t)$. Under the assumption that $\alpha << \omega$, the solution of the linear homogeneous equation takes the simple form, $p = p_0 \exp(i\omega t - \alpha t)$.

The figures below depict particular behaviors:

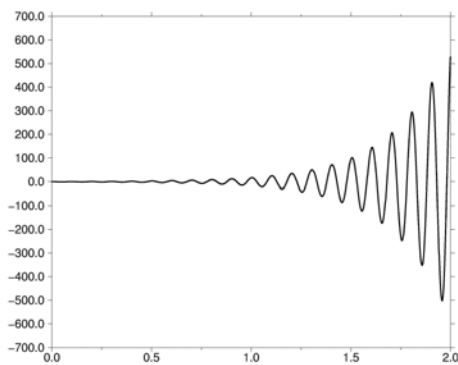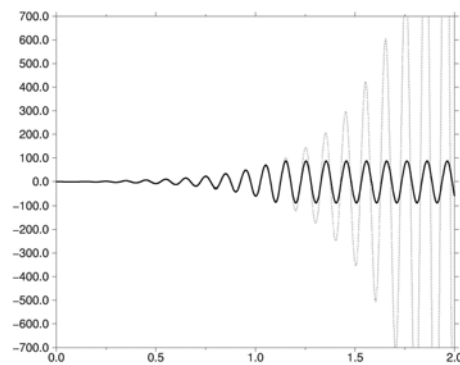

**Figure 2-a: Linearly Unstable.**



**Figure 2-b: Harmonically Forced Linearly Unstable and Non-Linearly Stable ($\alpha$ > 0 for Large Amplitudes).**
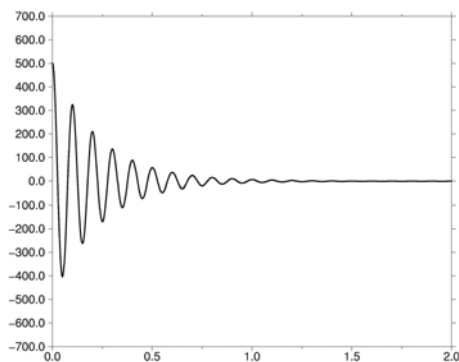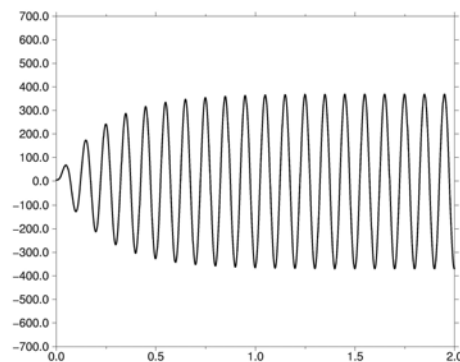


**Figure 2-c: Linearly Stable.**



**Figure 2-d: Linearly Stable, Harmonically Forced.**

It can be seen that cases b) and d) lead to limit amplitudes when some harmonic forcing functions are applied. Case d) is of particular interest since it may correspond to actual behaviors observed in large segmented space boosters, which while predicted linearly stable, exhibit limit amplitude cycles. For these cases, it is believed that periodic vortex-shedding could be the forcing function, although this point remains largely open to debate.

## Acoustic Balance

Before recalling the acoustic balance approach, it must be stressed that acoustic balance methods can be viewed as a linear analysis of the stability of chamber acoustic modes, much like the above simple oscillator examples. In the absence of forcing function, an inhomogeneous Helmoltz equation and its boundary conditions are derived from the linearized equations of motion. Inhomogeneities arise from considerations of the mean flow and the associated combustion, choked nozzle and two-phase flow effects. Solutions are sought as perturbations of reference acoustic modes, solutions of the homogeneous equations (in the absence of mean flow and associated phenomenons). That process establishes strong dependence on the acoustic point of view since the final solution can only be small (in the linear sense) perturbation to the acoustic reference mode. The validity of the final solution is thus limited by assumptions which underlie the reference acoustic solution.

The acoustic balance method was first proposed by Hart & McClure [3] and was given its most practical form by Culick [4-6]. The acoustic balance technique belongs to the asymptotic expansion methods. Every variable F is split into its mean, $\overline{F}$, and fluctuating, F', parts:

$$F = \overline{F} + F' \quad \text{with } \varepsilon = \left|F'\right|/\left|\overline{F}\right| \ll 1.$$

$\varepsilon$ is a perturbation parameter that characterizes the instability and is used to split the governing equations into successive powers of $\varepsilon$. A second perturbation parameter, $\overline{M}$, representing the mean flow Mach number, is used to simplify the equations. Assuming $\overline{M} \ll 1$ implies that the mean flow remains incompressible, which is a good approximation in the combustion chamber, for practical situations. The use of two perturbation parameters imposes to fix their respective order of magnitude. Considering that the unsteadiness is added to an existing mean flow, it is assumed that:

$$\lim_{\varepsilon, \overline{M} \to 0} \varepsilon/\overline{M} = 0$$

Then application of this technique to the fluid mechanic equations of mass, momentum and energy balance, leads to the following classes of problems:

| $\varepsilon$ | $\overline{M}$ | Problem |
|:---:|:---:|:---:|
| 0 | $\overline{M}$ | Steady, incompressible flow |
| $\varepsilon$ | 0 | Acoustic, without mean flow |
| $\varepsilon$ | $\overline{M}$ | Linear coupling: mean flow-acoustic |

The order $\varepsilon\overline{M}$ is the lower order that permits the description of the instabilities and corresponds to linear equations in $\varepsilon$. As a consequence, only the tendencies of infinitesimal perturbations to grow or decay can be determined in the form of a damping coefficient $\alpha$ ($F' \propto e^{-\alpha t}$). One of the advantages of the linear approach is that it permits to think additively. Indeed, the total damping is the sum of particular $\alpha_i$, that can be determined (or corrected) separately:

$$\alpha = \sum_i \alpha_i$$

The acoustic balance approach will be briefly described below, following Culick's paper (see [6]). Assuming that the combustion products form a two-phase mixture (subscript p represents the condensed phase of single class of size $D_p$), let $\rho_p$ be the apparent particulate density:

$$\rho_p = N\, m_p\,,$$

with N the number of particles per unit volume and $m_p$ the mass of a particle. The conservation equations can be written, for and inviscid fluid and inert particles, as follows (the primitive variables are used instead of conservative variables for convenience):

mass:

$$\frac{\partial \rho_g}{\partial t} + \frac{\partial}{\partial x_i}\left(\rho_g u_i\right) = 0 \tag{1}$$

$$\frac{\partial \rho_p}{\partial t} + \frac{\partial}{\partial x_i}\left(\rho_p u_{pi}\right) = 0 \tag{2}$$

momentum:

$$\rho_g \frac{\partial u_i}{\partial t} + \rho_g u_j \frac{\partial u_i}{\partial x_j} + \frac{\partial p}{\partial x_i} = F_{pi} \tag{3}$$

$$\rho_p \frac{\partial u_{pi}}{\partial t} + \rho_p u_{pi} \frac{\partial u_{pj}}{\partial x_j} = -F_{pi} \tag{4}$$

energy:

$$\rho_g C_V \frac{\partial T}{\partial t} + \rho_g C_V u_i \frac{\partial T}{\partial x_i} + p \frac{\partial u_i}{\partial x_i} = Q_p \tag{5}$$

$$\rho_p C \frac{\partial T_p}{\partial t} + \rho_p C u_{pi} \frac{\partial T_p}{\partial x_i} = -Q_p \tag{6}$$

$F_p$ is the drag force exerted by the particles on a unit volume of gas and $Q_p$ is the heat transferred to the gas from the particles. For the study of unsteady two-phase flow, it is generally assumed that the two phases are in equilibrium for the steady motions (the unsteady motions will be the cause of unequilibrium). This leads to the following notations:

$u_{pi} = u_i + \delta u_{pi}$ and $T_p = T + \delta T_p$, where $\delta$'s will have zero mean values. These definitions, together with eqns (4) and (6) lead to the following new inter-phase terms:

$$\delta F_{pi} = -\rho_p \left[ \frac{\partial \delta u_{pi}}{\partial t} + \delta u_{pi} \frac{\partial uj}{\partial x_j} + u_i \frac{\partial \delta u_{pj}}{\partial x_j} \right] \tag{7}$$

$$\delta Q_p = -\rho_p C \left[ \frac{\partial \delta T_p}{\partial t} + \delta u_{pi} \frac{\partial T}{\partial x_i} + u_i \frac{\partial \delta T_p}{\partial x_i} \right] \tag{8}$$

Finally, defining the mixture properties as:

$\kappa = \rho_p / \rho_g$

$\rho^* = (1 + \kappa) \rho_g$

$C_V^* = (C_V + \kappa C)/(1 + \kappa)$

$R^* = R_g/(1 + \kappa)$: mixture perfect gas constant

$p^* = p = R^* T/\rho^* = RT/\rho$: static pressure

$\gamma^* = 1 + R^*/C_V^* = \gamma(1 + \kappa C/C_p)/(1 + \kappa C/C_V)$

$$a^* = \left[ \frac{1 + \kappa\, C/C_p}{(1 + \kappa)\left(1 + \kappa\, C/C_V\right)} \right]^{1/2} a_g$$

equations (3) and (5) can be rewritten for the mixture:

$$\rho^* \frac{\partial u_i}{\partial t} + \rho^* u_j \frac{\partial u_i}{\partial x_j} + \frac{\partial p}{\partial x_i} = \delta F_{pi} \tag{9}$$

$$\rho^* C_V^* \frac{\partial T}{\partial t} + \rho^* C_V^* u_i \frac{\partial T}{\partial x_i} + p \frac{\partial u_i}{\partial x_i} = \delta Q_p \tag{10}$$

Then eqn (10) can be written for the pressure:

$$\frac{\partial p}{\partial t} + u_i \frac{\partial p}{\partial x_i} + \left( \frac{R^*}{C_V^*} + 1 \right) p \frac{\partial u_i}{\partial x_i} = \frac{R^*}{C_V^*} \delta Q_p \tag{11}$$

At this point it is interesting to note, that under the assumptions of a steady state motion and of inert particles, eqn. (2) gives:

$$\frac{\partial}{\partial x_i} \left( \kappa \rho_g u_i \right) = 0$$

which, using eqn. (1), leads to:

$$u_i \frac{\partial}{\partial x_i} \left( \kappa \right) = 0$$

implying that $\kappa$ is conserved on any streamline. Since $\kappa$ is uniform on the propellant surface, $\kappa$ is uniform throughout the chamber.

The next step is to develop eqns. (9) and (11) to first order in $\varepsilon$ and $\overline{M}$. It must be noted that the inter-phase equilibrium hypothesis permits to assimilate the mixture (superscript *) and the steady gas motion (notation ‾).

Steady state:

$$\frac{\partial}{\partial x_i}\left(\overline{u_i}\right) = 0 + O(\overline{M}^2)$$

$$\frac{\partial}{\partial x_i}\left(\overline{p}\right) = 0 + O(\overline{M}^2)$$

First order:

$$\frac{\partial p'}{\partial t} + \overline{u_i}\frac{\partial p'}{\partial x_i} + \gamma\overline{p}\frac{\partial u_i^{'}}{\partial x_i} = \frac{R}{C_V}\delta Q_p^{'} \tag{12}$$

$$\overline{\rho}\frac{\partial u_i^{'}}{\partial t} + \frac{\partial p'}{\partial x_i} = \delta F_{pi}^{'} - \overline{\rho}\left(\overline{u_j}\frac{\partial u_i^{'}}{\partial x_j} + u_j^{'}\frac{\partial \overline{u_i}}{\partial x_j}\right) \tag{13}$$

Then, taking the time derivative of eqn. (12) and combining with the divergence of eqn. (13) and assuming harmonic motions ( $F' = \tilde{F}\exp(i\omega t)$ ), one gets an inhomogeneous Helmoltz's equation for p. This equation is valid in the interior domain $\Omega$ where the mean flow can be assumed incompressible. Its boundary conditions are obtained by taking the scalar product of eqn. (13) with the outward unit normal vector, $n_i$, along the chamber boundaries:

$$\frac{\partial^2 \tilde{p}}{\partial x_i \partial x_i} + k^2 \tilde{p} = \tilde{h} \tag{14}$$

$$n_i \cdot \frac{\partial \tilde{p}}{\partial x_i} = -\tilde{f} \tag{15}$$

with:

$$k = \left(\omega + i\alpha\right)/a$$

$$\tilde{h} = i\frac{\omega}{a}\frac{\overline{u}_i}{a}\frac{\partial \tilde{p}}{\partial x_i} - i(\gamma-1)\frac{\omega}{a^2}\delta\tilde{Q}_p + \frac{\partial}{\partial x_i}\left(\delta\tilde{F}_{pi}\right)$$
$$- \overline{\rho}\frac{\partial}{\partial x_i}\left(\overline{u_j}\frac{\partial \tilde{u}_i}{\partial x_j} + \tilde{u}_j\frac{\partial \overline{u_i}}{\partial x_j}\right) \tag{16}$$

$$\tilde{f} = i\omega\overline{\rho}n_i\tilde{u}_i - n_i\delta\tilde{F}_{pi} - \overline{\rho}n_i\left(\overline{u_j}\frac{\partial \tilde{u}_i}{\partial x_j} + \tilde{u}_j\frac{\partial \overline{u_i}}{\partial x_j}\right) \tag{17}$$

For the unperturbed case (rigid boundaries [*], no mean flow and no particles), one has classically:

$$\frac{\partial^2 \tilde{p}_N}{\partial x_i \partial x_i} + k_N^2\tilde{p}_N = 0 \tag{18}$$

---

[*] This assumption is justified in most cases, except the cases with "long nozzles" where the nozzle admittance must be taken into account in eq. (19) (see ref. [7]).

$$n_i \cdot \frac{\partial \tilde{p}_N}{\partial x_i} = 0 \tag{19}$$

Combining eqns. (14) to (19) and taking a volume average over the domain $\Omega$, one can arrive, after some tedious algebra, for an expression (eqn. 20) for the perturbed wave number, k, valid at first order, and making use of the unperturbed eigen mode of the chamber:

$$\begin{aligned} \left(k^2 - k_N^2\right) E_N^2 &= -ik_N \int_{\partial\Omega} \left(A_n + \overline{M}_n\right) \tilde{p}_N^2 \, dS \\ &- \int_\Omega \delta \tilde{F}_{pi} \frac{\partial \tilde{p}_N}{\partial x_i} dV - i(\gamma-1) \frac{k_N}{a} \int_\Omega \delta \tilde{Q}_p \tilde{p}_N \, dV \end{aligned} \tag{20}$$

The following definitions are used:

$$E_N^2 = \int_\Omega \tilde{p}_N^2 \, dV$$

$$A_n = \overline{\rho} a \frac{\tilde{u}_i n'_i}{\tilde{p}}$$

$$M_n = \frac{\overline{u}_i n'_i}{a}$$

where $n'_i$ is the inward pointing unit normal vector.

It must be noted that to arrive at equation (20) one has to assume that the vector $\tilde{u}_i$ is proportional to the gradient $\partial \tilde{p}_N / \partial x_i$, imposing an irrotational field for the unsteady velocity. This assumption bears several limitations for the use of the acoustic balance. Indeed recent works have demonstrated that the unsteady velocity field may be highly rotational, as a consequence of the propellant side injection [e.g. 8-11]. Recent works propose a modification of the acoustic balance technique [10] to account for unsteady vorticity. It is outside the scope of this paper to discuss that matter. It must also be said that in situations where vortex shedding takes place, the assumption of an irrotational velocity field is also incorrect.

Equation (20) can be split in its real and imaginary parts to give the following equations for the frequency shift and the damping coefficient, brought by the perturbation (assuming that $\alpha^2 << \omega^2$):

$$\begin{aligned} \omega - \omega_N &= \frac{a}{2E_N^2} \int_{\partial\Omega} \text{Im}(A_n) \tilde{p}_N^2 \, dS \\ &- \frac{a}{2k_N E_N^2} \int_\Omega \text{Re}\left(\delta\tilde{F}_{pi} \frac{\partial \tilde{p}_N}{\partial x_i}\right) dV \\ &- (\gamma-1)\frac{1}{2E_N^2} \int_\Omega \text{Im}(\delta\tilde{Q}_p \tilde{p}_N) dV \end{aligned} \tag{21}$$

$$\begin{aligned} \alpha &= \frac{-a}{2E_N^2} \int_{\partial\Omega} \left(\text{Re}(A_n) + \overline{M}_n\right) \tilde{p}_N^2 \, dS \\ &- \frac{a}{2k_N E_N^2} \int_\Omega \text{Im}\left(\delta\tilde{F}_{pi} \frac{\partial \tilde{p}_N}{\partial x_i}\right) dV \\ &- (\gamma-1)\frac{1}{2E_N^2} \int_\Omega \text{Re}(\delta\tilde{Q}_p \tilde{p}_N) dV \end{aligned} \tag{22}$$

## Particular Contributions to the Acoustic Balance

The last two volume integrals of the above equations concern the particulate damping and will be discussed in a following section. Concentrating on eqn. (22), and discarding the particulate dampings, usual form will be given. The first surface integral can be broken over the following surfaces:

- Propellant surfaces: due to the propellant combustion, $M_n$ represents the injection Mach number, $M_{inj}$, and $A_n$ the propellant admittance. It is common practice to use the propellant burning rate response, $R_{MP}$, instead of the admittance. These two quantities are linked by the following relationship:

$$R_{MP} = \frac{v_c^{'}/\overline{v}_c}{p'/\overline{p}} = \frac{\rho^{'}/\overline{\rho}}{p'/\overline{p}} + \frac{\overline{p}}{aM_{inj}} \frac{u_i^{'}.n_i^{'}}{p'}$$

$$\Rightarrow R_{MP} = \frac{1}{\gamma M_{inj}} \left[ M_{inj} + A_n \right]$$

A global response is sometimes defined as: $R_c = R_{MP} + R_{TP}$, with $R_{TP}$ being the temperature response. Assuming isentropic oscillations leads to:

$$R_c = R_{MP} + \frac{T^{'}/\overline{T}}{p'/\overline{p}} = R_{MP} + \frac{\gamma - 1}{\gamma}$$

Then, assuming that the propellant combustion does not depend one the location, the combustion term $\alpha_c$ can be obtained as:

$$\alpha_c = -\gamma a M_{inj} \, \text{Re}(R_{MP}) \frac{\int_{S_{inj}} \widetilde{p}_N^2 \, dS}{2 \int_\Omega \widetilde{p}_N^2 \, dV} \tag{23}$$

- Inert walls: their contributions are obviously zero.

- Nozzle entrance plane: due to different normal vectors orientations, $M_n$ represents $-M_L$, and $A_n$ represent $-A_L$, with $M_L$ and $A_L$ being the nozzle inlet Mach number and acoustic admittance respectively. Assuming uniform properties across the nozzle entrance plane, the nozzle term is broken into the following convective, $\alpha_{NC}$, and radiative, $\alpha_{NR}$, parts:

$$\alpha_{NC} = a \overline{M}_L \frac{\int_{S_L} \widetilde{p}_N^2 \, dS}{2 \int_\Omega \widetilde{p}_N^2 \, dV} \tag{24}$$

$$\alpha_{NR} = a \, \text{Re}(A_L) \frac{\int_{S_L} \widetilde{p}_N^2 \, dS}{2 \int_\Omega \widetilde{p}_N^2 \, dV} \tag{25}$$

Once the propellant and nozzle properties are known, evaluating the motor linear stability is only a question of computing the reference acoustic mode, solution of eqns. (18) and (19), and evaluating the different stability integrals appearing in $\alpha_c$, $\alpha_{NC}$, and $\alpha_{NR}$. The resulting damping coefficient will then be $\alpha = \alpha_c + \alpha_{NC} + \alpha_{NR}$.

This will be illustrated for a simple cylindrical port motor displayed in fig. 3, and for the case of the $q^{th}$ longitudinal mode.
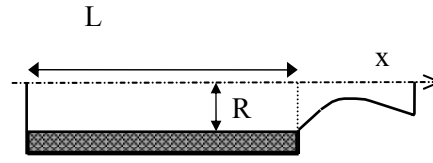
**Figure 3: Simple Cylindrical Motor.**

The following equations are used:

$$S_{inj} = 2\pi RL, \; S_L = \pi R^2, \; \Omega = \pi R^2 L$$

$$M_L = \frac{S_{inj}}{S_L} M_{inj}, \; M_{inj} = \frac{V_{inj}}{a}$$

$$\tilde{p}_N = \tilde{p}_{N0} \cos(k_N x) \text{ with } k_N = q\frac{\pi}{L}$$

Finally:

$$\alpha_c = -\gamma \frac{V_{inj}}{R} Re(R_{MP})$$

$$\alpha_{NC} = \frac{aM_L}{L} = \frac{2V_{inj}}{R}$$

$$\alpha_{NR} = \frac{aRe(A_L)}{L}$$

To estimate the effectiveness of the dampings, $\alpha$ must be compared to the frequency, $f_q = q\,a/(2L)$, so that:

$$\frac{\alpha_c}{f_q} = -\gamma \frac{2}{q} \frac{L}{R} M_{inj} Re(R_{MP})$$

$$\frac{\alpha_{NC}}{f_q} = \frac{2}{q} M_L = \frac{2}{q} \frac{2L}{R} M_{inj}$$

$$\frac{\alpha_{NR}}{f_q} = \frac{2}{q} Re(A_L)$$

It must be noted that for short nozzles, it is common to approximate the real part of the nozzle admittance, $A_L$, by its value derived from a quasi-steady analysis:

$$\frac{PA_c}{C^*} = (\rho UA)_L \quad \Rightarrow \quad \frac{p'}{\overline{P}} - \frac{1}{2}\frac{T'}{\overline{T}} = \frac{\rho'}{\overline{\rho}} + \frac{u'}{\overline{U}}$$

$$\text{with: } \quad \frac{T'}{\overline{T}} = \frac{p'}{\overline{P}} - \frac{\rho'}{\overline{\rho}}, \quad \frac{\rho'}{\overline{\rho}} = \frac{1}{\gamma}\frac{p'}{\overline{P}} \quad \text{and} \quad \overline{P} = \frac{\overline{\rho}\,a^2}{\gamma}$$

$$\text{hence: } \quad A_L = \overline{\rho}\,a\,\frac{u'}{p'} = \frac{\gamma-1}{2}\,\overline{M}_L$$

$$\Rightarrow Re(A_L) = \frac{\gamma-1}{2}\,\overline{M}_L$$

This permits to evaluate the relative order of magnitude of equations (24) et (25). Assuming $\gamma \approx 1.2$, it is found that the radiative term represents roughly 10% of the convective one. The fact that $Re(A_L)$ is a small number validates the assumption that the nozzle entrance plane behaves much like a rigid wall.

Then evaluating the resulting $\alpha$, one gets in this simple case:

$$\frac{\alpha}{f_q} = \frac{2}{q}\frac{L}{R}M_{inj}\left[-\gamma Re(R_{MP}) + 2 + \frac{\gamma-1}{2}\right] \tag{26}$$

From this equation it appears that unless $Re(R_{MP})$ is larger than $(\gamma+3)/2\gamma$ ($\approx 1.75$) stability will be predicted. This limit will be even higher when the flow-turning correction will be added to the acoustic balance (see next section).

In more complex situations, the stability integrals must be carried out numerically, as well as the determination of the reference acoustic mode. It can be seen from eqns. (23) and (24-25) that the location where the combustion takes place and/or where the nozzle is located with respect to the reference acoustic mode will affect the global balance. In particular, the most famous T burner, with its propellant samples at the chamber ends and its nozzle at the mid-chamber position, will favor motor instability (which is what it was designed for).

## Flow Turning Issue

The flow turning issue is a long debated subject (e.g. see [1, 2, 6, 8, 10, 12, 13]). It appeared from the fact that the results of the 1D acoustic balance are different from the 3D ones. An additional term is found in the form of a surface integral over the burning surface:

$$\alpha_{FT} = \frac{a}{2k_N^2 E_N^2}\int_{S_{inj}}\overline{M}_{inj}\left(\frac{d\widetilde{p}_N}{dx}\right)^2 dS \tag{27}$$

This term was extended to the 3D analysis by Culick [6]. It derives from the condition of a no-slip boundary condition that can be freely imposed in 1D whereas the 3D approach forces an irrotational unsteady field. This was interpreted as a viscous effects, due to acoustic boundary layers. However, a simplified viscous treatment, near the injecting surface, led to a different expression [8], resulting from the "apparent" propellant admittance. Indeed, the actual propellant admittance has to be corrected from the displacement effect of the viscous layers. In the case of the relatively strong blowings encountered in SRM, this correction had a limiting value, independent of the viscosity, which was troubling. This term, supposed to replace the $\alpha_{FT}$ term, was:

$$\alpha_{BL} = \frac{a}{2E_N^2}\int_{S_{inj}}\overline{M}_{inj}(\widetilde{p}_N)^2 dS \tag{28}$$

Please note that in the case of a pure cylindrical motor, both eqns. (27) and (28) give the same result, adding to the trouble. The discussion was further fed by full numerical solutions of the unsteady Navier-Stokes equations [9, 11] that clearly showed that the unsteady velocity field was clearly rotational, invalidating both the 1D and the 3D approaches and the $\alpha_{FT}$ term, but also that the so-called acoustic boundary layers were very thick, invalidating the admittance correction approach and the $\alpha_{BL}$ term. In several recent papers [e.g. 14], Majdalani *et al.* revisited the problem of unsteady vorticity in acoustic solutions and proposed a unified mathematical framework.

In any cases, most researchers agree to the fact that the uncorrected acoustic balance, as expressed in eqn. (26), underestimates the motor stability. Indeed, for the simple cylindrical motor, one gets:

$$\frac{\alpha_{FT}}{f_q} = \frac{\alpha_{BL}}{f_q} = \frac{2}{q}\frac{L}{R}M_{inj}$$

leading to the following expression:

$$\frac{\alpha}{f_q} = \frac{2}{q}\frac{L}{R}M_{inj}\left[-\gamma Re(R_{MP}) \ + \ 3 \ + \ \frac{\gamma-1}{2}\right] \tag{29}$$

which sets the stability limit to Re($R_{MP}$) larger than ($\gamma$+5)/2$\gamma$ ($\approx$ 2.58), which is a rather large value for the real part of the response function. One may then conclude, that if the combustion is the only driving mechanism, most motors should be stable on their longitudinal modes, which is unfortunately not the case. For transverse modes and especially the tangential modes, the above analysis leads to less marked conclusions, in particular due to the nozzle terms which contributes to only limited losses.

## Two-Phase Flows

Since most motors use metallized propellants, the combustion products carry some amount of condensed phase products, such as alumina droplets. These will add to the motor stability. In fact, one of the reasons to load propellants with metal powder, such as aluminum, is to increase the stability of the motors (another reason being the benefit of increased specific impulse).

Evaluation of the particulate terms in eqns. (21) and (22), can be done providing that ad-hoc laws are supplied for the drag force and the heat transferred between phases. Reference [15] describes the problem and proposes solution methods. It is common practice to evaluate the two-phase flow terms for the simplified Stokes regimes, valid for small (less than unity) particular Reynolds numbers ($Re_p = \rho\, D_p\, \Delta U_p\, /\mu$ , where $\Delta U_p$ is the velocity difference between the two phases). For low amplitude oscillations, this is consistent with the equilibrium hypothesis, since then:

$$(Re)_p = \frac{\rho_g D_p\left|\delta\widetilde{\mathbf{u}}_p\right|}{\mu}$$

Under these conditions, the drag coefficient takes the well known value of:

$$C_D = 24/(Re)_p$$

and the convective heat transfer coefficient is taken as:

$$h' = 2\lambda/Dp \text{ (Nusselt number = 2)},$$

This leads to the following linear relations:

$$\delta\mathbf{F}_p = N_p(3\pi\mu D_p)\delta\mathbf{u}_p$$

$$\delta Q_p = N_p(2\pi\lambda D_p)\delta T_p$$

At first order, eqns. (7) et (8) lead to:

$$\left|\delta\mathbf{u}_p\right| = \left|\delta\mathbf{u}_p\right|_0 e^{-\frac{t}{\tau_v}} \quad \text{with} \quad \tau_v = \frac{\rho_{ps} D_p^2}{18\mu}$$

$$\left|\delta T_p\right| = \left|\delta T_p\right|_0 e^{-\frac{t}{\tau_T}} \quad \text{with} \quad \tau_T = \frac{3}{2} Pr \frac{C}{C_p} \tau_v$$

Finally, expressing $\delta\mathbf{F}_p$ et $\delta Q_p$ as functions of the fluctuating velocity and temperature (which, at first order, can be directly linked to $\partial p_N / \partial x$ and $p_N$, one gets:

$$\delta F_{pi} = \kappa \frac{1 - i\omega\tau_v}{1 + (\omega\tau_v)^2} \frac{\partial \widetilde{p}_N}{\partial x_i}$$

$$\delta Q_p = -\kappa\omega \frac{C}{C_p} \frac{i + \omega\tau_T}{1 + (\omega\tau_T)^2} \widetilde{p}_N$$

These are then incorporated into eqns. (21) et (22). With some further approximations, valid for small $\kappa$ and for $C/C_p$ et $C/C_v$ close to unity, the particular damping term can be expressed as:

$$\alpha_p = \kappa \frac{\omega}{2} \left[ \frac{\omega\tau_v}{1 + (\omega\tau_v)^2} \frac{\int_\Omega \left(\frac{d\widetilde{p}_N}{dx}\right)^2 dV}{k_N^2 \int_\Omega \widetilde{p}_N^2 dV} + (\gamma - 1) \frac{C}{C_p} \frac{\omega\tau_T}{1 + (\omega\tau_T)^2} \right] \tag{30}$$

Please note that on the contrary to the preceding terms, this expression involves a volume effect.

For the simple cylindrical motor, this expression becomes:

$$\alpha_p = \kappa \frac{\omega}{2} \left[ \frac{\omega\tau_v}{1 + (\omega\tau_v)^2} + (\gamma - 1) \frac{C}{C_p} \frac{\omega\tau_T}{1 + (\omega\tau_T)^2} \right]$$

and finally:

$$\frac{\alpha_p}{f_q} = \kappa\pi \left[ \frac{\omega\tau_v}{1 + (\omega\tau_v)^2} + (\gamma - 1) \frac{C}{C_p} \frac{\omega\tau_T}{1 + (\omega\tau_T)^2} \right]$$

Neglecting the thermal term, the optimum damping is obtained for $\omega\tau_v = 1$, which leads to:

$$(\alpha_p)_{opt} = \kappa \frac{9\mu}{2\rho_{ps} D_p^2} \quad \text{and} \quad (f)_{opt} = \frac{9\mu}{\pi\rho_{ps} D_p^2}$$

$$(D_p)_{opt} = \sqrt{\frac{9\mu}{\pi\rho_{ps} f}}$$

This relation can be used to adjust the propellant loading to damp potentially unstable modes (most of the time, the feared tangential modes) by selecting the proper particle sizes.

## Conclusion/Limitations

The above sections described the engineer tools for predicting motor stability. In practical situations, which depart from the simple cylindrical motor considered here, this task involves the determination of the reference acoustic modes and the evaluation of the stability integrals. Inputs to the model are the propellant response function, the nozzle admittance and the particular phase sizes. These can be obtained from experiments, dedicated to that characterization effort, and bear some uncertainties, sometimes quite large, due to the complex physical mechanisms involved. This, added to the fact that some difficulties arise from the formulation itself (e.g. how to express the flow-turning loss or the nozzle admittance in complex geometries), makes the acoustic balance a "**useful tool of limited validity**". It is not surprising that stability is predicted most of the time, while unstable motors keep haunting the rocket engineers' nights.

## FLOW STABILITY

### Presentation

From what precedes, it is clear that some sources of instability are missing from the acoustic balance approach. Flandro and Jacobs [16] were the first to mention the "vortex-shedding" as a possible additional driving to the motor stability balance. It was viewed as a coupling between a shear layer instability (in the hydrodynamic sense) and the chamber acoustic. First works considered simple correlations in term of critical Strouhal numbers (see [17] for a detailed presentation). These Strouhal numbers were based on the mean axial velocity (U) and either on the port diameter (D): $(St)_D$ , or on the stand-off distance between the vortex generation point and its impact, $\ell$ , $(St)_\ell$:

$$(St)_D = fD/U \text{ and } (St)_\ell = f\ell/U$$

References [18-24] present interesting attempts to use correlations of this type. However, it must be stressed that such correlations have a limited predictive merit and can be compared to the celebrated "age of the capitain" formula (mast height divided by the ship speed): all the difficulty lies in the proportionality constant which has no universal quality. Reference [20] goes one step further in using the Rossiter's formula to correlate the observed frequencies. This approach uses the relative time delays of the vortex emission to the acoustic feedback. The figure hereafter illustrates this point of view.
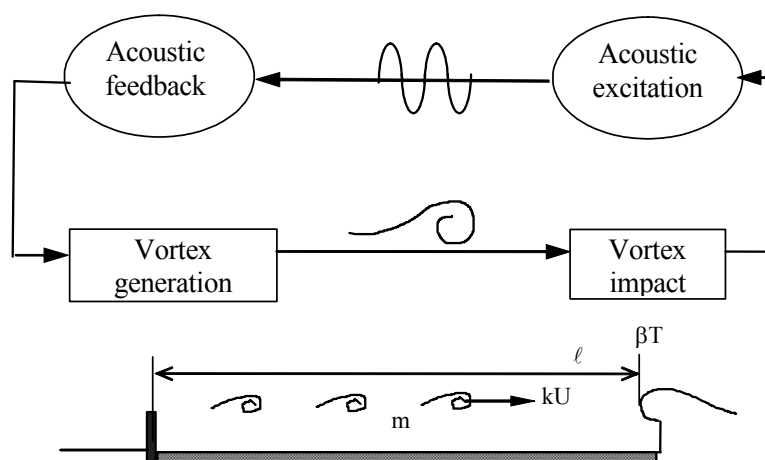


**Figure 4: Illustration of the Vortex-Shedding Phenomenon.**

Let T be the time period of the vortex-shedding, k the ratio of vortex displacement velocity to the mean axial flow velocity, U, β an empirical constant representing the time delay between vortex impact and acoustic wave emission and m the number of vortices on distance $\ell$ , then one gets:

$$mT = \ell/kU + \ell/c + \beta T$$

k and β are empirical constants that must be case adjusted from the measurement of the frequency.

Reference [20] uses this relationship to express $(St)_\ell$ as:

$$(St)_\ell = \frac{m-\beta}{\overline{\overline{M}}+1/k}$$

$$\text{leading to:} \quad f = \frac{U}{\ell} \frac{m-\beta}{\overline{M}+1/k} \approx k\frac{U}{\ell}(m-\beta) \tag{31}$$

M is the Mach number associated to U and can be neglected before 1/k (always greater than 1).

Application of this formula to the Titan SRMU leads to values of m in the range 5-12, and to *k = 0.58* and *β = 0.25*, which is in reasonable agreement with previous works (see [20]).

It is important to stress that such an approach is simplified and cannot be fully predictive. However it turns out to be quite useful in interpreting firing test measurements.

The most complete approach to this problem is that of Flandro [22]. Vortex properties (wave length, displacement speed) are derived from the hydrodynamic stability analysis of the velocity profile at the origin of vortex-shedding. The impact mechanisms are modelized through a localized volumetric force. References [17, 23-25] present applications of this method to the Ariane 5 MPS P230 solid boosters. The aim is to derive a vortex-shedding additional term, $\alpha_{VS}$ , to the acoustic balance results. However, non realist values are obtained (due to the strong linear growth of the vortices) and the method was limited to a qualitative analysis (driving or damping effects) that is based on the phase difference between the vortices at impact and the acoustic field. This method will not be further detailed here, although it represents a unique attempt to quantify the Rossiter's equation from first principles, because it was found to be extremely sensitive to unknown details, such as the precise location of the vortex origin. The interested readers are referred to references [22-25 and 17].

Looking back at the acoustic balance approach, it is interesting to look at the implications of rotational fields on the final equations (see [26, 17]). Indeed, assuming that the unsteady velocity is no longer aligned with the gradient of the acoustic pressure, additional terms result from the linearization of the **u.∇u** term in the RHS of eqn. (20). These terms take the following form:

$$\overline{\rho}\left\{ \int_\Omega k_N^2 \left[ \overline{\mathbf{u}}.(\widetilde{\mathbf{u}} - \widetilde{\mathbf{u}}_N) \right] \widetilde{p}_N \, dV + \int_\Omega (\overline{\boldsymbol{\omega}} \wedge \widetilde{\mathbf{u}}).\nabla \widetilde{p}_N \, dV + \int_\Omega (\widetilde{\boldsymbol{\omega}} \wedge \overline{\mathbf{u}}).\nabla \widetilde{p}_N \, dV \right\}$$

These integrals are difficult to evaluate in general and need to know the flow organization in the volume of the motor. However, it is interesting to note that the last integral implies unsteady vorticity and can be related to the vortex-shedding phenomenon. For a two-dimensional flow its integrand reduces to:

$$-\widetilde{\omega}_z \, \overline{v} \, \frac{\partial \widetilde{p}_N}{\partial x}$$

It can be argued that this integrand takes significant values at localized points inside the motor chamber, such as the nozzle entrance where $\widetilde{\omega}_z$  and  $\overline{v}$ are large, thus providing a natural way to introduce the

coupling between the vortical and the acoustic fields. The volume integral can then be reduced to a surface integral at the vortex "impact" point as proposed by Flandro.

## Intrinsic Non-Linear Nature

Attempts to complement the basic acoustic balance approach are impeded by difficulties linked to the departure of the unsteady field, in particular the velocity field, from the pure acoustic vision. Indeed, the flow-turning debate illustrates the difficulty in incorporating unsteady vorticity in the acoustic framework, while the vortex-shedding issue exemplifies the difficulties in taking care of flow instabilities in the linear framework.

The fact that the mean flow can become unstable by its own is now an accepted result. The fact that this unstable behavior cannot easily fit into the acoustic framework is also becoming evident. One of the reasons that one can invoke is that flow instability evolves on its own, as an independent mechanism, with no need to an acoustic reference. The attempts to treat separately these two independent mechanisms from variable decomposition: mean and fluctuating flows, with the fluctuating flow composed of an compressible irrotational (acoustic component) and an incompressible rotational (vortical component) components, at the basis of Flandro's approach, failed to provide useful results. The reason of failure lied not in the necessary coupling equations, which could be written, but rather in the difficulty to describe the vortical evolutions. Indeed, vortical flow can be characterized in its linear regime (initial growth of instability waves) with proven methods (Orr-Sommerfeld type approaches) but growth rates in this early linear regime are quite high and the vortical field rapidly enters some form of non-linear regimes which are much more complex to model. The fact that in most situations the interactions between the two unsteady fields occur when the vortical fields has become non-linear, may explain the failure of the above mentioned approaches.

Most of the time, **observable vortices are the results of a non-linear growth process**. As a consequence, our knowledge of such vortices and of their dependencies on the known parameters is blurred by the non-linear growth stage of initial unstable vortical waves, a process which most of the time remains beyond our present understanding. However it is of **major importance to better understand the initial destabilisation mechanisms**, simply because they have definite frequency signatures and sensitivities to flow characteristics which must be known in order to understand their potential effectiveness to couple with acoustic waves and produce harmful vortices. Controlling the early stage of flow instabilities is undoubtedly an effective mean of avoiding unwanted motor instabilities driven by some form of vortex-shedding. **In that view the knowledge of flow stability characteristics is an essential prerequisite to any attempt in controlling motor flow driven instabilities**. This is detailed in the second paper devoted to the stability theory.

## Model Requirements

From what precedes, it is clear that if motor flow driven instabilities have to be predicted, one has to rely on a model that has the ability to describe, in the same framework, both the acoustic waves and the vortical waves (including non-linear interactions). From that point of view, the full numerical solution of the compressible Navier-Stokes equations provides the needed framework.

However, since the instabilities can be viewed as resonance mechanisms that involve the motor chamber acoustic modes and unstable couplings of physical phenomenons linked to the mean flow, the Navier-Stokes equations have to be completed to include all the needed phenomenons. Considering the nature of the solid propellant rocket internal flows, identified physical mechanisms are:

- the mean flow itself, including sheared flows, nozzle flows, and turbulence,
- the propellant combustion at the burning surface,

- the combustion of aluminum droplets carried by the flow,

- the structure motions (as possibly affecting the mean and unsteady flows).

Finally, the model should be able:

a) to propagate the acoustic waves,

b) to describe the details of the internal flow, including the capture of acoustically forced vorticity waves as well as flow instabilities and their non-linear growth,

c) to include some form of condensed phase model (inert and reactive),

d) to couple with propellant combustion models,

e) to couple with solid mechanic models.

This analysis concluded that full solutions of the compressible unsteady Navier-Stokes equations, including reactive two-phase flow treatments should be sought. Indeed, as already mentioned, such solutions have the capability to describe both the acoustic and flow vorticity, without the need to separate the solution in several flow components. We have underlined that this poses some problems for describing each component in a compatible way. Further, such a model could be coupled through its boundary conditions to propellant combustion models and solid mechanic codes, to permit a complete description of the identified mechanisms. This would then provide an unprecedented tool for analyzing motor instabilities.

However, such a solution would necessarily rely on a numerical solution of the equations and some concerns were raised about the ability of the numerical procedure to faithfully describe the solution, due to numerical errors and grid size requirements. As a consequence, it was agreed that such a solution method should pass through a severe validation procedure before it could be safely used in predicting motor stability.

This validation requirement posed in turn some constraints which were the need for detailed measurements in known situations to provide the data against which the numerical results would be validated. This was quite a new constraint and it promoted a series of unique research works, sometimes of ingrate nature, that had to be performed to sustain the construction of this new tool. Here "ingrate" must be understood, not as scientifically uninteresting works but rather as far from actual motor applications and thus implying difficulties in being funded and fully appreciated by program managers. However, such works were essential and ranked from:

- Cold flow simulators in which detailed velocity measurements could be performed and compared to numerical simulation results,

- Analytical solutions of unstable flow regimes,

- Dedicated lab scale motors with high quality and numerous measurements to gain real firing tests data,

- Meticulous characterization efforts to provide the model inputs. These comprised condensed phase characterizations, details of the propellant composition, including characterizations of AP and aluminum size distributions, and unsteady propellant combustion responses function determinations,

- Dedicated models for combustion mechanisms and fluid-structure couplings,

- Dedicated and documented test cases for model evaluations.

Such works have be carried out in Europe thanks to the Ariane 5 related programs and represent a valuable asset for the development of a comprehensive model for motor stability predictions. For the first time,

at the end of that research effort, actual unstable motor behaviors could be simulated numerically and produced results that agreed both in frequency and in oscillatory amplitude, with motor measurements. Results of such quality were judged unattainable at the start of the research effort and are worth to be celebrated. Of course much remains to be done yet, to guarantee the capability of a priori predictions from scratch (i.e. before any firings are performed).

## STABILITY THEORY

This part is described in details in the second paper.

## DEALING WITH FLOW STABILITY

### Experimental Evidences

From early works of Flandro *et al.*, it was expected that flow instabilities could drive unstable motors. In particular, it was stressed that inflectional velocity profiles, as created above protruding obstacles or at propellant grain discontinuities could be at the origin of unstable flows, prone to produce vortex-shedding driven instabilities. The works carried out in the USA, relative to the Space Shuttle and the Titan boosters, clearly demonstrated that vortex-shedding could drive the first longitudinal modes of the motor [27-30, 18-22]. The works of Dunlap *et al.* [19] established that for such large segmented space boosters, protruding inhibitor rings, such those created by the front ends thermal insulations of propellant segments (typically the aft segments), could be at the origin of highly sheared flow that produced periodic vortex-shedding driving the motors unstable. This was also observed in Ariane 5 boosters [31]. The resulting mild pressure oscillations were disturbing since all these motors were predicted stable by the acoustic balance method and more annoying, they produced significant thrust oscillations, due to high pressure to thrust ratio (of the order of 10). This high value of the ratio can be straightforwardly explained from geometric and phase relationships. Moreover, the low frequencies associated with these large motors (recall that $f_{1L} \approx a/2L$) rendered such oscillations undesirable since they were able to couple to the structural modes and thus to propagate easily to the launcher structure and payloads.

The vortical origin of these oscillations can be traced to their particular frequency signatures. Indeed it was observed that instabilities followed peculiar frequency tracks, showing decreasing frequencies and sudden jumps around the pure acoustic frequency. For example, the figure below shows the time evolution of the head end pressure power spectral density for one subscale firing. The particular frequency tracks around chamber acoustic mode frequencies (solid lines) is evident. The decrease of the frequency during motor burn was viewed as an indication of the driving being the result of flow instabilities, linked to the mean flow axial velocity. Indeed in most solid propellant motors the axial velocity continuously decreases, due to increasing motor port area, as propellant burns out. The jumps were viewed as system adaptation to changing conditions: when the vortex driving frequency falls too far away from the acoustic frequency, an increase in the number of vortices occurs (see eqn. 31) to bring back the driving frequency in the acoustic range. Such behaviors could not be explained by the acoustic balance approaches and were considered as evidence of an hydrodynamic origin of the oscillations.
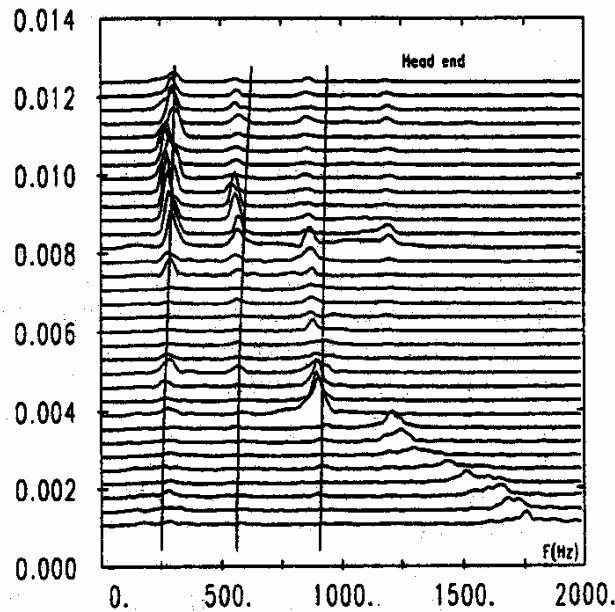
**Figure 5: Typical Frequency Tracks for Flow Driven Instabilities (LP3 E Firing).**

In Europe the development of the Ariane 5 segmented solid rocket motor promoted researches in that area, looking to unstable behaviors of segmented motors. A subscale motor was designed from a simplified, 1/15th scale, geometry of Ariane 5 P230 MPS solid rocket motor. Cylindrical propellant grains were used and a non-aluminized propellant was chosen. Since the emphasis was put on flow driven instabilities it was thought that details of the combustion should be of secondary importance. The overall P230 segmentation scheme was reproduced with a propellant loading composed of three segments: a short head end segment of limited burn time (roughly 20% of total burn time), two longer mid and aft segments. As in the full scale motor, a submerged nozzle assembly was retained. This motor was named LP3 and five configurations were fire tested [24, 32]. For each configuration, two firings were performed to check for reproducibility. The configurations differed between each other by segment arrangements, as depicted in figure 6 below.
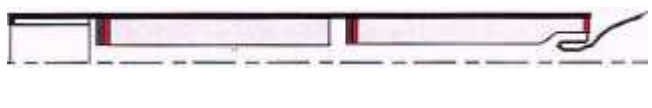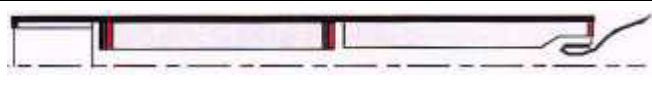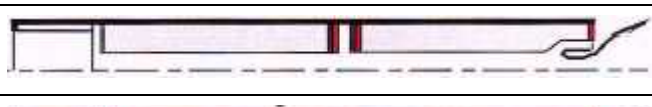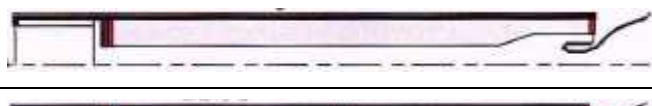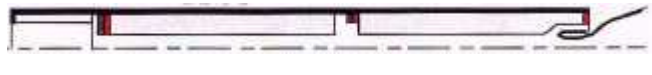
| LP3 A |  | Nominal configuration: mid and aft segments inhibited on their forward ends |
|-------|------|------|
| LP3 B |  | Inhibitor rings on both ends of the mid-segment. Aft segment free of inhibitor. |
| LP3 C |  | Mid segment inhibitor moved to segment aft end. |
| LP3 D |  | Mid and aft segment replaced by a single longer segment |
| LP3 E |  | Aft segment free of inhibitor |

**Figure 6: The LP3 Configurations.**

These configurations permitted a parametric study of the second inter-segment arrangement (termed IS2) which was suspected to be at the origin of the unstable sheared flow capable of driving motor instability.

Configurations A, D and E produced the most remarkable results, with clearly different behaviors. The figures below, taken from reference [33] illustrates these results. They show head end pressure power spectral densities (psd).
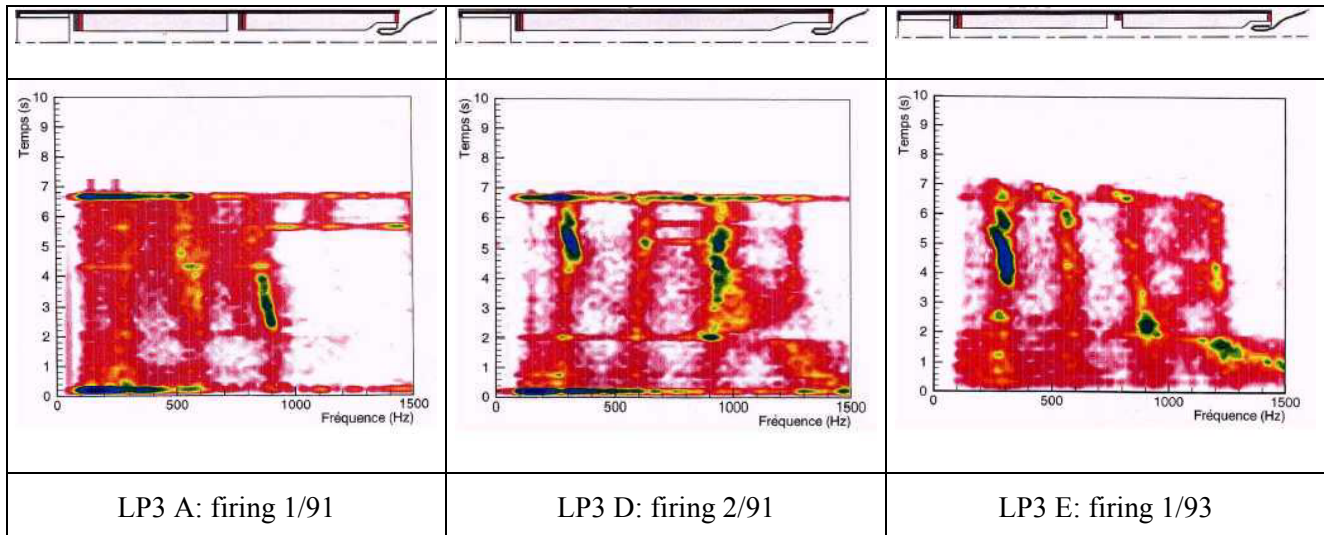


| LP3 A: firing 1/91 | LP3 D: firing 2/91 | LP3 E: firing 1/93 |

**Figure 7: Typical Results of LP3 Motors (Head-End Power Spectral Densities)**
**NB : $f_{1L} \approx 300$ Hz, $f_{2L} \approx 600$ Hz, $f_{3L} \approx 900$ Hz.**

These results show that all three configurations were unstable and that the frequency tracks were organized around the first three longitudinal modes. Decreasing frequency tracks with sudden jumps are clearly visible and indicate that the observed instabilities belong to flow driven instability regimes. References [24, 25] present the results of the acoustic balance approach that was applied to all LP3 configurations and concluded that the motors should be stable. These results were at the origin of a brand new understanding of flow instabilities. Before these results, it was accepted that in segmented motors, like those of the US Space Shuttle, US Titan launcher or the European Ariane 5 MPS, the protruding inhibitor ring at the IS2 location was the major source of vortex-shedding, due to the highly sheared flow around the obstacle created by the protrusion of the inhibitor. This situation is present in LP3 A and results show that it produces instabilities, early in the burn, at high frequencies (around the third longitudinal mode, close to 900 Hz). The other results were rather surprising, since significant amplitudes were recorded despite the motor configurations do not comprise protrusion of obstacle in the flow. This was viewed as an indication that another mechanism for flow instabilities was present. The fact that LP3 D configuration was unstable was in itself like an earthquake in our understanding. How such a simple geometry (at the time where instabilities are observed, the motor was very much a pure cylindrical grain) can produce flow instabilities ? This question motivated the throughout analysis of the Taylor's flow stability, as described in the second paper. The results of that analysis were beyond all expectations. They clearly showed that the simple Taylor's flow bore in itself the roots of instabilities [34]. This rather simple flow (velocity field expresses as mere sine and cosine laws) was found to undergo intrinsic destabilization at a moderate critical abscissa of x/R close to 3 (for axisymmetric configurations), and mostly independently of the flow Reynolds number. Moreover the frequencies of the early unstable waves were found to lie in the range of longitudinal acoustic mode frequencies. This opened the way for a radically new interpretation of unstable flow regimes, driven by intrinsic flow instability. This was supported by unprecedented full numerical simulations of motor instabilities [35]. These showed that observed instabilities in LP3 D and LP3 E configurations were of a same nature and implied a coupling of

Taylor's flow intrinsic unstable waves with longitudinal acoustic modes of the chamber. This coupling produced what was called parietal vortex-shedding: vortices are generated at the burning surface and move downstream until they interact with the submerged nozzle. Afterward, it was noted that first hints of Taylor's flow instabilities were mentioned and detailed in the synthesis article of Dunlap *et al.* [36].

## Simplified Approaches

In the quest for situations that would permit the full numerical model validation it was decided to use Flandro's approach to devise the simplest motor that could produce vortex-shedding driven instabilities. From the ingredients of Flandro's explanation to unstable motor it was retained that, in order to devise a "whistling motor", one would need to produce a mean flow with a localized inflectional profile whose unstable frequencies could match the chamber first longitudinal modes frequencies. That work, described in details in [17, 23], consisted in devising an unstable motor from first principles and is worth being related here as an example of the use of simplified methods to analyze flow driven instabilities. The starting point is a simple motor geometry used for code evaluation that comprises a prismatic grain geometry. This geometry produces an inflectional velocity profile at the exit of the cylindrical portion of the grain (here x=155 mm), as described in figure 8 below.
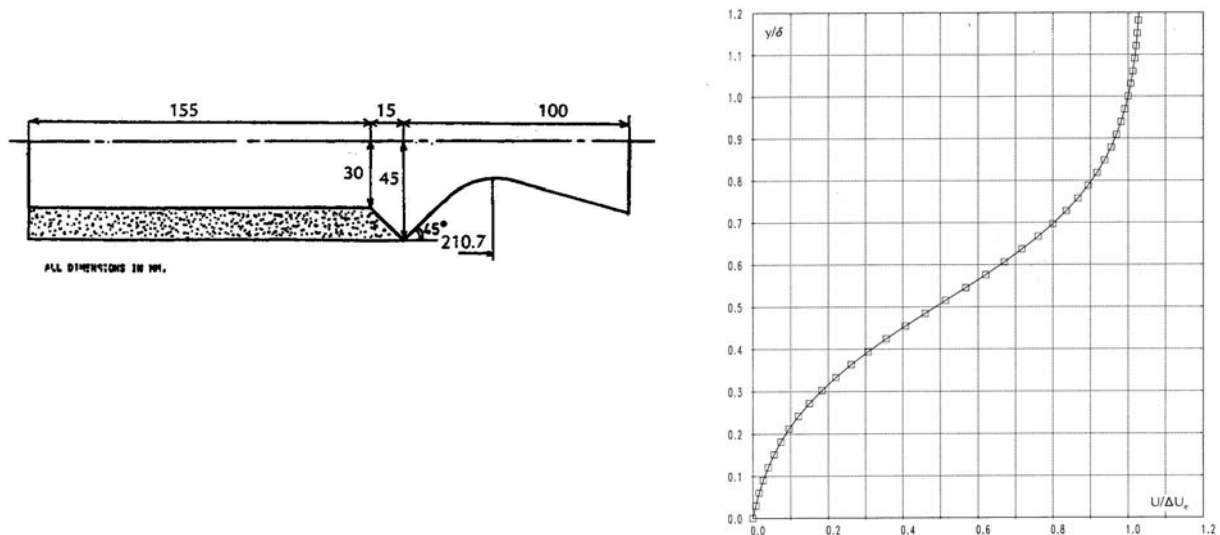


**Figure 8: Simple Motor Geometry Producing an Inflectional Velocity Profile at x=155 mm.**

Under the assumption of parallel flow, it is possible to characterize the stability properties of this profile from Orr-Sommerfeld type equations, in their spatial growth formulation. In this formulation velocities are expressed relative to $\Delta U$, the velocity difference across the shear layer and distances are expressed relative to $\delta$, the thickness of the shear layer. The time scale is thus $\delta/\Delta U$. The main result is the complex dimensionless wave number $a = a^r + ia^i$, obtained as a function of the real dimensionless frequency, expressed as a Strouhal number, $c^r = 2\pi f\delta/\Delta U$. The opposite of the imaginary part of the wave number, $-a^i$, represents the spatial growth rate and the ratio $K_v = c^r/a^r$ is the vortex phase velocity in $\Delta U$ units. These results are depicted in figure 9 below.

**Figure 9: Stability Properties of the Inflectional Profile.**

The results of the Orr-Sommerfeld solver can be viewed as universal curves, characterizing profiles of similar shapes, defined by their values for $\delta$ and $\Delta U$. For such profiles, the most unstable frequency is given by $c^r = 0.3$ with an associated vortical wave length, $\lambda_v = 2\pi\delta/a^r = K_v(2\pi\delta/c^r)$. From fig. 9 it is 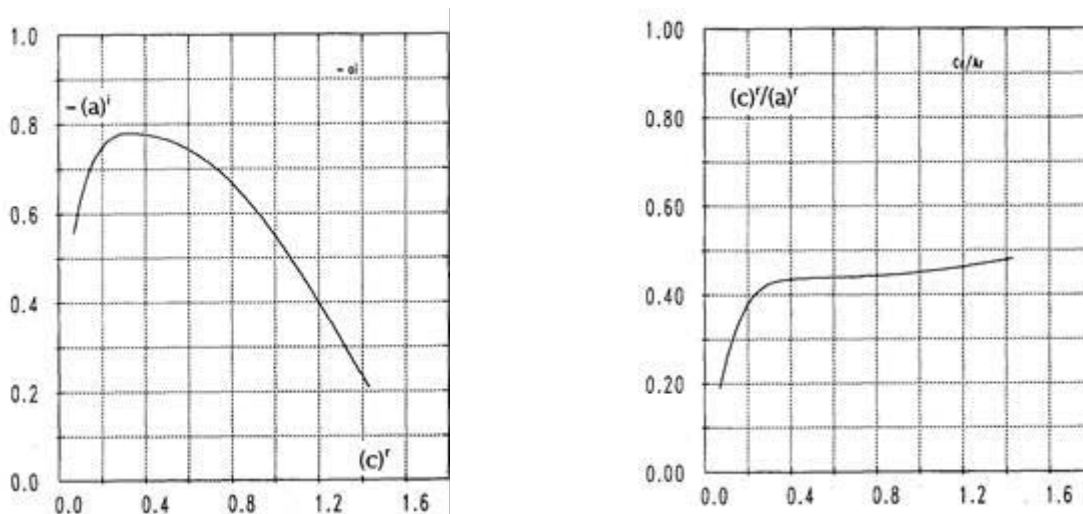useful to note that there exists an upper limit ($c^r \approx 1.6$) above which no unstable waves can be sustained. The coefficient $K_v$ is the ratio $c^r/a^r$ and is also a direct result of the velocity profile stability analysis. It represents the ratio of the vortex displacement velocity to the shear layer velocity difference $\Delta U$. This is a useful information if phase relationship have to be compared, as in the Rossiter's approach (coefficient k).

In order to devise a whistling motor, one has to verify that:

   a) the most unstable frequency of the vortical waves matches the chamber longitudinal acoustic mode frequency,

   b) the stand-off distance separating the vortex emission point to the interaction point, assumed to be localized at the nozzle entrance, is sufficient to contain an integer number of vortices of wave length $\lambda_v$.

These two conditions are necessary conditions to produce vortex driven instabilities. Experience show that they are also, in most cases, sufficient conditions.

It is then a simple matter to adjust the motor chamber length (which governs the frequency of the $q^{th}$ longitudinal mode, $f_q = q\, a_0/2L$), by increasing the distance between the downstream end of the propellant grain and the nozzle, to verify the two conditions stated above. Considering an actual motor, propellant combustion implies a continuous increase of the internal grain port diameter, D, and consequently a continuous decrease of the mean flow axial velocity, U, at the grain downstream end (from simple mass balance). Assuming that $\delta$ and $\Delta U$ are known functions of D and U: $\delta = K_\delta D$ and $\Delta U = K_U U$, one can follow the evolution of the vortical wave properties during motor burn. This will permit final adjustments. This exercise was performed on a laboratory scale motor configuration and resulted in the C1xb motor depicted in figure 10 below. The stand-off distance from propellant end to the nozzle entrance plane was adjusted to provide frequency match during most of the motor burn time. In the frequency versus propellant web distance burned plot, we followed the time evolution of the frequencies corresponding to $c^r = 0.3$ (most amplified frequency) and $c^r = 1.6$ (upper frequency limit of the unstable velocity profile) in the grid formed with the chamber acoustic mode frequencies (horizontal lines). It clearly appears that

the range of possibly excited modes rapidly narrows to the first acoustic mode, in the second half of the firing.
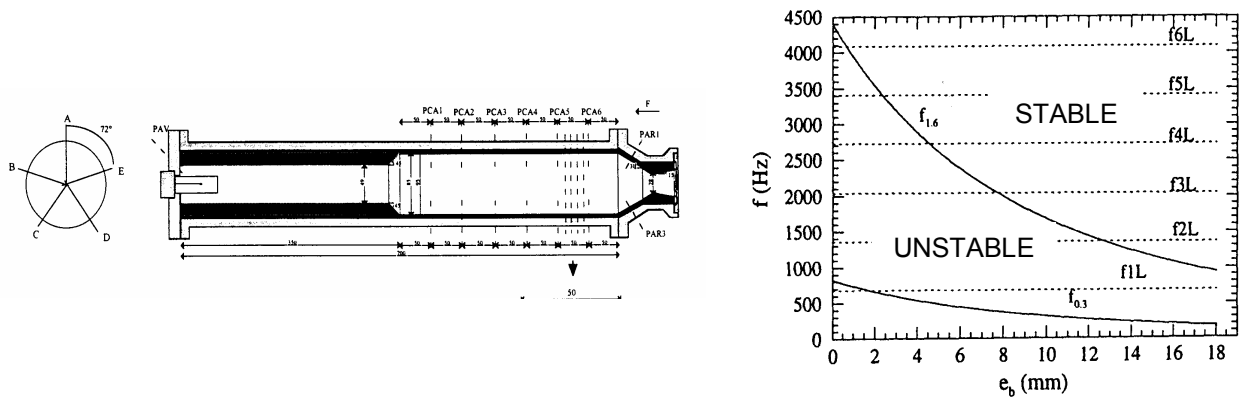


**Figure 10: C1xb Motor Design from the Simple Frequency Match.**

Although the acoustic frequencies never match the most amplified frequency, it was anticipated that the motor would be unstable. Indeed, a coupling path is available since the acoustic frequency of the first mode lies in the range of the shear layer unstable frequencies. In that vision, the shear layer is a mere broad band amplifier and will naturally tune to available frequencies. This actually worked. The C1xb motor was constructed and fired several time at ONERA, in the framework of J. Dupays's thesis [37, 38]. Good reproducibility was observed and the motor was used in the validation work of the full numerical approaches (see below). Figure 11 illustrates the results of one C1xb firing. It clearly shows that, after a first phase where higher frequencies are present a second phase occurs with a clear flow driven motor destabilization on the first mode frequency, around 700 Hz.
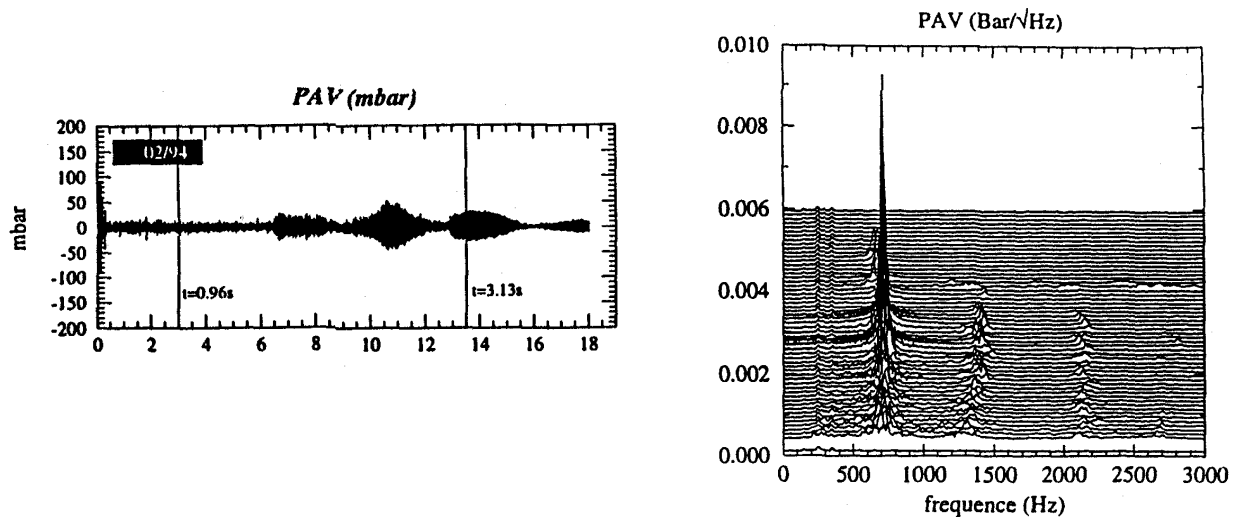


**Figure 11: Example of One C1xb Firing Test. Head end unsteady pressure time history and psd.**

The same simplified approach can be carried out from the stability properties of the Taylor's flow (detailed in the second part of this paper). The starting point is again the frequency range of early vortical waves. Again, the velocity and length scales are directly obtained from the stability analysis: $V_{inj}$ is the injection velocity, and h, the height (or radius) of the chamber. The knowledge of the frequencies of possible unstable waves, in $V_{inj}/h$ units, permits to identify configurations whose acoustic frequencies of

interest can be matched. This provides the necessary ingredients for positive coupling and permits to identify configurations that would be prone to acoustic resonances. Again this exercise was done for the 2D planar VECLA cold gas set-up and produced remarkable results [39-42]. Figure 12 below represents the results of the hydrodynamic stability analysis in the form of the wave growth factor as a function of dimensionless frequency and the dimensionless distance from the head-end.



**Figure 12: Results of the Stability Analysis of the Taylor's Flow. Spatial amplification factor as a function of dimensionless frequency and distance from the head-end.**

However, simple frequency match considerations are not always sufficient to describe conditions for acoustic resonances, in particular for the type of instability like Taylor's flow instability. Other parameters 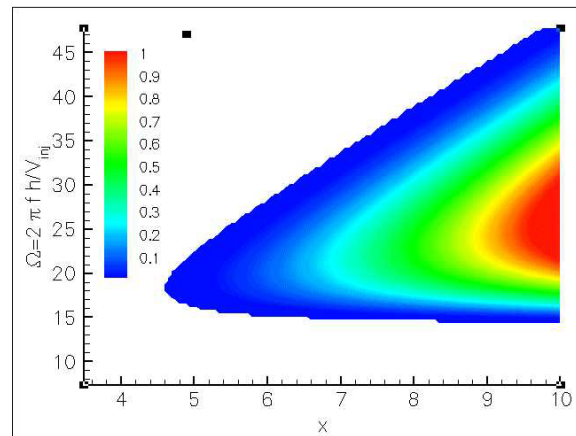must be included, such as vortical wave growth distance, non-linear saturation, amplitudes, non parallel nature of the flow (its stability properties depend on x) and phases and amplitudes at interaction points. Two critical interaction points have been identified: motor exit or nozzle entrance point where the vortices exchange energy with the acoustic waves and "receptivity" point where the acoustic waves feed back to the vortical waves. At the present time these issues are not yet fully settled, although some clear trends have been pointed out in B. Ugurtas and J. Griffond theses [43, 44].

Simple approaches are interesting because they permit to summarize the accumulated knowledge in simple relationships that help understanding the mechanisms that govern such delicate couplings. However they cannot provide quantitative results and full numerical approaches are then needed. It must be noted that although very powerful, the full numerical approaches would only give global results (much like an experiment) that will require, in turn, some form of analysis to build some knowledge.

## Full Numerical Approaches

The full numerical approaches provide an unprecedented mean to analyze the details of the flow field during flow driven motor instabilities. In particular, the ability to see the internal details of the flow field has proven to be useful in classifying the flow regimes that led to motor instabilities. We already mentioned the role of the numerical simulations in pinpointing the Taylor's flow instability origin of the instabilities in the LP3 D/E motor. The results of the full numerical approach permitted to identify three types of flows that led to motor instabilities.

• Obstacle vortex-shedding (termed VSO from the French acronym "vortex-shedding d'obstacle") where the shear layer responsible for the shedding of vortices is created by a protruding obstacle (such as an inhibitor ring). This corresponds to the first idea from the US experience on the Space Shuttle SRB and early Titan IIIC/D then 34D motors, but also to the nominal version of the LP3 subscale motor, LP3 A. This situation is illustrated below.

- Corner vortex-shedding (termed VSA from the French acronym "vortex-shedding d'angle") corresponding to simplest case where shedding was produced by an obstacleless shear layer (jetting effect) corresponding to the C1xb situation, illustrated below.
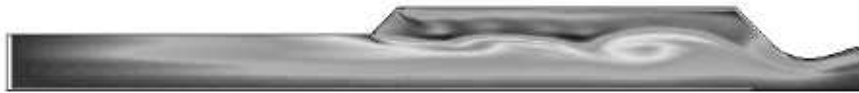


- Surface or parietal vortex-shedding (VSP from the French acronym "vortex-shedding pariétal") where the shedding results from an intrinsic instability of the internal flow, corresponding to versions D and E of the LP3 motor, without aft segment inhibitor rings, the cold flow set-up Vecla but also to the recent TITAN IV/SRMU motor. The figure below illustrates this situation.
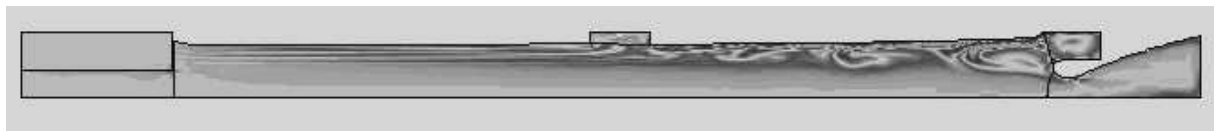


The benefits of the full approaches are not limited to this useful insight nor to the capability to treat both acoustic and vortical waves in the single framework of the compressible full (non-linear) Navier-Stokes equations. Although important these are not sufficient to open the way to useable stability previsions in real motors. We have seen that most of the time, mild pressure oscillations are present in motors predicted stable from acoustic balance method. The important information are then the frequency and the amplitude of these pressure oscillations, as well as their efficiency in translating to thrust oscillations. The full approaches must then have the capability in providing such information. This implies that some of the phenomenons identified in fig. 1 that are missing in the approach have to be taken care of. Since phenomenons numbered 2, 3 and 5 (nozzle flow, vorticity waves and vortex-shedding) are already included in the full Navier-Stokes approach, models must be devised for including the phenomenons numbered 1, 4 and 6 on fig. 1 (propellant combustion, two-phase flow and turbulence). To these internal phenomenons, the possible coupling with the motor case or elements of structure must be added. Under these conditions, the full numerical approaches will become a useful tool for an oscillation free motor design (quiet motor).

Research work is heading in that direction and the present state of the art is coming close to that requirement. This will be illustrated by three examples in the next section. Most of these examples have been obtained in the validation stage. Indeed, as already mentioned, the validation of the numerical tools is of first importance and represent the price to pay for a reliable prevision of motor stability and/or control. References [45-50] are examples worth mentioning to complement other cited references.

## Examples

### Example 1: The C1xb and VSA

From the beginning, the C1xb motor was designed as to be a first stage of validation at the laboratory scale. As described in J. Dupays' thesis the emphasis was put on the two-phase flow effects, combined with vortex-shedding driven oscillations. Following first demonstration of effective motor destabilization, as presented here above, the motor was fired with propellants having different inert particle loadings. Although this work produced unprecedented results, in particular on the influence of the inert particles on

oscillatory levels (to the contrary of the ideas inherited from the acoustic balance approach described earlier, amplitudes were not always decreased by the presence of condensed phase) it was limited by the difficulties in characterizing the propellant combustion response. A quantitative comparison in term of frequency and amplitude was nevertheless conducted few years later, once propellant characterization became available. This is described in [51] and the main results are presented below. The propellant response function is treated as an unsteady boundary condition that is derived from the linear relationship defining the pressure coupled response function $R_{MP}(\omega) = \dfrac{\dot{m}'(\omega)/\overline{\dot{m}}}{p'(\omega)/\overline{p}}$. Here $\dot{m}$ is the injected mass flow rate, prime denotes unsteady components and overbar mean values. Then the resulting unsteady injected mass flow rate is expressed as a convolution integral:

$$\dot{m}(t) = \overline{\dot{m}} + \frac{\overline{\dot{m}}}{\overline{p}} \int_0^{t-t_0} R(\tau)(p(t-\tau) - \overline{p})d\tau$$

with $R(\tau)$ being the impulse response associated to the frequency response $R_{MP}(\omega)$:

$$R(t) = TF^{-1}\left[R_{MP}(\omega)\right]$$

This simple boundary condition proved to be quite effective and produced quasi-perfect agreement between the experimental measurements and the computations. Due to uncertainties in the propellant characterization two response curves were considered. Although these curves largely differed, the results were found to be significantly improved with both response functions. The figure below presents the unsteady flow field in the C1xb motor at the 10.7 mm web distance burned which was chosen for the comparison, and the following table summarizes the quantitative results, in terms of pressure amplitudes and frequency.
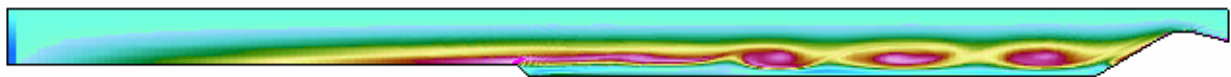


**Figure 13: C1xb Flow Field at 10.7 mm of Web Distance Burned.**

| | No response | Response #1 (mne) | Response #2 (glk) | **Experiment** |
|---|---|---|---|---|
| Head-end amplitude (hPa) (relative error) | 12.7 (71%) | 28.5 (35%) | 43.1 (2%) | **43.9** |
| Aft-end amplitude($P_{C6}$) (hPa) (relative error) | 15.5 (39%) | 20.6 (20%) | 26.6 (4%) | **25.6** |
| Frequency (Hz) (relative error) | 740 (3.8%) | 720 (1.0%) | 715 (0.3%) | **713** |
| Frequency resolution (Hz) | 23 | 23 | 23 | **10** |

The "no response" results were found to be improved for both response functions. In particular, the ratio of head-end to aft-end pressure amplitudes together with the oscillation frequency were found to better match the experimental measurements. Best results were obtained with the second response curve with an almost perfect agreement. It must be stressed that it was the first time that full approach results could be

compared to actual firing test measurements. The rather satisfactory agreement was seen as an evidence that the full approach was sound and could provide quantitative stability data, such as frequency and amplitude of limit cycle oscillations in actual motors.

**Example 2: The VECLA Set-Up and the VSP**

The VECLA cold flow set-up of ONERA was extensively used to understand the VSP mechanism and to validate the full numerical approach. The VECLA set-up is a modular air fed set-up. It is 2D planar and the length to height ratio can be varied through variation of chamber height (the length of the porous wall is fixed at 581 mm but the height can be varied from 30 to 10 mm). It can be tested with or without a choked nozzle. In the configuration without nozzle, the injection velocity can be easily varied by changing the air mass flow rate. This provided a very convenient mean to control the flow field inside the VECLA set-up.

At least three different behaviors were documented:

   a)  For large length to height ratio (h=10mm) transition to turbulence was observed inside the chamber.

   b)  For moderate length to height ratio (h=20mm) acoustic resonance could be produced for a definite range of injection velocity.

   c)  For small length to height ratio (h=30mm) no acoustic resonance nor turbulent transition are observed. However, the flow exhibits local instabilities that can be compared to the stability analysis.

All three regimes were used to validate the full numerical approach.

Case a) served to validate turbulence models [52] and will not be detailed here.

Case c) provided unprecedented check of the linear stability results, as described in the second paper. Unstable wave frequency range and spatial growth rate were found to match the stability results. These results were also used to check the full Navier-Stokes approach, as described in B. Ugurtas' thesis [43]. The claim was that the full Navier-Stokes solution contains the early hydrodynamically unstable waves. This was verified in case c). Simulations were performed and the unsteady field was extracted from the full Navier-Stokes solutions by Fourier transforms at given frequencies. The shape and growth rate of the unstable waves were compared to the linear stability results and showed good agreement, as illustrated by the figures 14 and 15 below.
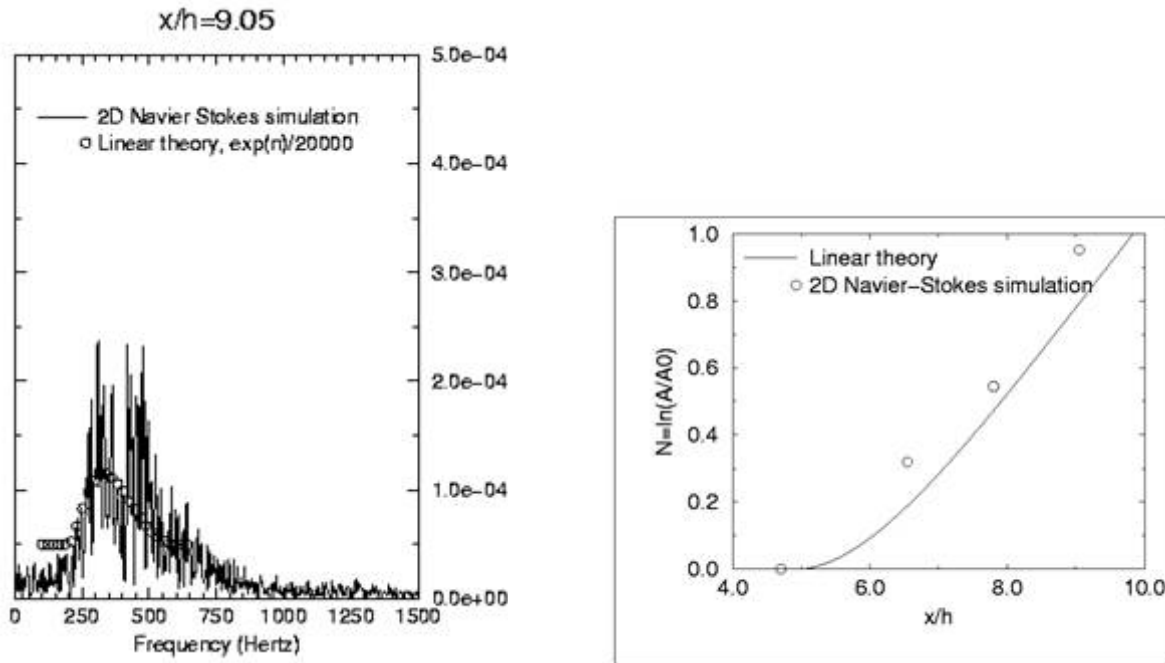
**Figure 14: Comparison of the Navier-Stokes Results with the Linear Stability Analysis. Velocity spectrum and spatial amplification factor.**
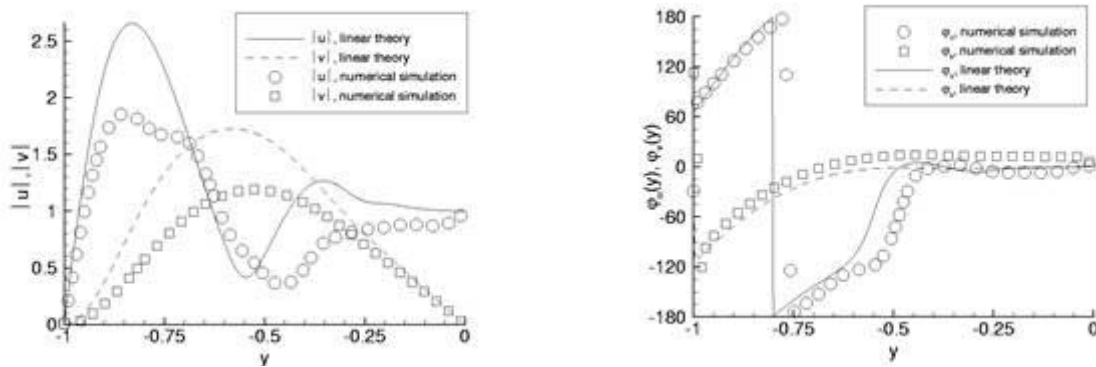


**Figure 15: Comparison of the Navier-Stokes Results with the Linear Stability Analysis. Amplitude and phase of the velocity radial profile.**

This established the ability of the Navier-Stokes solver to properly describe the early destabilization processes of the Taylor's flow.

Case b) was also used to check the ability of the full Navier-Stokes approach to reproduce acoustic resonance regimes. For this case, the ratio $V_{inj}/h$ could be adjusted so as the unstable stability wave frequencies match the chamber longitudinal mode frequencies. Clear cases of acoustic resonance could be observed in a definite injection velocity range. By imposing a time variation of the injection velocity in the Navier-Stokes simulations resonances could be simulated in good agreement with the experimental results. This is illustrated by figure 16 below.

**Figure 16: Comparison of the Navier-Stokes Results (right) with the Experimental Results (left). Velocity psd as a function of the injection velocity.**

Satisfactory qualitative agreement is observed, establishing the ability of the full approach to reproduce resonant regimes in VSP situations. However, the oscillatory amplitudes were found to be over-estimated. Reference [53] presents an effort to bridge the amplitude gap. In that work, the negative response function of the porous wall was included in the simulation (on the contrary to burning pro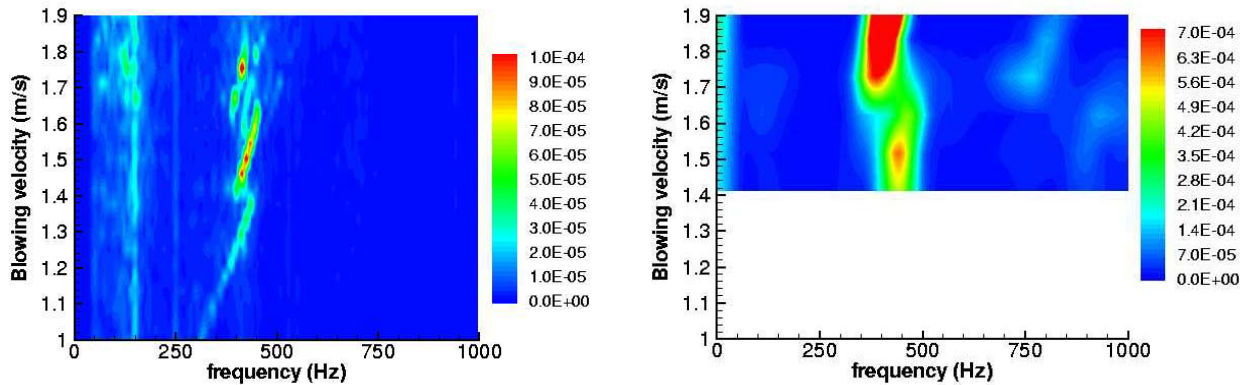pellant, the porous wall has a negative response to pressure waves, resulting in significant damping of the excited acoustic waves). In an attempt to better stick to the experiment, the flow destabilization in the numerical solution relied on a white noise, introduced at the porous surface vicinity, whose characteristic was matched with the measured injection noise. This produced a marked decrease of the simulated oscillatory amplitude being now comparable to actually measured amplitudes, as displayed in figure 17.
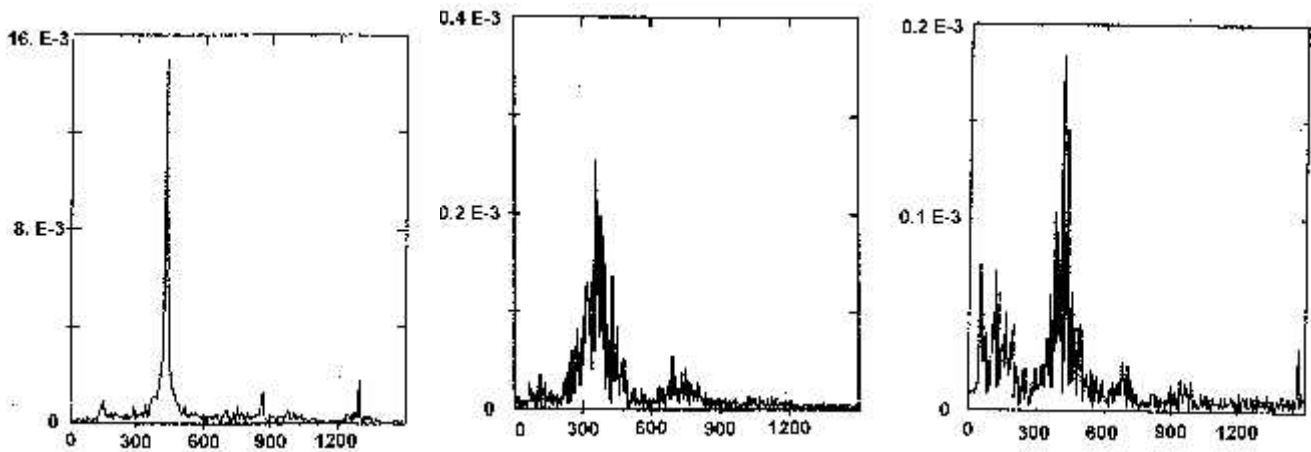


**Figure 17: Head-End Pressure Spectra. From left to right: a) Initial Navier-Stokes solution; b) Navier-Stokes with porous wall response and white noise model; c) Experiment.**

The exemplary simplicity of the VECLA set-up permitted to go one step further in establishing the validity of the full numerical approach and to actually see the so-called parietal vortices. Following Prof. Culick's suggestion, the injected flow was seeded with acetone and laser induced fluorescence permitted to actually see the vortices in the VECLA set-up [54]. It must be stressed that this constituted a world premiere that confirmed that the computed vortices were indeed present in the experimental set-up. Figure 18 below illustrates this result.
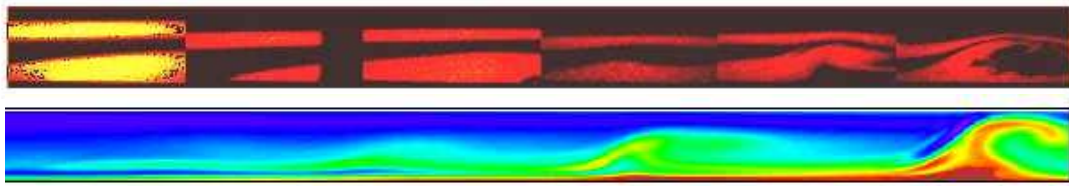
**Figure 18: PLIF Images of Vortices in VECLA Set-Up (top)
Compared to the Computed Vorticity Field (bottom).**

## Example 3: An Actual Motor (VSP + VSO)

Application to an actual full scale motor was rendered possible by the validation effort depicted in the preceding examples and completed by a two-phase flow model that was also validated [37-38, 55]. Considering that the actual Ariane 5 motor used an aluminized propellant, the two-phase flow solver was completed by a very basic aluminum combustion model. This model was based on the $d^2$ model that links the aluminum droplet burn time to the square of its diameter. Realistic value for the reaction heat was used. The inter-phase source terms in the balance equations were thus modified to include the mass and energy exchanges due to droplet combustion. This is detailed in reference [56].

Then the early K4 configuration of the Ariane 5 P230 was simulated, with or without the reactive two-phase model. The chosen time point was that of maximum of observed oscillatory amplitude. The retained experimental configuration was that of the M1 firing test at 95 s into the burn.

This work showed that simulations without aluminum combustion were not satisfactory since they could not reproduce the oscillation frequency and amplitude. Detailed analysis of the numerical results showed two competing mechanisms: the VSO vortices from the protruding inhibitor, at a higher frequency, close to the third acoustic mode frequency and the VSP vortices that developed along the aft segment, at the lower first mode frequency. This competition resulted in the absence of acoustic resonance. On the other hand, when aluminum combustion was introduced, the VSP was reinforced to the point that it became dominant and forced the VSO to tune to the first acoustic mode frequency. This resulted in marked resonance in better agreement with the experimental results. This is illustrated by the following figure.
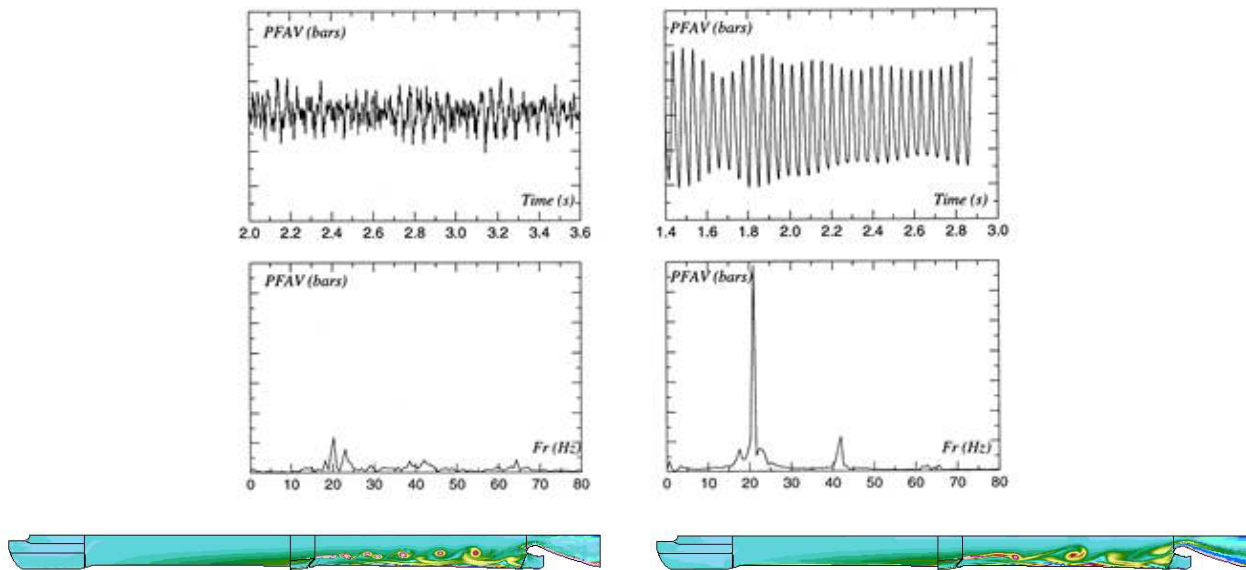


**Figure 19: M1 Results for the Single Phase (left) and Reactive Two-Phase (right) Models.
Head-end pressure time history and spectrum, vorticity field.**

The computed frequency was then close to the first acoustic mode frequency and the oscillatory amplitudes were comparable to the measured amplitudes. Of course, this result depends on the model inputs, particularly the size of the aluminum droplets and of the alumina residues, as well as on model details or inhibitor ring properties (deformation, vibrations, ...) which may have some incidences on the computed flow field. Such data are still not perfectly known and some characterization and modeling works are still needed before a satisfactory prediction can be guaranteed in such complex full scale motor configurations.

**Example 4: Active Control Demonstration**

To complete this example section, it is interesting to illustrate the capability of the full numerical approach to validate closed loop active control concepts. The idea was to use the full Navier-Stokes solution to evaluate control strategies and to demonstrate the feasibility to control flow driven instabilities. It was then decided to use the simulated flow field in the simplest VSA configuration. The test case C1 was used. This test case is the first configuration designed with the simplified approach, as described above for the C1xb motor. On the contrary to the C1xb motor, it is a purely numerical test case [23] that has been used at the beginning of the Navier-Stokes codes validation effort. It is fully documented and has been computed many times by many codes.

Roughly speaking, the active control loop is composed of:

- A transducer that records the state of the internal flow,

- An actuator that is capable of acting on the flow field,

- A controller that processes the transducer signal into a signal that is fed to the actuator.

This is completed by an identification step that defines the actual transfer function between the actuator and the transducer.

During operation, the controller adjusts its own transfer function to minimize the output signal of the transducer.

The work presented here is the result of a cooperation between the EM2C lab at ECP and ONERA. It is described in details in M. Mettenleiter's thesis and in reference [57, 58].

Transducer was normally taken as computed pressure at the nozzle entrance section but a numerical vorticity transducer was also tested. Actuator was modelized by distributed mass sources, representing an injection of a reactive fluid. Actuator was placed at the chamber head-end (case 1) but some tests were also performed with an actuator placed in the vicinity of the unstable shear layer (case 2). Figure 20 below presents the control scheme for C1 test case. Two main control strategies were tested. They belonged to anti-noise control and to noise source control. In the latter strategy the aim is to actively control the source at the origin of the acoustic resonance rather than controlling the resulting acoustic wave.
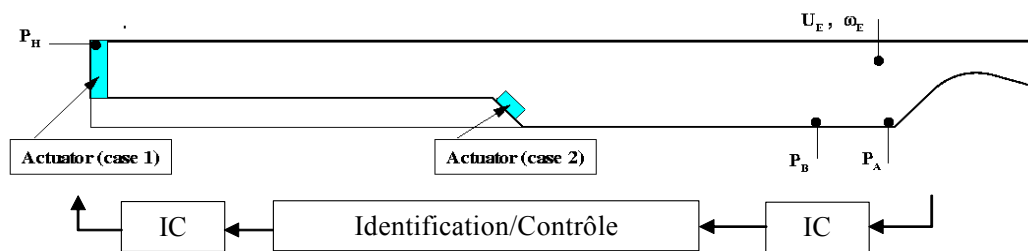


**Figure 20: Control Schemes for the C1 Test Case.**

The control algorithm was introduced as Fortran subroutines into the Navier-Stokes solver. Special attention was given to the calling sequence between the Navier-Stokes solver iterative time integration and the controller own process. Adapted filtering steps were added to the coupling procedure, in order to take care of the very different time scales between to two programs. Indeed, the time step of the explicit Navier-Stokes solver is of the order of $10^{-7}$ s, while the time scale of the controller is of the order of $10^{-4}$ s. Under such conditions, very significant reductions of the oscillatory amplitude could be demonstrated. One of the difficulty was that the acoustic resonance could occur in a large frequency range. This is illustrated on figure 10 that shows that at given web distance burned, several acoustic modes lie in the unstable range. The direct consequence was that once the motor was controlled on its initial resonant frequency, it shifted to another resonance at a higher frequency, corresponding to the next acoustic mode. Then the controller had to adjust itself to the new condition. This illustrated the benefit of an adaptive active control loop, as the one proposed by EM2C/ECP, for the flow driven instability under consideration.

Control was achieved in the standard configuration (nozzle end pressure transducer + head-end actuator) that could correspond to an actual motor configuration. However, the numerical approach permitted to test other configurations, not yet fully adaptable to an actual motor, such as the vorticity transducer combined with an actuator located in the vicinity of the unstable shear layer (case 2). Not surprisingly, this latter configuration exhibited better performance in term of time to control and residual amplitudes. Figure 21 below illustrates this performance.
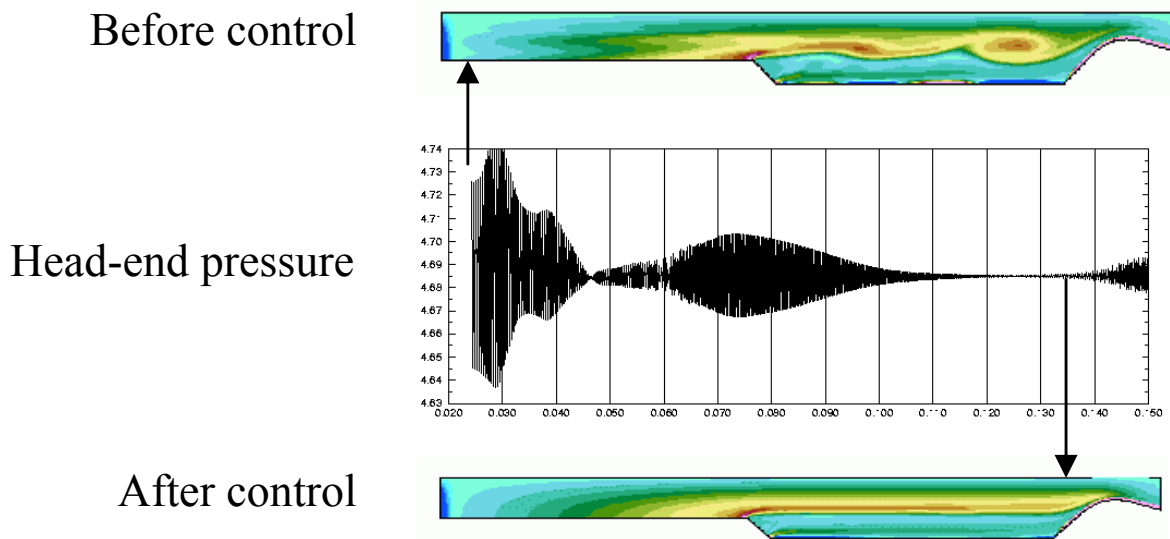


**Figure 21: Demonstration of Adaptive Active Control in C1 Test Case (Case 2).**

## CONCLUSIONS/UNSETTLED ISSUES

The intensive research effort conducted in the past 12 years in the framework of the European Ariane 5 launcher related programs has produced a new vision for motor instability. It is now clear that instabilities must be approached in a global fashion that puts the internal flow field and related phenomenons, such as gaseous and condensed phase combustion, vorticity (in the form of acoustically forced vorticity waves, developed vortices or early flow instability waves) and structural response, in the center of the investigation. The early acoustic balance approaches, although extremely profitable in term of understanding and isolating physical phenomenons, could not produce the expected answers for motor sustaining mild amplitude limit cycle pressure oscillations.

It has been shown that under the condition that the necessary validation and characterization efforts were conducted, the numerical solution to the full unsteady compressible Navier-Stokes equations, together with ad hoc models for coupled mechanisms, could produce valuable results in close agreement with experimental measurements.

Of course obtaining meaningful numerical solutions, in particular in such a challenging and delicate context remains a difficult task. The grid issue is undoubtedly one of the most crucial issue. In order to stay within acceptable limits in terms of computer CPU time and memory occupation, the grid must be tailored to each case. Our ability to produce adequate grids in then a direct function of our knowledge of what the important flow features are and where they are located. This clearly limits the use of the full numerical approach to documented situations and a priori predictions cannot be guaranteed in any situation. However, once the applicability has been established for a given type of configurations, the numerical approach can be used with large benefits to analyse and optimise the configuration.

Another limitation is the choice of the proper models to describe non flow related mechanisms such as combustion, structural response, ... These models bear their own limitations that are of two types: the physics that is included in the models and the necessary inputs to the models. Both limitations can impair the successful application of the model into the numerical solution. Aluminum combustion is presently one area where progresses are expected for both types of limitations. This implies dedicated experiments and analyses to better describe the complex mechanisms that govern the formation of aluminum droplets, their combustion and finally the production of alumina droplets in complex flow fields. In particular the question of droplet interactions in a large population of various sizes and compositions, remains open.

Finally, several years of experience with full numerical solutions, where most often several models are coupled in a non-linear fashion, have put to light many unexpected or surprising results. It is always surprising to realize that the resulting behavior is not the mere addition of individual effects or that a linearly damping mechanism can increase the limit cycle amplitude. This departure from the common linear thinking poses some problems when results are to be analyzed, understood and finally validated or accepted. This difficulty, far from being a mere curiosity, renders the progressive validation approach mandatory, in order to know how confident one can be when confronted to unexpected results. Often, the simplified approaches can be called in to help analyzing the results.

Most often success lies in a proper combination of both approaches. It is then recommended that the rocket engineer who has to deal with instabilities exercise in both approaches.

## ACKNOWLEDGEMENT

## REFERENCES

[1]    Kuentzmann P., "Combustion Instabilities," AGARD LS-180, September 1991.

[2]    Culick F.E.C. and Yang V., "Prediction of the Stability of Unsteady Motions in Solid Propellant Rocket Motors," Nonsteady Burning and Combustion Instability of Solid Propellants, Vol. 143, Progress in Astronautics and Aeronautics, Edited by L. De Luca, E.W. Price, and M. Summerfield, AIAA, New York, 1992, pp. 719-779.

[3] Hart R.W. and McClure F.T., "Theory of Acoustic Instability in Solid Propellant Rocket Combustion", 10th Symposium (international) on Combustion, pp. 1047-1065, 1965, The Combustion Institute, 1965, Pittsburgh PA.

[4] Culick F.E.C., "Acoustic Oscillations in Solid Propellant Rocket Chambers", Astronautica Acta, Vol. 12, No. 2, 1966, pp. 113-125.

[5] Culick F.E.C., "The Stability of One Dimensional Motions in a Rocket Motor", Combustion Science and Technology, 1973, Vol. 7, pp. 165-175.

[6] Culick F.E.C., "The Stability of Three Dimensional Motions in a Combustion Chamber", Combustion Science and Technology, 1975, Vol. 10, pp. 109-124.

[7] Vuillot F., "Acoustic Mode Determination in Solid Rocket Motor Stability Analysis", J. of Propulsion and Power, Vol. 3, No. 4, July-August 1987.

[8] Flandro G.A., "Solid Propellant Acoustic Admittance Corrections," Journal of Sound and Vibration, Vol. 36, No. 3, 1974, pp. 297-312.

[9] Vuillot F. and Avalon G., "Acoustic Boundary Layers in Solid Propellant Rocket Motors Using Navier-Stokes Equations", J. Propulsion and Power, Vol. 7, No. 2, March-April 1991, pp. 231-239.

[10] Flandro G.A., "Effects of Vorticity on Rocket Combustion Stability", J. of Propulsion and Power, Vol. 11, No. 4, July-August 1995, pp. 607-625.

[11] Vuillot F., "Numerical Computation of Acoustic Boundary Layers in Large Solid Propellant Space Booster", AIAA 91-0206, AIAA 29th Aerospace Sciences Meeting, Reno, Nevada, USA, January 1991.

[12] Vuillot F. and Kuentzmann P., "Flow Turning and Admittance Corrections: An Experimental Comparison", J. of Propulsion and Power, Vol. 2, No. 4, July-August 1986, pp. 345-353.

[13] Van Moorhem W., "Flow Turning in Solid Propellant Rocket Combustion Stability Analyses", AIAA Journal, Vol. 20, No. 10, pp. 1420-1425, October 1982.

[14] Majdalani J. and Van Moorhem W.K., "Laminar Cold-Flow Model for the Internal Gas Dynamics of a Slab Rocket Motor", Aerosp. Sci. Technol. 5 (2001) 193-207.

[15] Temkin S. and Dobbins R.A., "Attenuation and Dispersion of Sound by Particulate-Relaxation Processes", J. of Acoustical Society of America, Vol. 40, No. 2, 1966.

[16] Flandro G.A. and Jacobs H.R., "Vortex Generated Sound in Cavities", AIAA Paper 73 1014, Seattle, Washington, USA, October 1973.

[17] Vuillot F., "Vortex-Shedding Phenomena in Solid Rocket Motors", Journal of Propulsion and Power, Vol. 11, No. 4, pp. 626-639, July-August 1995.

[18] Dunlap R. and Brown R.S., "Exploratory Experiments on Acoustic Oscillations Driven by Periodic Vortex Shedding", AIAA J., Vol. 19, No. 3, 1981.

[19] Brown R.S., Dunlap R., Young S.W. and Waugh R.C., "Vortex Shedding as a Source of Acoustic Energy in Segmented Solid Rockets", J. of Spacecraft and Rocket, Vol. 18, No. 4, pp. 312-319, July-August 1981.

[20] Dotson K.W., Koshigoe S. and Pace K.K., "Vortex Shedding in a Large Solid Rocket Motor Without Inhibitors at the Segment Interfaces", J. of Propulsion and Power, Vol. 13, No. 2, March-April 1997, pp. 197-206.

[21] Flatau A. and Van Moorhem W., "Prediction of Vortex Shedding Responses in Segmented Solid Rocket Motors", AIAA-90-2073, AIAA 26th Joint Propulsion Conference, July 1990, Orlando, USA.

[22] Flandro G.A., "Vortex Driving Mechanism in Oscillatory Rocket Flows", Journal of Propulsion and Power, Vol. 2, No. 3, pp. 206-214, May-June 1986.

[23] Lupoglazoff N. and Vuillot F., "Numerical Simulation of Vortex Shedding Phenomenon in 2D Test Case Solid Rocket Motors," AIAA 92-0776, AIAA 30th Aerospace Sciences Meeting, Reno, Nevada, USA, January 1992.

[24] Vuillot F., Traineau J.C., Prevost M. and Lupoglazoff N., "Experimental Validation of Stability Assessment Methods for Segmented Solid Propellant Motors", AIAA 93-1883, AIAA 29th Joint Propulsion Conference, June 1993, Monterey, CA.

[25] Vuillot F., "Prise en compte du détachement tourbillonnaire dans les approches linéarisées par la méthode de Flandro", Colloque CNES-ONERA "Fonctionnement des Moteurs à Propergol Solide Segmentés pour Lanceurs Spatiaux", 8-9 decembre 1992, Châtillon, FRANCE.

[26] Brown R.S., Blackner A.M., Willoughby P. and Dunlap R., "Coupling Between Velocity Oscillations and Solid Propellant Combustion," AIAA Paper 86 0531 AIAA 24th Aerospace Sciences Meeting, January 1986, Reno, Nevada.

[27] Mason D.R., Folkman S.L. and Behring M.A., "Thrust Oscillations of the Space Shuttle Solid Rocket Booster Motor During Static Tests", AIAA Paper 79 1138, AIAA 15th Joint Propulsion Conference, Las Vegas, June 18-20, 1979.

[28] Mathes H.B., "Assessment of Chamber Pressure Oscillations in the Shuttle Solid Rocket Booster Motors", AIAA paper 80 1091, AIAA 16th Joint Propulsion Conference, Hartford CT, June 1980.

[29] Alden R.J., "Improved Performance 3.05 m (120 in.) Boosters for the Air Force Titan 34D Space Launch Vehicle," The 1983 JANNAF Propulsion Meeting, Vol. 1, pp. 15-27; 83N 35012.

[30] Blomshield F. and Mathes H.B., "Pressure Oscillations in Post Challenger Space Shuttle Redesigned Solid Rocket Motors", J. of Propulsion and Power, Vol. 9, No. 2, March-April 1993, pp. 217-221.

[31] Scippa S., Pascal Ph. and Zanier F., "Ariane 5 MPS Chamber Pressure Oscillations Full Scale Firings Results Analysis and Further Studies", AIAA paper 94-3068, 30th AIAA Joint Propulsion conference, June 27-29, 1994, Indianapolis, IN, USA.

[32] Prevost M., Vuillot F. and Traineau J.C., "Vortex-Shedding Driven Oscillations in Subscale Motors for the Ariane 5 MPS Solid Rocket Motors", AIAA96-3247, 32nd AIAA Joint Propulsion Conference, Orlando, USA, July 1-3, 1996.

[33] Prevost M., Dommee Y. and Maunoury J., "Programme POP, synthèse de la base de données expérimentales instationnaires (révision 5)", ONERA RT 4/05212 DMAE, juin 2001.

[34] Vuillot F., Casalis G., Avalon G. and Lupoglazoff N., "Mise en résonance acoustique d'une cavité par l'instabilité naturelle d'un écoulement généré par injection pariétale", CR Acad. Sci. Paris, t. 327, Série II b, p. 77-83, 1999.

[35] Lupoglazoff N. and Vuillot F., "Parietal Vortex Shedding as a Cause of Instability for Long Solid Propellant Motors. Numerical Simulations and Comparisons with Firing Tests", AIAA 96 0761, AIAA 34th Aerospace Sciences Meeting, Reno, Nevada, USA, January 1996.

[36] Dunlap R., Blackner A.M., Waugh R.C., Brown R.S. and Willoughby P., "Internal Flow Field Studies in a Simulated Cylindrical Port Rocket Chamber," J. of Propulsion and Power, Vol. 6, No. 6, November-December 1990, pp. 690-704.

[37] Dupays J., "Contribution à l'étude du rôle de la phase condensée dans la stabilité d'un MPS pour lanceur spatial", Thesis dissertation, INPT, novembre 1996.

[38] Dupays J., Prevost M., Tarrin P. and Vuillot F., "Effects of Particulate Phase on Vortex Shedding Driven Oscillations in Solid Rocket Motors", AIAA 96-3248, AIAA 32nd Joint Propulsion Conference, July 1-3 1996, Orlando, USA.

[39] Avalon G., Casalis G. and Griffond J., "Flow Instabilities and Acoustic Resonance of Channels with Wall Injection," AIAA paper 98-3218, AIAA 34th JPC, Cleveland, July 13-15, 1998.

[40] Casalis G., Avalon G. and Pineau J.-Ph., "Spatial Instability of Planar Channel Flow with Fluid Injection through Porous Walls", Phys. Fluids, 10 (10), October 1998.

[41] Ugurtas B., Avalon G., Lupoglazoff N. and Vuillot F., "Numerical Computations of Hydrodynamic Instabilities Inside Channels with Wall Injection", AIAA 99-2505, 35th AIAA-/ASME/SAE/ASEE Joint Propulsion Conference, 20-24 June 1999, Los Angeles, CA, USA.

[42] Ugurtas B., Avalon G., Lupoglazoff N., Vuillot F. and Casalis G., "Stability and Acoustic Resonance of Internal Flows Generated by Side Injection", in AIAA Progress in Astronautics and Aeronautics, Volume 185, Solid Propellant Chemistry, Combustion, and Motor Interior Ballistics, Vigor Yang, Thomas B. Brill, Wu-Zhen Ren Editors.

[43] Ugurtas B., "Etudes numérique et expérimentale des instabilités hydrodynamiques et du couplage aéro-acoustique dans un écoulement de Taylor", Thesis dissertation, Paris 6, décembre 2000.

[44] Griffond J., "Instabilité pariétale et accrochage aéroacoustique dans les conduits à parois débitantes simulant les moteurs à propergol solide d'Ariane 5", Thesis dissertation, ENSAE, septembre 2001.

[45] Lupoglazoff N. and Vuillot F., "Simulation numérique bidimensionnelle des écoulements instationnaires dans les propulseurs à propergol solide", La Recherche Aérospatiale, No.1992-2, pp. 21-41.

[46] Tissier P.Y., Godfroy F. and Jacquemin P., "Simulation of Three Dimensional Flows Inside Solid Propellant Rocket Motors Using a Second Order Finite Volume Method – Application to the Study of Unstable Phenomena", AIAA 92-3275, AIAA 28th Joint Propulsion Conference, July 1992, Nashville, USA.

[47] Lupoglazoff N. and Vuillot F., "Comparison between Firing Tests and Numerical Simulation of Vortex Shedding in a 2D Test Solid Motor" AIAA 93-3066, AIAA 24th Fluid Dynamics Conf., Orlando, FL, July 6-9, 1993.

[48] Godfroy F. and Tissier P.Y., "CFD Analysis of Vortex Shedding Inside a Subscale Segmented Motor", AIAA 94-2781, AIAA 30th Joint Propulsion Conference, June 1994, Indianapolis, IN.

[49] Morfouace V. and Tissier P.Y., "Two-Phase Flow Analysis of Instabilities Driven by Vortex Shedding in Solid Rocket Motors", AIAA 95-2733, 31st Joint Propulsion Conference July 10-12, 1995, San Diego.

[50] Vuillot F. and Lupoglazoff N., "Combustion and Turbulent Flow Effects in 2D Unsteady Navier-Stokes Simulations of Oscillatory Rocket Motors", AIAA 96 0884, AIAA 34th Aerospace Sciences Meeting, Reno, Nevada, USA, January 1996.

[51] Lupoglazoff N. and Vuillot F., "Simulations of Solid Propellant Rocket Motors Instability Including Propellant Combustion Response", 6th International Congress on Sound and Vibration, 5-8 July 1999, Lingby, Denmark.

[52] Chaouat B., "Numerical Predictions of Channel Flows with Fluid Injection Using Reynolds Stress Model", J. of Propulsion and Power, Vol. 18, No. 2, March-April 2002, pp. 295-303.

[53] Lupoglazoff N. and Vuillot F., "Numerical Simulations of Parietal Vortex-Shedding Phenomenon in A Cold Flow Set-Up", AIAA 98-3220, 34th AIAA/ASME/SAE/ASEE Joint Propulsion Conference, July 13-15 1998, Cleveland, USA.

[54] Avalon G., Ugurtas B., Grisch F. and Bresson A., "Numerical Computations and Visualization Tests of the Flow Inside a Cold Gas Simulation with Characterization of a Parietal Vortex Shedding", AIAA 2000-3387, 36th AIAA/ASME/SAE/ASEE Joint Propulsion Conference and Exhibit, Huntsville, AL, 16-19 July 2000.

[55] Vuillot F., Basset T., Dupays J., Daniel E. and Lupoglazoff N., "2D Navier-Stokes Stability Computation for Solid Rocket Motors: Rotational, Combustion and Two-Phase Flow Effects", AIAA 97-3326, 33rd AIAA/ASME/SAE/ASEE Joint Propulsion Conference, July 6-9 1997, Seattle, USA.

[56] Lupoglazoff N., Vuillot F., Dupays J. and Fabignon Y., "Numerical Simulations of the Unsteady Flow Inside Fegmented Solid-Propellant Motors with Burning Aluminum Particles", AIAA Paper 2002-0784, AIAA 40th Aerospace Sciences Meeting, Reno, Nevada, USA, January 2002.

[57] Mettenleiter M., "Contrôle adaptatif des instabilités aéroacoustiques. Application aux systèmes de propulsion", Thesis dissertation, Ecole Centrale Paris, 2000.

[58] Mettenleiter M., Vuillot F. and Candel S., "Numerical Simulation of Adaptive Control Application to Unstable Solid Rocket Motors", Symposium RTO, Applied Vehicle Technology Panel, on Active Control Technology, 8-11 May 2000, Braunschweig (Germany), accepted for publication in AIAA Journal, 2002.

# MOTOR FLOW INSTABILITIES - Part 2

## Intrinsic linear stability of the flow induced by wall injection

G. Casalis, F. Vuillot

ONERA Toulouse - 2, av. Ed. Belin BP 4025 - 31 055 Toulouse Cedex - FRANCE
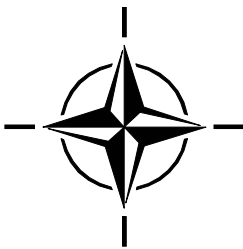ONERA - BP72 - 29 av. de la Div. Leclerc - F-92 322 Châtillon Cedex - FRANCE

casalis@onecert.fr, vuillotf@onera.f

RTO-AVT VKI Special Course on

INTERNAL AERODYNAMICS IN SOLID ROCKET PROPULSION

VKI Institut, 27-31 May, 2002

# Contents

# Introduction

Thrust oscillations generally occur in large solid propellant motor during a few seconds of the flight, they exactly correspond to the frequencies of the cavity modes. The excitation of cavity modes has been reproduced in small scale solid propellant motors and also in cold gas facilities. However as extensively exposed by F. Vuillot in the present VKI lecture series, there are different possible causes of this excitation and all of them may play a role. Among them, as suggested by F. Vuillot, see [1], there is the intrinsic instability.

Let us start with very simple models. Let be $\mathcal{L}(\omega)$ a linear differential operator for which some values of $\omega$ correspond to eigenmodes. It means that for these values, it exists a non zero solution $\hat{u}_\omega$ ($\hat{u}_\omega \not\equiv 0$) such as : $\mathcal{L}(\omega)(\hat{u}_\omega) = 0$. Now, $\omega$ is assumed to be such an eigenvalue and $\hat{u}_\omega$ the associated eigenfunction. If the system is forced by a non zero right hand side term $f$, we have to solve : $\mathcal{L}(\omega)(v) = f$. Thanks to the linear nature of the differential operator, if $f$ may be decomposed in different terms $f = \sum f_i$, the solution $v$ is the exact superposition of the solution of each isolated forcing $v = \sum v_i$ with $\mathcal{L}(\omega)(v_i) = f_i$. If $f_i$ does not correspond to the eigenmode $\hat{u}_\omega$, the amplitude $v_i$ remains as small as the one of the forcing $f_i$. On the other hand, if $f_{i,\omega}$ is an eigenmode (proportional to $\hat{u}_\omega$), then the amplitude of $v_{i,\omega}$ may become very large (it is the so-called secular terms in the framework of the multiple scale analysis, it is the so-called resonance phenomenon generally speaking). Consequently, after some transient, the contribution of $v_{i,\omega}$ in the sum $v = \sum v_i$ will be dominant, $v \approx v_{i,\omega}$ : the system has selected a single behaviour, the one corresponding to the resonant forcing.

Coming back to the solid propellant motor, the previous operator $\mathcal{L}(\omega)$ may be associated to the governing problem for the cavity mode, the matter is to determine the origin of the forcing. An intrinsic instability mechanism has been suspected by François Vuillot to be responsible of the forcing. If it is the case, the forcing would be itself an eigenmode, but for another dynamical system !

The present course is limited to the presentation of the linear stability theory. We will show the general philosophy which is behind a so-called "instability", the application of it for the special flow which is representative of the one in a solid propellant motor. We will also show that the present theory is very strange from a theoretical point of view, but very efficient in comparison with the available experimental results. Finally we will conclude as a "Public Prosecutor" against the intrinsic instability modes which are suspected to be the forcing terms with respect to the emergence of the dangerous cavity modes.

# Chapter 1

# Geometry, presentation

## 1.1 Experimental facilities

In real motors, the conditions are very severe (two-phase flow, high pressure, high temperature), so that detailed measurements inside the motor are nearly impossible. Cold gas experimental facilities have been thus especially designed for fundamental studies. They are much less expensive than the experiment which use solid propellant and detailed measurements are possible ; on the other hand some physical effects are missing such as the reactive two-phase flow or the slow regression of the wall (due to the combustion of the propellant).

For cold gas experiment, the flow inside the motor which comes from the burning surface in real motors is simulated by a wall injection of cold gas (air for example). This is usually realized by using a porous wall constituted by small bronze particles which are then compacted.

In the following, two types of geometry will be considered.

- The first one is of rectangular type. We will take benefit from only one facility of this kind :
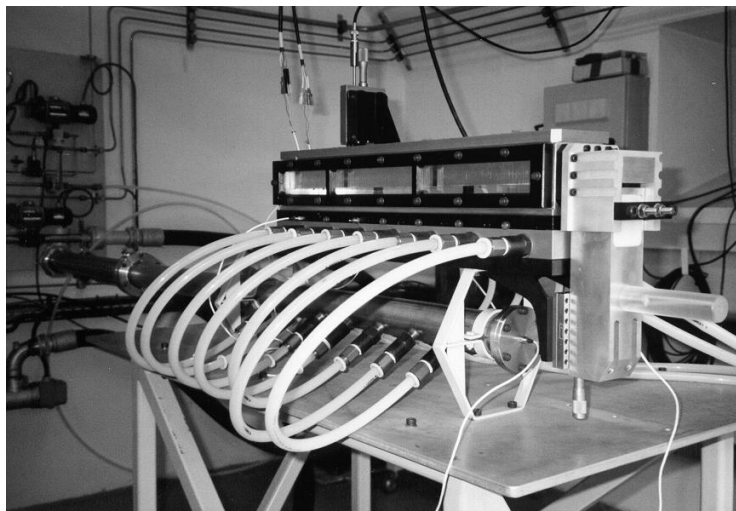


Figure 1.1: VECLA facility

---

the one called "VECLA", extensively studied by G. Avalon in ONERA Palaiseau, see [2] even if other facilities such as the so-called "Micat1" carried out in Poitiers, see [3], with which very interesting results have been obtained. A photo of VECLA is given in figure 1.1, whereas a sketch is given in figure 1.2. Its length and its breadth are fixed, 603 mm and 60 mm respectively.
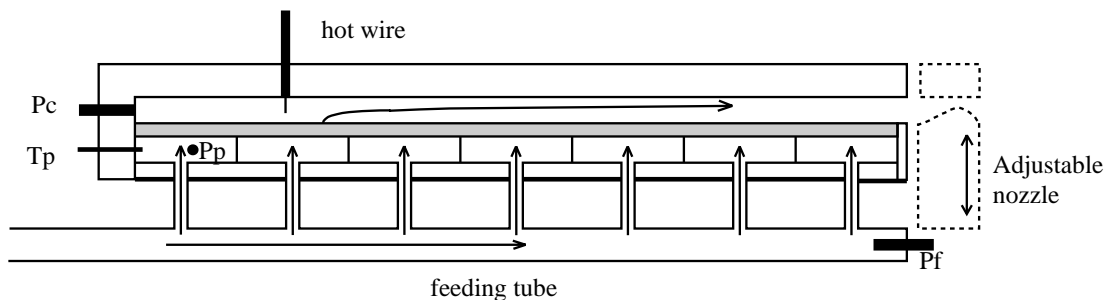


Figure 1.2: Sketch of the VECLA facility

On the other hand, the height can be modified, 10 mm, 20 mm and 30 mm have been tested. Air is injected only through the lower wall. The upper wall is solid and is perforated by small holes in order to maintain a hot wire anemometer used for measurement of the instantaneous velocity. The two lateral walls are in plexiglas allowing thus flow visualisations. In the theory presented in the following, we will considerer a plane case for which both lower and upper walls are used for the air injection. Finally the system is closed on one side by a front wall and ends on the other side by either nothing or by a non injecting nozzle leading to a throat. In the operating conditions, the flow is sonic at the throat. Without nozzle, the injection velocity may be varied continuously during the experience. It can also be fixed, typical values are around 1 m/s. The nozzle is adjustable, as indicated in figure 1.2, so that the injection velocity may be changed but not continuously during an experiment. In addition to some technical measurements necessary for the control of the flow, the measurements consist in the fluctuating pressure at the front wall (denoted by $Pc$ in figure 1.2) and the velocity (mean value and fluctuating one) inside the flow by using a hot wire. This one can be moved at several distances from the front wall and different distances from the porous wall can be analysed. By using the so-called periodogram process, the temporal velocity signal is finally converted into a spectral representation. Very interesting and recent results obtained with VECLA may be found [4].

- The second geometry is closer than the one of real solid propellant motors, it is a cylinder. Results of different facilities will be used in the present document. The oldest one (whose results are used in the present document) is located in the United States and has been extensively tested by Brown and co-workers, see [5] for example. Another one is in Belgium and has been realized and studied by Jérome Anthoine, see [6], manager of the present lecture series ! Finally a more recent one is currently investigated at ONERA-Palaiseau by G. Avalon. A photo of this last facility is provided in figure 1.3. In that case, there is a unique cylindrical porous wall, through which cold gas is injected. The diameter is 60 mm. This case is obviously closer to the real geometry, but only one diameter can be used for a given system. As for the first geometry, there is a front wall and either a free exit section (as it is the case for the photo 1.3) or a
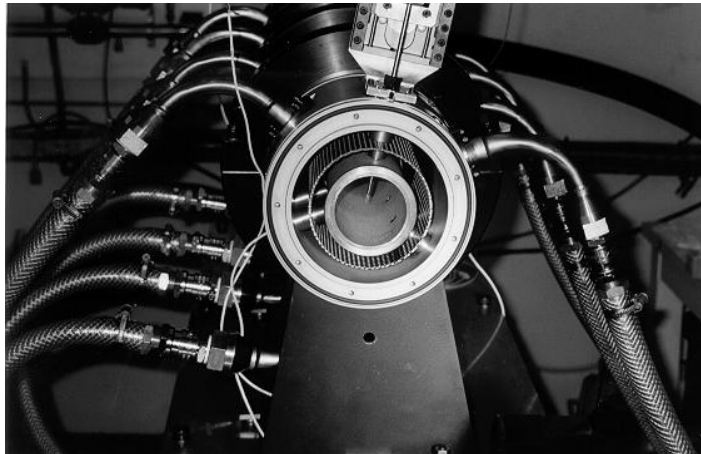
Figure 1.3: Photo of the VALDO facility

throat. As with VECLA, for a free exit section, the injection velocity can be varied more or less arbitrarily. Front wall pressure is measured and a hot wire is also used, it may be observed in photo 1.3. But for this type of installation with a hot wire passing through the porous wall, very few distances from the front wall can be analysed. In order to obtain finer experimental results for the evolution of the velocity with respect to the distance from the front wall, the hot wire has been installed on a very fine and long blade passing directly through the exit section.

## 1.2 Notations

### 1.2.1 Plane case

As sketched in figure 1.4, the $x$ coordinate is defined in the direction perpendicular to the front
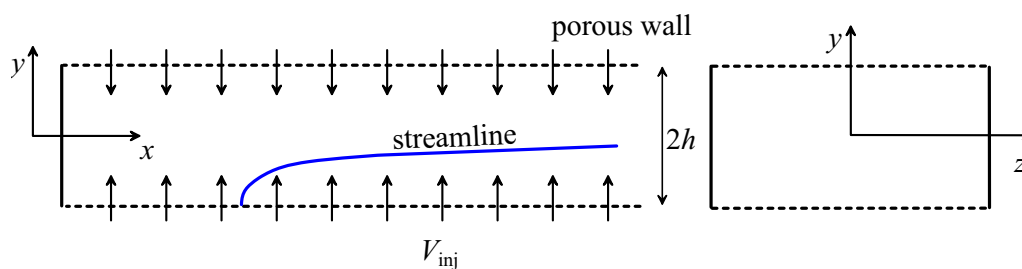


Figure 1.4: Plane notations

wall, $x = 0$ being located at this wall. The coordinate denoted by $y$ defines the distance from the upper and lower walls, $y = 0$ is located in the symmetry plane. Finally, the coordinate $z$ defines the broadness. The distance between the upper and lower walls is denoted by $2h$, so that $h$ is the physical distance between the two walls when considering the VECLA facility, for which the non porous wall is located at $y = 0$. The norm of the injection velocity through these walls is assumed

to be constant and uniform, it is noted $V_{\text{inj}}$.

### 1.2.2   Axisymmetric case

As in the first case, $x$ represents the distance from the front wall. Otherwise, $r$ denotes the radial coordinate and $\theta$ the azimuthal one. The geometry is sketched in figure 1.5. The diameter is noted by $2h$ and the norm of the injection velocity by $V_{\text{inj}}$, as for the plane case.
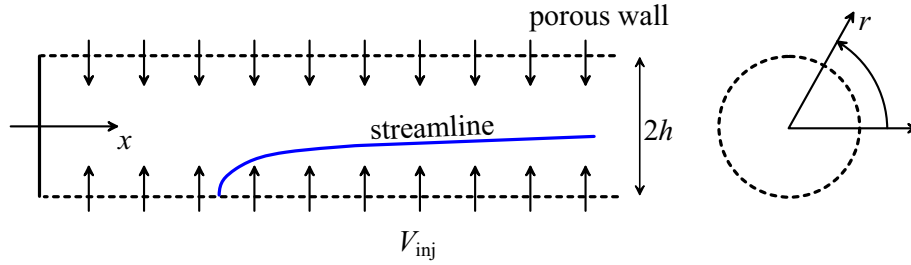


Figure 1.5: Axisymmetric notations

### 1.2.3   Dimensionless quantities, Reynolds number

In the following, all the quantities are dimensionless according to the reference velocity $V_{\text{inj}}$ and the reference length $h$, it means that the lengths are scaled by the radius (and not by the diameter) of the cylinder in case of the axisymmetric geometry. The reference time is $h/V_{\text{inj}}$ and the pressure is scaled with $\rho V_{\text{inj}}^2$, $\rho$ being the density (assumed to be constant). Thus, in the equations it appears a Reynolds number based on the injection velocity :

$$\mathcal{R} = \frac{h V_{\text{inj}}}{\nu}$$

where $\nu$ represents the kinematic viscosity. In the operating conditions, this Reynolds number is of order 1000. In some papers, like [7], another Reynolds number is used which is based on the longitudinal velocity in the middle of the channel at the considered distance from the front wall, see also figure 4.3 in the following.

## 1.3   General equations

### 1.3.1   Used assumptions

As previously mentioned, flow injection is assumed to be steady and uniform (independent of the location) and strictly perpendicular to the porous wall. Concerning the theoretical results, the geometry is assumed to be constant. In fact, as demonstrated in [8], a slow regression of the porous wall (compatible with the real time scale of the motion of the propellant surface in real motors) does not modify significantly the results presented in the following.

Finally the total length of the channel is assumed to be sufficiently short so that the flow remains subsonic inside the channel (it will be shown below that the flow is uniformly accelerated

in the $x$ direction due to the injection). As the temperature field is numerically observed to be more or less constant, we also assume that the flow is incompressible. Again this assumption has been validated, see [9].

### 1.3.2 Plane geometry

Assuming that the flow remains two-dimensional, all the quantities depend only on the time $t$ and on the spatial coordinates $(x, y)$. The two components of the instantaneous flow velocity are noted $(\tilde{u}, \tilde{v})$, the pressure $\tilde{p}$, so that the Navier-Stokes equations written for the incompressible flow in the cartesian $(x, y)$ coordinate system are :

$$\begin{cases} \dfrac{\partial \tilde{u}}{\partial x} + \dfrac{\partial \tilde{v}}{\partial y} = 0 \\[3mm] \dfrac{\partial \tilde{u}}{\partial t} + \tilde{u}\dfrac{\partial \tilde{u}}{\partial x} + \tilde{v}\dfrac{\partial \tilde{u}}{\partial y} + \dfrac{\partial \tilde{p}}{\partial x} = \dfrac{1}{\mathcal{R}}\Delta\tilde{u} \\[3mm] \dfrac{\partial \tilde{v}}{\partial t} + \tilde{u}\dfrac{\partial \tilde{v}}{\partial x} + \tilde{v}\dfrac{\partial \tilde{v}}{\partial y} + \dfrac{\partial \tilde{p}}{\partial y} = \dfrac{1}{\mathcal{R}}\Delta\tilde{v} \end{cases} \tag{1.1}$$

where $\Delta$ denotes the laplacian operator. The boundary equations must first express the no-slip condition together with the injection condition at the two horizontal porous walls. Concerning the front wall, the no-slip condition leads to a non self-coherent relation, especially at the two corners $(0, -1)$ and $(0, 1)$ in terms of $(x, y)$ coordinates. Assuming an injection at these points is not compatible indeed with the viscous no-slip relationship. A possible solution could be to simulate a boundary layer in the injection process in the neighbourhood of these two points. A simpler solution however consists in assuming that the front wall acts as a symmetry plane (allowing a mirror flow for negative values of $x$). This last solution leads to impose that only the $\tilde{u}$ component vanishes at $x = 0$. Finally the boundary conditions associated to the equations (1.1) are :

$$\begin{cases} \forall y \in [-1, +1] \qquad \tilde{u}(0, y) = 0 \\[3mm] \forall x \geq 0 \qquad \tilde{u}(x, -1) = 0, \quad \tilde{v}(x, -1) = 1, \quad \tilde{u}(x, 1) = 0, \quad \tilde{v}(x, 1) = -1 \end{cases} \tag{1.2}$$

For this type of flow, it may be useful to work with a stream function $\tilde{\psi}$ related to the velocity by :

$$\tilde{u} = \frac{\partial \tilde{\psi}}{\partial y} \qquad \tilde{v} = -\frac{\partial \tilde{\psi}}{\partial x}$$

In system (1.1), the continuity condition is automatically satisfied for $\tilde{\psi}$, whereas the pressure can be eliminated between the two momentum equations. Differentiating the first momentum equation with respect to $y$ and the second one with respect to $x$ and subtracting then these two equations lead to :

$$\frac{\partial}{\partial t}\left(\frac{\partial}{\partial y}\tilde{u} - \frac{\partial}{\partial x}\tilde{v}\right) + \tilde{u}\frac{\partial}{\partial x}\left(\frac{\partial}{\partial y}\tilde{u} - \frac{\partial}{\partial x}\tilde{v}\right) + \tilde{v}\frac{\partial}{\partial y}\left(\frac{\partial}{\partial y}\tilde{u} - \frac{\partial}{\partial x}\tilde{v}\right) = \frac{1}{\mathcal{R}}\Delta\left(\frac{\partial}{\partial y}\tilde{u} - \frac{\partial}{\partial x}\tilde{v}\right)$$

In terms of stream function, this writes :

$$\frac{\partial}{\partial t}\Delta\tilde{\psi} + \frac{\partial\tilde{\psi}}{\partial y}\frac{\partial}{\partial x}\Delta\tilde{\psi} - \frac{\partial\tilde{\psi}}{\partial x}\frac{\partial}{\partial y}\Delta\tilde{\psi} = \frac{1}{\mathcal{R}}\Delta\Delta\tilde{\psi} \tag{1.3}$$

The boundary conditions must then also be expressed in terms of $\tilde{\psi}$ :

$$\begin{cases} \forall y \in [-1,+1] \qquad \dfrac{\partial \tilde{\psi}}{\partial y}(0,y) = 0 \\[4mm] \forall x \geq 0 \qquad \dfrac{\partial \tilde{\psi}}{\partial y}(x,-1) = 0, \quad \dfrac{\partial \tilde{\psi}}{\partial x}(x,-1) = -1, \quad \dfrac{\partial \tilde{\psi}}{\partial y}(x,1) = 0 \quad \dfrac{\partial \tilde{\psi}}{\partial x}(x,1) = 1 \end{cases} \qquad (1.4)$$

### 1.3.3   Cylindrical geometry

In this case, $\tilde{p}$ remains the notation for the pressure and the three components of the instantaneous velocity write now as $(\tilde{u}_x, \tilde{u}_r, \tilde{u}_\theta)$, in the cylindrical $(x, r, \theta)$ coordinate system illustrated in figure 1.5. The Navier-Stokes equations become now :

$$\begin{cases} \dfrac{\partial \tilde{u}_x}{\partial x} + \dfrac{\partial \tilde{u}_r}{\partial r} + \dfrac{\tilde{u}_r}{r} + \dfrac{1}{r}\dfrac{\partial \tilde{u}_\theta}{\partial \theta} = 0 \\[4mm] \dfrac{\partial \tilde{u}_x}{\partial t} + \tilde{u}_x \dfrac{\partial \tilde{u}_x}{\partial x} + \tilde{u}_r \dfrac{\partial \tilde{u}_x}{\partial r} + \tilde{u}_\theta \dfrac{1}{r}\dfrac{\partial \tilde{u}_x}{\partial \theta} + \dfrac{\partial \tilde{p}}{\partial x} = \dfrac{1}{\mathcal{R}} \left( \dfrac{\partial^2 \tilde{u}_x}{\partial x^2} + \dfrac{\partial^2 \tilde{u}_x}{\partial r^2} + \dfrac{1}{r}\dfrac{\partial \tilde{u}_x}{\partial r} + \dfrac{1}{r^2}\dfrac{\partial^2 \tilde{u}_x}{\partial \theta^2} \right) \\[4mm] \dfrac{\partial \tilde{u}_r}{\partial t} + \tilde{u}_x \dfrac{\partial \tilde{u}_r}{\partial x} + \tilde{u}_r \dfrac{\partial \tilde{u}_r}{\partial r} + \tilde{u}_\theta \dfrac{1}{r}\dfrac{\partial \tilde{u}_r}{\partial \theta} - \dfrac{\tilde{u}_\theta^2}{r} + \dfrac{\partial \tilde{p}}{\partial r} \\[4mm] \qquad\qquad = \dfrac{1}{\mathcal{R}} \left( \dfrac{\partial^2 \tilde{u}_r}{\partial x^2} + \dfrac{\partial^2 \tilde{u}_r}{\partial r^2} + \dfrac{1}{r}\dfrac{\partial \tilde{u}_r}{\partial r} - \dfrac{\tilde{u}_r}{r^2} + \dfrac{1}{r^2}\dfrac{\partial^2 \tilde{u}_r}{\partial \theta^2} - \dfrac{2}{r^2}\dfrac{\partial \tilde{u}_\theta}{\partial \theta} \right) \\[4mm] \dfrac{\partial \tilde{u}_\theta}{\partial t} + \tilde{u}_x \dfrac{\partial \tilde{u}_\theta}{\partial x} + \tilde{u}_r \dfrac{\partial \tilde{u}_\theta}{\partial r} + \dfrac{\tilde{u}_\theta}{r}\dfrac{\partial \tilde{u}_\theta}{\partial \theta} + \dfrac{\tilde{u}_\theta \tilde{u}_r}{r} + \dfrac{1}{r}\dfrac{\partial \tilde{p}}{\partial \theta} \\[4mm] \qquad\qquad = \dfrac{1}{\mathcal{R}} \left( \dfrac{\partial^2 \tilde{u}_\theta}{\partial x^2} + \dfrac{\partial^2 \tilde{u}_\theta}{\partial r^2} + \dfrac{1}{r}\dfrac{\partial \tilde{u}_\theta}{\partial r} - \dfrac{\tilde{u}_\theta}{r^2} + \dfrac{1}{r^2}\dfrac{\partial^2 \tilde{u}_\theta}{\partial \theta^2} + \dfrac{2}{r^2}\dfrac{\partial \tilde{u}_r}{\partial \theta} \right) \end{cases} \qquad (1.5)$$

Concerning the boundary conditions, the same previous remark about the injection at the abscissa $x = 0$, close to the front wall, can be expressed. The boundary conditions are thus :

$$\begin{cases} \forall \theta \in [0, 2\pi[ \quad \forall r \in [0,1] \qquad \tilde{u}_x(0, r, \theta) = 0 \\[4mm] \forall x \geq 0, \quad \forall \theta \in [0, 2\pi[ \qquad \tilde{u}_x(x, 1, \theta) = 0, \quad \tilde{u}_r(x, 1, \theta) = -1, \quad \tilde{u}_\theta(x, 1, \theta) = 0 \end{cases} \qquad (1.6)$$

## 1.4   Basic flow

In this section, we will first determine a particular steady solution of the Navier-Stokes equations and associated boundary conditions. The following step of the analysis will be to determine its stability, this will be done in the following chapters. The physical quantities associated to the steady solution, we are looking for, will be noted in capital and overlined letters.

### 1.4.1   Plane case

It is possible to find a mathematical steady solution of the equations. A self-similar solution firstly proposed by Berman, see [10], may be sought for the stream function of the mean flow :

$$\bar{\psi} = xF(y)$$

that is $\bar{U} = xF'(y)$ and $\bar{V} = -F$ in terms of the velocity components. Equation (1.3) leads to

$$F'F'' - FF''' = \frac{1}{\mathcal{R}}F^{(IV)} \tag{1.7}$$

associated to the boundary conditions :

$$F(-1) = -1 \qquad F'(-1) = 0 \qquad F(1) = 1 \qquad F'(1) = 0$$

(the boundary condition at the front wall is automatically satisfied with this self-similar form). For large Reynolds numbers, a very accurate approximation of the basic flow is obtained with the so-called Taylor solution, see [11] :

$$\bar{U} = \frac{\pi x}{2}\cos\frac{\pi y}{2} \qquad \bar{V} = -\sin\frac{\pi y}{2} \tag{1.8}$$

which is strictly valid for the equations written for an inviscid flow. The (inviscid) pressure is then given by :

$$\bar{P} = -\frac{\pi^2 x^2}{8} - \frac{1}{2}\left(\sin\frac{\pi y}{2}\right)^2 + P_0$$

where $P_0$ is a constant. The associated stream function is :

$$\bar{\psi} = x\sin\frac{\pi y}{2} + k$$

with $k$ a constant.

### 1.4.2 Axisymmetric case

In the cylindrical case, a steady axisymmetric solution may be also determined in the self-similar form given by :

$$\bar{U}_x = \frac{1}{r}\frac{\partial\Phi}{\partial r} \qquad \bar{U}_r = -\frac{1}{r}\frac{\partial\Phi}{\partial x} \qquad \bar{U}_\theta = 0 \qquad \text{with} \quad \Phi(x,r) = xf(r)$$

where $\Phi$ is a cylindrical stream function of the flow. The function $f$ satisfies the following differential problem with the prime corresponding to the differentiation with respect to $r$ :

$$\begin{cases} \dfrac{1}{\mathcal{R}}\left[\dfrac{1}{r}\left\{r\left(\dfrac{f'}{r}\right)'\right\}'\right]' + \left\{\dfrac{f}{r}\left(\dfrac{f'}{r}\right)' - \left(\dfrac{f'}{r}\right)^2\right\}' = 0 \\[3mm] \left(\dfrac{f'}{r}\right)'(0) = 0 \qquad \dfrac{f}{r}(0) = 0 \qquad f'(1) = 0 \qquad f(1) = 0 \end{cases}$$

The two first boundary equations written above impose the leading order of the behaviour of the function $f$ close to the axis $r = 0$ in case of a viscous flow. Assuming a regular Taylor expansion of the form $f(r) = a_0 + a_1 r + a_2 r^2/2 + \dots$, it can be readily proved that $f$ satisfies $f(r) = \mathrm{O}(r^3)$ for $r$ close to 0. Without viscosity, only the second boundary condition in $r = 0$ is necessary and the leading order becomes then $f(r) = \mathrm{O}(r^2)$ for $r$ close to 0.

Again it is possible to find an analytical solution, which exactly satisfies the inviscid equations :

$$\bar{U}_x = \pi x\cos\frac{\pi r^2}{2} \qquad \bar{U}_r = -\frac{1}{r}\sin\frac{\pi r^2}{2} \qquad \bar{U}_\theta = 0 \tag{1.9}$$

with the pressure given by :

$$\bar{P} = -\frac{\pi^2 x^2}{2} - \frac{1}{r^2}\left(\sin\frac{\pi r^2}{2}\right)^2 + P_0$$

where $P_0$ is a constant. This solution constitutes a good approximation of the viscous case for large Reynolds numbers (typically $\mathcal{R} \geq 1000$).

### 1.4.3  Some remarks

Before analysing the stability properties of the mean flow described above, it may be interesting to note some remarkable features.

- First the approximate analytical solution has been checked to be quasi superposed to the exact self similar solution for the two types of geometry at least for the Reynolds numbers range considered in the present document, see [8] and [12].

- The mean flow depends on two spatial coordinates and accordingly there is a non zero vertical (or radial) velocity component, so that the flow is said to be non parallel. The plane Poiseuille flow, solution in an infinitely long and broad non injected rectangular duct, is strictly parallel, there is only one spatial direction in which the velocity is not homogeneous (the distance to the wall) and consequently the streamlines are strictly parallel. Conversely, the Taylor flow is non parallel, the streamlines start at the porous lines, turn and become more or less parallel far from the front wall. This is illustrated in figure 1.6 for both types of geometry. In fact, even for
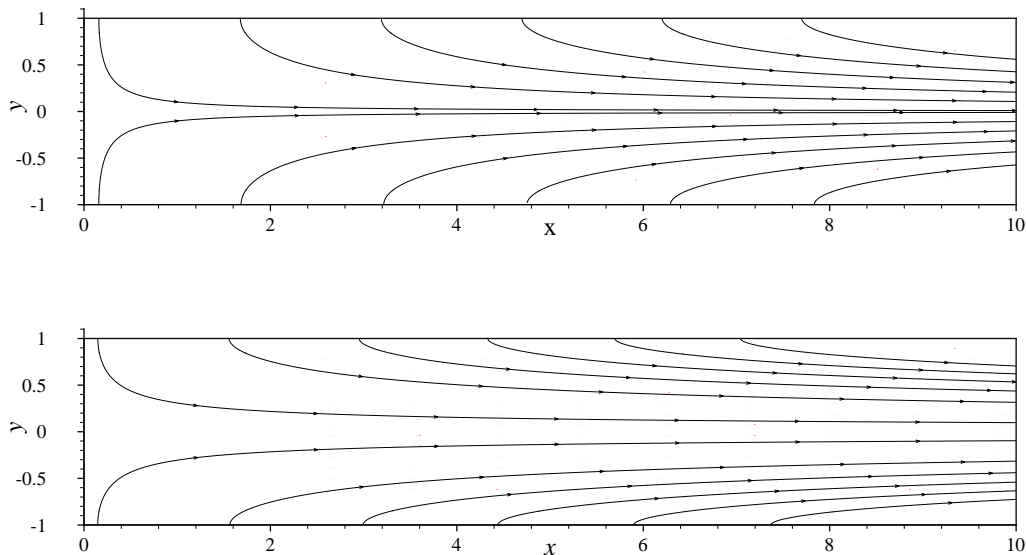


Figure 1.6: (Computed) streamlines of the Taylor flow (plane geometry in the upper figure, axisymmetric geometry in the lower one).

large values of $x$, it remains obviously a small region close to the porous wall in which the flow

is highly non parallel. This feature induces some difficulties with respect to the mathematical form of the perturbation considered in the stability analysis. This point will be discussed in some details in the following, see section 4.1.

- This $x$ dependence describes explicitly a linear increase of the longitudinal component of the velocity.

- Comparing the two types of geometry in figure 1.6, it appears clearly that at a given $x$ position the curvature of the streamlines is much larger in the axisymmetric case than in the plane case. This will strongly affect the stability results.
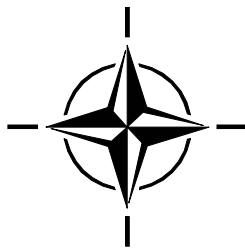
# Chapter 2

# Linear Stability Theory

## 2.1   A short philosophical escape

It must be emphasized that the mean flow described in the previous chapter is a possible solution of the equations. However finding such a possible solution does not prove that this solution will be the observed one in practice. This last point depends in fact on the stability of the proposed solution. A similar problem arise for example with a small ball placed on the top of a large sphere (where "top" refers to the direction of the gravity). The position on the top is a possible equilibrium location, however as it is unstable, it cannot be practically observed.

Coming back to the Taylor flow, the same question is relevant : is the particular flow described by expression (1.8) or (1.9) observed in practice, that is for example in the channel VECLA ? In fact the answer depends on the injection conditions (injection velocity and porosity of the material). The injected flow probably contains some turbulent structures which may excite continuously the channel flow. It has been observed that for a given porosity if the injection velocity is too large, the Taylor flow, as it is described by expression (1.8) or (1.9) is never observed. In that conditions, the flow inside the channel is turbulent everywhere, so that it exists large turbulent fluctuations, which interact between themselves leading by nonlinear mechanisms to a modification of the mean flow. The Taylor flow which is a possible solution of the averaged equations does not correspond then to the averaged observed (or measured) flow. This case will be no longer examined in the following part of the present document.

For small injection velocities and for small values of the porosity, the Taylor flow can be observed, at least in the upstream part of the channel. In fact, the measured flow does not correspond exactly to the Taylor flow, it always exists some fluctuations (for example those induced directly from the non-perfect injection system) superimposed to this theoretical solution. As all dynamical systems, the main flow which is continuously excited by the injection system exhibits two types of response with respect to this forcing. First there is the so-called forced response, whose amplitude is of the same order of the forcing amplitude. Secondly it may exist an eigenresponse the amplitude of which can be dangerously larger than the one of the forcing.

The amplitude of the eigenresponse may be in fact extremely large, it means that a micro phenomenon (small inhomogeneity of the injection) can generate a macro feature. This particular behaviour is the signature of an intrinsic instability. Obviously determining the physical character-

istics of the eigenresponse is very important (amplification rate, frequency, spatial shape), this is the goal of the stability studies. A well-known and classical presentation of the stability theory is published in [13], whereas a general presentation of the practical use of it in case of the boundary layer which exhibits some common feature with the present basic flow is nicely presented in [14] and finally the first attempt of a theoretical application for the Taylor flow has been done in Russia by Varapaev and Yagodkin and has been translated in [7].

## 2.2  Small perturbation technique

According to the previous comments, a particular solution (the Taylor flow in the present case) is supposed to be known, its stability is going to be analysed. The instantaneous flow is then assumed to result from a pure superposition of this particular flow, which will be called the "basic flow" in the following, and of a fluctuation to be determined. This is mathematically imposed by writing :

$$\tilde{q} = \bar{Q} + q \tag{2.1}$$

for any physical quantity $q$ (components of the velocity, pressure and also for example temperature, mass flux density in case of compressible fluids). The instantaneous flow is assumed to be realistic, thus it satisfies the general governing equations. The key point for the stability analysis is the following one. As we only focus on an eigenresponse (and not on a forced response), the boundary conditions written for the instantaneous flow must be strictly identical to those imposed for the determination of the basic flow.

Before writing the complete equations, it may be instructive to describe formally the procedure. Let us represent the complete equations together with the boundary conditions by a (non linear) operator $\mathcal{L}$, for example the one corresponding to the Navier-Stokes equations and associated boundary conditions. As explained above both basic flow and instantaneous flow are assumed to satisfy these equations and boundary conditions :

$$\mathcal{L}(\tilde{q}) = 0 \qquad \text{and} \qquad \mathcal{L}(\bar{Q}) = 0 \tag{2.2}$$

According to the superposition (2.1), the first equation becomes : $\mathcal{L}(\bar{Q} + q) = 0$. Then, the operator $\mathcal{L}$ being regularly dependent on the physical quantities, a first order Taylor expansion can be written :

$$\mathcal{L}(\bar{Q} + q) = \mathcal{L}(\bar{Q}) + \mathcal{M}(\bar{Q}).q + NLT$$

where $NLT$ means nonlinear terms with respect to the fluctuating quantities $q$ and $\mathcal{M}(\bar{Q})$ is a linear operator function of the basic flow which applies to the fluctuating quantities. It represents formally the gradient operator of $\mathcal{L}$. In this course, the fluctuation is assumed to be small in comparison to the basic flow : $q \ll \bar{Q}$, so that the nonlinear terms are small in comparison to the linear ones. Indeed in the linear stability theory these nonlinear terms are simply dropped, the previous Taylor expansion is thus simplified into :

$$\mathcal{L}(\bar{Q} + q) \simeq \mathcal{L}(\bar{Q}) + \mathcal{M}(\bar{Q}).q$$

Finally, as both instantaneous flow and basic flow satisfy the equations as expressed by (2.2), previous equation becomes :

$$\mathcal{M}(\bar{Q}).q = 0 \tag{2.3}$$

which represents the linearised Navier-Stokes equations (and boundary conditions). In the general case, the operator $\mathcal{M}(\bar{Q})$ is invertible so that the only solution is $q \equiv 0$, it means that there is no eigenresponse. However is some very specific cases, as for the present Taylor flow, possible non zero eigensolution may be found. This is mainly the case when the basic flow exhibits symmetry properties (usually invariance with respect to spatial and temporal coordinates) inducing then a special mathematical form for the fluctuation. This is described in the next section.

## 2.3 Normal mode form

In this section, the basic flow is assumed to be dependent on only one spatial variable : $y$ in the plane case and $r$ in the axisymmetric case. This is the parallel assumption. Of course, as mentioned above, this is not strictly the case for the Taylor flow, see section 4.1. In fact, to be more precise, the parallel assumption consists in assuming that only the physical quantities $\bar{Q}$, which are written in the linearised operator (2.3), are dependent on one spatial variable. For example for the plane Poiseuille flow, which is strictly parallel, the pressure depends on $x$ too, but, at least in the incompressible approximation, this pressure term does not appear explicitly in the linearised equations (2.3).

Just to fix the ideas, we will note $y$ the spatial variable in the non homogeneous direction : $\bar{Q} = \bar{Q}(y)$. Then, equation (2.3) represents a system of partial differential equations whose coefficients depend on the basic flow quantities $\bar{Q}$, hence on $y$ only. Thus with respect to each of the other variables, equation (2.3) appears as a system of linear equations with constant coefficients. It is well known that solutions in that case may be sought in an exponential form. Following this mathematical result, all the fluctuating quantities are sought with the so-called normal mode form :

$$q(x,y,t) = \hat{q}(y)e^{i(\alpha x - \omega t)} \qquad \text{plane case}$$

$$q(x,r,\theta,t) = \hat{q}(r)e^{i(\alpha x + m\theta - \omega t)} \qquad \text{axisymmetric case}$$

(2.4)

This notation needs to be explained. First, some quantities have complex values, for example $i$ is the imaginary number satisfying $i^2 = -1$, whereas the physical fluctuation must be obviously real. In fact, the physical fluctuating quantities correspond to the real part of the right hand side terms in (2.4). The functions $\hat{q}(y)$ and $\hat{q}(r)$ are complex and are called the amplitude functions, $m$ is an integer and is the azimuthal wave number and $\alpha$ and $\omega$ are generally complex numbers. Introducing real part and imaginary part of these two numbers by subscripts "$r$" and "$i$", the fluctuating quantities $q$ write :

$$q(x,y,t) = \hat{q}(y)e^{-\alpha_i x + \omega_i t}\, e^{i(\alpha_r x - \omega_r t)}$$

The second exponential term is of norm 1, it describes thus the wavy nature of the solution for the fluctuation, $\alpha_r$ is the longitudinal wave number, $\omega_r$ the circular frequency with $f = \omega/2\pi$ being the frequency itself. The first exponential term is real, it describes a possible amplification of the fluctuation with respect to the time and/or with the distance $x$ according to the sign of $\omega_i$ and $\alpha_i$. Usually at this step, two types of theory are distinguished : the temporal theory for which $\alpha_i \equiv 0$, the fluctuations only grow with time and the growth is governed by the temporal growth rate $\omega_i$ and the spatial theory for which on the other hand we have $\omega_i \equiv 0$, the fluctuations only grow in $x$

and the growth is governed by the spatial growth rate $-\alpha_i$. Between these two theories, it may be interesting to recall that in fact both theories usually provide very similar results by using the so-called Gaster transformation, see [15] :

$$-\alpha_i \simeq \frac{\omega_i}{V_g} \qquad \text{with} \quad V_g = \frac{\partial \omega}{\partial \alpha}$$

where $V_g$ is the group velocity (such an approximation is strictly valid in the vicinity of the neutral curve).

As suggested by the experimental results for the Taylor flow, which will be given in section 3.4, the relevant approach in the present case is the spatial theory. The mathematical form of the perturbation used in the present document is thus :

$$q(x,y,t) = \hat{q}(y)e^{-\alpha_i x}\, e^{i(\alpha_r x - \omega_r t)} = \hat{q}(y)e^{i(\alpha x - \omega t)} \tag{2.5}$$

with $\omega$ a real number and $\alpha$ a complex one. Assuming that the perturbation is convected in the same direction as the basic flow, that is for increasing values of $x$, the spatial evolution of the fluctuation and consequently the stability of the basic flow depends on the sign of $\alpha_i$, the results are given in table 2.1. The same conclusions are true for the perturbation form in the axisymmetric

| sign of $\alpha_i$ | basic flow |
|---|---|
| $\alpha_i > 0$ | stable |
| $\alpha_i < 0$ | unstable |
| $\alpha_i = 0$ | neutral (or marginal) |

Table 2.1: Stability criterion in term of spatial amplification growth rate

geometry.

Finally, the perturbation given by relation (2.4) in the "plane case" corresponds to a plane perturbation. A more general form of the perturbation must include the $z$-dependence, the perturbation writing then :

$$q(x,y,z,t) = \hat{q}(y)e^{i(\alpha x + \beta z - \omega t)}$$

It is known, see [13] for example, that for a strictly parallel basic flow, it is sufficient to limit the stability analysis to two-dimensional modes, as written in (2.4). This result comes from the so-called Squire's theorem. This one cannot be theoretically applied due to the nonparallel terms which are kept in the stability equations. However, systematic stability computations performed for a three-dimensional perturbation showed that the most amplified mode (which corresponds to the largest growth rate $-\alpha_i$) is obtained for $\beta = 0$, that is for a two-dimensional mode. This explains why the perturbation is assumed to be in the form (2.4) in the following.

## 2.4   Dispersion relation

The problem now is to determine the amplitude functions, the frequency and of course the complex wave number $\alpha$. The perturbation is required to satisfy the linearized equations (2.3). Consequently, the form (2.5) is introduced into these linearized equations, this yields :

$$\mathcal{N}(\bar{Q}, \alpha, \omega).\hat{q} = 0$$

where $\mathcal{N}$ is now an ordinary differential operator with respect to $y$ only. Differentiations with respect to $t$ and to $x$ simply become multiplications by $-i\omega$ and by $i\alpha$ respectively. In order to find a non zero solution $\hat{q}$, it is necessary to find values of $(\alpha, \omega)$ such as $\mathcal{N}(\bar{Q}, \alpha, \omega)$ is non invertible. The mean flow depends on $x$ and on $y$ but practically the stability analysis is performed for a fixed value of $x$. On the other hand, as this operator corresponds to the linearized form of the Navier-Stokes equations (1.1), the Reynolds number $\mathcal{R}$ is a parameter. Finally, the formal linearized equations may be written as :

$$\mathcal{N}(x, \mathcal{R}, \alpha, \omega).\hat{q} = 0 \tag{2.6}$$

Now we have to find conditions for which $\mathcal{N}(x, \mathcal{R}, \alpha, \omega)$ is not invertible. Again, it can be first noted that this operator is usually invertible, however it may be possible that for some specific conditions between the parameters $(x, \mathcal{R}, \alpha, \omega)$, the operator is not invertible. These (not known and not obvious) specific conditions are noted by a relation :

$$\mathcal{F}(x, \mathcal{R}, \alpha, \omega) = 0 \tag{2.7}$$

which is called a dispersion relation, because for $x$ and $\mathcal{R}$ being fixed, this equation binds the frequency and the phase velocity $\omega/\alpha$. Of course, this equation is usually not explicit, numerical computations are necessary. They are often performed in two steps (eigenvalues and then eigenfunctions). First, the differential continuous problem being discretised, a complex eigenvalue ($\alpha$ for example) is searched in such a way that a non zero solution for the perturbation may exist. In this step, equation (2.7) is solved in fact, even if the latter is not written explicitly. Then the optional second step consists in determining the non zero solution, with the obtained eigenvalue (which allows a non zero solution). Namely, this non zero solution is the eigenfunction associated to the obtained eigenvalue. Some insight about the numerical aspects are given in appendix.

## 2.5   Linearised equations

### 2.5.1   Plane case

As explained before, the small perturbation technique is used, by decomposing each quantity as written in relation (2.1). In this section, the perturbation is written with the normal mode form (2.4) even if it is not justified, according to the $x$ dependence of the mean flow. This problem related to the non parallel effects will be considered in section 4.1.

For the plane case, it is possible to use either the primitive variables $(u, v, p)$ or the stream function. Let us start with the first formulation. The procedure given in section 2.2 leads with (1.1) to :

$$\begin{cases} i\alpha\hat{u} + \dfrac{\partial \hat{v}}{\partial y} = 0 \\[2mm] -i\omega\hat{u} + i\alpha\bar{U}\hat{u} + \hat{u}\dfrac{\partial \bar{U}}{\partial x} + \bar{V}\dfrac{\partial \hat{u}}{\partial y} + \hat{v}\dfrac{\partial \bar{U}}{\partial y} + i\alpha\hat{p} = \dfrac{1}{\mathcal{R}}\left(\dfrac{\partial^2 \hat{u}}{\partial y^2} - \alpha^2\hat{u}\right) \\[2mm] -i\omega\hat{v} + i\alpha\bar{U}\hat{v} + \hat{u}\dfrac{\partial \bar{V}}{\partial x} + \bar{V}\dfrac{\partial \hat{v}}{\partial y} + \hat{v}\dfrac{\partial \bar{V}}{\partial y} + \dfrac{\partial \hat{p}}{\partial y} = \dfrac{1}{\mathcal{R}}\left(\dfrac{\partial^2 \hat{v}}{\partial y^2} - \alpha^2\hat{v}\right) \end{cases} \tag{2.8}$$

This system is associated to the following boundary conditions, coming from (1.2) :

$$\hat{u}(-1) = \hat{v}(-1) = \hat{u}(1) = \hat{v}(1) = 0$$

It can be easily shown that system (2.8) may be written under the form of a first order ordinary differential linear problem applied to the vector $(\hat{u}, \partial\hat{u}/\partial y, \hat{v}, \hat{p})$ of dimension 4, so that this system, associated to the four boundary conditions above is a well-posed problem. It remains to solve it numerically, see the appendix for some numerical details.

The stream function formulation has the advantage to define only one scalar unknown (the stream function amplitude). The superposition (2.1) is introduced in equation (1.3). After linearisation, this leads to

$$\left(-i\omega + i\alpha\bar{U} + \bar{V}D - \frac{1}{\mathcal{R}}(D^2 - \alpha^2)\right)(D^2 - \alpha^2)\hat{\psi} - \frac{\partial^2\bar{V}}{\partial y^2}D\hat{\psi} - i\alpha\frac{\partial^2\bar{U}}{\partial y^2}\hat{\psi} = 0 \qquad (2.9)$$

where $D$ represents the differentiation with respect to $y$. This equation corresponds exactly to equation (2.3) in case of equation (1.3). Associated to this equation, the following boundary conditions

$$\hat{\psi}(-1) = D\hat{\psi}(-1) = \hat{\psi}(1) = D\hat{\psi}(1) = 0 \qquad (2.10)$$

coming from (1.4), must be satisfied. The stream function of the perturbation is thus required to satisfy again a fourth order homogeneous ordinary differential equation (2.9) associated to four homogeneous boundary conditions. Obviously, the trivial $\hat{\psi} \equiv 0$ remains a possible solution. The goal is to find if for specific conditions between $\alpha$ and $\omega$ (dispersion relation), another solution may exist. It is also important to note that equation (2.9) contains three supplementary terms (due to the non zero $\bar{V}$ factor) in comparison with the classical Orr-Sommerfeld equation. The latter is obtained as explained before but for a strictly parallel mean flow, that is with a velocity of the form $(\bar{U}(y), 0)$. These additional terms are those associated with an odd order of derivation in (2.9).

### 2.5.2 Axisymmetric case

The same procedure can be applied in the axisymmetric geometry. Like the plane case, the basic flow does not depend on $r$ only, so that the normal mode is theoretically not applicable. However using it leads to :

$$
\begin{cases}
i\alpha\hat{u}_x + \dfrac{\partial\hat{u}_r}{\partial r} + \dfrac{\hat{u}_r}{r} + \dfrac{im}{r}\hat{u}_\theta = 0 \\[2ex]
-i\omega\hat{u}_x + i\alpha\bar{U}_x\hat{u}_x + \dfrac{\partial\bar{U}_x}{\partial x}\hat{u}_x + \bar{U}_r\dfrac{\partial\hat{u}_x}{\partial r} + \dfrac{\partial\bar{U}_x}{\partial r}\hat{u}_r + i\alpha\hat{p} \\[1ex]
\qquad = \dfrac{1}{\mathcal{R}}\left(-\alpha^2\hat{u}_x + \dfrac{\partial^2\hat{u}_x}{\partial r^2} + \dfrac{1}{r}\dfrac{\partial\hat{u}_x}{\partial r} - \dfrac{m^2}{r^2}\hat{u}_x\right) \\[2ex]
-i\omega\hat{u}_r + i\alpha\bar{U}_x\hat{u}_r + \dfrac{\partial\bar{U}_r}{\partial x}\hat{u}_x + \bar{U}_r\dfrac{\partial\hat{u}_r}{\partial r} + \dfrac{\partial\bar{u}_r}{\partial r}\hat{u}_r + \dfrac{\partial\hat{p}}{\partial r} \\[1ex]
\qquad = \dfrac{1}{\mathcal{R}}\left(-\alpha^2\hat{u}_r + \dfrac{\partial^2\hat{u}_r}{\partial r^2} + \dfrac{1}{r}\dfrac{\partial\hat{u}_r}{\partial r} - \dfrac{\hat{u}_r}{r^2} - \dfrac{m^2}{r^2}\hat{u}_r - \dfrac{2im}{r^2}\hat{u}_\theta\right) \\[2ex]
-i\omega\hat{u}_\theta + i\alpha\bar{U}_x\hat{u}_\theta + \bar{U}_r\dfrac{\partial\hat{u}_\theta}{\partial r} + \dfrac{\bar{U}_r\hat{u}_\theta}{r} + \dfrac{im}{r}\hat{p} \\[1ex]
\qquad = \dfrac{1}{\mathcal{R}}\left(-\alpha^2\hat{u}_\theta + \dfrac{\partial^2\hat{u}_\theta}{\partial r^2} + \dfrac{1}{r}\dfrac{\partial\hat{u}_\theta}{\partial r} - \dfrac{\hat{u}_\theta}{r^2} - \dfrac{m^2}{r^2}\hat{u}_\theta + \dfrac{2im}{r^2}\hat{u}_r\right)
\end{cases}
\qquad (2.11)
$$

This system of linear ordinary differential equations is associated to the boundary conditions :

$$\hat{u}_x(1) = \hat{u}_r(1) = \hat{u}_\theta(1) = 0$$

expressing, as for the plane case, that there is no fluctuating velocity (for determining the eigen-response) at the porous wall. The numerical resolution of system (2.11) presents a (small) difficulty at the axis $r = 0$, as usual when using the cylindrical coordinates system, see [16] for a possible treatment of this singularity.

# Chapter 3

# Stability results

## 3.1 Eigenmodes

The first task is to determine the solutions of the dispersion relation (2.7) if any. As the conclusions are very similar in the other cases, we will only consider the plane case formulated by the stream function, see (2.9). Then, in order to obtain the "complete" spectrum (i.e. the set of the eigenvalues) of the linearised equations, it is more convenient to fix $\alpha$ and to search all possible solutions in terms of $\omega$ for $\mathcal{R}$ and $x$ fixed. The reason comes from the fact that $\omega$ appears linearly in the Navier-Stokes equations, and $\alpha$ non linearly because it exists terms in $\partial^2/\partial x^2$ which lead to the factor $\alpha^2$. More precisely, equation (2.9) may be rewritten in :

$$\left\{ \left( i\alpha\bar{U} + \bar{V}D - \frac{1}{\mathcal{R}}(D^2 - \alpha^2) \right)(D^2 - \alpha^2) - \frac{\partial^2\bar{V}}{\partial y^2}D - i\alpha\frac{\partial^2\bar{U}}{\partial y^2} \right\} \hat{\psi} = i\omega(D^2 - \alpha^2)\hat{\psi}$$

which is formally of the type $\mathcal{A}\hat{\psi} = \omega\mathcal{B}\hat{\psi}$, that is of the type of a standard (generalised) eigenvalue problem. The differential problem being discretised, many mathematical libraries allow the determination of the "complete" spectrum.

As an example, the following parameters have been fixed : $\mathcal{R} = 1000$, $x = 10$ and $\alpha = 4$. Some eigenvalues are plotted in figure 3.1 in the complex $\omega$-plane. The horizontal line $\omega_i = 0$ separates the instability zone from the stability zone. The higher the points are, the most dangerous they are (according to the temporal theory). In the instability region, only two amplified modes have been found : $\omega \in \{31.59 + 1.6946i, 31.622 + 1.6296i\}$. They are thus very close together and seem in the figure to be only one. The other modes are damped modes, at least for the chosen values of the parameters. Moreover for smaller value of $\omega_i$ it exists many other modes, including possible continuous branches.

To analyse the two amplified modes and their differences, it is generally fruitful to calculate the corresponding eigenfunctions. Moreover, in order to illustrate the strong correspondence between the temporal and the spatial theory, we now move to the spatial theory and fix $\omega$ to a real number by $\omega = 31.6$, in the range of the two previous modes. Then by using a shooting method (Newton convergence from an initial guess of the root), two amplified modes are obtained, as in the temporal theory. They are given by $\alpha = 4.0037 - i0.366$ and $\alpha = 4.016 - i0.373$. The group velocity may be calculated, the nearly same value is found for both modes $V_g \simeq 4.4$. Gaster's
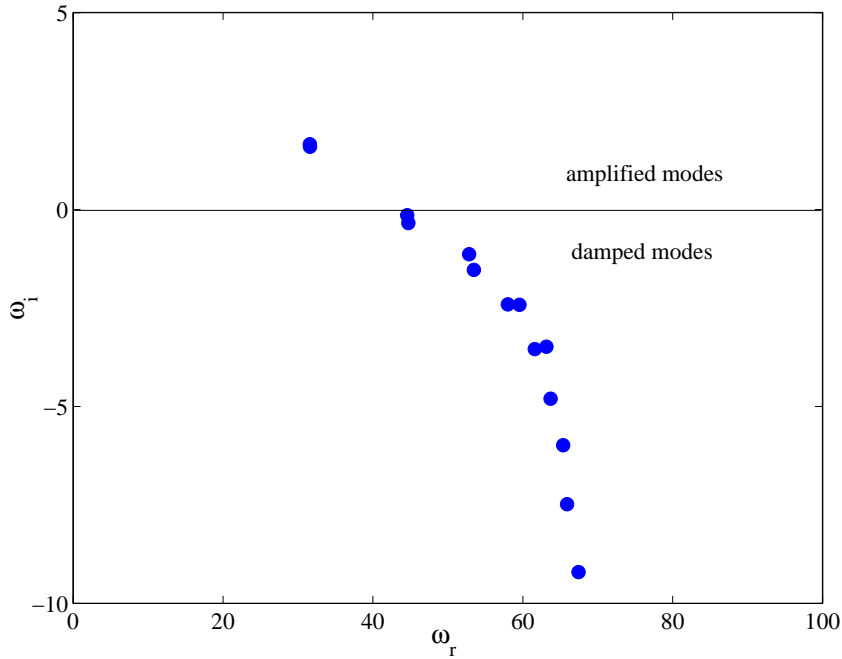
Figure 3.1: Spectrum, $\mathcal{R} = 1000$, $x = 10$, $\alpha = 4$, 300 points in the collocation method

transformation provides then temporal amplification rates which are of order 1.66, they constitute thus good predictions of the temporal growth rates which have been computed directly in the temporal theory.

The corresponding eigenfunctions are plotted in figure 3.2 for the first one and in figure 3.3 for the second one. The main difference between these two modes occurs close to the axis $y = 0$. For the first mode, plotted in figure 3.2, the transverse velocity $v$ is zero on the axis, whereas it is the longitudinal velocity $u$ which vanishes at the axis for the second mode. The first mode is called a varicose mode, and the second one a sinuous mode. Concerning the facility VECLA, it can be noted that with the solid wall (non porous) placed in the upper limit on the duct, only the varicose modes can be observed, the sinuous ones are not compatible with a non-penetration condition at this upper wall.

## 3.2 Amplitude and $n$ factor

### 3.2.1 Definition of the $n$ factor

In agreement with the experimental results, see section 3.4 for validations and explanations, the relevant theory is the spatial one, so that $\omega$ is a real number characterising the frequency of the wave. The dispersion relation is thus solved for fixed values of $(\mathcal{R}, x, \omega)$ (and additionally with the azimuthal wave number $m$ being fixed for the axisymmetric geometry) and the complex $\alpha$ value is computed in order to satisfy the dispersion relation (2.7).

The opposite of the imaginary part $\alpha_i$ of the complex wave number is the growth rate in

Figure 3.2: Norm of the longitudinal and transverse velocity component of the eigenmode $\alpha = 4.0037 - i0.366$ obtained for $\mathcal{R} = 900$, $x = 10$ and $\omega = 31.6$
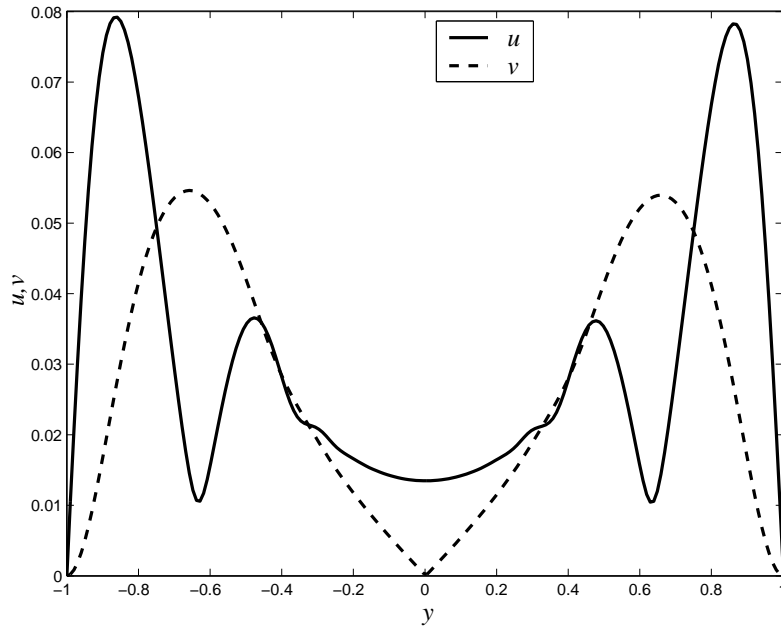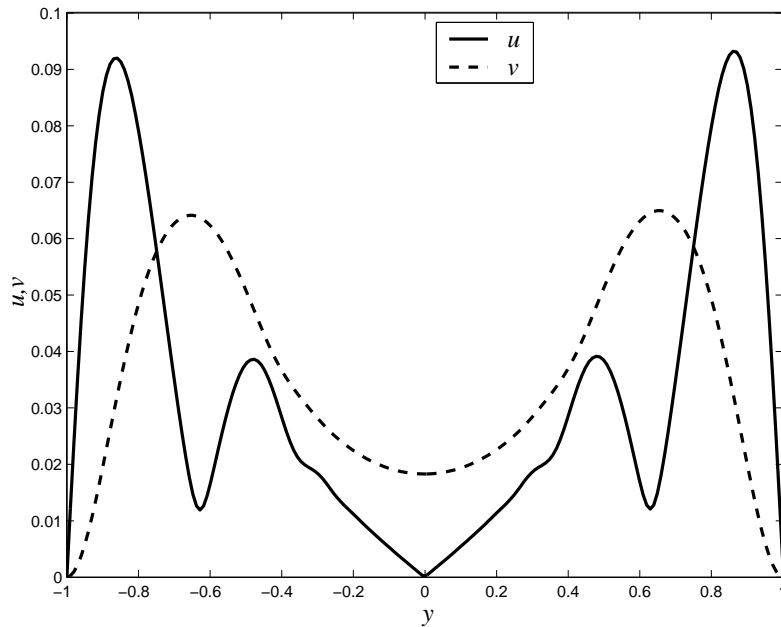


Figure 3.3: Norm of the longitudinal and transverse velocity component of the eigenmode $\alpha = 4.016 - i0.373$ obtained for $\mathcal{R} = 900$, $x = 10$ and $\omega = 31.6$

the $x$ direction. As it has been developed for the boundary layer [17], it is thus possible to define an amplitude $A$ for the eigenmode by :

$$-\alpha_i = \frac{1}{A}\frac{dA}{dx}$$

As suggested by (2.7), the growth rate depends on the parameters $\mathcal{R}$, $\omega$ and $x$. Thus this equation may be integrated in order to calculate the amplitude :

$$A(x;\omega,\mathcal{R}) = A_0 e^n \qquad \text{with} \quad n(x;\omega,\mathcal{R}) = \int_{x_0}^{x} -\alpha_i(\xi;\omega,\mathcal{R})\,d\xi \tag{3.1}$$

With the same meaning as used in the boundary layer, see [18], the factor $n$ gives the logarithm of the eigenmode amplitude. In equation (3.1), $x_0$ is the neutral position. If it exists, it is the point for given values of $(\mathcal{R},\omega)$ which separates upstream a stable region and downstream an unstable region. Generally, $x_0$ depends in fact on $(\mathcal{R},\omega)$, so that we may write $x_0 = x_0(\mathcal{R},\omega)$. In equation (3.1) $A_0$ is an amplitude, which corresponds to the amplitude at the abscissa $x_0$. It can be noted that the eigenmode is solution of a homogeneous problem, so that its definition is not univocal. For example, with the equation (2.9), if $\hat{\psi}$ satisfies the equation, $\lambda\hat{\psi}$, with $\lambda$ any complex constant, also satisfies the equation. For that reason, the amplitude $A_0$ cannot be determined within the linear stability theory. On the other hand, the $n$ factor is intrinsic.

### 3.2.2 Plane case

To be comparable to the experimental results obtained with VECLA, we only focus on the amplified varicose mode in this paragraph. To give an example, the injection Reynolds number $\mathcal{R}$ is fixed : $\mathcal{R} = 4000$. Then, the growth rate $-\alpha_i$ is computed for different frequencies, and for different values of $x$. Finally, for each considered frequency, the growth rate is integrated leading to the $n$ factor. The result is given in figure 3.4 in a diagram $(x,\omega)$. Some important feature may be deduced from this figure. First there is a critical abscissa, which is close to 5 for the considered Reynolds number[1]. It means that upstream the abscissa $x = 5$, the Taylor flow is stable, possible eigenmodes are damped in this region. On the other hand, downstream the critical abscissa, i.e. for $x \geq 5$, there is a range of frequencies for which the instability modes are amplified. Moreover, it can be noted that this range of "dangerous" frequencies increases with $x$. However, low frequencies (less than approximately 14) are never amplified, whereas large frequencies become amplified but for more and more large values of $x$.

The upstream curve corresponds to $n = 0$, i.e. to the neutral (or marginal) curve : the location of $x_0(\mathcal{R},\omega)$ with the notations of (3.1). Without any additional information, it is usually assumed that the amplitude $A_0$ is a constant at the abscissa $x_0(\mathcal{R},\omega)$. In fact this point is related to the receptivity process which describes the physical mechanism by which eigenmodes appear from the general ambiant turbulent noise or from any other types of excitations. If this ambiant noise does not contain any favoured frequencies, at least in the range of possible amplified frequencies, this uniform repartition of initial amplitude $A_0$ seems natural as a first approximation. In this case, the $n$ factors give exactly the amplitude of the eigenmodes up to a scale factor. Thus, figure 3.4

---

[1]In fact the exact value of the critical abscissa must be carefully considered. This is due to the non parallel effects which strongly increase for small values of $x$, see section 4.1.
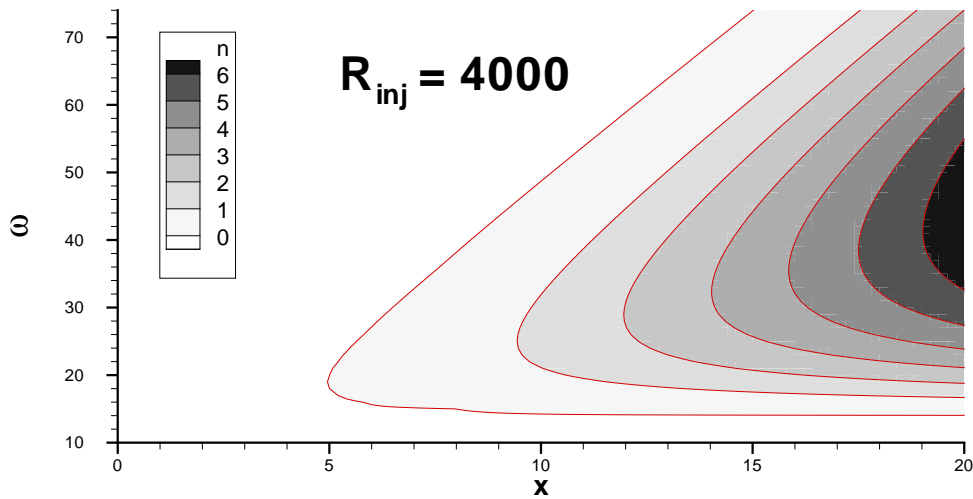
Figure 3.4: Iso-$n$ factors in a $(x, \omega)$ diagram, $\mathcal{R} = 4000$

also shows that the frequency which corresponds to the largest eigenmode at a given distance from the front wall is slightly (and quasi linearly) increasing with this distance.

Finally this figure quantifies the amplification, for example, at $x = 20$, the maximum of the $n$ factor is close to 7, it means that the perturbation is $e^7 \simeq 1000$ times larger than the perturbation at $x = 5$.

### 3.2.3 Axisymmetric case.

For reasonable values of the injection Reynolds number, the frequency and the values of $x$, only one mode (for each value of the azimuthal wave number) has been found to become amplified from some abscissa. The other modes remain damped. We obviously focus on this possibly amplified mode.

Similarly to figure 3.4, figure 3.5 gives for $m = 0$ (axisymmetric modes) and for the same Reynolds number as before $\mathcal{R} = 4000$, the values of the computed $n$ factor in a diagram $(x, \omega)$. The general shape is similar to the one obtained in the plane case. However some important differences exist, that must be noted. First the critical abscissa is located upstream in the axisymmetric case. Furthermore, the $n$ factors seems to be larger in this geometry than in the plane one. For example at $x = 15$, the $n$ factor is close to 11 in the axisymmetric geometry, it is only close to 3 in the plane geometry. Taken into account that the growth of the perturbation follows an exponential behaviour, this means that the axisymmetric Taylor flow is much more unstable than the plane Taylor flow. This difference may be related to the difference observed previously in figure 1.6 between the streamlines in the two cases. Indeed, one important question is to determine the origin of the present intrinsic instability. Even if it is not really demonstrated, it may be suggested that the instability comes from the strong curvature of the streamline close to the porous wall. This could be at least coherent with the following observations.
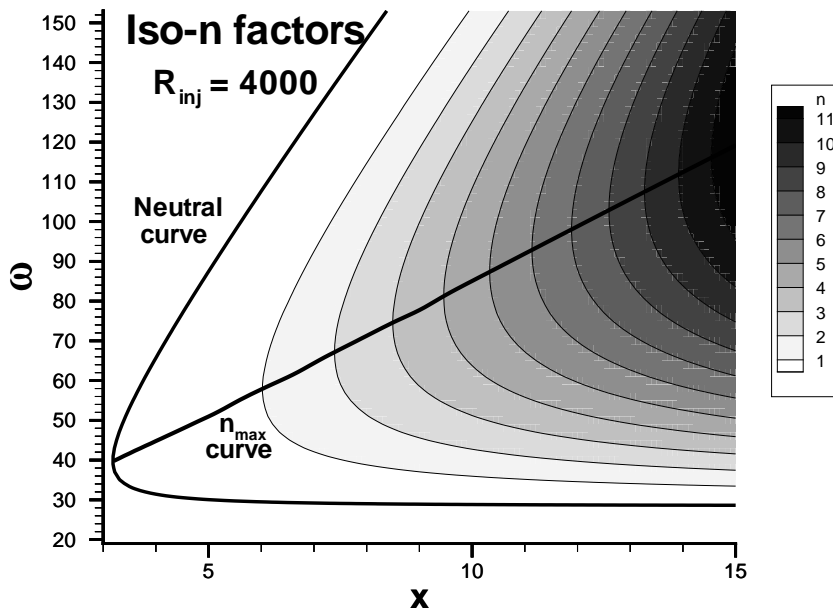
Figure 3.5: Iso-$n$ factor, $m = 0$, $\mathcal{R} = 4000$

1. The maximum of the fluctuating velocity is close to the porous wall.

2. The Taylor flow is stable upstream (where the curvature of the streamlines may be not large enough)

3. If the non parallel terms in $\bar{V}$ are suppressed in the stability equations, such as in (2.8), the basic flow is found to be always stable, see [19].

4. Finally, on one hand, the curvature is much more stronger in the axisymmetric case as in the plane one, as observed in figure 1.6 and, on the other hand, the growth rates are much more larger in the axisymmetric geometry.

The last difference between figures 3.4 and 3.5 concerns the frequency. It seems that the amplified frequencies are greater in the axisymmetric case than in the plane one. For example, the range of amplified frequencies for $x = 8$ is close to $\omega \in [30, 140]$ whereas it is only $\omega \in [15, 40]$ for the plane Taylor flow.

The results given above correspond to the two-dimensional (noted 2D) mode, that is for the azimuthal wave number $m = 0$. An important point concerns the nature of the most amplified mode. A well-known result is the Squire's theorem, which expresses that for a 2D strictly parallel basic flow, the first instability occurs for a 2D perturbation. However, it does not mean that a two-dimensional perturbation is always more amplified than any three-dimensional perturbation, see [20] for more information. However for the Taylor flow this theorem cannot be applied even in the plane case, considering that the stability equations contain some nonparallel terms which

makes unapplicable the mentioned theorem. Some direct computations in the plane case show however that the most amplified modes are approximately two-dimensional, these are the varicose and the sinuous modes. For the axisymmetric geometry, figure 3.6 shows the neutral curve and the
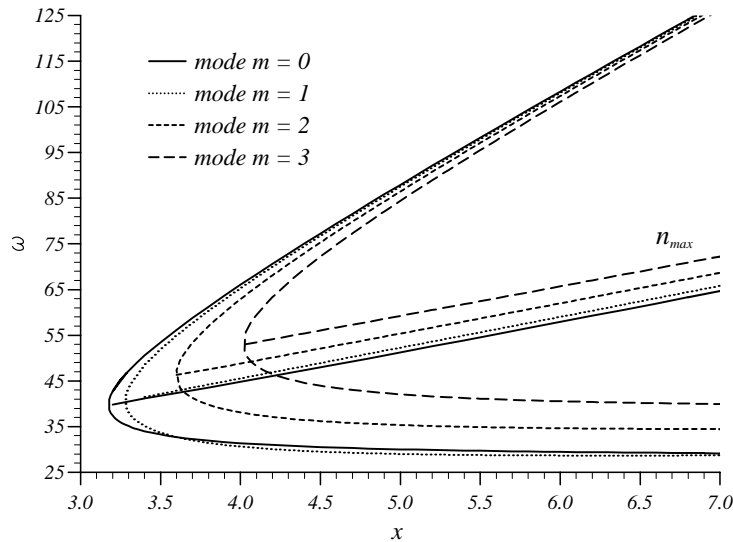


Figure 3.6: Marginal curves for $m = 0, 1, 2, 3$, $\mathcal{R} = 4000$

location of the maximum of the $n$ factor in the $(x, \omega)$ diagram for the four first positive azimuthal wave numbers. The first observation is that the results for $m = 0$ and $m = 1$ are quasi identical. This conclusion exactly corresponds to the similarity between the varicose and the sinuous modes previously observed for the plane geometry. On the other hand, larger azimuthal wave numbers seem to be less and less amplified, except for the high frequencies, for which the differences seem to be small. However the critical abscissa for $m = 3$ is close to the one of $m = 0$, for example it is clearly upstream the location of the $n = 1$ curve in figure 3.5. This means that if all the eigenmodes (characterised by $(m, \omega)$) start with the same initial amplitude $A_0$ at their neutral curve, the amplitude of the $m = 0$ mode at the critical abscissa of $m = 3$ is only a little larger than the amplitude of the $m = 1, 2, 3$ modes. Therefore, it is clear that at a given $x$ position, $x = 7$ for example, the perturbation should be the superposition of several modes corresponding to different values of $m$, so that for any hot wire measurement it should be very difficult to isolate the contributions of the different modes.

To conclude this overview of the typical stability results, it remains to analyse the real part of the complex wave number $\alpha$. It is then more suitable to work with the wavelength $\lambda$ which is defined by : $\lambda = 2\pi/\alpha_r$. Figure 3.7 gives the iso-$\lambda$ values, always in a $(x, \omega)$ diagram for the axisymmetric geometry with $\mathcal{R} = 4000$ and $m = 0$. It is interesting to note that at least for values of $x$ less than 15, the wavelength of the mode which corresponds to the largest amplitude is close to 1. With a dimensional point of view, this means that the largest mode presents a wavelength roughly equal to the radius of the duct. In particular the streamwise evolution of the
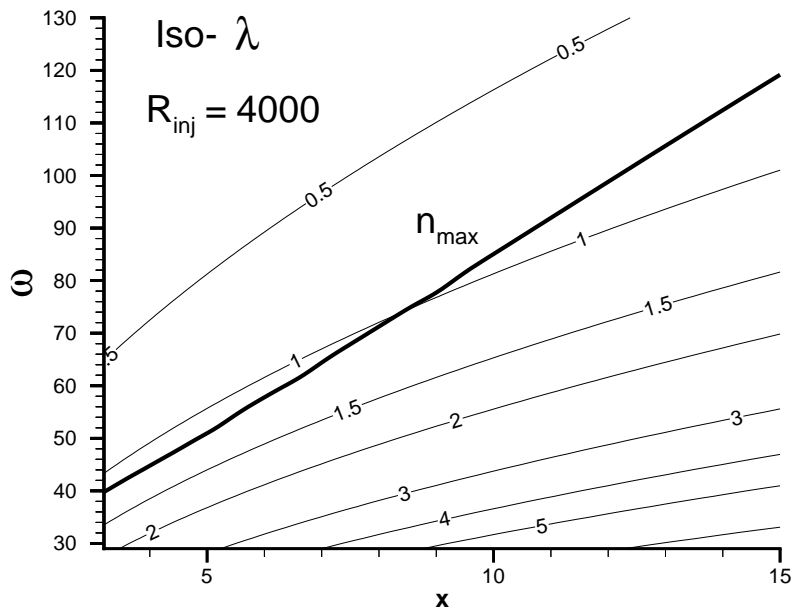
Figure 3.7: Iso-wavelength for $m = 0$, $\mathcal{R} = 4000$

eigenmodes occurs on a scale which is much shorter than the total length of the duct which scales the undesirable cavity modes. Due to this great difference of streamwise extend, it may be guessed that the instability alone is not very efficient as a possible exciting source of the cavity modes.

## 3.3  Influence of the Reynolds number

Concerning the dispersion relation, the influence of the different parameters $x$, $\omega$ and the azimuthal wave number for the axisymmetric geometry have been studied. It remains the influence of the injection Reynolds number. For example, the plane geometry is considered, with fixed $x$ and $\omega$ values : $x = 10$, $\omega = 31.6$ (which have been chosen in the spectrum analysis of the linearised operator, see figure 3.1). The result is plotted in figure 3.8 for the streamwise wave number $\alpha_r$ represented in dashed line and for the growth rate $-\alpha_i$ represented in full line. In this figure, the basic flow is always the one given by the analytical Taylor form (1.8) and only for the stability the Reynolds has been varied from 50 up to $10^5$. It is clear that there is an asymptotic behaviour when the Reynolds number increases. This means that the basic mechanism of this instability is mainly inviscid. Up to now, a clear physical explanation "with the hands" of the origin of the instability has not be found. As explained in the previous section, the instability appears to be related to the strong curvature of the streamlines of the mean flow close to the injecting wall, which is little affected by the viscosity.

However the wave number seems to tend to the inviscid value faster than the growth rate. Thus, especially for the estimation of the $n$ factor in practical case for which the Reynolds number
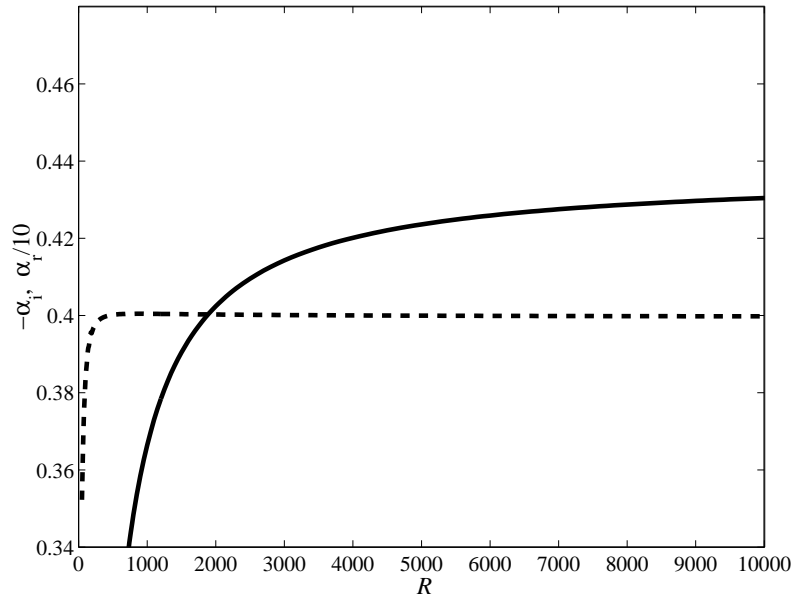
Figure 3.8: Influence of the Reynolds number on the complex streamwise wave number $\alpha$, plane case, $x = 10$, $\omega = 31.6$, varicose mode. The growth rate $-\alpha_i$ is in full line, the tenth of the wave number $\alpha_r/10$ in dashed line

is of order 1000, it is necessary to take into account the viscous effects, the difference could be of about 10% for inviscid computations. On the other hand, it is important to emphasize that for the mean flow, it is really not necessary to use the viscous mean flow given by (1.7) for Reynolds numbers greater than 100, the Taylor solution is accurate enough.

The same feature can be observed in the axisymmetric geometry, leading to the same conclusions.

## 3.4   Comparisons with the experiment

### 3.4.1   Preparation of the results for the comparison

Hot wire measurements give access to the instantaneous velocity at the position where the probe has been placed. Then, using different possible treatments of the signal, the latter is decomposed in two parts : the mean value and the fluctuating one upon which a Fourier transform is applied in order to get the spectral dependence of the fluctuating velocity or more often the power spectral density (DSP).

This spectral representation may be compared to the theoretical predictions. For each given frequency, the $n$ factor is computed by integrating in $x$ the amplification growth rate, so that the amplitude of the fluctuation is simply theoretically given by $A_0 \exp(n(x, \omega))$, with $A_0$ the initial amplitude coming from the receptivity conditions. In the following results, this constant $A_0$ is assumed to be independent of $\omega$, but to be a function of the experimental conditions (values of the injection velocity, of the height of the duct, of the porosity of the injecting walls, ...). Obviously, $A_0$

is independent of $x$. Consequently for given experimental conditions, the constant $A_0$ is adjusted once, in order to fit for one frequency and one value of $x$ the measured amplitude. In case of comparisons including $y$ variations, the same constant $A_0$ must be considered of course.

### 3.4.2 Effects of the dimensional height of the duct and injection velocity

It is interesting to test first the scaling effects by varying experimentally the injection velocity and the height. From the theoretical point of view, as the computation of the $n$ factor in the $(x, \omega)$ plane is performed with dimensionless quantities, changing the injection velocity and the height only modifies the Reynolds number. Comparisons with measurements obtained with the VECLA facility are reported in figure 3.9. Four comparisons are given, they correspond to four values of the pair (injection velocity $V_{\text{inj}}$, height $h$). The measured values are plotted in full line, the theoretical predictions by the open circles. In the four cases, the frequency is plotted between 0 and 2000 Hz. However the scale of the vertical axis, giving the amplitude of the fluctuation, differs from each other. The adjusted initial amplitude $A_0$ is also given for each comparison in the legend, it seems that the constant $A_0$ increases with the injection velocity and decreases with the height of the duct.

The overall comparison is quite satisfying (good prediction of the amplified frequencies and quite good shape of the spectral dependence), even if there are some differences which are mainly visible for $h = 10$ mm. It may be remarked however that for this height (the smallest one for the VECLA facility), the mean flow does not exactly coincide with the theoretical Taylor flow (or the viscous solution), it seems that small three-dimensional structures slightly modify the streamwise component of the mean velocity in comparison with the expected one. However the broadness of the amplified frequencies peak as well as the frequency associated to this peak are in good accordance with the linear stability results.

A similar comparison has been done for the axisymmetric geometry with the available experimental results, see [5]. However in this case, the experiment have been carried out in 1990, that is before the knowledge of the intrinsic instability described in the present document. Among other comparisons, which can be found in [16], figure 3.10 shows the power spectral density of the fluctuating axial velocity for three values of the injection velocity. The latter is represented by $M_w$, the wall injection Mach number. The left figures (experiment) are directly scanned from the publication, whereas the right ones give the theoretical results obtained for the four first positive azimuthal wave numbers. Three different initial amplitudes $A_0$ have been chosen for the three different injection velocities. As before, the range of the amplified frequencies seem to agree quite well with the experimental results, even if there are some discrepancies which are significantly larger than the ones observed with VECLA in the plane geometry.

### 3.4.3 Streamwise amplification

The previous comparisons proved the good agreement between the experimental results and the theoretical ones in terms of range of amplified frequencies. The goal of this section is to analyse carefully the instability process itself, that is the streamwise amplification, which is theoretically of exponential type. The fluctuating velocity at different values of $x$ must be then compared in the same experimental condition (in order to keep the same initial amplitude $A_0$ for the different

*Without nozzle, porosity = 18 $\mu m$, $y_0$ = 1 mm*
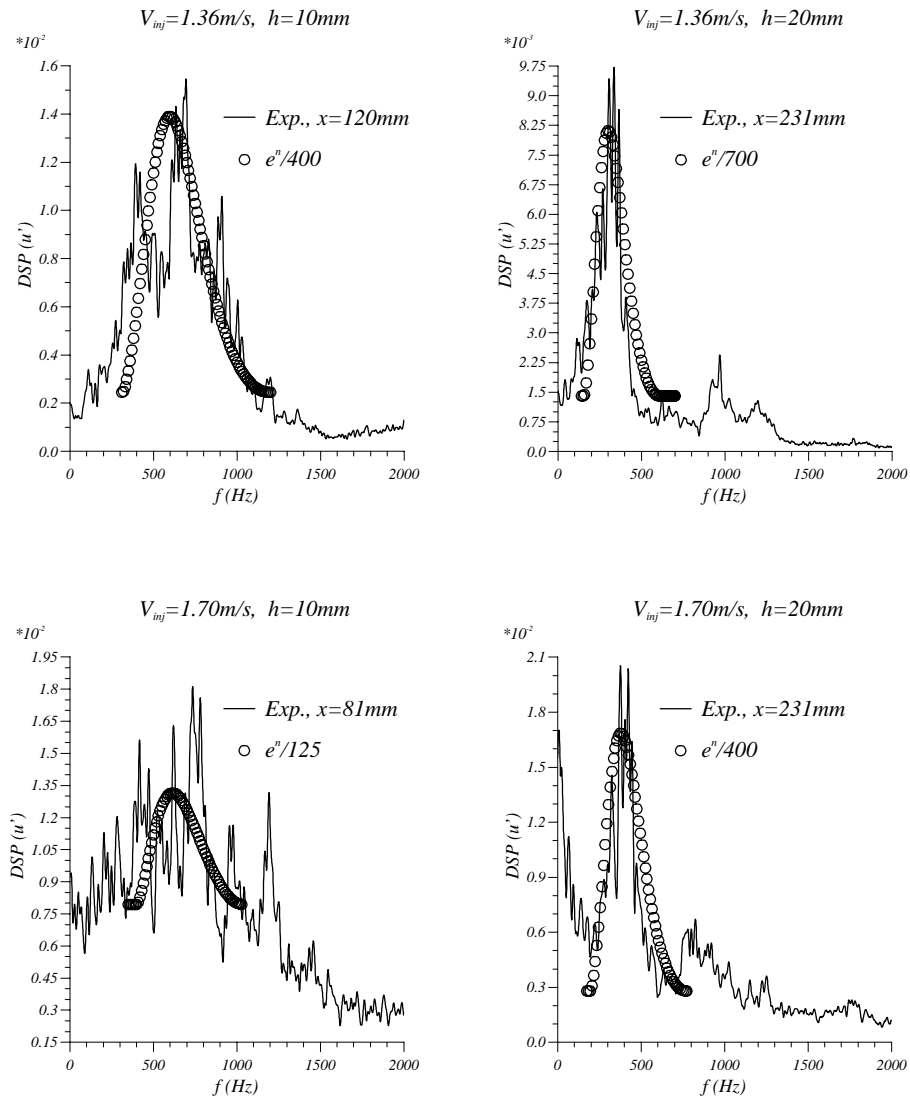


Figure 3.9: Comparisons between LST results and experimental ones with the VECLA facility
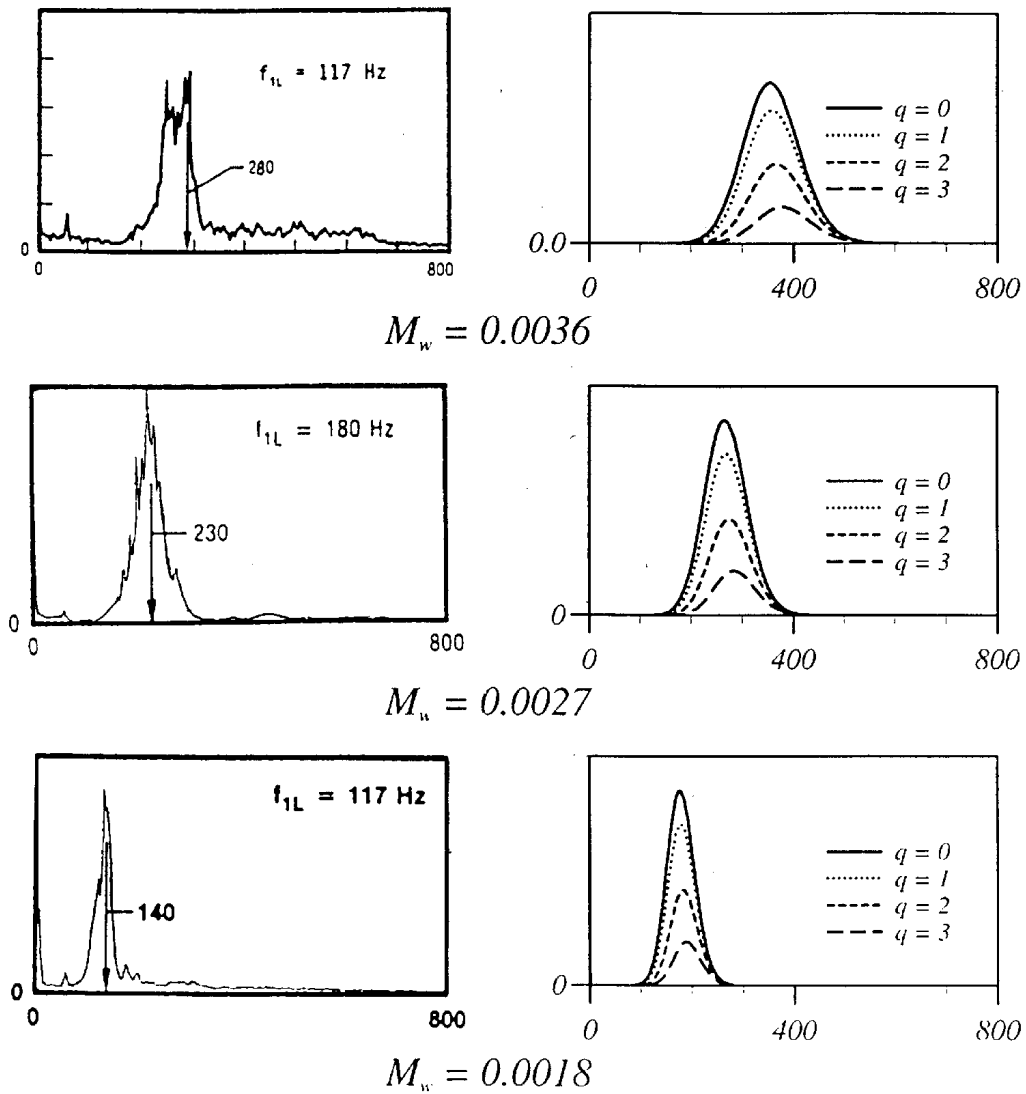
Figure 3.10: Comparisons between LST results and experimental ones obtained by Brown and co-workers

values of $x$).

A first comparison is given in figure 3.11. The height of the duct is 30 mm. The experimental results (lines) are given in six increasing abscissa, whereas the theoretical values (symbols) are reported for only the four largest values of $x$. The two first values are indeed upstream the critical abscissa. The comparison gives an excellent agreement between the experiment and the theory demonstrating undoubtedly on one hand the real existence of intrinsic instability for this type of flow and on the other hand the reliability of the present linear stability theory. To emphasize this comparison, let us mention : the range of amplified frequencies (as shown above), the streamwise amplification (as previously said, the same constant $A_0 = 1/6000$ has been used for the different abscissa). Furthermore, the increasing shift of the amplified frequencies with respect to $x$ is also clearly visible in this figure. Finally, the spectrum measured at $x = 570$ mm, the most downstream



Figure 3.11: Comparisons between LST results and experimental ones with the VECLA facility

position, exhibits an interesting (weakly) nonlinear phenomenon, that is the increase of $2\omega$ and $0\omega$ (steady) modes. These first nonlinear mechanisms are quite well understood in the framework of

the boundary layer stability, see [21]. The basic reason comes from the linear form

$$u_\varphi = \frac{1}{2}(\hat{u}\exp(i\omega) + \hat{u}^*\exp(-i\omega))$$

of the physical fluctuation (where $z^*$ represents the complex conjugate of $z$). The quadratic terms in the Navier-Stokes equations are formally expressed by the product $u_\varphi u_\varphi$. The product is converted into a sum of the exponential terms, leading thus to the frequencies $2\omega$ and $0$. And, as the linear step does not amplify only one mode, but a rather broad range, the quadratic interactions lead also to amplify a certain range around zero and another one corresponding to twice the linear range.

Similar comparisons can be also tested with the axiymmetric duct. In the present document,
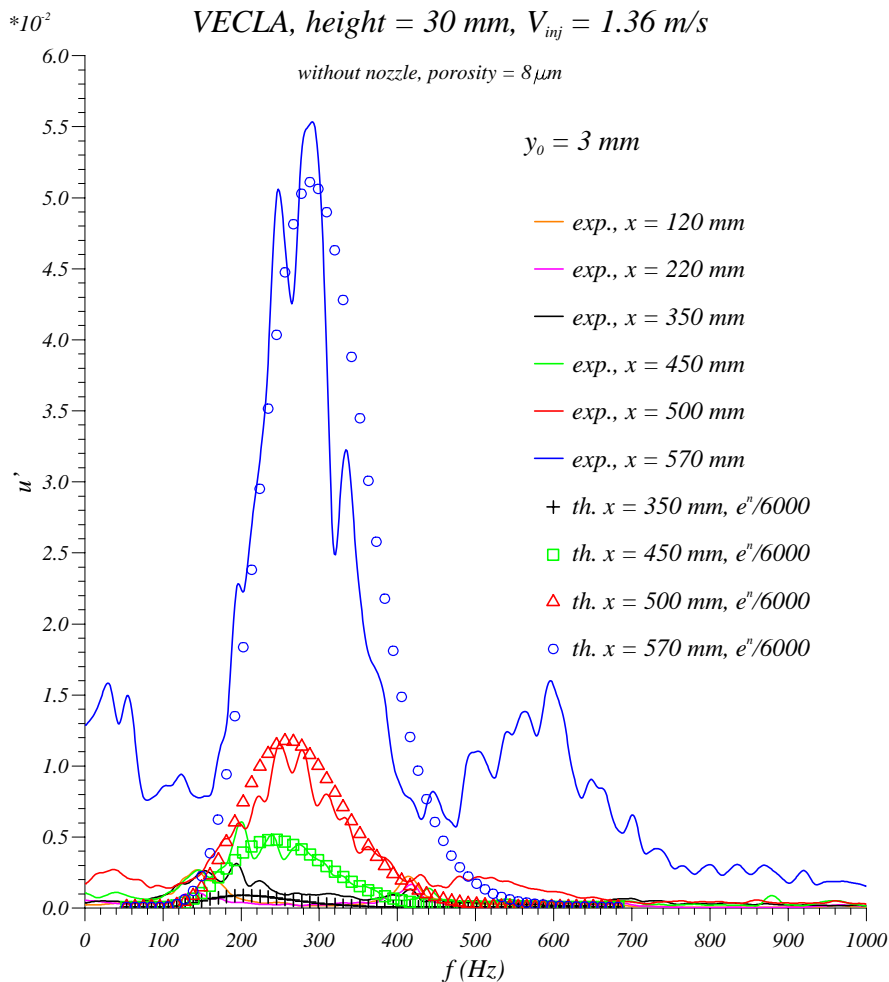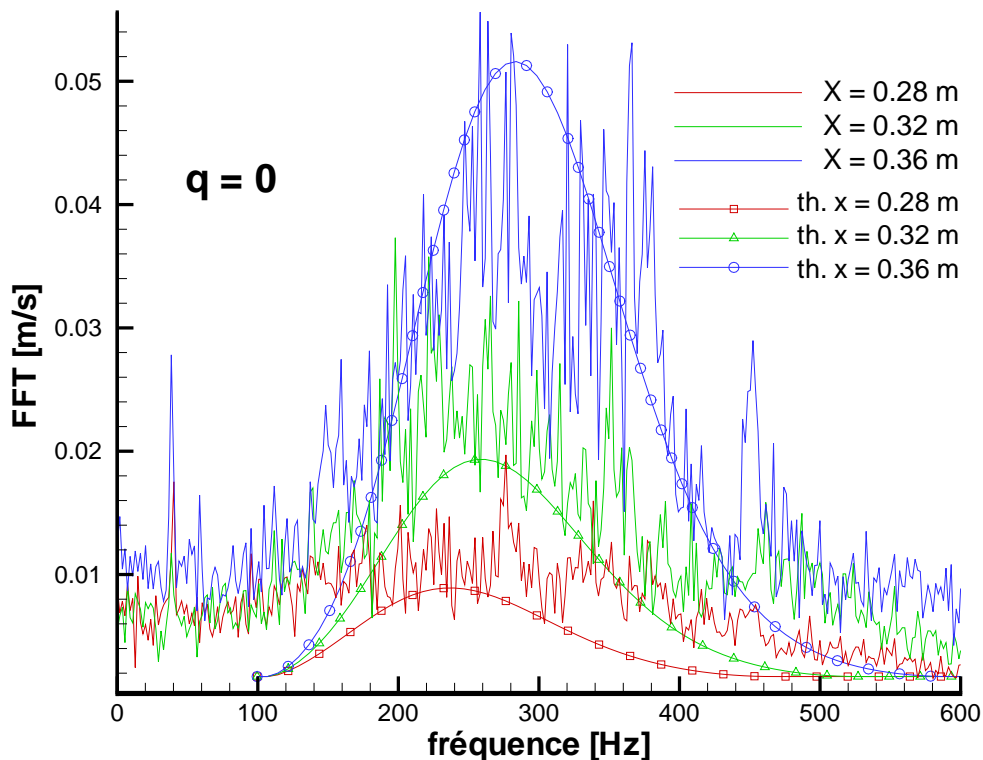


Figure 3.12: Comparisons between LST results and experimental ones obtained with the facility of the VKI. The full lines correspond to the experimental results, each of them at one value of $x$. They are ordered regularly : the large the FFT amplitude, the larger the value of $x$.

two different comparisons are shown, the experimental results coming from two different facilities. The first one is located in VKI and the results have been obtained by J. Anthoine, see [6]. As before, the axial fluctuating velocity spectrum is compared between both approaches, the results are given in figure 3.12. The injection velocity is 0.88 m/s, the radius of the duct 38 mm. The spectra are given for three values of $x$, between 7.4 and 10 in terms of dimensionless distances from the front wall. In comparison with the result given for the plane geometry, it appears immediately that the measured velocity is much less smooth than in figure 3.11.

Similar behaviour have been recently obtained by using the facility VALDO, see [22]. The results are reported in figure 3.13. The radius is 30 mm, the injection velocity 1.05 m/s, the chosen abscissa are thus close to 10.5 in dimensionless value.

From both figures, it may be concluded that there is a range of amplified frequencies which correspond roughly to the theoretical predictions. It seems also that there is a streamwise amplification but some discrepancies are clearly present between the theoretical results and the experimental ones. It is not easy to explain the reason of this noisy signal obtained in the axisymmetric facil-
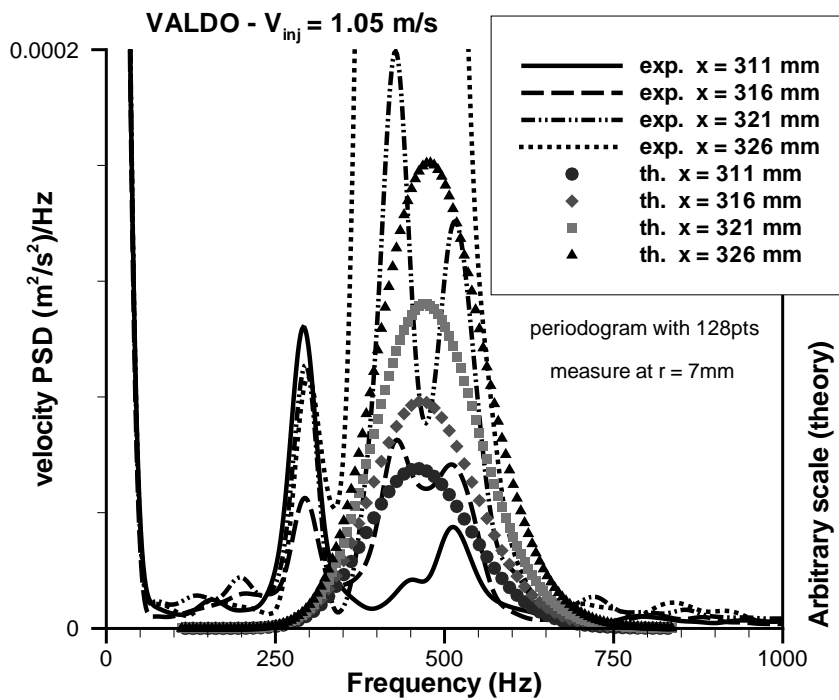


Figure 3.13: Comparisons between LST results and experimental ones obtained with the VALDO facility. Each curve corresponds to one of the four measurements, the same is true for the symbols giving the theoretical predictions

ity. This may be due to the existence of several modes (associated to different azimuthal wave numbers), but this may be also due to the measurement anemometer. In the plane case, the hot wire is parallel to the porous wall whereas in the other geometry, some corners effects may occur. As the probe is placed very close to the porous boundary, there are possible interactions between the mean flow and the corners of the probe which carry the hot wire itself. Anyway, it may be noted that the streamwise amplification is very large. For example, the result shown in figure 3.13 exhibits a huge amplification (factor about 20 in the experiment over a distance of only 1.5 cm).

# Chapter 4

# In(tro)spection of the used assumptions

Different assumptions have been made, their influences must be inspected in order to determine the generality of the results presented in the previous chapter.

## 4.1  Non parallel effects

### 4.1.1  Definitions

As explained before, the basic flow explicitly depends on the streamwise coordinate $x$ so that the exponential form $\exp(i\alpha x)$ used for the perturbation is not theoretically justified. For a two-dimensional basic flow, a dependence of the streamwise velocity coordinate with respect to $x$ is related to a non zero transverse velocity $\bar{V}$ through the continuity equation. This is the reason why this $x$ dependence is called a non parallel effect. In the following, the basic flow is assumed to be dependent on $x$ (even weakly).

For clarity, let us call the parallel approach the one when only the $\bar{U}$ is kept in the stability equations (leading to exactly the Orr-Sommerfeld equation) and the nonparallel approach the one for which all terms related to the basic flow are kept in the stability equations. Then, if the perturbation has the form of a normal mode for a parallel basic flow (or for a flow of which the non parallel terms are neglected), the corresponding approach will be noted by OSE (for Orr-Sommerfeld Equation). On the other hand, the (theoretically not justified) use of the normal mode for a non parallel basic flow will be noted by NNP (for Normal Non Parallel approach). All the results shown in the previous chapter have been obtained by using the NNP approach.

Now there are some questions : is the Taylor flow weakly non parallel (so that OSE is a more or less accurate approximation) ? Is it possible to justify the use of NNP ? Is it possible to perform a consistent and accurate non parallel stability analysis ? The following part of the present chapter is aimed to provide some answers to that questions.

### 4.1.2  Use of a parallel approximation ?

As explained above, the non parallel effects are connected with the magnitude of $\bar{V}$ with respect to $\bar{U}$. Using the Taylor analytical form (1.8), the ratio $\bar{V}/\bar{U}$ may be readily calculated :

$$\left|\frac{\bar{V}}{\bar{U}}\right| = \frac{2}{\pi x}\frac{\left|\sin\frac{\pi y}{2}\right|}{\cos\frac{\pi y}{2}} = \frac{2}{\pi x}\tan\frac{\pi|y|}{2}$$

This suggests that this ratio varies from 0 (at the symmetry axis) to $\infty$ at the porous walls. However if the dependence on $y$ is suppressed by a norm such as the maximum with respect to $y$, the ratio is simplified into $\bar{V}/\bar{U} = 2/\pi x$, which indicates that, according to this choice of norm, the non parallel effects decrease with respect to $x$ (the ratio is smaller than 0.05 for $x \geq 15$ for example). From these simple two remarks, it can be concluded that the Taylor flow may appear more and more parallel for large values of $x$ but, reciprocally, at any values of $x$ it exists a small region close to the injecting walls where the basic flow is strongly non parallel.

In order to illustrate the non parallel effects, a first possibility consists in solving the OSE with the streamwise velocity component $\bar{U}$ being the one given by Taylor, even if the mean flow given by the velocity $(\pi x/2\cos(\pi y/2), 0)$ obviously does not satisfy the steady equations. Figure 4.1 gives for the axisymmetric Taylor flow, with $\mathcal{R} = 4500$, $q = 0$ and $\omega = 80$, the evolution with respect
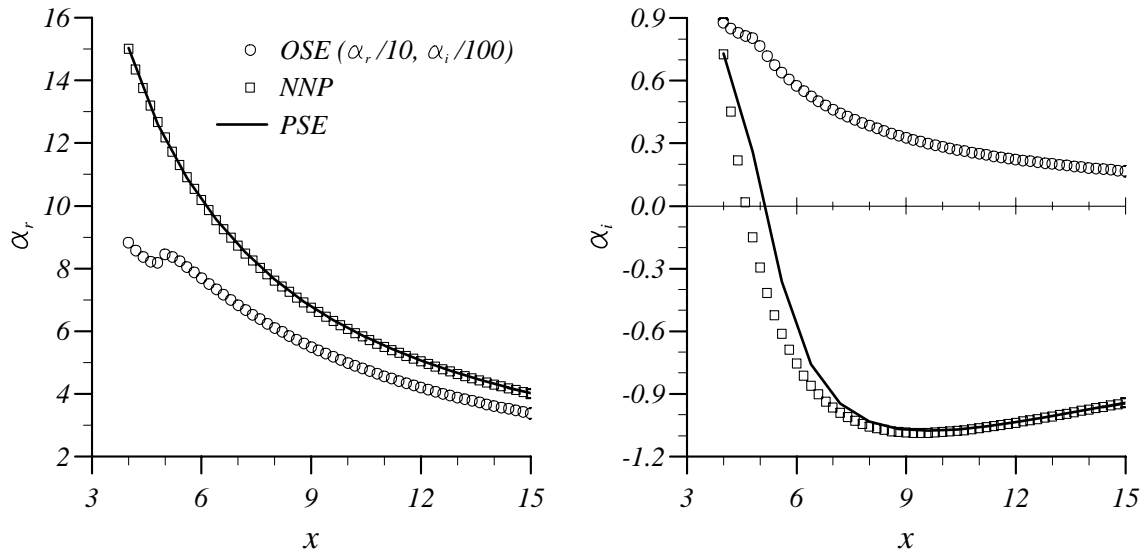


Figure 4.1: Comparison of OSE, NNP and PSE results for the axisymmetric Taylor flow, $\mathcal{R} = 4500$, $q = 0$ and $\omega = 80$. The wavenumber $\alpha_r$ is plotted in the left hand side, the growth rate $\alpha_i$ in the right hand side

to $x$ of the complex number $\alpha$ solved by the OSE, the NNP and the PSE approaches (see below for some explanations on the PSE method). It appears that on one hand NNP and PSE results are very similar, whereas OSE strongly differs from the two others, for example the growth rate remains always positive. Similar behaviour has been found in plane geometry, see [19].

This strong non parallel effect is also confirmed by the whole spectrum obtained with the OSE linearised operator with the same values of the parameters are for figure 3.1. The results

with respect to $y$. If we proceed in this way, the following equation is obtained

$$\left(-i\omega + i\alpha\bar{U} + \bar{V}D - \frac{1}{\mathcal{R}}(D^2 - \alpha^2)\right)(D^2 - \alpha^2)\hat{\psi} - \frac{\partial^2\bar{V}}{\partial y^2}D\hat{\psi} - i\alpha\frac{\partial^2\bar{U}}{\partial y^2}\hat{\psi} + \frac{\partial U}{\partial x}\alpha^2\hat{\psi} = 0 \quad (4.1)$$

which is NOT equation (2.9) as it ought to be in a consistent theory, the last term of (4.1) is not present in (2.9). Let us just recall that for a strictly parallel basic flow, both formulations are strictly equivalent, they lead both to the Orr-Sommerfeld equation.

The NNP approach is consequently not consistent, its results may depend on the formulation. To illustrate that point, comparisons between the two formulations have been performed, they are illustrated in figure 4.3. In addition, the published results of [7] and [23] have been indicated in
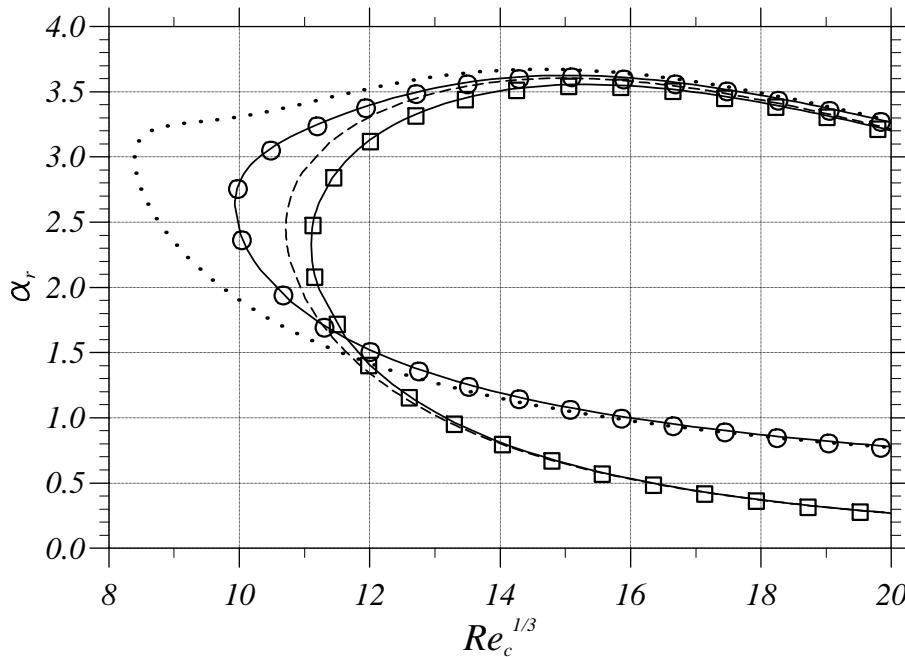


Figure 4.3: Comparisons between diverse published results and our results illustrating the inconsistency of the normal non parallel approach. Using the stream function formulation, results for the neutral curve for the sinuous modes in [7, 23] (circles) and for the varicose modes in [23] coincide with ours (full lines). They are significantly different from ours obtained with the primitive variable formulation for the varicose mode (dashed line) and for the sinuous mode (dotted line). Self-similar solution is used for the plane basic flow with $\mathcal{R} = 100$.

symbols. The neutral curve has been calculated for $\mathcal{R} = 100$ for both sinuous and varicose modes and with the two formulations. It is represented in the $(R_c^{1/3}, \alpha_r)$ diagram, where $R_c$ represents the Reynolds number based on the axial velocity (which is linearly dependent on $x$). All the published results seem to be accurately calculated, the differences between the full lines and the dashed or the dotted ones are intrinsic, they are due to the choice of the normal mode which is inconsistent with the present basic flow.

### 4.1.4   Is there any consistent and accurate non parallel approach ?

From a practical point of view, the inconsistent approach seems however to work with enough accuracy. For large Reynolds number as well as for large values of $x$, the differences between the two approaches discussed in the previous paragraph are quasi negligible. Furthermore, as shown in the previous chapter, the agreement with the experimental results is very good. Even for the axisymmetric geometry, for which the growth rates are larger and the involving $x$ values smaller, it may be guessed that for practical prediction the NNP approach provides a satisfactory estimation of the instability.

On the other hand, the present solution is clearly wrong for the small values of $x$. In particular the location of the neutral curve must be considered with care. Thus an alternative approach for the mathematical form of the perturbation, which would be more consistent and more accurate with respect to the non parallel characteristics of the basic flow, would be useful.

Some approaches already exist which are first consistent and whose goal secondly is to deal with the non parallel effects. The clearest one is based on the multiple scale analysis, see [25] or [26] for a general presentation and see [27] for an example of use in a non parallel stability analysis (in the framework of the boundary layer stability). A more recent approach, called PSE (for Parabolized Stability Equations), developed by Herbert and Bertolotti [28], also deals with the non parallel effects. This approach has been used for the present mean flow, the results are shown in figure 4.1. They prove that after a numerical transient in $x$, the PSE results rapidly agree with the NNP ones. Concerning the consistency, the multiple scale analysis is fully consistent, the PSE approach is quasi consistent, see [29] for more details. The (theoretical) problem with these approaches is that both consider the Orr-Sommerfeld equation as a first order solution, whereas it is not the case for the Taylor basic flow.

Another mathematical form for the perturbation has been proposed by J. Griffond, see [24]. The starting equation is the linearised form of the Navier-Stokes equations expressed with the stream function (1.3). Using the perturbation technique $\tilde{\psi} = \bar{\psi} + \psi$, the linearised problem is :

$$\frac{\partial}{\partial t}\Delta\psi + \frac{\partial\bar{\psi}}{\partial y}\frac{\partial}{\partial x}\Delta\psi + \frac{\partial}{\partial x}\Delta\bar{\psi}\frac{\partial\psi}{\partial y} - \frac{\partial\bar{\psi}}{\partial x}\frac{\partial}{\partial y}\Delta\psi - \frac{\partial}{\partial y}\Delta\bar{\psi}\frac{\partial\psi}{\partial x} = \frac{1}{\mathcal{R}}\Delta\Delta\psi \qquad (4.2)$$

with the following boundary conditions :

$$\begin{cases} \forall y \in [-1,+1] \qquad \dfrac{\partial\psi}{\partial y}(0,y) = 0 \\[2mm] \forall x \geq 0 \qquad \dfrac{\partial\psi}{\partial y}(x,-1) = 0, \quad \dfrac{\partial\psi}{\partial x}(x,-1) = 0, \quad \dfrac{\partial\psi}{\partial y}(x,1) = 0 \quad \dfrac{\partial\psi}{\partial x}(x,1) = 0 \end{cases} \qquad (4.3)$$

As shown before, a possible choice for one stream function associated to the Taylor basic flow is $\bar{\psi} = x\sin(\pi y/2)$. Equation (4.2) represents then a linear equation with coefficients which are dependent on $x$ and $y$ and independent of $t$. Thus a general form for the unknown function $\psi(x,y,t)$ may be chosen with an exponential dependence with respect to $t$ (normal mode in $t$) :

$$\psi(x,y,t) = e^{-i\omega t}\check{\psi}(x,y)$$

Equation (4.2) becomes then :

$$-i\omega\Delta\check{\psi} + \frac{\pi x}{2}\cos\frac{\pi y}{2}\frac{\partial}{\partial x}\Delta\check{\psi} - \frac{\pi^2}{4}\sin\frac{\pi y}{2}\frac{\partial\check{\psi}}{\partial y} - \sin\frac{\pi y}{2}\frac{\partial}{\partial y}\Delta\check{\psi} + \frac{\pi^3 x}{8}\cos\frac{\pi y}{2}\frac{\partial\check{\psi}}{\partial x} = \frac{1}{\mathcal{R}}\Delta\Delta\check{\psi}$$

whereas the associated boundary equations remain the same as (4.3), with $\check{\psi}$ instead of $\psi$. A possible solution could be to solve directly the stability problem given by the previous homogeneous partial differential equation. Such problems are currently investigated by some researchers (in case of the stability of a recirculating zone, a vortex, the boundary layer in the vicinity of the attachment line etc.) but there is a strong difficulty with the treatment of the boundary conditions. The proposed solution is to search $\check{\psi}$ in the form :

$$\check{\psi} = x^\lambda \hat{\psi}(y)$$

leading hence to ordinary differential equations (like with the normal mode) and avoiding therefore the difficulty with the boundary conditions. The idea with this mathematical form is to define a phase velocity, which is then uniformly accelerated with $x$, as is the basic Taylor flow, whereas with the normal mode, the phase velocity does not depend on $x$. With this form, equation (4.2) writes :

$$
\begin{aligned}
0 = &-\frac{1}{\mathcal{R}}D^4\hat{\psi} - i\omega D^2\hat{\psi} + \left[\frac{\lambda\pi}{2}\cos\frac{\pi y}{2} - \sin\frac{\pi y}{2}.D\right]\left(D^2\hat{\psi} + \frac{\pi^2}{4}\hat{\psi}\right) \\
&+ \frac{1}{x^2}\left[-\frac{2}{\mathcal{R}}D^2 - i\omega + \frac{\pi}{2}\cos\frac{\pi y}{2}(\lambda - 2) - \sin\frac{\pi y}{2}.D\right]\lambda(\lambda - 1)\hat{\psi} \\
&- \frac{1}{x^4}\frac{1}{\mathcal{R}}\lambda(\lambda - 1)(\lambda - 2)(\lambda - 3)\hat{\psi}
\end{aligned}
\tag{4.4}
$$

with $D$ the differentiation operator with respect to $y$. As it is the case with the normal mode, this form does not satisfy exactly the equations, so that $\lambda$ is not really independent of $x$. By using the so-called quasi-parallel approach, the value of $\lambda$ is recalculated at each considered value of $x$.

The advantage of this form is clearly to define a zero-order approximation which is asymptotically valid for large values of $x$ :

$$-\frac{1}{\mathcal{R}}D^4\hat{\psi} - i\omega D^2\hat{\psi} + \left[\frac{\lambda\pi}{2}\cos\frac{\pi y}{2} - \sin\frac{\pi y}{2}.D\right]\left(D^2\hat{\psi} + \frac{\pi^2}{4}\hat{\psi}\right) = 0 \tag{4.5}$$

On the other hand, let us return to the OSE and NNP approaches (obtained with the term $\exp(i\alpha x)$) for which, as proposed by J. Griffond, we define :

$$\lambda = ix\alpha$$

Then, the OSE approach gives :

$$-\frac{1}{\mathcal{R}}D^4\hat{\psi} - i\omega D^2\hat{\psi} + \frac{\lambda\pi}{2}\cos\frac{\pi y}{2}\left(D^2\hat{\psi} + \frac{\pi^2}{4}\hat{\psi}\right) + \frac{1}{x^2}\left[-\frac{2\lambda}{\mathcal{R}}D^2\hat{\psi} + \frac{\lambda^3\pi}{2}\cos\frac{\pi y}{2}\hat{\psi}\right] - \frac{1}{x^4}\frac{\lambda^4}{\mathcal{R}}\hat{\psi} = 0$$

whereas the NNP approach leads to :

$$
\begin{aligned}
0 = &-\frac{1}{\mathcal{R}}D^4\hat{\psi} - i\omega D^2\hat{\psi} + \left[\frac{\lambda\pi}{2}\cos\frac{\pi y}{2} - \sin\frac{\pi y}{2}.D\right]\left(D^2\hat{\psi} + \frac{\pi^2}{4}\hat{\psi}\right) \\
&+ \frac{1}{x^2}\left[-\frac{2\lambda^2}{\mathcal{R}}D^2\hat{\psi} + \left(\frac{\lambda\pi}{2}\cos\frac{\pi y}{2} - \sin\frac{\pi y}{2}.D\right)\lambda^2\hat{\psi}\right] - \frac{1}{x^4}\frac{\lambda^4}{\mathcal{R}}\hat{\psi}
\end{aligned}
$$

These equations show that for large values of $x$, the leading order (4.5) of (4.4) coincides exactly with the leading order of the NNP approach and NOT with the OSE approach. The inconsistent approach remains inconsistent obviously but is now justified (its leading order terms) for large values of $x$. Finally some comparisons between direct simulations (by using the code SIERRA developed by F. Vuillot, see [30]) and stability computations show a better agreement with (4.4) than with the NNP, see [24].

## 4.2    Physical assumptions

In addition to the assumption of a normal mode, there are several other aspects which have been neglected in the presentation given before. However, the effects of :

- compressibility,

- real geometry,

- presence of an acoustic mode,

- regression of the boundary wall

have been found to be nearly completely negligible. The intrinsic instability described before seems to be very robust.

The last point related to the linear stability theory, which appears to be important in the computations, see [31], concerns the effects of the presence of particles, especially of reactive particles. A first attempt in that direction has been achieved by taking into account non reactive particles. A first interesting result of [32] is that the particles may destabilise the flow, as it is illustrated in figure 4.4. This effect may be attributed to the appearing augmentation of the
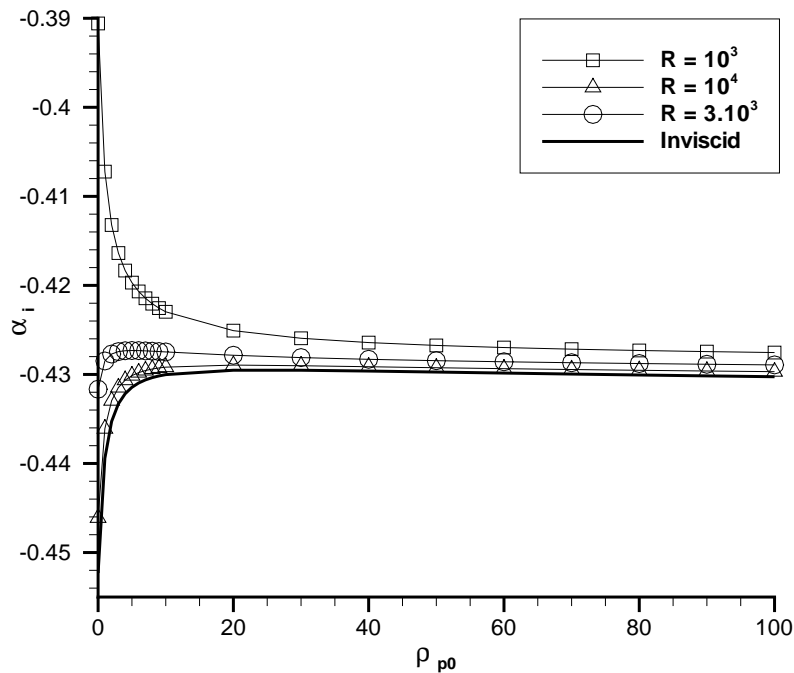


Figure 4.4: Evolution of the growth rate $\alpha_i$ as function of the density of the injected particles at the wall. The injection velocity of the particles is the same as the one of the fluid, the Stokes number is $10^{-3}$, and $x = 10$, $\omega = 30$.

Reynolds number due to the augmentation of the density thanks to the particles.

In addition to this two-phase flow effect, there is of course the linear assumption. But nonlinear mechanisms induced by instability are neither very easy nor very common. This could be another lecture ! See the thesis of J. Griffond [9] for detailed nonlinear analysis.

# Conclusion

Undoubtedly, an intrinsic instability exists in the flow induced by wall injection. A linear stability theory can be carried out, even if it presents some difficulties (mainly from the theoretical point of view) in relation with the non parallel characteristics of the considered mean flow. At least in the plane geometry, the experimental results confirm the predictions based on the linear stability theory. However in practice, the intrinsic perturbation cannot grow infinitely in $x$, as it could be according to the linear stability results. From flow visualisations performed in VECLA, we know that large structures are emitted somewhere, they are associated to fluctuations of large amplitude and are thus not compatible with a small perturbation approach leading to the linear theory. The perturbations grow in $x$, according to the linear instability mechanism and then become fully non linear. Moreover, for some configurations the experimental results of VECLA do not seem to exhibit any instability feature. Among these results, there is the resonance on an acoustic mode of large amplitude which is of course the most important configuration in practice.

Where does this resonance phenomenon come from ? Does the stability play any role ?

In order to try to give some answers to these questions, let us summarise the main ideas (coming from the experimental results, direct simulations and nonlinear stability theories) obtained at the end of the PhD of J. Griffond. The key point is the dimensional value of the abscissa of the motor exit section $x_s^*$. It seems that the abscissa related to the instability mechanisms (location of the iso-$n$ factor curves, location of the large structure emission) are mainly constant in term of dimensionless values, with the reference scale for the distance being the radius of the fluid $h$. But for a real motor, only $x_s^*$ remains constant, the value of $h$ grows continuously thanks to the regression of the injecting wall due to the combustion.

The proposed scenario is then the following one :

- At the beginning, $h$ is small. In that case, the flow becomes turbulent somewhere in the duct, the large structures which are emitted upstream in the laminar zone are dissipated by the turbulence, so that there is no coherent (i.e. quasi periodic in time) structure which passes through the exit section. Nothing happens with respect to the cavity modes.

- Later, $h$ becomes larger, the transition to turbulence moves downstream and at a given time, the turbulence zone is not sufficient to dissipate enough the large emitted structures. The frequency associated to this emission corresponds more or less to the one of the largest amplitude of the eigenmode at the abscissa from which nonlinear phenomena start to operate. At each time that a structure passes the throat (exit section), there is an emission of a reflecting pressure wave (it has been measured in the cold gas facilities). This wave arrives at the front wall and there is another reflecting wave, but now in the downstream direction. This wave may reasonably

excite the intrinsic instability mode (by the so-called receptivity mechanism) and mainly the one corresponding to its frequency. This mode is then fully favoured : it is an intrinsically amplified mode and it starts with a larger and larger amplitude due to the reflecting waves. Rapidly only one mode comes up. Then, at least in the VECLA and VALDO facilities, there are two cases : either the dominant frequency corresponds to the one of a cavity mode or not. The frequency obtained by the instability and the reflecting waves strongly depends on the injection velocity whereas the cavity frequencies are obviously mainly independent of this injection velocity. In the second case, the reflecting waves remain linear and the physics remains governed by the instability mechanism. In the first case, the amplitudes are very large and it may be guessed that the instability plays a role only in the transient which leads to the excitation of the cavity mode.

- Finally when $h$ is large, the emission of the large structure does not occur any more in the booster, it moved downstream, only small fluctuations (the intrinsic instability modes themselves) remain and do not provide enough energy for creating reflected pressure waves.

This scenario needs of course additional confirmations but it is fully consistent with the experiment, the numerical simulations and the investigated nonlinear stability approaches.

# Acknowledgement

# Bibliography

[1] Lupoglazoff N. and Vuillot F. Parietal vortex shedding as a cause of instability for long solid propellant motors. numerical simulations and comparisons with firing tests. aiaa 96-0761. In *34th Aerospace Sciences Meeting and Exhibit.* AIAA, 15-18 janvier Reno, Nevada 1996.

[2] G. Avalon. Caractérisation des phénomènes liés à l'instabilité naturelle de l'écoulement dans le montage VECLA - Etude des conditions permettant de réaliser l'accrochage acoustique. Rapport final CNES 90/6133EY, ONERA, juillet 1997.

[3] Couton D., Plourde F., and Doan-Kim S. Cold gas simulation of a solid propellant rocket motor. *AIAA Journal*, 34:1462–1464, 1996.

[4] Avalon G., Ugurtas B., Grisch F., and Bresson A. Numerical computations and visualizations tests of the flow in a cold gas simulation with characterization of a parietal vortex-shedding. In *36th Joint Propulsion Conference and Exhibit, AIAA/ASME/ASEE, AIAA 2000-3387*, Huntsville, Alabama, 16-19 July 2000.

[5] Dunlap R., Blackner A., Waugh R., Brown R., and Willoughby P. Internal flow field studies in a simulated cylindrical port rocket chamber. *J. Propulsion*, 6, 1990.

[6] J. Anthoine. *Experimental and numerical study of aeroacoustic phenomena in large solid propellant motors.* PhD thesis, Université libre, Bruxelles, October 2000.

[7] V.N. Varapaev and V.I. Yagodkin. Flow stability in a channel with porous wall. *Izv. AN SSSR. Mekhanika Zhidkosi i Gaza.*, vol. 4, No 5, 1969.

[8] J. Griffond. Stabilité linéaire dans un conduit à parois débitantes. Effet de la régression de la paroi. Technical report, Rapport de DEA, ENSTA et Univ. P. et M. Curie, septembre 1998.

[9] J. Griffond. *Instabilité linéaire et non linéaire en conduit à parois débitantes.* PhD thesis, ENSAE, Toulouse, 21-Sept. 2001.

[10] Berman A. Laminar flow in channels with porous walls. *J. of applied Physics*, 24(9), september 1953.

[11] G. I. Taylor. Fluid flow in regions bounded by porous surfaces. *Proc. of the Royal Soc. Series A, London*, 234(1199):456–475, 1956.

[12] J. Ph. Pineau. Stabilité linéaire d'un écoulement dans un conduit cylindrique à paroi débitante. Rapport de DEA, CERT-ONERA, septembre 1997.

[13] P.G. Drazin and W. Reid. *Hydrodynamic stability.* Cambridge University, 1985.

[14] L. M. Mack. Boundary layer linear stability theory. *Special course on stability and transition of laminar flow*, 709, 1984.

[15] M. Gaster. A note on the relation between temporally increasing and spatially increasing disturbances in hydrodynamic stability. *J. of Fluid Mech.*, 14:222–224, 1962.

[16] J. Griffond, G. Casalis, and J. Ph. Pineau. Spatial instability of flow in a semiinfinite cylinder with fluid injection through its porous walls. *European Journal of Mechanics, B/Fluids*, 19, issue 1, Janvier 2000.

[17] M. Gaster. On the effect of boundary layer growth on flow instability. *J. of Fluid Mech.*, 66, 1974.

[18] D. Arnal, M. Habiballah, and E. Coustols. Théorie de l'instabilité laminaire et critères de transition en écoulement bi et tridimensionel. *La Recherche Aérospatiale*, 2, Mars - Avril 1984.

[19] G. Casalis, G. Avalon, and J. Ph. Pineau. Spatial instability of planar channel flow with fluid injection through porous walls. *Physics of Fluid*, 10(10), October 1998.

[20] G. Casalis and F. Charru. *Instabilités hydrodynamiques.* Cours du D.E.A. de mécanique des fluides de Toulouse, 1995.

[21] S. Hein, A. Hanifi, and G. Casalis. Nonlinear transition prediction. In *European Congress on Computational Methods in Applied Sciences and Engineering, ECCOMAS*, Barcelona, 11-14 september 2000.

[22] Th. Feraille. Phd, in preparation.

[23] Lee Y. and Beddini R. Acoustically-induced turbulent transition in solid propellant rocket chamber flowfields. In *35th AIAA/ASME/ASEE Joint Propulsion Conference and Exhibit, AIAA-99-2508*, Los Angeles, California, 20-24 June 1999.

[24] J. Griffond and G. Casalis. On the dependence on the formulation of some nonparallel stability approaches applied to the taylor flow. *Physics of Fluids*, 12(2), February 2000.

[25] C.M. Bender and S.A. Orszag. *Advanced mathematical methods for scientists and engineers.* McGraw-Hill, 1981.

[26] G. Casalis. *Méthodes mathématiques pour la mécanique.* Cours SUPAERO, 2000.

[27] Bridges T.J. and Morris P.J. Boundary layer stability calculations. *Physics of Fluids*, 30, november 1987.

[28] Th. Herbert and F. P. Bertolotti. Stability analysis of non-parallel boundary layers. *Bull. Am. Phys. Soc.*, 32, 1987.

[29] Ch. Airiau and G. Casalis. Stabilité linéaire de la couche limite par un système d'équations parabolique. *La Recherche Aérospatiale*, 5, Septembre-Octobre 1993.

[30] Vuillot F. Numerical computations of acoustic boundary layers in large solid propellant space booster. In *29th Aerospace Sciences Meeting*. AIAA 91-0206, Reno, Nevada, January 1991.

[31] Lupoglazoff N., Vuillot F., Dupays J., and Fabignon Y. Numerical simulations of the unsteady flow inside Ariane 5 P230 SRM booster with burning aluminium particles. In *2nd European Conference on Launcher Technology, Space Solid Propulsion*, Roma, 21-24 november 2000.

[32] Féraille T. and Casalis G. Particles effects on solid propellant motors flow stability. In *38th AIAA/ASME/SAE/ASEE Joint Propulsion Conference & Exhibit*, Indianapoli, Indiana, United States, 7-10, July 2002.

[33] Canuto C., Hussaini M., Quarteroni A., and Zang T. *Spectral methods in fluid dynamics*. Springer, 1988.

[34] M.R. Khorrami M.R. Malik R.L. Ash. Application of spectral collocation techniques to the th stability of swirling flows. *J. Comput. Physics*, vol. 81:pp. 206–229, 1989.
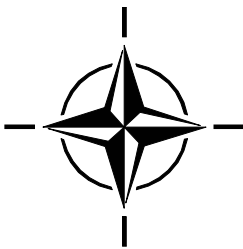
# ANNEX : Spectral collocation method for eigenvalue problem

## Description of the method

Several methods may be used for solving an eigenvalue problem or more generally any differential equations system. In the case of the plane Taylor flow, expressed in terms of stream function, equation (2.9), the simplest method is probably the spectral collocation method. In this annex, only a short view of it is given, more details together with other methods can be found in [33], an application of the spectral collocation technique in a particular stability problem is described in [34].

The goal is hence to solve the differential problem constituted by equation (2.9) and boundary conditions (2.10). The variable $y$ varies in $[-1, +1]$. Some definitions are necessary, let be first $T_n$ the $n^{\text{th}}$ Chebychev's polynomial of degree $n$. Then, an integer $N$ is assumed to be chosen, it characterises the chosen refinement for solving the differential problem, as it will be explained just below. Let be :

$$\xi_j = \cos\left(\frac{\pi j}{N}\right) \qquad j = 0, \dots, N$$

$N + 1$ points, which are called the ones of "Gauss-Lobatto". The unknown amplitude function, which will be noted $\psi$ in this annex, is approximated by the polynomial :

$$\psi(\xi) = \sum_{j=0}^{N} \lambda_j(\xi)\psi(\xi_j)$$

where $\lambda$ stands for

$$\lambda_j(\xi) = \left(\frac{1 - \xi_j^2}{\xi - \xi_j}\right)(-1)^{j+1}\frac{T_N'(\xi)}{N^2 c_j}$$

with $T_N'$ the derivative of the $N^{\text{th}}$ Chebychev's polynomial. The $N + 1$ discrete values

$$\psi_j = \psi(\xi_j)$$

are explicitly the unknown of the (discretised) problem. This is the reason why $N$ describes the used accuracy for computing the unknown. As $\psi$ is a solution of differential problem, we have now to link between the derivative $\psi'$ and the function $\psi$ itself. For this purpose, let be :

$$E_{jk} = \frac{c_j}{c_k}\frac{(-1)^{k+j}}{\xi_j - \xi_k} \qquad j \neq k$$

$$E_{jj} = -\frac{\xi_j}{2(1 - \xi_j^2)} \qquad j = 1, \dots, N - 1$$

$$E_{00} = -E_{NN} = \frac{2N^2 + 1}{6}$$

defining a square matrix $E$ with the coefficients $c_j$ given by :

$$c_0 = c_N = 2 \qquad c_j = 1 \qquad j = 1, \dots, N - 1$$

Then, it can be proved that the derivative exactly corresponds for the discrete values to the matrix multiplication by $E$ :

$$\frac{d\psi}{d\xi}(\xi_j) = \sum_{k=0}^{N} E_{jk}\psi_k$$

**Typical stability code**

Using the previous matrix multiplication as derivative operator leads to discretise the linearised stability equations into an algebraic problem for $X$ the vector of the unknowns $\psi_j$. Then, there are usually two approaches, either the complete spectrum of the discretised problem is looked for or by a shooting method a unique value of the spectrum is looked for.

**Spectrum.**   In this case, if the unknown is the complex number $\omega$, the discretised problem is written under the form :

$$A.X = \omega B.X$$

with $A$ and $B$ two matrices coming from derivation and intervention of the mean flow. All the lines of the matrices correspond to the discretisation of the continuous equations at the collocation points, for example ordered from -1 up to +1. Then the four homogeneous boundary conditions are included by substituting the first line by the condition $\hat{\psi}(-1) = 0$, the second line by $\hat{\psi}'(-1) = 0$ and the two last lines in the same way (by the boundary conditions in +1). Thus the previous algebraic problem is replaced by :

$$\tilde{A}.X = \omega \tilde{B}.X$$

The last step consists in determining the eigenvalues $\omega$ by an appropriate method.

**Shooting method.**   In this case, if the unknown is the complex number $\alpha$, the discretised problem is written under the form :

$$A(\alpha).X = 0$$

As in the previous case, each lines expresses the continuous equation written in the corresponding collocation point. The idea in this case is as before to introduce the boundary conditions, but only three. In addition, a non homogenous one is introduced, for example a condition on the pressure (or the second derivative of $\hat{\psi}$). This non homogeneous condition acts as a normalisation condition. The previous problem is then replaced by :

$$\tilde{A}(\alpha).X = b$$

The next step consists in inverting $\tilde{A}(\alpha)$ and thus in determining $X$. Then, the omitted boundary condition is examined and in fact all the described procedure is included into a loop : $\alpha$ is searched until the omitted boundary condition is satisfied.

## Code written in Matlab

A small program written using the commercial software Matlab is given below. The five routines are organised as described in figure 4.5. The main program is called "OrrSom". The initialisation defines the collocation points and the matrix used for the derivation. Then, it is possible to compute the whole spectrum of the linearised operator, this is achieved in the routine "spectre". Alternatively, the shooting method can be used, the initial guess is given in the main program, the routine "balai" defines possible parametric computations (by varying regularly one parameter among the Reynolds number, the frequency and the abscissa). This routine uses the one named "Newton" whose goal is to determine the eigenvalue by a standard Newton iterative procedure.
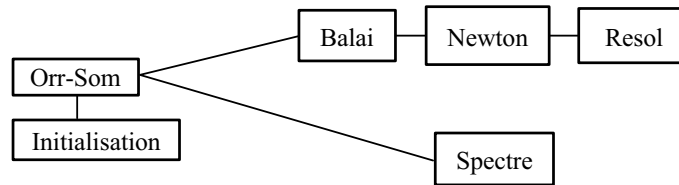
Figure 4.5: Representation of five Matlab routines for solving a stability problem with the spectral collocation method either with a shooting method (upper line "Balai - Newton - Resol") or by determining the whole spectrum (lower line "Spectre")

Each resolution of the stability equation called by "Newton" is performed thanks to the routine "Resol".

**Main program : orrsom.m**

```
%
% Programme principal ORRSOM.m
%
% résolution du problème de stabilité linéaire
% pour l'écoulement dans un conduit plan à parois débitantes.
%   perturbation en forme de mode normal,
%   formulation en fonction de courant
%
%
global npol xi e id alpha omega reynolds csol type_calcul xloc;
%
% valeurs de départ
%2.48746e-001 9.70805e-001
reynolds = 1000;
xloc = 10;
omega = 31.6;
alpha = complex(4.0158,-0.373);
%
type_calcul = 'spectre';
%
initialisation;
%
switch lower(type_calcul)
    case 'balai'
        balai;
    case 'spectre'
        spectre;
    otherwise
        disp('Orr-Som, non implémenté')
end
```

Subroutine : initialisation.m

```
%
% Sous-programme initialisation.m
%
% Initialisation dans la méthode de collocation spectrale
%  npol est le nombre de points de collocation
%  e    est la matrice de dérivation
%  id   est la matrice identité
%  xi   est le vecteur des points de collocation
%
global npol xi e c id;
%
% Préliminaires
%
npol = 100;
iaff = 0;
xi = zeros(npol,1); c = zeros(npol,1); id = zeros(npol,npol); e = zeros(npol,npol);
%
% Calcul du vecteur xi et du vecteur technique c
%
for j = 0:npol
    j1 = j+1;
    xi(j1,1) = cos(pi*j/npol); c(j1,1) = 1;
end
id = diag(c,0);
c(1,1)=2; c(npol+1,1)=2;
%
% Calcul de la matrice e
%
for j = 0:npol
    j1 = j+1;
    for k = 0:npol
        k1 = k+1;
        if (k~=j)
            e(j1,k1) = c(j1,1)*(-1)^(k+j)/(c(k1,1)*(xi(j1,1)-xi(k1,1)));
        else
            if (j~=0 & j~=npol)
                e(j1,j1) = -xi(j1,1)/(2*(1-xi(j1,1)*xi(j1,1)));
            end
        end
    end
end
e(1,1) = (2*npol*npol+1)/6; e(npol+1,npol+1) = -(2*npol*npol+1)/6;
```

Subroutine : spectre.m

```
%
```

```
% Sous-programme spectre.m
%
%  Détermination du spectre de l'opérateur d'Orr-Sommerfeld
%    on écrit le probleme sous la forme :
%          mat1.v = omega . mat2.v
%
% Paramètres
%
global npol xi e id alpha omega reynolds csol type_calcul vp xloc;
%
% initialisation
%
e2 = zeros(npol,npol); mat1 = zeros(npol,npol); mat2 = zeros(npol,npol) ;
ci = complex(0,1); e2=e*e ; e3=e2*e ;
%
% écoulement de base
%
u = pi*xloc*cos(pi*xi/2)/2; ddu = e2*u;
v = -sin(pi*xi/2); ddv = e2*v;
%
% remplissage des matrices mat1 et mat2
%
for i = 0:npol
    i1 = i+1;
    for j=0:npol
        j1=j+1;
        mat1(i1,j1) = -ci*alpha*(ddu(i1)+alpha*alpha*u(i1))*id(i1,j1);
        mat1(i1,j1) = mat1(i1,j1)+ci*alpha*u(i1)*e2(i1,j1);
        mat1(i1,j1) = mat1(i1,j1)-(alpha*alpha*v(i1)+ddv(i1))*e(i1,j1);
        mat1(i1,j1) = mat1(i1,j1) + v(i1)*e3(i1,j1);
    end
end
z1 =-1/reynolds; z2 = 2*alpha*alpha/reynolds ; z3 = -alpha.^4/reynolds;
mat1 = mat1 + z1*e2*e2 + z2*e2 + z3*id ;
mat2 = -ci*(alpha*alpha*id-e2) ;
%
% Conditions aux limites
%
for i = 0:npol
    i1=i+1;
    mat1(1,i1) = 0;mat2(1,i1) = 0;
    mat1(2,i1) = e(1,i1);mat2(2,i1) = 0;
    mat1(npol,i1) = e(npol+1,i1); mat2(npol,i1) = 0;
    mat1(npol+1,i1) = 0; mat2(npol+1,i1) = 0;
end
mat1(npol+1,npol+1) = 1; mat1(1,1) = 1;
%
```

```
% calcul des valeurs propres (généralisées)
%
bmat = eye(size(mat1));
l = eig(mat1,mat2);
%
% représentation graphique
%
plot(real(l),imag(l),'ob','MarkerSize',6,'MarkerFaceColor','b')
axis([0 100 -10 5])
```

## Subroutine : balai.m

```
%
% Sous-programme balai.m
%
% calcul de valeurs propres avec Newton par variation de l'un des paramètres
%
% Ce paramètre peut etre :
%   le nombre de Reynolds
%   la position en abscisse
%   la fréquence
%
%
global alpha omega reynolds xloc;
%
% Valeurs initiales pour la variation
%
type_balai = 'reynolds';
nparam = 1; dparam = 100;
%
% Lecture du fichier où sont écrites les valeurs précédentes
%
fid = fopen('C:\GREG\ONERA\SPADA\StabMatlab\varirey.txt','a+');
%
[vect,count] = fscanf(fid,'%f %f %e %e %e',inf);
nligne = count/5; indice = 5*(nligne-1);
reynolds = vect(indice+1); xloc = vect(indice+2);
omega = vect(indice+3);
alpha = complex(vect(indice+4),vect(indice+5));
%
% Valeurs pour démarrer le calcul
%
alphainit = alpha; omegainit = omega;
reynoldsinit = reynolds; xlocinit = xloc;
%
% Variation suivant le paramètre choisi
%
switch lower(type_balai)
```

```
    case 'frequence'
        domega = dparam; dreynolds = 0; dxloc = 0;
    case 'abscisse'
        domega = 0; dreynolds = 0; dxloc = dparam;
    case 'reynolds'
        domega = 0; dreynolds = dparam; dxloc = 0;
    otherwise
        disp('non implémenté (ou erreur) dans balai')
end
%
%  Boucle pour la variation du paramètre choisi
%
for iparam = 1:nparam
    omega    = omegainit    + (iparam-1)*domega;
    reynolds = reynoldsinit + (iparam-1)*dreynolds;
    xloc     = xlocinit     + (iparam-1)*dxloc;
    %
    % Estimation des valeurs initiales
    %
    switch lower(iparam)
    case 1
        alpha = alphainit;
    case 2
        alpha = alpha1;
    case 3
        alpha = 2*alpha2 - alpha1;
    otherwise
        alpha = 3*(alpha3-alpha2) + alpha1;
    end
    %
    % Appel à la convergence, méthode de Newton
    %
    newton;
    %
    % Stockage des au plus 3 dernières valeurs convergées
    %
    switch lower(iparam)
    case 1
        alpha1 = alpha;
    case 2
        alpha2 = alpha;
    case 3
        alpha3 = alpha;
    otherwise
        alpha1=alpha2; alpha2=alpha3; alpha3=alpha;
    end
    %
```

```
    % Affichage écran des résultats
    %
    fprintf('iparam = %d, R = %0.1f, X = %0.1f, w = %0.5e, ar = %0.5e, ai = %0.5e\n\n\n',...
        iparam,reynolds,xloc,omega,real(alpha),imag(alpha))
    %
    % Ecriture sur fichier des résultats
    %
    fprintf('\n')
    fprintf(fid,'%0.1f %0.1f %0.5e %0.5e %0.5e \n ',...
        reynolds,xloc,omega,real(alpha),imag(alpha));
end
%
status = fclose(fid);
```

## Subroutine : newton.m

```
%
% Sous-programme Newton.m
%
% Méthode de Newton complexe pour
%  résoudre csol = 0, alpha est l'inconnue complexe
%
global npol xi e id alpha omega reynolds csol type_calcul;
%
% Initialisation Newton
%
dval = 1E-4;
err = 1;
it = 0;
alphan = alpha ;
%
% Méthode de Newton (utilisation des relations de Cauchy)
%
while (err > 1E-08 & it < 10)
   it = it + 1;
   alpha = alphan;
   resol; csol0 = csol ;
   alpha = alphan + dval;
   resol; csolm = csol;
   dcsol = (csolm-csol0)/dval; cor = csol0/dcsol;
   err = abs(cor)/abs(alphan);
   alphan = alphan - cor;
end
if (err > 1E-06)
    disp('problème Newton')
    break
end
```

Subroutine : resol.m

```
%
% Sous-programme resol.
%
% On ecrit Orr-Sommerfeld sous la forme mat.X = b
%
%    e2  : matrice de dérivée seconde e2 = e*e
%
global npol xi e id c alpha omega reynolds csol xloc;
%
% initialisation
%
b = zeros(npol,1); e2 = zeros(npol,npol); mat = zeros(npol,npol);
e3 = zeros(npol,npol);
ci = complex(0,1); e2=e*e; e3=e2*e;
%
% écoulement de base
%
u = pi*xloc*cos(pi*xi/2)/2; ddu = e2*u;
v = -sin(pi*xi/2); ddv = e2*v;
%
% remplissage de la matrice mat
%
for i = 0:npol
    i1 = i+1;
    for j=0:npol
        j1=j+1;
        mat(i1,j1) = -ci*alpha*(ddu(i1)+alpha*alpha*u(i1))*id(i1,j1);
        mat(i1,j1) = mat(i1,j1)+ci*alpha*u(i1)*e2(i1,j1);
        mat(i1,j1) = mat(i1,j1)-(alpha*alpha*v(i1)+ddv(i1))*e(i1,j1);
        mat(i1,j1) = mat(i1,j1) + v(i1)*e3(i1,j1);
        mat(i1,j1) = mat(i1,j1) -ci*omega*e2(i1,j1) ;
    end
end
z1 =-1/reynolds; z2 = 2*alpha*alpha/reynolds ;
z3 = -alpha.^4/reynolds + ci*omega*alpha*alpha ;
mat = mat + z1*e2*e2 + z2*e2 + z3*id ;
%
% conditions aux limites
% on écrit psi"(1) = 1, psi'(1) = 0, psi'(-1) = 0, psi(-1) = 0
%
for i = 0:npol
    i1=i+1;
    mat(1,i1) = e2(1, i1);
    mat(2,i1) = e(1,i1);
    mat(npol,i1) = e(npol+1,i1);
    mat(npol+1,i1) = 0;
```

```
        b(i1) = 0;
    end
mat(npol+1,npol+1) = 1; b(1) = 1;
%
% inversion
%
sol_v = mat\b ;
%
% si iaff=0, c'est Newton sur v(1), sinon affichage de la fonction propre
%
iaff = 0;
if (iaff == 0)
    csol = sol_v(1);
else
    sol_dv = e*sol_v;
    plot(xi,abs(sol_v),xi,abs(sol_dv),'LineWidth',2)
    set(gca,'DefaulttextFontName','Times New Roman');set(0,'DefaulttextFontSize',14);
    xlabel('{\it y}','FontName','Times New Roman','FontSize',16);
    ylabel('{\it u,v}','FontName','Times New Roman','FontSize',16);
    legend('u','v',0);
end
```

# Numerical Modeling of Internal Flow Aerodynamics
## Part 1: Steady State Computations

**Jean-François Guéry**
SNPE Propulsion
Centre de Recherche du Bouchet
F-91710 Vert-le-Petit
FRANCE

## NOTATIONS

| | | | |
|---|---|---|---|
| $E$ | total energy per unit of mass (J/kg) | $T_f$ | propellant flame temperature (K) |
| $F$ | convective flux vector in the x direction | $u$ | velocity component in the $x$-longitudinal direction (m/s) |
| $G$ | convective flux vector in the y direction | | |
| $H$ | convective flux vector in the z direction | $u_v$ | axial mean velocity (m/s) |
| $S$ | source term vector | $v$ | velocity component in the $y$-lateral direction (m/s) |
| $k$ | turbulent kinetic energy | | |
| $\dot{m}_w$ | mass flow rate per injecting surface unit (kg/m$^2$) | $v_{inj}$ | wall injection velocity (m/s) |
| | | $w$ | velocity component in the $w$-lateral direction (m/s) |
| $P$ | pressure (Pa) | | |
| $P'$ | fluctuating pressure (Pa) | $x,y,z$ | co-ordinate system (m) |
| $Q$ | conservative variables vector of Navier-Stokes equations | $\varepsilon$ | turbulent dissipation rate |
| $q_m$ | total mass flow rate (kg/s) | $\kappa$ | thermal conductivity (W/mK) |
| $r_b$ | burning rate (mm/s) | $\mu$ | dynamic viscosity (kg/ms) |
| $T$ | temperature of the flow (K) | $\rho$ | density (kg/m$^3$) |
| | | $\rho_s$ | propellant density (kg/m$^3$) |

**Dimensionless Parameter**

$Re_c$    axial Reynolds number: $\rho\, u_v\, D_c/\mu$, where D$_c$ is a characteristic diameter of the SRM

$Re_s$    wall injection Reynolds number: $\rho\, v_w\, D_c/\mu$

$\gamma$    isentropic exponent, equal to the specific heat ratio for a perfect gas

## INTRODUCTION [1]

Internal ballistics in a SRM can be solved with various ways and for various objectives [2]. The motor design engineer wants to predict or understand the burning characteristics and the global performances of the motor, seek the efficiency of thermal insulation and nozzle design, check the reliability of ignition and motor design for the life cycle of the motor, take into account variability induced by manufacturing processes, etc.

Different ways can be followed to reach the same goal. The reasons why a project manager uses numerical simulations are multiple. In the predictive mode, the aim is to design the system which fulfils the specifications at the lowest development cost (by minimizing the number of prototypes and tests). In the explanatory mode, the desire is to explain an observed and unknown phenomenon that happened during the development phase of a program.

For solid rocket motors, the objectives of internal flow computations are to predict the global performance and reliability of the rocket, avoid, minimize or master undesired behaviors (like thrust oscillations, erosive burning), take into account flow/grain and casing interactions (mechanical and thermal loads), etc.

The internal aerodynamics inside a solid rocket motor can be modeled with increasing degrees of complexity from the simplest global equations to a full 3D numerical simulations. An AGARD Lecture Series has already been organized on the Design Methods in Solid Rocket Motors [3]. The objective of this special course is not to duplicate the materials developed in AGARD-LS-150. We will focus on multidimensional simulations of internal flows.

Example of objectives and constraints:

- assessment of stability

- prediction of performances

- prediction of reliability

- prediction of variability, for instance thrust imbalance (important when using simultaneously more than one identical motor)

Conception:

- choose the right propellant for the application, and design the initial geometry of the solid propellant charge that will deliver, with surface regression, the required time history of the gas flow

- assess reliability of the designed motor (mechanical loads, ignition, casting process and raw materials variability, thrust oscillations, …)

Challenges of numerical modeling:

- two-phase reacting flow (aluminized propellants)

- gas in a wide range of temperatures

- multi-species and turbulence

- two or three dimensional geometry

- moving boundaries

- fluid/structure coupling, with heterogeneous surface combustion

- steady and unsteady compressible flows, with all range of Mach number

The impact of numerical modeling in designing motors of new generation had a recent increase due to mainly three causes:

- large progress of computer power (hardware) and in computational fluid dynamics (software) in the last decades

- objective of cost reduction (mainly in the development phase of a new motor)

- new objectives of performance and reliability

An improved prediction reduces the number of qualifying fires, and for large and expensive motors, this is of prime importance.

This lecture series will be divided in two special courses. The first one presents the general models for solving internal steady state aerodynamic in solid rocket motors, the second one focus on pressure and thrust oscillations modeling.

## GENERAL EQUATION FOR AERODYNAMICS

At a starting point, the general equations describing fluid flows inside a solid rocket motor begins with the Navier-Stokes equation. We remind them as an introduction.

The general form of the conservation equations for a three dimensional viscous flow can be written in the following form:

$$\frac{\partial Q}{\partial t} + \frac{\partial F}{\partial x} + \frac{\partial G}{\partial y} + \frac{\partial H}{\partial z} = S$$

where:

$$Q = \begin{bmatrix} \rho \\ \rho u \\ \rho v \\ \rho w \\ \rho E \end{bmatrix}$$

$$F = \begin{bmatrix} \rho u \\ \rho u^2 + P - \sigma_{xx} \\ \rho uv - \sigma_{xy} \\ \rho uw - \sigma_{xz} \\ (\rho E + P)u - u\sigma_{xx} - v\sigma_{xy} - w\sigma_{xz} - \kappa\frac{\partial T}{\partial x} \end{bmatrix}$$

$$G = \begin{bmatrix} \rho v \\ \rho uv - \sigma_{xy} \\ \rho v^2 + P - \sigma_{yy} \\ \rho vw - \sigma_{yz} \\ (\rho E + P)v - u\sigma_{xy} - v\sigma_{yy} - w\sigma_{yz} - \kappa\frac{\partial T}{\partial y} \end{bmatrix}$$

$$H = \begin{bmatrix} \rho w \\ \rho uw - \sigma_{xz} \\ \rho vw - \sigma_{yz} \\ \rho w^2 + P - \sigma_{zz} \\ (\rho E + P)w - u\sigma_{xz} - v\sigma_{yz} - w\sigma_{zz} - \kappa \dfrac{\partial T}{\partial z} \end{bmatrix}$$

and $S$ is the source term vector.

These equations must be solved with appropriate solvers and on appropriate grids.

Over the last twenty years, different grid technologies have been developed. Based on experience on finite difference schemes and for the sake of simplicity in software management, structured grids have been widely used. A structured grid is a grid where each component can be identified by two indices (i,j) in 2D and three indices (i,j,k) in 3D. Each index refers to a space dimension. Hence, the grid points are ordered, giving the name of "structured grid". However, this technology was shown very precise and efficient for a simple geometry but limited for a complex geometry. Techniques of multiple structured domains overlapping have been developed, but with special difficulties for ensuring global conservation among the different domains and a good efficiency on distributed memory parallel computers.

For an unstructured flow solver, the computational domain is tessellated using a grid composed of simplices, which are quadrilaterals or triangles in two dimensions and generally tetrahedras, pyramids, pentagons, prisms and hexahedras in three dimensions. Unstructured grids provide flexibility for tessellating about complex geometry and for adapting to flow features, such as shocks and boundary layers.

On a given grid, one has the option of locating the variables at the cell centers or at the vertices of the grid, giving rise to cell-centered and cell-vertex schemes. Alternatively, it is possible to deal strictly with averages defined over volumes. This approach has certain advantages for higher order schemes. In the case of finite volume schemes, the governing equations are discretized. This allows discontinuities to be captured as part of the solution.

## SOLID PROPULSION MODELS

General modern CFD codes for computing flows in solid rocket motors have the following features:

- solves the 2D axisymmetrical, plane and 3D Navier-Stokes equations for laminar or turbulent flows

- uses unstructured meshes for complex geometry treatment

- has the possibility for treating the chemical reactions of multi-species and the coupling between a gas phase and a condensed phase, inert or not, with specific models

- has moving mesh facilities

- incorporates specific solid propulsion models for the burning rate, from simple laws (regression rate) to several coupling (ignition, erosive burning, unsteady combustion) as well as solid propellant grain coupling (mechanical, surface-burnback).

# COMBUSTION AND EROSIVE BURNING

Erosive burning is a phenomenon commonly experienced in a solid propellant rocket motor, represented by an increase of the local propellant burning rate due to high velocity combustion gas flow across the burning surface. Most propellants have a minimum cross-flow velocity below which erosive burning is not observed, referred to as the "threshold velocity".

The erosive burning mechanism is believed to be due to the:

- increase in gas-to-solid heat feedback caused by the increase in transport coefficients

- turbulence-enhanced mixing and chemical reaction of the oxidizer and fuel rich gases pyrolized for composite propellants

Steady combustion is a complex mechanism including chemical and physical effects (nature and details of energetic materials and additives, particle size distribution, operating conditions: pressure, initial temperature, radiation, …). For erosive burning, the cross-flow velocity (parallel to the solid propellant burning surface) constitutes an additional operating condition of extreme importance.

Several theoretical approaches have been reported, which can be grouped in five categories, following Kuo and coworkers [4]:

1) phenomenological heat transfer theories

2) modification of the propellant combustion mechanism

3) integral boundary layer analysis

4) chemically reacting turbulent boundary layer analysis

5) others

We focus on models 1 and 4. Models in the category 1 will have an interest for engineering design problems while models in the category 4, relying on more fundamental viewpoint, are thought to be more precise and thus more appropriate for being incorporated in complex CFD codes.

## Phenomenological Heat Transfer Theories

Most of these models are based on or derived from Lenoir & Robillard [5] approach, giving the general expression for the burning rate in the form:

$$r_b = aP^n + \frac{\alpha G^g}{f(D_h)} e^{-\frac{\beta \rho_s r_b}{G}}$$

where $\alpha$, $\beta$ and $g$ are three constants, $G$ is the mass flux through the port, and $D_h$ is the hydraulic diameter. The expression $f(D_h)$ can include scale effects. In the original form, $f(D_h)=D_h^{0.2}$, $\beta=53$ is found to be independent of the propellant type, and $g=0.8$ (based on Chilton-Coburn correlation for evaluating the convective heat transfer coefficient ).

This approach is well suited for 1D analysis.

## Chemically Reacting Turbulent Boundary Layer Analysis

These models are well suited to aerothermochemical analysis of erosive burning of composite propellants, and many authors have contributed (King [6], Beddini, Kuo, and people from ONERA). We will focus on ONERA approach [7,8] used at SNPE.

The turbulent flow is solved in a high Reynolds approach and the propellant surface is treated as a wall zone. In this region, Couette equations are solved, from the propellant surface to the first integration point of the flow in the port. The temperature gradient in the flame is then computed, leading to the heat flux to the surface. A flame height criterion is used, assuming that the combustion between oxidizing and fuel gases is limited by the diffusion (valid for medium and large AP sizes). In the erosive regime, the solution of the Couette flow is coupled with the flame height criterion, including the turbulent contribution. This coupled system is solved in an iterative way, until the velocity and temperature profiles match the values of the first integration point in the flow. At convergence, the erosive burning rate is immediately obtained.

Since it is driven by viscous effects, the erosive burning in a SRM will be sensitive to the scale of the motor.



a) Scale effect on the flame zone
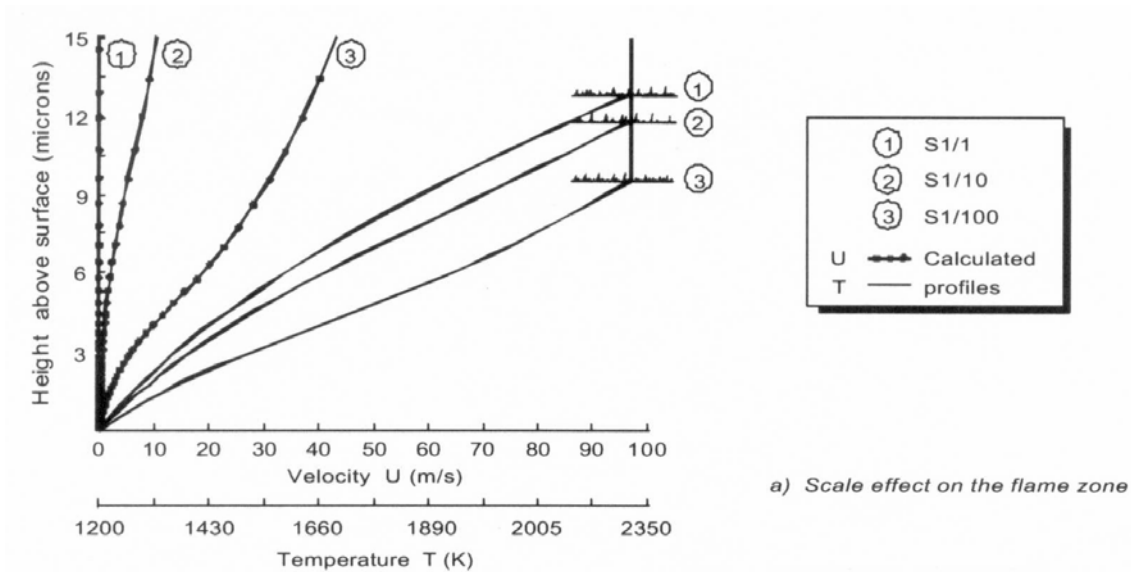
**Figure 1: Flame Zone Computed by the ONERA Model at Different Scales (1, 1/10 and 1/100).**
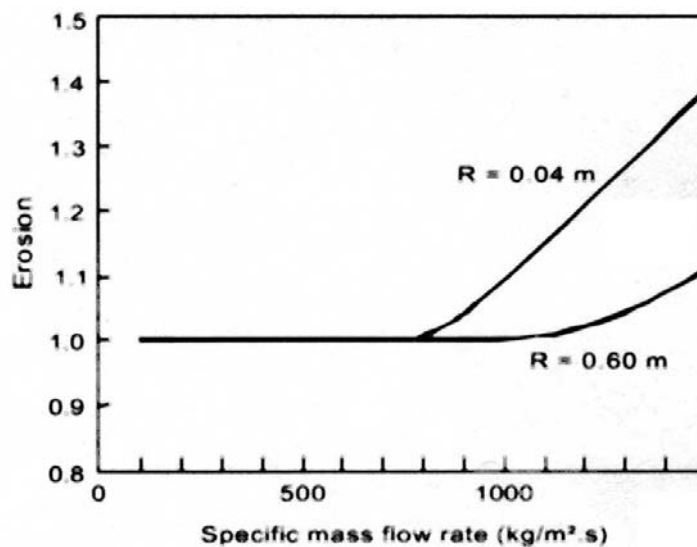


**Figure 2: Erosive Behavior as a Function of the Motor Scale (ONERA Model).**

c) Erosive mass flow rate threshold as from the model
and various small scale experiments
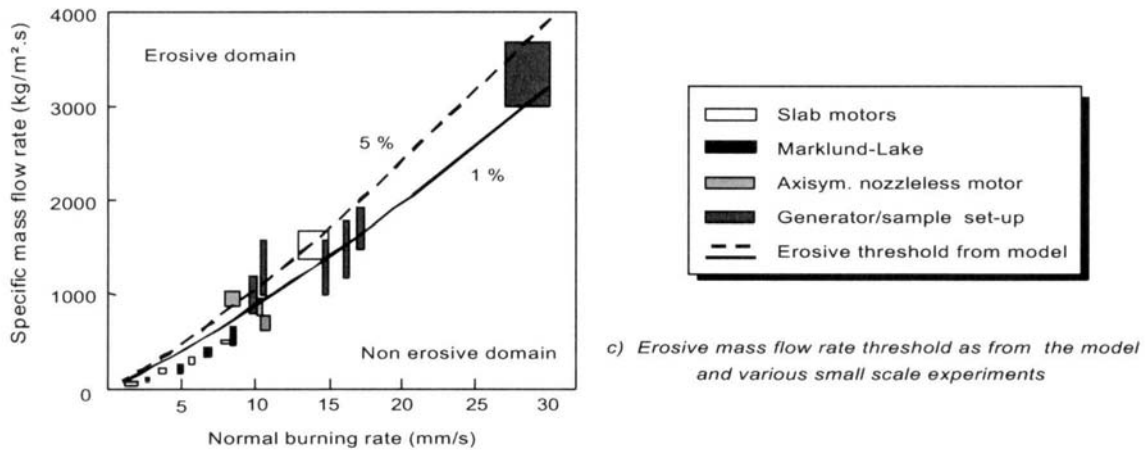
**Figure 3: Erosive Threshold in Various Configurations (ONERA Model).**

## TURBULENCE

Turbulence modeling in the port becomes necessary for the evaluation of heat transfer and/or diffusion related phenomena (erosive burning, heat flux over thermal inhibitors and material decomposition, …).

Cold flow experiments with wall injection have shown that this kind of flow have a delayed turbulent transition, as illustrated on Figure 4. The important parameter is the injection Reynolds number (defined with injection velocity at the blowing surface and port radius). For injection Reynolds number above 50, the transition from a laminar to a turbulent flow is delayed.
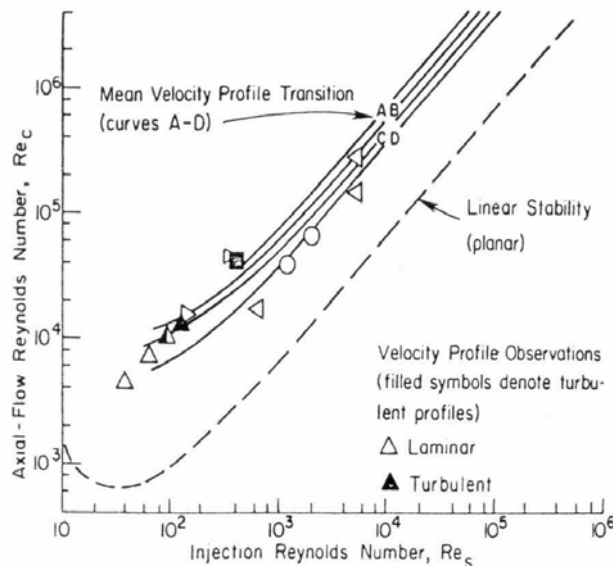


**Figure 4: Laminar / Turbulent Transition as a Function of the Injection Reynolds Number.**

The difficulty in simulating turbulence in a SRM comes from the fact that the transition is always inside the port, since the velocity at the head-end is equal to zero. So, turbulence modeling must compute correctly the transition. A schematic view of laminar-turbulence interaction is given in Figure 5.
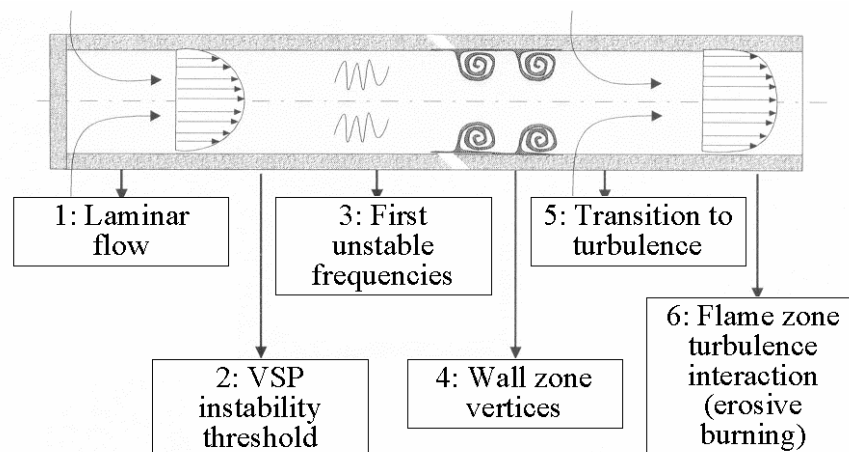
**Figure 5: Schematic View of Laminar-Turbulence Transition in a SRM.**

Usually, classical turbulence models are used for internal flows in SRM. As in the usual treatment of turbulence, the velocity field *u* and pressure *P* are decomposed into mean *u, P* and fluctuating *u', P'* parts with Favre's average for compressible flows.

Two-equation models, like the *k-ε* model, solves transport equations for the turbulent kinetic energy *k* and the dissipation rate *ε*. Source terms (S) are accounted for modeling turbulence creation and dissipation. The eddy viscosity is expressed as a function of $k^2/\varepsilon$ and the Boussinesq hypothesis is used for computing the turbulent stresses.

Classical *k-ε* turbulence models are isotropic, and this hypothesis is very restrictive for flows in SRM. Anisotropic turbulence models, like Algebraic Stress Models (ASM) are an efficient way for improving turbulence modeling without a dramatic CPU increase.

Flow turbulence modeling must always be associated with a consistent injection modeling. As the difficulty is in predicting turbulence transition, the flow features must be well described at injection. This can be done by solving the boundary zone with Couette or Prantl equations, as for the erosive burning modeling, or with approximated laws [9].
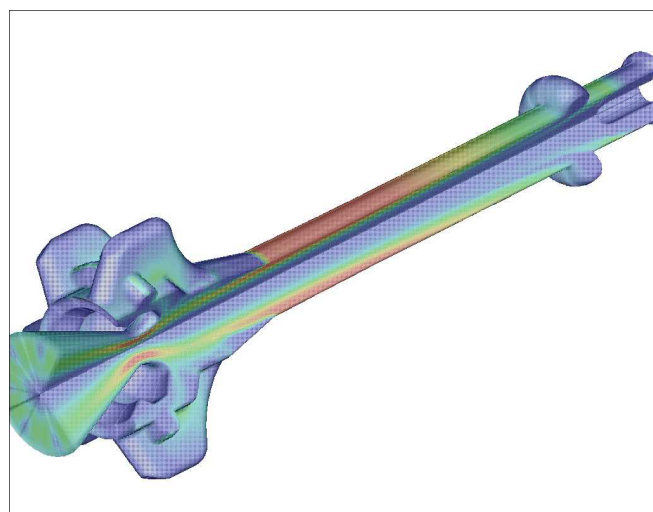


**Figure 6: Computation of Turbulence Level in a Finocyl SRM (SNPE).**

## TWO-PHASE FLOW EFFECTS

Many solid rocket motors use aluminized propellants in order to improve their performances. The aluminum combustion produce a condensed phase (aluminum oxide), and therefore a two-phase flow in the rocket chamber.

An important consequence of the presence of this liquid phase is two-phase losses, and in the case of large segmented motors with a submerged nozzle, slag accumulation, which may have several consequences on specific impulse, thermal insulation behavior and thrust vectoring.

Continuous efforts have been done, for many years, in the USA, in Russia and in France, in order to develop numerical models able to predict accurately losses and the slag formation.

More details can be fond in Salita special course [10].

An eulerian or a lagrangian description can be used for the condensed phase.

In the eulerian description, the condensed phase is assumed to be a continuous medium, and the conservation equation are derived from integrals of conservative quantities (mass, momentum and energy) on control volumes. The following vectors are added to the gas phase vector in the previous form of the conservation equation [11]:

$$Q_p = \begin{bmatrix} \rho_p \\ \rho_p u_p \\ \rho_p v_p \\ \rho_p w_p \\ \rho_p E_p \end{bmatrix}$$

$$F_p = \begin{bmatrix} \rho_p u_p \\ \rho_p u_p{}^2 \\ \rho_p u_p v_p \\ \rho_p u_p w_p \\ (\rho_p E_p) u_p \end{bmatrix} \quad G_p = \begin{bmatrix} \rho_p v_p \\ \rho_p u_p v_p \\ \rho_p v_p{}^2 \\ \rho_p v_p w_p \\ (\rho_p E_p) v_p \end{bmatrix} \quad H_p = \begin{bmatrix} \rho_p w_p \\ \rho_p u_p w_p \\ \rho_p v_p w_p \\ \rho_p w_p{}^2 \\ (\rho_p E_p) w_p \end{bmatrix}$$

and the source term S account for gas-condensed phase interactions. In these expressions, subscript $_p$ refers to the particulate phase. The volume fraction of the dispersed phase is noted $\alpha_p$ and is supposed to be small (for being neglected in the gas phase equations). Apparent condensed phase density, $\rho_p$, is equal to $\rho_p = \alpha_p \varrho_p$ where $\varrho_p$ is the condensed phase true density.

The eulerian method is well suited for particles with a fixed diameter. Generally, aluminum oxide particle show a bi or trimodal distribution after aluminum combustion (resulting from smoke, nominal aluminum residues and agglomerated aluminum residues). According to its small size and relaxation time, the smoke can be treated with the equivalent gas. Generally, one or two classes (diameter) or particles are used in the computation. Even if it is possible in the eulerian form, for coupling the particle velocity field with turbulence or taking into account complex phenomena such as coalescence or break-up, the lagrangian method is more appropriate.

In the lagrangian method, group of particles are emitted from the propellant surface and are explicitly followed in the flow. It allows more complex physics to be taken into account since it approaches the "discrete form" of the condensed phase, but the lagrangian method is CPU time consuming for a correct treatment of the flow (approaching the apparent particle density in the flow).
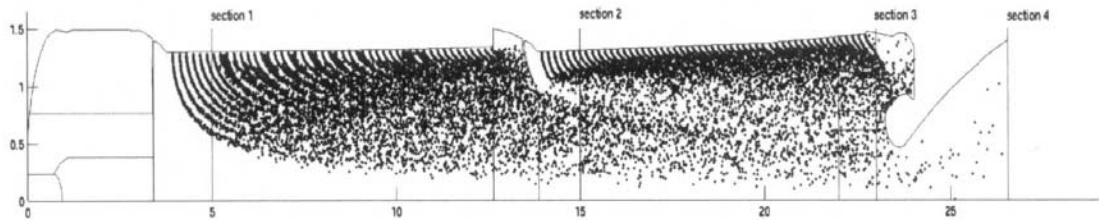


**Figure 7: Lagrangian Computation of the Two-Phase Flow in Ariane 5 SRM [13].**

## Two-Phase Losses

These losses are created by the non equilibrium between gas and condensed phase from the chamber to the throat. In the converging part of the nozzle, the flow is accelerated and the condensed phase is accelerated by the flow. An important parameter will be the ratio of condensed phase relaxation time over the transit time in the nozzle. If we note $R$ this ratio:

- for small $R$, the particles are in equilibrium with the gas, they are accelerated and give their thermal energy (temperature) to the gas, contributing to the impulse;

- for large $R$, particles will be in non-equilibrium with the gas, and an impulse deficit will be created.

Additional phenomena to take into account are particles break-up and phase changes.

## Investigation of the Slag Formation [12]

Slag is generated, either when aluminum oxide droplets impinge on some portion of the back-face of the nozzle, or when they are captured in the recirculation zone behind the submerged nozzle. This phenomenon generally produces a slag pool in the aft end of the motor and an aluminum oxide liquid film on some part of the nozzle wall.
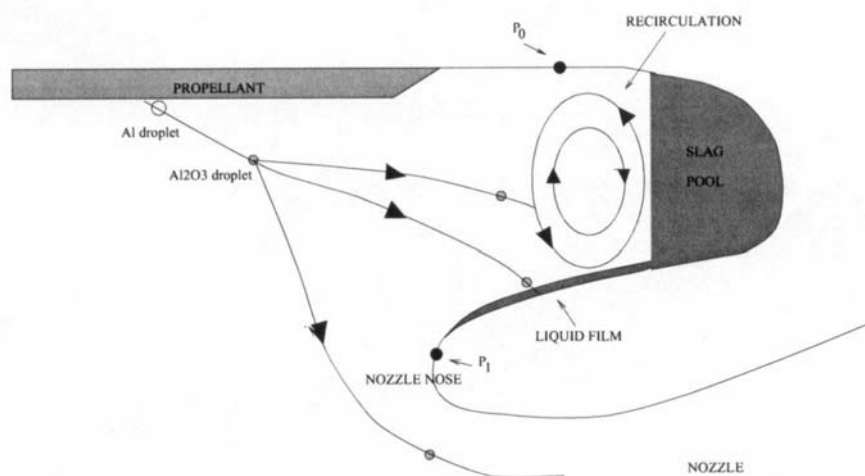


**Figure 8: Schematic View of Main Phenomena Leading to Slag Formation.**

Different strategies can be applied to the slag formation investigation: a fully coupled numerical computation, or a two step, uncoupled, computation.

The principle of a two-step uncoupled calculation can be summarized as follows [13]:

1) The steady state of the gas flowfield must be calculated with an appropriate turbulence model; the presence of the liquid phase must be taken into account by assuming that the two phases are at equilibrium everywhere in the booster (same temperature, same velocity and constant density ratio deduced from the propellant composition), using the equivalent gas (see chapter on thermochemistry).

2) The condensed phase consists only of aluminum oxide droplets, ejected directly from the propellant surface; when the combustion zone is small compared to motor geometry, no combustion model need to be used; the droplet size distributions, used in the simulations, must follow the experimental distribution, measured with a quench bomb.

3) If the motion of the droplets is simulated by a Lagrangian method, all the trajectories are calculated on the steady gas flowfield and a stochastic model can be used to take into account the influence of the turbulence field on the droplet dispersion.

4) The total slag rate can be calculated by summing the weights of all the droplets which impinged the nozzle back-face in the stagnation zone or which are trapped in the recirculation zone in the aft end of the motor.

If the motor is unstable, a coupling may exists between vortex-shedding and particles behavior in the flow. In that particular case, an unsteady computation of this coupling is necessary [14].



**Figure 9: Computation of the Coupling between Vortex-Shedding and Two-Phase Flow in an Unstable Segmented Solid Rocket Motor (Particles Volume Fraction).**

## THERMOCHEMISTRY

Since the flame zone in SRM is very small compared to motor length, we can consider that the injected gas from the burning surface are the final combustion products.

Generally, their thermochemical properties are computed from equilibrium computer codes, most of them based on the original Gordon and Mc Bride CEC71 code [15]. Since classical computations are done with constant thermodynamic properties, the validity of assumptions made for computing them must be checked. Classically, two thermodynamic parameters are taken: the frozen heat capacity and $\gamma$ in the motor. As an illustration, the evolution of the frozen heat capacity of a composite solid propellant is given as a function of the Mach number in a SRM (from the chamber to the throat) in Figure 10.
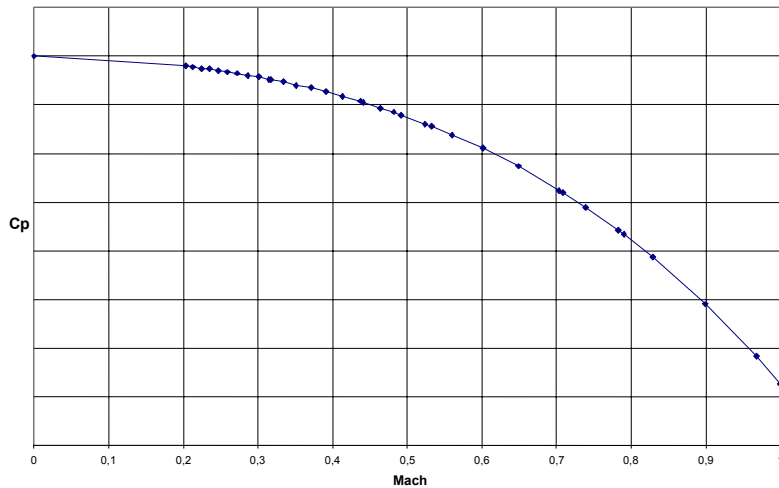
**Figure 10: Example of the Evolution of the Heat Capacity with
the Mach Number in the Convergent Part of a Nozzle.**

Another approximation can be made by writing the combination of Saint-Venant and enthalpy conservation equation:

$$T_f = T(1 + \frac{\gamma - 1}{2} M^2)$$

and using this equation at the throat (M=1) for computing an approximated γ with the value of the temperature at the throat computed by the thermodynamical code.

This equation also shows that temperature and velocity or pressure and density are correlated in a SRM, and that temperature and pressure are independant.

The other thermodynamic parameter, for instance the specific heat capacity, can be adjusted for giving the correct characteristic velocity c*, hence the correct pressure.
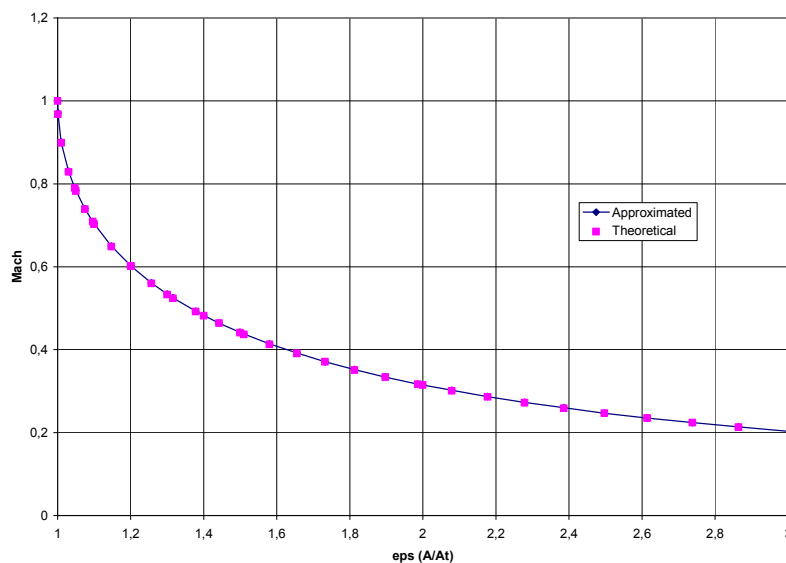


**Figure 11: Comparison of Theoretical and Approximated Pressure in a Nozzle.**
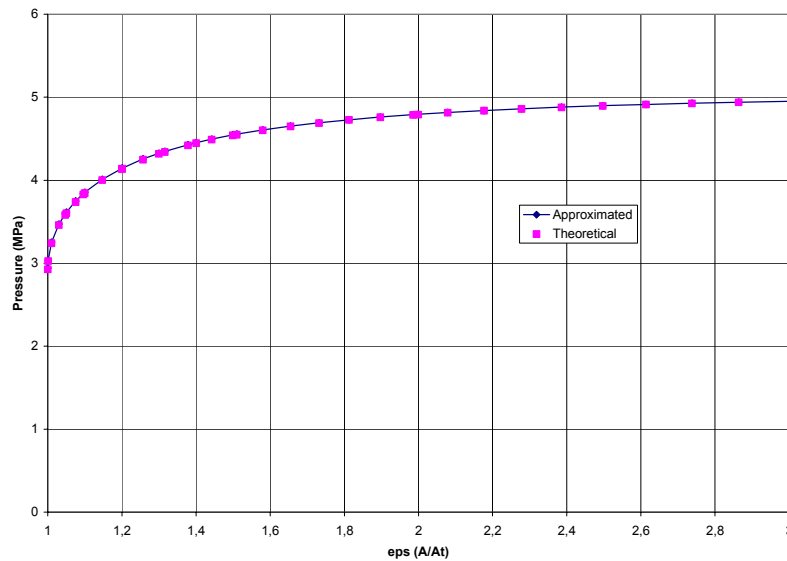
**Figure 12: Comparison of Theoretical and Approximated Pressure in a Nozzle.**

For a two-phase flow approximation, the following relations must be written for the heat capacity and specific heat ratio:

$$c_p{}^g = (1 + C_m)c_p - C_m c_p{}^p$$

$$\gamma^g = \frac{1}{1 - (1 + C_m)\dfrac{c_p}{c_p{}^g}\dfrac{\gamma - 1}{\gamma}}$$

where the subscripts $^g$ and $^p$ are for the gaz and particulate phase in the two-phase approximation, and $C_m$ is the condensed phase / gas phase mass flow rate ratio.

## RECENT DEVELOPMENTS: FLUID-STRUCTURE INTERACTION [16]

Fully coupled solution of fluid flows with structural interactions is called fluid-structure interaction. The range of its applications is important in many engineering disciplines [17]. Some current applications are pressure waves in a piping system, sound waves traveling through fluid-solid media, biomedical problems such as blood flow in a diseased artery or coupled instabilities in power systems. Computer-aided techniques for design optimization have been much promoted over the past decades and have subsequently reached a high level of sophistication within many single disciplines such as fluid or structural mechanics. However, because of complexity and computational cost issues, most often the coupling effects are neglected. For example, in aerodynamics optimization, the structure is assumed to be rigid. Another reason for separate treatment is the schismatic split-up of engineering disciplines, which makes it difficult for one person to have in-depth knowledge on all of these. With the computer power increasing and the advent of parallel processing, research on fluid-structure interaction in the field of numerical aeroelastic simulations has received growing interest in the last ten years.

In fluid-structure interactions, the combined effects of inertial, elastic and aerodynamic forces impact the movement of the fluid and solid boundaries. The fluid movement exerts aerodynamic forces on the structure that reacts and in turn forces the flow to evolve at the interface with an interface velocity. This produces the coupling effect and suitable computational strategies need to be developed. The problem

of the motion of the fluid-structure interface that occurs in coupled aeroelastic problems is generally addressed by solving the fluid equations on moving dynamic meshes with an Arbitrary Lagrangian Eulerian formulation.

Fluid structure computation has applications in solid propellant grain mechanical design and unsteady simulations.

## Main Features of the Modeling

Mathematical models of coupled problems are usually coupled partial differential equations in space and time. Often, different discretization techniques are used on the different physical components. The most difficult part of handling numerically the fluid-structure coupling arises from the fact that the structural equations are usually formulated with lagrangian coordinates while the flow equations are expressed using eulerian coordinates. These physically heterogeneous system components are computationally treated as isolated entities that are separately advanced in time. Interaction effects are viewed as forcing effects that are communicated between the individual components.

## Arbitrary Lagrangian Eulerian Formulation

The ALE formulation consists in solving the conservation equation on a moving grid. Since if the grid is fixed, the method is called eulerian, and the method is called lagrangian for grid points having the material velocity, the ALE formulation is a generalization.

Numerical fluxes must be computed correctly through the moving faces [17].

In order to solve the problem, the computational mesh has to be moved or deformed during the time integration of the fluid. A common technique to deform a mesh is the spring analogy. The force exerted by the nodes $j$ which are connected to the node $i$ is mathematically expressed by:

$$\sum_{j} \kappa_{ij} (\vec{x}_j - \vec{x}_i)$$

where $\kappa_{ij}$ is the stiffness of the spring between nodes $i$ and $j$. At equilibrium state, the force at every node $i$ has to be zero. After regrouping the terms, the iterative equation to be solved yields:

$$\vec{x}_i^{k+1} = \sum_{j} \kappa_{ij} \, \vec{x}_j^k \Big/ \sum_{j} \kappa_{ij}$$

## Structural Model

The structural model can go from a simple reduction of stiffness, mass and damping matrices of the finite element mechanical model on the fluid boundary to the full resolution with a non linear structural mechanics code.

## Fluid-Structure Coupling Algorithm

The coupling algorithm is performed in a staggered way. Structure and fluid are integrated on the same time scale (given by the fluid time step required by the fluid solver) although the characteristic scales for the structural system and for the fluid flow may be very different.

The fluid and structure equations are coupled by imposing that at the boundary, the structure stress tensor is in equilibrium with the fluid pressure and that wall boundary condition occurs on the fluid-structure interface. It implies that the forces and energies exchanged at the fluid-structure interface are balanced. Moreover, mesh and structure motions are also coupled by continuity conditions on the interface.

A complete cycle takes place as follows:

1)  The fluid transmits to the structure a pressure profile obtained at time $n$ to evaluate the pressure forces exerted by the fluid $F^n$.

2)  The structure model determines the displacements $q^{n+1}$.

3)  This structure configuration is transmitted to the fluid model.

4)  Fluid variables $W$ are then advanced at time $n+1$.

5)  Back to step 1.

The position of the structure at time $n+1$ is advanced with pressure force input $F^n$ defined from a fluid pressure profile and then the flow state vector $W^{n+1}$ is computed from the mesh configurations $x^n = q^n$ to $x^{n+1} = q^{n+1}$. The position of the dynamic fluid mesh does not lag behind that of the surface of the structure.

With no damping matrix $[D]$, the structural energy expresses as:

$$E_s = \frac{1}{2} \, {}^t q \left[ K \right] q + \frac{1}{2} \, {}^t \dot{q} \left[ M \right] \dot{q} + {}^t q \, F_0$$

and its variation during a time step is $\Delta E_s = E_s^{n+1} - E_s^n = \left( {}^t q^{n+1} - {}^t q^n \right) F^n$ deriving from the structural time integrator. On the other hand, the transferred energy through an element of the fluid-structure interface can be written as $\Delta E_f = \left( {}^t x^{n+1} - {}^t x^n \right) P$ where $P$ is the nodal fluid force whose expression depends on the fluid pressure values used by the flow solver to compute the fluxes across the fluid-structure interface. The force and energy exchanged between the fluid and the structure at their interface must be opposed. To ensure these principles, a procedure enforcing momentum or energy conservation is used at the interface in step 4. To do it, fluid pressure involved in the boundary flux is re-adjusted. The simplest way is to estimate $P$ and $F^n$ with the mean value of the gas pressure available at the beginning of cycle.

## CONCLUDING REMARKS

In this lecture, on overview of general problems and models used in CFD code for SRM steady interior flows has been made. The second paper will focus on unsteady phenomena.

## REFERENCES

[1]  A. Davenas et al, "Solid Rocket Propulsion Technology", Pergamond Press, 1993.

[2]  F. Godfroy and G. Delannoy, "La Modélisation des Ecoulements dans les systèmes propulsifs et les dispositifs pyrotechniques", Revue Scientifique de la Défense, 1997-3, pp. 63-74.

[3]  AGARD-LS-150, "Design Methods in Solid Rocket Motors".

[4]   K.K. Kuo and M. Summerfield et al, "Fundamentals of Solid Propellant Combustion", AIAA PAAS Vol. 90.

[5]   J.M. Lenoir and G. Robillard, "A Method to Predict the Effects of Erosive Burning in Rocket Motors", 6th Symposium on Combustion, 1957.

[6]   M.K. King, "Erosive Burning of Solid Propellants", Combustion of Solid Propellants, AGARD-LS-180, 1991.

[7]   J.C. Godon, J. Duterque and G. Lengellé, "Solid Propellant Erosive Burning", Journal of Propulsion and Power, 8(4), pp. 741-747, 1992.

[8]   J.C. Godon, J. Duterque and G. Lengellé, "Erosive Burning in Solid Propellant Motors", Journal of Propulsion and Power, 9(6), pp. 806-811, 1993.

[9]   I. Tseng, I-Shih and V. Yang, "Combustion of a Double-Base Homogeneous Propellant in a Solid Rocket Motor", Combustion and Flame, Vol. 96-4, 1994.

[10]  M. Salita, "Two-Phase Flows in Rocket Motors", RTO-AVT-VKI Special Course, Internal Aerodynamics in Solid Rocket Propulsion, May 2002.

[11]  V. Morfouace and P.Y. Tissier, "Two-Phase Flow Analysis of Instabilities Driven by Vortex-Shedding in Solid Rocket Motors", AIAA-95-2733, July 1995.

[12]  J. Dupays, Y. Fabignon, P. Villedieu, G. Lavergne and J.L. Estivalezes, "Some Aspects of Two-Phase Flows in Solid Propellant Rocket Motors", in Solid Propellant Chemistry, Combustion and Motor Interior Ballistics, Progress in Astronautics and Aeronautics, Vol. 185, 2000.

[13]  P. Villedieu, Y. Fabignon, J.F. Guéry, F. Godfroy, P. Le Helley, J. Hylkema, L. Jacques and G. Lavergne, "Slag Accumulation in Large Segmented Solid Rocket Motors with a Submerged Nozzle", Space Solid Propulsion Conference, Rome, November 2000.

[14]  F. Godfroy and J.F. Guéry, "Unsteady Eulerian Two-Phase Flow Analysis of Solid-Propellant Rocket Motor Slag", AIAA-97-2859, July 1997.

[15]  S. Gordon and B.J. McBride, "Computer Program for Calculation of Complex Chemical Equilibrium Compositions, Rocket Performance, Incident and Reflected Shocks and Chapman-Jouguet Detonation", NASA-Lewis Research Center, SP-273, 1971.

[16]  P. Della Pieta et al, "Numerical Simulations of Some Fluid-Structure Interaction Phenomena Found in Solid Rocket Motors", paper submitted for publication to the Journal of Propulsion and Power.

[17]  A. Dervieux et al, "Fluid-Structure Interaction", Revue Européenne des Eléménts Finis, Vol. 9, October 2000.

# Numerical Modeling of Internal Flow Aerodynamics
# Part 2: Unsteady Flows

**Jean-François Guéry**
SNPE Propulsion
Centre de Recherche du Bouchet
F-91710 Vert-le-Petit
FRANCE

## NOTATIONS

$a$      sound velocity (m/s) = $\sqrt{\gamma r T}$

$f_{nL}$      n$^{th}$ longitudinal acoustic mode (Hz)

     (= $\dfrac{na}{2L}$ in a closed duct assumption)

$\dot{m}_w$      mass flow rate per injecting surface unit (kg/m$^2$)

$P$      pressure (Pa)

$q_m$      total mass flow rate (kg/s)

$R$      port radius

$r_b$      burning rate (mm/s)

$T$      temperature of the flow (K)

$T_f$      propellant flame temperature (K)

$u$      unsteady mean velocity component in the $x$-longitudinal direction (m/s)

$u_v$      axial mean velocity (m/s)

$v$      unsteady mean velocity component in the $y$-lateral direction (m/s)

$v_{inj}$      wall injection velocity (m/s)

$w$      unsteady mean velocity component in the $w$-lateral direction (m/s)

$x,y,z$      co-ordinate system (m)

$\rho$      density (kg/m$^3$)

$\rho_s$      propellant density (kg/m$^3$)

**Dimensionless Parameter**

$Re_c$      Reynolds number: $\rho\, u_v\, D_c/\mu$, where $D_c$ is a characteristic diameter of the SRM

$Re_w$      wall injection Reynolds number: $\rho\, v_w\, h_c/\mu$

$\gamma$      specific heat ratio

## INTRODUCTION

It has been widely reported in the open literature that large segmented and axisymmetric Solid Rocket Motors (SRM) are subject to pressure oscillations caused by vortex shedding at annular restrictors or cavities in the grain, and acoustic feedback resulting from impingement of the vortices on the nozzle or other obstacles. If they are well suited for combustion instabilities studies in tactical rocket motors, acoustic balance methods have proven inefficient in predicting stability of large segmented rocket motors (e.g. Ariane 5 MPS and Titan IV SRMU).

For those situations, the full unsteady numerical simulation of the internal flow becomes the adequate solution. In general, simulations are done within two objectives:

- **Explanation**: this is the numerical simulation of a geometry defined at the time (web thickness) of maximum pressure oscillation after the firing of a SRM. This simulation will be generally made in a fixed geometry corresponding at that web thickness for a few acoustic periods. Frequencies and levels are expected from numerical simulation. The objective is to compute and explain the non linear coupling mechanisms between hydrodynamic instabilities and acoustics leading to such levels, with associated processes (conditions for resonance, aluminum combustion, fluid-structure coupling, ...).

- **Prediction**: in this simulation, we want to assess the effect of a change in SRM geometry, propellant, burning rate [1],... on thrust oscillations, before any firing. In that case, all the firing has to be examined since there is no way to determine a priori the time of maximum pressure oscillation.

The studies carried out in France during the last 10 years (POP and ASSM CNES programs) have displayed that vortex shedding due to annular restrictors is not the only process explaining the thrust oscillations of large SRM. It comes actually that pressure oscillations in large L/D ratio SRM could be due to three different vortex shedding phenomena [2]:

- Vortex shedding from annular restrictors,

- Vortex shedding over intersegment cavities,

- Surface vortex shedding [3].

This lecture will focus on some models used in CFD code for internal aerodynamics in SRM, validation cases, confrontations between experiments and simulations, and recent improvements.


## GRAIN REGRESSION EFFECT

If we do not want to simulate the entire firing, but concentrate on a typical event (burst) some time during the firing, care must be taken for defining properly the computation initial conditions.

During the burning of a solid propellant grain, the internal geometry evolves continuously, leading to an evolution of the aerodynamic flow field and acoustic modes. When a hydrodynamic instability matches an acoustic mode, this slow evolution creates slow frequency changes, and waterfalls on successive acoustic modes.

We can define some characteristic times.

For the sake of simplicity, a global approach is given. In a SRM and in the steady state, pressure and temperature fields can be shown independent. We define $u_v(x)$ to be the axial mean velocity at an x axial position in the motor:

$$u_v = \frac{\dot{m}(x)}{\rho(x)A(x)}$$

with $\dot{m}(x)$ being the mass flow rate through the port cross area A(x) at abscissa x. This expression shows that this means velocity can vary for at least three reasons:

- a variation of the forward mass flow $\dot{m}(x)$

- a variation of the density (that is to say the mean pressure)

- a variation of the port cross area

Hence, four characteristic times can be defined:

1) $t_m = \dfrac{\dot{m}(x)}{\dfrac{d(\dot{m}(x))}{dt}}$

2) $t_p = \dfrac{P}{\dfrac{d(P)}{dt}}$

3) $t_b = \dfrac{R}{r_b}$

4) $t_u = \dfrac{u_v(x)}{\dfrac{d(u_v(x))}{dt}}$

The two first characteristic times can be any during some events in the burning (for instance when the burning surface reaches the structure).

The third characteristic time describes the slow evolution of the internal geometry.

The last characteristic time, related to the evolution of the mean velocity, can characterize constant Strouhal evolution rates.

Dimensionless parameters can be obtained through the product of these times with $f_{1L}$. For instance, in Ariane 5 SRM and in the last third of the firing, $t_b f_{1L}$ is around of 3000. It means that during 30 periods of the first acoustic mode, the port internal radius has varied of 1%.

These considerations show that in the majority of applications, the geometry can be considered fixed, defined by a ballistics restitution, when we want to compute the unsteady internal flow during a few first acoustic mode periods, and a way for verifying this hypothesis can be by computing these characteristic times.


## PHYSICAL MODELS

In order to extend the credibility of numerical calculations as a predicting tool to be used for industrial applications either in development phases or in conceptual analysis phases, one needs to improve the level of accuracy of physical models and the effectiveness of numerical schemes. Numerical schemes are the "classical" ones used in CFD (generally, finite volume methods based on approximate Riemann solvers, with at least second order accuracy in space and time). Important physical models are two-phase and unsteady combustion models.


### Unsteady Combustion Modeling

The pressure-coupled response links the fluctuations of the propellant injected specific mass flow rate to the fluctuations of the pressure, both being functions of the frequency through the pulsation $\omega = 2\pi f$:

$$R_{mp}(\omega) = \frac{\dot{m}'/\bar{m}}{p'/\bar{p}} \qquad (1)$$

This linear expression accounts for the coupling between unsteady combustion phenomena in the propellant and fluctuating pressure above the burning surface. The real part of the response indicates the portion of the mass burning rate which fluctuates in phase with the pressure, which means energy is exchanged between the pressure waves in the gas phase and the propellant burning surface. According to the sign of the real part of $R_{mp}$, pressure waves will be amplified ($Re(R_{mp})>0$) or damped ($Re(R_{mp})<0$) by the combustion. The analytical expression of the response can be deduced by modeling the heat flux transfer from the flame to the propellant surface and the heat diffusion inside the solid phase. Several non-linear models were proposed [20-22], and they usually differ one from the other in the expression of the instantaneous heat flux transmitted to the propellant.

Culick [21] has shown that all these models could lead to a same form for the linear response function, which is the two-parameter function:

$$R_{mp}(\omega) = \frac{nAB}{S + A/S - (1+A) + AB} \qquad (2)$$

where:

- $n$ is the pressure exponent of the steady-state burning rate law $V_c = \alpha p^n$ .

- $A$ and $B$ are non-dimensional parameters which characterize the propellant and depend on its physical and chemical properties. $A$ is related to the pyrolysis kinematics and $B$ to the energy released at the surface of the propellant.

- $S$ is a Laplace variable, here defined by equation: $S(S - 1) = i\Omega$, where $\Omega = a\omega/V_c^2$, a being the propellant thermal diffusivity.

In an internal CFD code, the pressure-coupled response can be modeled through a detailed physical model, CPU time consuming, or in a very simpler way (Traineau et al.) [16]. The ONERA representation of the unsteady propellant combustion prescribes the instantaneous specific injected mass flow rate as:

$$\dot{m}(t) = \overline{\dot{m}} + \frac{\overline{\dot{m}}}{\overline{p}} \int_0^{t-t_0} R(\tau)\big[p(t - \tau) - \overline{p}\big]d\tau \qquad (3)$$

where $R(\tau)$ is the impulse response associated with propellant pressure-coupled response and quantities with an overbar are mean values.

Assuming the response function $R_{mp}$ is known (i.e. the values of $A$ and $B$ are determined from experimental points) for a given frequency range [0-$f_{max}$], its associated impulse response can be deduced easily by applying an inverse Fourier Transform to $R_{mp}$. The time resolution of the impulse response function has to be adjusted according to the time step of the Navier-Stokes simulation.

The model implementation mainly consists in replacing the propellant boundary condition used in Navier-Stokes solvers (calculation of the injected mass flow rate from the steady-state burning rate law in $\alpha p^n$) by a new boundary condition derived from equation (3). The injected specific mass flow rate is computed from Eq. (3) on each grid cell on the propellant surface, not necessarily for each time step dt since usually d$\tau$ is much greater than dt. One has to note that the use of this unsteady propellant combustion model implies the user has previously performed a reference computation with a steady-state burning rate, as expression (3) requires the estimate and storing of the means values of the pressure and injected mass flow rate, for each cell on the propellant burning surface.

## Two-Phase Flows

Aluminized propellants give liquid aluminum oxide in the chamber. This two-phase-flow can significantly influence motor performance in terms of acoustic stability, slag accumulation, nozzle erosion, two-phase losses, and so on…

The internal unsteady two-phase flows can be solved with eulerian or lagrangian approaches and are described in the previous lecture [4].

The condensed phase can be considered inert or reactive. Most of aluminum combustion models are derived from Law's model [5].

## TURBULENCE

Specific turbulence models must be used for studying unsteady flows in SRM. Usually, two kind of models are used: URANS and LES. These models must also take two-phase flow effects into account.

## VALIDATION CASES

Many strategies can be used to validate multidimensional computations. The more logical one is to go from confrontations to simple 1D analytical results to full scale comparison with experiments.

### Comparison to Analytical Results

Most of them are 1D theories. For instance, Morfouace and Tissier [6] have studied the acoustic wave damping of a two-phase flow in a duct in a very simple test case: the geometry in an open duct, a sinusoidal pressure signal is applied at the entrance, and a non reflecting boundary condition is used at the exit. They compared their results to Culick [7] and Temkin and Dobbins [8] theories.
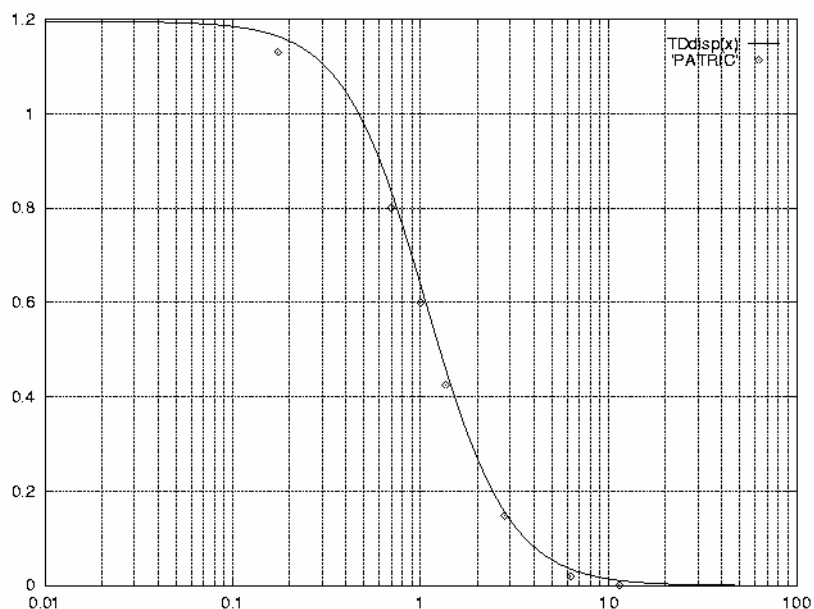


**Figure 1: Comparison between 1D Computation (PATRIC) and TD Theory**
**(Dispersion vs Dimensionless Frequency).**
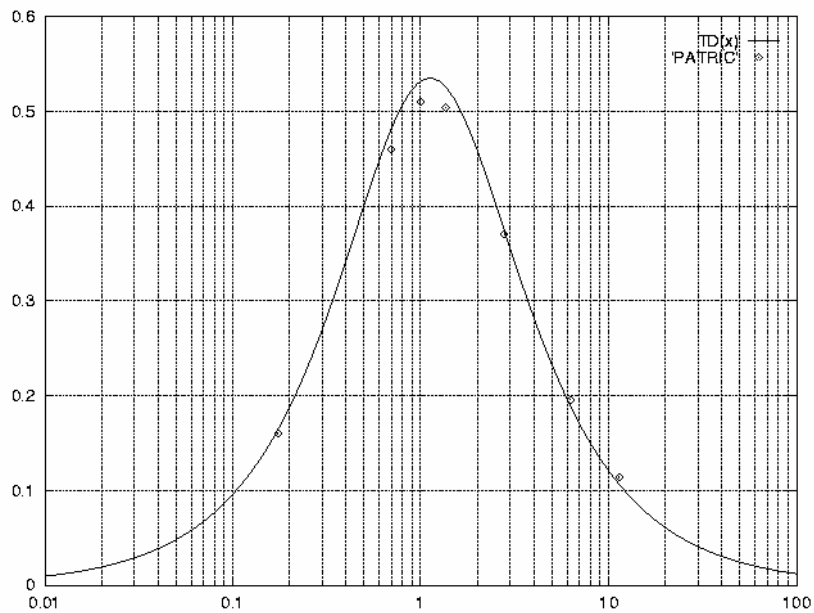
**Figure 2: Comparison between 1D Computation (PATRIC) and TD Theory**
**(Damping vs Dimensionless Frequency).**

## Comparison to Acoustic Balance

Vuillot et al. [9] have extended the validation to two-dimensional situation. In their paper, 2D Navier-Stokes stability computations are performed on a simple cylindrical port motor.
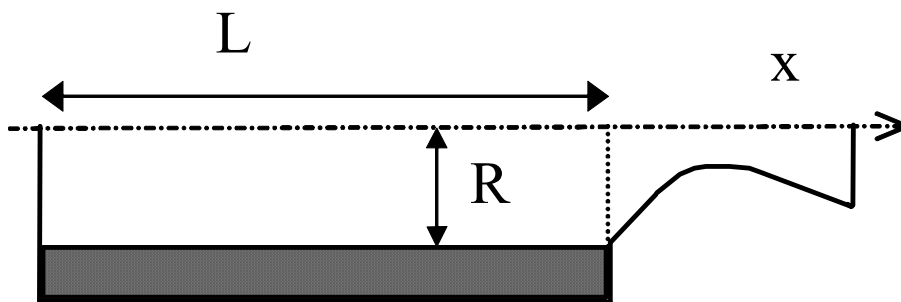


**Figure 3: Schematic View of Vuillot et al. Test Case.**

The 2D results, in terms of motor frequency and damping, as well as in terms of full acoustic field, are compared to classical 1D linear acoustic balance performed for the first longitudinal mode. The 2D computations are performed in the following way: after convergence toward a steady state solution, the motor is excited close to its first longitudinal mode by means of one period of head end forcing. Then the response of the flow field to that perturbation is analyzed, in term of frequency and exponential damping. The 2D computations are performed with models representing the propellant combustion response and two-phase flow behavior. The models are used separately and then together.

The results obtained for various model parameter settings as well as for various griddings are compared to linear results.

Noting $\Omega$ the interior of the chamber, $\partial\Omega$ its boundary, considering harmonic motions ($F' = \tilde{F}\exp(i\omega t)$) and using the following notations:

$$k_N = \frac{\omega_N}{a}$$

$$E_N^2 = \int_\Omega \tilde{p}_N^2 \, dV, \quad A_n = \overline{\rho} a \frac{\tilde{u}_i n'_i}{\tilde{p}}, \quad M_n = \frac{\overline{u}_i n'_i}{a}$$

where $n'_i$ is the inward pointing unit normal vector, the linear stability results are:

$$\omega - \omega_N = \frac{a}{2E_N^2}\int_{\partial\Omega} Im(A_n)\tilde{p}_N^2 \, dS - \frac{a}{2k_N E_N^2}\int_\Omega Re\left(\delta\tilde{F}_{pi}\frac{\partial\tilde{p}_N}{\partial x_i}\right)dV + (\gamma-1)\frac{1}{2E_N^2}\int_\Omega Im(\delta\tilde{Q}_p \tilde{p}_N)dV$$

$$\alpha = \frac{-a}{2E_N^2}\int_{\partial\Omega}\left(Re_7(A_n) + \overline{M}_n\right)\tilde{p}_N^2 \, dS - \frac{a}{2k_N E_N^2}\int_\Omega Im\left(\delta\tilde{F}_{pi}\frac{\partial\tilde{p}_N}{\partial x_i}\right)dV - (\gamma-1)\frac{1}{2E_N^2}\int_\Omega Re(\delta\tilde{Q}_p \tilde{p}_N)dV$$

The surface integral is usually split over the propellant surface (combustion driving, $\alpha_C$) and the nozzle entrance plane (nozzle damping expressed as the sum of a convective part $\alpha_{NC}$ and a radiative part $\alpha_{NR}$). It is a common use to add a so-called "flow-turning" damping term, $\alpha_{FT}$, or to correct the propellant admittance for the displacement effect of the ABL ($\alpha_{BL}$). The last two volume integrals are directly linked with the condensed phase and disappear for a one phase flow. $\delta F$ and $\delta Q$ are respectively the drag force exerted by the particles on the gas and the heat exchanged between the two phases. The overall expression for the resulting frequency shift and damping is:

$$\Delta\omega = \Delta\omega_C + \Delta\omega_{NR} + \Delta\omega_p$$

$$\alpha = \alpha_C + \alpha_{BL} \text{ (or } \alpha_{FT}) + \alpha_{NC} + \alpha_{NR} + \alpha_p$$

The integral over the burning surface can be simplified by making use of the propellant pressure coupled combustion response, $R_{MP}$, defined as:

$$R_{MP} = \frac{v'_c/\overline{v}_c}{p'/\overline{p}} = \frac{\rho'/\overline{\rho}}{p'/\overline{p}} + \frac{\overline{p}}{aM_{inj}}\frac{u'_i.n'_i}{p'}$$

$$\Rightarrow R_{MP} = \frac{1}{\gamma M_{inj}}\left[M_{inj} + A_n\right]$$

so that: $\alpha_c = -\gamma a M_{inj} Re(R_{MP})\dfrac{\int_{S_{inj}} \tilde{p}_N^2 \, dS}{2\int_\Omega \tilde{p}_N^2 \, dV}$

For the simple cylindrical port, the damping take simplified expressions. The following relationships apply for this simple situation:

$$S_{inj} = 2\pi R L,$$

$$S_L = \pi R^2,$$

$$\Omega = \pi R^2 L$$

$$M_L = \frac{S_{inj}}{S_L} M_{inj},$$

$$M_{inj} = \frac{V_{inj}}{a}$$

$$\widetilde{p}_N = \widetilde{p}_{N0} \cos(k_N x) \quad with \quad k_N = q\frac{\pi}{L}$$

leading to:

$$\alpha_c = -\gamma \frac{V_{inj}}{R} Re(R_{MP})$$

$$\alpha_{NC} = \frac{aM_L}{L} = \frac{2V_{inj}}{R}$$

$$\alpha_{NR} = \frac{aRe(A_L)}{L}$$

$$\alpha_{FT} = \alpha_{BL} = \frac{V_{inj}}{R}$$

$$\alpha_p = \kappa \frac{\omega}{2}\left[\frac{\omega\tau_v}{1+(\omega\tau_v)^2} + (\gamma-1)\frac{C}{C_p}\frac{\omega\tau_T}{1+(\omega\tau_T)^2}\right]$$

$\kappa$ is the particle to gas mass ratio ($\kappa = C_m/(1-C_m)$, where $C_m$ is the propellant particle loading). $\tau_u$ and $\tau_T$ are relaxation times given by $\tau_u = \dfrac{\rho_{material}D_p^2}{18\mu}$ and $\tau_T = \dfrac{3}{2}\Pr\dfrac{C}{Cp}\tau_u$ with $Pr$, the Prandtl number.

Comparison of linear acoustic balance and 2D computation on coarse and fine grids are given in Figure 4 and Figure 5.
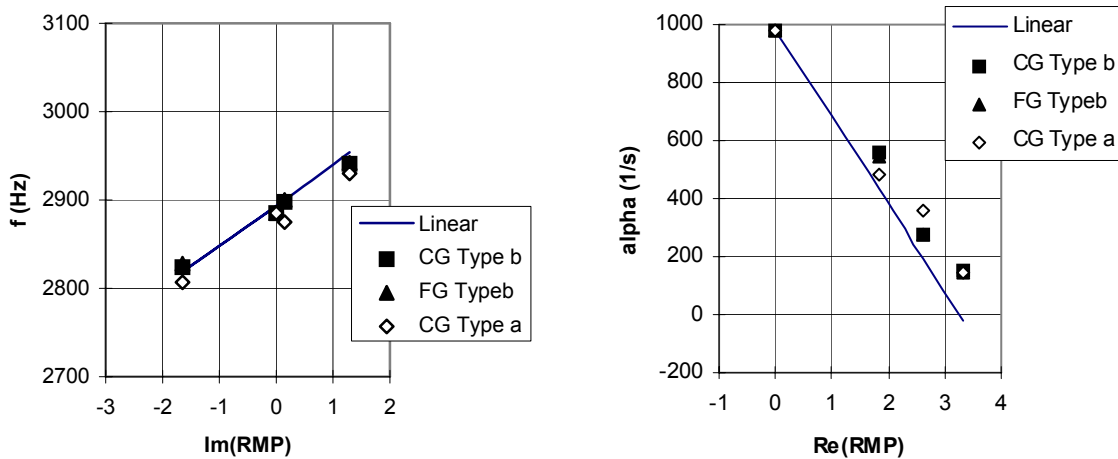
**Figure 4: Summary of Computations with the Propellant Response Function Model
(Coarse grid CG, fine grid FG, and two types of propellant response).**
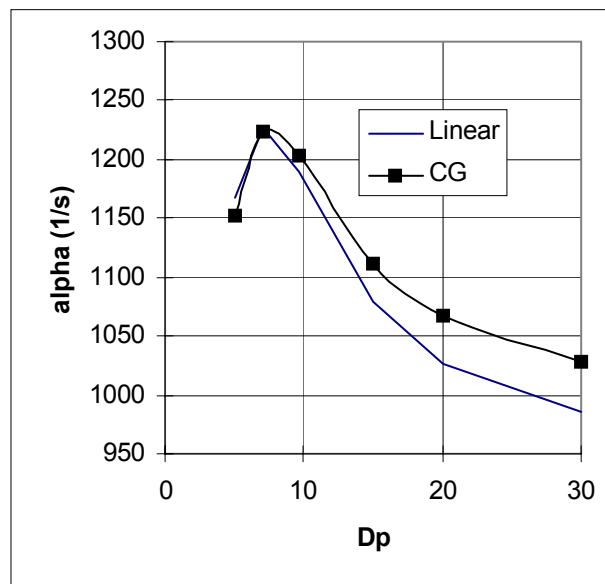


**Figure 5: Particle Size Effect on Two-Phase Flow Damping.**

The results show that the overall tendencies are correctly obtained over a large range of model parameter settings. Surprisingly it is found that the 2D results do not depend on the grid spatial resolution and that the details of the so-called acoustic boundary layer (ABL) do not need to be resolved.

This finding is also true for the two-phase flow damping. Analysis of the computed 2D acoustic field show that the ABL displacement effect is an effective damping source (even for an ABL penetrating into the core of the flow) and that an extra damping exists which is not incorporated into the classical acoustic balance.

## Cold Flows

Since the internal flows in a solid-propellant rocket motor are difficult to instrument, cold flow experimental simulations are an alternative tool for a detailed aerodynamic effects understanding

(see Guéry et al [18]). The three different instability behaviours can be obtained. If absolute instabilities can be naturally computed by solving the Navier-Stokes equations, the surface vortex-shedding instability, as a convective instability, is more complex to obtain. Ugurtas [10] injects a gaussian noise with an amplitude of 0.4% $v_{inj}$ to simulate the VECLA experiments. Apte and Yang [11] forces the head end with a pressure oscillation equal to 5% of the head-end mean pressure at imposed acoustic frequencies in order to analyse unsteady flow organisation in Hervat and Traineau [12] cold flow simulation of a nozzleless rocket motor.
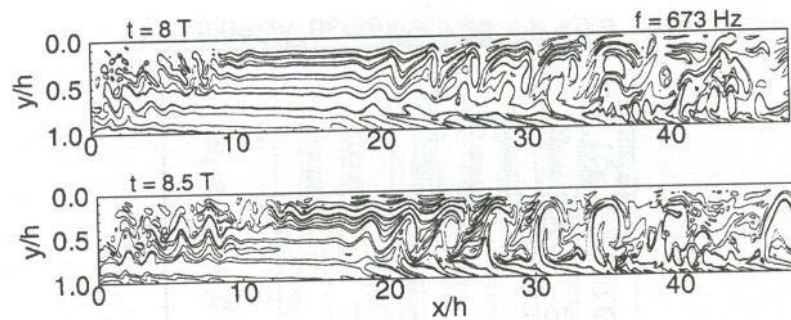


**Figure 6: Eddy Motions in the Forced Acoustic Environment [11].**

## Validation on Simplified Rocket Motors

Dupays [13] developed a whistling motor (small and naturally unstable, based on VSA instability). He studied the effect of inert particulate phase in the propellant on the instabilities (vortex-shedding) by adding alumina or zirconium silicate particles in a AP/HTPB propellant. Different sizes and loading were used. Pressure oscillations were identified on all the firings, with some burst corresponding to self-sustained phenomena.

Experimental results are well reproduced by computations. When studying the particulate loading effect, with 5, 10 and 20 % of condensed phase, he noticed a curious effect: oscillations levels are larger with 10 % loading than 5 %, whereas 20 % loading damps out all the signal. These results are in contradiction with linear theory, and are not explained until now (particles/eddies interactions?).
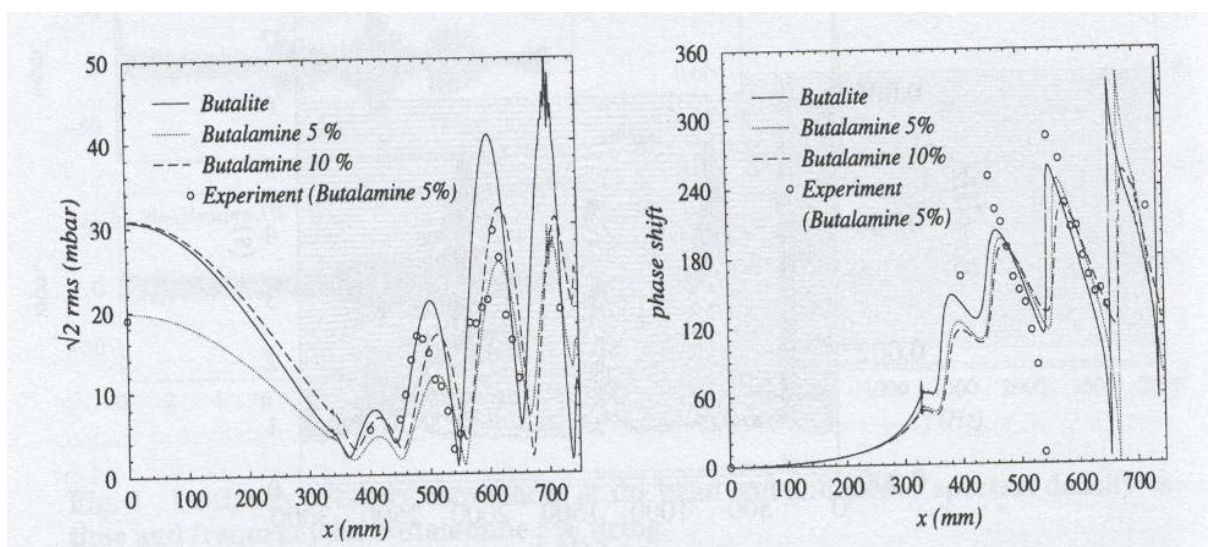


**Figure 7: Comparison between Experiments and Computations (Dupays [13]).**

# RECENT IMPROVEMENTS

## Full Motor Firing Simulation

The main project actually in the world leading to the detailed full numerical simulation of a SRM is the CSAR project at UIUC [14], and when GEN2 family codes (the last generation) will be operational, a large step in prediction will have been done.

SNPE developed the CPS and MOPTI® computer codes for CFD computations inside SRM. CPS solves the two and three dimensional compressible unsteady Navier-Stokes equations for turbulent, reactive, multi-species, two-phase flows with a cell-centered finite volume method on an unstructured mesh with triangular and quadrilateral control cells in 2D and with hexahedrons, pentahedrons, pyramids, prisms and tetrahedrons in 3D. It incorporates fluid-structure coupling facility, and is parallel. MOPTI® manages exchanges between two principal computational modules:

- A varying burning rate surface burnback module,
- CFD code CPS.

MOPTI® has been precisely described in reference [1]. The global structure of MOPTI is presented on Figure 8.
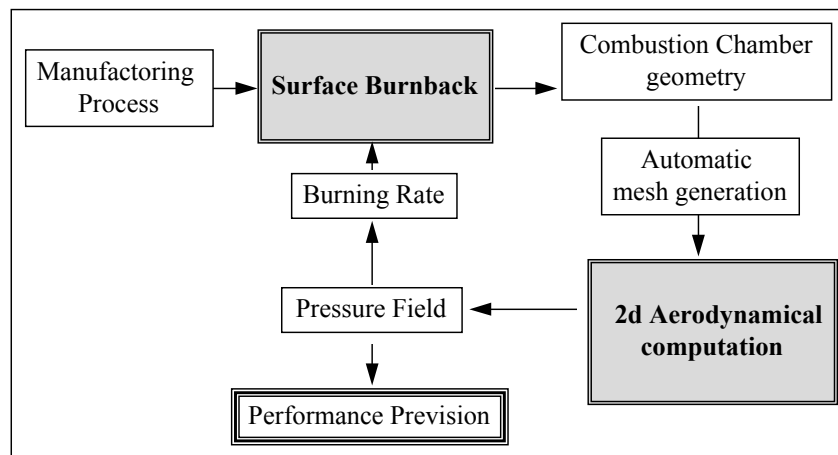


**Figure 8: Structure of MOPTI®.**

A MOPTI® simulation of the Ariane 5 1/15 subscale motor (LP6) is given [15]. On Figure 9 numerical vorticity fields are presented. They show that the flow becomes unstable after t≅5s. Before this time, the pressure signal is stable.
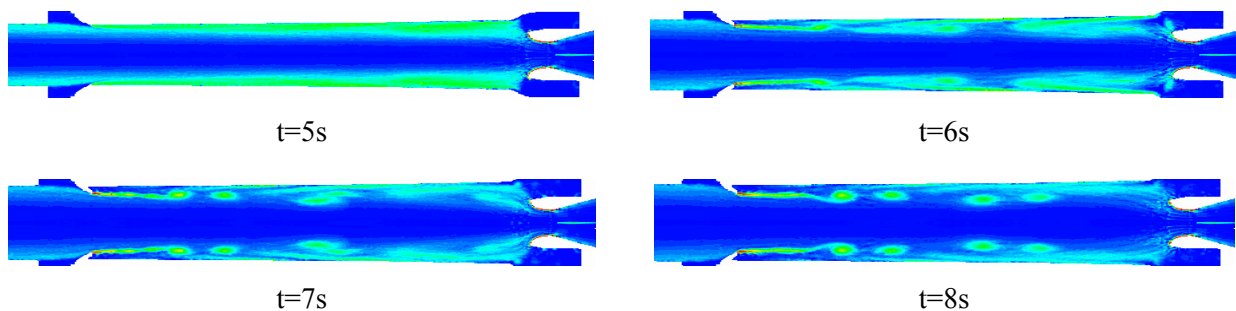


**Figure 9: Numerical Vorticity Fields.**

Those figures show a very good agreement between numerical and experimental results. The first oscillations occur after t≅5s. A first waterfall on the first longitudinal acoustic mode is observed between 5 an 6.5s. The levels are stronger on computational results but the global form is similar. The principal waterfall occurs between 6.5 and 8s, and a last one in the combustion tail off between 8 and 10s. For both waterfalls the numerical and experimental results are in really good agreement. The same comparison may be done on the second acoustic mode.
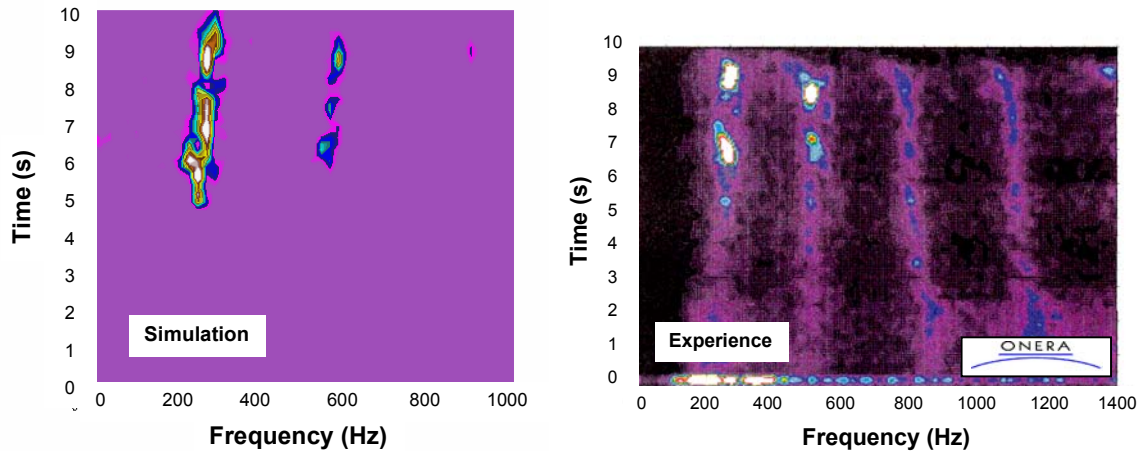


**Figure 10: PSD Contours – Comparison of Experimental and Computational Results.**

## Fluid-Structure Coupling

In segmented motors with inhibited faces, a strong effect of the static bending of the emerging thermal inhibitors on pressure oscillation levels has been observed [16]. In order to investigate the influence of the dynamic behavior of the thermal inhibitor, CPS fluid-structure coupling facility has been used [17].
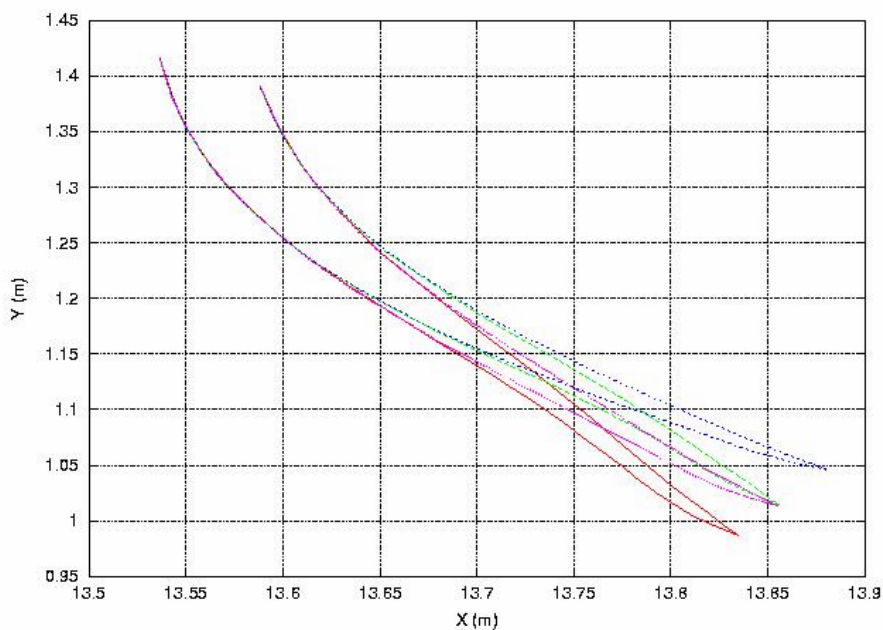


**Figure 11: Deformed Shape of the Inhibitor at Different Times in the FSC Computation.**

This computation is noted FSC. Unsteady pressure signal and its Fourier analysis is given in Figure 12. A strong influence of this phenomenon is found in this configuration since the fluctuation levels reach 3.5 times configuration without FSC.



**Static inhibitor**                    **Fluid structure coupling**
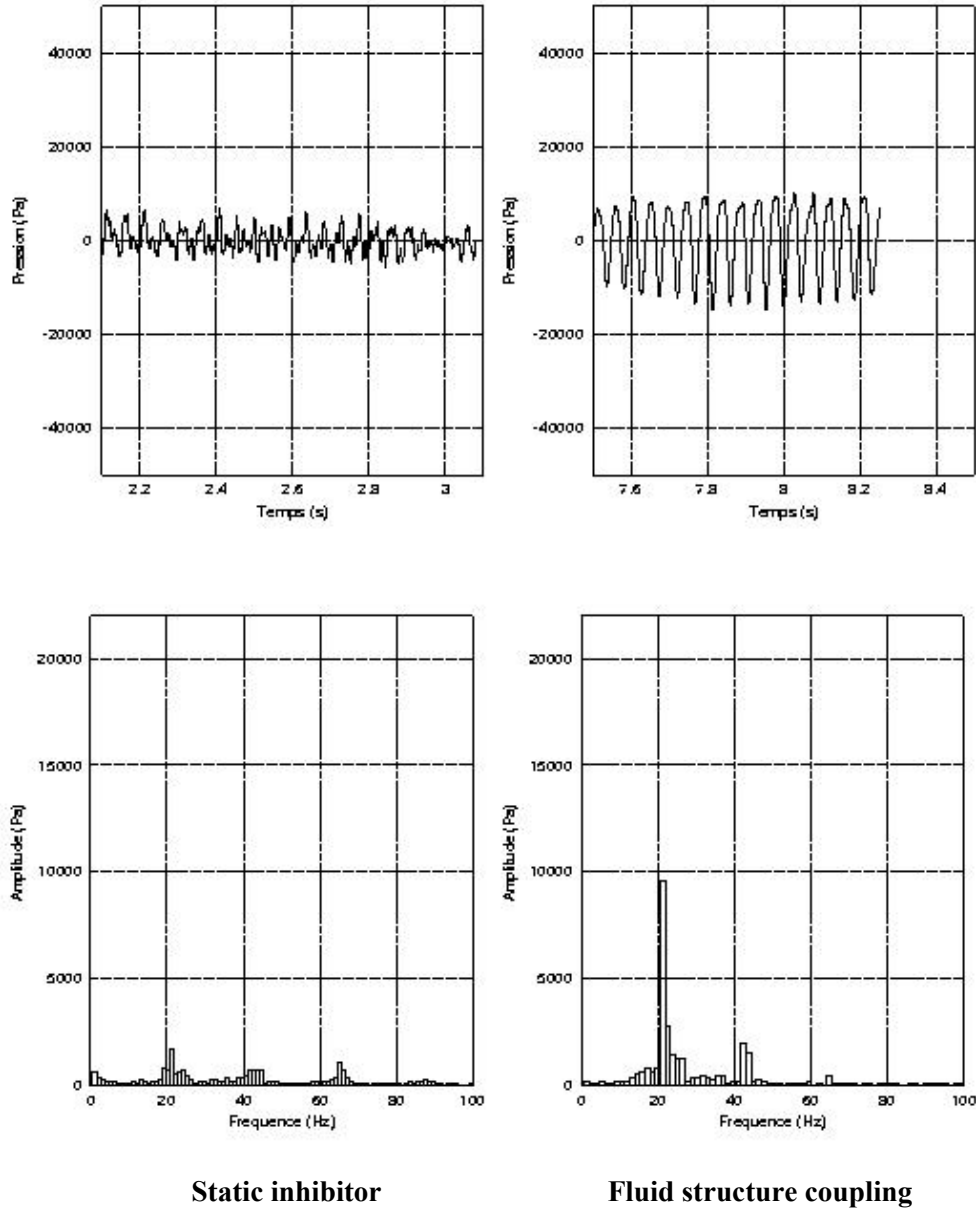
**Figure 12: Head End Pressure Signal and its Fourier Transform.**

This influence needs to be investigated in details. That could be done through cold flow experiments [18].

**Effects of Aluminum Combustion**

It is believed that aluminum distributed combustion and alumina droplets behavior might affect pressure oscillations of AP/Al propellant SRM, releasing heat inside the core of the flow. Such an eventuality has been assessed by using two-phase flow capabilities first at ONERA [15], then at SNPE [19]. A simplified combustion model has been used.

In these computations, Figure 13, particle distribution clearly displays vortex shedding and shows that momentum of particles are too large for their coming into vortex cores. The temperature map exhibits that combustion takes place very close to the surface and that some particles burn while passing round the vortices. Figure 14 presents pressure signals at the head end compared to the single phase computation in time and frequency space. It clearly points out a periodic signal and levels more than 4 times higher that those obtained with single phase computations.
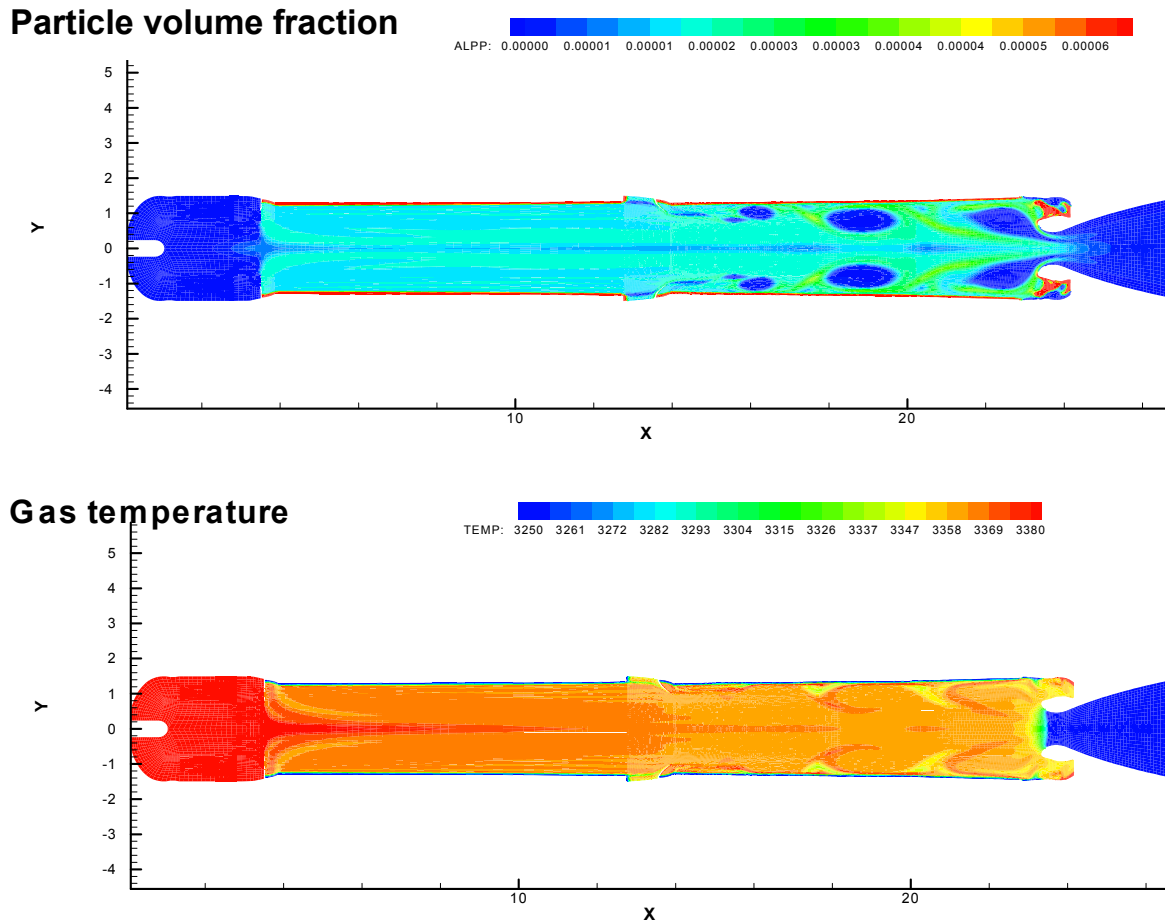
**Figure 13: Particle Volume Fraction (up) and Gas Temperature (down).**
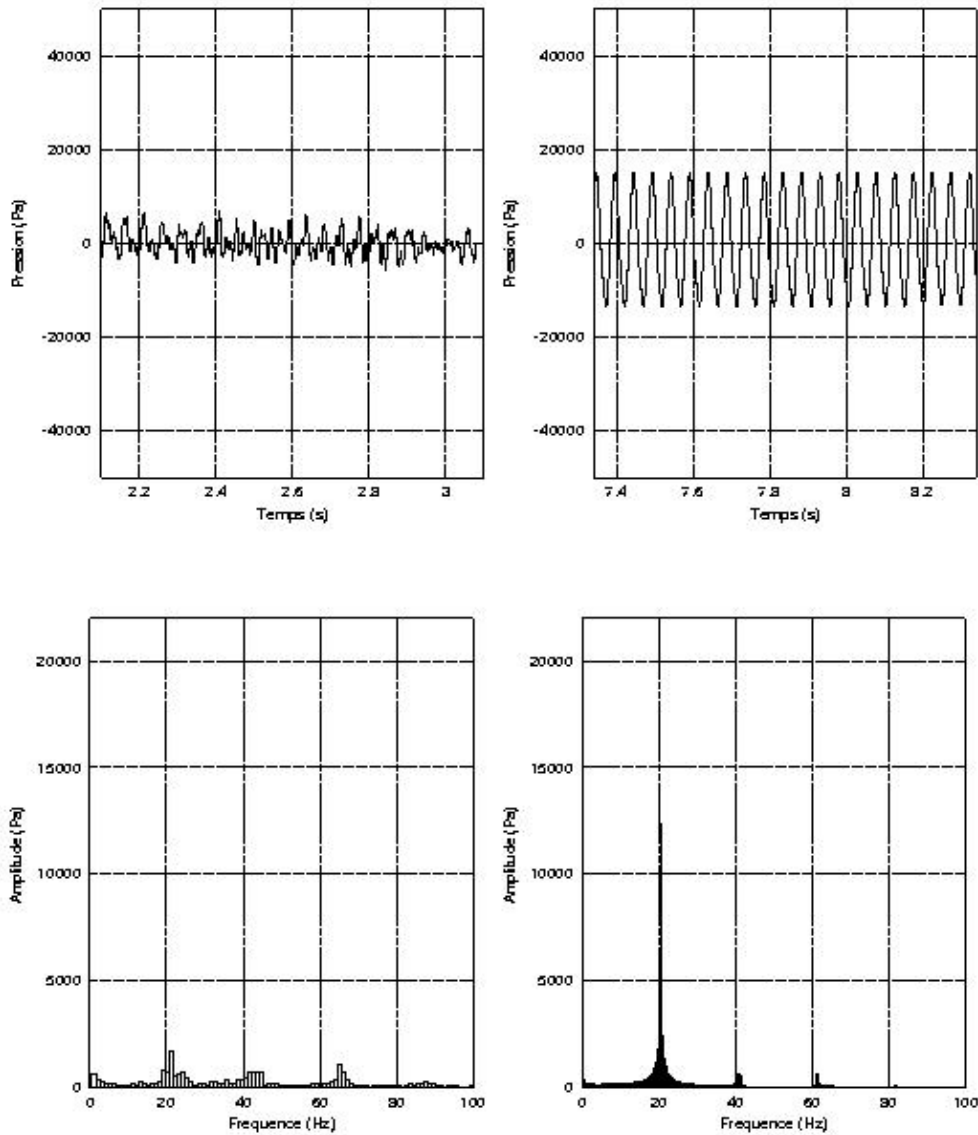
**Bended inhibitor**                 **Al Combustion**

**Figure 14: Head End Pressure Signal and its Fourier Transform.**

# CONCLUDING REMARKS

Ten years after Kuentzmann [20] AGARD Lecture Series on combustion instabilities, we can measure the progress made in the numerical simulations of aerodynamic/acoustics coupling in SRM. This fantastic progress is due to two reasons. The first one is the continuously increasing performance of computers, giving scientists and engineers the opportunities for continuously increasing the accuracy of both numerical and physical models. But computer codes are nothing without validated models. The second reason has been the support of research programs in the US and France (ASSM and POP CNES programs for the French part).

During these ten years, numerical computation has gone from an academic research topic to an industrial powerful tool. And this was the second challenge for driving progress in SRM conception.

## REFERENCES

[1]    P. Le Breton, D. Ribéreau and F. Godfroy. "SRM Performance Analysis by Coupling Bidimensional Surface Burnback and Pressure Field Computations", AIAA 98-3968, July 1998.

[2]    D. Ribéreau, J.-F. Guery and P. Le Breton, "Numerical Simulation of Thrust Oscillations of Ariane 5 Solid Rocket Boosters", Space Solid Propulsion, November 2000.

[3]    N. Lupoglazoff and F. Vuillot, "Parietal Vortex Shedding as a Cause of Instability for Long Solid Propellant Motors. Numerical Simulations and Comparisons with Firing Tests", AIAA 96-0761, January 1996.

[4]    J.F. Guéry, "Numerical Modeling of Internal Flow Aerodynamics", RTO-AVT-VKI Special Course, Internal Aerodynamics in Solid Rocket Propulsion, May 2002.

[5]    C.K. Law, "A Simplified Theoretical Model for the Vapor-Phase Combustion of Metals Particles", Combustion Science and Technology, Vol. 7, N° 3-6, 1973.

[6]    V. Morfouace and P.Y. Tissier, "Two-Phase Flow Analysis of Instabilities Driven by Vortex-Shedding in Solid Rocket Motors", AIAA 95-2733, July 1995.

[7]    F.E.C. Culick, "Combustion Instability in Solid Rocket Motors", CPIA Publication 290, January 1981.

[8]    S. Temkin and R.A. Dobbins, "Attenuation and Dispersion of Sound by Particulate-Relaxation Processes", J. of the Acoustical Society of America, Vol. 40, N° 2, 1966.

[9]    F. Vuillot, J. Dupays, N. Lupoglazoff, Th. Basset and E. Daniel, "2D Navier-Stokes Stability Computations for Solid Rocket Motors: Rotational, Combustion and Two-Phase Flow Effects", AIAA 97-3326, July 1997.

[10]  B. Ugurtas, G. Avalon, N. Lupoglazoff, F. Vuillot and G. Casalis, "Stability and Acoustic Resonance of Internal Flows Generated by Side Injection", in Solid Propellant Chemistry, Combustion and Motor Interior Ballistics, Progress in Astronautics and Aeronautics, Vol. 185, 2000.

[11]  S. Apte and V. Yang, "Simulated Nozzleless Rocket Motor", in Solid Propellant Chemistry, Combustion and Motor Interior Ballistics, Progress in Astronautics and Aeronautics, Vol. 185, 2000.

[12]  J.C. Traineau, P. Hervat and P. Kuentzmann, "Cold Flow Simulation of a Two-Dimensional Nozzleless Solid Rocket Motor", AIAA 86-1447, June 1986.

[13]  J. Dupays, Y. Fabignon, P. Villedieu, G. Lavergne and J.L. Estivalezes, "Some Aspects of Two-Phase Flows in Solid Propellant Rocket Motors", in Solid Propellant Chemistry, Combustion and Motor Interior Ballistics, Progress in Astronautics and Aeronautics, Vol. 185, 2000.

[14]  W.A. Dick, M.T. Heath and R.A. Fiedler, "Integrated 3D Simulations of Solid Propellant Rockets", AIAA 2001-3949, July 2001.

[15]  P. Le Breton, J.F. Guéry, F. Vuillot and M. Prevost, "Recent Advances in the Prediction of SRM Thrust Oscillations", Colloque Vibration des Lanceurs, Toulouse, November 1999.

[16] J.C. Traineau, M. Prévost, F. Vuillot, P. Le Breton, J. Cuny and N. Preioni, "A Subscale Test Program to Assess the Vortex Shedding Driven Instabilities in Segmented Solid Rocket Motors", AIAA-973247, July 1997.

[17] P. Della Pieta et al, "Numerical Simulations of Some Fluid-Structure Interaction Phenomena Found in Solid Rocket Motors", paper to be submitted for publication to the Journal of Propulsion and Power.

[18] J.F. Guéry, F. Vuillot, G. Avalon, F. Plourde, J. Anthoine and B. Platet, "Use of Cold Flow Experiment in the ASSM Program: Lessons and Results" Space Solid Propulsion, Rome, November 2000.

[19] J.F. Guéry, S. Gallier, P. Della Pieta, F. Godfroy, A. Guichard, P. LeBreton and D. Ribéreau, "Numerical Simulation of Thrust Oscillations of Segmented AP/Al Solid Rocket Motors", IAF-01-S.2.05, October 2001.

[20] P. Kuentzmann, "Combustion Instabilities", AGARD-LS-180, 1991.
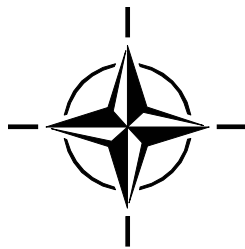
# COMBUSTION INSTABILITIES IN
# SOLID PROPELLANT ROCKET MOTORS

## F.E.C. Culick
California Institute of Technology
1200 E. California Blvd., MC 205-45
Pasadena, CA 91125, U.S.A.

## Notes for Two Lectures given as part of the Special Course "Internal Aerodynamcis in Solid Rocket Propulsion"

## von Kármán Institute
## 27–31 May 2002

# Contents

CONTENTS

CONTENTS

CONTENTS

# COMBUSTION INSTABILITIES IN SOLID PROPELLANT ROCKET MOTORS

F.E.C. Culick
California Institute of Technology
1200 E. California Blvd., MC 205-45
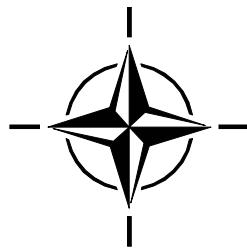Pasadena, CA 91125, U.S.A.

## ABSTRACT

These notes for two lectures are intended to provide the basic ideas for understanding and interpreting coherent oscillations is solid propellant rocket motors. The discussion is concerned mainly with the dynamics of a system consisting of two coupled sub-systems: the chamber containing combustion products; and the combustion processes confined almost entirely to a thin region adjacent to the surface of burning propellant. Coupling between the sub-systems is always present due to the sensitivity of the ocmbustion processes to local values of pressure and velocity. Thus the primary mechanisms for instabilities in solid rockets are related to those interactions. A second mechanism involves vortex shedding, a cause of instabilities mainly in large motors, notably the Space Shuttle and Ariene V boost motors. Following a brief review of the history of combustion instabilities in solid rockets, the mechanisms and their quantitative representations are discussed. The remainder of the lectures is devoted to an approximate analysis providing a general framework convenient for understanding, predicting and interpreting combustion instabilities.

## 1. A BRIEF SURVEY OF COMBUSTION INSTABILITIES IN SOLID ROCKETS

Chemical propulsion systems depend fundamentally on the conversion of energy stored in molecular bonds to mechanical energy of a vehicle in motion. The first stage of the process, combustion of oxidizer and fuel, takes place in a vessel open only to admit reactants and to exhaust the hot products. Higher performance is achieved by increasing the rate of energy release per unit volume. For example, the power density in the Atlas engine (1950s) was 146.4 gigawatts/m$^3$. The power densities in solid rockets are much less. For a cylindrical bore, the values are approximately $0.25(r/D)$ gigawatts/m$^3$, where $r$ is the linear burning rate, typically a few centimeters per second, and $D$ is the diameter. Thus the power densities rarely exceed one gigawatt/m$^3$. These are indeed very large power densities. We cannot be surprised that such enormous power densities should be accompanied by relatively small fluctuations whose amplitudes may be merely annoying or possibly unacceptable in the worst cases.

We are concerned in these lectures with the dynamics of combustion systems using solid propellants. The motivation for addressing the subject arises from particular problems of combustion instabilities observed in all types of solid rockets. Typically the instabilities are observed as pressure oscillations growing spontaneously out of the noise during a firing. As a practical matter, combustion instabilities are more likely encountered during development of new combustion systems intended to possess considerable increases of performance in some sense. The present state of theory and experiment has not provided a sufficiently strong foundation to provide a complete basis for prediction. Hence there are only a few guidelines available to help designers avoid combustion instabilities. In that respect, more is known about the dynamical behavior of solid rockets than about corresponding problems in other propulsion systems.

Under such conditions, it is extremely important to pay attention to the experience gained in the laboratory as well as in full-scale tests of devices: theory alone is quite helpless because of the impossibility of obtaining quantitative results solely from first principles. Moreover, because of the many properties of the behavior common to the various systems, much is to be gained from understanding the characteristics of systems other than the one that may be of immediate concern. It is therefore proper to begin with a survey of some typical examples drawn from many years' experience. Theory is an indispensable aid to making sense of observational results. Conversely, discussion of various experimental observations is a natural place to introduce many of the basic ideas contained in the theory.

From the beginning of this subject, the central practical question has been: What must be done to eliminate combustion instabilities? Traditionally, the approach taken has been based on passive measures, largely *ad hoc* design changes or notably for solid propellant rockets, favorable changes of propellant composition. During the past few years, considerable effort has been expended on the problem of applying active feedback control to combustion systems. It's an attractive proposition to control or eliminate instabilities with feedback control, particularly because one implication, often made explicit, is that the use of feedback will somehow allow one to get around the difficult problems of understanding the details of the system's behavior. Many laboratory, and several full-scale demonstrations with gas turbines support that point of view. Proposals have been made for active control of solid rockets but there seem to be no successful demonstrations. In any case, for at least two reasons, serious application of feedback control must be based on understanding the dynamics of the system to be controlled:

(i) all experience in the field of feedback control generally has demonstrated that the better the controlled plant is understood, the more effective is the control;

(ii) without understanding, development of a control system for a full-scale device is an *ad hoc* matter, likely to involve expensive development with neither guarantee of success nor assurance that the best possible system has been designed.

Consequently, whatever one's motivation for investigating combustion instabilities, it is essential to have a good understanding of experiences with as many systems as possible. Therefore we begin this book with a lengthy survey of combustion instabilities observed in various systems. The theoretical framework is constructed to accommodate these observations, but later emerges also as a perfect vehicle for investigating the use of active feedback control.

**1.1. Introduction.** For the kinds of propulsion systems normally used, combustion chambers are intended to operate under conditions that are steady or vary little. The central questions addressed in the monograph concern the stability and behavior subsequent to instability of steady states in combustors. If a state is unstable to small disturbances, then an oscillatory motion usually ensues. Such combustion instabilities commonly exhibit well-defined frequencies ranging from 15 hz or less to many kilohertz. Even at the highest amplitudes observed in practice, the instabilities consume only a small fraction of the available chemical energy. Thus, except in extremely severe instances, the oscillations do not normally affect the mean thrust or steady power produced by the systems. Serious problems may nevertheless arise due to structural vibrations generated by oscillatory pressures within the chamber or by fluctuations of the thrust. In extreme cases, internal surface heat transfer rates may be amplified ten-fold or more, causing excessive erosion of the chamber walls.

An observer perceives an unstable motion in a combustion chamber as "self-excited," a consequence of the internal coupling between combustion processes and unsteady motion. Except in cases of large disturbances (e.g. due to passage of a finite mass of solid material through the nozzle), the amplitude of the motion normally seems to grow out of the noise without the intrusion of an external influence. Two fundamental reasons explain the prevalence of instabilities in combustion systems:

(i) an exceedingly small part of the available energy is sufficient to produce unacceptably large unsteady motions;

(ii) the processes tending to attenuate unsteady motions are weak, chiefly because combustion chambers are nearly closed.

These two characteristics are common to all combustion chambers and imply that the possibility of instabilities occurring during development of a new device must always be recognized and anticipated. Treating combustion instabilities is part of the price to be paid for high-performance chemical propulsion systems. It is a corollary of that condition that the problem will never be totally eliminated. Advances in research will strengthen the methods for solution in practical applications, and will provide guidelines to help in the design process.

The fact that only a small part of the total power produced in a combustor is involved in combustion instabilities suggests that their existence and severity may be sensitive to apparently minor changes in the system. That

conclusion is confirmed by experience. Moreover, the complicated chemical and flow processes block construction of a complete theory from first principles. It is therefore essential that theoretical work always be closely allied with experimental results, and vice versa. No single analysis will encompass all possible instabilities in the various practical systems. There are nevertheless many features common to all combustion chambers. Indeed, it is one theme of this book that the characteristics shared by propulsion systems in many respects dominate the differences. While it is not possible to predict *accurately* the occurrence or details of instabilities, a framework does exist for understanding their general behavior, and for formulating statements summarizing their chief characteristics. For practical purposes, the theory often serves most successfully when used to analyze, understand, and predict *trends* of behavior, thereby also providing the basis for desirable changes in design. Experimental data are always required to produce quantitative results and their accuracy in turn is limited by uncertainties in the data.

Special problems may be caused by combustion instabilities interacting with the vehicle. Because the frequencies are usually well-defined in broad ranges, resonances with structural modes of the vehicle or with motions of components are common. Perhaps the best known form of this sort of oscillation is the POGO instability in liquid rockets. Strong couplings between chamber pressure oscillations, low-frequency structural vibrations, and the propellant feed system sustain oscillations. The amplitudes may grow to unacceptable limits unless measures are taken to introduce additional damping. A striking example occurred in the Apollo vehicle. The central engine of the cluster of five in the first stage was routinely shut off earlier than the others in order to prevent growth of POGO oscillations to amplitudes such that the astronauts would be unable to read instruments. Comments on the vibrations and the early shut off may be heard in communications recorded during the launch phase of several Apollo missions.

In the U.S., and possibly in other countries, notably Germany and Russia before and during World War II, combustion instabilities were first observed in solid and liquid propellant rocket engines. Subsequent to the war, considerable effort was expanded in Russia and in the U.S. to solve the problem, particularly in large liquid systems. Probably the most expensive program was carried out during development of the F-1 engine for the Apollo vehicle (Ofelein and Yang, 1993).

Liquid-fueled, air-breathing propulsion systems also commonly suffer combustion instabilities. Axial oscillations in ramjet engines are troublesome because their influence on the shock system in the inlet diffuser can reduce the inlet stability margin. Owing to their high power densities and light construction, thrust augmenters or afterburners are particularly susceptible to structural failures.

For any afterburner, conditions can be found under which steady operation is not possible. As a result, the operating envelope is restricted by the requirement that combustion instabilities cannot be tolerated. Due to structural constraints placed on the hardware, combustion instabilities in afterburners are particularly undesirable and are therefore expensive to treat.

In recent years combustion instabilities in the main combustor of gas turbines have become increasingly troublesome. The chief reason is ultimately due to requirements that emission of pollutants, notably oxides of nitrogen, be reduced. A necessary strategy, particularly for applications to flight, is reduction of the average temperature at which combustion takes place. Generation of $NO$ by the thermal or 'Zel'dovich' mechanism is then reduced. Lower combustion temperature may be achieved by operating under lean conditions, when the flame stabilization processes tend to be unstable. Fluctuations of the flame cause fluctuations of energy release, which in turn may produce fluctuations of pressure, exciting acoustical motions in the chamber and affecting the generation of nitrogen oxides.

Finally, almost all solid rockets exhibit instabilities, at least during development, and occasionally motors are approved even with low levels of oscillations. Actual failure of a motor itself is rare in operations, but vibrations of the supporting structure and of the payload must always be considered. To accept the presence of weak instabilities in an operational system one must have sufficient understanding and confidence that the amplitudes will not unexpectedly grow to unacceptable levels. One purpose of these lectures is to provide an introduction to the foundation for gaining the necessary understanding.

In the most general sense, a combustion instability may be regarded as an unsteady motion of a dynamical system capable of sustaining oscillations over a broad range of frequencies. The source of energy associated

with the motions is ultimately related to the combustion processes, but the term 'combustion instability,' while descriptive, is misleading. In most instances, and always for the practical problems we discuss in this book, the combustion processes themselves are stable: uncontrolled explosions and other intrinsic chemical instabilities are not an issue. Observations of the gas pressure or of accelerations of the enclosure establish the presence of an instability in a combustion chamber. Excitation and sustenance of oscillations occur because coupling exists between the combustion processes and the gasdynamical motions, both of which may be stable. What is unstable is the entire system comprising the propellants, the propellant supply system, the combustion products that form the medium supporting the unsteady motions, and the containing structure.

If the amplitude of the motions is small, the vibrations within the chamber are usually related to classical acoustic behavior possible in the absence of combustion and mean flow. The geometry of the chamber is therefore a dominant influence. Corresponding to classical results, traveling and standing waves are found at frequencies approximated quite well by familiar formulas depending only on the speed of sound and the dimensions of the chamber. If we ignore any particular influences of geometry, we may describe the situation generally in the following way, a view valid for any combustion instability irrespective of the geometry or the type of reactants.

Combustion processes are generally sensitive to fluctuations of pressure, density, and temperature of the environment. A fluctuation of burning produces local changes in the properties of the flow. Those fluctuations propagate in the medium and join with the global unsteady field in the chamber. Under favorable conditions, the field develops to a state observable as a combustion instability. As illustrated schematically in Figure 1.1, we may view the process abstractly in analogy to a feedback amplifier in which addition of feedback to a stable oscillator can produce oscillations. Here the oscillator is the combustion chamber, or more precisely, the medium within the chamber that supports the unsteady wave motions. Feedback is associated with the influences of the unsteady motions on the combustion processes or on the supply system, which in turn generate fluctuations of the field variables. The dynamical response of the medium converts the local fluctuations to global behavior. In the language of control theory, the field in the chamber is the 'plant,' described by the general equations of motion.
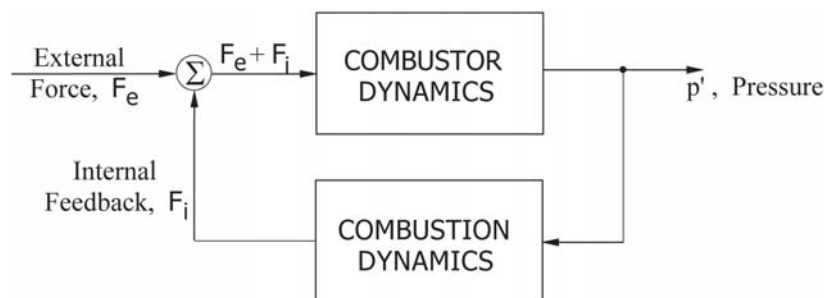


FIGURE 1.1. Schematic Diagram of a Combustion System as a Feedback Amplifier

The diagram in Figure 1.1 illustrates the global point of view taken here. Broadly, the subjects covered divide into two categories: those associated with the plant—the fluid mechanics and other physical processes comprising the *combustor dynamics;* and those connected primarily with the feedback path, chiefly combustion processes and their sensitivity to time-dependent changes in the environment, the *combustion dynamics.* Splitting is particularly clear for solid rockets because practically all of the combustion processes are completed in a thin region adjacent to the burning propellant. The theory we will describe encompasses all types of combustion instabilities in a general framework having the organization suggested by the sketch. External forcing functions are accommodated as shown in the sketch, but the causes associated with the feedback path are far more significant in practice.

Figure 1.1 is motivated by more than a convenient analogy. For practical purposes in combustion systems, we generally wish to eliminate instabilities. Traditionally that has meant designing systems so that small disturbances are stable, or adding some form of energy dissipation to compensate the energy gained from the combustion processes, that is, *passive control.* However, in the past few years interest has grown in the possibility of *active control* of instabilities. If that idea is to be realized successfully, it will be necessary to combine modern control theory with the sort of theory described here. It is advantageous to think from the beginning in terms that encourage this merger of traditionally distinct disciplines.

We will return to the subject of passive control for solid rockets at the end of these lectures. Any method of control is rendered more effective the more firmly it rests on understanding the problem to be solved. Understanding a problem of combustion instabilities always requires a combination of experiment and theory. For many reasons, including intrinsic complexities and inevitable uncertainties in basic information (e.g., material properties, chemical dynamics, turbulent behavior of the flow field, ...), it is impossible to predict from first principles the stability and nonlinear behavior of combustion systems. Hence the purpose of theory is to provide a framework for interpreting observations, both in the laboratory and full-scale devices; to suggest experiments to produce required ancillary data or to improve the empirical base for understanding; to formulate guidelines for designing full-scale systems; and globally to serve, like any good theory, as the vehicle for understanding the fundamental principles governing the physical behavior, thereby having predictive value as well.

All theoretical work in this field has been carried out in response to observational and experimental results. We therefore spend much of the remainder of this introductory chapter on a survey of the characteristics of combustion instabilities observed, and occasionally idealized, for combustion systems generally to be analyzed in later chapters. The general point of view taken throughout the book will then be formulated in heuristic fashion, based on experimental results.

**1.2. Historical Background.** Some of the consequences and symptoms of combustion instabilities were first observed in the late 1930s and early 1940s, roughly at the same time for liquid and solid propellant rockets, and apparently somewhat earlier in the Soviet Union than in the U.S. With the later development of turbojet engines, high-frequency instabilities were found in thrust augmenters or afterburners in the late 1940s and early 1950s. Although the problem had been encountered in ramjet engines in the 1950s, it became a matter of greater concern in the late 1970s and 1980s. The introduction of compact dump combustors led to the appearance of longitudinal or axial oscillations that interfered with the inlet shock system, causing loss of pressure margin and 'unstart' in the most severe cases. Owing to availability, almost all of the data cited here as examples will be derived from liquid rockets, solid rockets and laboratory devices. Figure 1.2 is a qualitative representation of the chronology of combustion instabilities. Due to the accessibility of documentation and the experiences of the author, particular cases cited are mainly those reported in the U.S.
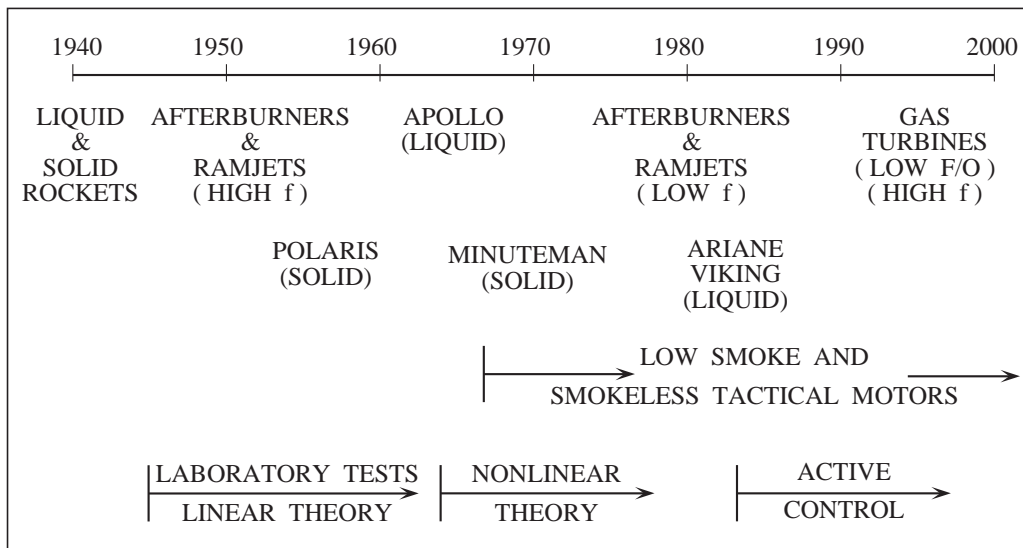


FIGURE 1.2. A Chronology of Combustion Instabilities

Several reviews of early experiences with combustion instabilities have been prepared for liquid rockets (Ross and Datner 1954) and for solid rockets (Wimpress 1950; Price 1968; Price and Flandro 1992). The details are not important here, but the lessons learned certainly are. Often forgotten is the most important requirement of good high-frequency instrumentation to identify and understand combustion instabilities in full-scale as well as in laboratory systems. Until the early 1940s, transducers and instrumentation for measuring pressure had inadequate dynamic response to give accurate results for unsteady motions. Ross and Datner note that "Prior to 1943,

the resolution of Bourdon gauges, photographed at 64 and 128 fps, constituted the principal instrumentation." Recording oscillographs were introduced sometime in 1943, but not until the late 1940s were transducers available with sufficient bandwidth to identify instabilities at higher frequencies (hundreds of hertz and higher).

The situation was even more difficult with solid rockets because of the practical difficulties of installing and cooling pressure transducers. Probably the experience with cooling chamber and nozzle walls helps explain why quantitative results were obtained for instabilities in liquid rockets earlier than for solid rockets (E. W. Price, private communication). Prior to the appearance of high-frequency instrumentation, the existence of oscillations was inferred from such averaged symptoms as excessive erosion of inert surfaces or propellant grains due to increased heat transfer rates; erratic burning appearing as unexpected shifts in the mean pressure; structural vibrations; visible fluctuations in the exhaust plume; and, on some occasions, audible changes in the noise produced during a firing.

Experimental work progressed for several years before various unexplained anomalies in test firings were unambiguously associated with oscillations. By the late 1940s, there was apparently general agreement among researchers in the U.S. and Europe that combustion instabilities were commonly present in rocket motors and that they were somehow related to waves in the gaseous combustion products. In addition to measurements with accelerometers, strain gauges, and pressure transducers, methods for flow visualization soon demonstrated their value, mainly for studies of liquid propellant rockets (Altseimer 1950; Berman and Logan 1952; and Berman and Scharres 1953). Characteristics of the instabilities as acoustic vibrations, or weak shock waves, were revealed.

It is much more difficult to observe the flow field in a solid rocket motor and during the early years of development, the only results comparable to those for liquid rockets were obtained when excessive chamber pressures caused structural failures. Partially burned grains often showed evidence of increased local burning rates, suggesting (possibly) some sort of influence of the gas flow. The same events also produced indications of unusual heating of the unburned solid propellant, attributed to dissipation of mechanical vibrational energy (Price and Flandro, 1992). Subsequently that interpretation was confirmed by direct measurements (Shuey, 1987).

High-frequency or 'screech' oscillations were also first encountered in afterburners in the late 1940s; as a result of the experience with rockets and the availability of suitable instrumentation, the vibrations were quickly identified as combustion instabilities. The staff of the Lewis Laboratory (1954) compiled most of the existing data and performed tests to provide a basis for guidelines for design.

Thus by the early 1950s most of the basic characteristics of combustion instabilities had been discovered in both liquid-fueled and solid-fueled systems. Many of the connections with acoustical properties of the systems, including possible generation of shock waves, were recognized qualitatively. Although the frequencies of oscillations found in tests could sometimes be estimated fairly closely with results of classical acoustics, no real theory having useful predictive value existed. During the 1950s and the 1960s the use of sub-scale and laboratory tests grew and became increasingly important as an aid to solving problems of combustion instabilities occurring in the development of new combustion systems.

**1.3. Solid Propellant Rocket Motors.** Since the late 1950s, serious concern with instabilities in solid propellant motors has been sustained by problems arising in both small (tactical) and large (strategic and large launch systems) rockets. The volume of collected papers compiled and edited by Berle (1960) provides a good view of the state of the field at the end of the 1950's in the Western countries. The level of activity remained high and roughly unchanged through the 1960's, due entirely to the demands of the Cold War: the use of solid rocket boosters in systems for launching spacecraft, and for changing trajectories, came later. During the 1950's and 1960's strong emphasis was already placed on sub-scale and laboratory tests, a strategy dictated at least partly by the large costs of full-scale tests. As a result, more is understood about combustion instabilities in solid rockets than in other systems. Moreover, methods and viewpoints developed by the solid rocket community have strongly influenced the approaches to treating combustion instabilities in other systems. The theory developed in this book is an example of that trend.

A problem with the third stage of the Minuteman II launch vehicle in the late 1960's (Joint Prop. Mtg 1972) initially motivated considerable research activity during the following decade, sponsored largely by the Air Force Rocket Propulsion Laboratory. The causes of three failures in test flights had been traced to the presence of

combustion instabilities. Thorough investigation showed that although oscillations had been present throughout the history of the motor, a significant change occurred during production, apparently associated with propellant Lot 10. Figure 1.3 shows the main observable features.
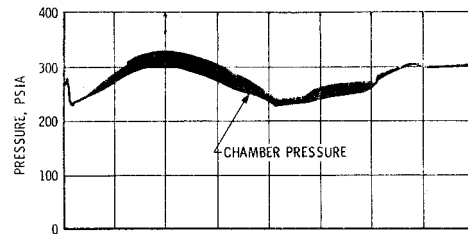


(a)
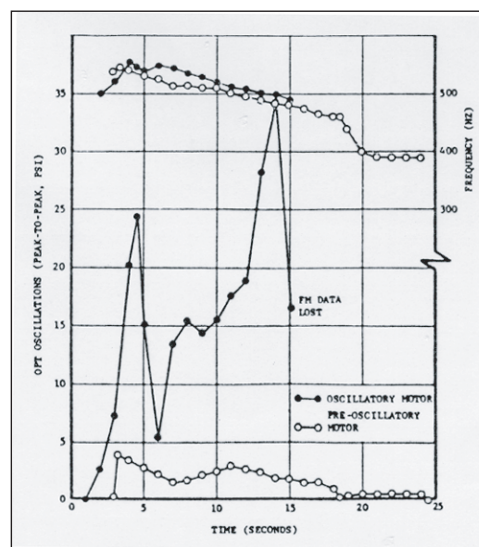


(b)

FIGURE 1.3. Frequencies and Amplitudes of Combustion Instabilities in the Minuteman II, Stage 3 Motor: (a) A Pressure Record from a Flight Test; (b) Frequencies and Amplitudes Measured During Static Tests.

The oscillations existed during the first fifteen seconds of every firing and always had frequency around 500 Hertz. Whatever occurred with production Lot 10 caused the maximum amplitudes of oscillations to be unpredictably larger in motors containing propellant from that and subsequent lots. The associated structural vibrations caused failures of a component in the thrust control system.

This example exhibits several characteristics common to many instances of combustion instabilities in solid rockets. In test-to-test comparisons, frequencies are reproducible and amplitudes show only slight variations unless some change occurs in the motor. Any changes must be of two sorts: either geometrical, i.e. the internal shape of the grain, or chemical, consequences of variations in the propellant. Chemical changes, i.e. small variations in the propellant composition, are most likely to affect the dynamics of the combustion processes and indirectly other physical processes in the motor. That is apparently what happened in the Minuteman.

Between production of propellant Lots 9 and 10, the supplier of aluminum particles was changed, because the original production facility was accidentally destroyed. The new aluminum differed in two respects: shapes of the particles, and the proportion of oxide coating. Testing during investigation of the instability led to the conclusion that consequent changes in the processes responsible for the production of aluminum oxide products of combustion generated smaller particle sizes of $Al_2O_3$. The smaller sizes less effectively attenuated acoustic waves; the net tendency to excite waves therefore increased. As a result, the motors were evidently more unstable and also supported larger amplitudes of oscillation. The second conclusion was purely speculative at the time of

the investigation, but can now be demonstrated with the theory covered in this book. Nevertheless, the details explaining why the change in the aluminum supplied led eventually to the significant changes in the combustion products remain unknown.

Subsequent to the Minuteman problem, the Air Force Rocket Propulsion Laboratory supported a substantial program of research on many of the most important problems related to combustion instabilities in solid rockets. Broadly, the intellectual centroid of that program lay closer to the areas of combustor dynamics and combustion dynamics than to the detailed behavior of propellants. The synthesis, chemistry and kinetics of known and new materials belonged to programs funded by other agencies in the U.S. and in Europe, notably ONERA in France. By far most of the related work in Russia has always been concerned with the characteristics and combustion of propellants, with relatively little attention to the dynamics of combustors.

As the research activities related specifically to solid rockets decreased during the 1980s and new programs began for liquid-fueled systems, the communities, previously quite separate, grew closer together. For example, prompted by contemporary concern with problems in ramjets, a workshop sponsored by JANNAF (Culick 1980) was organized partly with the specific intention to bring together people experienced in the various propulsion systems. During the 1980s there was considerable interchange between the various research communities and since that time, a significant number of people have worked on both solid and liquid-fueled systems. That shift in the sociology of the field has provided the possibility and much of the justification for this book. Events of the past decade have confirmed that the field of combustion instabilities is very usefully approached as a unification of the problems arising in all systems.

In Europe during the 1990's, work on combustion instabilities in solid propellant rockets has been motivated largely by low frequency oscillations in the booster motors for the Ariane 5. The most intensive and comprehensive recent work in the U.S. has been carried out in two Multiuniversity Research Initiators (MURI) involving 15 different universities. An unusual characteristic of those programs, active for five years beginning in 1995, was the inclusion of coordinated research on all aspects of problems of combustion instabilities in solid propellant rockets, from fundamental chemistry to the internal dynamics of motors. Results of recent works will be covered here in the appropriate places.

**1.4. Mechanisms of Combustion Instabilities.** Just as for steady operation, the chief distinctions among combustion instabilities in different combustors must ultimately be traceable to differences in geometry and the states of the reactants. The root causes, or 'mechanisms', of instabilities are imbedded in that context and are often very difficult to identify with certainty. Possibly the most difficult problem in this subject is to quantify the mechanism. Solving that problem requires finding an accurate representation of the relevant dynamics.

The simplest and most convenient characterization of an unstable oscillation is expressed in terms of the mechanical energy of the motion. Linear theory produces the result that the rate of growth of the amplitude is proportional to the fractional rate of change of energy, the sum of kinetic and potential energies. The idea is discussed further in the following section. What matters at this point is that the term 'mechanism' refers to a process that causes transfer of energy to the unsteady motion from some other source. Thus, mechanisms form the substance of the feedback path in Figure 1.1. Generally there are only three sorts of energy sources for unsteady motions in a combustor: the combustion processes; the mean flow, which of course itself is caused by combustion; and a combination of combustion and mean flow simultaneously acting. The distinction is important because the physical explanations of the energy transfer are very different in the three cases.

Combustion processes are sensitive to the macroscopic flow variables, particularly pressure, temperature and velocity. Even slow changes of those quantities affect the energy released according to rules that can be deduced from the behavior for steady combustion. In general, however, representations of that sort, based on assuming quasi-steady behavior, are inadequate. Combustion instabilities normally occur in frequency ranges such that genuine dynamical behavior is significant. That is, the transient changes of energy release do not follow precisely in phase with imposed changes of a flow variable such as pressure.

The next simplest assumption is that the combustion processes behave as a first order dynamical system characterized by a single time delay or relaxation time. That idea was apparently first suggested by Karman as a basis for interpreting instabilities discovered in early experiments with liquid propellant rockets at Caltech

(Summerfield, 1941). That representation, which came to be called the '$n - \tau$ model' was developed most extensively by Crocco and his students at Princeton during the 1950s and 1960s. Time delays may be due, for example, to processes associated with ignition of reactants. Subsequent to injection as the reactants flow downstream, finite times may be required for vaporization, mixing, and for the kinetics mechanism to reach completions. Both effects may be interpreted as a convective time delay. Under unsteady conditions, the initial state of the reactants, their concentrations, pressure, and velocity, also fluctuate, causing the delay time to be both nonuniform in space and in time. As a result, rate of energy release downstream in the chamber is also space- and time-dependent, and acts as a source of waves in the combustor.

The approximation of first order behavior fails entirely for the dynamics of burning solid propellants (Culick 1968). Although in good first approximation dominated by unsteady heat transfer in the condensed phase, a diffusive process, the combustion dynamics in this case exhibits behavior closer to that of a second order system. The frequency response of that burning rate tends normally to have a large broad peak centered at a frequency falling well within the range of the frequencies characteristic of the chamber dynamics. Hence there is a clear possibility for a resonance and instability suggested by the diagram in Figure 1.1. The chief mechanisms for instabilities in solid rockets are discussed in the following chapter.

Generation of oscillations by the average flow is due to causes roughly like those active in wind musical instruments. In all such cases, flow separation is involved, followed by instability of a shear layer and formation of vortices. Direct coupling between the vortices and a local velocity fluctuation associated with an acoustic field is relatively weak; that is, the rate of energy exchange is in some sense small. However, the interaction between the velocity (or pressure) fluctuation and the initial portion of the shear layer is normally a basic reason that feedback exists between the unsteady field in the volume of the combustor and vortex shedding.

It has long been known experimentally that vortices shed in a chamber more effectively generate acoustic waves if they impinge in an obstacle downstream of their origin (Flandro and Jacobs, 1975; Magiawala and Culick, 1979; Flandro, 1986). The first example of this phenomenon was the solid rocket booster for the Shuttle launch system in the 1970s. It was that problem that motivated the works just cited, but since then vortex shedding has been recognized as a mechanism for generating acoustic oscillations in other systems as well, notably the booster motors on the Space Shuttle and on the Ariane 5.

**1.5. Physical Characteristics of Combustion Instabilities.** Owing to the difficulty of making direct measurements of the flow field within a combustion chamber, virtually all that is known about combustion instabilities rests on close coordination of experiment and theory. The subject is intrinsically semi-empirical, theoretical work being founded on observational data both from full-scale machines and laboratory devices. Conversely, the theoretical and analytical framework occupies a central position as the vehicle for planning experimental work and for interpreting the results. The chief purpose of this section are to summarize briefly the most important basic characteristics of observed instabilities; and to introduce the way in which those observations motivate the formulation of the theoretical framework.

In tests of full-scale propulsion systems, only three types of data are normally available; obtained from pressure transducers, accelerometers, and strain gauges. Measurements of pressure are most direct but are always limited, and often not possible when the necessary penetration of the enclosure to install instruments is not allowed. Hence the unsteady internal pressure field is often inferred from data taken with accelerometers and strain gauges. In any case, because it is the fundamental variable of the motions, the pressure will serve here as the focus of our discussion.

Figure 1.4a and 1.4b is an example of a fully developed instability, shown with its power spectral densities. The well-defined peaks reflect the clear presence of several frequencies in the waves, the larger amplitudes occurring at the lower frequencies, as commonly happens. A substantial background of broad-band noise is of course always present due to turbulent fluctuations of the flow, noise emission by combustion processes, and possibly other unsteady motions such as flow separation. Some recent laboratory tests have shown that the level of noise depends on the presence and amplitude of combustion instabilities, but the cause is unknown and no such observations exist for full-scale combustors.
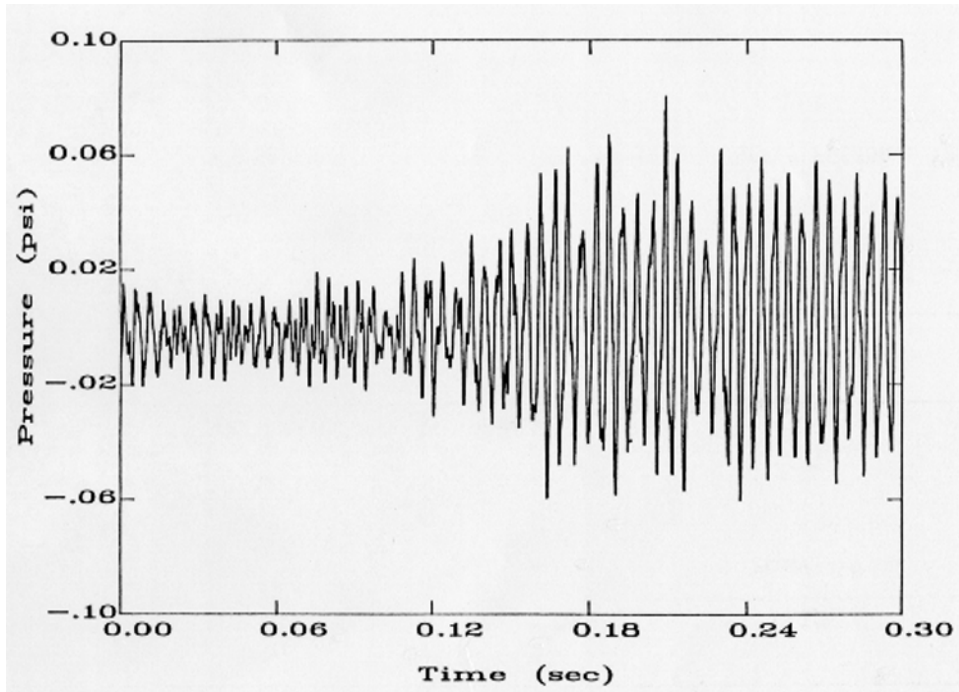
(a)
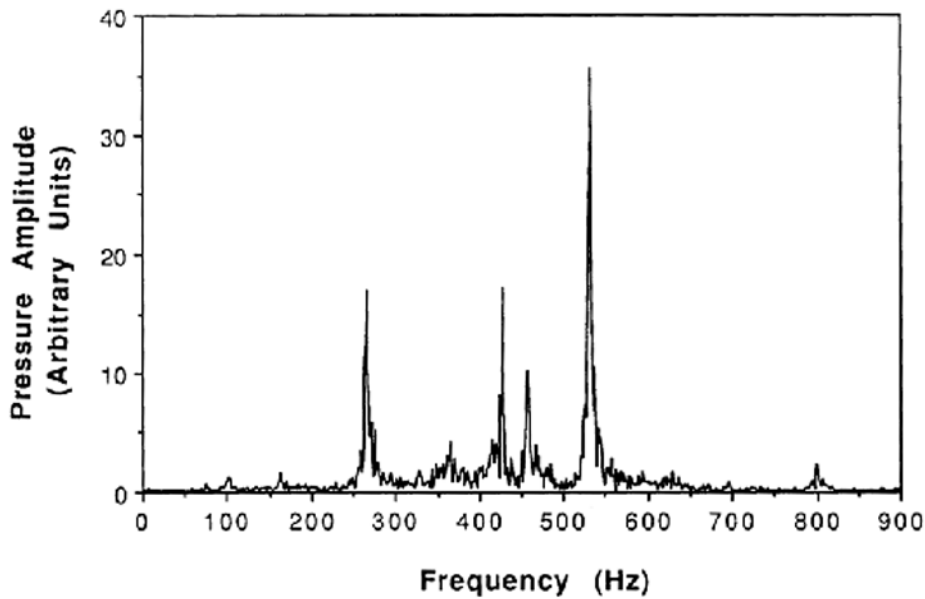


(b)

FIGURE 1.4. Waveform and Spectrum for an Instability in the Caltech Dump Combustor

Much of these lectures is devoted to understanding the origins of the behavior illustrated by the examples in Figures 1.3 and 1.4. The classical theory of acoustics has provided the basis for under standing combustion instabilities since early recognition that some unexpected observations could be traced to pressure oscillations. Many basic results of classical acoustics have been applied directly and with remarkable success to problems of instabilities. It is often taken for granted that well-known acoustics formulas should be applicable—their use can in fact be justified on fundamental grounds. However, in the first instance, it is surprising that they work so well,

because the medium is far from the ideal uniform quiescent gas assumed in the classical acoustics of resonating chambers.

A combustion chamber contains a non-uniform flow of chemically reacting species, often present in condensed as well as gaseous phases, exhausting through a nozzle that is choked in rockets, ramjets, and afterburners. Moreover, the flow is normally turbulent and may include regions of separation. Yet estimates of the frequencies of oscillations computed with acoustics formulas for the natural modes of a closed chamber containing a uniform gas at rest commonly lie within 10–15 percent or less of the frequencies observed for combustion instabilities, if the speed of sound is correctly chosen.

There are three main reasons that the classical view of acoustics is a good first approximation to wave propagation in combustion chamber: (1) the Mach number of the average flow is commonly small, so convective and refractive effects are small; (2) if the exhaust nozzle is choked, incident waves are efficiently reflected, so for small Mach numbers the exit plane appears to be nearly a rigid surface; and (3) in the limit of small amplitude disturbances, it is a fundamental result for compressible flows that any unsteady motion can be decomposed into three independent modes of propagation, of which one is acoustic (Chu and Kovazsnay 1956). The other two modes of motion are vortical disturbances, the dominant component of turbulence, and entropy (or temperature) waves. Hence even in the highly turbulent non-uniform flow usually present in a combustion chamber, acoustic waves behave in good first approximation according to their own simple classical laws. That conclusion has simplified enormously the task of gaining qualitative understanding of instabilities arising in full-scale systems as well as in laboratory devices.

Of course, it is precisely the departures from classical acoustics that define the class of problems we call combustion instabilities. In that sense, this book is concerned chiefly with perturbations of a very old problem, standing waves in an enclosure. That point of view has significant consequences; perhaps the most important is that many of the physical characteristics of combustion instabilities can be described and understood quite well in a familiar context. The remainder of this chapter is an elaboration of that conclusion.

The most obvious evidence that combustion instabilities are related to classical acoustic resonances is the common observation that frequencies measured in tests agree fairly well with those computed with classical formulas. Generally, the frequency $f$ of a wave equals its speed of propagation, $a$, divided by the wavelength, $\lambda$:

$$f = \frac{a}{\lambda} \tag{1.1}$$

On dimensional grounds, or by recalling classical results, we know that the wavelength of a resonance or normal mode of a chamber is proportional to a length, the unobstructed distance characterizing the particular mode in question. Thus the wavelengths of the organ-pipe modes are proportional to the length, $L$, of the pipe, those of modes of motion in transverse planes of a circular cylindrical chamber are proportional to the diameter, $D$, and so forth. Hence (1.1) implies

$$f \sim \frac{a}{L} \quad \text{longitudinal modes}$$

$$\tag{1.2 a, b}$$

$$f \sim \frac{a}{D} \quad \text{transverse modes}$$

There are two basic implications of the conclusion that the formulas (1.2 a, b), with suitable multiplying constants, seem to predict observed frequencies fairly well: evidently the geometry is a dominant influence on the special structure of the instabilities; and we can reasonably define some sort of average speed of sound in the chamber, based on an approximation to the temperature distribution. In practice, estimates of a use the classical formula $a = \sqrt{\gamma RT}$ with $T$ the adiabatic flame temperature for the chemical system in question, and with the properties $\gamma$ and $R$ calculated according to the composition of the mixture in the chamber. Usually, mass-averaged values, accounting for condensed species, seem to be close to the truth. If large differences of temperature exist in the chamber, as in a flow containing flame fronts, nonuniformities in the speed of sound must be accounted for to obtain good estimates of the frequencies.

Even for more complicated geometries, notably those often used in solid rockets, when the simple formulas (1.2 a, b) are not directly applicable, numerical calculations of the classical acoustic motions normally give good

RTO-EN-023

approximations to the natural frequencies and pressure distributions. Thus quite generally we can adopt the point of view that combustion instabilities are acoustical motions excited and sustained in the first instance by interactions with combustion processes. That the classical theory works so well for estimating frequencies and distributions of the unsteady motions means that computation of those quantities is not a serious test of a more comprehensive theory. What is required first of a theory of combustion instabilities is a basis for understanding how and why combustion instabilities differ from classical acoustics.

In particular, two global aspects of minor importance in most of classical acoustics, are fundamental to understanding combustion instabilities: transient characteristics and nonlinear behavior. Both are associated with the property that with respect to combustion instabilities, a combustion chamber appears to an observer to be a *self-excited system*: the oscillating appear without the action of externally imposed forces. Combustion processes are the sources of energy which ultimately appear as the thermal and mechanical energy of the fluid motions. If the processes tending to dissipate the energy of a fluctuation in the flow are weaker than those adding energy, then the disturbance is unstable.

**1.6. Linear Behavior.** When the amplitude of a disturbance is small, the rates of energy gains and losses are usually proportional to the energy itself which in turn is proportional to the square of the amplitude of the disturbance; the responsible processes are said to be linear because the governing equations are linear in the flow variables. An unstable disturbance then grows exponentially in time, without limit if all processes remain linear. Exponential growth of the form $A_0 e^{\alpha t}$, where $A_0$ is the amplitude of the initial small disturbance, is characteristic of the initial stage of an instability in a self-excited system, sketched in Figure 1.5(a). In contrast, the initial transient in a linear system forced by an invariant external agent grows according to the form $1 - e^{-\beta t}$, shown in Figure 1.5(b). The curve $e^{\alpha t}$ is concave upward and evolves into a constant limiting value for a physical system only if nonlinear processes are active. However, the plot of $1 - e^{-\beta t}$ is concave downward and approaches a limiting value for a linear system because the driving agent supplies only finite power.



(a)   (b)
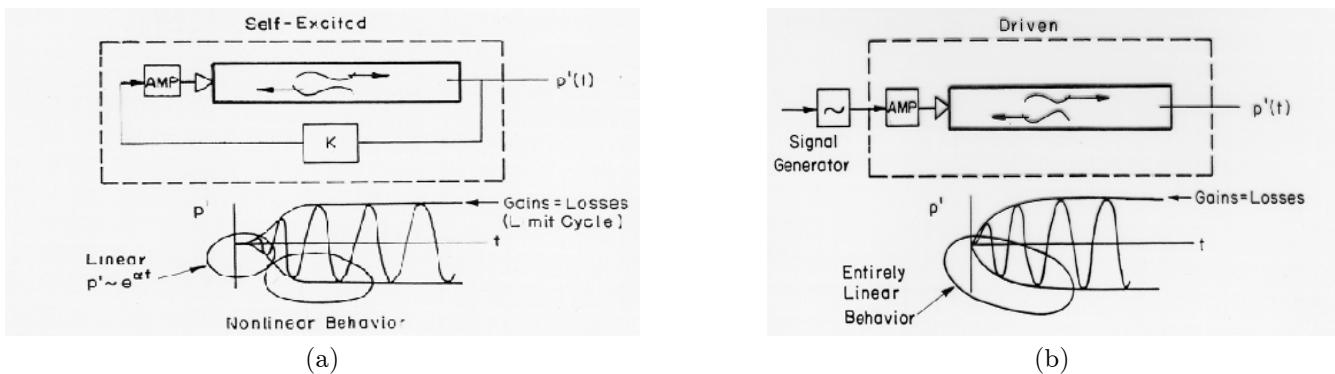
FIGURE 1.5. Transient behavior of (a) Self Excited Linearly Unstable Motions; (b) Forced Motions.

Data of the sort reproduced in Figure 1.4 leave no doubt that the unstable motions in combustion chambers are self-excited, having the characteristics shown in Figure 1.5(a). The physical origin of this behavior is the dependence of the energy gains and losses on the motions themselves. For combustion instabilities, the 'system' is the dynamical system whose behavior is measured by the instrument sensing the pressure oscillations. Thus, in view of earlier remarks, the dynamical system is in some sense the system of acoustical motions in the chamber coupled to the mean flow and combustion processes (recall Figure 1.1).

It is a fundamental and extremely important conclusion that by far most combustion instabilities are motions of a self-excited dynamical system. Probably the most significant implication is that in order to understand fully the observed behavior, and how to affect it and control it, one must understand the behavior of a nonlinear system. When the motion in a combustion chamber is unstable, except in unusual cases of growth to destruction, the amplitude typically settles down to a finite value: the system then executes a limiting motion, usually a periodic limit cycle. For practical applications, it is desirable to know how the amplitude of the limit cycle depends on the parameters characterizing the system. That information may serve as the basis for changing the characteristics to reduce the amplitude, the goal in practice being zero. In any case, good understanding of the properties of the

limit cycle will also provide some appreciation for those variables which dominate the behavior and to which the motions may be most sensitive, a practical matter indeed.

Our global view, then, is that a combustion instability is an oscillatory motion of the gases in the chamber, which can in first approximation be synthesized of one or more modes related to classical acoustic modes. The mode having lowest frequency is a 'bulk' mode in which the pressure is nearly uniform in space but fluctuating in time. Because the pressure gradient is everywhere small, the velocity fluctuations are nearly zero. This mode corresponds to the vibration of a Helmholtz resonator obtained, for example, by blowing over the open end of a bottle. The cause in a combustion chamber may be the burning process itself, or it may be associated with oscillations in the supply of reactants, caused in turn by the variations of pressure in the chamber.

Structural vibrations of a solid rocket are not normally influential, but an instability of the bulk mode (there is only one bulk mode for a given geometry) has often been a problem in motors designed for use in space vehicles. In those cases, the term L*-instability has been used because the stability of the mode is predominantly a function of the L* of the motor and the mean pressure (Sehgal and Strand 1964). The instability is associated with the time lag between fluctuations of the burning rate and of mass flux through the nozzles: that time lag is proportional to the residence time, and hence L*, for flow in the chamber. L*-instabilities occur in motors qualified for space flight because they arise in the lower ranges of pressure at which such rockets operate.

Whatever the system, most combustion instabilities involve excitation of the acoustic modes, of which there are an infinite number for any chamber. The values of the frequencies are functions primarily of the geometry and of the speed of sound, the simplest examples being the longitudinal and transverse modes of a circular cylinder, with frequencies behaving according to 1.2 a, b. Which modes are unstable depends on the balance of energy supplied by the exciting mechanisms and extracted by the dissipating processes. We consider here only linear behavior to illustrate the point.

In general the losses and gains of energy are strongly dependent on frequency. For example, the attenuation due to viscous effects typically increases with the square root of the frequency. Other sources of energy loss associated with interactions between the oscillations and the mean flow tend to be weaker functions of frequency. That is the case, for example for reflections of waves by a choked exhaust nozzle. The gains of energy usually depend in a more complicated way on frequency.

The sources of energy for combustion instabilities i.e. the mechanisms responsible for their existence, present the most difficult problems in this field. For the present we confine our attention to qualitative features of energy exchange between combustion to unsteady motions. For example, the magnitude of the energy addition due to coupling between acoustic waves and combustion processes for a solid propellant normally rises from some relatively small quasi-steady value at low frequencies, passes through a broad peak, and then decreases to zero at high frequencies. Recent experimental results suggest that flames may exhibit similar behavior (Pun 2001). Energy is transferred to a pressure oscillation having a particular frequency at a rate proportional to the part of the coupling that is in phase with the pressure at that frequency.[1] Figure 1.6 is a schematic illustration of this sort of behavior.

In Figure 1.6, the gains exceed the losses in the frequency range $f_1 < f < f_2$. Modes having frequencies in that range will therefore be linearly unstable. An important characteristic, typical of combustion chambers generally, is that in the lower ranges of frequency, from zero to somewhat above the maximum frequency of instability, the net energy transfer is a small difference between relatively larger gains and losses. That implies the difficulty, confirmed by many years' experience, of determining the net energy flow accurately. Unavoidable uncertainties in the gains and losses themselves become much more significant when their difference is formed. That is the main reason for the statement made earlier that analysis of combustion instabilities has been useful in practice chiefly for predicting and understanding trends of behavior rather than accurate calculations of the conditions under which a given system is unstable. The ultimate source of all of these difficulties is the fact, cited in Section 1.1, is the property that the motions in question consume and contain only small portions of the total energy available within the system. Hence in both laboratory tests and in operational systems one is confronted with determining the characteristics of essentially small disturbances imbedded in a complicated dynamic environment.

---

[1]It is possible, due to the behavior of the phase angle, that in a range of high frequencies the combustion processes may in fact extract energy from the acoustic waves and hence contribute to the losses of energy.
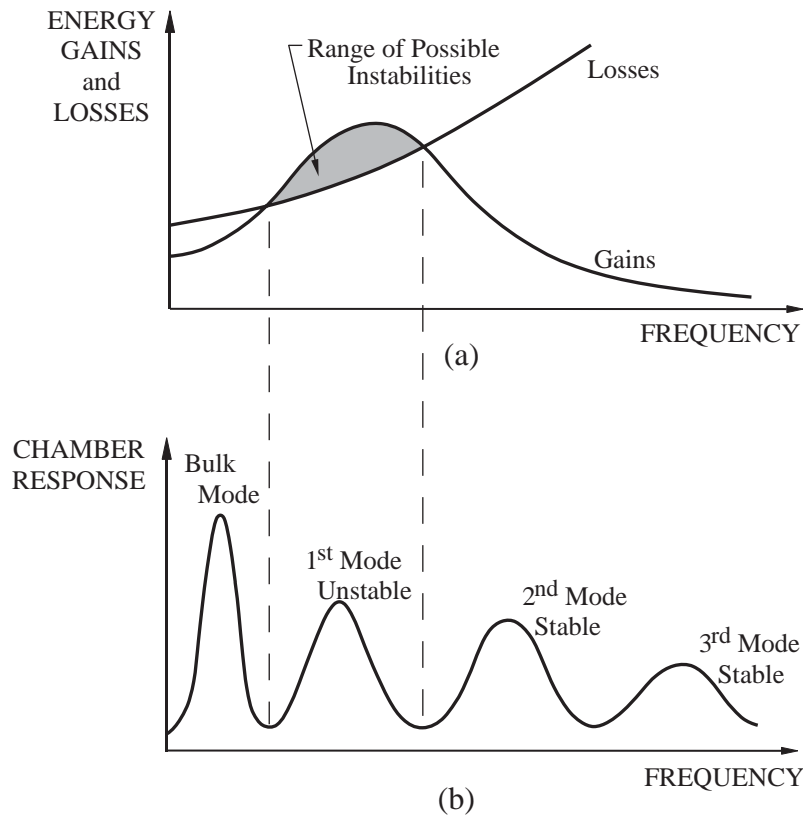
FIGURE 1.6. Qualitative Dependence of (a) Energy Gains and Losses; and (b) the Frequency Response of a Combustor.

The best and most complete data illustrating the preceding remarks have been obtained with solid propellant rockets. There are several reasons for that circumstance. First, the ignition period — the time to cause all of the exposed propellant surface to begin burning — is relatively short and the average conditions in the chamber quickly reach their intended values. Unless oscillations are severely unstable, and growing rapidly during the ignition transient, there is a good opportunity to observe the exponential growth characteristic of a linear instability. The measurements shown in Figures 1.4(a) and (b) are good examples.

Secondly, it is probably true that more effort has been spent on refining the measurements and predictions of linear stability for solid rockets than for other systems because of the expense and difficulty of carrying out replicated tests. There is no practical, routine way of interrupting and resuming firings and it is the nature of the system that an individual motor can be fired only once. Particularly for large motors used in space launch vehicles, successive firings involve great expense. Development by empirical trial-and-error is costly and there is considerable motivation to work out methods of analysis and design applicable to individual tests.

1.6.1. *Gains and Losses of Acoustic Energy; Linear Stability.* It is a general result of the theory of linear systems that if a system is unstable, a small disturbance of an initial state will grow exponentially in time:

$$\text{amplitude of disturbance} \sim e^{\alpha_g t} \tag{1.3}$$

where $\alpha_g > 0$ is called the *growth constant.* If a disturbance is linearly stable, then its amplitude decays exponentially in time, being proportional to $e^{-\alpha_d t}$ and $\alpha_d > 0$ is the *decay constant.* The definition (1.3) implies that for a variable of the motion, say the pressure, having maximum amplitude $\hat{p}_0$ in one cycle of a linear oscillation:

$$p'(t) = \hat{p}_0 e^{\alpha_g (t-t_0)} \tag{1.4}$$

where $\hat{p}_0$ is the amplitude at time $t = t_0$. Then if $p'_1$, $p'_2$ are the peak amplitudes at time $t_1$, $t_2$ as indicated in Figure 1.7,

$$\frac{\hat{p}_2}{\hat{p}_1} = \frac{p'(t = t_2)}{p'(t = t_1)} = \frac{e^{\alpha_g(t_2-t_0)}}{e^{\alpha_g(t_1-t_0)}} = e^{\alpha_g(t_2-t_1)} \tag{1.5}$$

The logarithm of (1.5) is

$$\log \frac{\hat{p}_2}{\hat{p}_1} = \alpha_g(t_2 - t_1) \tag{1.6}$$

In practice, $t_2 - t_1$ is taken equal to the period $\tau$, the time between successive positive (or negative) peaks. Then the logarithm of the ratio $\hat{p}_2/\hat{p}_1$ for a number of pairs of successive peaks is plotted versus the time $t_1$ or $t_2$ at which the first or second peak occurs. The line is straight, having slope $\alpha_g$.

Whatever the system, the analytical treatment of linear stability is essentially the same. There is really only one problem to solve: find the growth and decay constants and the frequencies of the modes. Determining the actual mode shapes is part of the general problem, but is often not essential for practical purposes. Typically, both the frequency and the mode shape for small-amplitude motions in a combustion chamber are so little different from their values computed classically as to be indistinguishable by measurement in operating combustors. By "classical" we mean here a computation according to the equations of classical acoustics for the geometry at hand, and with account taken of large gradients in the temperature, which affect the speed of sound. The presence of combustion processes and a mean flow field are not accounted for explicitly, but it may be necessary for satisfactory results, to include a good approximation to the boundary condition applied at the exhaust nozzle, particularly if the average Mach number is not small.
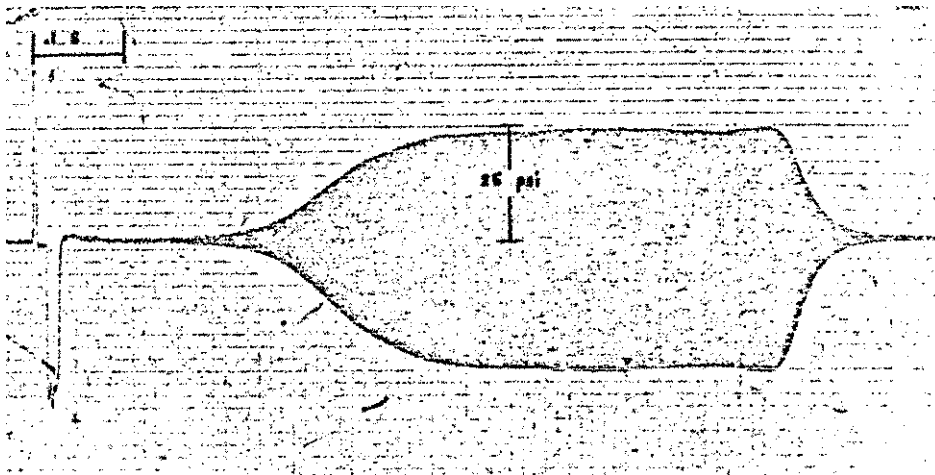


FIGURE 1.7. Exponential Growth of a Linearly Unstable Motion (Perry 1968)

Hence the linear stability problem is really concerned with calculations of the growth and decay constants for the modes corresponding to the classical acoustic resonances. An arbitrary small amplitude motion can, in principle, be synthesized with the results, but that calculation is rarely required for practical applications. Results for the net growth or decay constant have been the central issue in both theoretical and practical work. In combustors, processes causing growth of disturbances and those causing decay act simultaneously. Hence an unstable disturbance is characterized by a net growth constant that can be written $\alpha = \alpha_g - \alpha_d$. Because the problem is linear, the growth constants can quite generally be expressed as a sum of the contributions due to processes accounted for in the formulation, as for example:

$$\alpha := \alpha_g - \alpha_d = (\alpha)_{\text{combustion}} + (\alpha)_{\text{nozzle}} + (\alpha)_{\text{mean flow}} + (\alpha)_{\text{condensed}} + (\alpha)_{\text{structure}} + \cdots \tag{1.7}$$

The labels refer to processes of interaction between the acoustic field and combustion, the nozzle, the mean flow, condensed species, the containing structure,.... Structural interactions comprise not only the vibrations mentioned earlier as a necessary part of the POGO instability, but also quite generally any motions of mechanical components, including propellant. For example, in large, solid propellant rockets, motions of the viscoelastic

material of the grain may be a significant source of energy losses through internal dissipation (McClure, Hart, and Bird 1960).

The stability boundary—the locus of parameters marking the boundary between unstable ($\alpha > 0$) and stable ($\alpha < 0$) oscillations—is defined by $\alpha = 0$ in (1.7). That statement is a formal rendition of the physical condition that the energy gained per cycle should equal the energy lost per cycle:

$$\alpha_g = \alpha_d \tag{1.8}$$

Usually the main source of energy is combustion and in terms of the contributions shown in (1.7), this relation becomes

$$(\alpha)_{\text{combustion}} = -(\alpha)_{\text{nozzle}} - (\alpha)_{\text{mean flow}} - (\alpha)_{\text{condensed}} - (\alpha)_{\text{structure}} \tag{1.9}$$

There are situations in which the acoustic/mean flow interactions may provide a gain of energy. That is, energy is transferred from the average flow to the unsteady motions (as happens, for example, in wind instruments and sirens), but there is no need to consider the matter at this point.

As simple as it appears, equation (1.7) defining $\alpha$, and its special form (1.8) defining the stability boundary, are basic and extremely important results. There is no evidence, for any propulsion system, contradicting the view that these results are correct representations of actual linear behavior. Difficulties in practice arise either because not all significant processes are accounted for, or, more commonly, insufficient information is available to assign accurately the values of the various individual growth or decay constants.
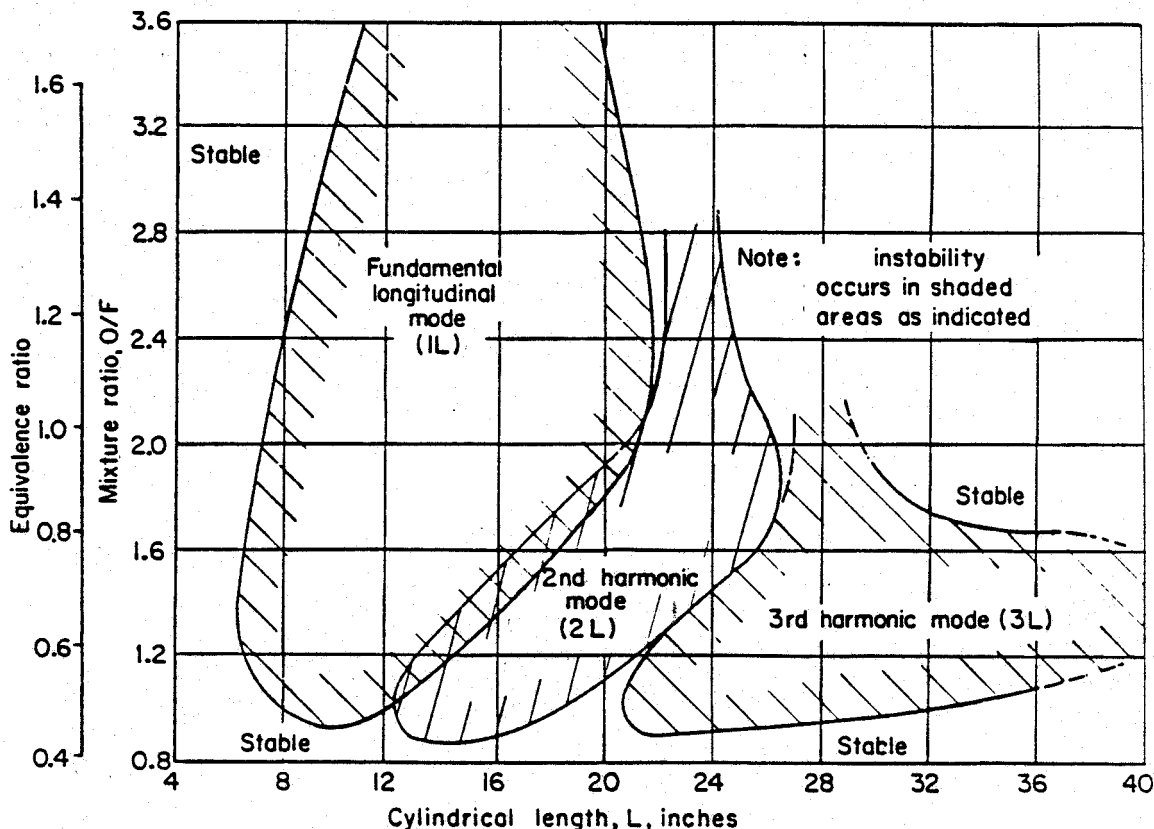


FIGURE 1.8. Stability Boundary for a Laboratory Gas-Fueled Rocket (Crocco, Grey, and Harrje)

As examples, Figure 1.8 shows stability boundaries computed for longitudinal oscillations in a gas-fueled laboratory rocket motor (Crocco, Grey, and Harrje 1960) and Figure 1.9 shows the results of calculations for a large, solid propellant rocket (Beckstead 1974). Those results illustrate the two uses mentioned above for the

formula (1.9). In the case of the gas-fired rocket, the calculations contained two parameters not known from first principles, namely $n$ and $\tau$ arising in the time-delay model of the interactions between combustion and the acoustic field. All other parameters defining the geometry and the average flow field were known. The purpose of the work was to compare the calculations with measurements of the stability boundary to infer values of $n$ and $\tau$.
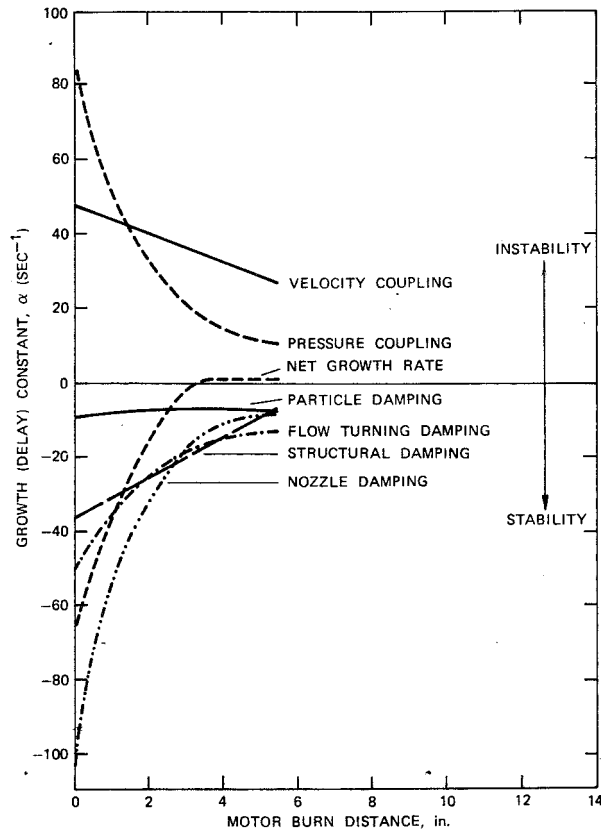


FIGURE 1.9. Predicted Stability Boundary for a Large Solid Propellant Rocket Motor, and the Separate Contributions to $\alpha_d$ and $\alpha_g$. (Beckstead 1974)

The purpose of the results reproduced in Figure 1.9 was to predict the stability of a full-scale motor prior to test firing. In that case, all of the parameters appearing in (1.7) must be known. Usually some of the information is available only from ancillary laboratory tests, notably those required to characterize the coupling between propellant combustion and the acoustic field.

Indeed, an important application of the formulas (1.11) and (1.12) is to do exactly that for a laboratory device called the "T-burner". It is not necessary to restrict attention to the stability boundary if good measurements of the growth constant can be made. Then if all the losses can be computed, one can find the value of the growth constant due to combustion (or, more generally all energy gains) as the difference

$$\alpha_{\text{combustion}} = \alpha - \alpha_{\text{losses}} \tag{1.10}$$

Results for $\alpha_{\text{combustion}}$ can either be adapted for use directly in computing the stability of a motor; or they can be interpreted with models of the combustion processes to obtain better understanding of unsteady combustion. That procedure has been used extensively to assess the combustion dynamics of solid propellants and to investigate trends of behavior with operating conditions and changes of composition.

The growth constant has a simple interpretation beyond that given by 1.10 as the slope of a semi-logarithmic plot of the peak amplitudes versus time: twice $\alpha$ is the fractional rate of change of time-averaged energy in the classical acoustic field. We will prove the result more rigorously in Chapter 3 but this interpretation is so central to all problems of linear stability that it is useful to have it in hand from the beginning. By the definition of $\alpha$,

both the pressure and velocity oscillations have the time dependence

$$p' \sim e^{\alpha t} \cos \omega t; \quad u' \sim e^{\alpha t} \sin \omega t$$

multiplied by their spatial distributions. The acoustic energy density is the sum of the local kinetic energy, proportional to $u'^2$, and potential energy, proportional to $p'^2$:

$$\text{K.E.} \sim e^{2\alpha t} \cos^2 \omega t; \quad \text{P.E.} \sim e^{2\alpha t} \sin^2 \omega t$$

If we assume that the period of oscillation, $\tau = 2\pi/\omega$, is much smaller then the decay rate, $1/\alpha$, then the values of these functions averaged over a cycle of the oscillation are proportional to $e^{2\alpha t}$. Hence the acoustic energy density is itself proportional to $e^{2\alpha t}$. Integrating over the total volume of the chamber we find that the total averaged energy $\langle \mathcal{E} \rangle$ in the acoustic field has the form

$$\langle \mathcal{E} \rangle = \langle \mathcal{E}_0 \rangle e^{2\alpha t} \tag{1.11}$$

where $\langle \mathcal{E}_0 \rangle$ is a constant depending on the average flow properties and the geometry. We then find directly from (1.11) the result claimed:

$$2\alpha = \frac{1}{\langle \mathcal{E} \rangle} \frac{d\langle \mathcal{E} \rangle}{dt} \tag{1.12}$$

Another elementary property worth noting is that $1/\alpha$ is the time required for the amplitude of oscillation to decay to $1/e$ of some chosen initial value. Also, the fractional change of the peak value in one cycle of oscillation $(t_2 - t_l = \tau = 2\pi/\omega)$ is

$$|p_2'| - |p_1'| = \delta|p'|_m \sim e^{\alpha t_1} - e^{\alpha t_2} = e^{\alpha t_2} \left[ e^{\alpha(t_1 - t_2)} - 1 \right]$$

where $|\quad|_m$ denotes the magnitude of the peak amplitude. We assume as above that the fractional change in one period $\tau$ is small so

$$e^{\alpha(t_1 - t_2)} \approx 1 + \alpha(t_1 - t_2) = 1 + \alpha\tau$$

The amplitude itself is approximately proportional to $e^{\alpha t_2}$ or $e^{\alpha t_1}$ and we can write the fractional change as

$$\frac{\delta|p'|_m}{|p'|_m} \approx \alpha\tau = \frac{\alpha}{f} \tag{1.13}$$

where $f$ is the frequency in cycles per second, $f = 1/\tau$. The dimensionless ratio $f/\alpha$ is a convenient measure of the growth or decay of an oscillation. According to the interpretation of $1/\alpha$ noted above, $(1/\alpha)/\tau = f/\alpha$ is the number of cycles required for the maximum amplitudes of oscillation to decay to $1/e$ or grow to $e$ times an initial value.

The ratio $\alpha/f$ must be small for the view taken here to be valid. Intuitively, $\alpha$ must in some sense be proportional to the magnitude of the perturbations of the classical acoustics problem. We will find that the most important measure of the perturbations is a Mach number, $\bar{M}_r$, chacterizing the mean flow; for many significant processes, $\alpha/f$ equals $\bar{M}_r$ times a constant of order unity. Roughly speaking, then, the measured value of $\alpha/f$ is an initial indication of the validity of the view that a combustion instability can be regarded as a motion existing because of relatively weak perturbations of classical acoustics.

**1.7. Nonlinear Behavior.** It is a fundamental and extremely important conclusion that combustion instabilities are motions of a self-excited nonlinear dynamical system. Probably the most significant implication is that in order to understand fully the observed behavior, and how to affect or control it, one must ultimately understand the behavior of a nonlinear system. When the motion in a combustion chamber is unstable, except in unusual cases of growth to destruction, the amplitude typically settles down to a finite value: the system then executes a limiting motion, usually a periodic limit cycle. For practical applications, it is desirable to know how the amplitude of the limit cycle depends on the parameters characterizing the system. That information may serve as the basis for changing the characteristics to reduce the amplitude, the goal in practice being zero. In any case, good understanding of the properties of the limit cycle will also provide some appreciation for those variables which determine the behavior and to which the motions may be most sensitive, a practical matter indeed.

Rarely do the motions in a combustion chamber exhibit clear limit oscillations of the sort commonly encountered with simpler mechanical systems. Figure 1.3 and 1.4 illustrate the point. It appears that combustion devices

are subject to influences, probably not easily identified, that prevent constant frequencies and amplitudes in the limit motions. The motions seem not to be limit cycles in the strict sense. However, experience gained in the past few years suggests that the deviations from the well-defined behavior of simpler systems are normally due to secondary influences. There are several possibilities, although not enough is known about the matter to make definite statements. Recent analysis (Burnley, 1996; Burnley and Culick, 1999) has demonstrated that noise, and interactions between random and acoustical motions can cause departures from purely periodic limit cycles appearing very similar to those found in pressure records for operating combustors. The random or stochastic motions are likely associated with flow separation, turbulence, and combustion noise.

Probably other causes of departures from strictly periodic limit cycles are associated with the parameters characterizing steady operation of a combustor; and with 'noise' or random fluctuation of flow variables. As we have already emphasized, the unsteady motions require only a negligibly small part of the energy supplied by the combustion processes. Relatively minor variations in the combustion field, due, for example, to small fluctuations in the supplies of reactants, may alter the rates of energy transfer to instabilities and hence affect features of a limit cycle. Similarly, adjustments in the mean flow, notably the velocity field and surface heat transfer rates, will directly influence the unsteady field. Laboratory experiments clearly show such phenomena and considerable care is required to achieve reproducible results. In solid propellant rockets, the internal geometry necessarily changes during a firing. That happens on a time scale much longer than periods of unsteady motions, but one obvious result is the decrease of frequencies normally observed in tests. Because there is ample reason to believe that the phenomena just mentioned are not essential to the global nonlinear behavior of combustion instabilities, we ignore them in the following discussion.

1.7.1. *Linear Behavior Interpreted as the Motion of a Simple Oscillator.* Intuitively we may anticipate that nonlinear behavior may be regarded in first approximation as an extension of the view of linear behavior described in the preceding section, made more precise in the following way. Measurement of a transient pressure oscillation often gives results similar to those shown in Figures 1.5(a). The frequency in each case varies little, remaining close to a value computed classically for a natural resonance of the chamber, and the growth of the peak amplitude during the initial transient period is quite well approximated by the rule for a linear instability, $e^{\alpha t}$. Thus the behavior is scarcely distinguishable from that of a classical linear oscillator with damping, and having a single degree of freedom. The governing equation for a simple mass $(m)$/ spring $(k)$/ dashpot $(r)$ system is

$$m\frac{d^2x}{dt^2} + r\frac{dx}{dt} + kx = 0 \tag{1.14}$$

It is surely tempting to model a linear combustion instability by identifying the pressure fluctuation, $p'$, with the displacement $x$ of the mass. Then upon dividing (1.14) by $m$ and tentatively replacing $x$ by $p'$, we have

$$\frac{d^2p'}{dt^2} + 2\alpha\frac{dp'}{dt} + \omega_0^2 p' = 0 \tag{1.15}$$

where $2\alpha = r/m$ and the undamped natural frequency is $\omega_0 = \sqrt{k/m}$. The familiar solution to (1.15) has the form of the records shown in Figures 1.5(a), $p' = \hat{p}_0 e^{\alpha t} \cos \Omega t$ where $\Omega = \omega_0\sqrt{1 - (\alpha/\omega_0)^2}$ and $\hat{\rho}_0$ is the value of $p'$ at $t = 0$.

The preceding remarks suggest the course we should follow to investigate the linear behavior of combustion instabilities, and indeed is the motivation behind the general view described earlier. But this is purely descriptive heuristic reasoning. No basis is given for determining the quantities 'mass,' 'damping coefficient,' and 'spring constant' for the pressure oscillation. The procedure for doing so is developed in Chapter 4; the gist of the matter is the following, a brief description of the method used later to analyze combustion instabilities.

According to the theory of classical acoustics for a sound wave, we may identify both kinetic energy per unit mass, proportional to the square of the acoustic velocity $u'$, and potential energy per unit mass, proportional to the square of the acoustic pressure $p'$. The acoustic energy per unit volume is

$$\frac{1}{2}\left(\bar{\rho}u'^2 + \frac{p'^2}{\bar{\rho}\bar{a}^2}\right) \tag{1.16}$$

where $\bar{\rho}$ and $\bar{a}$ are the average density and speed of sound. This expression corresponds to the formula for the energy of a simple oscillator,

$$\frac{1}{2}(m\dot{x}^2 + kx^2) \tag{1.17}$$

Now consider a stationary wave in a closed chamber. Both the velocity and pressure fluctuations have spatial distributions such that the boundary condition of no velocity normal to a rigid wall is satisfied. Hence the local pressure $p'$ in equation (1.15) must depend on position as well as time. However, the frequency $\omega_0$ depends on the geometry of the entire chamber and according to equation (1.12), we should be able to interpret $2\alpha$ in equation (1.15) as the fractional rate of change of averaged energy in the entire volume. Therefore, we expect that the parameters $m$, $k$, and $r$ implied by the definitions $\alpha = r/2m$ and $\omega_0 = k/m$ must be related to properties of the entire chamber. The approximate analysis used in most of this book is based partly on spatial averaging defined so that the properties ascribed to a particular mode are local values weighted by the spatial distribution of the mode in question, and averaged over the chamber volume.

Locally in the medium, the 'spring constant' is supplied by the compressibility of the gas, and the mass participating in the motion is proportional to the density of the undisturbed medium. When the procedure of spatial averaging is applied, both the compressibility and the density are weighted by the appropriate spatial structure of the acoustical motion. As a result, the damping constant and the natural frequency are expressed in terms of global quantities characterizing the fluctuating motion throughout the chamber. We will find rigorously that in the linear limit, an equation of the form (1.15) does apply, but instead of $p'$ itself, the variable is $\eta_n(t)$, the time dependent amplitude of an acoustic mode represented by

$$p'_n = \bar{p}\eta_n(t)\psi_n(\vec{r}) \tag{1.18}$$

where $\bar{p}$ is the mean pressure and $\psi_n(\vec{r})$ is the spatial structure of the classical acoustic mode identified by the index $(\quad)_n$. Hence the typical equation of motion is

$$\frac{d^2\eta_n}{dt^2} + 2\alpha_n\frac{d\eta_n}{dt} + \omega_n^2\eta_n = 0 \tag{1.19}$$

The constants $\alpha_n$ and $\omega_n$ contain the influences of all linear processes distinguishing the oscillation in a combustion chamber from the corresponding unperturbed classical motion governed by the equation

$$\frac{d^2\eta_n}{dt^2} + \omega_{n0}^2\eta_n = 0 \tag{1.20}$$

if dissipation of energy is ignored. Because damping in a mechanical system causes a frequency shift, and the actual frequency is not equal tot he unperturbed value, $\omega_{n0}$.

For technical reasons not apparent at this point, it is convenient to regard the linear perturbing process as a force $F_n(\eta_n, \dot{\eta}_n)$ is acting on the 'oscillator' and equation (1.19) is written

$$\frac{d^2\eta_n}{dt^2} + \omega_{n0}^2\eta_n = F_n^L(\eta_n, \dot{\eta}_n) \tag{1.21}$$

The superscript $(\quad)^L$ identifies the 'force' as linear, and for simplicity $\omega_{n0}^2$ is written $\omega_n^2$. We will consistently use the symbol $\omega_n$ for the unperturbed classical acoustic frequency. If there is no linear coupling between the modes (typically linear coupling is small), the force $F_n^L$ consists of two terms, one representing the damping of the mode and one the frequency shift:

$$F_n^L = -\Delta\omega_n^2\eta_n + 2\alpha_n\dot{\eta}_n \tag{1.22}$$

Equations (1.21) and (1.22) produce (1.19) with $\omega_n^2$ replaced by $\omega_n^2 + \Delta\omega_n^2$.

With the above reasoning we have heuristically constructed equation (1.21) as the fundamental equation for a linear combustion instability corresponding to a classical acoustic mode of the chamber. Its simplicity masks the fact that a great amount of effort is required to determine realistic functions $F_n^L(\eta_n, \dot{\eta}_n)$ applicable to the motions in a combustion chamber. The approximate analysis developed later provides a framework for accommodating all linear processes but does not contain explicit formulas for all of them. Most importantly, there are terms

representing interactions between combustion processes and the unsteady motions, but their computation requires modeling the mechanisms that cause combustion instabilities. Some of the purely gasdynamical processes, arising with coupling between mean and fluctuating motions, are given explicitly.

According to classical acoustic theory, a closed chamber of gas at rest has an infinite number of normal or resonant modes. The spatial structures (mode shapes) and resonant frequencies are found as solutions to an eigenvalue problem. A general motion in the chamber, having any spatial structure, can then be represented as a linear superposition of the normal modes. The process of spatial averaging, leading to equation (1.20), amounts to representing any motion as an infinite collection of simple oscillators, one associated with each of the normal modes. That interpretation holds as well for equation (1.21) except that now each mode may suffer attenuation ($\alpha_n < 0$) or excitation ($\alpha_n > 0$). It is this point of view that allows natural extension of the analysis to nonlinear behavior.

1.7.2. *Nonlinear Behavior Interpreted as the Motion of a Nonlinear Oscillator.* In view of the observation that measurements often show development of limit cycles like those shown in Figure **??**, it is tempting simply to add a nonlinear term to the oscillator equation (1.21) and assume that a combustion instability involves only a single mode. Thus, for example, we could add to the right-hand side a force $F_n^{nL} = c_1 \eta_n^2 + c_2 \ddot{\eta}_n^2 + c_3 \eta_n \dot{\eta}_n + c_4 |\eta_n| + \cdots$ where the constants $c_1,...$ may be chosen by fitting the solution to data. Culick (1971) showed that quite good results could be obtained with this approach applied to limited data. Figure 1.10 shows one example. Of course this is a purely *ad hoc* approach and provides no means of computing the coefficients from first principles.
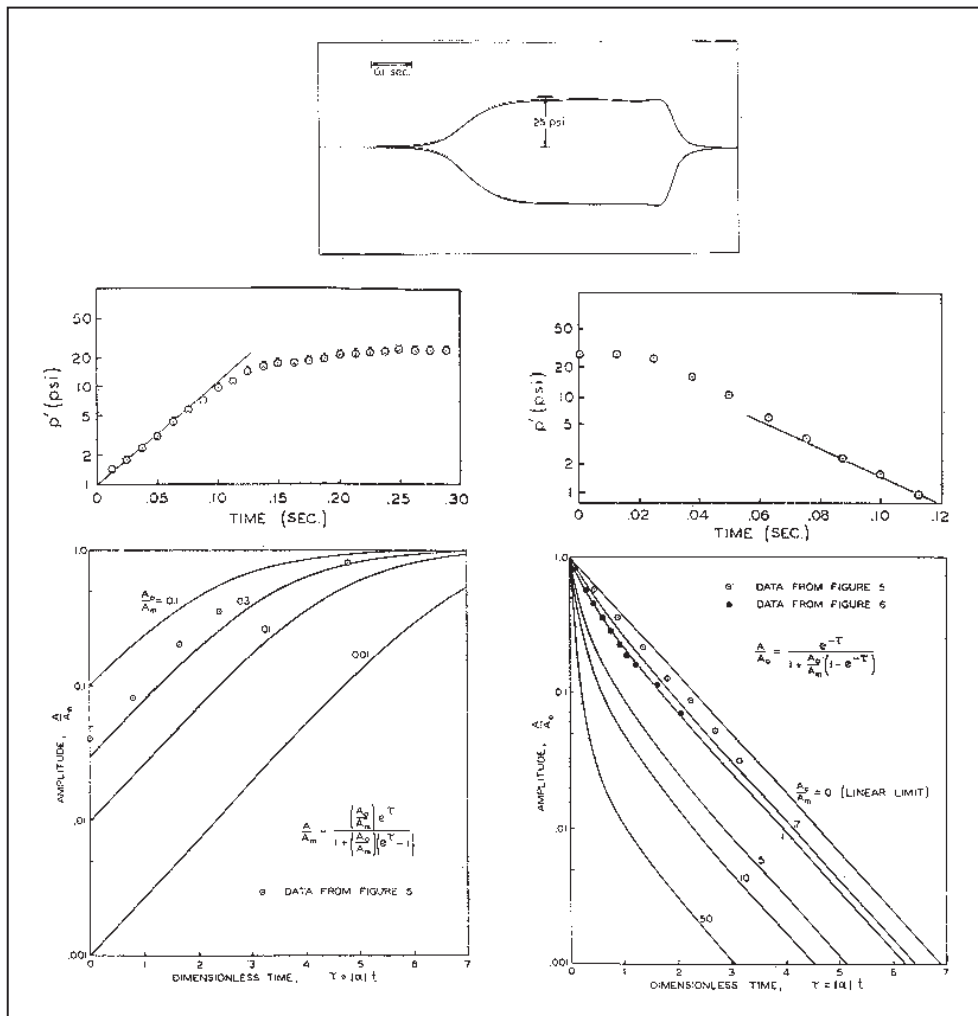


FIGURE 1.10. An Example of Fitting T-Burner Data with the Model of a Simple Nonlinear Oscillator (Culick 1971).

Subsequently, Jensen and Beckstead (1973) applied that procedure to extensive data taken in laboratory devices intended for measuring the characteristics of unsteady burning of solid propellants. The chief result was that the data could be matched equally well with rather broad ranges of the constants, and no particular kind of nonlinearity seemed to dominate the motions. Consequently, representation with a single mode was not successful. Even though analysis of pressure records for limit cycles often showed relatively small (it seemed) amounts of harmonics of the principle mode, it appeared necessary to account for two modes at least, with coupling due to nonlinear processes.

In other contexts, that conclusion is surely not surprising. The development of a small amplitude compressive disturbance into a shock wave is the oldest and most familiar example in gasdynamics. Steepening of a smooth wave arises primarily from two nonlinear influences: convection of the disturbance by its own motion, and dependence of the speed of sound on the local temperature, itself dependent on the wave motion. A good approximation to the phenomenon is obtained if viscous stresses and heat conduction are ignored. If the disturbance is regarded as a combination of various modes, the flow of energy from modes in the low frequency range to those having higher frequencies is favored by the nonlinear gasdynamic coupling. The rapid growth of the higher-frequency modes having shorter wavelengths produces the steepening, eventually limited, in real flows, by the actions of various effects. In a combustion chamber possible consequences of nonlinear combustion processes cannot be ignored.

In extreme cases of combustion instabilities, particularly in liquid and solid rockets, the approximately sinusoidal motions, substantially systems of stationary waves, may be absent or evolve into a different form. The motions then appear to be weak shock waves, or pulses having measurable width, propagating in the chamber. Instabilities of that type are commonly produced subsequent to excitation by finite pulses. Examples were observed early in tests of liquid rockets, typically involving motions mainly transverse to the axis, identified as 'spinning' transverse modes. Their presence is particularly harmful due to the greatly increased surface heat transfer rates causing unacceptable scouring of the chamber walls.

The corresponding cases in solid rockets usually are longitudinal motions. They rarely occur in large motors and seem to have been first observed in pulse testing of laboratory motors (Dickenson 1962; Brownlee 1964). An example is reproduced in Figure 1.11 (Brownlee, 1964). Often this sort of instability is accompanied by a substantial increase of the mean pressure, seriously affecting the steady performance of the motors. The primary cause of the pressure rise is evidently the increased burn rate, although precisely why the rate increases is not well understood. More recently, these pulsed instabilities have been the subject of successful comparisons between laboratory test results and numerical simulations (Baum and Levine 1982; Baum, Levine, and Lovine 1988). Figure 1.12 shows an example of their results.

For combustion instabilities, the situation is very different from that for shock waves in a pure gas because the processes governing the transfer of energy from combustion to the gasdynamical motions cannot be ignored and in general depend strongly on frequency. Indeed, it may happen, as seems sometimes to be the case for combustion of solid propellants, that the coupling may cause attenuation of higher frequencies. For that reason, the tendency for steepening by the gasdynamics is partially compensated by the combustion processes, may be linear or nonlinear. As a result, in a chamber, a limit cycle may be formed having very closely the spatial structure and frequency of the unstable mode (commonly, but not always, the fundamental mode) and relatively modest amounts of higher modes. It is that behavior that seems to be important in many combustion problems, explaining in part why the approach taken in the approximate analysis has enjoyed some success.

Naturally the preceding is a greatly simplified and incomplete description of the events actually taking place in a given combustion chamber. The essential conclusion that nonlinear gasdynamical processes are partly augmented and partly compensated by combustion processes seems to be an important aspect of all combustion instabilities. It appears that the idea was first explicitly recognized in work by Levine and Culick (1972, 1974), showing that realistic limit cycles could be formed with nonlinear gasdynamics and linear combustion processes. Perhaps the most important general implication of those works is that the nonlinear behavior familiar in flows of pure nonreacting gases is not a reliable guide to understanding the nonlinear behavior in combustion chambers.

For nonlinear problems, the governing equations obtained after spatial averaging have the form
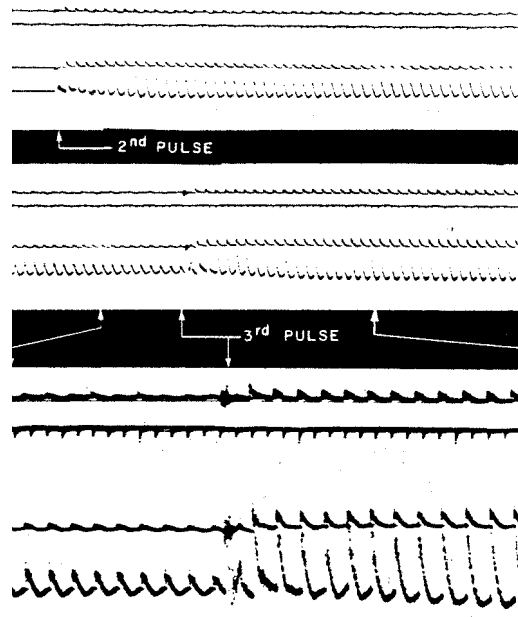
FIGURE 1.11. Steep-fronted Waves Observed in Solid Propellant Rocket Motors (Brownlee, 1964)
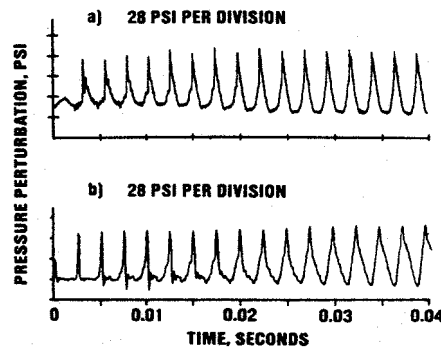


FIGURE 1.12. A Comparison of Observed and Simulated Steep-Fronted Waves in a Solid Propellant Rocket Motor. (a) Observed; (b) numerical Simulation (Baum and Levine, 1982).

$$\frac{d^2\eta_n}{dt^2} + \omega_n^2 \eta_n = F_n^L(\eta_n, \dot{\eta}_n) + F_n^{NL}(\eta_i, \dot{\eta}_i) \tag{1.23}$$

where $F_n^{NL}(\eta_i, \dot{\eta}_i)$ is the nonlinear force depending on all amplitudes $\eta_i$, including $\eta_n$ itself. Thus we may regard a combustion instability as the time-evolution of the motions of a collection of nonlinear oscillators, one associated with each of the classical acoustic modes for the chamber. In general the motions of the oscillators may be coupled by linear as well as nonlinear processes, although linear coupling seems rarely to be important. The analytical framework established by the dynamical system (1.23) will serve throughout this book as the primary means for analyzing, predicting, and interpreting combustion instabilities.

Representation of unsteady motions in a combustion by expansion in acoustic modes ('modal expansion') and application of spatial averaging was first accomplished by Culick (1961, 1963) using a Green's function. The work by Jensen and Berkstead cited above motivated extension to nonlinear behavior (Culick 1971 and 1975; and Zinn and Powell (1970a, 1970b) first used an extension of Galerkin's method to treat nonlinear behavior is in liquid rockets; the method was subsequently extended to solid rockets by Zinn and Lores (1972). In practice, application of a method based on modal expansion and spatial averaging is normally useful only if a small number of modes is required. Yet there are a large number of experimental results showing the presence of steep-fronted waves, often sufficiently steep to be interpreted as shock waves. Hence an analysis of the sort followed here would

seem to be quite seriously limited unless one is prepared to accommodate a large number of modes. That is, one would expect that wave motions exhibiting rapid temporal changes and large spatial gradients must contain significant amounts of higher modes. However, results have also shown that due to fortunate phase relationships, a surprisingly small number of modes serves quite well even to represent many features of waves having steep fronts. The method gives quite a good approximation to both the limiting motions and the transient development of disturbances into weak shock waves.

**1.8. Analysis and Numerical Simulations of Combustion Instabilities.** In these lectures, the vehicle for unification is a theoretical framework originating in the late 1960s and early 1970s with treatments of instabilities in liquid rockets (Culick 1961, 1963; Powell 1968; Zinn and Powell 1968; and Powell and Zinn 1971) and in solid rockets (Culick 1971, 1976). Those analyses differed from previous work mainly in their use of a form of spatial averaging, in some instances related to Galerkin's method, to replace the partial differential equations of conservation by a system of ordinary differential equations. The dependent variables are the time-dependent amplitudes of the acoustic modes used as the basis for series expansion of the unsteady pressure. It is the process of spatial averaging over the volume of the chamber that produces a formulation convenient for handling models of widely different geometries and physical processes. Consequently, in return for the approximate nature of the analysis (for example, the series must be truncated to a finite number of terms), one obtains both convenience and a certain generality of applications not normally possible when partial differential equations are used directly. In general form, this approach is applicable to all types of combustors. Different systems are distinguished by different geometries and the forms in which the reactants are supplied (liquid, solid, gas, slurry, . . . ). Those differences affect chiefly the modeling of the dominant physical processes.

Some analysis of combustion instabilities has customarily accompanied experimental work as an aid to interpreting observations. The paper by Grad (1949) treating instabilities in solid rockets is probably the first entirely theoretical work dealing with small amplitude acoustical motions in a mean flow field with combustion sources. During the 1950s and 1960s, many theoretical works were published on the subject of oscillations in solid rockets (Bird, McClure, and Hart 1963; Cheng 1954, 1962; Hart and McClure 1959, 1965; Cantrell and Hart 1964; Culick 1966) and in liquid rockets (Crocco 1952, 1956, 1965; Crocco and Cheng 1956; Reardon 1961; Culick 1961, 1963; Sirignano 1964; Sirignano and Crocco 1964; Zinn 1966, 1968, 1969; Mitchell, Crocco, and Sirignano 1969). It was during that period that the view of combustion instability as a perturbation of classical acoustics was first extensively developed.

Most of the analyses cited in the previous paragraph (those by Sirignano, Zinn and Mitchell are notable exceptions) were restricted to linear problems. Their chief purpose was to compute the stability of small amplitude motions. Indeed, since the earliest works on combustion instabilities, practical and theoretical considerations were directed mainly to the general problem of linear stability: the reasoning is that if the system is stable to small disturbances (e.g. associated with 'noise' always present in a combustion chamber) then undesirable instabilities cannot arise. There is a flaw in that reasoning: the processes in a combustion chamber are nonlinear, so a linearly stable system may in fact be unstable to sufficiently large disturbances. In any case, oscillations in combustors reach limiting amplitudes due to the action of nonlinear processes. Hence understanding nonlinear behavior is the necessary context in which one can determine what changes to the system may reduce the amplitudes. Ultimately, a complete theory, and therefore understanding, must include nonlinear behavior, a subject covered at considerable length in these lectures, largely within the context cited in the first paragraph.

Recognition of the practical implications of the deficiencies of a view founded on linear behavior motivated the development of the technique of "bombing" liquid rocket chambers in the 1960s by NASA in its Apollo program. The idea is to subject an operating combustion chamber to a succession of increasingly large disturbances (generated by small explosive charges) until sustained oscillations are produced. Then the size of the disturbance required to "trigger" the instability is evidently a measure of the relative stability of the chamber. Another measure is the rate of decay of oscillations subsequent to a pulse injected into a linearly stable system; the method was invented by NASA during the development of engines for the Apollo vehicle in the 1960's. What constitutes the correct 'measure' of relative stability cannot of course be determined from experiments alone, but requires deeper understanding accessible only through theoretical work. This is part of the reason that the nonlinear analyses cited above were carried out; also an extensive program of numerical calculations was supported. Owing to the limitations of computing resources at that time, those early numerical calculations involved solutions to quite restricted problems, commonly sectors or annular regions of chambers. It was not possible to compute what are

less emphasis on the last. The integration of those activities forms a body of knowledge within which one may understand, interpret and predict physical behavior.

It is important to realize that experimental information about unsteady motions in combustion chambers is very limited. Commonly only measurements of pressure are available. Accelerometers and strain gauges mounted in a chamber may provide data from which some characteristics of the pressure field can be inferred. Quantitative surveys of the internal flow are virtually unavailable owing to the high temperatures, although optical methods are useful in laboratory work to give qualitative information and, occasionally, useful quantitative data.

As a practical matter we are therefore justified in assuming only that the pressure is available, at most as a function of time and position on the surface of the chamber. That restriction is a fundamental guide to the way in which the theory and methods of analysis for combustion instabilities are developed. Throughout these lectures we emphasize determining and understanding the unsteady pressure field. The approximate analysis constituting the framework in which we will discuss instabilities is based on the pressure as the primary flow variable.

## 2. MECHANISMS OF COMBUSTION INSTABILITIES IN SOLID PROPELLANT ROCKETS

Identifying the ultimate cause, the mechanism, is probably the single most important task in understanding combustion instabilities in full-scale systems. The term "mechanism" refers to that phenomenon or collection of processes forming the chief reason that the instability exists. There may be more than one mechanism, but in any case the ultimate reason for an instability is that energy is transferred from the combustion processes, or the mean flow, to unsteady organized motions. Instabilities are commonly observed as nearly periodic oscillations having time-dependent amplitudes. As a practical matter, the chief goal is to reduce the amplitudes to acceptable levels. For that purpose it is essential first to understand the cause, and then to work out the connections with the chamber dynamics.

In the context defined by Figure 1.1, understanding the mechanism of combustion instabilities is equivalent to understanding combustion dynamics. It is essential to keep in mind always that by its very definition, combustion involves chemistry and chemical kinetics within the setting of fluid mechanics. Depending on the mechanism, one or another of those phenomena may dominate. Hence, for example, in some cases involving the dynamics of vortex formation and shedding, we may find that burning is not a central issue. Nevertheless, the presence of the flow field supporting the vortices is itself produced by combustion of reactants. We may therefore justifiably include the phenomenon under the general label 'combustion dynamics.' Hence all of the topics comprising the subject of mechanisms belong largely to the feedback path in Figure 1.1.

In some respects combustion in a solid propellant rocket chamber appears to be less complicated than those in any other type of combustor. The burning processes occur almost entirely within a thin region, normally less than one millimeter thick, adjacent to the propellant surface. Although some residual combustion normally occurs when the propellant contains aluminum or other metallic additives, there is no unambiguous evidence that combustion within the volume contribute significantly as a cause of combustion instabilities. We assume that to be the case, leaving surface combustion and purely fluid mechanical processes as origins of possible mechanisms. Of these, the dynamics of surface combustion is by far the most common and most important. The four chief mechanisms for instabilities in solid rockets are shown in Figure 2.1 surface combusiton; vortices shed from obstacles, or growing out of the shear flow at a burning surface; and residual combustion within the volume of the chamber.

Vortex shedding from obstacles—as in the Shuttle solid rocket booster—or vortices produced at the lateral surface ('parietal vortex shedding')—as in the Ariane 5 solid rocket booster—have been identified as mechanisms only in large motors. Excitation of acoustic waves by vortices is of course a well-known phenomenon in a wide variety of wind musical instruments. The idea that vortices might be responsible for oscillations in a combustion chamber seems to have been proposed first by Flandro and Jacobs (1974).

The dynamics of residual combustion far from the burning surface—mostly likely associated with aluminum or other metal fuel additives not completely burned at the surface—remains poorly understood. Although some attention has been given to the process (Beckstead *et al.* 1987), analysis of the dynamics is incomplete. No calculations exist assessing quantitatively the possible contributions of residual combustion to linear stability relative to those of surface combustion.

On the other hand, there is no disagreement that the dynamics of surface combustion is the dominant mechanism causing most combustion instabilities in all types and sizes of solid rockets. We therefore begin with examination of that subject.

**2.1. Qualitative Interpretation of the Basic Mechanism.** The dependence of the burning rate of a solid propellant on the pressure has long been known as a basic characteristic. Experiment and theory for the combustion of gases shows that the reaction rates vary strongly with both pressure and temperature. It is therefore not surprising that the burning rate of a solid is sensitive to the impressed temperature and pressure. What **is** surprising is that the processes in the gas and condensed phases in the vicinity of the burning conspire to produce a dynamical response that exhibits significant dependence in frequency. That dependence on frequency is particularly important because the response is noticeably greater over a rather broad frequency range. In that range the combustion processes act to amplify pressure fluctuations. That is, some of the energy released in chemical reactions is transformed to mechanical energy of motions in the combustion products. Hence the

(a)  Pressure  Coupling



(b)  Velocity  Coupling



(c)  Vortex  Shedding



(d)  Residual  Combustion
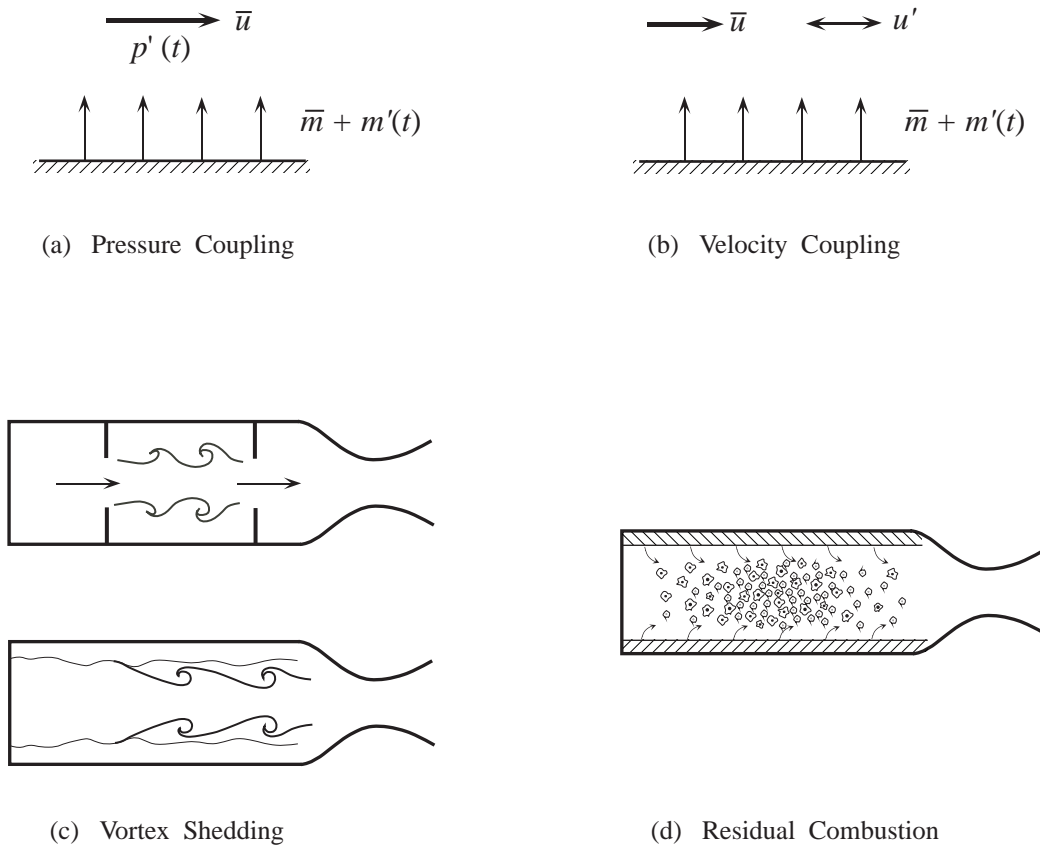
FIGURE 2.1.  The Four Chief Mechanisms for Combustion Instabilities in Solid Rockets

dynamics in the feedback path, Figure 1.1, not only provide feedback but as well promote an unstable situation. The burning surface exhibits a sort of resonant behavior but without possessing the inertial and spring-like (i.e. restoring) forces associated with a resonant oscillating system such as the simple mass/spring oscillator.

Since the cavity in a solid rocket possesses its own acoustic resonances, we have a system of two coupled oscillators. If it should happen that resonant frequencies of the two oscillators are close, then conditions clearly favor an instability. That is the situation commonly occurring in solid rockets and is the simplest direct explanation for the widespread occurrences of instabilities in tactical as well as strategic motors (Blomshield, 2000).
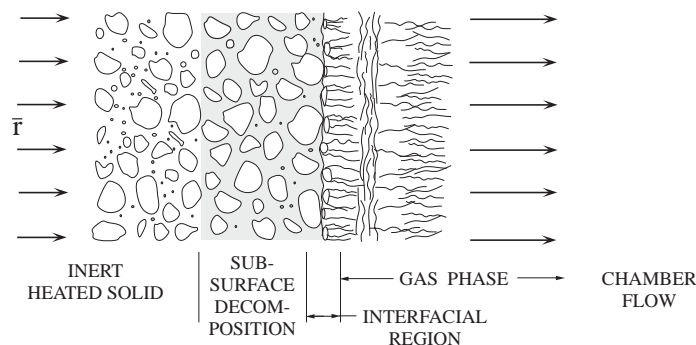


FIGURE 2.2.  Sketch of Unsteady Combustion of a Solid Propellant.

The essential features of the combustion processes dominating the behavior just described have long been known. Figure 2.2 is an idealized sketch showing the main characteristics of a burning composite propellant exposed to an oscillation of the chamber pressure. Ultimately it is the fluctuation of velocity of gases leaving the

combustion zone that is the essence of the mechanism. Oscillation of the flow causes the surface to appear like an acoustic speaker, a source of acoustic waves. Formally the situation is identical to a planar array of monopoles having zero-average mass flow superposed on the mean flow due to combustion. However, the fluctuation of burning rate is a consequence of fluctuating heat transfer so we can understand the mechanism best by examining the behavior of the temperature profile. We will treat the propellant as if it were a perfectly homogeneous isotropic material in the condensed phase, and use the one-dimensional approximation throughout, from the cold condensed solid phase to the hot combustion products. Figure 2.3 is one frame from a film of a burning solid taken at the Naval Weapons Center, suggesting that any sort of one-dimensional approximation seems unrealistic. That is certainly true on the scale of the particle sizes (10s to 100s of microns).

However, the variations of velocity and pressure in the chamber occur over distances of the order of the chamber dimensions. Hence it is appealing to suppose that for interactions between the combustion zone and the motions in the chamber, the heterogeneous character propellant can be overlooked in some sense. For example, the linear burning rate of a propellant is measured without special regard for spatial variations on the small scale of compositional inhomogeneities. No instrument is available to do otherwise. That is not to say, of course, that the burn rate and the combustion dynamics do not depend on spatial variations of the condensed material and the gas phase. Rather, we suppose that dependence in such things as the size distribution of oxidizer particles is accounted for by some sort of averaging procedure. Thus, parameters appearing in the final results, such as A and B in the QSHOD model discussed here, must depend on, for example, an average particle size. No rules exist for the averaging, but recently impressive progress has been made for computed steady burning rates using a "random packing" model (Kochevets and Buckmaster, 2001). In all of the discussion here we adhere to the one-dimensional approximation with no attention paid to the possible errors incurred. In any case it seems a good assumption that if the averaging process is good, any errors are likely to be less than uncertanties arising in other parts of the problem, e.g. material properties.

The mechanism in question here is, broadly speaking, primarily a matter of combustion dynamics. It has become customary to represent the mechanism quantitatively as an admittance or response function. We use the latter here, defined generally as the fluctuation of mass flow rate of gases departing the combustion zone to the imposed fluctuation of either the pressure or the velocity. Thus the response function for pressure fluctuations (referred to as the "response to pressure coupling") is defined in dimensionless form as $R_\rho$,

$$R_\rho = \frac{m'/\overline{m}}{p'/\overline{p}} \tag{2.1}$$

where $(\ )'$ means fluctuation and $\overline{(\ )}$ is an average value. The average value $\overline{m}$ represents the average inflow of mass due to the propellant burning. In almost all applications, the fluctuations are steady sinusoidal oscillations, written as

$$\frac{m'}{\overline{m}} = \frac{\hat{m}}{\overline{m}} e^{-i\omega t}$$
$$\frac{p'}{\overline{p}} = \frac{\hat{p}}{\overline{p}} e^{-i\omega t} \tag{2.2)a,b}$$

and

$$R_\rho = \frac{\hat{m}/\overline{m}}{\hat{p}/\overline{p}} \tag{2.3}$$

where $(\hat{\ })$ denotes the amplitude of the oscillation, including both magnitude and phase. Because generally the oscillations of mass flux rate are not in phase with the pressure oscillations, the function $R_p$ is complex, the real part representing that part of $m'/\overline{m}$ that is in phase with the pressure oscillation.

Although the response function for pressure coupling is most commonly used, there is a second response function, that associated with velocity coupling, which under some practical circumstances is far more important. At this point we confine our remarks to the response function for pressure coupling.

A simple interpretation of the response function explains its importance to combustion instabilities. According to the definition (2.3), a pressure oscillation having amplitude $\hat{p}/\overline{p}$ produces the oscillation $\hat{m}/\overline{m}$ of mass flow into

the chamber

$$\frac{\hat{m}}{\bar{m}} = R_\rho \frac{\hat{p}}{\bar{p}} \tag{2.4}$$

Viewed from the chamber, the boundary appears then to oscillate. The apparent motion is entirely analogous to that of a speaker or piston mounted at the boundary. Thus pressure waves are generated in a fashion similar to that of a loudspeaker in a room. Through a complicated sequence of processes whose details are not germane here, those waves coalesce and combine with the original pressure waves causing the fluctuations of mass flux. Whether or not that merging process augments or subtracts from the existing wave system in the chamber depends on the phase between $\hat{m}$ and $\hat{p}$. The part of $\hat{m}$ in-phase with $\hat{p}$ increases the amplitude of the wave system and is therefore destabilizing. For a particular motor, the tendency for combustion dynamics to drive instabilities is proportional to the integral of $R_p$ over the entire area of burning surface. Hence it is clearly essential to know the response function for the propellant used.
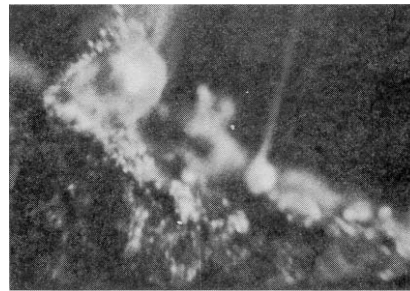


FIGURE 2.3. View of the Surface of a Burning Solid Propellant Containing Aluminum.

Traditional composite propellants using ammonium perchlorate as oxidizer, as well as advanced propellants using higher energy oxidizers and binder, burn in qualitatively similar fashion. The interface between the condensed and gas phases is fairly well defined, may be dry or wet, and may exhibit local dynamical activity owing to the presence of solid particles and responsive collections of liquid pools or drops. The dynamics of the interfacial region is particularly noticeable in microcinematography when the propellant contains aluminum. The metal collects in molten droplets, mobile and ignitable on the surface; those not fully consumed are carried away by the gaseous products of the interface. The high temperature at the surface is sustained by a balance between heat flow away from the interface, required to heat the cool propellant advancing to the surface; energy required to effect the phase changes at and near the interface; and the heat transfer supplied to the interfacial region from the combustion zone in the gas phase. It's a delicate balance, easily disturbed by changes in the chemical processes in the interfacial region, particularly within the subsurface region in the condensed phase. Figure 2.4 is a sketch of the temperature field, showing also the possible consequences of additional exothermic reactions in the sub-surface condensed phase. Note that in this figure we imagine that the temperature exists in a spatially averaged sense. Local variations on the scale of oxidizer particles are smeared out in the averaging procedure and explicit effects of inhomogeneities are absent.



(a) Flame Front    (b) Distributed Combustion
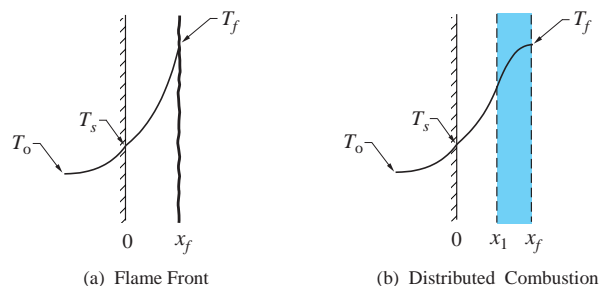
FIGURE 2.4. Representation of the Temperature Field in a Burning Solid Propellant.

The essentials of the behavior represented macroscopically by response functions can be described as a sequence of elementary steps, described here in simplified form with reference to Figure 2.4:

(i) Suppose that for some reason the rate of reactions in the combustion zone increases-perhaps due to a fluctuation of pressure, or temperature, or to increased local mixing associated with greater intensity of turbulence locally in the chamber.

(ii) Increased reaction rates produce a rise in the rate of energy release and an increase of temperature of the combustion zone.

(iii) Due both to radiation and heat conduction, the heat transfer from the combustion zone to the interfacial region increases, having at least two possible consequences: the temperature at the surface is increased; and the rate at which condensed material is converted to gas is also increased.

(iv) Because the temperature in the interfacial region rises, so also does the heat flow to the subsurface region and further into the solid, tending to cool the interface.

(v) If there are subsurface reactions, the heat flow will tend to increase their rate, with consequences depending on the associated energy release (or absorption) rate.

(vi) Exothermic subsurface reactions will act to maintain higher temperature locally, thereby encouraging the conversion of condensed material to gas at the interface, but also tending to increase the heat flow to the cooler solid.

(vii) The net result may be that if the fluctuation of heat flow, and reduction of temperature, at the interface does not happen too quickly, the enhanced reaction rate assumed in Step (i) may produce a fluctuation of mass flow leaving the surface, that is in phase with the initial perturbation. Hence in this event the entire process is destabilizing in the sense that the initial disturbance has the result that the disturbed mass flow into the chamber tends to augment that initial disturbance.

Whether or not the preceding sequence will be destabilizing depends entirely on details of the processes involved. Notably, if sub-surface reactions are endothermic, then the sequence (v)–(vii) leads to the conclusion that the reactions may cause the propellant combustion to be less sensitive to disturbances.

The model we will analyze first is the simplest possible capturing a dominant contribution to the combustion dynamics. Only unsteady heat transfer in the condensed phase causes true dynamical behavior, i.e. dependence of the response to pressure coupling. That process must in any case be present. This problem (model) is therefore the reference always used to assess the possible influences of other dynamical processes, in particular, those in the gas phase and decomposition in the condensed phase. The substance of the model is defined by the following assumptions:

(i) **q**uasi-**s**teady behavior of all processes except unsteady conductive heat transfer in the condensed phase;

(ii) **h**omogeneous and constant material properties, non-reacting condensed phase;

(iii) **o**ne-**d**imensional variations in space;

(iv) conversion of condensed material to gas phase at an infinitesimally thin interface.

The acronym QSHOD for this model derives from the five letters in assumptions (i)–(iii).

During the early years of this subject, from the mid-1950s to the mid-1960s, roughly ten analyses of the response function were published in the Western literature, giving apparently distinct results. Culick (1968) showed that, due to the fact that all of the models were based in the same set of assumptions (i)–(iv), the results were dynamically identical. That is, all had the same dependence on frequency and, with appropriate values for the various parameters involved, give coincident numerical values. Hence the term QSHOD is a useful term referring to a class of models. Differences between the models are associated with different detailed models of the steady processes, notably the flame structure in the gas phase.

A different approach to compute the combustion response was taken by Zel'dovitch (1942) in Russia and elaborated in great depth by Novozhilov (1965, 1973, 1996). The result has come to be known as the Z-N model. The Z-N representation of the response has certain distinct advantages, most importantly giving convenient connections between the parameters in the response function and quantities easily measured in steady combustion. The idea is explained in Section 2.

**2.2. Analysis of the QSHOD Model.** Analysis of the model sketched in Figure 2.2 amounts to quantitative representation of the sequence (i)–(iv). Even in the simplest form described here, the problem is too

complicated for a closed form solution. Apart from recent results obtained numerically for the entire region, covering the cold solid to the hot combustion products the usual procedure, familiar in many problems of this sort, is based on solutions found for the separate regions defined above, and matched the results at the interfaces. The solutions and the matching conditions are based on the one-dimensional equations of motion. In the approach taken here, the interfaces move, a feature that must be correctly incorporated in the analysis.

The following remarks are based on the review cited above, Culick (1968). Since that time much work has been done to determine the consequences of relaxing the assumptions on which the following analysis (the QSHOD model) is based. We will later examine some of those ideas. In this section we assume that the combustion proceeds as transformation of a condensed phase at a single flat interface to the gas phase, requiring that solutions be matched at only one interface. We choose a reference system with origin $(x = 0)$ fixed[2] to the average position of the interface. Hence the cold unreacted solid material progresses inward from the lift. Figure 2.5 shows this definition and the matching conditions that must be satisfied at the interface. Note that the velocity $\dot{x}_s$ of the interface appears explicitly in these conditions and is to be determined as part of the solution to the complete problem.
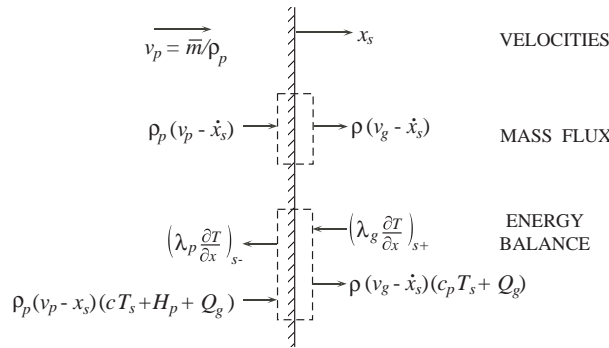


FIGURE 2.5. Reference System and Matching Conditions for the QSHOD Model.

For the simple model used here, the analysis involves only three steps: solution for the temperature field in the solid phase; solution for the temperature field in the gas phase; and matching the two solutions at the interface. Because the temperature field is central to the analysis, the final results should correctly be regarded as a thermal theory of steady and unsteady combustion of a solid propellant. No diffusive contributions are accounted for and the pressure is uniform throughout the region considered: the momentum of the flow does not enter the problem.

**(a) Solid Phase**

The energy equation for the temperature in the solid phase assumed to have uniform and constant properties, is

$$\lambda_p \frac{\partial^2 T}{\partial x^2} - \overline{m}c\frac{\partial T}{\partial x} - \rho_p c\frac{\partial T}{\partial t} = -\dot{Q}_d \tag{2.5}$$

where $\overline{(\ )}$ means time-averaged value; $(\ )_p$ denotes propellant; $c$ is the specific heat of the solid; $\overline{m} = \rho_p \overline{r}$ is the average mass flux in the reference system defined in Figure 2.5; and $\dot{Q}_d$ is the rate at which energy is released per unit volume due to decomposition of the solid ($\dot{Q}_d > 0$ for exothermic decomposition). We assume $\dot{Q}_d = 0$ here an assumption to be relaxed in Section 2. It is convenient to use the dimensionless variables

$$\xi_p = \frac{\overline{r}}{\kappa_c}x \ ; \quad \tau = \frac{T}{\overline{T}_s} \tag{2.6}$$

---

[2]Alternatively, the reference frame may be fixed to the instantaneous position of the surface and therefore is not an inertial frame for the unsteady problem. For the linear problem, it is easy to show the equivalence of the results obtained with the two choices of reference systems. If more than three regions are treated—e.g. when an additional decomposition zone is included in the condensed phase—it may be more convenient to take $x_s = 0$ and account for the motions of the remaining interfaces.

where values at the interface are identified by subscript $s$ and $\kappa_p = \lambda_p/\rho_p c$ is the thermal diffusivity of the propellant. Equation (2.5) becomes

$$\frac{\partial^2 \tau}{\partial \xi^2} - \frac{\partial \tau}{\partial \xi_p} - \frac{\lambda_p \rho_p}{\overline{m}^2 c} \frac{\partial \tau}{\partial t} = 0 \tag{2.7}$$

Solution to (2.7) with the time derivative dropped gives the formula for the normalized mean temperature

$$\overline{\tau} = \overline{\tau_c} + (1 - \overline{\tau_c})e^{\xi_p} \tag{2.8}$$

satisfying the conditions $\overline{\tau} = \overline{\tau_s} = 1$ at the surface and $\overline{\tau_c} = \overline{T_c}/\overline{T_s}$ far upstream $(\overline{T} = \overline{T_c})$ in the cold propellant.

For harmonic motions, with $\tau = \overline{\tau} + \tau'$ and[3] $\tau' = \hat{\tau}e^{-i\omega t}$, $\hat{\tau}$ being the amplitude, a complex function of position in the solid material. Substitution in (2.7) leads to the equation for $\hat{\tau}(\xi_p)$, easily solved to give

$$\tau' = \hat{\tau}_0 e^{\lambda \xi_p} e^{-i\omega t} \tag{2.9}$$

where $\lambda$ satisfies the relation

$$\lambda(\lambda - 1) = -i\Omega \tag{2.10}$$

and $\Omega$ is the important dimensionless frequency,

$$\Omega = \frac{\lambda_p \rho_p}{\overline{m}^2 c}\omega = \frac{\kappa_p}{\overline{r}^2}\omega \tag{2.11}$$

In order that $\tau' \to 0$ for $x \to -\infty$, the solution of (2.10) with positive real part must be used; $\lambda = \lambda_r - i\lambda_r$ and

$$\lambda_r = \frac{1}{2}\left\{1 + \frac{1}{\sqrt{2}}\left[(1 + 16\Omega^2)^{1/2} + 1\right]^{1/2}\right\}$$

$$\lambda_i = \frac{1}{2\sqrt{2}}\left[(1 + 16\Omega^2)^{1/2} - 1\right] \tag{2.12a,b}$$

Due to the choice of reference system, $\hat{\tau}$ in (2.9) is the fluctuation of temperature at the average position of the interface ($\xi_p = 0$). However, matching conditions at the interface requires values and derivatives of the temperature at the interface itself, having position $x_s$ and velocity $\dot{x}_s$. Values at the interface are calculated with Taylor series expansions about $x = 0$; only the first order terms are retained for the linear problem, and on the solid side of the interface[4]:

$$\overline{T}_s(x_s) = \overline{T}(0) + x_s\left(\frac{d\overline{T}}{dx}\right)_{0-} \quad ; \quad \left(\frac{d\overline{T}}{dx}\right)_{s-} = \left(\frac{d\overline{T}}{dx}\right)_{0-} + x_s\left(\frac{d^2\overline{T}}{dx^2}\right)_{0-}$$

$$T_s'(x_s) = T_{0-}'(0) + x_s\left(\frac{\partial\overline{T}}{\partial x}\right)_{0-} \quad ; \quad \left(\frac{\partial T'}{\partial x}\right)_{s-} = \left(\frac{\partial T'}{\partial x}\right)_{0-} + x_s\left(\frac{\partial^2 T'}{\partial x^2}\right)_{0-} \tag{2.13}$$

Hence the required results for the upstream side of the interface cannot be completed until the interfacial region is analyzed.

### (b) Interfacial Region

Three relations govern the behavior at the interface: conservation of mass and energy, and the law for conversion of solid to gas. The first two are established by considering a small control volume placed about the true burning surface, as sketched in Figure 2.5. The volume is then collapsed to give "jump" conditions associated with the total unsteady mass and energy transfer in the upstream $(s-)$ and downstream $(s+)$ sides of the interface:

$$\frac{\rho_p \dot{x}_s}{\overline{m}} = -\left[1 - \frac{\overline{\rho}_{gs}}{\rho_{ps}}\right]\frac{m_s'}{\overline{m}} \approx -\frac{m_s'}{\overline{m}}$$

$$\left[\lambda_g \frac{\partial T}{\partial x}\right]_{s+} = \left[\lambda_p \frac{\partial T}{\partial x}\right]_{s-} + \overline{m}\left[1 - \frac{\overline{\rho}_p \dot{x}_s}{\overline{m}}\right](L_s) \tag{2.14a,b}$$

---

[3]Note that consistently throughout these notes we use the negative exponential, $\exp(-i\omega t)$. In some of the literature the positive exponential is used, so care must be taken when making comparisons of results.

[4]The temperature is continuous at the interface, but on $x = 0$, the fluctuations $T_{0-}'$ and $T_{0+}'$ computed from the solutions for the solid and gas phase need not be continuous.

The mean gas density $\overline{\rho}$ near the surface is much smaller than the density of the condensed phase, for cases of current interest, so the term $\overline{\rho}/\rho_p \ll 1$ will hereafter be dropped. For an exothermic surface reaction, the change $L_s = h_{s+} - h_{s-}$ of the enthalpy is positive and may be viewed as a 'latent heat'. The heat fluxes $[\lambda_p \partial T/\partial x]_{s-}$ and $[\lambda_g \partial T/\partial x]_{s+}$ are respectively flows of heat *from* the interface to the condensed phase and *to* the interface *from* the gas phase.

An Arrhenius law has commonly been assumed for the conversion of solid to gas, giving the total surface mass flux

$$m_s = Bp^{n_s}e^{-E_s/R_0 T_s} \tag{2.15}$$

To first order in small quantities, the perturbed form of (2.15) is

$$\frac{m_s'}{\overline{m}} = Ee^{i\omega\tau_1}\tau_s' + n_s e^{i\omega\tau_2}\frac{p'}{\overline{p}} \tag{2.16}$$

where $E = E_s/R_0 T_s$ is the dimensionless activation energy for the surface reaction. Time delays or lags $\tau_1$ and $\tau_2$ are included in (2.16), but presently there is no way to compute them; hence they will largely be ignored here except for some results given in Section 2.6.

For steady combustion, the energy balance (2.14)b, with (2.8) substituted for $d\overline{T}/dx$, becomes

$$\left(\lambda_g \frac{d\overline{T}}{dx}\right)_{s+} = \overline{m}\left[c\left(\overline{T}_s - T_c\right) + L_s\right] \tag{2.17}$$

The linear unsteady part of (2.14)b is

$$\left(\lambda_g \frac{\partial T}{\partial x}\right)_{s+}' = \left(\lambda_p \frac{\partial T}{\partial x}\right)_{s-}' + m_s'\overline{L}_s + \overline{m}(c_p - c)T_s' \tag{2.18}$$

Combination of (2.8) and (2.9) and the appropriate parts of (2.13) gives the formula for the heat transfer into the condensed phase from the interface:

$$\left(\lambda_p \frac{\partial T}{\partial x}\right)_{s-}' = \overline{m}c\left[\lambda T_s' + \frac{1}{\lambda}\left(\overline{T}_s - T_c\right)\frac{m_s'}{\overline{m}}\right] \tag{2.19}$$

In this result, the approximation in (2.14)a has been used. Substitution of (2.19) in (2.18) leads to the boundary condition to be set on the unsteady temperature at the downstream side of the interface:

$$\left(\lambda_g \frac{\partial T}{\partial x}\right)_{s+}' = \overline{m}c\left[\lambda T_s' + \left(\frac{c_p}{c} - 1\right)T_s' + \left\{\frac{1}{\lambda}\left(\overline{T}_s - T_c\right) + \frac{L_s}{c}\right\}\frac{m_s'}{\overline{m}}\right] \tag{2.20}$$

This results contains two assumptions:

(i) $\overline{\rho}_g/\overline{\rho}_p \ll 1$ $(x = x_s)$
(ii) nonreacting condensed phase having constant and uniform properties

Normally, the first is reasonable. However, the second is restrictive, possibly seriously so according to some analyses; see Section 2.5. The important point is that (2.20) explicitly contains the transient behavior (the dynamics) associated with unsteady heat transfer in a benign solid material. If no further dynamics is attributed to the processes at the interface or in the gas phase, then the response function found with this analysis reflects only the dynamics of unsteady heat transfer in the condensed phase. That is the QSHOD result. Hence it is apparent that the form of the dependence of the response function in frequency *will necessarily in this case be independent of the model chosen for the quasi-static behavior of the gas phase.* The details of the model selected will affect *only* the particular values of parameters appearing in the formula for the response function.

Thus, to complete the analysis, it is best at this stage to choose the simplest possibility. We assume that the thermal conductivity is uniform in the gas phase and that the combustion processes (i.e. the rate of energy release per unit volume) are also uniform in a region beginning some distance from the interface and extending downstream, ending at a location, that is, by definition, the edge of the flame zone. This is a useful model containing two simple limits: uniform combustion beginning at the interface; and a flame sheet, obtained by

letting the thickness of the combustion zone become infinitesimally thin. Figure 2.6 is a sketch of the model. Analysis of the model for steady burning was given by Culick (1969) with the following results.
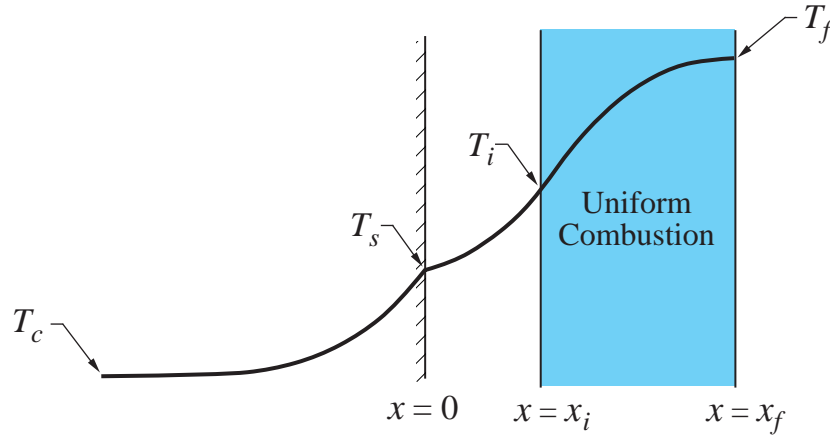


FIGURE 2.6. Sketch of the Model of a Solid Propellant Burning with Uniform Combustion in the Gas Phase.

The governing equation for this thermal theory is

$$mc_p\frac{dT}{dx} - \frac{d}{dx}\left(\lambda_g\frac{dT}{dx}\right) = \rho_g Q_f \dot{s} \tag{2.21}$$

where $Q_f$ is the energy released per unit mass of reactant mixture (assumed to be constant), $\rho_g$ is the local gas density and $\dot{s}$ is the local rate of reaction. At the downstream edge of the combustion zone, the boundary conditions are

$$T = T_f \; ; \quad \frac{dT}{dx} = 0 \quad (x = x_f) \tag{2.22)a,b}$$

where $T_f$ is the adiabatic flame temperature. On the interface,

$$T = T_s \tag{2.23}$$

and the energy balance at the interface gives

$$\left(\lambda_g\frac{dT}{dx}\right)_{s+} = \overline{m}\left[c\left(\overline{T}_s - T_c\right) + L_s\right] \tag{2.24}$$

For steady combustion, consideration of the energy flow across the gas phase gives

$$\left(\lambda_g\frac{dT}{dx}\right)_{s+} = \overline{m}\left[Q_f - c_p\left(T_f - T_s\right)\right] \tag{2.25}$$

On the other hand, integration of (2.21) across the combustion zone, and application of the boundary conditions (2.22)a,b and (2.23) leads to

$$\left(\lambda_g\frac{dT}{dx}\right)_{s+} = \int_0^\infty \rho_g Q_f \dot{s}\,dx - mc_p\left(T_f - T_s\right) \tag{2.26}$$

Because $Q_f$ is constant, comparison of (2.25) and (2.26) leads to the requirement on the overall reaction rate

$$\int_0^\infty \rho_g \dot{s}\,dx = m \tag{2.27}$$

We assume $\lambda_g$ constant (an assumption that is easily relaxed) and transform from $x$ to the dimensionless variable $\zeta$:

$$\zeta = e^{\frac{mc_p}{\lambda_g}x} \tag{2.28}$$

The energy equation (2.21) becomes

$$-\zeta^2 \frac{d^2 T}{d\zeta^2} = \Lambda^2 \tag{2.29}$$

where the eigenvalue $\Lambda^2$ is

$$\Lambda^2 = \frac{\lambda_g Q_f w}{m^2 c_p^2 T_s} \tag{2.30}$$

and

$$w = \rho_g \dot{\epsilon} \tag{2.31}$$

Generally, of course, $\dot{\epsilon}$ and hence $w$ and therefore $\Lambda^2$ are dependent at least on temperature, so $\Lambda^2$ is implicitly a function of $\zeta$. However, we assume $\Lambda^2$ constant, defining the condition of uniform combustion. Then with $\zeta_i$ the value of $\zeta$ at the beginning of the combustion zone (where ignition is assumed to occur) and $\zeta_f$ the value at the downstream edge of the flame, the first integral of (2.29) gives

$$\left( \frac{dT}{d\zeta} \right)_{s+} = \left( \frac{\zeta_f - \zeta_i}{\zeta_f \zeta_i} \right) \Lambda^2 \tag{2.32}$$

Thus

$$\left( \lambda_g \frac{dT}{dx} \right)_{s+} = \frac{\lambda_g Q_f}{c_p} \left( \frac{1}{\zeta_i} - \frac{1}{\zeta_f} \right) \frac{w}{m} \tag{2.33}$$

For $\zeta_f \gg \zeta_i$, and in the limit of combustion beginning at the solid/gas interface so $\zeta_i = 1$,

$$\left( \lambda_g \frac{dT}{dx} \right)_{s+} = \frac{\lambda_g Q_f}{c_p} \frac{w}{m} \tag{2.34}$$

The assumption of quasi-steady behavior implies that the fluctuation of heat transfer at the surface is given simply by the linearized form of (2.33):

$$\left( \lambda_g \frac{dT}{dx} \right)'_{s+} = \overline{m} c_p \overline{T}_s \Lambda^2 \left( \frac{w'}{\overline{w}} - \frac{m'}{\overline{m}} \right) \tag{2.35}$$

We also find as the linearized form of (2.25):

$$\left( \lambda_g \frac{dT}{dx} \right)'_{s+} = m' \left[ Q_f - c_p \left( \overline{T}_f - \overline{T}_s \right) \right] - \overline{m} c_p \left( \overline{T}_f - \overline{T}_s \right) \tag{2.36}$$

This equation gives a formula for the fluctuation of flame temperature,

$$T'_f = T'_s + \frac{m'}{\overline{m}} \left[ \frac{Q_f}{c_p} - \left( \overline{T}_f - \overline{T}_s \right) \right] - \frac{1}{\overline{m} c_p} \left( \lambda_g \frac{dT}{dx} \right)'_{s+} \tag{2.37}$$

Substitution of (2.35) for the last term gives the formula for computing $T'_f$ when the combustion is uniform. In general, $T'_f$ is not equal to the local fluctuation of temperature due to acoustical motions in the gas phase, the difference appearing the temperature fluctuation associated with an entropy wave carried by the mean flow departing the combustion zone.

By letting $\zeta_i \to \zeta_f$, the corresponding results can be obtained for a flame sheet; see Culick (1969; 2002). We will consider here only the case of finite combustion zone; the response functions found for the two cases differ only in small details.

To progress further, we must specify the form of $w = \rho_g \dot{s}$; the reaction rate per unit volume. For the quasi-steady part of the processes, we assume that the mass flow provided by the surface is well-approximated by the Arrhenius law (2.15) and its fluctuation is (2.16) with zero time delays,

$$\frac{m'}{\overline{m}} = E \frac{T'_s}{\overline{T}_s} + n_s \frac{p'}{\overline{p}} \tag{2.38}$$

Due to the assumption of quasi-steady behavior, this formula represents the fluctuation of mass flow throughout the gas phase.

Finally, we need an explicit form for $w$ as a function of the flow variables. To construct a consistent formula for the reaction rate in the gas phase, we equate the two results for heat transfer to the interface during steady burning: (2.24), the energy balance generally valid at the interface; and (2.34) found for the special case of uniform combustion. We find the expression for $w$:

$$w = \frac{c_p}{\lambda_g Q_f} m^2 \left[ c\left(\overline{T}_s - T_c\right) + L_s \right] \tag{2.39}$$

We assume that the right-hand side can be written as a function of pressure only by approximating the pyrolysis law $m = a(T_s)p^n$ as

$$m = ap^n = b(T_s - T_c)^s p^{n_s} \tag{2.40}$$

so

$$T_s - T_c = \left( \frac{a}{b} p^{n-n_s} \right)^{\frac{1}{s}} \tag{2.41}$$

Then (2.39) becomes

$$w = \frac{c_p}{\lambda_g Q_f} (ap^n)^2 \left[ c\left( \frac{a}{b} p^{n-n_s} \right)^{\frac{1}{s}} + L_s \right] \tag{2.42}$$

The fluctuation $w'$ of the reaction rate is then

$$\frac{w'}{\overline{w}} = \frac{\left( 1 - \frac{T_c}{\overline{T}_s} \right)}{\Lambda^2} \frac{c}{c_p} w \frac{p'}{\overline{p}} \tag{2.43}$$

where $\Lambda^2$ is given by (2.30) for the steady problem,

$$\Lambda^2 = \frac{\lambda_g Q_f \overline{w}}{\overline{m}^2 c_p^2 \overline{T}_s} \tag{2.44}$$

and

$$w = \left[ 2(1+H) + \frac{c_p}{c} \frac{1 - \frac{n_s}{n}}{c} \right]$$
$$H = -\frac{L_s}{c(\overline{T}_s - T_c)} \tag{2.45}a,b$$

Instead of the calculations leading from (2.34) to (2.43) one could as well simply assume $w' \sim p'$. The only purpose of these remarks is to give an example of relating fluctuations of the reaction rate to the pressure for a well-defined model of combustion in the gas phase.

**(c) Construction of the Response Function**

We find the formula for the response function in the following way:

(i) Substitute the pyrolysis law (2.38) in (2.20) which combines the interfacial conditions for energy and mass transfer:

$$\frac{1}{\overline{m}c\overline{T}_s} \left( \lambda_g \frac{\partial T}{\partial x} \right)'_{st} = \left( \lambda + \frac{A}{\lambda} \right) \frac{T'_s}{\overline{T}_s} + \left( \frac{c_p}{c} - 1 + \frac{LA}{1 - \frac{T_c}{\overline{T}_s}} \right) \frac{T'_s}{\overline{T}_s} + n_s \left( L + \frac{1 - \frac{T_c}{\overline{T}_s}}{\lambda} \right) \frac{p'}{\overline{p}} \tag{2.46}$$

where

$$L = \frac{L_s}{c\overline{T}_s}$$
$$A = (1 - \frac{T_c}{\overline{T}_s})(\alpha_s + \frac{E_s}{R_o \overline{T}_s}) \tag{2.47}a,b$$

(ii) Substitute the reaction rate (2.43) into the expression (2.35) for the heat loss from the gas phase:

$$\frac{1}{\overline{m}c\overline{T}_s}\left(\lambda_g \frac{\partial T}{\partial x}\right)'_{st} = \left(1 - \frac{T_c}{\overline{T}_s}\right)w\frac{p'}{\overline{p}} - \frac{c_p}{c}\Lambda^2\frac{m'}{\overline{m}} \tag{2.48}$$

(iii) Equation (2.46) and (2.48), use the pyrolysis law to eliminate $T'_s/\overline{T}_s$; this step leaves an equation which can be rearranged to give the ratio defined to be the response function for pressure coupling:

$$R_p = \frac{m'/\overline{m}}{p'/\overline{p}} = \frac{\left(AW + \frac{c_p}{c}n_s\right) + n_s(\lambda - 1)}{\lambda + \frac{A}{\lambda} + \left[\frac{c_p}{c}E\Lambda^2 - HA + \frac{c_p}{c} - 1\right]} \tag{2.49}$$

(iv) Write (2.49) in the form

$$R_p = \frac{c_1 + n_s(\lambda - 1)}{\lambda + \frac{A}{\lambda} + c_2} \tag{2.50}$$

For the assumed steady burning rate law, $m = ap^n$, the fluctuation can be written

$$R_p = \frac{m'/\overline{m}}{p'/\overline{p}} = n \tag{2.51}$$

Thus in the limit of zero frequency ($\lambda = 1$), the right-hand side of (2.50) must equal $n$, giving the condition

$$\frac{c_1}{1 + A + c_2} = n$$

Define $B$ with

$$c_1 = nB$$

and

$$c_2 = B - (1 + A)$$

Hence (2.50) becomes

$$R_p = \frac{nB + n_s(\lambda - 1)}{\lambda + \frac{A}{\lambda} - (1 + A) + B} \tag{2.52}$$
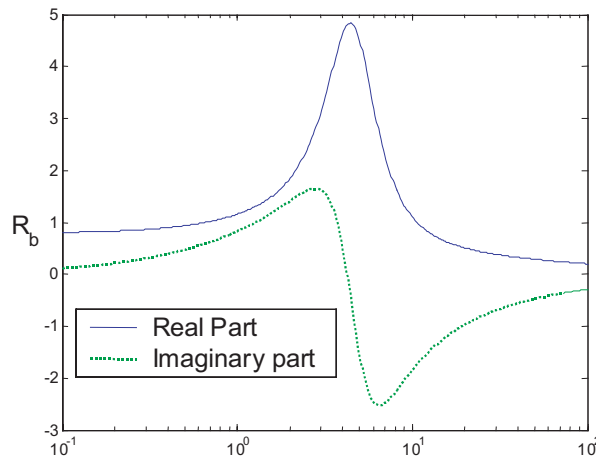


FIGURE 2.7. Real and Imaginary Parts of a QSHOD Response Function Computed with Equation 2.52.

Figure 2.7 shows typical results for the real and imaginary parts of this formulas when $n_s = 0$. Experimental results given in the following section have long established that the QSHOD model captures a major contribution to the dynamical behavior, due to unsteady heat transfer in the condensed phase. Thus it is important to inderstand the preceding analysis. However, even with the large experimental errors associated with all current

experimental methods, it seems there is little doubt that other dynamical processes cannot be ignored for many propellants, especially in the range of frequencies above that where the broad peak of the real part of $R_b$ appears.

**2.3. Measurements of the Response Function; Comparison of Experimental Results and the QSHOD Model.** For more than forty years, measurement of the response function has been the most important task is research on combustion instabilities in solid rockets. Without accurate data, the truth of theoretical results cannot be assessed; predictions and interpretations of instabilities in motors are uncertain; and the ability to screen propellants for optional behavior is seriously compromised. Unfortunately no entirely satisfactory method exists for accurate measurements of the combustion response, irrespective of cost. Two recent reports of extended programs (Caltech MURI, 2002 and UIUC MURI, 2002) have led to this conclusion after five years' investigation of the five main existing methods:

  (i) T-burner
 (ii) ultrasonic apparatus
(iii) laser recoil method
 (iv) magnetohydrodynamic method
  (v) microwave technique

A sixth method based on using a burner (e.g. an L* burner) in which bulk oscillations are excited, was not investigated, partly because it is intrinsically limited to low frequencies.

It is not our purpose here to review these methods; see the two MURI reports; Couty (1999) and references contained in those works for all discussions of all but the last. The microwave technique was introduced in the 1970's and has been continually improved, but the accuracy of the data remains inadequate, particularly for metallized propellants for which the method is useless under some conditions.

The central question for modeling and theory is: how good is the agreement between predicted and measured values? It appears that the first extensive comparison for this purpose were carried out many years ago (Beckstead and Culick, 1971) soon after the recognition that all the available models/analyses were equivalent to the QSHOD (A,B) model. With only two parameters available to adjust the theoretical results to fit data, the task of comparing theory and experiment became manageable. At that time, only T-burner data were available. Figures 2.8 and 2.9 show two results.
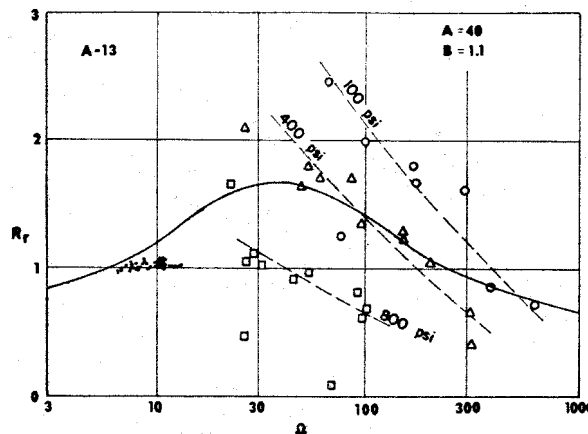


FIGURE 2.8. The real part of the response function vs. the non-dimensional frequency, $\alpha_t \omega / r^2$ for A-13 propellant: the solid curve is calculated from the QSHOD formula for the values of $A$ and $B$ shown; the dashed curves represent the T-burner data at the indicated pressures. (Beckstead and Culick 1969).

One purpose of the report by Beckstead and Culick was to combine the formula for the QSHOD response function with results obtained from analyses of the T-burner and the L*-burner to obtain formulas for the
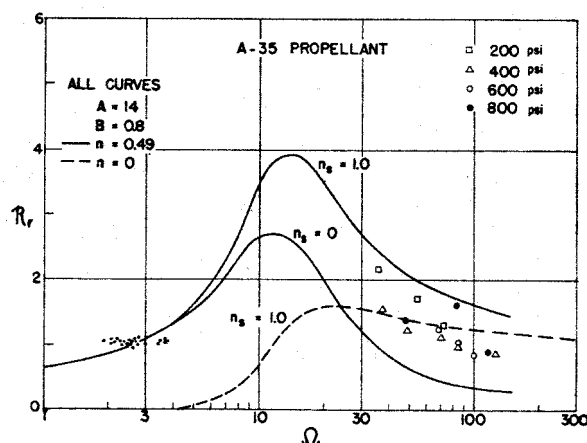
FIGURE 2.9. The real part of the response function vs. the non-dimensional frequency for A-35 propellant; the curves were calculated from the QSHOD formula. (Beckstead and Culick 1969).

parameters A and B in terms of measurable quantities. The main conclusion was that unique values of A and B could not be obtained for a given propellant tested at a chosen value of operating pressure. Consequently, large differences existed between the data and curves of the sort shown in Figure 2.7.

Since that time, many examples of using the A, B model to fit data have been given. Most, if not all, approach the matter as a two-parameter (A and B) curve fitted to data for the real part of the response function only. Strictly, that tactic is incorrect and could produce misleading results. The proper approach requires that the two-parameter representation be used to fit simultaneously the real and imaginary parts of the response function. There are also cases in which investigators have failed to respect the distinction between the response function $R_p \sim m'/p'$ and the admittance function $A_p \sim u'/p'$ defined for velocity fluctuations.

Without attention to both of those points, any comparisons between data and a model are suspect. Despite those common deficiencies, there is no doubt that the QSHOD model cannot and does not represent the dynamics of actual propellants. One would anticipate even without experimental results that the assumption of quasi-steady behavior in the gas phase must fail at high frequencies, commonly believed to be around 1000 Hertz and higher. Moreover, observations of steady combustion have shown that important decomposition processes take place in the sub-surface zone near the interface of most propellants. Hence at least two improvements of the QSHOD model should be made.

Before examining examples of more complicated models, we review the essentials of another approach to deriving the QSHOD model, the Z-N model.

**2.4. The Zel'dovich-Novozhilov (Z-N) Model .** Zel'dovich (1942) was first to consider true combustion dynamics for solid propellants. He was concerned with problems of transient burning—i.e. what happens to combustion of a propellant when the impressed pressure is changed rapidly—but now explicitly with the response function. Novozhilov (1965) later used Zel'dovich's basic ideas to find a formula for the response of a burning propellant to sinusoidal oscillations of pressure. The result has exactly the same dependence on frequency as the QSHOD model, i.e. it is identical with the formula obtained by Denison and Baum four years earlier.

The Z-N model incorporates quasi-steady behavior of the burning in a clever and instructive fashion. More-over, the parameters—there are, of course two corresponding to A and B in the QSHOD model—are so defined as to be assigned values from measurements of steady combustion of the propellant in question. Hence there is no need to become enmeshed in the details of modeling the combustion processes in the gas phase. If the measurements could be done accurately, it would be possible to obtain good predictions of the combustion response for propellants, subject of course to all the assumptions built into the QSHOD model. Unfortunately, the required quantities are difficult to measure accurately. Confirmation of the results still requires measurements of both the real and imaginary parts of the response function.

The condensed phase and interfacial region are treated as described in Section 2.2 for the QSHOD model. Instead of detailed analysis of the gas phase, that is, construction of a "flame model", the assumption of quasi-steady behavior is applied by using relations among the properties of steady combustion, the burning rate and the surface temperature as functions of the initial temperature of the cold propellant and the operating pressure:

$$m = m(T_c, p)$$
$$T_s = T_s(T_c, p)$$

(2.53)a,b

The assumption is also made that these functions are known sufficiently accurately that their derivatives can also be formed, introducing the four parameters

$$\nu = \left( \frac{\partial \ln \overline{m}}{\partial \ln \overline{p}} \right)_{T_c}$$

$$\mu = \frac{1}{\overline{T}_s - T_c} \left( \frac{\partial \overline{T}_s}{\partial \ln \overline{p}} \right)_{T_c}$$

$$k = \left( \overline{T}_s - T_c \right) \left( \frac{\partial \ln \overline{m}}{\partial T_c} \right)_{\overline{p}}$$

$$r_{ZN} = \left( \frac{\partial \overline{T}_s}{\partial T_c} \right)_{\overline{p}}$$

(2.54)a,b,c,d

Subscript $ZN$ is attached to $r$ to distinguish it from the linear burning rate. It is not apparent from the remarks here why the four parameters (2.54)a,b are significant in this theory.

Recall from Section 2.2 that the sole reason for analyzing a model of combustion in the gas phase was to produce a formula for the heat feedback, $\lambda_g (\partial T/\partial x)_{s+}$, to the interface. That is the central problem here as well: to find the heat feedback from considerations of steady combustion and assume (the quasi-steady approximation) that the form of the result holds under unsteady conditions. The trick is to work out the relation between the feedback and the properties of steady combustion. It is in that process that the parameters (2.54)a–d appear.

The formula for the response function corresponding to (2.52) is usually written (e.g. Cozzi, DeLuca and Novozhilov 1999)

$$R_p = \frac{\nu + \delta(\lambda - 1)}{r_{ZN}(\lambda - 1) + k \left( \frac{1}{\lambda} - 1 \right) + 1}$$

(2.55)

where

$$\delta = \nu r_{ZN} - \mu k$$

(2.56)

Comparison of (2.52) and (2.55) gives the formulas connecting the parameters in the two formulations:

$$A = \frac{k}{r_{ZN}} , \quad B = \frac{1}{k} , \quad n = \nu , \quad n_s = \frac{\delta}{r_{ZN}}$$

(2.57)

Much emphasis has been placed in the Russian literature on the "boundary of intrinsic stability", the locus of values of (A,B), or $(k, r_{ZN})$ for which the denominator of (2.55) vanishes. Under those conditions, the propellant burn rate suffers a finite perturbation in the limit of a vanishingly small change of pressure. Hence, from measured values of $\nu$ and $r_{ZN}$, one can infer how close an actual propellant is to that stability boundary.

With these models, the opportunity exists to use experimental results to determine how accurately the QSHOD approximations capture the combustion dynamics of solid propellants:

(1) measure $\nu, \mu, k, r_{ZN}$ from tests of steady combustion;
(2) measure the real and imaginary parts of $R_p$;
(3) compute $R_p$ from (2.52) or (2.55) and compare with (2)

There seem to be no published reports of results for this procedure.

**2.5. Revisions and Extensions of the QSHOD Model.** As we have already noted in Section 2.3, even with the large uncertainties accompanying the experimental results obtained with current methods, it is clear that the QSHOD model does not capture some important dynamical processes. Considerable effort has been devoted to improving the model, with a certain amount of success, but unfortunately the deficiencies in the experimental procedures still prevent definitive identification of the most significant contributions.

Attention has been given to all three of the regions sketched in Figure 2.2. It is important to recognize that simply changing the model for steady combustion—for example including a finite zone of decomposition in the solid phase—will not change the form of the QSHOD result. Any additional spatial zones or processes must also contain new dynamics, a lesson the author learned the hard way (Culick 1969).

Here we will only cite a few of the recent works without giving details of the analyses. To be possibly unseemly parochial, Section 2.6 contains a more extensive, but brief description of recent work at Caltech.

2.5.1. *Additional Dynamics in the Condensed Phase.* It seems that three types of processes have been considered:

1) temperature-dependent thermal properties;
2) phase transitions; and
3) decomposition zones.

Louwers and Gadiot (1999) have reported results for numerical calculations based on a model of HNF. Melting at some interface within the condensed phase is accounted for, as well as energy released by sub-surface reactions. Combustion in the gas phase is also treated numerically. The computed response functions also show that the new processes may increase the values of $R_p^{(r)}$ by as much as 10–30% and more in the frequency range above the peak. The peak value is unchanged.

Brewster and his students at the University of Illinois have produced a number of interesting works treating additional dynamics related to chemical processes in the condensed phase and at the interface (Zebrowski and Brewster, 1996; Brewster and Son, 1995).

Gusachenko, Zarko and Rychkov (1999) have investigated the effects of melting in the response function, finding quite significant consequences. Lower melting temperatures and larger energy absorption in the melt layer increase the magnitude of the response function.

Cozzi, DeLuca and Novozhilov (1999) worked out an extension of the Z-N method to account for phase transition at an infinitesimally thin interface in the condensed phase. The analysis includes new dynamics by allowing different properties of the thermal waves on the two sides of the interface. Additional heat release is allowed only at the interface of the transition and with conversion of condensed material to gaseous products. They found that the response function is increased by exothermic reaction at the internal interface and by reduced temperature of the phase transition.

2.5.2. *Additional Dynamics in the Gas Phase.* DeLuca (1990; 1992) has given thorough reviews of the various models used for the dynamics of the gas phase. Most, however, involve no dynamics, so there are no effects on the dependence of the response function on frequency. Truly dynamical effects are covered in the next section.

**2.6. Modeling the Effects of Velocity Coupling on the Global Dynamics of Combustion Chambers.** The research summarized in this section has been reported in a Ph.D. Thesis (Isella, 2001) and in three publications (Culick, Isella and Seywert, 1998; Isella and Culick, 2000a; 2000b). Chiefly two general problems have been addressed:

1) develop a simple general analysis of the combustion dynamics of a solid propellant that will conveniently accommodate models of the relevant chemical and physical processes, especially those in the interfaced region; and
2) investigate the influences of changes in the combustion response function on observable features of the combustor dynamics, particularly properties of limit cycles.

Both of these problems were chosen to try to determine answers to the question: what properties of a solid propellant are responsible for the often observed sensitivity of the dynamics of a solid rocket to apparently small (sometimes not well-known) changes in the composition of the propellant. The main conclusions are:

(i) small changes in the composition and thermodynamic properties of a propellant have significant consequences for dynamical behavior due to pressure coupling only if the propellant is burning near its intrinsic instability boundary; and

(ii) on the contrary the dynamics due to velocity coupling is evidently significantly sensitive to small compositional changes.

If these conclusions are true, then future work in the area of combustion instabilities must include intensive attention to modeling and measuring the combustion dynamics-i.e. the response function-associated with velocity coupling.

2.6.1. *The Model Framework.* One important purpose of the work cited above was to construct a framework within which it should be possible easily to investigate the consequences of various processes participating in the combustion of a solid. Representation of the combustion dynamics must be in a form required for analyzing the global dynamics (Section 3.2). The simplest approach is an extension of the well-known one-dimensional analysis producing the QSHOD response function for pressure coupling (Culick, 1968; Beckstead *et al.*, 1969; T'ien, 1972; among many works). Others have followed a similar tack (e.g. Louwers and Gadiot, 1999); the main novel aspect of this work is inclusion simultaneously of surface physical dynamics (e.g. due to mobility of liquid or solid particles); dynamics, rather than quasi-steady behavior, of the gas phase; and an elementary representation of velocity coupling.

On the submillimeter scale, a burning solid is heterogeneous both in the region adjacent to the interface and in the gas phase where much of the conversion to products takes place. The flow field in the chamber, in particular the unsteady acoustic field, has spatial variations normally the order of centimeters and larger. The dynamics of the combustion processes at the surface are formally accommodated as a boundary condition, a response function of some sort, in the analytical framework for the global dynamics. Hence the vast difference in characteristic scales is accommodated, in principle, by spatially averaging the combustion dynamics. The averaging is done over a surface in some sense far from the interface so far as the propellant combustion is concerned, but practically at the interface so far as the field within the chamber is concerned. In that way, the results of solution to the "inner" problem of combustion dynamics in the surface region are used as the boundary conditions for solution to the "outer" problem of the unsteady flow field in the chamber.

We are not concerned here with the matter of spatial averaging: we assume it can be done, not necessarily an easy or obvious process. It's an important part of the general problem. Therefore we proceed from the beginning with a one-dimensional analysis. The spatial framework for the model shown in Figure 2.10.
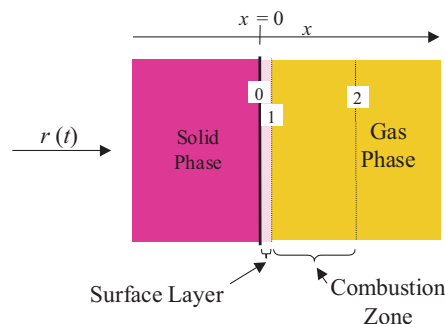


FIGURE 2.10. Spatial Definition of the Model

The strategy of the analysis is not novel and has been used in many previous works: solve the relevant equations, or postulate a model, governing the behavior in each of the three regions: solid phase; surface layer; and gas phase, including the region called 'combustion zone' in Figure 2.10. A major purpose of the analysis

has been to determine the quantitative effects of the dynamics in the surface layer and gas phase in the response function found from the QSHOD model. Hence throughout the work we assume the same model for the solid phase: the dynamics is due to unsteady heat transfer in a homogeneous material having uniform and constant properties.

Separate solutions or representations are obtained for each of the three regions. Unspecified constants or functions are then eliminated by satisfying boundary conditions and applying matching conditions at the two interfaces. Initially we intended, or hoped, to find such a form for the general behavior that different models for the surface layer and gas phase could easily be substituted and their consequences assessed. That goal has not been realized and probably is unattainable. Results require detailed numerical calculations before interesting information is obtained.

2.6.2. *Models of the Surface Layer.* From the beginning of this work we anticipated, because the dynamics of the gas phase are fast (owing to the relatively low material density), that the dynamics of the surface region should have greater effect on the combustion response function. We investigated two models of the region:

(i) first order dynamics represented by a constant time lag; and
(ii) unsteady heat transfer, with material properties different from those in the solid phase.

The idea of using a time lag is of course an old one, having been used by Grad (1949) in the first analysis of combustion instabilities, and later by Cheng (1982) as part of the Princeton group's extensive investigations (nearly a technical love affair) of time lag representations of unsteady combustion. The result in the present work, for the fluctuation of mass flux is

$$\frac{m'/\overline{m}}{p'/\overline{p}} = R_p \frac{e^{-i\Omega t}}{\sqrt{1+(\Omega t)^2}}$$

where $R_p$ (sometimes written as $R_b$) is the response function found in the QSHOD theory. Thus $R_p$ has the familiar two-parameter (A,B) representation. The dimensionless frequency is $\Omega = \omega\kappa/F^2\kappa$ is the thermal diffusivity and $\overline{r}$ is the linear burning rate and $\tau$ is the dimensionless time lag, equal to the physical time lag divided by $\kappa/\overline{r}^2$. Figure 2.11 shows a typical result (A = 14; B = 0.85; $\tau$ = 1.5). The graphs illustrate clearly a basic problem with a time lag theory: if the time lag is assumed constant (i.e. independent of frequency) the response (in this case the real part) possesses an oscillatory behavior with period increasing with frequency. Such behavior has never been observed.
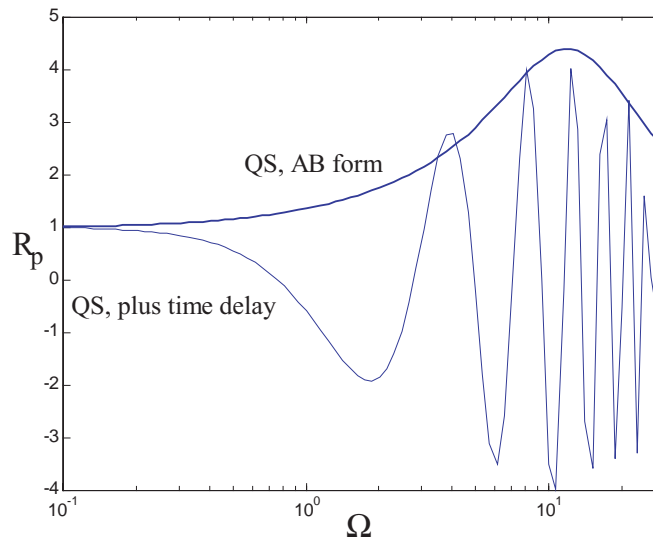


FIGURE 2.11. QSHOD Response Function with a Time lag: Thick Line, QSHOD Theory; Thin Line, QSHOD Model Including a Surface Layer Having First Order (time lag) Dynamics.

It is true that any response function can be written in a form showing a time lag behavior, but in general the time lag varies with frequency (Culick, 1968). If the physical model is sufficiently detailed, the dependence of t on frequency is found as part of the solution. In particular, the QSHOD theory gives $\tau(\Omega)$ such that the amplitude of the response function decays smoothly for frequencies higher than that at which the single peak occurs.

The second model for the surface is the only one considered for the following results. It is a simple representation of the dynamical behavior making use of the same solution as that for the homogeneous solid phase, with two differences:

(i) the uniform and constant properties are different from those of the condensed solid material;
(ii) the solution is forced to satisfy matching conditions of continuous temperature and heat transfer at the interfaces with the condensed phase and the gas phase.

2.6.3. *Models of the Gas Phase.* In this analysis, all combustion processes are assumed to occur in the gas phase; upstream only phase changes are accounted for, assumed to take place at the interfaces. We assume distributed combustion of a simplified form, a single one-step reaction as previous treatments have used (T'ien, 1972; Huang and Micci, 1990; Lazmi and Clavin, 1992). Solutions must then be found numerically for the steady and linear unsteady temperature distributions, and subsequently matched to the solution for the surface layer.

2.6.4. *Some Results for the Combustion Response Function.* Many experimental results exist suggesting that the responses of actual propellants tend often to be higher than that predicted by the QSHOD model for high frequencies. Initially the strongest motivation for this work on the response function was to determine in simple and relatively crude fashion what processes might have greatest effect on the values of the pressure-coupled response at frequencies greater than that at which the peak magnitude occurs. Roughly what that means, is finding one or more processes having 'resonant behavior' or characteristic times in the appropriate range. Unfortunately the analysis is sufficiently complicated that it has not been possible yet to deduce any explicit 'rules of thumb.' Therefore we present here a few plots of computed results to illustrate the behavior.

Figure 2.12 shows the basic or reference response function computed from the simple QSHOD model. The influences of dynamics in the surface layer and gas phase will be shown relative to that reference.
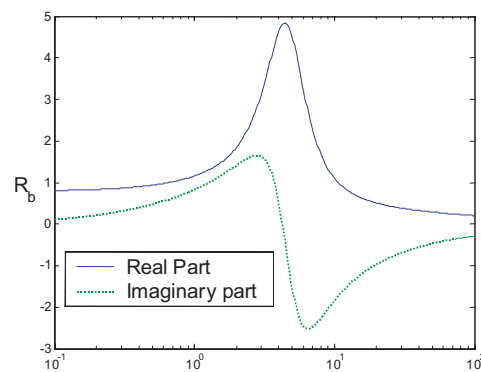


FIGURE 2.12. Reference Case: QSHOD Result with A = 6.0, B = 0.60.

**(i) Influence of Gas Phase Dynamics.**

Figure 2.13 is the result when only the dynamics in the gas phase is added to the QSHOD model. The results are similar to those found by T'ien (1972) and Lazmi and Clavin (1992), not a surprising conclusion. As expected, the dynamics of the gas phase introduce a single additional peak at a frequency higher than that of the peak caused by unsteady heat transfer in the condensed phase.

**(ii) Combined Influences of the Dynamics of the Surface Layer and the Gas Phase.**
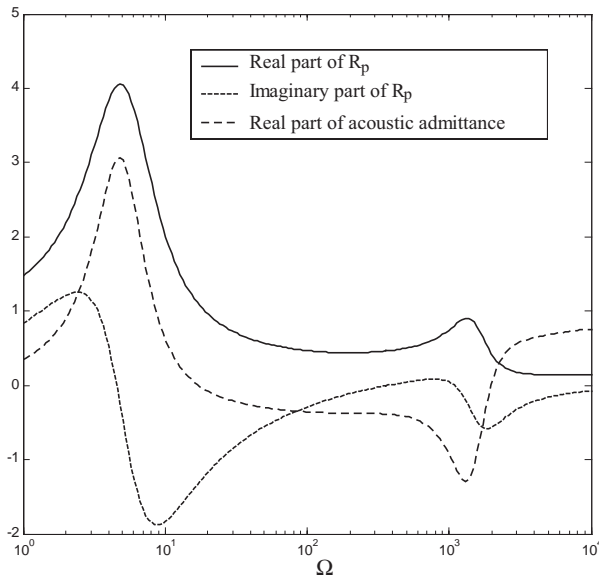
FIGURE 2.13. Combustion Response, QSHOD Model with Gas Phase Dynamics

The dynamics of the surface layer itself is the same as those of the condensed phase, but with different values of the defining parameters Figure 2.14 illustrates the effects of changing the surface activation energy and the material density on a function characterizing the response of heat transfer in the layer. The shape of this function differs from that (Figure 2.12) of the basic response function because it depends on the dependence of several flow variables on frequency.
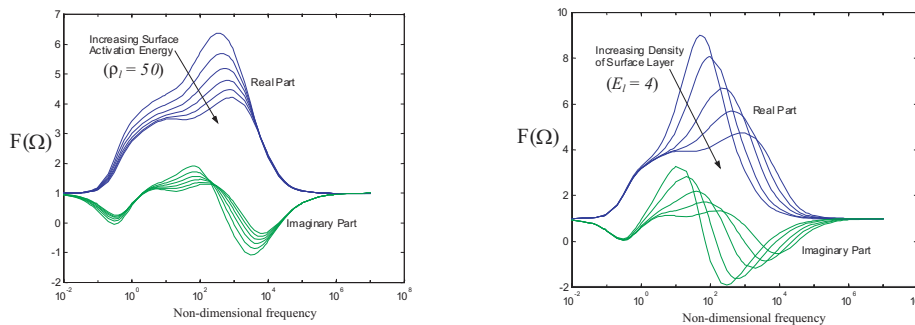


FIGURE 2.14. Effects of Activation Energy and Density on the Dynamics of the Surface Layer.

Finally, Figure 2.15 shows the result for one example of the response function with the dynamics of both the surface layer and the gas phase accounted for. Evidently for the conditions examined here the dynamics of the gas phase has more obvious influence on the response, in the higher frequency range, than does the surface layer.

One way of summarizing the results is shown in Figure 2.16, showing the contributions to the response function by the solid (condensed) phase, the surface layer and the gas phase. The overall response function for the propellant is the product of the three contributions.

**2.7. Velocity Coupling, the Combustion Response, and Global Dynamics.** The research summarized in this section amounts to using some characteristics of the global combustor dynamics—the amplitudes and harmonic context of limit cycles—to draw some inferences about qualitative features of the combustion dynamics.
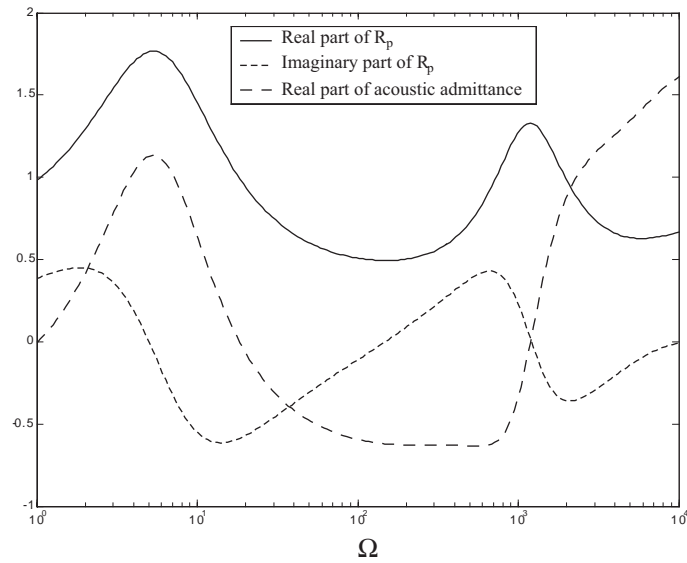
FIGURE 2.15. Combustion Response Function Including the Dynamics of the Surface Layer and the Gas Phase.
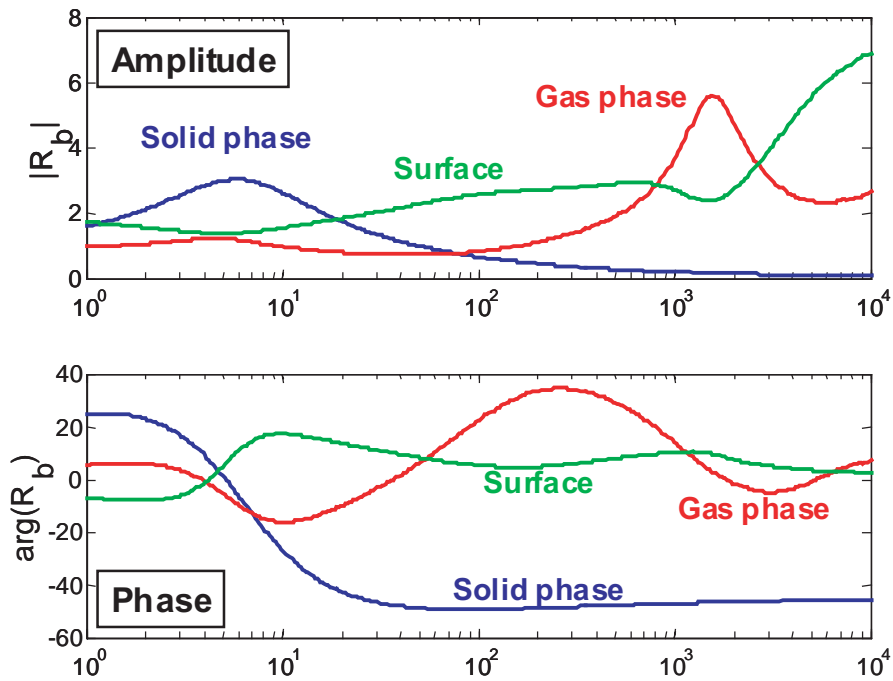


FIGURE 2.16. The Combustion Response Function Represented as Magnitudes and Phases of Individual Contributions.

At the beginning of the MURI program, during completion of his dissertation, Burnley (1996) showed that rectification associated with a velocity-coupled response function having also a threshold velocity, could be responsible for nonlinear or pulsed instabilities in a solid rocket motor. This result confirmed a conclusion reached several years previously by Levine and Baum (1983). That was the first example of using the behavior of the global dynamics as essentially a diagnostic tool to learn about the influences of the combustion dynamics on observable phenomena.

In the current work, the main questions at hand have to do with the apparent sensitivity of the global dynamics to small changes of propellant composition (see remarks (i) and (ii) in the introductory part of the section). We assume that small changes of composition likely have relatively small effects on the magnitude and phase of the response function. Therefore, we are really investigating the effects of small changes in the response function on the observable global dynamics. Our main conclusion is that the sensitivity of the dynamics to changes in the response associated with velocity coupling is significantly greater than that for the response due to pressure coupling. The implications for directions in future research are substantial.

Isella (2001) and Isella and Culick (2000) have reported the main results. Here we will only cite a couple of examples. The idea is to use the framework described in Section 3.2 below to compute the growth and limiting amplitudes for limit cycles. Essentially a modest parameter study has been done, the response function itself (i.e. the combustion dynamics) being the parameter. Following the tactic first introduced by Culick, Isella and Seywert (1998), it is helpful to display the response function, as a function of frequency, and the amplitudes of the modes forming a limit cycle, as two parts of the same figure, such as Figure 2.17 prepared for a typical case for the QSHOD response function. The chamber is cylindrical, 0.6 m long, 0.025 m in diameter, operated at a chamber mean pressure equal to $1.06 \times 10^7$ Pa. It is the same motor considered by Culick and Yang (1992).
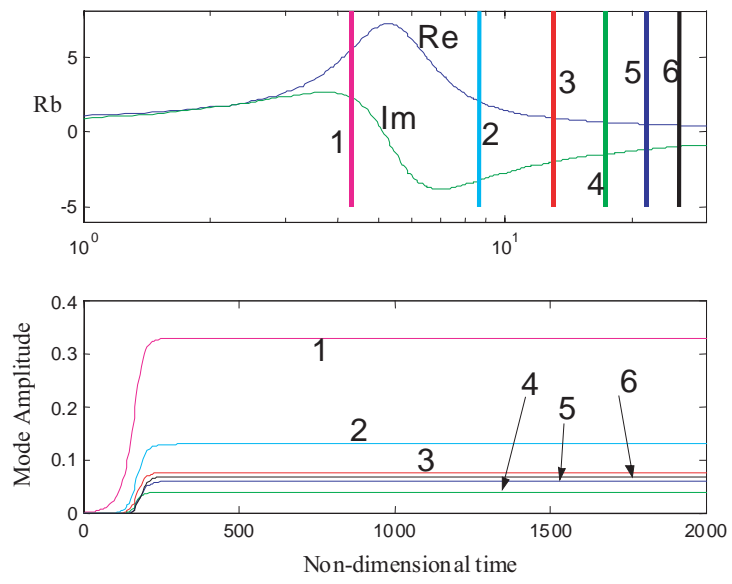


FIGURE 2.17. Results of a Simulation with a QSHOD Combustion Response (Pressure Coupling: A= 8.0, B = 0.6, n = 0.8).

Figures 2.18–2.20 show results obtained for the same motor and basic combustion response but including, respectively, a time delay; surface layer dynamics; and dynamics of both a surface layer and gas phase, all according to the analysis described above.

Owing to the significantly different dynamics added to the basic QSHOD model, the three examples illustrated in Figures 2.18–2.20 show quite different response functions—all, it must be emphasized-representing responses due to pressure coupling. The question here concerns the sensitivity of the response function to changes of composition (not the qualitative dynamics) and consequently the sensitivity of the global chamber dynamics.

For the examples chosen, the waveforms in the limit cycles are similar whether or not dynamics of the surface layer and gas phase are accounted for. This result is due mainly to the substantial attenuation of higher harmonics due to particle damping (Culick and Yang, 1992). If the damping is reduced, the amplitudes and amounts of higher harmonics are substantially affected, as Figures 2.21 and 2.22 show.
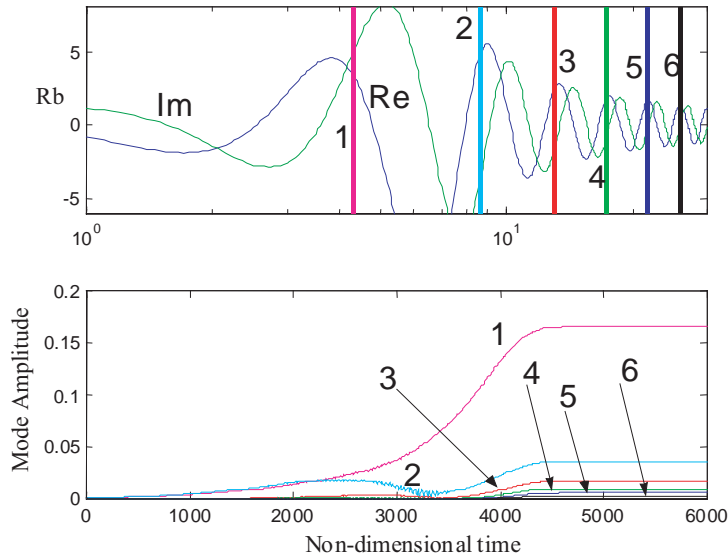
FIGURE 2.18. Results of a Simulation Including a Time Delay ($\tau = 1.5$)
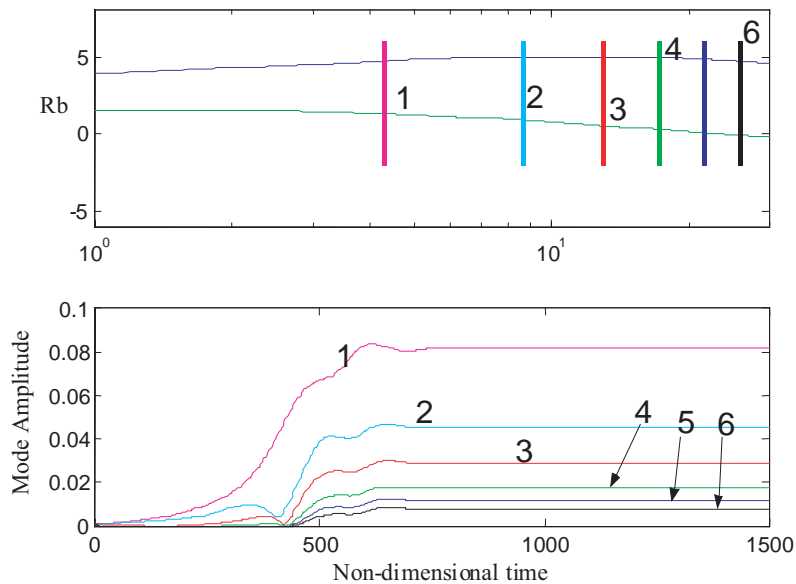


FIGURE 2.19. Results of a Simulation Including Dynamics of a Surface Layer

In general, models based on pressure coupling do not show dramatic sensitivity of the combustor dynamics to small changes of composition. Hence we investigated similar problems with a simple model of the response due to velocity coupling. The idea is based on the model introduced by Levine and Baum (1988).

Some recent work done on the dynamics resulting from functional form of the equations used in the analysis by Ananthkrishnan (2002) (See attachment to these notes.) seems to prove that the absolute value function in itself, as it appears in a simple model of velocity coupling, is sufficient to produce a subcritical bifurcation (pitchfork) followed by a fold (saddle-node bifurcation).
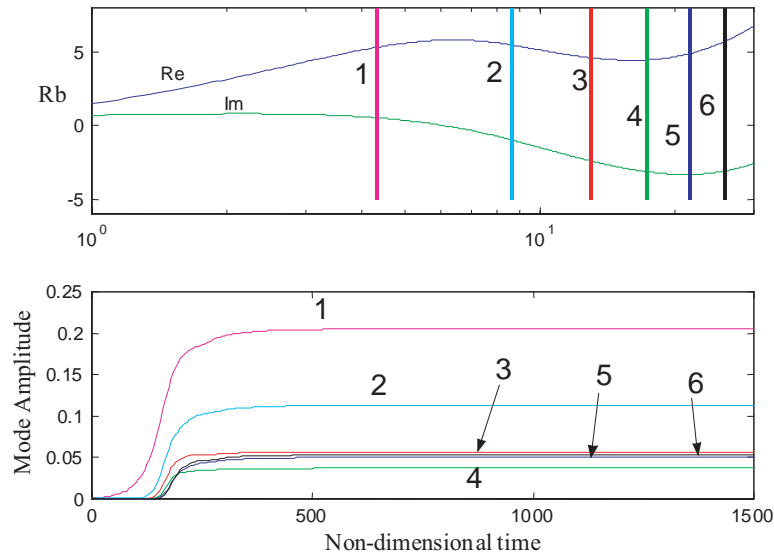
FIGURE 2.20. Results of a Simulation Including Dynamics of a Surface Layer and the Gas Phase
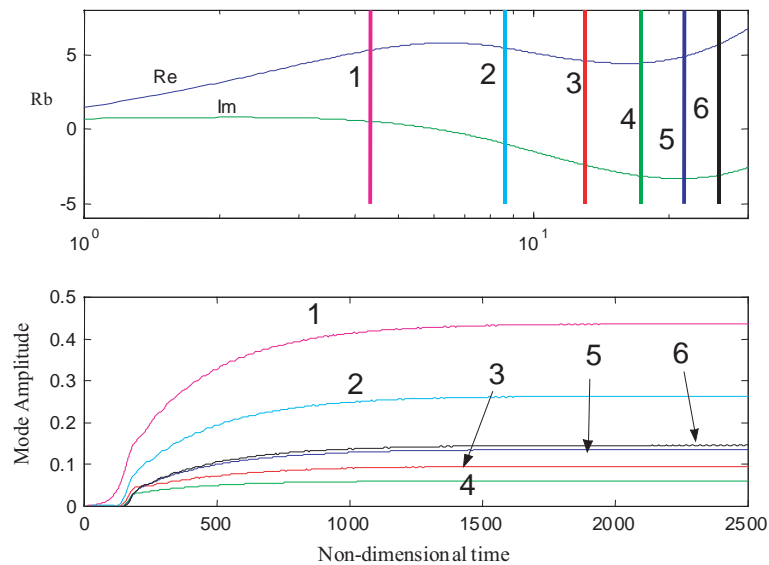


FIGURE 2.21. Simulations with Dynamics of the Surface Layer and Gas Phase Included, but with Reduced Particle Damping (10% Reduction Over the Entire Frequency Range)

In order to analyze the effect of velocity coupling on the overall dynamics, the following two relative sensitivities are defined:

$$S_{\tilde{R}_{\nu c}}^{A_{LC}} = \frac{1}{A_{LC}} \frac{\partial A_{LC}}{\partial \tilde{R}_{\nu c}} \tag{2.58}$$

$$S_{\tilde{R}_{\nu c}}^{\alpha_{BP}} = \frac{1}{\alpha_{BP}} \frac{\partial \alpha_{BP}}{\partial \tilde{R}_{\nu c}} \tag{2.59}$$

where $A_{LC}$ is the amplitude of the limit cycle (defined at a fixed value of $\alpha$), and $\alpha_{BP}$ is the value of the growth rate at which the unstable fold turns to a stable fold. Equation (2.58) defines the relative sensitivity of
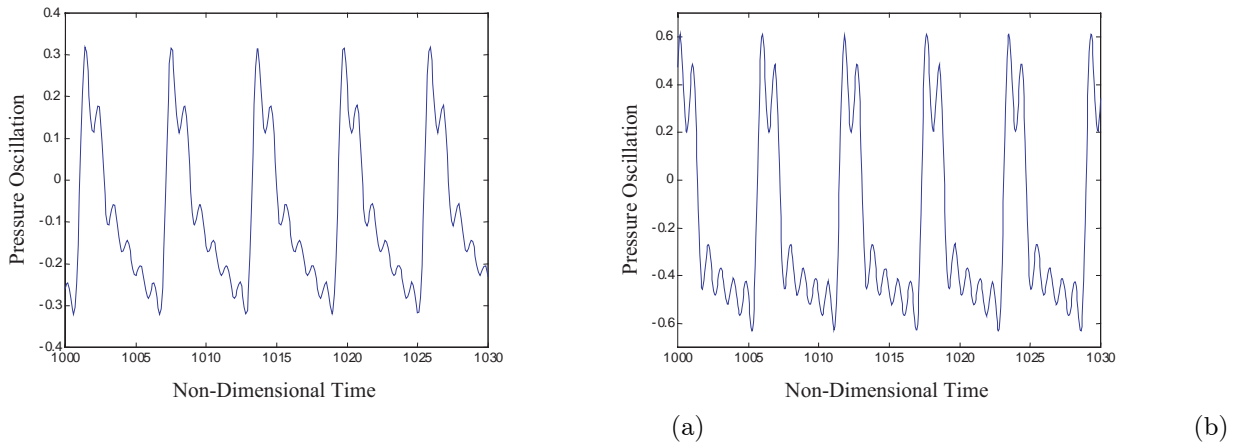
FIGURE 2.22. Waveforms for the Limit Cycles (a) Figure 2.20; (b) Figure 2.21.
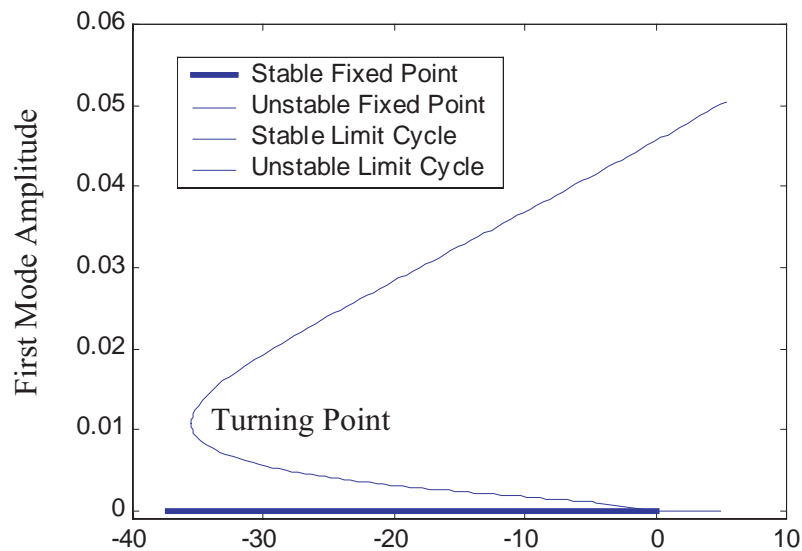


FIGURE 2.23. Bifurcation Diagram

the amplitude of the limit cycle to variations in the velocity coupling coefficient; equation (2.59) refers to the sensitivity of the turning point to the same coefficient.

Figure 2.24 shows a plot of the sensitivities, calculated for the combustion chamber used in the examples of the previous section, and using a six mode approximation of the system. Note that the sensitivity of the turning point is very high, and also the sensitivity of the amplitude of the limit cycle is quite large in the range 0.15 to 0.25 of the coupling coefficient.

We now analyze the same combustor described in Section 2.6 with the introduction of the extra terms due to velocity coupling. For reference, Figure 2.25 presents the results of the simulation for the system with a combustion response based on the quasi-steady theory. The top section presents the combustion response function; the vertical lines mark the non-dimensional frequencies of the acoustic modes of the combustion chamber considered in the simulations. The bottom half shows the time evolution of the amplitude of each mode. The values of the parameters are: A = 6.0, B = 0.55, n = 0.50.
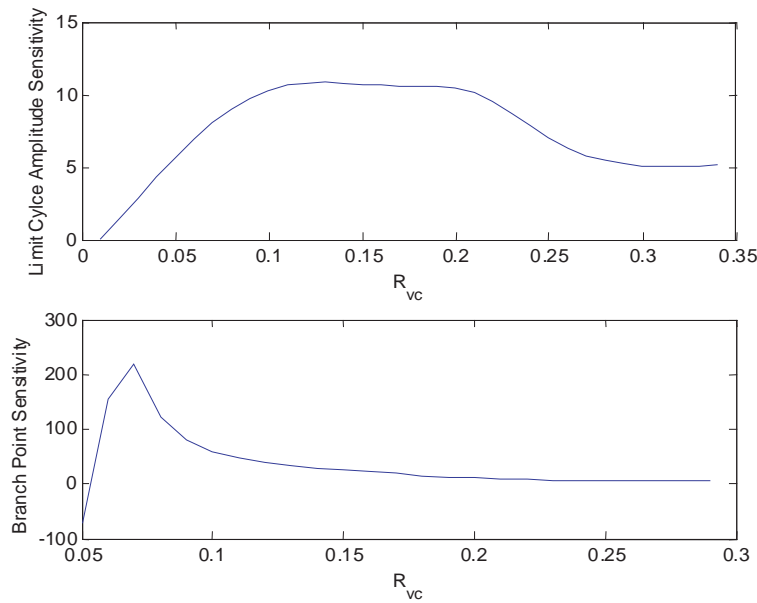
FIGURE 2.24. Sensitivity of Global Dynamics to Variations of the Coupling Coefficient
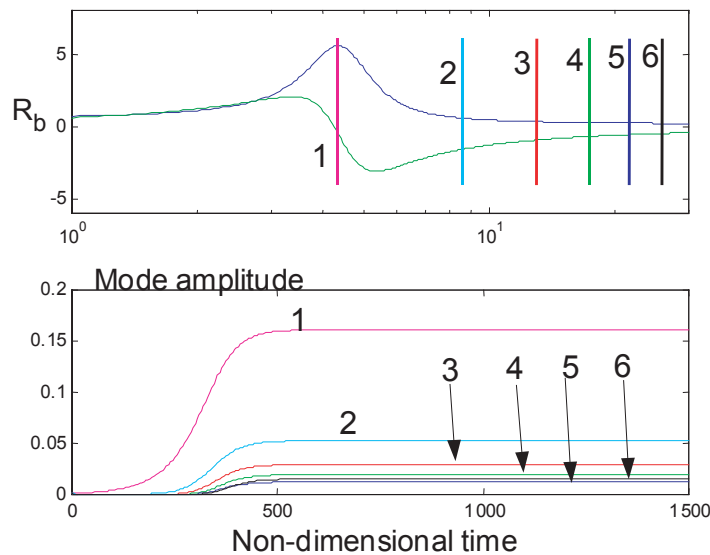


FIGURE 2.25. Simulation Results for QSHOD Combustion Response

The first mode is unstable and rapidly grows to a limit amplitude, while the other modes are all stable, and draw energy from the first mode (allowing the system to enter a limit cycle).

Figure 2.24 shows that there is a region of high sensitivity of the amplitude of the limit cycle for variations in the velocity-coupling coefficient. Figure 2.26 presents the global response for a small variation of the velocity coupling coefficient ($\tilde{R}_{\nu c} = 0.15$ and $\tilde{R}_{\nu c} = 0.165$).

The simulation uses the same coefficients for the pressure coupling as in the results of Figure 2.25, with the addition of the velocity coupling terms. Figure 2.27 and 2.28 show the pressure trace and the harmonic content for the same two cases.
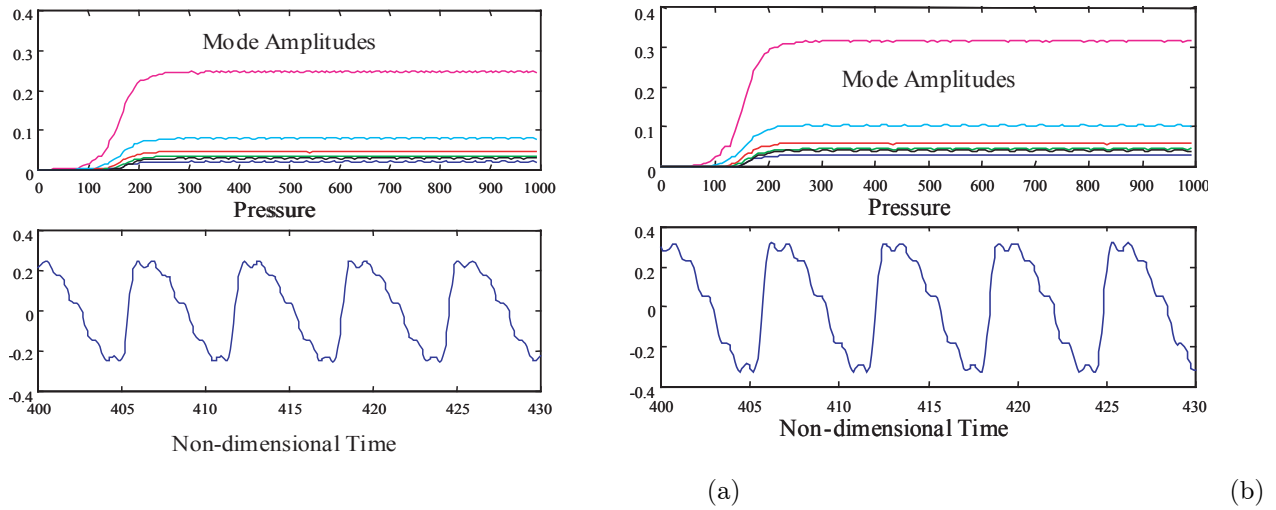
FIGURE 2.26. Simulations with Velocity Coupling for: (a) $\tilde{R}_{\nu c} = 0.15$, (b) $\tilde{R}_{\nu c} = 0.165$.
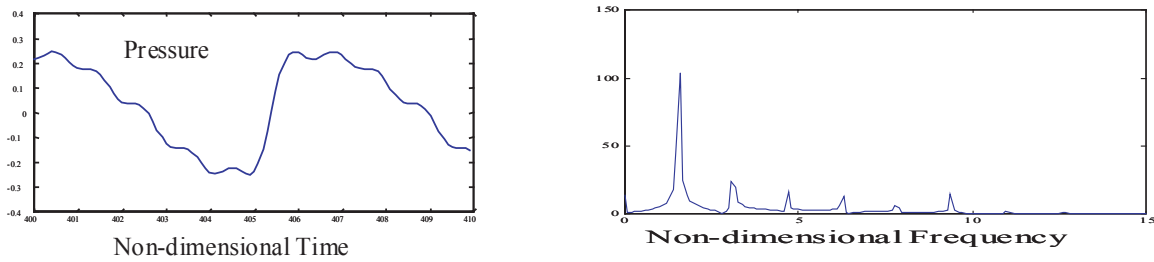


FIGURE 2.27. Pressure Trace and Harmonic Content for the Case $\tilde{R}_{\nu c} = 0.15$
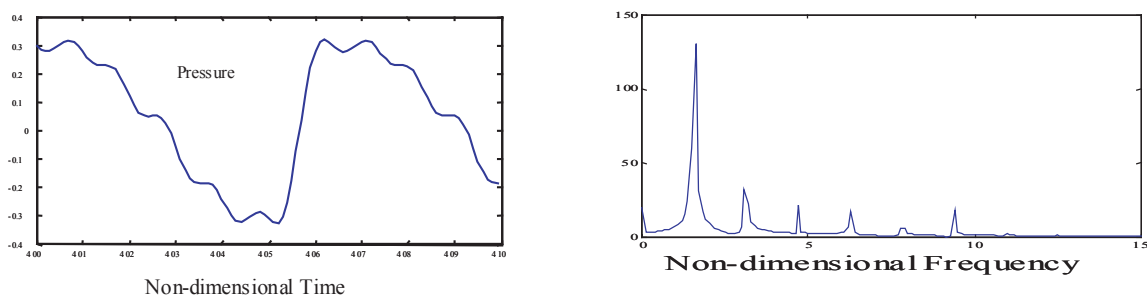


FIGURE 2.28. Pressure Trace and Harmonic Content for the Case $\tilde{R}_{\nu c} = 0.165$

In summary, we have shown with these calculations that the global dynamics of a solid propellant motor seem to be affected more significantly by small changes in the combustion response to velocity coupling then in the combustion response to pressure coupling. We cannot claim at this time that this is a universal result but the possible implications are important. It appears in any case that to determine why small changes of propellant composition seem on a number of occasions to have relatively large effects in the chamber dynamics, one must investigate the phenomenon of velocity coupling. The most serious need is experimental. Attention must be paid to developing a method for measuring the combustion dynamics associated with velocity coupling.

**2.8. Generation of Vorticity and Vortex Shedding.** There are two principal connections between vorticity and combustion instabilities in solid rockets:

1) generation of unsteady vorticity at burning surfaces; and

2) coupling between acoustical motions and large vortices shed at obstacles or growing out of the region adjacent to the lateral burning surface.

Both of these phenomena have motivated much interesting work—analytical, numerical and experimental. And although both sorts of behavior fundamentally involve production of vorticity, their characters and the positions they occupy in the area of oscillatory behavior are very different.

2.8.1. *Generation of Vorticity.* The generation of vorticity at a burning surface is special to solid rockets. It occurs whenever there is a variation of pressure fluctuation in the direction tangential to a surface from which there is average mass flow normal to surface into the chamber. The vorticity is created because the velocity inward is perpendicular to the surface—the 'no-slip' boundary condition. Imposition of a tangential velocity fluctuation, due to the non-uniform pressure along the surface, on the average inward flow constitutes an inviscid mechanism of vorticity generation. Moreover, conservation of mass in the region close to the surface causes a periodic pumping action normal to the surface. Both the vorticity generation and the pumping exist at the expense of work done by the impressed acoustic field and therefore ultimately appear as losses to the acoustic field in the chamber.

An oversimplified and incomplete interpretation of the phenomenon is that the incoming average flow normal to the surface gains some kinetic energy because it must acquire the oscillatory motion parallel to the surface. Thus there is effectively a "turning" of the flow. The inelastic acceleration of the mass flow causes a loss that is the unsteady counterpart of the loss accompanying mass injection into a duct flow. This "flow-turning loss" was, not surprisingly, discovered in an analysis of unsteady one-dimensional flow with mass injection at the lateral surface (Culick 1970). However, the connection with vorticity generation was not pointed out. It was Flandro (1995) who clarified the phenomenon in terms of the unsteady production of vorticity, emphasizing the central importance of the no-slip boundary condition. Flandro carried out the first rigorous formal analysis of the problem, work that has since prompted a stream of calculations on the basic problem at hand, as well as variations (e.g. Majdalani, 1999; Kassoy, 1999; Majdalani, Flandro and Roh, 2000; and many others).

Generation of vorticity can provide a significant contribution to the loss of acoustic energy and hence to stability. That is why it has become the subject of some controversy in the community of researchers concerned with combustion instabilities. There is not presently uniform agreement on the true effects of vorticity generation on linear stability (unfortunately). The situation in the analyses is more complicated than that described superficially above. Besides the dissipation of vorticity in the chamber—due both to laminar viscous effects and interactions between the vorticity and turbulence, there are one or two effects not mentioned above. Hence depending on interpretation of the basic phenomenon, and also on the particular configuration of motor considered, the next effect of vorticity generation may be stabilizing or de-stabilizing. The matter remains unresolved and deserves resolution, but not in these notes.

We should note that there are also many experimental results related to this problem, some obtained in university laboratories, and some gained in subscale practical configurations (e.g. Dunlap *et al.* 1990).

2.8.2. *Shedding of Large Scale Vortices.* So far as practical consequences are concerned, the production of large vortices in motors has been far more significant than has the generation of vorticity discussed above. The latter is present in all solid rockets, and contributes always to linear stability, although the true quantitative value remains controversial. On the other hand, while the prediction and influences of vortex shedding may contain uncertainties, it is fair to say that the general characteristics are well-known and settled. Moreover, vortex shedding has been identified unambiguously as the mechanism for oscillation observed in several large motors including the Space Shullte SRM, the Titan IV SRMV and the Ariane 5 SRM. Note that the mechanism is apparently active only in large motors.

The main reason for that conclusion seems to be the required special near-coincidence between the frequency of sheding and the frequency of an acoustic mode. Simple laboratory tests demonstrate that basic feature (Magiawala and Culick 1979; Nomoto and Culick 1982; Aaron and Culick 1984): satisfaction of the condition requires suitable combinations of geometry, mean flow speed, thichness of shear layer at the origin of the vortex shedding and acoustic frequency which depends mainly on the speed of sound and length of chamber.

Vortex shedding in large motors has appeared in two forms: shedding from obstacles or sharp edges; and growth out of the region of reletively high shear near the lateral burning surface. Motivated by some experimental results (Price *et al.* 1972) involving vortex shedding, Flandro and Jacobs (1974) first proposed the excitation of acoustic modes in a chamber due to coupling with vortices shed from an obstacle. Within a couple of years that process was discovered[5] as the mechanism for potentially serious pressure oscillations in the Space Shuttle SRM (Mathes 1980).

The appearance of vortex shedding in the Titan motors caused formation of a very useful program of extensive tests of a subscale cold-flow model of the motor (Dunlap and Brown 1981; Brown *et al.* 1981). Those tests produced extensive date for the internal flow fields, eventually including results that formed part of the basis for the theoretical work on unsteady vorticity cited in the preceeding section.

In 1986, Flandro reported his collaboration and extension of the analysis he had carried out with Jacobs twelve years earlier. The work brought together previous ideas of instability of a shear layer as the initiation of a shear wave; growth and roll-up of the wave into a vortex; propagation of the vortex at a speed something less than that of the average flow; and impingement of the vortices on a solid surface, producing a pulse of pressure that can excite and sustain acoustic waves in the chamber. An acoustic pulse will propagate upstream to the region of the shear instability, possibly to initiate another disturbance to be amplified within the layer, later to develop into another vortex... The process will continue, becoming periodic when the frequency of the vortex shedding is nearly equal to the acoustic frequency.

When that behavior occurs in a rocket, toroidal vortices are shed from the inner edge of an annular obstruction, as in the Shuttle and Titan motors, or at the transition from slots to primary cylindrical chamber (Figure 2.29). The acoustic frequency is determined mainly by the length of the chamber, while the vortex shedding frequency
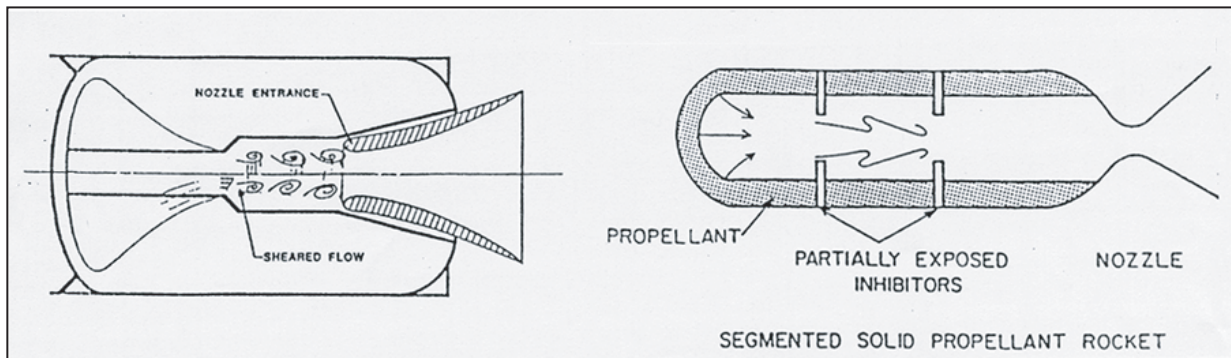


FIGURE 2.29. Vortex Shedding from (a) a transition zone in a rocket chamber; and (b) a residual annulus of inhibitor material (Flandro 1986).

is influenced by the local geometry and average flow. The local geometry determines the growth of the shear layer and in particular its momentum thickness, a fundamental parameter defining the conditions for instability. Flandro's analysis—an adaptation of earlier work by Michalle—and experimental results have confirmed that the vortex shedding is characterized by the value of the Strouhal number $S$ at which the growth rate of an unstable disturbance is maximum. The Strouhal number is defined as the product of shedding frequency $f_s$ times a characteristic length $\delta$ divided by a characteristic speed $U$ so the shedding frequency is given by the formula

$$f_s = S \frac{U}{\delta} \qquad (2.60)$$

where $S$ has some value roughly constant and set by the geometry. The frequencies of the acoustic modes are only weakly dependent on the mean flow of the Mach number so small but do depend strongly on the geometry. For a chamber having length $L$ and closed at both ends[6], the longitudinal modes have frequencies given by

$$f_a = \ell \pi \frac{a}{L} \qquad (2.61)$$

---

[5]The initial report of those oscillations prompted the laboratory demonstration reported by Culick and Magiawala (1979).

[6]A rocket physically closed at one end and exhausting through a choked nozzle appears to acoustic waves as if it is approximately closed at both ends.

where $a$ is the speed of sound and $\ell = 1, 2, \ldots$ identifies the mode.

Some interesting results reported by Nomoto and Culick (1982) confirm the truth of the preceding ideas for a simple laboratory apparatus consisting of two annuli fitted in a tube, separated by some distance $\ell$ and having a mean flow in the axial direction. Figure 2.30 shows lines drawn according to (2.60) and (2.61) and data points indicating the occurences of oscillations without regard to amplitude. For the conditions of the experiment, significant oscillations were excited only in regions in which (2.60) and (2.61) are simultaneously satisfied. Note that the separate diagonal lines for shedding frequency given by (2.60) represent cases in which there are $1, 2, 3, \ldots$ vortices existing between the annuli at any given time.
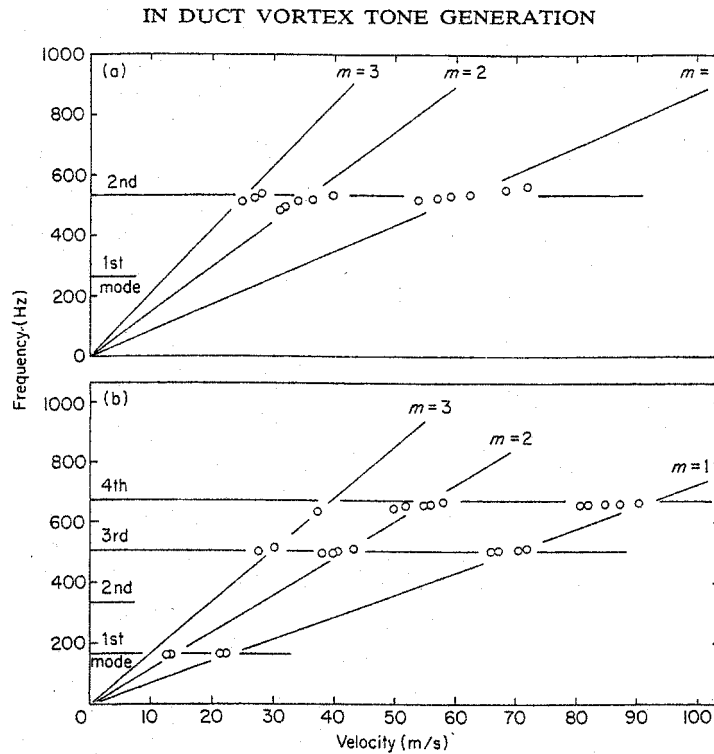


FIGURE 2.30. Experimental Results for the Excitation of Acoustic Modes by Vortex Shedding (Nomoto and Culick 1982).

An important implication of Figure 2.30 is that the dependence of the observed frequency of oscillation may not have a simple—or obvious—dependence on the length and mean flow speed during the firing of a solid rocket. In fact, as several researchers have noted (see, e.g., Vuillot 1995) the shift of frequency with time is a good basis for distinguishing vortex shedding as the mechanism for oscillations.

Instabilities sustained by feedback involving combustion dynamics almost always show dependence on geometry closely given vy the formulas of classical acoustics: $f_a \sim 1/L$. Thus, if there is little or no propellant cast at the head end, the longitudinal frequency is nearly constant in time. Or, if, as usually is the case for large motors, there are slots and fins at the head end, the effective length of the chamber tends to increase during a firing and hence the frequency of oscillation decreases.

However, according to the results given in Figure 2.30, because the mean velocity may increase during a burn as more propellant is exposed, the frequency may increase. It is possible (and has been observed) that the frequency suffers discrete changes, corresponding to transition between groups of data points shown in Figure **??**, that is the state of the oscillating system shifts because the number of shed vortices present between the shedding and impingement points changes.

An important and very interesting second cause of vortex shedding was discovered several years ago by Vuillot and his colleagues at ONERA while investigating the mechanism for unstable oscillations observed in teh Ariane

5 solid rocket boosters. Subscale firings of motors showed that large vortices were initiated, grew, and were shed from the region near the burning surface. (Vuillot *et al.* 1993; Traineau *et al.* 1997). Hence the phenomenon was called "parietal vortex shedding" by Lupuglazoff and Vuillot (1996).

In an exemplary systematic research program, the group at ONERA have established most of the characteristics of parietal vortex shedding relevant to practical applications. Some issues of scale apparently remain, but very good agreement has been found between subscale hot firings; subscale tests with flow visualization (Avalon *et al.* 2000); and numerical analyses of stability and vortex shedding. LeBreton *et al.* (1999) have given a good review of the subject, including some results for the effects of resudual combustion.

Possibly the most important aspect of this subject is weak understanding of nonlinear behavior. No simple explanation exists for the amplitudes of oscillations that can be generated by coupling with the shedding of large vortices. According to LeBreton *et al.* (1999) parietal vortex shedding produces, in their examples, larger amplitudes of oscillation than shedding from an annulus (inhibitor ring in a segmented rocket). It would clearly be a significant aid to design and development if a rule of thumb could be constructed to place an upper limit to the amplitudes of oscillation caused by vortex shedding. Because the mechanism involves conversion of mechanical energy of the near flow to acoustic energy, it is likely that the maximum possible amplitudes must be much smaller than those that can be generated by coupling between acoustics and combustion dynamics.

**2.9. Distributed Combustion.** Combustion of the major components of a solid propellant—the primary oxidizer and the binder in the case of composite solids—normally takes place to completion near the burning surface. Thus the term 'distributed combustion' refers to combustion of particles as they are carried into the volume of the chamber. Almost all attention has been directed to residual combustion of aluminum for which there is much photographic evidence. Steady combustion of aluminum particles has long been and continues to be a subject of research owing to its vital importance to the efficiency and performance of motors, and in the formation of slag.

Relatively little notice has been taken of the possible influences of residual combustion on the stability of motors. Probably the main reason for this lack of interest is the general view that generally the existence of combustion instabilities in motors can be satisfactorily explained by other mechanisms, notably the dynamics of surface combustion and vortex shedding. It appears that the dynamics of aluminum combustion within the volume of the chamber must provide at most a small contribution to stability. There are at least two reasons for this conclusion: the available data contain uncertainties too large to allow identification of the influences of unsteady aluminum combustion; and any destabilizing tendencies of the particles are roughly compensated by the attenuation of unsteady motions due to the presence of particles. The second is known to be significant if the particles are inert and have suitable sizes for the frequencies of the instability in question.

Several works (Marble and Wooten (1970); Dupays and Vuillot 1998) have treated the effects of condensation and vaporization of non-burning particles, on attenuation of acoustic waves. Whether the attenuation is increased or decreased depends on many factors, including the sizes of particles and the rates at which the particles gain or lose mass. When, for example, a particle is vaporizing, it seems that in the presence of an acoustic wave, the phenomenon of 'flow turning' discussed in the preceding section should cause increased attenuation for a given particle size and frequency. However, while the analysis by Wooten (1966) supports that conclusion, recent work by Dupays (1999) suggests that the result is not always true. Moreover, suggestions have been made by investigators of combustion instabilities in ramjets (Sirignano) and in liquid rockets (Merkl) that the process of vaporization of liquid drops is destabilizing. Those conclusions may be misleading because due to implied direct connections between the vaporization and burning rates. It may in fact be the case that the destabilization found is due to combustion rather than vaporization *per se.*

Owing to the necessary connection between vaporization and combustion of particles, the problem of residual combustion presents certain difficulties of distinguishing what process is really responsible for attenuation or driving of waves. The most extensive work is the problem has been done by Beckstead and his students (Brooks and Beckstead, 1995; Raun and Beckstead, 1993; Beckstead, Richards and Brewster, 1984). Probably the most compelling reason for investigating the manner was the discover of anomalous (and still not completely understood) results obtained with a device called the 'velocity-coupled T-burner'. In this configuration, large areas of propellant

are mounted in the lateral boundary to emphasize the interactions between surface combustion and velocity fluctuations parallel to the surface.

For reasons not discussed here, Beckstead concluded that residual combustion was possibly a reason that unusually large values of the response function were found. The idea was based partly on the suspicion that the tangential velocity disturbances can strip incompletely burned aluminum from the surface. Subsequently, with both calculations and further experiments (Raun and Beckstead, 1993). Beckstead has strengthened his case that the effects of unsteady residual combustion should not be dismissed out-of-hand. However, there is presently no analysis accommodating the process in computations of combustion instabilities in solid rockets. It is worth noting the conclusion by Brooks and Beckstead (1995) that the greatest effect of residual combustion (of aluminum) on stability was indirect, due to its effect on the mean temperature profile.

## 3. EQUATIONS FOR UNSTEADY MOTIONS IN COMBUSTION CHAMBERS

The examples described in Section 1, and many others, establish a firm basis for interpreting unsteady motions in a combustor in terms of acoustic modes of the chamber. That view has been formalized during the past fifty years and has led to the most widely used methods for analyzing combustor dynamics. In this section, we present the foundations of a particularly successful version of methods based on expansion in normal modes and spatial averaging. We assume familiarity with most of the required background in classical fluid dynamics and acoustics. Section 5 covers the principles and chief results of classical acoustics required as part of the foundation for understanding combustion instabilities. The discussions in this and the following sections are quite formal, intended to serve as the basis for a general framework within which unsteady motions, especially combustion instabilities, in all types of combustors may be treated. Analyses using *ad hoc* models will be covered when particular systems are considered, as in Section 2.

**3.1. Modes of Wave Motion in a Compressible Medium.** In this section, the term 'modes' refers not to natural motions or resonances of a chamber but rather to a *type* or class of motions in compressible flows generally. The brief discussion here is intended to address the question: how is it possible that apparently coherent nearly-classic acoustic waves exist in chambers containing highly turbulent non-uniform flow? It's a fundamentally important observation that such is the case. The explanation has been most thoroughly clarified by Chu and Kovasznay (1957), who elaborated and combined some results known for nearly a century. Their conclusions most significant for present purposes may be summarized as follows:

(1) Any small amplitude (linear) disturbance may be synthesized of three modes of propagation: *entropy waves* or 'spots', small regions having temperatures slightly different from the ambient temperature of the flow; *vortical* or *shear waves* characterized by nonuniform vorticity; and *acoustic waves.*

(2) In the linear approximation, *if the flow is uniform,* the three types of waves propagate independently, but may be coupled at boundaries (e.g. nozzles) or in combustion zones.

Entropy and vortical waves propagate with the mean flow speed ('convected') but acoustic waves propagate with their own speeds of sound. Moreover, in this linear limit, only acoustic waves carry disturbances of pressure. All three types of waves are accompanied by velocity fluctuations. If the flow is non-uniform or at finite amplitudes, the three modes become coupled. As a result, each of the waves then carries pressure, temperature and velocity fluctuations. Extension of the fundamental theory has not been accomplished completely (see Chu and Kovasznay). Some of the consequences of these types of modal coupling arise in the theory developed here, but much remains to be investigated. In particular, interactions between turbulence and an acoustic field is an important process represented by coupling of the basic linear modes of propagation.

**3.2. Equations of Motion for a Reacting Flow.** Combustion systems commonly contain condensed phases: liquid fuel or oxidizer, and combustion products including soot and condensed metal oxides. Hence the equations of motion must be written for two phases consisting of at least one species each. For investigating the dynamics of combustors, it is entirely adequate to represent each phase as its mass average over all member species. For a medium consisting of a multicomponent mixture of reacting gases and, for simplicity, a single liquid phase, it is a straightforward matter to construct a system of equations representing a single fluid. The procedure is summarized in Appendix A. As a result we can treat combustor dynamics under broad conditions as unsteady motions of a fluid having the mass-averaged properties of the actual medium.[7] The dimensional governing equations are (A.9)–(A.14)

---

[7]We now use $C_v, \gamma, R, \cdots$ to stand for the mass-averaged properties represented by bold-face symbols in Appendix A.

*Conservation of Mass*

$$\frac{\partial \rho}{\partial t} + \mathbf{u} \cdot \nabla \rho = -\rho \nabla \cdot \mathbf{u} + \mathcal{W} \tag{3.1}$$

*Conservation of Momentum*

$$\rho \left[ \frac{\partial \mathbf{u}}{\partial t} + \mathbf{u} \cdot \nabla \mathbf{u} \right] = -\nabla p + \boldsymbol{\mathcal{F}} \tag{3.2}$$

*Conservation of Energy*

$$\rho C_v \left[ \frac{\partial \mathbf{T}}{\partial t} + \mathbf{u} \cdot \nabla T \right] = -p \nabla \cdot \mathbf{u} + \mathcal{Q} \tag{3.3}$$

*Equation for the Pressure*

$$\frac{\partial p}{\partial t} + \mathbf{u} \cdot \nabla p = -\gamma p \nabla \cdot \mathbf{u} + \mathcal{P} \tag{3.4}$$

*Equation for the Entropy*

$$\rho \left[ \frac{\partial s}{\partial t} + u \cdot \nabla s \right] = \frac{1}{T} \mathcal{S} \tag{3.5}$$

*Equation of State*

$$p = R\rho T \tag{3.6}$$

All definitions are given in Appendix A.

It is particularly important to realize that the source functions $\mathcal{W}$, $\boldsymbol{\mathcal{F}}$, $\mathcal{Q}$ and $\mathcal{P}$ contain all relevant processes in the systems to be analyzed here. They include, for example, the modeling and representations of the actions of actuation mechanisms used for active control. Eventually, the most difficult problems arising in this field are associated with modeling the physical processes dominant in the problems addressed.

Both for theoretical and computational purposes it is best to express the equations in dimensionless variables using the reference values:

$$L \; : \text{reference length}$$
$$\rho_r, p_r, T_r, a_r \; : \text{reference density, pressure, temperature and speed of sound}$$
$$C_{vr}, C_{pr}, R_r \; : \text{reference values of } C_v, C_p, R$$

Then define the dimensionless variables represented by $\mathbf{M}$ and the same symbols used for dimensional variables:

$$\mathbf{M} = \frac{\mathbf{u}}{a_r}; \quad \frac{\rho}{\rho_r} \rightarrow \rho; \quad \frac{p}{\rho_r a_r^2} \rightarrow p; \quad \frac{T}{T_r} \rightarrow T; \quad \frac{C_v}{C_{vr}} \rightarrow C_v, \text{ etc.}; \quad \frac{s}{C_{vr}} \rightarrow s$$

The dimensionless source functions are

$$\frac{L}{\rho_r a_r} \mathcal{W} \rightarrow \mathcal{W}; \quad \frac{L}{\rho_r a_r^2} \boldsymbol{\mathcal{F}} \rightarrow \boldsymbol{\mathcal{F}}; \quad \frac{L}{\rho_r a_r^3} \mathcal{Q} \rightarrow \mathcal{Q}; \quad \frac{L}{\rho_r a_r} \mathcal{P} \rightarrow \mathcal{P}; \quad \frac{\mathcal{S}}{\rho_r a_r C_{vr}} \rightarrow \mathcal{S}$$

Substitution of these definitions in equations (3.1)–(3.6) leads to the set of dimensionless equations for the single fluid model:

$$Mass: \qquad \frac{D\rho}{Dt} = -\rho \nabla \cdot \mathbf{M} + \mathcal{W} \tag{3.7}$$

$$Momentum: \qquad \rho \frac{D\mathbf{M}}{Dt} = -\nabla p + \boldsymbol{\mathcal{F}} \tag{3.8}$$

$$Energy: \qquad \rho C_v \frac{DT}{Dt} = -p \nabla \cdot \mathbf{M} + \mathcal{Q} \tag{3.9}$$

$$Pressure: \qquad \frac{Dp}{Dt} = -\gamma p \nabla \cdot \mathbf{M} + \mathcal{P} \tag{3.10}$$

$$Entropy: \qquad \rho \frac{Ds}{Dt} = \frac{1}{T} \mathcal{S} \tag{3.11}$$

$$State: \qquad p = \rho RT \tag{3.12}$$

and

$$\frac{D}{Dt} = \frac{\partial}{\partial t} + \mathbf{M} \cdot \nabla \tag{3.13}$$

We emphasize again that the source terms accommodate all relevant physical processes and can be interpreted to include the influences of actuation used in active control.

**3.3. Two-Parameter Expansion of the Equations of Motion.** The general equations (3.7)–(3.13) are written in the form suggestive of problems that are dominated by fluid mechanical processes, a tactic dictated by the observations described earlier. This point of view is the basis for the approach taken here to construct a general framework within which both practical and theoretical results can be obtained by following systematic procedures.

We are not concerned at this point with simulations or other methods relying essentially on some sort of numerical anaylsis and large scale computations. The nature of the problems we face suggests perturbation methods. If the source terms $\mathcal{W}, \ldots$ were absent from (3.7)–(3.11), the homogeneous equations then represent nonlinear inviscid motions in a compressible fluid: Nonlinear acoustics in a medium without losses. One useful method for investigating such problems is based on expansion of the equations in a small parameter, $\varepsilon$, measuring the amplitude of the motion. Specifically, $\varepsilon$ can be taken equal to $M_r'$, a Mach number characteristic of the fluctuating flow, $\varepsilon := M_r'$.

The problems we are concerned with here are defined essentially by the non-zero functions $\mathcal{W}, \ldots$ . Because observed behavior seems to be dominated by features recognizable as 'acoustical', those sources which excite and sustain the actual motions must in some sense be small. They should therefore be characterized by at least one additional small parameter. It has become customary to select only one such parameter, $\mu := \bar{M}_r$, a Mach number $\bar{M}_r$ characterizing the mean flow, for the following reasons.[8]

Any operating combustion chamber contains an average steady flow produced by combustion of the fuel and oxidizer to generate products. The intensity of the flow, partly measurable by the Mach number, is therefore related to the intensity of combustion and both processes can in some sense be characterized by the same quantity, namely the Mach number of the average flow. Thus many of the processes represented in the source functions may be characterized by $\mu$, in the sense that their influences become vanishingly small as $\mu \to 0$ and are absent when $\mu = 0$.

---

[8]We use the symbols $\varepsilon$ and $\mu$ rather than $M_r'$ and $\bar{M}_r$ to simplify writing.

It is important to understand that the two small parameters $\varepsilon$ and $\mu$ have different physical origins. Consequently, they also participate differently in the formal perturbation procedures. Familiar nonlinear gas dynamical behavior is, in the present context, governed by the parameter $\varepsilon$; steepening of compressive waves is a notable example. In the expansion procedure worked out here, the term 'nonlinear behavior' refers to the consequences of terms higher order in $\varepsilon$.

On the other hand, the parameter $\mu$ characterizes perturbations of the gasdynamics due in the first instance to combustion processes and the mean flow. Terms of higher order in $\mu$, but linear in $\varepsilon$, represent linear processes in this scheme. Failure to recognize this basic distinction between $\varepsilon$ and $\mu$ can lead to incorrect applications of formal procedures such as the method of time-averaging. Instances of this point will arise as the analysis is developed.

3.3.1. *Expansion in Mean and Fluctuating Values.* There is no unique procedure for carrying out a two-parameter expansion. We begin here by writing all dependent variables as sums of mean ($\bar{\ }$) and fluctuating ( )$'$ parts without regard to ordering

$$p = \bar{p} + p', \quad \mathbf{M} = \bar{\mathbf{M}} + \mathbf{M}', \dots, \quad \mathcal{W} = \bar{\mathcal{W}} = \mathcal{W}', \quad \boldsymbol{\mathcal{F}} = \bar{\boldsymbol{\mathcal{F}}} + \boldsymbol{\mathcal{F}}', \dots \tag{3.14}$$

We take the fluctuations of the primary flow variables ($p'$, $\mathbf{M}'$, $\rho'$, $T'$, $s'$) to be all of the same order in the amplitude $\varepsilon$ of the unsteady motion. Generally, the source terms are complicated functions of the flow variables and therefore their fluctuations will contain terms of many orders in $\varepsilon$. For example, suppose $\mathcal{W} = kp^3$. Then setting $p = \bar{p} + p'$ and expanding, we have

$$\mathcal{W} = k(\bar{p} + p')^3 = k\left[\bar{p}^3 + 3\bar{p}^2 p' + 3\bar{p}p'^2 + p'^3\right]$$

Hence we define orders of the fluctuations of the source $\mathcal{W}$ and write

$$\mathcal{W} = \bar{\mathcal{W}} + \mathcal{W}'_1 + \mathcal{W}'_2 + \mathcal{W}'_3 + \mathcal{W}'_4 + \dots$$

where the subscript denotes the order with respect to the amplitude: Here, for the example $\mathcal{W} = kp^3$, $\mathcal{W}'_2 = (2k\bar{p})p'^2$. All source functions are written symbolically in the general form shown for $\omega$, but modeling is required to give explicit formulas.

Most combustors contain flows of relatively low Mach number, say $\bar{\mathbf{M}} \lesssim 0.3$ or so. Thus we can assume that for a broad range of circumstances, processes depending on the square of $\bar{\mathbf{M}}$, i.e. of order $\mu^2$, probably have small influences on the unsteady motions. We therefore neglect all terms of order $\mu^2$ and higher in the equations. As a practical matter, the equations are greatly simplified with this assumption.

After substituting all variables split into sums of mean and fluctuating values, and collection of terms by orders, we can rewrite (3.7)–(3.13) as[9]

$$\left[\frac{D\bar{\rho}}{Dt} + \bar{\rho}\nabla \cdot \bar{\mathbf{M}} - \bar{\mathcal{W}}\right] + \left[\frac{\partial \rho'}{\partial t} + \bar{\rho}\nabla \cdot \mathbf{M}'\right] + \left[\bar{\mathbf{M}} \cdot \nabla \rho' + \rho'\nabla \cdot \bar{\mathbf{M}} + \mathbf{M}' \cdot \nabla \bar{\rho} + \nabla \cdot (\rho'\mathbf{M}')\right] - \mathcal{W}' = 0 \tag{3.15}$$

$$\left[\bar{\rho}\frac{D\bar{\mathbf{M}}}{Dt} + \nabla \bar{p} - \bar{\boldsymbol{\mathcal{F}}}\right] + \left[\bar{\rho}\frac{\partial \bar{\mathbf{M}}}{\partial t} + \nabla p'\right] + \left[\bar{\rho}\left(\bar{\mathbf{M}} \cdot \nabla \mathbf{M}' + \mathbf{M}' \cdot \nabla \bar{\mathbf{M}}\right) + \bar{\rho}\frac{\bar{D}\bar{\mathbf{M}}}{Dt}\right]$$
$$+ \left[\rho'\frac{\partial \mathbf{M}'}{\partial t} + \bar{\rho}\mathbf{M}' \cdot \nabla \mathbf{M}' + \rho'\left(\bar{\mathbf{M}} \cdot \nabla \mathbf{M}' + \mathbf{M}' \cdot \nabla \bar{\mathbf{M}}\right)\right] + \left[\rho'\mathbf{M}' \cdot \nabla \mathbf{M}'\right] - \boldsymbol{\mathcal{F}}' = 0 \tag{3.16}$$

---

[9]We do not include here terms $O(\bar{M}_r M_r'^2)$, i.e. first order in the mean flow and second order in fluctuations.

$$\left[\bar{\rho}C_v\frac{D\bar{T}}{Dt} + \bar{p}\nabla\cdot\bar{\mathbf{M}} - \bar{\mathcal{Q}}\right] + C_v\left[\bar{\rho}\frac{\partial T'}{\partial t} + \bar{p}\nabla\cdot\mathbf{M}'\right] + \left[\bar{\rho}C_v\left(\bar{\mathbf{M}}\cdot\nabla T' + \mathbf{M}'\cdot\nabla\bar{T}\right) + C_v\rho'\frac{\bar{D}\bar{T}}{Dt} + p'\nabla\cdot\bar{\mathbf{M}}\right]$$

$$+ \left[C_v\bar{\rho}\frac{\partial T'}{\partial t} + C_v\rho'\left(\bar{\mathbf{M}}\cdot\nabla T' + \mathbf{M}'\cdot\nabla\bar{T}\right) + C_v\rho'\mathbf{M}'\cdot\nabla T' + p'\nabla\cdot\mathbf{M}'\right] + \left[C_v\bar{\rho}\mathbf{M}'\cdot\nabla T'\right] - \mathcal{Q}' = 0 \tag{3.17}$$

$$\left[\frac{\partial\bar{p}}{\partial t} + \bar{\mathbf{M}}\cdot\nabla\bar{p} + \gamma\bar{p}\nabla\cdot\bar{\mathbf{M}} - \bar{\mathcal{P}}\right] + \left[\frac{\partial p'}{\partial t} + \gamma\bar{p}\nabla\cdot\mathbf{M}'\right] + \left[\bar{\mathbf{M}}\cdot\nabla p' + \mathbf{M}'\cdot\nabla\bar{p} + \gamma p'\nabla\cdot\bar{M}\right]$$

$$+ \left[\mathbf{M}'\cdot\nabla p' + \gamma p'\nabla\cdot\mathbf{M}'\right] - \mathcal{P}' = 0 \tag{3.18}$$

$$\left[\bar{\rho}\bar{T}\frac{\bar{D}\bar{s}}{Dt} - \bar{\mathcal{S}}\right] + \left[\bar{\rho}\bar{T}\frac{\partial s'}{\partial t}\right] + \left[\bar{\rho}\bar{\mathbf{M}}\cdot\nabla s' + \rho'\bar{T}\frac{\bar{D}\bar{s}}{Dt} + \bar{\rho}\bar{T}\mathbf{M}'\cdot\nabla\bar{s} + \bar{\rho}T'\bar{\mathbf{M}}\cdot\nabla\bar{s}\right]$$

$$+ \left[\rho'\bar{T}\frac{\bar{D}s'}{Dt} + \rho'T'\frac{\bar{D}\bar{s}}{Dt} + \rho'\bar{T}\mathbf{M}'\cdot\nabla\bar{s} + \bar{\rho}T'\mathbf{M}'\cdot\nabla\bar{s} + \bar{\rho}T'\frac{\partial s'}{\partial t}\right]$$

$$+ \left[\left(\bar{\rho}T' + \rho'\bar{T}\right)\mathbf{M}'\cdot\nabla s' + \rho'T'\left(\mathbf{M}'\cdot\nabla\bar{s} + \bar{\mathbf{M}}\cdot\nabla s'\right)\right]$$

$$+ \left[\rho'T'\mathbf{M}'\cdot\nabla s'\right] - \mathcal{S}' = 0 \tag{3.19}$$

$$\left[\bar{p} - R\bar{\rho}\bar{T}\right] + \left[p' - R\left(\bar{\rho}T' + \rho'\bar{T}\right)\right] + \left[-R\rho'T'\right] = 0 \tag{3.20}$$

where the convective derivative following the mean flow is

$$\frac{\bar{D}}{Dt} = \frac{\partial}{\partial t} + \bar{\mathbf{M}}\cdot\nabla \tag{3.21}$$

As a convenience in writing, it is useful to introduce some symbols defining groups of ordered terms. The set of equations (3.15)–(3.21) then become:

$$\left[\frac{\bar{D}\bar{\rho}}{Dt} + \bar{\rho}\nabla\cdot\bar{\mathbf{M}} - \bar{\mathcal{W}}\right] + \left(\frac{\partial\rho'}{\partial t} + \bar{\rho}\nabla\cdot M'\right) + \{[\rho]\}_1 + \{\rho\}_2 - \mathcal{W}' = 0 \tag{3.22}$$

$$\left[\bar{\rho}\frac{\bar{D}\bar{\mathbf{M}}}{Dt} + \nabla\bar{p} - \bar{\boldsymbol{\mathcal{F}}}\right] + \left(\bar{\rho}\frac{\partial\mathbf{M}'}{\partial t} + \nabla p'\right) + \{[\mathbf{M}]\}_1 + \{\mathbf{M}\}_2 + \{\mathbf{M}\}_3 - \boldsymbol{\mathcal{F}}' = 0 \tag{3.23}$$

$$\left[\bar{\rho}C_v\frac{\bar{D}\bar{T}}{Dt} + \bar{p}\nabla\cdot\bar{\mathbf{M}} - \bar{\mathcal{Q}}\right] + \left(\bar{\rho}C_v\frac{\partial T'}{\partial t} + \bar{p}\nabla\cdot M'\right) + \{[T]\}_1 + \{T\}_2 + \{T\}_3 - \mathcal{Q}' = 0 \tag{3.24}$$

$$\left[\frac{\bar{D}\bar{p}}{Dt} + \gamma\bar{p}\nabla\cdot\bar{\mathbf{M}} - \bar{\mathcal{P}}\right] + \left(\bar{\rho}C_v\frac{\partial P'}{\partial t} + \bar{p}\nabla\cdot M'\right) + \{[p]\}_1 + \{p\}_2 - \mathcal{P}' = 0 \tag{3.25}$$

$$\left[\bar{\rho}\frac{\bar{D}\bar{s}}{Dt} - \bar{\mathcal{S}}\right] + \left(\bar{\rho}\bar{T}\frac{\partial s'}{\partial t}\right) + \{[s]\}_1 + \{s\}_2 + \{s\}_3 + \{s\}_4 = 0 \tag{3.26}$$

$$\left[\bar{p} - R\bar{\rho}\bar{T}\right] + \{p - R\rho T\}_1 + \{R\rho'T\}_2 = 0 \tag{3.27}$$

The definitions of the bracketted terms $\{\rho\}_1, \cdots$ etc. are given in Appendix A, Section A.2; the subscript $\{\ \}_n$ on the brackets identifies the orders of terms with respect to the fluctuations of flow variables, and the square brackets [ ] indicate that the terms are first order in the average Mach number. We have shown here

in each equation terms of the highest order fluctuations generated by the purely fluid mechanical contributions plus sources that must be expanded to orders appropriate to particular applications. Only the entropy equation produces terms of fourth order.

Time derivatives of quantities identified with the mean flow are retained to accommodate variations on a time scale long relative to the scale of the fluctuations. This generality is not normally required for treating combustion instabilities and unless otherwise stated, we will assume that all averaged quantities are independent of time.

3.3.2. *Equations for the Mean Flow.* At this point we have two choices. Commonly the assumption is made that the equations for the mean flow 'satisfy their own equations'. That implies that the square brackets [ ] in (3.22)–(3.27) vanish identically. With the time derivatives absent, the equations for the mean flow are:

$$\bar{\mathbf{M}} \cdot \nabla \bar{\rho} + \bar{\rho} \nabla \cdot \bar{\mathbf{M}} = \bar{\mathcal{W}} \tag{3.28}$$

$$\bar{\rho} \bar{\mathbf{M}} \cdot \nabla \bar{\mathbf{M}} + \nabla \bar{p} = \bar{\boldsymbol{\mathcal{F}}} \tag{3.29}$$

$$\bar{\rho} C_v \bar{\mathbf{M}} \cdot \nabla \bar{T} + \bar{p} \nabla \cdot \bar{\mathbf{M}} = \bar{\mathcal{Q}} \tag{3.30}$$

$$\bar{\mathbf{M}} \cdot \nabla \bar{p} + \gamma \bar{p} \nabla \cdot \bar{\mathbf{M}} = \bar{\mathcal{P}} \tag{3.31}$$

$$\bar{\rho} \bar{T} \bar{\mathbf{M}} \cdot \nabla \bar{s} = \bar{\mathcal{S}} \tag{3.32}$$

$$\bar{p} = R \bar{\rho} \bar{T} \tag{3.33}$$

This set of equations certainly applies when the average flow is strictly independent of time and there are no fluctuations. The time derivatives cannot be ignored when the flow variables change so slowly that the motion may be considered as 'quasi-steady' and fluctuations are still ignorable.

It is possible that when fluctuations are present, interactions among the flow variables cause transfer of mass, momentum and energy between the fluctuating and mean flows, generating time variations of the averaged variables. Then the appropriate equations are obtained by time-averaging (3.22)–(3.27) to give[10]

$$\frac{\bar{D}\bar{\rho}}{Dt} + \bar{\rho} \nabla \cdot \bar{\mathbf{M}} = \bar{\mathcal{W}} - \overline{\{[\rho]\}}_1 - \overline{\{\rho\}}_2 + \overline{\mathcal{W}}' \tag{3.34}$$

$$\bar{\rho} \frac{\bar{D}\bar{\mathbf{M}}}{Dt} + \nabla \bar{p} = \bar{\boldsymbol{\mathcal{F}}} - \overline{\{[\mathbf{M}]\}}_1 - \overline{\{\mathbf{M}\}}_2 - \overline{\{\mathbf{M}\}}_3 + \overline{\boldsymbol{\mathcal{F}}'} \tag{3.35}$$

$$\bar{\rho} C_v \frac{\bar{D}\bar{T}}{Dt} + \bar{p} \nabla \cdot \bar{\mathbf{M}} = \bar{\mathcal{Q}} - \overline{\{[T]\}}_1 - \overline{\{T\}}_2 - \overline{\{T\}}_3 + \bar{\mathcal{Q}}' \tag{3.36}$$

$$\frac{\bar{D}\bar{p}}{Dt} + \gamma \bar{p} \nabla \cdot \bar{\mathbf{M}} = \bar{\mathcal{P}} - \overline{\{p\}}_1 - \overline{\{p\}}_2 + \overline{\{p\}}_3 \tag{3.37}$$

$$\bar{\rho} \bar{T} \frac{\bar{D}\bar{s}}{Dt} = \bar{\mathcal{S}} - \overline{\{s\}}_1 - \overline{\{s\}}_2 - \overline{\{s\}}_3 - \overline{\{s\}}_4 \tag{3.38}$$

$$\bar{p} = \mathbf{R} \bar{\rho} \bar{T} - \overline{\{\rho T\}}_1 - \overline{\{\rho T\}}_2 \tag{3.39}$$

---

[10]Note that the fluctuations of the source terms, $\mathcal{W}' \cdots$ etc., actually contain squares and higher order products of the dependent variables; hence their time averages will generally be non-zero.

If the mean flow is strictly independent of time, then time averages of all first-order brackets, $\overline{\{\ \ \}}_1$, must vanish. For generality we allow them to be nonzero. There seem to be no analyses in which their variations have been taken into account.

The two sets of equations governing the mean flow in the presence of unsteady motion define two distinct formulations of the general problem. In the first, equations (3.28)–(3.33), computation of the mean flow is uncoupled from that of the unsteady flow. Hence formally we are concerned with the stability and time evolution of disturbances superposed on a given, presumed known, mean flow unaffected by the unsteady motions. That is the setting for all investigations of combustion instabilities founded on the splitting of small flow variables into sums of mean and fluctuating values. This approach excludes, for example, possible influences of oscillations on the mean pressure in the chamber (often called 'DC shift'), not an unusual occurrence in solid propellant rockets. When they occur, DC shifts of this sort are almost always unacceptable in operational motors; they may or may not be significantly and directly affected by the fluctuations.

In contrast, the set (3.34)–(3.39) is strongly coupled to the fluctuating field. The situation is formally that producing the problem of 'closure' in the theory of turbulent flows (see, for example, Tennekes and Lumley, 1972). We will not explore the matter here, but we note only that the process of time averaging terms on the right-hand sides of the equations introduces functions of the fluctuations that are additional unknowns. Formal analysis then requires that those functions be modeled; perhaps the most familiar example in the theory of turbulence is the introduction of a 'mixing length' as part of the representation of stresses associated with turbulent motions.

Numerical simulations of combustion instabilities do not exhibit the problem of closure if the complete equations are used, avoiding the consequences of the assumption (3.14). Thus, for example, the results obtained by Baum and Levine (1982, 1988) do show time-dependence of the average pressure in examples of instabilities in solid rockets. Another possible cause of that behavior, probably more important in many cases, is nonlinear dependence of the burning rate on the pressure or velocity near the surface of a solid propellant rocket. Within the structure given here, that behavior may arise from time-averaged functions of $p'$, $\mathbf{M}'$, ... contained in the boundary conditions, or from some nonlinear dependence such as $|\mathbf{M}'|$.

We use in these lectures the formulation assuming complete knowledge of the mean flow, given either by suitable modeling or by solution to the governing equations (3.28)–(3.33) or (3.34)–(3.39).

3.3.3. *Systems of Equations for the Fluctuations.* The general equations of motion (3.22)–(3.27) and those for the mean flow written in Section 3.3.1 contain a restriction only on the magnitude of the average Mach number. Such generality blocks progress with the analysis and for many applications is unnecessary. The set of equations (3.22)–(3.27) must be simplified to forms that can be solved to give useful results. Many possibilities exist. We follow here a course that previous experience has shown to be particularly fruitful for investigations of combustor dynamics. The choices of approximations and tactics are usually motivated by eventual applications and the type of analysis used.

First we assume that the mean flow is determined by its own system of equations; that is, we avoid the problem of closure and use the first formulation, equations (3.28)–(3.33), discussed in Section 3.3.1. Consequently, the mean flow is taken to be independent of time and the combinations in square brackets [ ], equations (3.22)–(3.27), vanish identically. Using the definitions of the remaining brackets,

$$\frac{\partial \rho'}{\partial t} + \bar{\rho}\nabla \cdot \mathbf{M}' = -\{[\rho]\}_1 - \{\rho\}_2 + \mathcal{W}' \tag{3.40}$$

$$\bar{\rho}\frac{\partial \mathbf{M}'}{\partial t} + \nabla p' = -\{[\mathbf{M}]\}_1 - \{\mathbf{M}\}_2 - \{\mathbf{M}\}_3 + \boldsymbol{\mathcal{F}}' \tag{3.41}$$

$$\bar{\rho}C_v\frac{\partial T'}{\partial t} + \bar{p}\nabla \cdot \mathbf{M}' = -\{[T]\}_1 - \{T\}_2 - \{T\}_3 + \mathcal{Q}' \tag{3.42}$$

$$\frac{\partial p'}{\partial t} + \gamma \bar{p} \nabla \cdot \mathbf{M}' = -\{[p]\}_1 - \{p\}_2 + \mathcal{P}' \tag{3.43}$$

$$\bar{\rho}\bar{T}\frac{\partial s'}{\partial t} = -\{[s]\}_1 - \{s\}_2 - \{s\}_3 - \{s\}_4 + \mathcal{S}' \tag{3.44}$$

The various brackets are defined in Section A.2 of Appendix A. They are formed to contain terms ordered with respect to both the mean Mach number and the amplitude of the fluctuations:

$$
\begin{aligned}
[\ \ ] &: 1^{st} \text{ order in } \bar{\mathbf{M}}; \ 1^{st} \text{ order in } \mathbf{M}', \ O(\varepsilon) \\
\{\ \ \}_2 &: 0^{th} \text{ order in } \bar{\mathbf{M}}; \ 2^{nd} \text{ order in } \mathbf{M}', \ O(\varepsilon^2) \\
\{\ \ \}_3 &: 0^{th} \text{ order in } \bar{\mathbf{M}}; \ 3^{rd} \text{ order in } \mathbf{M}', \ O(\varepsilon^3) \\
\{\ \ \}_4 &: 0^{th} \text{ order in } \bar{\mathbf{M}}; \ 4^{th} \text{ order in } \mathbf{M}', \ O(\varepsilon^4)
\end{aligned} \tag{3.45}
$$

No terms have been dropped in passage from the set (3.22–(3.27) to the set (3.40)–(3.44), but fluctuations of the sources $\mathcal{W}', \cdots, \mathcal{S}'$ are not now classified into the various types defined by the brackets (3.45).

We have put the equations in the forms (3.40)–(3.44) to emphasize the point of view that we are considering classes of problems closely related to motions in classical acoustics. If the right-hand sides are ignored, (3.40)–(3.44) become the equations for linear acoustics of a uniform non-reacting medium at rest. The perturbations of that limiting class arise from three types of processes:

(i) interactions of the linear acoustic field with the mean flow, represented by the terms contained in the square brackets, $\{[\ \ ]\}$;

(ii) nonlinear interactions between the fluctuations, represented by the curly brackets conveniently referred to as: $\{\ \ \}_2$, second order acoustics; $\{\ \ \}_3$, third order acoustics; and $\{\ \ \}_4$, fourth order acoustics;

(iii) sources associated with combustion processes, represented by the source terms $\mathcal{W}', \boldsymbol{\mathcal{F}}', \mathcal{Q}', \mathcal{P}'$ and $\mathcal{S}'$.

By selectively retaining one or more of these types of perturbations we define a hierarchy of problems of unsteady motions in combustors. We label these classes of problems O, I, II, III, IV according to the orders of terms retained in the right-hand side when the left-hand side comprise only the terms of order $\varepsilon := \mathbf{M}'_r$ defining clssical linear acoustics.

O. **Classical Acoustics**, $(\mu = 0, \varepsilon \to 0)$

Perturbations to first order in $\varepsilon$ are retained in (3.40)–(3.44):

$$
\begin{aligned}
\frac{\partial \rho'}{\partial t} + \bar{\rho}\nabla \cdot \mathbf{M}' &= \mathcal{W}' \\
\bar{\rho}\frac{\partial \mathbf{M}'}{\partial t} + \nabla p' &= \boldsymbol{\mathcal{F}}' \\
\bar{\rho}C_v\frac{\partial T'}{\partial t} + \bar{p}\nabla \cdot \mathbf{M}' &= \mathcal{Q}' \\
\frac{\partial p'}{\partial t} + \gamma\bar{p}\nabla \cdot \mathbf{M}' &= \mathcal{P}' \\
\bar{\rho}\bar{T}\frac{\partial s'}{\partial t} &= \mathcal{S}'
\end{aligned} \tag{3.46} \text{ a-e}
$$

I. **Linear Stability**, $O(\varepsilon, \mu\varepsilon)$

Retain interactions linear in the average Mach number and in the fluctuations:

$$\frac{\partial \rho'}{\partial t} + \bar{\rho}\nabla \cdot \mathbf{M}' = -\{[\rho]\}_1 + \mathcal{W}'$$

$$\bar{\rho}\frac{\partial \mathbf{M}'}{\partial t} + \nabla p' = -\{[\mathbf{M}]\}_1 + \boldsymbol{\mathcal{F}}'$$

$$\bar{\rho}C_v\frac{\partial T'}{\partial t} + \bar{p}\nabla \cdot \mathbf{M}' = -\{[T]\}_1 + \mathcal{Q}' \qquad \text{(3.47) a-e}$$

$$\frac{\partial p'}{\partial t} + \gamma\bar{p}\nabla \cdot \mathbf{M}' = -\{[p]\}_1 + \mathcal{P}'$$

$$\bar{\rho}\bar{T}\frac{\partial s'}{\partial t} = -\{[s]\}_1 + \mathcal{S}'$$

II. **Second Order Acoustics**, $O(\varepsilon, \mu\varepsilon, \varepsilon^2)$

Retain the linear interactions and the nonlinear second order acoustics:

$$\frac{\partial \rho'}{\partial t} + \bar{\rho}\nabla \cdot \mathbf{M}' = -[\{[\rho]\}_1 + \{\rho\}_2] + \mathcal{W}'$$

$$\bar{\rho}\frac{\partial \mathbf{M}'}{\partial t} + \nabla p' = -[\{[\mathbf{M}]\}_1 + \{\mathbf{M}\}_2] + \boldsymbol{\mathcal{F}}'$$

$$\bar{\rho}C_v\frac{\partial T'}{\partial t} + \bar{p}\nabla \cdot \mathbf{M}' = -[\{[T]\}_1 + \{T\}_2] + \mathcal{Q}' \qquad \text{(3.48) a-e}$$

$$\frac{\partial p'}{\partial t} + \gamma\bar{p}\nabla \cdot \mathbf{M}' = -[\{[p]\}_1 + \{p\}_2] + \mathcal{P}'$$

$$\bar{\rho}\bar{T}\frac{\partial s'}{\partial t} = -[\{[s]\}_1 + \{s\}_2] + \mathcal{S}'$$

III. **Third Order Acoustics**, $O(\varepsilon, \mu\varepsilon, \varepsilon^2, \varepsilon^3)$

Retain the linear interactions and the nonlinear acoustics up to third order:

$$\frac{\partial \rho'}{\partial t} + \bar{\rho}\nabla \cdot \mathbf{M}' = -[\{[\rho]\}_1 + \{\rho\}_2] + \mathcal{W}'$$

$$\bar{\rho}\frac{\partial \mathbf{M}'}{\partial t} + \nabla p' = -[\{[\mathbf{M}]\}_1 + \{\mathbf{M}\}_2 + \{\mathbf{M}\}_3] + \boldsymbol{\mathcal{F}}'$$

$$\bar{\rho}C_v\frac{\partial T'}{\partial t} + \bar{p}\nabla \cdot \mathbf{M}' = -[\{[T]\}_1 + \{T\}_2 + \{T\}_3] + \mathcal{Q}' \qquad \text{(3.49) a-e}$$

$$\frac{\partial p'}{\partial t} + \gamma\bar{p}\nabla \cdot \mathbf{M}' = -[\{[p]\}_1 + \{p\}_2] + \mathcal{P}'$$

$$\bar{\rho}\bar{T}\frac{\partial s'}{\partial t} = -[\{[s]\}_1 + \{s\}_2 + \{s\}_3] + \mathcal{S}'$$

Four other classes of problems possible to define in this context will not be considered here since no results have been reported: second order acoustics with mean flow interactions; fourth order acoustics; and third and fourth order acoustics with nonlinear acoustics/mean flow interactions.

In problems I–III, the source terms $\mathcal{W}', \cdots$ must be expanded to order consistent with the orders of the fluid-mechanical perturbations retained.

**3.4. Nonlinear Wave Equations for the Pressure Field.** Practically all of the subsequent material in this book will be either directly concerned with pressure waves, or with interpretations of behavior related pressure waves. The presence of unsteady vorticity causes important revisions of such a restricted point of view, as we have already mentioned in Section 3.1, but the basic ideas remain in any event. Hence the wave equation

for pressure fluctuations occupies a meaningful position in all five classes of problems defined in the preceding section. Its formation follows the same procedure used in classical acoustics.

Define $\mathbf{\mathcal{M}}$ and $\mathcal{R}$ to contain all possible terms arising in the sets of equations constructed for the problems O–III:

$$\bar{\rho}\frac{\partial \mathbf{M}'}{\partial t} + \nabla p' = -\mathbf{\mathcal{M}} + \boldsymbol{\mathcal{F}'} \tag{3.50}$$

$$\frac{\partial p'}{\partial t} + \gamma \bar{p}\nabla \cdot \mathbf{M}' = -\mathcal{R} + \mathcal{P}' \tag{3.51}$$

where

$$\mathbf{\mathcal{M}} = \{[\mathbf{M}]\}_1 + \{\mathbf{M}\}_2 + +\{\mathbf{M}\}_3 \tag{3.52}$$

$$\mathcal{R} = \{[p]\}_1 + \{p\}_2 \tag{3.53}$$

Differentiate 3.50 with respect to time and substitute 3.50 for $\partial \mathbf{M}'/\partial t$:

$$\frac{\partial^2 p'}{\partial t^2} - \gamma \bar{p}\nabla \cdot \left[ -\frac{1}{\bar{\rho}}\nabla p' - \frac{1}{\bar{\rho}}\left(\mathbf{\mathcal{M}} - \boldsymbol{\mathcal{F}'}\right)\right] = -\frac{\partial \mathcal{R}}{\partial t} + \frac{\partial \mathcal{P}'}{\partial t}$$

Rearrange the equation to find

$$\nabla^2 p' - \frac{1}{\bar{a}^2}\frac{\partial^2 p'}{\partial t^2} = h \tag{3.54}$$

with

$$h = -\bar{\rho}\nabla \cdot \left[\frac{1}{\bar{\rho}}\left(\mathbf{\mathcal{M}} - \boldsymbol{\mathcal{F}'}\right)\right] + \frac{1}{\bar{a}^2}\frac{\partial}{\partial t}(\mathcal{R} - \mathcal{P}') + \frac{1}{\bar{\rho}}\nabla\bar{\rho}\cdot\nabla p' \tag{3.55}$$

The boundary condition for the pressure field is found by taking the scalar product of the outward normal, at the chamber boundary, with:

$$\hat{\mathbf{n}}\cdot\nabla p' = -f \tag{3.56}$$

$$f = -\bar{\rho}\frac{\partial \mathbf{M}'}{\partial t}\cdot\hat{\mathbf{n}} + \left(\mathbf{\mathcal{M}} - \boldsymbol{\mathcal{F}'}\right)\cdot\hat{\mathbf{n}} \tag{3.57}$$

Replacing $\mathbf{\mathcal{M}}$ and $\mathcal{R}$ by their definitions (3.52), we have the formulation based on the inhomogeneous nonlinear wave equation and its boundary condition:

$$\nabla^2 p' - \frac{1}{\bar{a}^2}\frac{\partial^2 p'}{\partial t^2} = h$$
$$\hat{\mathbf{n}}\cdot\nabla p' = -f \tag{3.57 a,b}$$

with

$$\begin{aligned} h = &-\left[\bar{\rho}\nabla\cdot\frac{1}{\bar{\rho}}\{[\mathbf{M}]\}_1 - \frac{1}{\bar{a}^2}\frac{\partial\{[p]\}_1}{\partial t}\right] - \left\{\bar{\rho}\nabla\cdot\frac{1}{\bar{\rho}}\{\mathbf{M}\}_2 - \frac{1}{\bar{a}^2}\frac{\partial\{p\}_2}{\partial t}\right\} - \bar{\rho}\nabla\cdot\frac{1}{\bar{\rho}}\{\mathbf{M}\}_3 \\ &+ \frac{1}{\bar{\rho}}\nabla\bar{\rho}\cdot\nabla p' + \bar{\rho}\nabla\cdot\frac{1}{\bar{\rho}}\boldsymbol{\mathcal{F}'} - \frac{1}{\bar{a}^2}\frac{\partial\mathcal{P}'}{\partial t} \end{aligned} \tag{3.58}$$

$$f = \bar{\rho}\frac{\partial \mathbf{M}'}{\partial t}\cdot\hat{\mathbf{n}} + \hat{\mathbf{n}}\cdot\left[\{[\mathbf{M}]\}_1 + \{\mathbf{M}\}_2 + \{\mathbf{M}\}_3\right] - \boldsymbol{\mathcal{F}'}\cdot\hat{\mathbf{n}} \tag{3.59}$$

With this formulation, the wave equations and boundary conditions for the classes of problems defined in Section 3.3 are distinguished by the following functions $h$ and $f$:

O. **Classical Acoustics**

$$h_O = \bar{\rho} \nabla \cdot \frac{1}{\bar{\rho}} \boldsymbol{\mathcal{F}}' - \frac{1}{\bar{a}^2} \frac{\partial \mathcal{P}'}{\partial t}$$

$$f_O = \bar{\rho} \frac{\partial \mathbf{M}'}{\partial \mathbf{t}} \cdot \hat{\mathbf{n}} - \boldsymbol{\mathcal{F}}' \cdot \hat{\mathbf{n}}$$

(3.60) a,b

I. **Linear Stability**

$$h_I = -\left[ \bar{\rho} \nabla \cdot \frac{1}{\bar{\rho}} \{[\mathbf{M}]\}_1 - \frac{1}{\bar{a}^2} \frac{\partial \{[p]\}_1}{\partial t} \right] + \frac{1}{\bar{\rho}} \nabla \bar{\rho} \cdot \nabla p' + \bar{\rho} \nabla \cdot \frac{1}{\bar{\rho}} \boldsymbol{\mathcal{F}}' - \frac{1}{\bar{a}^2} \frac{\partial \mathcal{P}'}{\partial t}$$

$$f_I = \bar{\rho} \frac{\partial \mathbf{M}'}{\partial t} \cdot \hat{\mathbf{n}} + \hat{\mathbf{n}} \cdot \{[\mathbf{M}]\}_1 - \boldsymbol{\mathcal{F}}' \cdot \hat{\mathbf{n}}$$

(3.61) a,b

Allowing $\boldsymbol{\mathcal{F}}'$ and $\mathcal{P}'$ to be non-zero gives the opportunity for representing sources of mass, momentum, and energy both within the volume and at the boundary. The first term in $f_0$ accounts for motion of the boundary.

II. **Second Order Acoustics**

$$h_{II} = -\left[ \bar{\rho} \nabla \cdot \frac{1}{\bar{\rho}} \{[\mathbf{M}]\}_1 - \frac{1}{\bar{a}^2} \frac{\partial \{[p]\}_1}{\partial t} \right] - \left\{ \bar{\rho} \nabla \cdot \frac{1}{\bar{\rho}} \{\mathbf{M}\}_2 - \frac{1}{\bar{a}^2} \frac{\partial \{p\}}{\partial t} \right\}$$
$$+ \frac{1}{\bar{\rho}} \nabla \rho' \cdot \nabla p' + \bar{\rho} \nabla \cdot \frac{1}{\bar{\rho}} \boldsymbol{\mathcal{F}}' - \frac{1}{\bar{a}^2} \frac{\partial \mathcal{P}'}{\partial t}$$

$$f_{II} = \bar{\rho} \frac{\partial \mathbf{M}'}{\partial t} \cdot \hat{\mathbf{n}} + \hat{\mathbf{n}} \cdot [\{[\mathbf{M}]\}_1 + \{\mathbf{M}\}_2] - \boldsymbol{\mathcal{F}}' \cdot \hat{\mathbf{n}}$$

(3.62) a,b

III. **Third Order Acoustics**

$$h_{III} = -\left[ \bar{\rho} \nabla \cdot \frac{1}{\bar{\rho}} \{[\mathbf{M}]\}_1 - \frac{1}{\bar{a}^2} \frac{\partial \{[p]\}_1}{\partial t} \right] - \left\{ \bar{\rho} \nabla \cdot \frac{1}{\bar{\rho}} \{\mathbf{M}\}_2 - \frac{1}{\bar{a}^2} \frac{\partial \{p\}_2}{\partial t} \right\}$$
$$- \bar{\rho} \nabla \cdot \frac{1}{\bar{\rho}} \{\mathbf{M}\}_3 + \frac{1}{\bar{\rho}} \nabla \bar{\rho} \cdot \nabla p' + \bar{\rho} \nabla \cdot \frac{1}{\bar{\rho}} \boldsymbol{\mathcal{F}}' - \frac{1}{\bar{a}^2} \frac{\partial \mathcal{P}'}{\partial t}$$

$$f_{III} = \bar{\rho} \frac{\partial \mathbf{M}'}{\partial t} \cdot \hat{\mathbf{n}} + \hat{\mathbf{n}} \cdot [\{[\mathbf{M}]\}_1 + \{\mathbf{M}\}_2 + \{\mathbf{M}\}_3] - \boldsymbol{\mathcal{F}}' \cdot \hat{\mathbf{n}}$$

(3.63) a,b

With these definitions of the functions $h$ and $f$, the definitions of the four classes of problems considered here are complete, forming the basis for the analysis worked out in the remainder of these lectures. Only problems within classical acoustics can be solved easily. All others require approximations, both in modeling physical processes and in the method of solution. Modeling will be discussed in the contexts of specific applications; a few remarks help clarify the approximate method of solution described in the following section.

**Remarks:**

i) The classes of problems I–III defined here are described by inhomogeneous equations that even for linear stability cannot be generally solved in closed form. The chief obstacles to solution arise because the functions $h$ and $f$ contain not only the unknown pressure but also the velocity and temperature. For given functions $\boldsymbol{\mathcal{F}}'$ and $\mathcal{P}'$, numerical solutions could be obtained for a specified combustor and mean flow field. The results would apply only to the special case considered. To obtain some understanding of general behavior it would be necessary to consider many special cases, a tedious and expensive procedure.

ii) Therefore, we choose to work out an approximate method of solution applicable to all classes of problems. Numerical solutions, or 'simulations' then serve the important purpose of assessing the validity and accuracy of the approximate results.

iii) The approximate method of solution is based first on spatial averaging, followed by an iteration procedure involving extension of the expansion in two small parameters defined in this section. This method has been most widely used and confirmed in applications to combustion instabilities in solid propellant rockets, but it can be applied to problems arising in any type of combustor.

iv) Instabilities in solid rockets have been particularly helpful in developing the general theory for at least three reasons: 1) the mean flow field, nonuniform and generated by mass addition at the boundary, requires careful attention to processes associated with interactions between the mean flow and unsteady motions; 2) more experimental results for transient behavior have been obtained for solid rockets than for any other combustion system; and 3) although still far from being satisfactorily understood, the dynamics of burning solid propellants is better known than for any other combustion system.

v) The fluctuations of the source terms, $\mathcal{W}'$, $\mathcal{F}'$, ... $\mathcal{S}'$ will be made explicit as required in particular applications.

## 4. MODAL EXPANSION AND SPATIAL AVERAGING; AN ITERATIVE METHOD OF SOLUTION

From the point of view represented in Figure 1.1, we are concerned in this section with representing the combustor dynamics. The procedure, often called 'modeling' is based on the equations of motion constructed in the preceding section and hence in principle will contain all relevant physical processes[11]. For the purposes here, all modeling of combustor dynamics and of combustion dynamics—the mechanisms and feedback in Figure 1.1—must be done in the context developed in Section 1. Thus we always have in mind the idea of wave motions somehow generated and sustained by interactions between the motions themselves and combustion processes, the latter also including certain aspects of the mean flow within the combustor.

The simplest model of the combustion dynamics is a single wave, a classical acoustic resonance as in an organ pipe, but decaying or growing due to the other processes in the chamber. In practice, the combustion processes and nonlinear gasdynamical effects inevitably lead to the presence of more than one acoustic mode. We need a relatively simple yet accurate means of treating those phenomena for problems of the sort arising in the laboratory and in practice. Modeling in this case begins with construction of a suitable method for solving the nonlinear wave equations derived in Section 3.4. In this context we may regard the analysis of the Rijke tube covered in Section 2 as a basic example of the procedure stripped of the formalism covered in this section.

The chief purpose of the analysis constructed here is, to devise methods capable of producing results useful for prediction and interpretation of unsteady motions in full-scale combustion chambers as well as for laboratory devices. That intention places serious demands on the methods used for at least two reasons:

1. processes that must be modeled are usually complicated and their theoretical representations are necessarily approximate to extents which themselves are difficult to assess; and
2. almost all input data required for quantitative evaluation of theoretical results are characterized by large uncertainties.

In this situation it seems that for practical and, as it will turn out, for theoretical purposes as well, the most useful methods will be based on some sort of spatial averaging. Direct solution of the partial differential equations, even for linear problems, is practically a hopeless task except for very special cases for simple geometries. Direct numerical simulations (DNS) or numerical solutions to the partial differential equations are not yet a real alternative for practical purposes at this time, and are usually less attractive for obtaining basic understanding. However, as we will see later, numerical solutions offer the only means for assessing the validity of approximate solutions and always can treat more complicated (realistic?) problems than we can reasonably handle with the analytical methods discussed here. In any event, one should view theory and analysis on the one hand, and numerical simulations on the other, as complementary activities.

The material on analysis and theory of combustion instabilities treated in these two lectures is based on a method of spatial averaging. The essential idea is of course not new, the method being nearly identical with similar methods used in other branches of continuum mechanics. There are a few special characteristics associated with applications to combustor that will appear in the course of the following discussion.

**4.1. Application of a Green's Function for Steady Waves.** The method used later to analyze nonlinear behavior has its origins in an early analysis of linear combustion instabilities in liquid rocket engines (Culick, 1961, 1963). That work was based on solution to problems of steady waves by introducing a Green's function. It is an effective strategy for this application because departures from a known soluble problem are small, due either to perturbations within the volume or at the boundary, all of order $\mu$ in the context developed in Section 3.

---

[11]That seems to be what some people (notably electrical engineers it seems) mean by the term 'physics-based modeling.' What would otherwise be the basis for acceptable modeling of a physical system has not been explained.

The problem to be solved is defined by equation (3.54) and its boundary conditions (3.56) derived in Section 3.4,

$$\nabla^2 p' - \frac{1}{\bar{a}^2}\frac{\partial^2 p'}{\partial t^2} = h$$
$$\hat{\mathbf{n}} \cdot \nabla p' = -f$$
(4.1) a,b

with $h$ and $f$ given by (3.61) a,b for linear stability. Because $h$ and $f$ are linear, various methods are available to build general solutions by applying the principle of superposition to elementary solutions representing steady waves. Hence we assume that the fluctuating pressure field is a steady wave system within the given chamber, having unknown spatial structure and varying harmonically in time:

$$p' = \hat{p}e^{i\bar{a}kt}$$
(4.2)

where $k$ is the complex wavenumber, also initially unknown,

$$k = \frac{1}{\bar{a}}(\omega - i\alpha)$$
(4.3)

As defined here, $\alpha$ positive means that the wave has growing amplitude, $p' \sim e^{\alpha t}$. Of course the wave is not strictly stationary, a condition existing only if $\alpha = 0$, certainly true when $h = f = 0$, as in classical acoustics.

Even when $h, f$ are non-zero, it is still possible that $\alpha = 0$, now defining a state of *neutral stability*. In general one must expect $\alpha \neq 0$; it is a basic assumption in all of the analysis covered in this book that $\alpha$ is small compared with $\omega$, so the waves are slowly growing or decaying—they are 'almost' stationary, and their spatial structure does not change much in time. However, the results obtained are quite robust and seem often to be usable even when $\alpha/\omega$ is not small.

The problem here is to determine the spatial distribution $\hat{p}$ and the complex wavenumber $k$. For steady waves we can write

$$h = \kappa\hat{h}e^{i\bar{a}kt} \ ; \ f = \kappa\hat{f}e^{i\bar{a}kt}$$

where again $\kappa$ is a small parameter[12] characterizing the smallness of $h$ and $f$. Substitution in (4.1) a,b and dropping the common exponential time factor gives

$$\nabla^2\hat{p} + k^2\hat{p} = \kappa\hat{h}$$
$$\hat{\mathbf{n}} \cdot \nabla\hat{p} = -\kappa\hat{f}$$
(4.4) a,b

This is of course a well-known classical problem thoroughly discussed in many books. Many methods of solution are available for the linear problem. We use here a procedure based on introducing a Green's function discussed, for example, by Morse and Feshbach (1952, Chapter 10). This is an attractive method for several reasons, including:

1. Conversion from a differential equation, and the iterative method of solution this suggests, is an effective means for minimizing the consequences of the uncertainties inherent in problems of combustor dynamics;

2. Explicit results can be obtained for real and imaginary parts of the complex wavenumber in forms that are easily interpreted and remarkably convenient both for theoretical work and for applications;

3. The method has motivated a straightforward extension to nonlinear problems, with considerable success.

Define a Green's function satisfying the homogeneous boundary and the wave equation homogeneous except at the single point where a source is located having zero spatial extent and infinite strength such that is integral over space is finite. Thus the source is represented by a delta function $-\delta(\mathbf{r} - \mathbf{r}_0)$ and $G$ is determined as a solution to the problem

$$\nabla^2 G(\mathbf{r}|\mathbf{r}_0) + k^2 G(\mathbf{r}|\mathbf{r}_0) = \delta(\mathbf{r} - \mathbf{r}_0)$$
$$\hat{\mathbf{n}} \cdot \nabla G(\mathbf{r}|\mathbf{r}_0) = 0$$
(4.5) a,b

---

[12]Later, $\kappa$ will be identified with $\mu$ introduced in Section 3.3 but it is useful in this discussion to maintain a distinction.

The notation $\mathbf{r}|\mathbf{r}_0$ as the argument of $G(\mathbf{r}|\mathbf{r}_0)$ represents the interpretation of the Green's function as the wave observed at point $\mathbf{r}$ due to a steady oscillatory point source at $\mathbf{r}_0$.

Multiply ((4.4) a,b)a by $G(\mathbf{r}|\mathbf{r}_0)$, ((4.5) a,b)a by $\hat{p}(\mathbf{r})$, subtract the results and integrate over volume (in the present case the volume of the chamber) to find

$$\iiint_V \left[ G(\mathbf{r}|\mathbf{r}_0)\nabla^2 \hat{p}(\mathbf{r}) - \hat{p}(\mathbf{r})\nabla^2 G(\mathbf{r}|\mathbf{r}_0) \right] dV + k^2 \iiint_V \left[ G(\mathbf{r}|\mathbf{r}_0)\hat{p}(\mathbf{r}) - \hat{p}(\mathbf{r})G(\mathbf{r}|\mathbf{r}_0) \right] dV$$
$$= \kappa \iiint_V G(\mathbf{r}|\mathbf{r}_0)\hat{h}(\mathbf{r}) - \iiint \hat{p}(\mathbf{r})\delta(\mathbf{r}-\mathbf{r}_0)dV \tag{4.6}$$

Because $G(\mathbf{r}|\mathbf{r}_0)$ and $\hat{p}(\mathbf{r})$ are scalar functions the second integral on the right-hand side vanishes. The first integral is rewritten using a form of Green's theorem, and the basic property of the delta function is applied to the second integral on the right-hand side:

$$\iiint_V F(\mathbf{r})\delta(\mathbf{r}-\mathbf{r}_0)dV = F(\mathbf{r}) \qquad (\mathbf{r}_1, \mathbf{r}_0 \text{ in } V) \tag{4.7}$$

Hence (4.6) becomes

$$\oiint_S \left[ G(\mathbf{r}|\mathbf{r}_0)\nabla\hat{p}(\mathbf{r}) - p(\mathbf{r})\nabla G(\mathbf{r}|\mathbf{r}_0) \right] \cdot \hat{\mathbf{n}}dS = \kappa \iiint_V G(\mathbf{r}|\mathbf{r}_0)\hat{h}(\mathbf{r})dV - \hat{p}(\mathbf{r}_0)$$

where $\hat{\mathbf{n}}$ is the outward normal at the surface of the volume $V$ in question.

Now apply the boundary conditions (4.4) a,b and (4.5) a,b and the last equation can be written in the form

$$\mathbf{p}(\hat{r}_0) = \kappa \left\{ \oiint_V G(\mathbf{r}|\mathbf{r}_0)\hat{h}(\mathbf{r})dV + \iint_S G(\mathbf{r_s}|\mathbf{r}_0)\hat{f}(\mathbf{r}_s)dS \right\} \tag{4.8}$$

Subscript $(\ )_s$ means the point $\mathbf{r}_s$ lies on the boundary surface (actually on the inside surface of the boundary). Because the operator for scalar waves is *self-adjoint* (see Morse and Feshbach 1952, Chapter 10), the Green's function possesses the property of symmetry

$$G(\mathbf{r}|\mathbf{r}_0) = G(\mathbf{r}_0|\mathbf{r}) \tag{4.9}$$

This property has the appealing physical interpretation that the wave observed at $\mathbf{r}$ due to a point source at $\mathbf{r}_0$ has the same amplitude and relative phase as for the wave observed at $\mathbf{r}_0$ when a point source is located at $\mathbf{r}$. With (4.9) we can interchange $\mathbf{r}$ and $\mathbf{r}_0$ in (4.8) to find for the steady field at position $\mathbf{r}$:

$$\hat{p}(\mathbf{r}) = \kappa \left\{ \iiint_V G(\mathbf{r}|\mathbf{r}_0)\hat{h}(\mathbf{r}_0)d\mathbf{V}_0 + \oiint_S G(\mathbf{r}|\mathbf{r}_{0s})\hat{f}(\mathbf{r}_{0s})dS \right\} \tag{4.10}$$

Equation (4.10) is not an explicit solution for the pressure field due to the source functions $\hat{h}$ and $\hat{f}$, but is rather, an integral equation because $\hat{h}$ and $\hat{f}$ in general depend on the fluctuating pressure and velocity fields themselves. However, because the sources are assumed to be small perturbations of the classical field having no sources, $\kappa$ is small and $\hat{p}$ will not differ greatly from a solution to the homogeneous problem defined by $h = f = 0$. The result (4.10) represents the solution to the inhomogeneous problem; the complete solution is (4.10) plus a homogeneous solution. Advantage will be taken of the smallness of $\kappa$ to find an approximate explicit solution for $\hat{p}$ by an iterative procedure discussed in Section 4.1.1.

Whatever tactic one may choose to follow, the result (4.10) is of no practical value without having a representation of $G(\mathbf{r}|\mathbf{r}_0)$. The most convenient form of $G(\mathbf{r}|\mathbf{r}_0)$ for our purpose is expansion in eigenfunctions $\psi_n(\mathbf{r})$, here the normal modes of the classical acoustics problem with no sources in the volume and homogeneous boundary conditions: $G(\mathbf{r}|\mathbf{r}_0)$ is therefore expressed as a *modal expansion*,

$$G(\mathbf{r}|\mathbf{r}_0) = \sum_{n=0}^{\infty} A_n \psi_n(\mathbf{r}) \tag{4.11}$$

where the $\psi_n$ satisfy

$$\nabla^2 \psi_n + k_n^2 \psi_n = 0$$
$$\hat{\mathbf{n}} \cdot \nabla \psi_n = 0$$

$$(4.12) \text{ a,b}$$

and the $\psi_n$ are orthogonal functions,

$$\iiint_V \psi_m(\mathbf{r})\psi_n(\mathbf{r})dV = E_n^2 \delta_{mn} \tag{4.13}$$

Substitute (4.11) in ((4.5) a,b)a, multiply by $\psi_m(\mathbf{r})$ and integrate over the volume to find

$$\iiint_V \psi_m \sum_{n=0}^{\infty} A_n \nabla^2 \psi_n dV + k^2 \iiint_V \psi_m \sum_{n=0}^{\infty} A_n \psi_n dV = \int \psi_m(\mathbf{r})\delta(\mathbf{r} - \mathbf{r}_0)dV$$

With (4.7), ((4.12) a,b) and (4.13), this equation produces the formula for $A_n$:

$$A_n = \frac{\psi_n(\mathbf{r}_0)}{k_n^2 - k^2} \tag{4.14}$$

Thus the expansion (4.11) for $G(\mathbf{r}|\mathbf{r}_0)$ is

$$G(\mathbf{r}|\mathbf{r}_0) = \sum_{n=0}^{\infty} \frac{\psi_n(\mathbf{r})\psi_n(\mathbf{r}_0)}{E_n^2(k^2 - k_n^2)} \tag{4.15}$$

the modal expansion of the Green's function. Substitution of (4.15) in (4.10) leads to the formal modal expansion of the pressure field,

$$\hat{p}(\mathbf{r}) = \kappa \sum_{n=0}^{\infty} \frac{\psi_n(\mathbf{r})}{E_n^2(k^2 - k_n^2)} \left\{ \iiint_V \psi_n(\mathbf{r}_0)\hat{h}(\mathbf{r}_0)dV_0 + \oiint_S \psi_n(\mathbf{r}_{0s})\hat{f}(\mathbf{r}_{0s})dS_0 \right\} \tag{4.16}$$

Suppose that for $\kappa$ tending to zero, $\hat{p}(\mathbf{r})$ approaches the unperturbed mode shape $\psi_N$; let the corresponding function $\hat{p}$ be denoted $\hat{p}_N$, so

$$\hat{p} \xrightarrow[\kappa \to 0]{} \hat{p}_N = \psi_N \tag{4.17}$$

Now separate the $N^{th}$ term from the sum in (4.16) and write

$$\hat{p}(\mathbf{r}) = \psi_N(\mathbf{r})\frac{\kappa}{E_N^2(k^2 - k_N^2)} \left\{ \iiint_V \psi_N(\mathbf{r}_0)\hat{h}(\mathbf{r}_0)dV_0 + \oiint_S \psi_N(\mathbf{r}_{0s})\hat{f}(\mathbf{r}_{0s})dS_0 \right\}$$

$$+ \kappa \sum_{n=0}^{\infty}{}' \frac{\psi_n(\mathbf{r})}{E_n^2(k^2 - k_n^2)} \left\{ \iiint_V \psi_n(\mathbf{r}_0)\hat{h}(\mathbf{r}_0)dV_0 + \oiint_S \psi_n(\mathbf{r}_{0s})\hat{f}(\mathbf{r}_{0s})dS_0 \right\} \tag{4.18}$$

where the prime in the summation sign means that the term $n = N$ is missing. This form is consistent with the requirement (4.17) only if the factor multiplying $\psi_N(\mathbf{r})$ is unity, giving the formula for the perturbed wavenumber

$$k^2 = k_N^2 + \frac{\kappa}{E_N^2} \left\{ \iiint_V \psi_N(\mathbf{r}_0)\hat{h}(\mathbf{r}_0)dV_0 + \oiint_S \psi_N(\mathbf{r}_{0s})\hat{f}(\mathbf{r}_{0s})dS_0 \right\} \tag{4.19}$$

and (4.18) becomes

$$\hat{p}(\mathbf{r}) = \psi_N(\mathbf{r}) + \kappa \sum_{n=0}^{\infty}{}' \frac{\psi_n(\mathbf{r})}{E_n^2(k^2 - k_n^2)} \left\{ \iiint_V \psi_n(\mathbf{r}_0)\hat{h}(\mathbf{r}_0)dV_0 + \oiint_S \psi_n(\mathbf{r}_{0s})\hat{f}(\mathbf{r}_{0s})dS_0 \right\} \tag{4.20}$$

Another more direct derivation of (4.19) very useful in later analysis, may be had by first multiplying ((4.4) a,b)a by $\psi_N$ and integrating over the volume:

$$\iiint_V \psi_N \nabla^2 \hat{p} dV + k^2 \iiint_V \psi_N \hat{p} dV = \kappa \iiint_V \psi_N \hat{h} dV$$

Application of Green's theorem to the first integral gives

$$\iiint_V \hat{p}\nabla^2\psi_N dV + \oiint_S [\psi_n\nabla\hat{p} - \hat{p}\nabla\psi_n]\cdot\hat{\mathbf{n}}dS + k^2\iiint_V \psi_n\hat{p}dV = \oiint_S \psi_N\hat{h}dV$$

after inserting $\nabla^2\psi_N = -k_N^2\psi_N$ and $\nabla\psi_N\cdot\hat{\mathbf{n}} = 0$, rearrangement gives

$$k^2 = k_N^2 + \frac{\kappa}{\iiint_V \psi_N\hat{p}dV}\left\{\iiint_V \psi_N(\mathbf{r})\hat{h}(\mathbf{r})dV + \oiint_S \psi_N(\mathbf{r}_s)\hat{f}(\mathbf{r}_s)dS\right\} \tag{4.21}$$

The integral of $\psi_N\hat{p}$ in the denominator of (4.21) can be evaluated by using (4.20) and is exactly $E_n^2$, providing the series in (4.20) converges. Hence (4.21) is identical to (4.19). This simple calculation has shown that (4.19) and (4.20) are consistent.

The preceding calculation contains several basic ideas behind much of the analysis used in these lectures. In summary, the original problem described by the differential equation ((4.4) a,b)a and its boundary condition ((4.4) a,b)b are converted to an integral equation, in this case (4.10), established by introducing a Green's function. This is not an explicit solution because the functions $h$ and $f$ generally depend on the dependent variable $\hat{p}$. However, formulation as an integral equation forms a convenient basis for approximate solution by iteration.

4.1.1. *Approximate Solution by Iteration.* To apply an iterative procedure, it is necessary first to give the Green's function $G(\mathbf{r}|\mathbf{r}_0)$ explicit form. The natural choice for problems of waves in a chamber is a series expansion in the natural modes of the chamber, a modal expansion, (4.15). For the small parameter $\kappa$ tending to zero (i.e. all perturbations of the classical acoustics problem are small), a straightforward argument produces the formula (4.19) for the wavenumber and the integral equation (4.20) for $\hat{p}(\mathbf{r})$.

Equation (4.20) must be solved to give $\hat{p}$ before the wavenumber can be computed with (4.19). We should emphasize that for many practical purposes, it is really $k$ that is required, because its imaginary part determines the linear stability of the system ($\alpha = 0$). The great advantage of this approach may be seen clearly with a simple example. Suppose $\hat{f} = 0$ and $\hat{h} = K(1 + \hat{p})$ in (4.4) a,b. Then (4.20) and (4.19) become

$$\hat{p}(\mathbf{r}) = \psi_N(\mathbf{r}) + \kappa K\sum_{n=0}^\infty{}' \frac{\psi_n(\mathbf{r})}{E_n^2(k^2-k_n^2)}\iiint_V \psi_n(\mathbf{r}_0)(1+\hat{p})dV_0 \tag{4.22}$$

$$k^2 = k_N^2 + \frac{\kappa K}{E_N^2}\iiint_V \psi_N(1+\hat{p})dV_0 \tag{4.23}$$

Because $\kappa$ is assumed to be small, solution by successive approximation, i.e. an iterative procedure, is a logical way to proceed. The initial (zeroth) approximation to the mode shape $\hat{p}$ is (4.22) for $\kappa = 0$, $\hat{p}^{(0)} = \psi_N$. Substitution in (4.23) gives $k^2$ correct to first order in $\kappa$:

$$\begin{aligned}(k^2)^{(1)} &= k_N^2 + \frac{\kappa K}{E_N^2}\iiint_V \psi_N(1+\psi_N)dV_0 \\ &= k_N^2 + \kappa\frac{KI_N}{E_N^2}\end{aligned} \tag{4.24}$$

where $I_N$ stands for the integral.

Calculation of $\hat{p}$ to first order in $\kappa$ requires setting $\hat{p}$ and $k^2$ to their *zeroth* order values on the right-hand side of (4.22), $\hat{p}^{(0)} = \psi_N$, $(k^2)^{(0)} = k_N^2$:

$$\begin{aligned}\hat{p}^{(1)}(\mathbf{r}) &= \psi_N(\mathbf{r}) + \kappa K\sum_{n=0}^\infty{}' \frac{\psi_n(\mathbf{r})}{E_n^2(k_N^2-k_n^2)}\iiint_V \psi_n(\mathbf{r}_0)(1+\psi_N(\mathbf{r}_0))dV_0 \\ &= \psi_N + \kappa\sigma_N\end{aligned}$$

Substitution of this formula for $\hat{p}$ under the integral in (4.23) then gives the second approximation $(k^2)^{(2)}$ to $k^2$:

$$
(k^2)^{(2)} = k_N^2 + \frac{\kappa K}{E_N^2} \iiint\limits_V \psi_N (1 + \psi_N + \kappa \sigma_N) dV_0
$$

$$
= (k^2)^{(1)} + \kappa^2 \frac{K}{E_N^2} \iiint\limits_V \psi_N \sigma_N dV_0
$$

(4.25)

A wonderful property of the procedure is already apparent: Calculation of the wavenumber to some order $l$ in the small parameter requires knowing the modal functions only to order $l-1$. That is the basis for the current standard practice of computing linear stability for solid propellant rockets (the Standard Stability Prediction Program, Nickerson *et al.* 1983) using the unperturbed acoustic modes computed for the geometry in question.

The "perturbation-iteration" procedure just described is an old and widely used method to obtain solutions to nonlinear as well as linear problems. Often much attention is paid to achieving more accurate solutions by carrying the iterations to higher order in the small parameter. That is a legitimate process providing the equations themselves are valid to the order sought. In Section 3 we emphasized the importance of the expansion procedure largely for that reason. If the equations are valid, say, only to second order in the amplitude ($\varepsilon$), there is no need—in fact no justification—to try to find a solution to order $\varepsilon^3$ and higher. Similar remarks apply to the expansion in the average Mach number ($\mu$). The procedure is fully explained in Section 4.5 for the equations derived in Section 3.4.

**4.2. An Alternative Derivation of the First Order Formula.** The results (4.19) and (4.21) for the complex wavenumber and mode shape can be constructively obtained in a different way. Both formulas provide means for computing the differences $k^2 - k_N^2$ and $\hat{p} - \psi_N$ between the actual (perturbed) quantities and the unperturbed quantities. It is reasonable that those results should somehow follow from comparison of the perturbed ($\kappa \neq 0$) and unperturbed ($\kappa = 0$) problems. The idea is to average the difference between the two problems weighted respectively by the other's mode shape. That is, subtract $\hat{p}$ times equation ((4.12) a,b)a from $\psi_n$ times ((4.4) a,b)a and integrate the result over the volume of the chamber:

$$
\iiint\limits_V \left[ \psi_N \nabla^2 \hat{p} - \hat{p} \nabla^2 \psi_N \right] dV + \iiint\limits_V (k^2 - k_N^2) \psi_n \hat{p} dV_0 = \kappa \iiint\limits_V \psi_N \hat{h} dV
$$

Now apply Green's theorem to the first integral, substitute the boundary conditions ((4.4) a,b)b and ((4.12) a,b)b and rearrange the result to find (4.21):

$$
k^2 = k_N^2 + \frac{\kappa}{\iiint\limits_V \psi_N \hat{p} dV} \left\{ \iiint\limits_V \psi_N(\mathbf{r})\hat{h}(\mathbf{r})dV + \oiint\limits_S \psi_N(\mathbf{r}_s)\hat{f}(\mathbf{r}_s)dS \right\}
$$

(4.26)

If $k^2$ is to be calculated to first order in $\kappa$, then $\hat{p}$ must be replaced by its zero order approximation $\hat{p} = \psi_N$. Because the correction to $k_N^2$ contains the multiplier $\kappa$, any contributions of order $\kappa$ multiplying $\kappa$ give terms of order $\kappa^2$. Hence to first order, (4.26) of course becomes (4.19).

This approach does not provide a recipe for computing the modal or basis functions to higher order. That does not cause difficulty here because we have the procedure given in the preceding section. We will find later that the simple derivation just given suggests a useful extension to time-dependent nonlinear problems. In that situation there is no result corresponding to (4.20) for computing the mode shapes to higher order. That deficiency is a serious obstacle to further progress, a subject of current research.

**4.3. Approximate Solution for Unsteady Nonlinear Motions.** The method covered in the preceding two sections, based essentially in the use of Green's functions, was the first application of modal expansions and spatial averaging to combustion instabilities (Culick 1961, 1963). In the early 1970's the procedure was extended

to treat nonlinear problems, necessarily involving time-dependence (Culick 1971, 1975). We summarize that approach here.[13]

We begin with the general problem (4.1) a,b and assume an approximation $\tilde{p}'(\mathbf{r})$ to the pressure field as a truncated expansion in a set of basis functions $\psi_m$,

$$\tilde{p}'(\mathbf{r}, t) = \bar{p}_r \sum_{m=0}^{M} \eta_m(t) \psi_m(\mathbf{r}) \tag{4.27}$$

In this work we will always take the $\psi_m$ to be acoustic modes defined by the geometry, the distribution of average temperature and suitable boundary conditions.[14] We would like the right-hand side of (4.27) to become more nearly equal to the actual pressure field in the combustor as more terms are included in the series, so that $\tilde{p}' \equiv p'$ in the limit:

$$\lim_{M \to \infty} \tilde{p}(\mathbf{r}; t) = \lim_{M \to \infty} \sum_{m=0}^{M} \eta_m(t) \psi_m(\mathbf{r}) \tag{4.28}$$

Because the $\psi_m$ do not satisfy the correct boundary conditions, this pointwise property certainly cannot be satisfied at the boundary. It is reasonable, however, to expect convergence in integral-squared sense; that is the integral of the square of the difference between the exact solution and (4.27) satisfies

$$\lim_{M \to \infty} \iiint \left[ p'(\mathbf{r}, t) - \bar{p}_r \sum_{m=0}^{M} \eta_m(t) \psi_m(\mathbf{r}) \right]^2 dV = 0 \tag{4.29}$$

We will not prove this properly, but assume its truth.

Convergence in the sense asserted by (4.29) is a common idea arising, for example, in formal treatments of Sturm-Liouville problems; see Hildebrand 1952 for a very readable discussion. The matter of convergence of approximate solutions in the present context is more complicated because one must take into account the fact that the governing equations and their solutions are expanded in the two small parameters $\mu$ and $\varepsilon$ introduced in Section 3. We will also not discuss that problem.

The synthesis of the pressure field expressed by (4.27) does not restrict in any practical fashion the generality of the method. For definitions here we assume that the modal functions satisfy the homogeneous Neumann condition $\hat{\mathbf{n}} \cdot \nabla \psi_n = 0$, but for some applications a different boundary condition, perhaps over only part of the boundary, may serve better. Hence we will assume here that the $\psi_n$ are eigensolutions to the problem (4.12) a,b.

We require that the approximation (4.27) to $p'$ satisfy equation (4.1) a,b. Multiply (4.12) a,b written for $\psi_N$ by $\tilde{p}'(\mathbf{r}, t)$, subtract from (4.1) a,b written for $\tilde{p}'$ multiplied by $\psi_N$; and integrate the difference over the volume of the chamber to give

$$\iiint_V \left[ \psi_N \nabla^2 \tilde{p}' - \tilde{p}' \nabla^2 \psi_N \right] dV - \iiint_V \frac{1}{\bar{a}^2} \frac{\partial^2 \tilde{p}'}{\partial t^2} dV - k_N^2 \iiint_V \tilde{p}' \psi_N dV = \iiint_V \psi_N h \, dV$$

---

[13]An alternative form based on an form of Galerkin's method, extended to accommodate the sorts of problems arising in the present context, was introduced first by Zinn and his students. That procedure and the present method give identical equations before the expansion procedure is applied and further approximations are used. The applicability of that method seems to have been blunted in some cases by use of a velocity potential, thereby requiring that the unsteady field be irrotational. It seems also that the ordering procedure (in terms of the small parameters $\bar{M}_r$ and $\bar{M}_r'$) (i.e. $\mu$ and $\varepsilon$) has not been followed consistently, causing confusion in some derivations and conclusions. Those matters are discussed elsewhere. It seems likely that the extended form of Galerkin's method could give the same (or nearly so) results as found by the method discussed here, but the early works were not pursued further. There is no basis for comparison.

[14]The selection of boundary conditions is part of the art of applying this method. Examples covered later will clarify the point. For the present, it is helpful to think of the $\psi_m$ as classical acoustic modes for a volume having rigid walls and the same shape as the combustion chamber in question. The $\psi_m$ therefore do not satisfy exactly the boundary conditions actually existing in a combustor. Hence the right-hand side of (4.27) is an approximation in two respects: the series is truncated to a finite number of terms and it does not satisfy the correct boundary conditions. However, the solution carried out to the next order *does* satisfy the boundary conditions to first order. This important point is discussed in Chapter 10 of Morse and Feshbach (1952). The approximate nature of the modal expansion will be clarified as the analysis proceeds.

Apply Green's theorem to the first integral, substitute the boundary conditions (4.1) a,b and (4.12) a,b and rearrange the result to give

$$\iiint\limits_V \frac{1}{\bar{a}^2} \frac{\partial^2 \tilde{p}'}{\partial t^2} \psi_N dV + k_N^2 \iiint\limits_V \tilde{p}' \psi_N dV = - \left\{ \iiint\limits_V h\psi_N dV + \oiint\limits_S f\psi_N dS \right\} \tag{4.30}$$

Now substitute the modal expansion (4.27) in the right-hand side:

$$\frac{\bar{p}_r}{\bar{a}_r^2} \sum_{m=0}^{M} \ddot{\eta}_m(t) \iiint\limits_V \left(\frac{\bar{a}_r}{\bar{a}}\right)^2 \psi_m \psi_N dV - k_n^2 \bar{p}_r \sum_{m=0}^{M} \eta_m \iiint\limits_V \psi_m \psi_N dV = E_N^2 \frac{\bar{p}_r}{\bar{a}_r^2} F_N \tag{4.31}$$

where

$$F_N = -\frac{\bar{a}_r^2}{\bar{p}_r E_N^2} \left\{ \iiint\limits_V h\psi_N dV + \oiint\limits_S f\psi_N dS \right\} \tag{4.32}$$

and $\bar{a}_r$ is a constant reference speed of sound. The second sum reduces, due to the orthogonality of the $\psi_m$, to $\eta_n E_n^2$. Under the first integrals, write

$$\Delta_a = 1 - \left(\frac{\bar{a}_r}{\bar{a}}\right)^2 \tag{4.33}$$

Then the first sum in (4.31) is

$$\sum_{m=0}^{M} \ddot{\eta}_m(t) \iiint\limits_V (1 - \Delta_a) \psi_m \psi_N dV = E_N^2 \ddot{\eta}_N - \sum_{m=0}^{M} \ddot{\eta}_m(t) \iiint\limits_V \Delta_a \psi_m \psi_N dV \tag{4.34}$$

With these changes, equation (4.31) becomes

$$\ddot{\eta}_N + \omega_N^2 \eta_N = F_N + \frac{1}{E_N^2} \sum_{m=0}^{M} \ddot{\eta}_m(t) \iiint\limits_V \Delta_a \psi_m \psi_N dV \tag{4.35}$$

The sum on the right-hand side represents part of the effect of a non-uniform speed of sound in the chamber (if $\Delta_a \neq 0$). To simplify writing we will ignore this term until we consider special problems in later chapters. For solid rockets it is a negligible contribution. If the combustor contains flame sheets, the temperature is piecewise uniform and this term also doesn't appear, but the presence of the discontinuities generates corresponding terms arising from $F_N$. Thus there are useful situations in which we deal with the system of equations:

$$\ddot{\eta}_N + \omega_N^2 \eta_N = F_N \tag{4.36}$$

This result, a set of coupled nonlinear equations with the forcing function $F_N$ given by (4.34), is the basis for practically all of the analysis and theory discussed in the remainder of this book. A corresponding result is given in Appendix B for a purely one-dimensional formulation. In anticipation of later discussions, several general remarks are in order.

(i) The formulation expressed by (4.36) accommodates all relevant physical processes. In the derivation of the conservation equations in Appendix A, only inconsequential approximations were made, notably the neglect of multi-component diffusion and the representation of the reacting multi-phase medium by a single-fluid model. However, only the basic gasdynamics are known explicitly. All other processes must be modeled in suitable forms.

(ii) Despite the apparent generality of (4.36) attention must be paid to an assumption implied in the application of Green's theorem in spatial averaging. That is, the functions involved must possess certain properties of continuity within the volume of averaging. The condition is not satisfied, for example, at a flame sheet, where the velocity is discontinuous, an important exception.

(iii) The selection of functions for the modal expansion (4.27) is not unique; possible alternatives must always be considered. What works best depends on the nature of the boundary conditions. The closer the boundary is to a rigid reflecting surface, the more effective is the choice $\hat{\mathbf{n}} \cdot \nabla \psi_N = 0$, meaning that the acoustic velocity vanishes on the boundary. Because a

combustor must provide for inflow of reactants and exhaust of products, it is simply not possible that the actual enclosure be everywhere rigid and perfectly reflecting. For $\hat{\mathbf{n}} \cdot \nabla \psi_N = 0$ to be a good approximation, as it should be for the modal expansion to serve successfully as a zeroth approximation to the pressure field, the boundary must be 'nearly' reflecting. Choked inlets and outlets satisfy the condition if the Mach number at the chamber side is small (that is, the flow within the volume is consistent with the assumption $\mu \ll 1$). Also, the dynamical response of burning solid propellants is normally such that requiring $\hat{\mathbf{n}} \cdot \nabla \psi_N = 0$ is a good choice. Hence, over a broad useful range of practical conditions, defining the modal expansion functions with (4.12) a,b is a reasonable choice. Exceptions are not rare, however, and care must be exercised. For example, a Rijke tube (Section 2) will contain a heater, or a thin combustion region within the duct. Continuous functions $\psi_N$ may not be good zeroth approximations to the actual behavior discontinuous at the heating zone; moreover, in that case $\hat{\mathbf{n}} \cdot \nabla \psi_N = 0$ at the ends is the proper choice for boundary conditions on the modal functions. More generally, if the temperature field is highly non-uniform, then the zeroth order expansion functions should take that feature into account.

(iv) An enormous advantage of the result (4.36) is its clear interpretation. A general unsteady motion in a combustor is represented by the time-evolution of a system of coupled nonlinear oscillators in one-to-one correspondence with the modes $\psi_N$. Although the left-hand side of (4.36) describes the motion of a linear oscillator, the forcing function $F_N$ will in general contain terms in $\eta_N$ representing linear and nonlinear damping, springiness and inertia. Consequently, as we will see, it is easy to find familiar nonlinear differential equations as special cases of (4.36). Such special results aid greatly interpretation of complicated observed behavior in terms of simpler elementary motions. Thus it is important to understand the connections between parameter defining the oscillators, the characteristics of the modes, and the definitions provided in the process of spatial averaging.

(v) Different problems are distinguished chiefly in two respects: Geometry of the combustor; and the form of the forcing function $F_N$. The forcing function contains the influences of gasdynamics explicitly, but all other processes must be modeled, either with theory or based on experimental results. The geometry and the boundary conditions determine the modal expansion functions $\psi_N$ and the frequencies $\omega_N$. For complicated geometries, as for many large solid propellant rockets and for most gas turbine combustors, computation of the $\psi_N$ and $\omega_N$ has been a time-consuming and expensive process. That situation is gradually changing with the development of more capable software.

(vi) The relatively general context in which the oscillator equations have been derived does not exclude simpler problems which can either be treated as special cases or constructed without reference to the procedures worked out here. However, it is then often more difficult to be certain that all important processes are accounted for or properly ignored.

**4.4. Application of Time-Averaging.** To this point the expansion procedure based on two small parameters has been used only to derive the systems of equations describing successively more difficult classes or problems in Section 3.3.2. There are at least two additional reasons for introducing that procedure. Later we will see how an iterative method based partly on the expansion reduces those systems of equations to more readily soluble forms. In this section we apply time-averaging to convert the second-order equations (4.36) to first order equations. First, two remarks:

(i) Use of time-averaging is motivated by the experimental observation that combustion instabilities commonly show slowly varying amplitudes and phases of the modes contributing to the motions. That behavior is a consequence of the relative weakness of the disturbing processes and is therefore measured by the small parameter $\mu$ characteristic of the Mach number of the mean flow. It is essential to understand that it is not the amplitudes themselves (i.e. the parameter $\varepsilon$) that matters. Thus the application of time-averaging in the present context is *not* intended to treat nonlinear behavior, but is based on the weak coupling between the mean flow and the unsteady motions.

(ii) Two-time scaling is an alternative method to time-averaging. The results obtained are identical up to second order acoustics (Section 3.3.3(II) and 3.4), a conclusion not shown here but consistent with similar previous works in other fields.

According to the discussion in Section 3.3.2, we can characterize the functions $h$ and $f$, and hence the forcing function $F_n$, as sums of terms each of which is of order $\mu$ and of zeroth or first order in $\varepsilon$. Thus for example, the right-hand side of (3.62) a,b has the form

$$-\mu\varepsilon\left\{\{[\mathbf{M}]\}_1 + \frac{\varepsilon}{\mu}\{\mathbf{M}\}_2\right\}$$

The divergence of these terms eventually appears in $h$ and $F_n$. Hence we are justified in taking $F_n$ of order $\mu$; to show this explicitly write (4.36) as

$$\ddot{\eta}_N + \omega_N^2 \eta_N = \mu G_N \tag{4.37}$$

In any event, for $\mu$ small, the $\eta_N$ differ but little from sinusoids so (without approximation) it is reasonable to express $\eta_N(t)$ in the equivalent forms

$$\eta_N(t) = r_N(t)\sin\left(\omega_N t + \phi_N(t)\right) = A_N(t)\sin\omega_N t + B_N(t)\cos\omega_N t \tag{4.38}$$

and

$$A_N(t) = r_N\cos\phi_N \; ; \quad B_N = r_N\sin\phi_N$$
$$r_N = \sqrt{A_N^2 + B_N^2} \; ; \quad \phi_N = \tan^{-1}\left(\frac{A_N}{B_N}\right) \tag{4.39}$$

One way to proceed follows a physical argument based on examining the time evolution of the energy of the oscillator having amplitude $\eta_N$ (Culick 1976). The energy $\mathcal{E}_N$ is the sum of kinetic and potential energies,

$$\mathcal{E}_N(t) = \frac{1}{2}\dot{\eta}_N^2 + \frac{1}{2}\omega_N^2\eta_N^2 \tag{4.40}$$

The time-averaged values of the energy and power input to the oscillator, due to the action of the force $\mu G_N$, are

$$\langle \mathcal{E}_N \rangle = \frac{1}{\tau}\int_t^{t+\tau} \mathcal{E}_N dt' \; ; \quad \langle \mu G_N \dot{\eta}_N \rangle = \frac{1}{\tau}\int_t^{t+\tau} \mu G_N \dot{\eta}_N dt' \tag{4.41}$$

Conservation of energy requires that the time-averaged rate of change of energy equal the time-averaged rate of work done by $\mu G_N$ on the oscillator:

$$\frac{d}{dt}\langle \mathcal{E}_N \rangle = \mu\langle G_N \dot{\eta}_N \rangle \tag{4.42}$$

From (4.38), the velocity is

$$\dot{\eta}_N = \omega_N r_N \cos\left(\omega_N t + \phi_N\right) + \left[\dot{r}_N \sin\left(\omega_N t + \phi_N\right) + \dot{\phi}_N r_N \cos\left(\omega_N t + \phi_N\right)\right] \tag{4.43}$$

Following Krylov and Bogoliubov (1947) we apply the 'strong' condition that the velocity is always given by the formula for an oscillator is force-free-motion,

$$\dot{\eta}_N = \omega_N r_N \cos\left(\omega_N t + \phi_N\right) \tag{4.44}$$

Hence (4.43) is consistent with this requirement only if

$$\dot{r}_N \sin\left(\omega_N t + \phi_N\right) + \dot{\phi}_N r_N \cos\left(\omega_N t + \phi_N\right) = 0 \tag{4.45}$$

Now use the definitions (4.36), (4.38), (4.39) and (4.42) to find

$$\mathcal{E}_N = \frac{1}{2}\omega_N^2 r_N^2$$
$$\mu G_N \dot{\eta}_N = \mu G_N \omega_N r_N \cos\left(\omega_N t + \phi_N\right) \tag{4.46 a,b}$$

The statement "slowly varying amplitude and phase" means that the fractional changes of amplitude and phase are small in one cycle of the oscillation and during the interval of averaging $\tau$ if $\tau$ is at least equal to the period of the fundamental mode:

$$\frac{\tau}{r_N}\frac{dr_N}{dt} \ll 1 \; ; \quad \frac{\tau}{2\pi}\frac{d\phi_N}{dt} \ll 1 \tag{4.47}$$

These inequalities imply that $r_N$ and $\phi_N$ may be treated as constants during the averaging carried out in (4.41). To see this, imagine that $r_N$ for example, is expanded in Taylor series for some time $t_1$ in the interval $\tau$, $t < t_1 < t+\tau$:

$$r_N(t) = r_N(t_1) + (t - t_1)\left(\frac{dr_N}{dt}\right)_{t_1} + \cdots$$

For $r_N$ slowly varying, $\dot{r}_N$ doesn't vary much during a period and may be assigned some average value. The increment $t - t_1$ has maximum value $\tau$; so the second term is negligible according to the first of (4.41). Therefore $r_N(t) \approx r_N(t_1)$ for any $t_1$ in the interval of averaging and the assertion is proved.

Substitution of (4.46) a,b in (4.42) then gives

$$\omega_N r_N \frac{dr_N}{dt} = \mu \frac{r_N}{\tau} \int_t^{t+\tau} G_N \cos(\omega_N t' + \phi_N) dt'$$

and

$$\frac{dr_N}{dt} = \mu \frac{1}{\omega_N \tau} \int_t^{t+\tau} G_N \cos(\omega_N t' + \phi_N) dt' \tag{4.48}$$

The corresponding equation for the phase $\phi_N(t)$ is found by substituting (4.38) and (4.39) in (4.45) to give

$$r_N \frac{d\phi_N}{dt} = -\frac{\mu}{\omega_N} G_N \sin(\omega_N t + \phi_N) \tag{4.49}$$

Now time average this equation over the interval $\tau$, the left-hand side is approximately constant for theorem give above, and the equation for $\phi_N(t)$ is

$$r_N \frac{d\phi_N}{dt} = -\mu \frac{1}{\omega_N \tau} \int_t^{t+\tau} G_N \sin(\omega_N t' + \phi_N) dt' \tag{4.50}$$

With the relations (4.39), equations (4.48) and (4.50) can be converted to equations for $A_N$ and $B_N$:

$$\frac{dA_N}{dt} = \frac{\mu}{\omega_N \tau} \int_t^{t+\tau} G_N \cos \omega_N t' dt'$$

$$\frac{dB_N}{dt} = -\frac{\mu}{\omega_N t} \int_t^{t+\tau} G_N \sin \omega_N t' dt' \tag{4.51} \text{ a,b}$$

Whichever pair one chooses to use, (4.48) and (4.50) or (4.51) a,b, the general formal problem of solving a system of coupled second order equations (4.37) for the oscillators, has been converted to the simpler approximate formal problem of solving a system of coupled first order equations. The essential basis for that conversion is the removal of the fast oscillatory behavior with the definition (4.38), a transformation made possible because the changes of amplitudes and phases take place on a much slower (i.e. longer) time scale than do the oscillations. The presence and role of two time scales is more evident in the following alternative derivation:

From the second equality of (4.38), we find the velocity

$$\dot{\eta}_N = \omega_N \left[A_N \cos \omega_N t - B_N \sin \omega_N t\right] + \left[\dot{A}_N \sin \omega_N t + \dot{B}_N \cos \omega_N t\right]$$

Now enforce the condition corresponding to (4.45),

$$\dot{A}_N \sin \omega_N t + \dot{B}_N \cos \omega_N t = 0 \tag{4.52}$$

and the velocity is

$$\dot{\eta}_N = \omega_N \left[A_N \cos \omega_N t - B_N \sin \omega_N t\right] \tag{4.53}$$

Substitution in (4.37) gives

$$\omega_N \left[ \dot{A}_N \cos \omega_N t - \dot{B}_N \sin \omega_N t \right] + \omega_N^2 \left[ -A_N \sin \omega_N t - B_N \cos \omega_N t \right]$$
$$+ \omega_N^2 \left[ A_N \sin \omega_N t + B_N \cos \omega_N t \right] = \mu G_N$$

and

$$\dot{A}_N \cos \omega_N t - \dot{B}_N \sin \omega_N t = \frac{\mu}{\omega_N} G_N$$

Multiply by $\cos \omega_N t$ and substitute (4.52) for $\dot{B}_N \cos \omega_N t$ to give

$$\dot{A}_N \cos^2 \omega_N t - \sin \omega_N t \left[ -\dot{A}_N \sin \omega_N t \right] = \frac{\mu}{\omega_N} G_N \cos \omega_N t$$

so

$$\frac{dA_N}{dt} = \frac{\mu}{\omega_N} G_N \cos \omega_N t \tag{4.54}$$

Similarly,

$$\frac{dB_N}{dt} = -\frac{\mu}{\omega_N} G_N \sin \omega_N t \tag{4.55}$$

We now introduce two time-scales, $\tau_f$ the first scale, of the order of the period of the fundamental oscillation (in fact, we might as well set $\tau_f = 2\pi/\omega_1$); and $\tau_s$, the slow scale characterizing transient changes of the amplitudes and phases of the oscillations. Two corresponding dimensionless time variables can be defined, $t_f = t/\tau_f$ and $t_s = t/\tau_s$. Thus we consider the amplitudes and phases to be functions of the slow variable $t_s$ while the forcing functions $G_N$ depend on both $t_f$ and to because they depend on the $\eta_N$, $(i = 1, 2, \cdots)$

$$\eta_N = A_N(t_s) \sin \left( 2\pi \frac{\omega_N}{\omega} t_f \right) + B_N(t_s) \cos \left( 2\pi \frac{\omega_N}{\omega_1} t_f \right)$$

In terms of the dimensionless time variables,

$$\frac{1}{\tau_s} \frac{dA_N}{dt_s} = \frac{\mu}{\omega_N} G_N \cos \omega_N t$$

and averaging over the fast variable we have

$$\frac{1}{\tau_s} \int_{t_f}^{t_f + \tau_f} \frac{1}{\tau_s} \frac{dA_N}{dt'_s} dt'_f = \frac{\mu}{\omega_N} \frac{1}{\tau_f} \int_{t_f}^{t+\tau_f} G_N \cos \left( 2\pi \frac{\omega_N}{\omega_1} t'_f \right) dt'_f$$

On the left-hand side, $dA_N/dt'_s$ is assume to be sensibly constant in the interval $\tau_f$ and we have

$$\frac{1}{\tau_s} \frac{dA_N}{dt'_s} = \frac{\mu}{\omega_N \tau_f} \int_{t_f}^{t+\tau_f} G_N \left( t'_f, t'_s \right) \cos \left( 2\pi \frac{\omega_N}{\omega_1} t'_f \right) dt'_f \tag{4.56}$$

Those parts of $G_N$ depending on $t'_s$ are taken also to be constant and if we now rewrite this equation in terms of dimensional variables, we recover (4.51)a with $\tau = \tau_f = 2\pi/\omega$. Similar calculations will produce again (4.51)b. Note that due to the nonlinear coupling, the amplitude and phases of all modes normally change on roughly the same scale as that for the fundamental mode; thus the single interval of averaging works for all modes.

In Section 7.2 we will use a continuation method to assess the ranges of parameters and other conditions for which the first order equations give accurate results when compared with solutions to the complete oscillator equations. In the development of the theoretical matters described in this book, the sets of first order equations have been central. They remain extremely useful both for theoretical work and for applications.

**4.5. The Procedure for Iterative Solution.** The oscillator equations (4.33) and (4.34) are not yet in a form that can be readily solved because the functions $F_N$, defined by (4.30) contain not only $p'$ but also the dependent variables $\rho'$, $T'$ and $\mathbf{u}'$ in the functions $h$ and $f$. With the two-parameter expansion as the basis, the iteration procedure provides a means for expressing $F_N$ in terms of $p'$ only. Thus eventually the oscillator equations become a system soluble for the modal amplitudes $\eta_N(t)$. There are of course approximations required, but magnitudes of their effects can always be estimated in terms of the parameters $\varepsilon$ and $\mu$. To appreciate how the procedure is constructed, it is helpful always to keep in mind the correspondence between the smallness of $\varepsilon$ and $\mu$, and the distortions they represent of the unperturbed classical acoustic field.

There are two chief types of distortions or perturbations: Those represented by $\varepsilon$, arising as nonlinear effects of finite amplitudes,[15] classified generally as energy transfer between modes; and those measured by $\mu$, consequences of interactions, hence energy transfer, between the steady and unsteady fields. Each of those types of perturbations may be identified within the volume in question and at the boundary. Quite generally, then, we must take into account perturbations of the classical acoustic field, associated with three kinds of energy transfer: linear transfer between the mean and fluctuating motions; nonlinear transfer between modes, or mode coupling, independent of the average flow field; and nonlinear energy transfer between the mean flow and fluctuating fields. The way in which we view and accommodate those perturbations determines our choice of basis functions $\psi_N$ used in the modal expansion (4.27).

4.5.1. *Linear Energy Transfer Between the Mean and Fluctuating Motions.* Any combustor designed for steady, or at most slowly varying conditions on the acoustic time scale, must have provision for supplying reactants and exhausting products. There must therefore be average flow within the volume and through openings in the enclosing boundary. If the reactants are liquid or gaseous, then openings exist for both inflow and outflow. In combustors for solid propellants, flow enters at the boundary but there are not openings for that purpose.

### (A) Volumetric Interactions

The general equations of motion in principle contain all interactions between the mean and fluctuating motions within the volume. Many are shown explicitly as the bracketted terms $[\bar{\mathbf{M}}]$, $\{\bar{\mathbf{M}}\}$, $[\rho_1]$, $\{p_1\}$, $\cdots$ defined in Section (3.3). Those terms in the forms given there account for interactions of the mean flow velocity with the acoustic field and have long served that purpose well in investigations of combustion instabilities. Additional consideration are required to treat interactions associated with entropy and vorticity waves, including turbulence and noise, a subject covered in Section (7.4).

Special effects also arise when the average temperature field is nonuniform; the last term in (4.33) represents one consequence of nonuniform average temperature but others are contained in the formula given for $h$, equation (3.55). Nonuniformities of temperature cause nonuniformities in the speed of sound which may be regarded as nonuniformities in the index of refraction for acoustic waves. Thus in the general context of wave motions, phenomena such as refraction and diffraction must arise. However, the analysis covered here for wave systems slowly varying on the acoustic time scale, obscures wave phenomena of that sort; they have rarely been addressed explicitly in the field of combustion instabilities and then only in connection with very special problems. However, the consequences of refraction and diffraction are contained implicitly in distortions of the structure of the steady waves.

It is extremely important that large differences in the average speed of sound be accounted for as accurately as possible. That is best done by including them in the functions used in the modal expansion. Formally that amounts to including all terms in $h$ representing linear interactions between the acoustic and mean fields, in the equations for the $\psi_m$. That is, such large perturbations are better not included in the procedure best suited for dealing with small perturbations. In practice, the only example of this tactic have been concerned with flows in ducts containing a compact zone of heating thin relative to the acoustic wavelength. The modal functions are then formed in piecewise fashion, the usual wave equation being solved separately for the two regions characterized by different uniform temperatures upstream and downstream of the zone of heating treated as a surface of discontinuity. Then the functions are joined with suitable matching conditions.

For the most part, therefore, energy transfer between the acoustic field and the mean flow within the volume of a combustor is due to interactions with the mean velocity, characterized by the parameter $\mu$. The analysis is strictly limited to perturbations linear in the Mach number of the mean flow (see the footnote in the preceding page).

### (B) Boundary Conditions

The situation in respect to processes at the boundary is considerably more complicated and in fact cannot be placed in a firm basis without detailed examination of ancillary problems. Only two possibilities have so far been

---

[15]Recall that in this work, nonlinear behavior is measured in terms of the amplitude $\varepsilon$ of the unsteady motions. It is intrinsic to their derivation (Section 3) that the governing equations are linear in $\mu$, i.e. in the Mach number of the mean flow.

of practical interest: physical openings in the boundary of the combustor; and a burning surface. Conditions to be set on the acoustic field at an opening depend on the flow field through and outside the boundary. In classical acoustics with no flow, an opening into an atmosphere held at constant pressure is almost perfectly reflecting, with the fluctuating pressure nearly zero in the plane of the opening. A perfectly reflecting rigid wall causes the fluctuating velocity to vanish there. Thus in those two limits, the boundary conditions to $0^{th}$ order on the pressure field are respectively $p' = 0$ and $\hat{\mathbf{n}} \cdot \nabla p' = 0$.

Subsonic flow through an orifice presents a boundary condition to acoustic waves closer to the case of no flow, $p' \approx 0$, than to a rigid wall. On the other hand, if the inlet flow is choked upstream close[16] to the orifice, or the outlet flow exhausts through a choked nozzle, the boundary condition is closer to the for a rigid wall, $\hat{\mathbf{n}} \cdot \nabla p' \approx 0$. That is the case for propulsion systems, with the possible exception of the primary combustion chamber in a gas turbine. The actual boundary conditions are more complicated but for linear behavior can be represented by impedance or admittance functions defined for steady waves. For the more common case of choked flows, that boundary condition is expressed as

$$\hat{\mathbf{n}} \cdot \hat{\mathbf{u}}\left(\mathbf{r}_s, w\right) = A_s\left(\mathbf{r}_s, w\right)\hat{p}\left(\mathbf{r}_s, w\right) = \mu a_s\left(\mathbf{r}_s, w\right)\hat{p}\left(\mathbf{r}_s, w\right) \tag{4.57}$$

where $A_s = \mu a_s$ is the dimensional admittance function shown here to be proportional to the Mach number of the average flow. (Tsien 1952; Crocco and Cheng 1956; Culick 1961, 1963) Generally, $A_s$ is a complex function,

$$A_s = |A_s|e^{i\phi_A} = \mu|a_s|e^{i\phi_A} \tag{4.58}$$

The representation (4.57) is based on the idea that when exposed to an oscillatory fluctuation of pressure, a physical surface responds in first approximation such that its velocity normal to itself is proportional to the impressed pressure, possibly with a phase or time delay. That idea is extended in the present context to describe fluctuations of flow at a fictious surface forming part of the boundary enclosing the combustor volume, or at the downstream edge of the combustion zone at a burning surface. Thus we have a simple and direct way of making explicit the first term in the definition (3.57) of the boundary function $f$ for steady waves:

$$\bar{\rho}\frac{\partial \mathbf{M}'}{\partial t} \cdot \hat{\mathbf{n}} = \bar{\rho}\bar{a}\frac{\partial \mathbf{u}'}{\partial t} \cdot \hat{\mathbf{n}} = \bar{\rho}\bar{a}\frac{\partial}{\partial t}\left[\hat{\mathbf{n}} \cdot \hat{\mathbf{u}}\left(\mathbf{r}_s, w\right)e^{i\bar{a}kt}\right]$$
$$= \mu\bar{\rho}\bar{a}a_s\left(\mathbf{r}_s, t\right)i\bar{a}k\hat{p}\left(\mathbf{r}_s, w\right)e^{i\bar{a}kt} \tag{4.59}$$
$$= \mu\bar{\rho}\bar{a}^2k\left(i|a_s|e^{i\phi_a}\right)\hat{p}\left(\mathbf{r}_s, w\right)e^{i\bar{a}kt}$$

An equivalent form is

$$\bar{\rho}\frac{\partial \mathbf{M}'}{\partial t} \cdot \hat{n} = \mu\bar{\rho}\bar{a}^2k\left\{-Im(a_s) + i\,Re(a_s)\right\}\hat{p}\left(\mathbf{r}_s, w\right)e^{i\bar{a}kt} \tag{4.60}$$

Although the admittance function is defined for steady waves initially, (4.49) can be converted to a form approximately applicable to problems having arbitrary dependence on time. The time derivative of some function $\varphi$ for steady waves, so we can make the correspondence

$$\frac{\partial \varphi}{\partial t} \longleftrightarrow i\bar{a}k\frac{\partial \varphi}{\partial t}$$

Hence we write (4.49) as

$$\bar{\rho}\frac{\partial \mathbf{M}'}{\partial t} \cdot \hat{\mathbf{n}} = \mu\bar{\rho}\bar{a}\left[\bar{a}k\,Im\left\{a_s\right\}p' + Re\left\{a_s\right\}\frac{\partial p'}{\partial t}\right] \tag{4.61}$$

This form of a boundary condition will be useful in later applications.

The chief point here is that for choked inlet and exhaust flows, the function $f$ in the boundary condition $\hat{\mathbf{n}} \cdot \nabla p' = -f$ is of order $\mu$. That is, perturbations from the condition defining a rigid impermeable wall are all proportional to the magnitude of the Mach number of the mean flow. Corresponding reasoning applies to the less important case of subsonic flow exhausting into surroundings held at constant pressure.[17] Now we set the

---

[16]'Close' means within a short distance relative to the wavelength of the dominant oscillation.

[17]Less important for practical applications. However there are many laboratory devices operating at close to atmospheric pressure and exhausting into the atmosphere for which the condition treated here is appropriate.

boundary condition by using (3.51) evaluated at the boundary; for linear steady waves we have

$$p' = \frac{1}{\bar{a}k}\left[\gamma\bar{p}\nabla\cdot\mathbf{M}_1' + \mu\{[p]_1\} - \frac{1}{\varepsilon}\mathcal{P}'\right]_{\mathbf{r}=\mathbf{r}_s} \tag{4.62}$$

Again we may define an admittance function to eliminate $\nabla\cdot\mathbf{M}_1'$ in favor of the local pressure fluctuation. We leave the calculation to special applications.

We conclude that for linear problems, perturbations of the classical acoustics problem due to energy transfer between the mean and unsteady fields are represented to order $\mu$, both within the volume and at the boundary. This result is of course consistent with the order to which the differential equations are valid within the approximation used here (see a remark following equation (3.39). For that reason, we cannot in any event carry terms of higher order in $\mu$ unless the governing equations used here are re-derived.

As an example to illustrate some implications of the preceding remarks, consider the case of flow through a uniform duct of length $L$, supplied through choked valves and exhausting through a choked nozzle. Suppose that by some means, for example by installing a speaker, oscillations can be excited and sustained in the duct. If there were no flow and rigid plates were placed at both ends ($z = 0, L$), classical 'organ pipe' acoustic modes would be found experimentally, having frequencies $\omega_N = n(\bar{a}/L)$. The velocity and pressure distributions for these steady axial modes are proportional to $\sin k_N x$ and $\cos k_N x$ respectively. Suppose we set, for example,

$$p'(z,t) = \hat{p}_0 \cos k_N z \cos \omega_N t \tag{4.63}$$

where $\omega_N = \bar{a}k_N$. The unperturbed acoustic momentum equation,

$$\bar{\rho}\frac{\partial\mathbf{u}'}{\partial t} = -\nabla p'$$

is satisfied with (4.52) if $\mathbf{u}'$ has only the axial component,

$$u'(z,t) = \frac{\hat{p}_0}{\bar{\rho}\bar{a}}\sin k_N z \sin \omega_N t \tag{4.64}$$

The velocity field has nodes ($u' = 0$) at the ends and the pressure field has anti-nodes, reaching maximum amplitude $\hat{p}_0$ when $t = 0, 2\pi/\omega_N, 4\pi/\omega_N, \cdots$. Now suppose that average flow is introduced and that the cross-sectional areas available for the flow upstream and downstream are small fractions of the cross-sectional area of the duct. Then the average Mach numbers at $z = 0, L$ are small ($\mu \ll 1$). Hence the distortions of the classical organ pipe modes are small. In particular, the modes of the velocity field are slightly displaced by the same amounts downstream of their unperturbed positions at $x = 0, L$. Thus the wavelength and frequency of the modes are unchanged and the unperturbed mode shapes are close approximations to the actual shapes with the flow, as sketched in Figure 4.1.
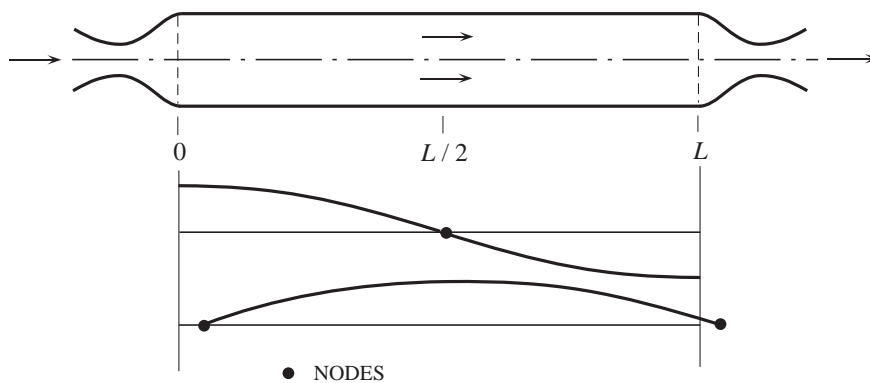


FIGURE 4.1. Fundamental Longitudinal Mode, Velocity Mode Shape: $----$ Classical (no flow); —— Duct with flow choked upstream and downstream

If the Mach numbers at the entrance ($z = 0$) and at the exit ($z = L$) are not small, then the nodes of the velocity wave are displaced by larger amounts, but the wavelength, and hence the frequency, suffer only small changes. This behavior suggests what is true quite generally in practice, that the processes in a combustion

chamber have relatively small effects in the frequencies of the normal modes. Consequently, as we will emphasize repeatedly, comparison of observed frequencies with those predicted is not a useful basis for assessing the correctness of the theory in question.

4.5.2. *Energy Transfer Between Modes; Nonlinear Mode Coupling.* If the functions $\psi_N$ used in the modal expansion are those computed according to classical acoustics, then in general linear coupling between modes will appear in the right-hand sides of the systems (4.33) and (4.34). When the mean flow field is nonuniform, interactions between the mean and fluctuating fields will cause linear mode coupling proportional to the average Mach number. Formally such contributions are included among those discussed in the preceding section, i.e. they are of order $\mu$.

In principle, linear coupling between modes can be formally eliminated by transformation to a new set of modal expansion functions by diagonalizing the matrix of coefficients (Culick 1997). There may be some applications for which the linear coupling should be explicitly treated, but here we assume that either linear coupling is absent on physical grounds or has been eliminated by suitable transformation.

Hence energy transfer between modes is of order $\varepsilon^2$ or higher and is necessarily nonlinear; calculations in the next section show that we can write the system (4.34) schematically in the form

$$\ddot{\eta}_N + \omega_N^2 \eta_N = -\mu \left( D_N \dot{\eta}_N + E_N \eta_N \right) + F_N^{NL} \tag{4.65}$$

The function $F_N^{NL}$ contains all nonlinear processes. According to its development in Section 3 consists of a sum of groups of terms of order $\varepsilon$, $\varepsilon^2$, $\cdots$, $\mu\varepsilon$, $\mu\varepsilon^2$, $\cdots$. In general, $F_N$ cannot be represented by a diagonal matrix: Nonlinear coupling of the modes always exists and, among other consequences, is an important process in the evolution of linear unstable motions into stable limit cycles.

4.5.3. *Zeroth and First Order Solutions to the Oscillator Equation.* We defer to a later section analysis including nonlinear energy transfer of order $\mu\varepsilon$, and we assume that the average temperature is approximately uniform, so the last term of (4.33) is negligible. The problem comes down to solving (4.34) for the $\eta_N(t)$,

$$\ddot{\eta}_N + \omega_N^2 \eta_N = F_N \tag{4.66}$$

with

$$F_N = -\frac{\bar{a}_r^2}{\bar{p}_r E_N^2} \left\{ \iiint_v h\psi_N dV + \oiint_S f\psi_N dS \right\} \tag{4.67}$$

and $h$ and $f$ are given by (3.55) and (3.57):

$$
\begin{aligned}
h = &- \bar{\rho} \left[ \nabla \cdot \left( \bar{\mathbf{M}} \cdot \nabla \mathbf{M}' + \mathbf{M}' \cdot \nabla \bar{\mathbf{M}} \right) - \frac{1}{\bar{a}^2} \frac{\partial}{\partial t} \left( \bar{\mathbf{M}} \cdot \nabla p' + \gamma p' \nabla \cdot \bar{\mathbf{M}} \right) \right] \\
&- \left\{ \bar{\rho} \nabla \cdot \left( \mathbf{M}' \cdot \nabla \mathbf{M}' + \frac{\rho'}{\bar{\rho}} \frac{\partial \bar{\mathbf{M}}'}{\partial t} \right) - \frac{1}{\bar{a}^2} \frac{\partial}{\partial t} \left( \mathbf{M} \cdot \nabla p' + \gamma p' \nabla \cdot \mathbf{M} \right) \right\} \\
&+ \left[ \frac{1}{\bar{\rho}} \nabla \cdot \left( \frac{1}{\bar{\rho}} \boldsymbol{\mathcal{F}}' \right) - \frac{1}{\bar{a}^2} \frac{\partial \boldsymbol{\mathcal{P}}'}{\partial t} \right] + \left\{ \frac{1}{\bar{p}} \nabla \cdot \left( \frac{1}{\bar{\rho}} \boldsymbol{\mathcal{F}}' \right) - \frac{1}{\bar{a}^2} \frac{\partial \boldsymbol{\mathcal{P}}'}{\partial t} \right\}
\end{aligned}
\tag{4.68}
$$

$$f = \bar{\rho} \frac{\partial \mathbf{M}'}{\partial t} \cdot \hat{\mathbf{n}} + \hat{\mathbf{n}} \cdot \left[ \bar{\rho} \mathbf{M}' \cdot \nabla \bar{\mathbf{M}} + \bar{\mathbf{M}} \cdot \nabla \mathbf{M}' \right] + \hat{\mathbf{n}} \cdot \left\{ \bar{\rho} \mathbf{M}' \cdot \nabla \mathbf{M}' + \rho' \frac{\partial \mathbf{M}'}{\partial t} \right\} + [\boldsymbol{\mathcal{F}}'] \cdot \hat{\mathbf{n}} + \{\boldsymbol{\mathcal{F}}'\} \cdot \hat{\mathbf{n}} \tag{4.69}$$

Recall that the left-hand side of (4.55) follows upon inserting in the linear wave operator the modal expansion (4.27) for $p'$;

$$p' = \bar{p}_r \sum_{m=1}^{M} \eta_m(t) \psi_m(\mathbf{r}) \tag{4.70}$$

The iterative procedure is a way of expressing the driving forces $F_N$ in terms of the amplitudes $\eta_m$, so (4.55) becomes a system of equations for the amplitudes. As we have explained earlier (Section 3.3) we use $\varepsilon$ as a

measure of the size of the pressure disturbance and write always

$$p' = \varepsilon p_1(\mathbf{r}_1, t) \tag{4.71}$$

However, we must allow the other dependent variables vary with $\varepsilon$ in a more complicated manner; it is reasonable at this point to assume dependence as a power series in $\varepsilon$:

$$\mathbf{M}' = \varepsilon \mathbf{M}_1 + \varepsilon^2 \mathbf{M}_2 + \cdots$$
$$T' = \varepsilon T_1 + \varepsilon^2 T_2 + \cdots \tag{4.72}$$

and so forth. All components of the fluctuations, $p_1$, $\mathbf{M}_1$, $\mathbf{M}_2$, $\cdots$, $T_1$, $T_2$, $\cdots$ become distorted by the mean flow. That possibility is taken into account by writing

$$p' = \varepsilon p_1 = \varepsilon \left[ p_{10} + \mu p_{11} + \mu^2 p_{12} + \cdots \right]$$
$$\mathbf{M}' = \varepsilon \mathbf{M}_1 + \varepsilon^2 \mathbf{M}_2 + \cdots = \varepsilon \left[ \mathbf{M}_{10}' + \mu \mathbf{M}_{11} + \cdots \right]$$
$$+ \varepsilon^2 \left[ \mathbf{M}_{20}' + \mu \mathbf{M}_{21} + \cdots \right] \tag{4.73}$$
$$T = \varepsilon T_1 + \varepsilon^2 T_2 + \cdots = \varepsilon \left[ T_{10} + \mu T_{11} + \cdots \right]$$
$$+ \varepsilon^2 \left[ T_{20} + \mu T_{21} + \cdots \right]$$

It is apparent that the number of functions to be determined rapidly gets out of hand as more terms are retained in the series expansion. However to the order we choose to investigate here, that difficulty doesn't appear, for the following reason. Examine a typical terms in $h$ say the first in each of the brackets:

$$h = -\bar{\rho} \left[ \nabla \cdot \left( \bar{\mathbf{M}}_1 \cdot \nabla \mathbf{M}' \right) + \cdots \right] - \left\{ \bar{\rho} \nabla \cdot \left( \mathbf{M}' \cdot \nabla \mathbf{M}' \right) + \cdots \right\} + \cdots$$
$$= -\mu \bar{\rho} \nabla \cdot \left[ \bar{\mathbf{M}}_1 \cdot \nabla \left( \varepsilon \mathbf{M}_1' + \varepsilon^2 \mathbf{M}_2' + \cdots \right) + \cdots \right] - \bar{\rho} \left\{ \nabla \cdot \left( \varepsilon \mathbf{M}_1' + \varepsilon^2 \mathbf{M}_2' + \cdots \right) \cdot \nabla \left( \varepsilon \mathbf{M}_1' + \varepsilon^2 \mathbf{M}_2' + \cdots \right) + \cdots \right\} + \cdots$$

Now substitute (4.62) to give

$$h = -\mu \bar{\rho} \nabla \cdot \left[ \bar{\mathbf{M}}_1 \cdot \nabla \left( \varepsilon \mathbf{M}_{10}' + \varepsilon \mu \mathbf{M}_{11}' + \cdots + \varepsilon^2 \mathbf{M}_{20}' + \varepsilon^2 \mu \mathbf{M}_{21}' + \cdots \right) + \cdots \right] =$$
$$- \bar{\rho} \nabla \cdot \left\{ \left( \varepsilon \mathbf{M}_{10} + \varepsilon \mu \mathbf{M}_{11}' + \cdots \right) \cdot \nabla \left( \varepsilon \mathbf{M}_{10}' + \varepsilon \mu \mathbf{M}_{11}' + \cdots \right) + \cdots \right\} + \cdots$$

Multiplying the various brackets and showing explicitly only those terms to be retained, we find

$$h = -\mu \varepsilon \bar{\rho} \nabla \cdot \left[ \bar{\mathbf{M}}_1 \cdot \nabla \mathbf{M}_{10}' + \cdots \right] - \bar{\rho} \nabla \cdot \left\{ \varepsilon^2 \mathbf{M}_{10} \cdot \nabla \mathbf{M}_{10} + \cdots \right\} + \cdots$$

This procedure leads eventually to the forms for $h$ and $f$ with only terms of order $\mu \varepsilon$ and $\varepsilon^2$:

$$h = -\mu \varepsilon \left[ \bar{\rho} \nabla \cdot \left( \bar{\mathbf{M}}_1 \cdot \nabla \mathbf{M}_{10} + \mathbf{M}_{10} \cdot \nabla \bar{\mathbf{M}}_1 \right) - \frac{1}{\bar{a}^2} \frac{\partial}{\partial t} \left( \bar{\mathbf{M}}_1 \cdot \nabla p_{10} + \gamma p_{10} \nabla \cdot \bar{\mathbf{M}}_1 \right) \right]$$
$$- \varepsilon^2 \left\{ \bar{\rho} \nabla \cdot \left( \mathbf{M}_{10} \cdot \nabla \mathbf{M}_{10} + \frac{\rho_{10}}{\bar{\rho}} \frac{\partial \mathbf{M}_{10}}{\partial t} \right) - \frac{1}{\bar{a}^2} \frac{\partial}{\partial t} \left( \mathbf{M}_{10} \cdot \nabla p_{10} + \gamma p_{10} \nabla \cdot \mathbf{M}_{10} \right) \right\} \tag{4.74}$$
$$+ \mu \varepsilon \left[ \frac{1}{\bar{\rho}} \nabla \cdot \left( \frac{1}{\bar{\rho}} \boldsymbol{\mathcal{F}}' \right) - \frac{1}{\bar{a}^2} \frac{\partial \boldsymbol{\mathcal{P}}'}{\partial t} \right] + \varepsilon^2 \left\{ \frac{1}{\bar{\rho}} \nabla \cdot \left( \frac{1}{\bar{\rho}} \boldsymbol{\mathcal{F}}' \right) - \frac{1}{\bar{a}^2} \frac{\partial \boldsymbol{\mathcal{P}}'}{\partial t} \right\}_{\varepsilon^2}$$

$$f = \bar{\rho} \left[ \frac{\partial \mathbf{M}'}{\partial t} \cdot \hat{\mathbf{n}} \right]_{\mu \varepsilon} + \bar{\rho} \left\{ \frac{\partial \mathbf{M}'}{\partial t} \cdot \hat{\mathbf{n}} \right\}_{\varepsilon^2} + \mu \varepsilon \bar{\rho} \hat{\mathbf{n}} \cdot \left[ \mathbf{M}_{10} \cdot \nabla \bar{\mathbf{M}}_1 + \bar{\mathbf{M}}_1 \cdot \nabla \mathbf{M}_{10} \right]$$
$$+ \varepsilon^2 \bar{\rho} \hat{\mathbf{n}} \cdot \left\{ \mathbf{M}_{10} \cdot \nabla \mathbf{M}_{10} \right\} + \mu \varepsilon \left[ \boldsymbol{\mathcal{F}}' \cdot \hat{\mathbf{n}} \right]_{\mu \varepsilon} + \varepsilon^2 \left\{ \boldsymbol{\mathcal{F}}' \cdot \hat{\mathbf{n}} \right\}_{\varepsilon^2} \tag{4.75}$$

## 5. SOME FUNDAMENTALS OF ACOUSTICS

According to the experiences related in Section 1, combustion instabilities may be regarded as unsteady motions closely approximated as classical acoustical motions with perturbations due ultimately to combustion processes. That view, initially an emprical conclusion, motivated the general form of the analytical framework constructed in Section 4. Relatively little knowledge of classical acoustics is required to understand and apply that construction formally.

However, interpretation of the details of observed behavior, and effective use of the theory to develop accurate representations of actual motions in combustors require firm understanding of the fundamentals of acoustics. The purpose of this section is to provide a condensed summary of the basic parts of the subject most relevant to the main subject of this book. We therefore ignore those processes distinguishing combustion chambers from other acoustical systems. Except for brief discussion of nonlinear gas dynamics, we restrict attention to the Problem O defined in Sections 3.3.3 and 3.4.

**5.1. The Linearized Equations of Motion; The Velocity Potential.** We will be concerned here with unsteady motions in a pure non-reacting gas at rest. The governing equations are 3.40 for Problem O, Classical Acoustics, leading to the corresponding wave equation and its boundary condition, equations 3.52 with $h_0$ and $f_0$ given by 3.55 for constant average density $\bar{\rho}$ and written with dimensional variables:

$$\nabla^2 p' - \frac{1}{\bar{a}^2}\frac{\partial^2 p'}{\partial t^2} = \nabla \cdot \boldsymbol{\mathcal{F}}' - \frac{1}{\bar{a}^2}\frac{\partial \mathcal{P}'}{\partial t}$$

$$\hat{\mathbf{n}} \cdot \nabla p' = -\bar{\rho}\frac{\partial \mathbf{u}'}{\partial t} \cdot \hat{\mathbf{n}} - \boldsymbol{\mathcal{F}}' \cdot \hat{\mathbf{n}}$$

(5.1) a,b

In the absence of condensed material, the definitions (A.18) and (A.20) of the unperturbed functions $\boldsymbol{\mathcal{F}}$ and $\mathcal{P}$ are:

$$\boldsymbol{\mathcal{F}} = \nabla \cdot \overset{\leftrightarrow}{\boldsymbol{\tau}}_v + \mathbf{m}_e - \mathbf{u}w_e \tag{5.2}$$

$$\mathcal{P} = \frac{R}{C_v}\left[\overset{\leftrightarrow}{\boldsymbol{\tau}}_v \cdot \nabla \cdot \mathbf{u} - \nabla \cdot \mathbf{q} - Q_e\right] + RTw_e \tag{5.3}$$

where

$\overset{\leftrightarrow}{\boldsymbol{\tau}}_{\boldsymbol{v}}$ : viscous stress tensor (force/area)

$\mathbf{q}$ : rate of conductive heat transfer (energy/area-s)

$\mathbf{m}_e$ : rate of momentum addition by external sources (mass-velocity/volume-s)

$w_e$ : rate of mass addition by external sources (mass/volume-s)

$Q_e$ : rate of energy addition by external sources (energy/volume-s)

Thus the function $\boldsymbol{\mathcal{F}}$ contains all processes causing changes of momentum of the gas, except for that due to internal pressure differences; and $\mathcal{P}$ represents all sources of energy addition. The linearized forms of the source terms will be constructed as required for specific problems. For most of this section we will treat only problems for which $h_0$ and $f_0$ vanish, giving the simplest equations for classical acoustics,

$$\nabla^2 p' - \frac{1}{\bar{a}^2}\frac{\partial^2 p'}{\partial t^2} = 0$$

$$\hat{\mathbf{n}} \cdot \nabla p' = 0$$

(5.4) a,b

With no sources in the volume or on the boundary, motions exist only for initial value problems in which the pressure and its time derivative are specified at some initial time, $t_0$.

In this case, the wave equation is used to describe freely propagating waves following an initial disturbance or, when the boundary condition (5.13)b is enforced, the normal modes for a volume enclosed by a rigid boundary. The condition $\hat{\mathbf{n}} \cdot \nabla p' = 0$ means that the velocity normal to the boundary is zero, because the acoustic velocity is computed from the acoustic momentum (3.40)b written in dimensional form with $\boldsymbol{\mathcal{F}} = 0$:

$$\bar{\rho}\frac{\partial \mathbf{u}'}{\partial t} = -\nabla p' \tag{5.5}$$

so

$$\hat{\mathbf{n}} \cdot \nabla p' = \bar{\rho} \frac{\partial \mathbf{u}'}{\partial t}$$

from which

$$\frac{\partial}{\partial t} \left( \hat{\mathbf{n}} \cdot \mathbf{u}' \right) = -\frac{1}{\bar{\rho}} \hat{\mathbf{n}} \cdot \nabla p' = 0 \tag{5.6}$$

Hence $\hat{\mathbf{n}} \cdot \mathbf{u}' = 0$ always

We have just derived the equations for classical acoustics by specializing the general equations of unsteady motion. It is also useful to arrive at the same conclusion in a slightly different way, beginning with the equations for inviscid motion in a homogeneous medium:

$$\textit{Conservation of Mass}: \qquad \frac{\partial \rho}{\partial t} + \nabla \cdot (\rho \mathbf{u}) = 0 \tag{5.7}$$

$$\textit{Conservation of Momentum}: \qquad \rho \frac{\partial \mathbf{u}}{\partial t} + \rho \mathbf{u} \cdot \nabla \mathbf{u} + \nabla p = 0 \tag{5.8}$$

$$\textit{Conservation of Energy}: \qquad \rho \frac{\partial}{\partial t} \left( e + \frac{1}{2} u^2 \right) + \rho \mathbf{u} \cdot \nabla \left( e + \frac{1}{2} u^2 \right) + \nabla \cdot (p \mathbf{u}) = 0 \tag{5.9}$$

$$\textit{Equation of State}: \qquad p = \rho R T \tag{5.10}$$

Remove the kinetic energy from the energy equation by subtracting $\mathbf{u} \cdot$ (momentum equation) to give

$$\rho \frac{De}{Dt} + p \nabla \cdot \mathbf{u} = 0 \tag{5.11}$$

where $\frac{D}{Dt} = \frac{\partial(\ )}{\partial t} + \mathbf{u} \cdot \nabla(\ )$. Because all irreversible processes have been ignored the entropy of a fluid element remains constant, $\frac{Ds}{Dt} = 0$, a result that follows directly by substituting the mass and energy equations in the thermodynamic definition of the entropy of an element:

$$\rho \frac{Ds}{Dt} = \rho \frac{De}{Dt} - \frac{p}{\rho} \frac{D\rho}{Dt} = -p \nabla \cdot \mathbf{u} + \frac{p}{\rho} \left( \rho \nabla \cdot \mathbf{u} \right) = 0 \tag{5.12}$$

Taking the density to be a function of pressure and entropy, we can write for an isentropic process

$$d\rho = \left( \frac{\partial \rho}{\partial s} \right)_p ds + \left( \frac{\partial \rho}{\partial p} \right)_s dp = \left( \frac{\partial \rho}{\partial p} \right)_s dp = \frac{1}{a^2} dp \tag{5.13}$$

where

$$a^2 = \left( \frac{\partial \rho}{\partial p} \right)_s \tag{5.14}$$

will turn out to be the speed of propagation of small disturbances, the 'speed of sound'. With this definition, we can rewrite the continuity equation (5.7) for the pressure:

$$\frac{\partial p}{\partial t} + \rho a^2 \nabla \cdot \mathbf{u} + \mathbf{u} \cdot \nabla p = 0 \tag{5.15}$$

This result is quite general: in particular, its derivation did not involve using the special characteristics of a perfect gas.

Alternatively, we may derive this equation for the special case of a perfect gas for which $de = C_v(T)dT$ and the equation of state is (5.10). Add $T$ times (5.7) to $C_v^{-1}$ times (5.11) with $de = C_v dT$; then use (5.10) to find

$$\frac{\partial p}{\partial t} + \left( 1 + \frac{R}{C_V} \right) p \nabla \cdot \mathbf{u} + \mathbf{u} \cdot \nabla p = 0 \tag{5.16}$$

But $R = C_p - C_v$, so $R/C_v = \gamma - 1$ for a perfect gas. Comparison of (5.14) and (5.15) gives the formula for the speed of sound in a perfect gas:

$$a^2 = \sqrt{\frac{\gamma p}{\rho}} = \sqrt{\gamma R T} \tag{5.17}$$

For an isentropic process of a perfect gas, equation (5.13) can be integrated,

$$d\rho = a^2 dp = \frac{\rho}{\gamma p} dp$$

which gives

$$p = p_0 \left( \frac{\rho}{\rho_0} \right)^\gamma \tag{5.18}$$

where $\rho_0$, $p_0$ are constant reference values.

We may now eliminate the density from the momentum equation (5.8) to find

$$\frac{\partial \mathbf{u}}{\partial t} + \mathbf{u} \cdot \nabla \mathbf{u} + \frac{1}{\rho_0} \left( \frac{p_0}{p} \right)^{1/2} \nabla p = 0 \tag{5.19}$$

Finally, we obtain the wave equation for the pressure by differentiating (5.16) with respect to time and substituting (5.19) and $a^2 = \gamma p / \rho$:

$$\frac{\partial^2 p}{\partial t^2} - a_0^2 \frac{p}{p_0} \nabla \cdot \left[ \frac{\nabla p}{(p/p_0)^{1/\gamma}} \right] = \gamma p \nabla \cdot (\mathbf{u} \cdot \nabla \mathbf{u}) - \gamma \frac{\partial p}{\partial t} \nabla \cdot \mathbf{u} - \frac{\partial}{\partial t} (\mathbf{u} \cdot \nabla p) \tag{5.20}$$

The boundary condition is defined by taking the component of (5.19) normal to the boundary:

$$\hat{\mathbf{n}} \cdot \nabla p = - \left( \frac{p}{p_0} \right)^{1/2} \rho_0 \left[ \hat{\mathbf{n}} \cdot \frac{\partial \mathbf{u}}{\partial t} + \hat{\mathbf{n}} \cdot \nabla (\mathbf{u} \cdot \nabla \mathbf{u}) \right] \tag{5.21}$$

Equation (5.20) and its boundary condition are easily linearized by assuming that the gas is at rest and that the fluctuations are all of the same order. To second order in the fluctuations we find

$$\frac{\partial^2 p'}{\partial t^2} - a_0^2 \nabla^2 p' = \left\{ p_0 \nabla \cdot (\mathbf{u}' \cdot \nabla \mathbf{u}') - \gamma \frac{\partial p'}{\partial t} \nabla \cdot \mathbf{u}' - \frac{\partial}{\partial t} (\mathbf{u}' \cdot \nabla p') \right\}$$
$$+ \rho_0 \left\{ (\gamma - 1) \left( \frac{p'}{p_0} \right) \nabla^2 \left( \frac{p'}{p_0} \right) - \left( \nabla \frac{p'}{p_0} \right)^2 \right\} \tag{5.22}$$

$$\hat{\mathbf{n}} \cdot \nabla p' = -\rho_0 \frac{\partial \mathbf{u}'}{\partial t} \cdot \hat{\mathbf{n}} - \rho_0 \left\{ \frac{1}{\gamma} \left( \frac{p'}{p_0} \right) \frac{\partial \mathbf{u}'}{\partial t} \cdot \hat{\mathbf{n}} + \hat{\mathbf{n}} \cdot (\mathbf{u}' \cdot \nabla \mathbf{u}') \right\} \tag{5.23}$$

Equations (5.4) a,b are recovered when the second order terms are neglected.

5.1.1. *The Velocity Potential.* It is often convenient to introduce scalar and vector potentials $\Phi$ and $\mathbf{A}$ from which the velocity is found by differentiation:

$$\mathbf{u} = -\nabla \Phi + \nabla \times \mathbf{A} \tag{5.24}$$

With this representation, the dilation and curl (rotation) of the velocity field are separated:

$$\nabla \cdot \mathbf{u}' = -\nabla^2 \Phi ; \quad \nabla \times \mathbf{u}' = \nabla \times \nabla \times \mathbf{A} \tag{5.24}$$

In general, both potentials are required if the mean velocity is non-zero or sources are present in the flow. The boundary conditions may also induce non-zero rotational flow. Here only the scalar potential is required for small amplitude motions because in that limit, the classical acoustic momentum is (5.5); taking the curl with uniform average density gives

$$\bar{\rho} \frac{\partial}{\partial t} (\nabla \times \mathbf{u}') = -\nabla \times (\nabla p') = 0$$

Hence if $\nabla \times \mathbf{u}' = 0$ initially, it remains so and we can take $\mathbf{A} = 0$.

The acoustic equations for momentum, 3.40 and 3.40 in dimensional variables are

$$\frac{\partial \mathbf{u}'}{\partial t} + \frac{1}{\bar{\rho}} \nabla p' = 0$$
$$\frac{\partial p'}{\partial t} + \gamma \bar{\rho} \nabla \cdot \mathbf{u}' = 0 \tag{5.25 a,b}$$

Differentiate the first with respect to time and insert the second to give the wave equation for the velocity fluctuation,

$$\frac{\partial^2 \mathbf{u}'}{\partial^2} - \bar{a}^2 \nabla^2 \mathbf{u} = 0 \tag{5.26}$$

Now substitute $\mathbf{u}' = -\nabla\Phi$ to give

$$\nabla \left[ \frac{\partial^2 \Phi}{\partial t^2} - \bar{a}^2 \nabla^2 \Phi \right] = 0$$

which is satisfied if the terms in brackets are a function of time only, so

$$\frac{\partial^2 \Phi}{\partial t^2} - \bar{a}^2 \nabla^2 \Phi = f(t) \tag{5.27}$$

The right-hand side represents a source field for the potential, uniform over all space. We may absorb $f(t)$ by defining a new potential $\Phi_1 = \Phi + \int^t dt' \int^{t'} f(t_1) dt_1$ and relabel $\Phi_1 \to \Phi$ to find[18] the wave equation for $\Phi$:

$$\frac{\partial^2 \Phi}{\partial t^2} - \bar{a}^2 \nabla^2 \Phi = 0 \tag{5.28}$$

When the velocity potential is used, the acoustic velocity is calculated with (5.24) and $\mathbf{A} = 0$

$$\mathbf{u}' = -\nabla\Phi \tag{5.29}$$

The acoustic pressure is found by setting $\mathbf{u}' = -\nabla\Phi$ in the momentum equation (5.25) a,b, giving

$$\nabla \left( -\frac{\partial \Phi}{\partial t} + \frac{1}{\bar{\rho}} p' \right) = 0$$

This solution is satisfied if the terms in parentheses are a function of $t$ only, $g(t)$, so

$$p' = \bar{\rho} \left( \frac{\partial \Phi}{\partial t} + g(t) \right) \tag{5.30}$$

As above, we may define a new potential $\Phi(t) + \int^t g(t')dt' = \Phi_1(t)$ and hence absorb $g(t)$ so we may redefine $\Phi_1 \to \Phi$ and

$$p' = \bar{\rho}\frac{\partial \Phi}{\partial t} \tag{5.31}$$

The conditions under which the acoustic field can be completely described by a velocity potential alone are precise and, so far as problems involving combustion are concerned, very restrictive. Any analysis or theory based on the velocity potential alone must also include demonstration that the vector potential can be ignored, i.e. set equal to a constant or zero. In general, the presence of a non-uniform mean flow field and various kinds of sources in the problems we are concerned with in this work, require that the velocity field be derived from both scalar and vector potentials. Use of the unsteady pressure as the primary flow variable provides a simpler approach for many purposes, but, as we will find later, apparently possesses unavoidable fundamental limitations.

**5.2. Energy and Intensity Associated with Acoustic Waves.** In this section we establish definitions of energy density and the intensity—i.e. the flow of energy—for classical acoustic waves. The definitions are only approximate under the more complicated conditions existing in a combustor but the general ideas remain.

Following Landau and Lifschitz (1959) we return to the basic energy equation (5.9) for inviscid flow. The idea is to establish a connection between the rate of change of something (the energy) within a volume and the flow of something (the intensity) through the closed boundary of that volume. Integrate the energy equation over a volume fixed in space; and apply Gauss' theorem to the terms on the right-hand side:

$$\frac{\partial}{\partial t} \int \rho \left( e + \frac{u^2}{2} \right) dV = -\int \nabla \cdot \left[ \rho \mathbf{u} \left( e + \frac{u^2}{2} \right) \right] dV - \int \nabla \cdot (\rho \mathbf{u}) dV$$

$$= -\oiint \left( e + \frac{u^2}{2} \right) \rho \mathbf{u} \cdot d\mathbf{S} - \oiint \rho \mathbf{u} \cdot d\mathbf{S}$$

---

[18]Alternatively, one can reason that when the velocity is found by taking the gradient of $\Phi + \iint f$, the term in $f$ contributes nothing and hence can be simply dropped. The desired solution is unaffected by setting $f = 0$.

This relation must be written to second order in the isentropic fluctuations; for example,

$$\rho e = \bar{\rho}\bar{e} + \rho'\left[\frac{\partial}{\partial\rho}(\rho e)\right]_{\bar{\rho}} + \frac{1}{2}\rho^{'2}\left[\frac{\partial^2(\rho e)}{\partial\rho^2}\right]_{\bar{\rho}\bar{e}} + \dots$$

$$= \bar{\rho}\bar{e} + \rho'\bar{k} + \frac{1}{2}\frac{\rho^{'2}}{\bar{\rho}\bar{a}^2} + \dots$$

Eventually the result is

$$\frac{\partial}{\partial t}\int \mathcal{E}dV = -\oiint \mathcal{E}\mathbf{u}\cdot d\mathbf{S} - \oiint p'\mathbf{u}'\cdot d\mathbf{S} \qquad (5.32)$$

where

$$\mathcal{E} = \frac{1}{2}\frac{p^{'2}}{\bar{\rho}\bar{a}^2} + \frac{1}{2}\bar{\rho}u^{'2} \qquad (5.33)$$

is the acoustic energy per unit volume and $p'\mathbf{u}'$ is the **intensity**, the flux of acoustic energy through an area normal to the direction of propagation (energy/area-S).

The first term on the right-hand side of (5.32) is third order in the fluctuations and must be dropped. Hence we have the important result interpreted in Figure 5.1.

$$\frac{\partial\mathcal{E}}{\partial t} + \nabla\cdot(p'\mathbf{u}') = 0$$
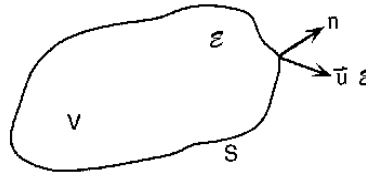


FIGURE 5.1. Acoustic Energy and Intensity

Table 5.1 summarizes the basic properties of plane sinusoidal waves. Brackets $\langle\ \ \rangle$ denote time averages over some interval $\tau$

$$\langle(\ \ )\rangle = \frac{1}{\tau}\int_T^{t+\tau}(\ \ )dt' \qquad (5.34)$$

**5.3. The Growth or Decay Constant.** In practice, due to natural dissipative processes, freely propagating waves and oscillations in a chamber will decay in space and time if there is no external source or energy. If there is an internal source of energy, waves may be unstable, having amplitudes increasing in time. The basic measure of the growth or decay of waves is the constant appearing in the exponent describing the sinusoidal spatial and temporal dependence of small amplitude waves, the definitions (5.62). For 'standing' or 'stationary' waves in a chamber, the wavelength, and hence wavenumber, is real and constant, but the frequency is complex:

$$\omega \rightarrow \omega + i\alpha \qquad (5.35)$$

and the variables of the motion have the behavior in time

$$e^{-i(\omega+i\alpha)t} \equiv e^{-i\omega t}e^{\alpha t} \qquad (5.36)$$

For this definition (5.34), $\alpha < 0$ means that the waves decay.

Normally in practice, $\left|\frac{\alpha}{\omega}\right| \ll 1$, implying that the fractional change of amplitude is small in one cycle of the oscillation. Thus when time averaging is carried out over one or a few cycles, $e^{\alpha t}$ may be taken as roughly constant, and the average energy density computed with (5.32) and (5.33), is

$$\langle\mathcal{E}\rangle = e^{2\alpha t}\frac{1}{4}\left[\frac{|\hat{p}|^2}{\bar{\rho}\bar{a}^2} + \bar{\rho}|\hat{u}|^2\right] \qquad (5.37)$$

TABLE 5.1.

Results for Rightward and Leftward Traveling Sinusoidal Waves

| Wave to Right | Wave to Left |
|---|---|
| $p'_+ = \hat{p}_+ e^{-i(\omega t - kx)}$ | $p'_- = \hat{p}_- e^{-i(\omega t + kx)}$ |
| $u'_+ = \hat{p}_+ e^{-i(\omega t - kx)}$ | $u'_- = \hat{u}_- e^{-i(\omega t + kx)}$ |
| $\hat{u}_+ = \frac{\hat{p}_+}{\rho_0 a_0}$ | $\hat{u}_- = -\frac{\hat{p}_-}{\rho_0 a_0}$ |
| $\varepsilon_+ = \frac{p'^2_+}{\rho_0 a_0}$ | $\varepsilon_- = \frac{p'^2_-}{\rho_0 a_0}$ |
| $l_+ = p'_+ u'_+ = \frac{p'^2_+}{\rho_0 a_0}$ | $l_- = p'_- u'_- = -\frac{p'^2_-}{\rho_0 a_0^2}$ |

$$\langle (\quad) \rangle = \frac{1}{\tau} \int_t^{t+\tau} (\quad) dt'$$

| | |
|---|---|
| $\langle p'^2_+ \rangle = \frac{1}{2}\hat{p}^2_+$ | $\langle p'^2_- \rangle = \frac{1}{2}\hat{p}^2_-$ |
| $\langle \varepsilon_+ \rangle = \frac{\hat{p}^2_+}{2\rho_0 a_0^2}$ | $\langle \varepsilon_- \rangle = \frac{\hat{p}^2_-}{2\rho_0 a_0^2}$ |
| $\langle l_+ \rangle = \frac{\hat{p}^2_+}{2\rho_0 a_0}$ | $\langle l_- \rangle = \frac{p^2_-}{2\rho_0 a_0}$ |

More generally: $p' = \hat{p} e^{i(\omega t + \varphi)}$ ; $\bar{u}' = \hat{\mathbf{u}} e^{i(\omega t + \varphi)}$

$$\langle \varepsilon \rangle = \frac{1}{4}\left[ \frac{|\hat{p}|^2}{\rho_0 a_0^2} + \rho_0|\hat{u}|^2 \right] = \frac{1}{4}(p'p'^* + \rho_0 \mathbf{u}' \cdot \mathbf{u}'^*)$$

$$\langle l \rangle = \frac{1}{2}|\hat{p}||\hat{\mathbf{u}}|\cos(\varphi - \psi) = \frac{1}{4}(p'^*\mathbf{u}' + p'\mathbf{u}'^*)$$

where $(\quad)^*$ denotes complex conjugate.

Hence we have the important interpretations which serve as the basis for measuring values of $\alpha$:

$$\alpha = \frac{1}{|\hat{p}|}\frac{d|\hat{p}|}{dt}$$
$$\alpha = \frac{1}{2\langle \mathcal{E} \rangle}\frac{d\langle \mathcal{E} \rangle}{dt}$$

(5.38) a,b

The sign of $\alpha$ is a matter of definition and has no fundamental significance. If the time dependence is taken to be $e^{i(\omega + i\alpha)t}$ then $\alpha < 0$ means that waves are amplified.

The formulas (5.39) define local values of the growth constant. It is often more meaningful to know the value for the entire volume of the system in question, found by using $\int \langle \mathcal{E} \rangle dV$ rather than $\langle \mathcal{E} \rangle$:

$$\alpha = \frac{1}{2\int\langle \mathcal{E} \rangle dV}\frac{d}{dt}\int \langle \mathcal{E} \rangle dV$$

(5.39)

**5.4. Boundary Conditions: Reflections from a Surface.** In the absence of other sources, the linearized boundary condition on the pressure at a surface is the first term of (5.1 b), here in dimensional form:

$$\hat{\mathbf{n}} \cdot \nabla p' = -\bar{\rho}\frac{\partial \mathbf{u}'}{\partial t} \cdot \hat{\mathbf{n}}$$

(5.40)

The acoustic surface impedance $z_a$ is defined by

$$\mathbf{u}' \cdot \hat{\mathbf{n}} = \frac{1}{z_a} p' \tag{5.41}$$

and the acoustic surface admittance $y_a$ is the reciprocal of the admittance:

$$y_a = \frac{1}{z_a} \tag{5.42}$$

Then for harmonic motions, $p' = \hat{p} e^{-i\omega t}$, we can rewrite (5.40) as

$$\hat{\mathbf{n}} \cdot \nabla p' = -i \frac{\bar{\rho}\omega}{z_a} p' = -i\bar{\rho}\omega y_a p' \tag{5.43}$$

The units of impedance are (pressure/velocity) $\equiv$ (density $\times$ velocity). Hence for the medium, the product $\bar{\rho}\bar{a}$ is called the characteristic impedance, having value 42 g/cm$^2$-s. at standard conditions. Dimensionless forms are defined as:

$$\begin{aligned}\text{acoustic impedance ratio:} \quad & \zeta_a = \frac{z_a}{\bar{\rho}\bar{a}} \\ \text{acoustic admittance ratio:} \quad & \eta_a = \frac{1}{\zeta_a}\end{aligned} \tag{5.44}$$

In general, impedance functions are complex; the real and imaginary parts are called:

$$\begin{aligned}Re(z_a): \quad & \text{acoustic resistance} \\ Im(z_a): \quad & \text{acoustic reactance}\end{aligned} \tag{5.45}$$

From (5.41) and (5.42), the surface admittance is

$$y_a = \frac{\mathbf{u} \cdot \hat{\mathbf{n}}}{p'}$$

and the dimensionless surface admittance ratio is

$$\eta_a = \bar{\rho}\bar{a} y_a = \frac{\bar{\rho}\bar{a}^2}{\bar{p}} \frac{\bar{\mathbf{M}}' \cdot \hat{\mathbf{n}}}{p'/\bar{p}} = \gamma \frac{M'_n}{p'/\bar{p}} \tag{5.46}$$

where $M'_n$ is the fluctuation of the Mach number normal to the surface.

If the surface is impermeable, the velocity at the surface is the velocity of the surface itself. However, if the surface is permeable, or, as for a burning propellant, mass departs the surface, then the impedance and admittance functions are defined in terms of the local velocity fluctuations presented[19] to the acoustic field, no matter what their origin.

Quite generally then, the admittance function represents the physical response of processes at the surface. It is of course an assumption that in response to an impressed pressure fluctuation, the fluctuation of velocity normal to the surface is proportional to the pressure change. Alternative definitions of quantities representing the acoustic boundary condition at a surface will arise when we consider special situations.

5.4.1. *Reflections of Plane Waves at a Surface.* Confinement of waves in a chamber to form modes necessarily involves reflections at the boundary surfaces. In solid propellant rockets the processes causing reflection are complicated, being responsible not only for confining the waves but also are the dominant means for transferring energy to the oscillating field in the chamber. Even at inert surfaces, more than the simple process of reflection is involved. Viscous stresses and heat conduction in the region adjacent to a surface cause dissipation of energy, discussed in Section 5.6.

Here we assume that all activity at the surface can be represented by a complex impedance or admittance function. The calculation follows that discussed by Morse and Ingard (1968). We consider reflection of a planar wave, Figure 5.2, allowing for the possibility of unequal angles of incidence and reflection, and for simplicity we

---

[19]For burning propellants, care must be taken with definition of the surface at which the boundary condition is imposed. Usually the velocity at the 'edge' of the combustion zone in the gas phase is the most convenient choice. Thus the admittance presented to the acoustic field is not that at the burning surface itself.

assume that there is no transmitted wave. The incident wave travels in the direction defined by the unit vector $\hat{\mathbf{k}}_i$ and the wavenumber vector is

$$\mathbf{k} = \frac{2\pi}{\lambda}\hat{\mathbf{k}} \tag{5.47}$$

We can represent the acoustic pressure and velocity in this plane wave by
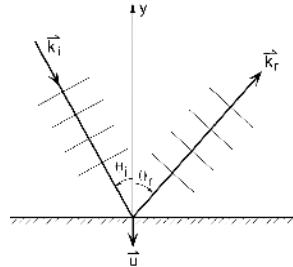


FIGURE 5.2. Reflection of a Plane Wave. Plane waves propagating in direction $\mathbf{k} = \frac{2\pi}{\lambda}\hat{\mathbf{k}}$

$$p'(\mathbf{r};t) = g_i(\mathbf{k}_i \cdot \mathbf{r} - \omega t)$$
$$\mathbf{u}'(\mathbf{r};t) = \frac{\hat{k}_r}{\rho\bar{a}}g_i(\mathbf{k}_i \cdot \mathbf{r} - \omega t) \tag{5.48 a,b}$$

Similar formulas hold for the reflected wave with $\mathbf{k}_i$ replaced by $\mathbf{k}_r$ lying in the direction defined by the unit vector $\hat{\mathbf{k}}_r$. The representations are therefore:

| **Incident Wave** | | | **Reflected Wave** | | |
|---|---|---|---|---|---|
| $p'_i$ | $=$ | $u_i(\xi_i)$ | $p'_r$ | $=$ | $g_r(\xi_r)$ |
| $\mathbf{u}'_i$ | $=$ | $\hat{\mathbf{k}}_i\frac{1}{\rho\bar{a}}g_i(\xi_i)$ | $\mathbf{u}'_r$ | $=$ | $\hat{\mathbf{k}}_r\frac{1}{\rho\bar{a}}g_r(\xi_r)$ |
| $\xi_i$ | $=$ | $\mathbf{k}_i \cdot \mathbf{r} - \omega t$ | $\xi_r$ | $=$ | $\mathbf{k}_r \cdot \mathbf{r} - \omega t$ |
| | $=$ | $k(x\sin\theta_i - y\cos\theta_i) - \omega t$ | | $=$ | $k(x\sin\theta_r - y\cos\theta_r) - \omega t$ |

Because the frequency is the same for the incident and reflected waves, so are the magnitudes of the wavenumbers:

$$|\mathbf{k}_i| = \frac{\omega}{\bar{a}} = |\mathbf{k}_r| \tag{5.49}$$

Reflection is assumed to occur at $y = 0$. By definition of $z_a$, the surface impedance, with the normal velocity outward from the surface equal to $u_y = \mathbf{u} \cdot \hat{\mathbf{j}} = -\mathbf{u} \cdot \hat{\mathbf{n}}$ where $\hat{\mathbf{n}}$ is the unit outward normal vector:

$$z_a = \left(\frac{p'}{u'_y}\right)_{y=0} = \bar{\rho}\bar{a}\frac{g_i(kx\sin\theta_i - \omega t) + g_r(kx\sin\theta_r - \omega t)}{\cos\theta_i g_i(kx\sin\theta_i - \omega t) - \cos\theta_r g_r(kx\sin\theta_r - \omega t)} \tag{5.50}$$

In general $z_a$ is variable along the surface. Suppose that in fact $z_a$ is constant, independent of $x$. That can be true if

$$\theta_i = \theta_r = \theta$$
$$g_r(\xi) = \beta g_i(\xi) \tag{5.51}$$

Then (5.50) becomes

$$z_a \cos\theta = \bar{\rho}\bar{a}\frac{1+\beta}{1-\beta} \tag{5.52}$$

and the complex reflection coefficient $\beta$ is related to the surface impedance by

$$\beta = \frac{z_a \cos\theta - \bar{\rho}\bar{a}}{z_a \cos\theta + \bar{\rho}\bar{a}} \tag{5.53}$$

This result is special because no transmitted wave has been accounted for. For example, if $z_a = \bar{\rho}\bar{a}$—perfect impedance matching exists at the interface—(5.52) gives $\beta = 0$ when $\theta = 0$, so there is no reflected wave. That is true in one sense because in physical terms $z_a = \bar{\rho}\bar{a}$ means that the same gas exists in both sides of the interface. Thus we are simply describing wave propagation in a continuous medium. On the other hand, the physical picture treated here accommodates no transmitted wave, which means that when there is no reflection, processes must exist at the interface providing perfect absorption.

Now suppose $\theta \neq 0$ but $z_a = \bar{\rho}\bar{a}$. Then (5.52) gives $\beta$ non-zero, i.e. partial absorption and some of the incident wave is reflected.

**5.5. Wave Propagation in Tubes; Normal Modes.** The simplest form of combustor is a straight tube, having generally non-uniform cross-section and not necessarily axisymmetric. Although the changes of cross-section may be abrupt—even discontinuous—experience has shown that good results may be obtained by assuming that the velocity fluctuations are uniform at every section and parallel to the axis: the flow is treated as one-dimensional. The governing equations are given in Appendix B, equations (B.2)–(B.4) with no sources:

$$\text{Conservation of Mass}: \qquad \frac{\partial\rho'}{\partial t} + \frac{\partial}{\partial x}(\bar{\rho}u'S_c) = 0 \tag{5.54}$$

$$\text{Conservation of Momentum}: \qquad \bar{\rho}\frac{\partial u'}{\partial t} + \frac{\partial p'}{\partial x} = 0 \tag{5.55}$$

$$\text{Conservation of Energy}: \qquad \bar{\rho}C_v\frac{\partial T'}{\partial t} + \bar{p}\frac{1}{S_c}\frac{\partial}{\partial x}(u'S_c) = 0 \tag{5.56}$$

The wave equation for the pressure is:

$$\frac{1}{S_c}\frac{\partial}{\partial x}\left(S_c\frac{\partial p'}{\partial x}\right) - \frac{1}{\bar{a}^2}\frac{\partial^2 p'}{\partial t^2} = 0 \tag{5.57}$$

5.5.1. *Waves in Tubes.*

### (a) Normal Modes for a Tube Closed at Both Ends

Results for a tube closed at both ends not only contain many ideas basic to general oscillations in chambers, but also are widely useful for practical applications. For a tube closed by rigid walls, the boundary conditions at the ends are that the velocity must vanish. The momentum equation (5.54) then states that acceleration and therefore the pressure gradient must vanish at the ends for all time:

$$\frac{\partial p'}{\partial x} = 0 \qquad x = 0, L; \quad \text{all } t \tag{5.58}$$

General linear motions within the tube can be constructed as superpositions of *normal modes* defined in general by two properties:

    (i) sinusoidal variations in time

    (ii) the motion at any point bears always a fixed phase relation with that at any other point in the volume

Those conditions imply here that the pressure can be expressed as

$$p'(x;t) = \hat{p}(x)e^{-i\bar{a}kt} \qquad (5.59)$$

where $k$ is the complex wavenumber, related in general to the complex frequency by the formula

$$\bar{a}k = \omega + i\alpha \qquad (5.60)$$

Because there are no dissipative processes in this problem, $\alpha = 0$ so the wavenumber is real. Substitution of (5.59) in (5.57) with $S$ independent of $x$ gives

$$\frac{d^2\hat{p}}{dx^2} + k^2\hat{p} = 0 \qquad (5.61)$$

A solution to (5.61) satisfying (5.58) at $x = 0$ is $\hat{p} = A\cos kx$. To satisfy the condition at $x = L$, $\cos kL = 0$. Then $k$ can assume only certain values $k_l$, called *characteristic* or *eigen* values:[20]

$$k_l = l\frac{\pi}{L} \qquad (l = 0, 1, 2, \cdots) \qquad (5.62)$$

Corresponding to each $k_l$ is a *characteristic function,* or *eigenfunction,*

$$\frac{\hat{p}_l}{\bar{p}_0} = A_l\cos(k_l x) \qquad (5.63)$$

For the problems we treat in this book, the motions represented by the $k_l$, $\hat{p}_l$, and $\hat{u}_l$ are usually called *normal modes,* $\bar{a}k_l = \omega_l$ being the *normal* or *modal frequency,* and $\hat{p}_l$, $\hat{u}_l$ are the *mode shapes* of pressure and velocity. All of these terms are used for two- and three-dimensional motions as well.

A normal mode is characterized by its frequency and the spatial distributions, or 'shapes' of all dependent variables. The mode shape for the velocity is derived from the mode shape (5.63) by integrating the acoustic momentum equation (5.55) written for $\hat{u}_l$:

$$-i\bar{a}k_l\hat{u}_l = -\frac{1}{\bar{\rho}}\frac{d\hat{p}_l}{dx} = \frac{k_l}{\bar{\rho}}\bar{p}_l A_l\sin k_l x$$

Thus

$$\hat{u}_l = i\frac{\bar{p}_l}{\bar{\rho}\bar{a}}A_l\sin k_l x \qquad (5.64)$$

or, written as the Mach number of the mode,

$$\hat{M}_l = i\frac{1}{\gamma}A_l\sin k_l x \qquad (5.65)$$

### (b) Normal Modes for a Tube Open at Both Ends

In this case, the pressure is assumed fixed at the ends, for example because the tube is immersed in a large reservoir having constant pressure, and $p' = 0$. For isentropic motions, $\frac{\rho'}{\bar{\rho}} = \frac{1}{\gamma}\frac{p'}{\bar{p}}$ so $\rho' = \frac{1}{\bar{a}^2}p'$ and the continuity equation (5.54) is

$$\frac{\partial p'}{\partial t} + \frac{\bar{a}^2}{\bar{\rho}}\frac{\partial u'}{\partial x} = 0 \qquad (5.66)$$

Hence if $p'$ is fixed, the velocity gradient must vanish at the ends. Set $p' = Ae^{-i\bar{a}kt}\sin kx$ and substitute in (5.66)

$$i\frac{\bar{a}}{\bar{p}}kAe^{-i\bar{a}kt}\sin kx = -\frac{\bar{a}^2}{\bar{\rho}}\frac{\partial u'}{\partial x}$$

---

[20]Only for $l \geq 1$ do we find wave modes. For $l = 0$, a qualitatively different mode exists for which the pressure is uniform in the volume but pulsates at a frequency well below that for the fundamental wave mode. The velocity is practically zero and the oscillator is sustained by some sort of external action. A prosaic example is the low frequency sound one can create by blowing across the narrow opening at the neck of a bottle. In this case the mode is called the *Helmholtz mode* and the bottle is behaving as a *Helmholtz resonator.*

The left-hand side vanishes (and hence $\partial u'/\partial x = 0$) at $x = 0$ for any $k$, but at $x = L$, we must have $\sin k_l L = 0$. Hence $k_l = (2l + 1)\frac{\pi}{L}$ and the normal mode shape and frequency are

$$\frac{\hat{p}_l}{\bar{p}} = A_l \sin(k_l x) \quad ; \qquad k_l = l\frac{\pi}{L} \quad (l = 1, 2, \cdots) \tag{5.67}$$

and the mode shape for the velocity is

$$\frac{\hat{u}_l}{\bar{a}} = \hat{M}_l = i\frac{1}{\gamma} A_l \cos k_l x \tag{5.68}$$

### (c) Normal Modes for a Tube Closed at One End and Open at the Other

Reasoning similar to the above leads in this case to the normal modes when the tube is closed at $x = 0$:

$$\frac{\hat{p}_l}{\bar{p}} = A_l \cos(k_l x) \quad ; \qquad \left( k_l = (2l + 1)\frac{\pi}{2L} \right) \quad (l = 1, 2, \cdots)$$

$$\frac{\hat{u}_l}{a} = -i\frac{1}{\gamma} A_l \sin(k_l x)$$

5.5.2. *Normal Modes for Tubes Having Discontinuities of Cross-Sectional Area.* Combustors having discontinuous area distributions are commonly used in solid propellant rockets and in various laboratory devices. Consider the example sketched in Figure 5.3. The boundary conditions at the ends are:

$$x = 0 : \qquad \frac{d\hat{p}}{dx} = 0$$
$$x = \beta L : \qquad \hat{p} = 0 \tag{5.69 a,b}$$
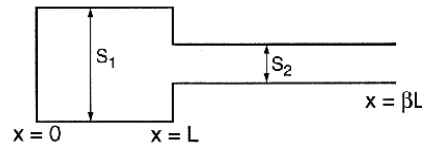


FIGURE 5.3. A Uniform Tube Having a Single Discontinuity.

Possible solutions in the regions to the left and right of the discontinuity are:

$$\frac{\hat{p}}{\bar{p}} = A \cos kx \qquad (0 \le x \le L)$$
$$\frac{\hat{p}}{\bar{p}} = B \sin k(\beta L - x) \qquad (L < x \le \beta L) \tag{5.70 a,b}$$

Note that $k = \omega/\bar{a}$ is the same throughout the tube because the motion occurs everywhere at the same frequency.

Completing the problem comes down to determining the conditions for matching the solutions. Two are required:

(i) continuity of pressure:

$$\lim_{\varepsilon \to 0} [\hat{p}(L - \varepsilon) - \hat{p}(L + \varepsilon)] = 0$$

which gives

$$A \cos kL = B \sin(\beta - 1)kL \tag{5.71}$$

(ii) continuity of acoustic mass flow:

Integrate the wave equation (for harmonic motions) across the discontinuity,

$$\int_{L-\varepsilon}^{L+\varepsilon} \left[ \frac{d}{dx}(S_c \frac{d\hat{p}}{dx} + k^2 S_c \hat{p} \right] dx = 0$$

Because $\hat{p}$ is continuous, this relation becomes

$$\lim_{\varepsilon \to 0} \left[ \left( S_c \frac{d\hat{p}}{dx} \right)_{L+\varepsilon} - \left( \frac{d\hat{p}}{dx} \right)_{L-\varepsilon} \right] = 0$$

Thus, with $\bar{\rho}$ constant and $\frac{d\hat{p}}{dx} \sim \hat{u}$:

$$(\bar{\rho} S_c \hat{u})_{L+\varepsilon} - (\bar{\rho} S_c \hat{u})_{L-\varepsilon} \tag{5.72}$$

After substituting the waveforms (5.70) a,b, and using (5.71) we find the transcendental equation for the modal wavenumbers:

$$\frac{S_1}{S_2} \tan k_l L = \cot k_l (\beta - 1) L \tag{5.73}$$

This method of solving a problem with discontinuities is only approximate: a practical question is: how large are the errors? To gain some idea of the errors incurred, tests at ambient temperature ('cold flow tests') were carried out by Mathis, Derr and Culick (1973) for the geometry of a T-burner used for measuring the combustion response of burning solid propellants. Results are shown in Figure 5.4. The measured values of both the frequencies and the mode shapes are surprisingly well-predicted by this theory. The principal reason is that the influence of a discontinuity is confined to a relatively small region near the change of area, but the characteristics of the normal modes depend on the motion in the entire volume.
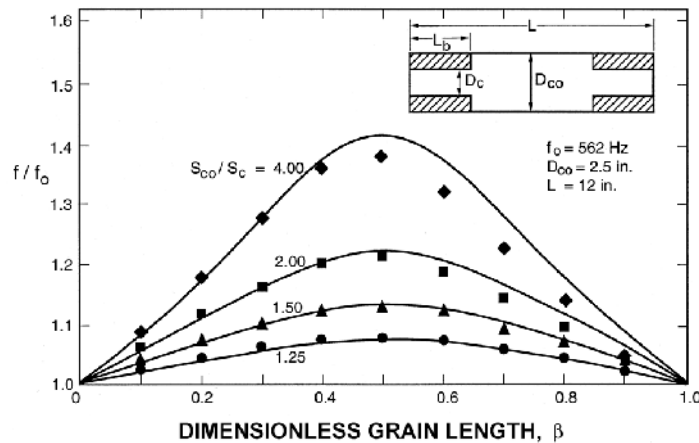


FIGURE 5.4. Comparison of Experimental and Theoretical Results for Normal Frequencies in a T-Burner (Ambient Temperature)

**5.6. Normal Acoustic Modes and Frequencies for a Chamber.** We now consider a volume of any shape enclosed by a rigid boundary and containing a uniform gas at rest. Unsteady small amplitude motions therefore satisfy the linear wave equation (5.4) a,b and its boundary condition ((5.4) a,b)b requiring that the velocity normal to the boundary vanish at all times. By this definition given in Section 5.5.1, normal modes are solutions to this problem which oscillate sinusoidally in time and have fixed phase relations throughout the volume. We assume the form[21] $p' = \psi e^{-i\bar{a}kt}$. The formal problem is to find $\psi$ satisfying the scalar wave equation, also called the Helmholtz wave equation, with vanishing normal gradient at the surface:

$$\nabla^2 \psi + k^2 \psi = 0$$
$$\hat{n} \cdot \nabla \psi = 0 \tag{5.74 a,b}$$

---

[21]Consistent with the general character of this problem, we replace $\hat{p}$ by $\psi$, introducing a common notation for normal modes. The velocity potential $\Phi$ satisfies the same pair of equations, a result reflected by equation (5.31) which for sinusoidal motions means that $p'$ and $\Phi$ are proportional: $p' = i\bar{a}k\bar{\rho}\Phi$.

There are many well-written books covering this problem and its solution, for example Hildebrand (1952), Morse and Feshbach (1952), and Morse and Ingard (1968). The simplest approach is based on the method of separation of variables, applicable for closed form solutions in thirteen coordinate systems; see, e.g., Morse and Feshbach (1952). In practical applications to combustors, only rectangular and circular cylindrical chambers are important.

5.6.1. *Normal Modes for Rectangular Chambers.* The wave equation in Cartesian coordinates is

$$\frac{\partial^2 \psi}{\partial x^2} + \frac{\partial^2 \psi}{\partial y^2} + \frac{\partial^2 \psi}{\partial z^2} + k^2 \psi = 0$$

and $\hat{n} \cdot \nabla \psi$ must vanish on the six flat surfaces each perpendicular to a coordinated axis, Figure 5.5. Applying the method of separation of variables leads to a solution having the form

$$\psi = A \cos(k_x x) \cos(k_y y) \cos(k_z z) \tag{5.75}$$

and

$$k^2 = k_x^2 + k_y^2 + k_z^2 \tag{5.76}$$
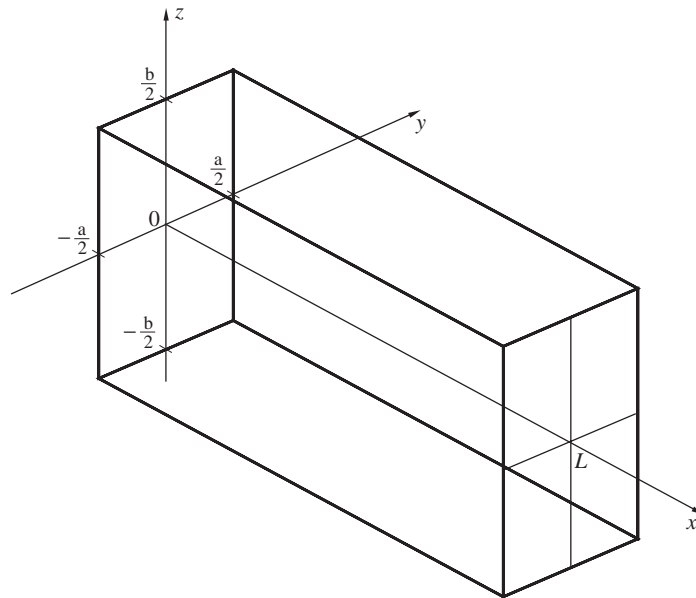


FIGURE 5.5. Rectangular Chamber

The boundary conditions must be satisfied:

$$\frac{\partial \psi}{\partial x} = 0 \qquad x = 0, L$$

$$\frac{\partial \psi}{\partial y} = 0 \qquad y = -\frac{a}{2}, \frac{a}{2} \tag{5.77 a,b,c}$$

$$\frac{\partial \psi}{\partial z} = 0 \qquad z = -\frac{b}{2}, \frac{b}{2}$$

Reasoning similar to that given in Section 5.5.1 leads to the values of the wavenumbers

$$k_x = l\frac{\pi}{L}$$

$$k_y = m\frac{\pi}{b} \tag{5.78 a,b,c}$$

$$k_z = n\frac{\pi}{c}$$

and the mode shapes are

$$\psi_{lmn} = A_{lmn} \cos\left(l\frac{\pi}{L}x\right) \cos m\frac{\pi}{a}\left(y+\frac{a}{2}\right) \cos n\frac{\pi}{b}\left(z+\frac{b}{2}\right) \tag{5.79}$$

The distributions of pressure therefore have the same form in all directions; of course the components (5.78) a,b,c can assume any of the allowed values, and the frequency is given by (5.76), $\omega = \bar{a}k$.

5.6.2. *Normal Modes for a Circular Cylindrical Chamber.* Let $x$ be the polar axis (Figure 5.6) and the wave equation in circular cylindrical coordinates is

$$\frac{1}{r}\frac{\partial}{\partial r}\left(r\frac{\partial\psi}{\partial r}\right) + \frac{1}{r^2}\frac{\partial^2\psi}{\partial\theta^2} + \frac{\partial^2\psi}{\partial x^2} + k^2\psi = 0 \tag{5.80}$$
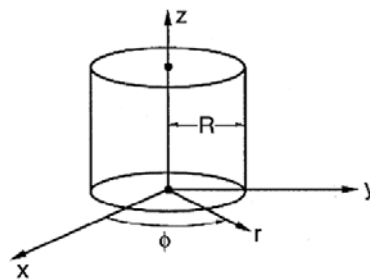


FIGURE 5.6. Circular Cylindrical Coordinates

The boundary condition requires that $\hat{n}\cdot\nabla\psi$ vanish at the ends and on the lateral boundary:

$$\begin{aligned}\frac{\partial\psi}{\partial x} &= 0 & x &= 0, L\\[2mm] \frac{\partial\psi}{\partial r} &= 0 & r &= R\end{aligned} \tag{5.81}$$

Application of the method of separation of variables leads to a solution of the form

$$\psi(r, x, \theta; t) = A \begin{Bmatrix}\cos n\theta\\ \sin n\theta\end{Bmatrix} \cos k_l z\, J_m\left(\kappa_{mn}\frac{r}{R}\right) \tag{5.82}$$

To satisfy the boundary conditions, the values of $k_l$ are integral multiples of $\pi/L$ as above and the $\kappa_{mn}$ are the roots of the derivative of the Bessel function:

$$\frac{dJ_m(\kappa_{mn})}{dr} = 0 \tag{5.83}$$

Figure 5.7 shows the lowest six modes in the transverse planes, and the identifying values of $n$ and $m$. More extended results are given in standard texts and collections of special functions.
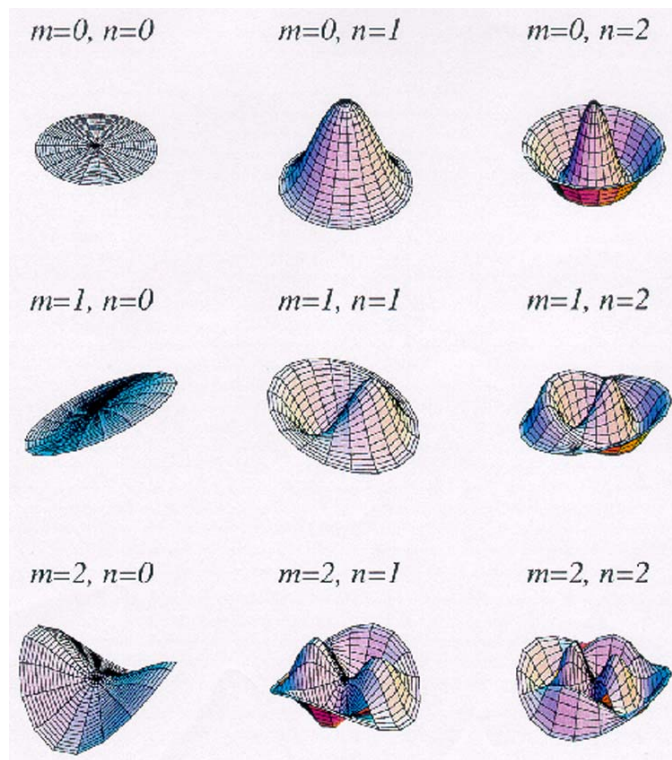
FIGURE 5.7. The First Six Transverse Modes in a Circular Cylinder

## 6. LINEAR STABILITY OF COMBUSTOR DYNAMICS

All problems of unsteady motion in combustion systems can be divided into the two classes: linearized and nonlinear. From the earliest discoveries of their transient behavior until the late 1950s 'combustion instabilities' implied small amplitude unsteady (and unwanted) motions growing out of a condition of linear instability. Even with the expanding awareness that the nonlinear properties must be understood as well, the linear behavior remains an essential part of understanding all aspects of combustion instabilities, including the consequences of nonlinear processes.

The literature of linear combustion instabilities contains many papers dealing with special problems. There seems often to be a tendency to regard the results as somehow disconnected. However, apparent differences arise chiefly from the differences in the processes accounted for and in the choices of models for those processes. So long as the problems are dominated by oscillating behavior in combustors, probably most, if not practically all of the results can be obtained in equivalent forms by suitable applications of the methods explained here. That statement is not as outrageous as it may seem, following as it does from the generality of the expansion procedures and the method of averaging covered in Section 4.

**6.1. Solution for the Problem of Linear Stability.** By 'solution' we mean here formulas for calculating the amplitudes $\eta_n(t)$ of modes retained in the expansion for the pressure field, $p'(\mathbf{r}, t) = \bar{p}\Sigma\eta_n(t)\psi_n(\mathbf{r})$. The amplitudes satisfy the oscillator wave equations (4.36)

$$\frac{d^2\eta_n}{dt^2} + \omega_n^2\eta_n = F_n + F_n^c \tag{6.1}$$

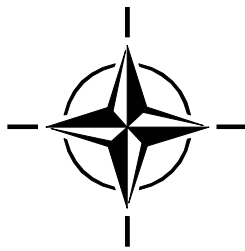where $F_n^c$ stands for the generalized 'force' associated with the exercise of control; and $F_n$ is the spatial average of that part (sometimes called the 'projection' on the basis function $\psi_n$) of the internal processes affecting the motion of the $n^{th}$ oscillator, given by (4.32):

$$F_n = -\frac{\bar{a}^2}{\bar{p}E_n^2}\left\{\int h\psi_n dV + \oiint f\psi_n dS\right\} \tag{6.2}$$

Here we ignore $F_n^c$ because we are concerned only with the internal behavior of the system. In general, the $F_n$ contain contributions associated with the motions of oscillators other than the $n^{th}$—i.e. the modes are coupled. For analysis of linear stability we are justified in ignoring that coupling, for reasons given by Culick (1997). Each $F_n$ is therefore a linear function of the amplitude and velocity of the oscillator, having the form

$$F_n = F_n^\eta\eta_n + F_n^{\dot{\eta}}\frac{d\eta_n}{dt} \tag{6.3}$$

where the $F_n^\eta$ and $F_n^{\dot{\eta}}$ are constants, depending only on the mode.

With these assumptions, the oscillator equations (6.1) are the uncoupled set

$$\frac{d^2\eta_n}{dt^2} - F_n^{\dot{\eta}}\frac{d\eta_n}{dt} + \left(\omega_n^2 - F_n^\eta\right)\eta_n = 0 \tag{6.4}$$

Because the equations are uncoupled, the normal modes $\psi_n$ for the corresponding classical acoustic problem are also the normal modes for the linear problem of combustor dynamics. The general problem of determining linear stability has therefore come down to the problem of determining the stability of the normal modes. In the usual fashion we assume sinusoidal time dependence with complex frequency:

$$\eta_n(t) = \hat{\eta}_n e^{i\Omega t} \tag{6.5}$$

Equation ((5.4) a,b) gives the quadratic equation for $\Omega_n$:

$$\Omega^2 - iF_n^{\dot{\eta}}\Omega + \left(\omega_n^2 - F_n^\eta\right) = 0 \tag{6.6}$$

with solution

$$\Omega = i\frac{1}{2}F_n^{\dot{\eta}} + \omega_n\sqrt{1 - \frac{1}{\omega_n^2}\left[F_n^\eta + \frac{1}{4}\left(F_n^{\dot{\eta}}\right)^2\right]} \tag{6.7}$$

where we take the $(+)$ sign on the radical to give a positive real frequency. Hence the amplitudes are

$$\eta_n(t) = e^{\frac{1}{2}F_n^{\dot{\eta}}t}e^{-i\omega_n\sqrt{1-\zeta_n^2}t} \tag{6.8}$$

and

$$\zeta_n = \frac{1}{\omega_n}\sqrt{F_n^{\eta} + \frac{1}{4}\left(F_n^{\dot{\eta}}\right)^2} \tag{6.9}$$

The $n^{th}$ mode is stable of

$$F_n^{\dot{\eta}} < 0 \tag{6.10}$$

That is, the coefficient of $\dot{\eta}_n$ in the expression for $F_n$ must be positive for the $n^{th}$ mode to be stable.

Now according to the methods of Fourier analysis, an arbitrary disturbance at some initial time (say $t = 0$) in the chamber can be synthesized of the normal modes. The time-evolution of the disturbance is therefore determined by the $\eta_n(t)$. In particular, an arbitrary disturbance in a combustor is stable if (and only if) all of the normal modes are stable and we arrive at the general result for the linear stability of a combustor:

(i) Write the linearized function for the force acting on the $n^{th}$ oscillator (spatially averaged acoustic mode) in the form

$$F_n = F_n^{\eta}\eta_n + F_n^{\dot{\eta}}\frac{d\eta_n}{dt}$$

(ii) Then any initial disturbance in a combustor is stable if and only if all the $F_n^{\dot{\eta}}$ are negative:

$$\text{Linear Stability} \iff F_n^{\dot{\eta}} < 0 \quad (\text{all } n)$$

The preceding calculation and its conclusion, illustrate further a point first made in Section 3. We have found a means of computing the linear stability of a combustor without knowing the linear motions themselves. The complex frequency (6.7) is in fact the frequency for the actual linear modes including the influences of all the processes accounted for. But calculation of the $F_n^{\eta}$ and $F_n^{\dot{\eta}}$ with the formula (6.2) requires knowledge only of the unperturbed normal modes—their frequencies $\omega_n$ and shapes $\psi_n(\mathbf{r})$. The formal statement of this property is that the eigenvalues $(\Omega_n)$ to any order in the relevant expansion parameter (here $\bar{M}_r := \mu$) can be computed knowing the eigenfunctions $(\psi_n)$ only to one less order. The eigenvalues $\Omega_n$ are here given to first order in the Mach number of the average flow but only the unperturbed classical eigenfunctions $\psi_n$ are required. This is the basic characteristic of the expansion procedures with spatial averaging that makes the method devised here so useful in practice.

**6.2. An Alternative Calculation of Linear Stability.** An equivalent calculation of the result for linear stability makes direct use of the formula for the wavenumber. Write

$$\eta_n = \hat{\eta}_n e^{-i\bar{a}kt} \quad ; \qquad F_n = \hat{F}_n e^{-i\bar{a}kt}$$

and substitute in (6.1) with $F_n^c$ ignored to find

$$(\bar{a}k)^2 = (\bar{a}k_n)^2 + \frac{1}{\hat{\eta}_n}\left(\hat{F}_n^{(r)} + i\hat{F}_n^{(i)}\right) \tag{6.11}$$

With $\bar{a}k = \omega + i\alpha$, this formula is

$$\omega^2 + i(2\alpha\omega) - \alpha^2 = \omega_n^2 + \frac{1}{\hat{\eta}_n}\left(\hat{F}_n^{(r)} + i\hat{F}_n^{(i)}\right)$$

where $(\quad)^{(r)}$ and $(\quad)^{(i)}$ stand for real and imaginary parts. Because $\alpha$ and $\hat{F}_n$ are of first order in the expansion parameter and terms of higher order must be dropped[22], we ignore $\alpha^2$ with respect to $\omega^2$. Then the real and imaginary parts of the last equation give

$$\omega^2 = \omega_n^2 + \frac{1}{\hat{\eta}_n}\hat{F}_n^{(r)}$$

$$\alpha = -\frac{1}{2\omega_n}\hat{F}_n^{(i)}$$

---

[22]Recall the remarks in Section 4.

where $\omega$ has been set equal to $\omega_n$ in the right-hand sides to ensure that higher order terms are not retained. Now take the square root of the first equation and again drop higher order terms to find

$$\omega = \omega_n - \frac{1}{2\omega_n}\frac{\hat{F}_n^{(r)}}{\hat{\eta}_n}$$
$$\alpha = -\frac{1}{2\omega_n}\frac{\hat{F}_n^{(i)}}{\hat{\eta}_n}$$

(6.12) a,b

The system is unstable if $\hat{F}_n^{(i)}$ is negative. This condition is essentially a generalized form of Rayleigh's criteria discussed further in Section 6.4.

After higher order terms are dropped from (6.7), the real and imaginary parts of $\omega$ are

$$\omega = \omega_n - \frac{1}{2\omega_n}F_n^\eta$$
$$\alpha = \frac{1}{2}F_n^{\dot{\eta}}$$

(6.14) a,b

Comparison of (6.12) a,b and 5.14 gives the connections between the two representations of the forcing function[23]:

$$F_n^\eta = \frac{\hat{F}_n^{(r)}}{\hat{\eta}_n}$$
$$F_n^{\dot{\eta}} = -\frac{1}{\omega_n}\frac{\hat{F}_n^{(i)}}{\hat{\eta}_n}$$

(6.15) a,b

Generally $F_n$ will contain several processes, each of which will depend linearly on $\eta_n$ and $\frac{d\eta_n}{dt}$ and appears additively in $F_n$. Hence formulas corresponding to (6.15) a,b apply to each of the individual processes. They are often useful, if only for checking correctness, in detailed calculations.

**6.3. An Example: Linear Stability with Distributed Sources of Heat and Motion of the Boundary.** As a first approximation to problems of combustion instabilities it is useful to ignore all processes involving interactions between the unsteady and steady fields, and focus attention on the two generic causes of instabilities: time-dependent energy addition and motions of the boundary. With suitable interpretation the second may represent the influence of unsteady combustion of a solid propellant. Then in dimensional variables the linearized pressure and momentum equations ((3.46) a-e)d and ((3.46) a-e)b, and the boundary condition (3.57) on the pressure fluctuations are

$$\frac{\partial p'}{\partial t} + \gamma\bar{p}\nabla \cdot \mathbf{u}' = \frac{R}{C_v}\dot{Q}'$$

(6.12)

$$\bar{\rho}\frac{\partial u'}{\partial t} + \nabla p' = 0$$

(6.13)

$$\hat{\mathbf{n}} \cdot \nabla p' = -\bar{\rho}\frac{\partial \mathbf{u}'}{\partial t} \cdot \hat{\mathbf{n}}$$

(6.14)

Now form the wave equation as in Section 3.4, so the problem is governed by the two equations

$$\nabla^2 p' - \frac{1}{\bar{a}^2}\frac{\partial^2 p'}{\partial t^2} = h$$
$$\hat{\mathbf{n}} \cdot \nabla p' = -f$$

(6.19) a,b

where

$$h = -\frac{1}{\bar{a}^2}\frac{R}{C_v}\frac{\partial \dot{Q}'}{\partial t}$$
$$f = -\bar{\rho}\frac{\partial \mathbf{u}'}{\partial t} \cdot \hat{\mathbf{n}}$$

(6.20) a,b

---

[23]The $(-)$ sign in (6.15) a,b arises from the $(-)$ sign in the exponential time dependence.

The expansion procedure and application of spatial averaging leads to the explicit oscillator equations (4.36):

$$\frac{d^2\eta_n}{dt^2} + \omega_n^2 \eta_n = -\frac{\bar{a}^2}{\bar{p}E_n^2}\left\{\int\left[-\frac{1}{\bar{a}^2}\frac{R}{C_v}\frac{\partial\dot{Q}'}{\partial t}\right]\psi_n dV + \iint\left[-\bar{\rho}\frac{\partial\mathbf{u}'}{\partial t}\cdot\hat{\mathbf{n}}\right]\psi_n dS\right\} \tag{6.21}$$



$$Q$$

$$0 \qquad\qquad L$$

FIGURE 6.1. A Tube with Distributed Heat Addition and an Oscillating Piston to Drive Waves

As a simple example, consider the one-dimensional problem of waves excited in a tube fitted with a piston, Figure 6.1, and with distributed heat addition provided by an electrically heated coil. Only longitudinal modes are accounted for, and

$$\psi_n = \cos(k_n x) \quad , \qquad k_n = n\frac{\pi}{L} \quad , \qquad E_n^2 = \frac{1}{2}S_c L \tag{6.21}$$

where $S_c = \pi R^2$ is the cross-section area of the tube. We ignore any average motion in the tube, and suppose that the average thermodynamic properties are maintained constant and uniform by suitable steady heat losses through the walls of the tube. The heat addition and motion of the piston are sinusoidal, having phases $\phi_Q$ and $\phi_n$ with respect to pressure oscillations:

$$\dot{Q}' = \left|\hat{\dot{Q}}(x)\right|e^{-i(\bar{a}kt-\phi_Q)}$$
$$\mathbf{u}_p'\cdot\hat{\mathbf{n}} = |\hat{u}_p|e^{-i(\bar{a}kt-\phi_p)} \tag{6.22 a,b}$$

Hence for use in $h$ and $f$:

$$\frac{\partial\dot{Q}'}{\partial t} = -i\bar{a}k\left|\hat{\dot{Q}}(x)\right|e^{-i(\bar{a}kt-\phi_Q)}$$
$$\frac{\partial}{\partial t}\left(\mathbf{u}_p'\cdot\hat{\mathbf{n}}\right) = -i\bar{a}k\,|\hat{u}_p|\,e^{-i(\bar{a}kt-\phi_u)} \tag{6.23 a,b}$$

With $\eta_n = \hat{\eta}_n e^{i\bar{a}kt}$, substitution in the oscillator equations (6.21) leads to

$$\left[-(\bar{a}k)^2 + \omega_n^2\right]\hat{\eta}_n = -\frac{\bar{a}^2}{\bar{p}E_n^2}\left\{-\frac{1}{\bar{a}^2}\frac{R}{C_v}(-i\bar{a}k)\int\cos(k_n x)\left|\hat{\dot{Q}}(x)\right|e^{i\phi_Q}dV\right.$$
$$\left. + i\bar{\rho}\bar{a}k\oiint\cos(k_n x)|\hat{u}_p|e^{i\phi_u}\right\}$$

After some rearrangement, and setting $\bar{a}k = \omega - i\alpha$, we find

$$(\omega + i\alpha)^2 = \omega_n^2 - i(\omega + i\alpha)\frac{\bar{a}^2}{\bar{p}(\frac{1}{2}S_c L)}\left\{\frac{1}{\bar{a}^2}\frac{R}{C_v}S_c\int_0^L\cos(k_n x)\frac{\left|\hat{\dot{Q}}(x)\right|}{\hat{\eta}_n}e^{i\phi_Q}dx\right.$$
$$\left. -\bar{\rho}S_c\frac{|\hat{u}_p|}{\hat{\eta}_n}e^{i\phi_p}\right\}$$

Because $|\hat{\dot{Q}}|$ and $|\hat{u}_p|$ are small perturbations we can write this equation to first order in small quantities:

$$\omega^2 - i(2\alpha\omega) = \omega_n^2 - i\omega_n\frac{2}{\bar{p}L}\frac{R}{C_v}\int_0^L\left[\cos(k_n x)\frac{\left|\hat{\dot{Q}}(x)\right|}{\hat{\eta}_n}e^{i\phi_p}dx + i\omega_n\frac{2\gamma}{L}\frac{|\hat{u}_p|}{\hat{\eta}_n}e^{i\phi_u}\right]dx$$

Take the real and imaginary parts to find

$$\omega^2 = \omega_n^2 + \frac{2\omega_n}{\bar{p}L}\left(\frac{R}{C_v}\right)\int_0^L\left[\cos(k_n x)\frac{\left|\hat{\dot{Q}}(x)\right|}{\hat{\eta}_n}\sin\phi_Q dx - \frac{2\gamma\omega_n}{L}\frac{|\hat{u}_p|}{\hat{\eta}_n}\sin\phi_u\right]dx$$

$$\alpha = \frac{1}{\bar{p}L}\frac{R}{C_v}\int_0^L\left[\cos(k_n x)\frac{\left|\hat{\dot{Q}}(x)\right|}{\hat{\eta}_n}\cos\phi_Q dx - \frac{\gamma}{L}\frac{|\hat{u}_p|}{\hat{\eta}_n}\cos\phi_u\right]dx$$

(6.24) a,b

Internal feedback, and hence a condition for instability, exists of either or both $|\hat{\dot{Q}}|$ and $|\hat{u}_p|$ depend on the fluctuating pressure (or velocity). For example, set

$$|\hat{\dot{Q}}| = q_0\hat{\eta}_n\psi_n = q_0\hat{\eta}_n\cos k_n x$$
$$|\hat{u}_p| = u_0\hat{\eta}_n$$

(6.25) a,b

and (6.24) a,b becomes

$$\omega^2 = \omega_n^2 + 2\omega_n\left(Aq_0\sin\phi_q - Bu_0\sin\phi_u\right)$$

where

$$A = \frac{1}{2\bar{p}}\frac{R}{C_v}\quad;\qquad B = \frac{\gamma}{L}$$

(6.26)

To first order in small quantities we find the results for the frequency and decay or growth constant:

$$\omega = \omega_n + Aq_0\sin\phi_Q - Bu_0\sin\phi_u$$
$$\alpha = Aq_0\cos\phi_Q - Bu_0\cos\phi_u$$

(6.27) a,b

**Remarks:**

(i) the $n^{th}$ mode is unstable if $Aq_0\cos\phi_Q > Bu_0\cos\phi_u$

(ii) the first term in $\alpha$ is an example of Rayleigh's criterion discussed in Section 6.3:

    a) if $0 \le \phi_u \le \frac{\pi}{2}$ then a necessary condition for instability is $0 \le \phi_Q \le \frac{\pi}{2}$.

    b) instability of the $n^{th}$ mode is encouraged if $|\hat{\dot{Q}}(x)|\cos k_n x$ is larger,
       i.e. if the heat addition is greater where the mode shape of the pressure.

It is important also to notice that due to the spatial averaging, one cannot distinguish the ultimate effects of volumetric and surface processes. There is an equivalence of the influences of the various processes, their importance in respect to position within the chamber being dominated by their location with respect to the mode shapes. That characteristic has far-reaching consequences.

**6.4. Rayleigh's Criterion and Linear Stability.** As part of his research on the excitation of acoustic waves by heat addition in chambers, Lord Rayleigh (1878, 1945) formulated the following explanation for the production of tones in a Rijke tube:

> "If heat be periodically communicated to, and abstracted from, a mass of air vibrating (for example) in a cylinder bounded by a piston, the effect produced will depend upon the phase of the vibration at which the transfer of heat takes place. If heat be given to the air at the moment of greatest condensation, or be taken from it at the moment of greatest rarefaction, the vibration is encouraged. On the other hand, if heat be given at the moment of greatest rarefaction, or abstracted at the moment of greatest condensation, the vibration is discouraged."

That paragraph has become probably the most widely cited explanation for the presence of combustion instabilities generally. For easy reference, the explanation has long been referred to as "Rayleigh's Criterion."

It is important to realize that Rayleigh addressed only the conditions under which unsteady heat addition 'encourages' oscillations, i.e. is a destablilizing influence. Other processes, stabilizing or destabilizing are neither

excluded nor included, and there is certainly no implication that satisfaction of the criterion is either a necessary or a sufficient condition for instability to exist. Several published examples exist of quantitative realizations of the criterion (Putnam 1971; Chu 1956; Zinn 1986; Culick 1987, 1992). The purpose of this section is to establish a generalized form of Rayleigh's Criterion by using the analysis based on spatial averaging.

The main idea is that a positive change of the time-averaged energy of a modal oscillator in a cycle of oscillation is exactly equivalent to the principle of linear instability, that the growth constant should be positive for a motion to be unstable. To establish the connection we use the oscillator equations,

$$\frac{d^2\eta_n}{dt^2} + \omega_n^2 \eta_n = F_n \tag{6.27}$$

The instantaneous energy[24] of the $n^{th}$ oscillator is

$$\mathcal{E}_n = \frac{1}{2}\left(\dot{\eta}_n^2 + \omega_n^2 \eta_n^2\right) \tag{6.28}$$

and the change of energy in one cycle is the integral over one period of the rate at which work is done by the force $F_n$:

$$\Delta\mathcal{E}_n = \int_t^{t+\tau_n} F_n(t')\dot{\eta}_n(t')dt' \tag{6.29}$$

Under the integral, $F_n$ and $\dot{\eta}_n$ must be real quantities: here we use the real parts of both functions,

$$\eta_n = \hat{\eta}_n e^{-i\bar{a}kt} = |\hat{\eta}_n|e^{-i\bar{a}kt}$$
$$F_n = \hat{F}_n e^{-i\bar{a}kt} = |\hat{F}_n|e^{-i(\bar{a}kt+\phi_F)} = |\hat{F}_n|\left(\cos\phi_F - i\sin\phi_F\right)e^{-i\bar{a}kt} \tag{6.31 a,b}$$

We measure all phases with respect to the pressure, so $\hat{\eta}_n$ is real and, being the maximum amplitude, is positive. Substitution in the oscillator equations gives

$$k^2 = \frac{1}{\bar{a}^2}\left(\omega_n^2 - \frac{\hat{F}_n}{\hat{\eta}_n}\right)$$

of which the real and imaginary parts are to first order in small quantities:

$$\omega^2 = \omega_n^2 - Re\left(\frac{\hat{F}_n}{\hat{\eta}_n}\right) = \omega_n^2 - \left|\frac{\hat{F}_n}{\hat{\eta}_n}\right|\cos\phi_F$$

$$\alpha_n = \frac{1}{2\omega_n}Im\left(\frac{\hat{F}_n}{\hat{\eta}_n}\right) = \frac{-1}{2\omega_n}\left|\frac{\hat{F}_n}{\hat{\eta}_n}\right|\sin\phi_F \tag{6.32 a,b}$$

Also for use in (6.29) we have

$$\dot{\eta}_n = i\bar{a}k|\hat{\eta}_n|e^{-i\bar{a}kt} = \bar{a}k|\hat{\eta}_n|e^{-i\left(\bar{a}kt+\frac{\pi}{2}\right)} \approx \omega_n|\hat{\eta}_n|e^{-i\left(\omega_n t+\frac{\pi}{2}\right)}$$

so

$$Re(\dot{\eta}_n) = \omega_n|\hat{\eta}_n|\cos\left(\omega_n t + \frac{\pi}{2}\right) = -\omega_n|\hat{\eta}_n|\sin\omega_n t \tag{6.33}$$

The real part of $F_n$ is

$$Re(F_n) = |\hat{F}_n|\cos\left(\omega_n t + \phi_F\right) = |\hat{F}_n|\left\{\cos\omega_n t \cos\phi_F - \sin\omega_n t \sin\phi_F\right\} \tag{6.34}$$

Hence the right-hand side of (6.29) is

$$\Delta\mathcal{E}_n = \int_t^{t+\tau_n} Re(F_n)Re(\eta_n)dt' = \omega|\hat{F}_n|\int_t^{t+\tau_n}\left\{\sin^2\omega_n t'\sin\phi_F - \frac{1}{2}\sin 2\omega_n t'\cos\phi_F\right\}dt'$$

$$= \omega|\hat{F}_n||\hat{\eta}_n|\frac{\tau_n}{2}\sin\phi_F$$

Substitution of (6.32)a,b leads to the formula

$$\Delta\mathcal{E}_n = 2\pi\alpha_n\omega_n|\hat{\eta}_n|^2 \tag{6.35}$$

which establishes the desired connection between Rayleigh's criterion and linear stability:

---

[24]$\mathcal{E}_n$ is not the energy of the $n^{th}$ acoustic mode, which is given by the integral of (5.33) over the volume of the chamber.

**Remarks:**

(i) Positive $\alpha_n$ (the system is linearly unstable) implies that the average energy of the oscillator increases, and vice-versa.

(ii) Rayleigh's original criterion is equivalent to the principle of linear instability **if** only heat exchange is accounted for and is **neither** a necessary **nor** a sufficient condition for existence of a combustion instability.

(iii) The extended form (6.35) of Rayleigh's criterion is exactly equivalent to the principle of linear instability.

Putnam (1971) has made the widest use of Rayleigh's Criterion in practical situations. His book and papers give many examples of applying the Criterion as an aid to making changes of design to avoid oscillations generated by heat release, particularly in power generating and heating systems.

In the past fifteen years many groups have been making direct observations on laboratory systems to check the validity of the Criterion's implications. The key step is based on the assumption that radiation by certain intermediate species in hydrocarbon reactions (CH and OH are the most common indentifiers) can be interpreted as a measure of the rate of chemical reactions taking place and hence of the rate at which energy is released. Simultaneous measurement we made of the spatial distribution of radiation in a system, and of the pressure oscillations, the results then allow at least a qualitative assessment of the extent to which the oscillations are being driven by the energy released in the combustion field, or whether other mechanisms may be active.

It seems that the first report of that sort of effort appeared in a Ph.D. thesis (Sterling, 1987; Sterling and Zukoski, 1991). Figure 6.2 is a sketch of the dump combustor used as the test device, and Figure 6.3 shows the main result.



FIGURE 6.2. The Caltech Dump Combustor (Sterling 1985)

**6.5. Explicit Formulas For Linear Stability.** The term 'stability of motions' has several interpretations for flows in combustion chambers, including:

(i) the stability of laminar average flow when viscous and inertial properties of the medium dominate, leading to turbulence, a field of distributed vorticity if the steady flow is unstable;

(ii) the stability of shear layers, commonly producing large scale vortex motions when a shear layer is unstable;

(iii) the stability of laminar flame fronts, responsible for one source of turbulent combustion when fronts are unstable;

(iv) the stability of small disturbances which, when the compressibility and inertia of the medium dominate, can develop into acoustic waves.

In terms of the modes of motion mentioned in Section 3.1 and discussed further in Section 3.3, the phenomena (i)–(iii) are classified as waves of vorticity and the fourth comprises acoustic waves. Here we are concerned only with the stability of acoustic waves. The results are very general, accommodating all relevant processes and applicable, in principle, to any combustion chamber. Eventually the obstacles to successful applications are associated almost entirely with problems of modeling. In the first instance, the formal results given here establish explicitly what modeling is required.

6.5.1. *Linear Stability in Three Dimensions.* The formulas (6.14) a,b are general, restricted only by the approximations used in formulating the analytical framework. Hence the problem of obtaining results specific to any given problem comes down to finding explicit forms for $F_n^\eta$ and $F_n^{\dot\eta}$, i.e. evaluating the integrals defining $F_n$,
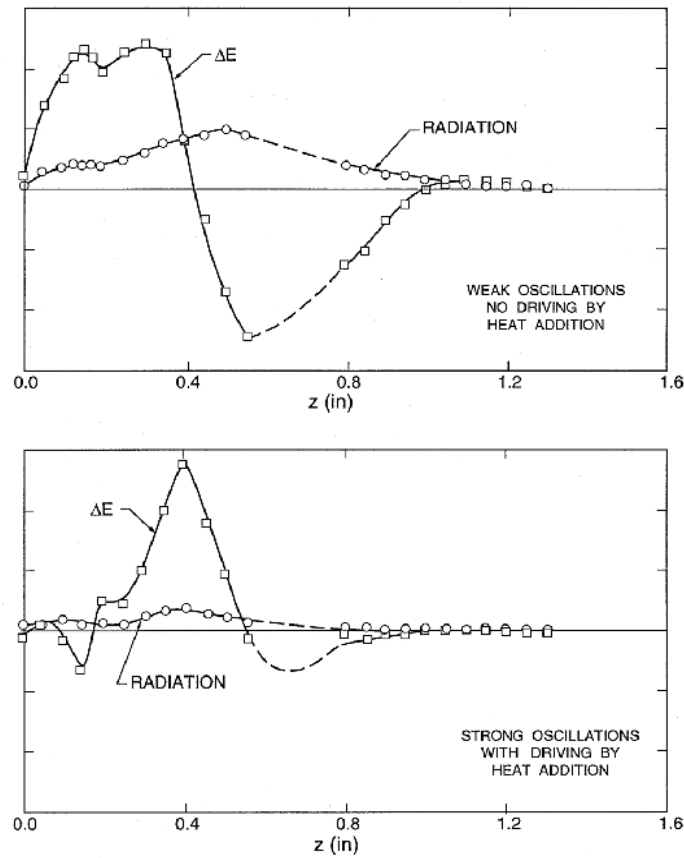
FIGURE 6.3. Experimental Confirmation of Rayleigh's Criteria (Sterling and Zukoski, 1991)

equation (6.2). The functions $h$ and $f$ are given by (4.72) and (4.73) to second order in the fluctuations. Here we need only the linear parts, terms of order $\mu\varepsilon$. With $\mu$ and $\varepsilon$ absorbed in the definitions of the variables, we have

$$
\begin{aligned}
h = &-\bar{\rho}\nabla \cdot \left(\bar{\mathbf{M}} \cdot \nabla\mathbf{M}' + \mathbf{M}' \cdot \nabla\bar{\mathbf{M}}\right) - \frac{1}{\bar{a}^2}\frac{\partial}{\partial t}\left(\bar{\mathbf{M}} \cdot \nabla p' + \gamma p' \nabla \cdot \bar{\mathbf{M}}\right) \\
&+ \left[\frac{1}{\bar{\rho}}\nabla \cdot \left(\frac{1}{\bar{\rho}}\mathcal{F}'\right) - \frac{1}{\bar{a}^2}\frac{\partial P'}{\partial t}\right]_{\mu\varepsilon}
\end{aligned}
\tag{6.36}
$$

$$
f = \bar{\rho}\left[\frac{\partial\mathbf{M}'}{\partial t} \cdot \hat{n}\right]_{\mu\varepsilon} + \bar{\rho}\hat{n} \cdot \left(\bar{\mathbf{M}} \cdot \nabla\mathbf{M}' + \mathbf{M}' \cdot \nabla\bar{\mathbf{M}}\right) + [\hat{n} \cdot \mathcal{F}']_{\mu\varepsilon}
\tag{6.37}
$$

where the subscript $\mu\varepsilon$ means that the quantity in expanded to include only terms of first order in the mean flow and the fluctuations, i.e. terms $O(\bar{M}_r M_r')$.

Substitution of (6.36) and (6.37) and some rearrangement leads to the result

$$
\begin{aligned}
\int \hat{h}\psi_n dV + \oiint f\psi_n dS = &\ \bar{\rho}k_n^2\int\left(\bar{\mathbf{M}} \cdot \hat{\mathbf{M}}\right)\psi_n dV \\
&- \bar{\rho}\int\left(\hat{\mathbf{M}} \times \nabla \times \bar{\mathbf{M}}\right) \cdot \nabla\psi_n dV \\
&+ i\frac{k_n}{\bar{a}}\int\psi_n\left[\bar{\mathbf{M}} \cdot \nabla\hat{p} + \gamma\hat{p}\nabla \cdot \bar{\mathbf{M}}\right]dV \\
&- i\frac{k_n}{\bar{a}}\int\psi_n\hat{\mathcal{P}}dV - \int\hat{\mathcal{F}} \cdot \nabla\psi_n dV \\
&+ \bar{p}\bar{a}k_n\oiint\psi_n\hat{\mathbf{M}} \cdot \hat{n}dS
\end{aligned}
\tag{6.38}
$$

Note that we have removed the exponential time factor for linear harmonic motions and (6.38) contains the amplitudes of fluctuations, denoted by ( $\hat{}$ ). Two remarks are important:

(i) the mean flow field may be rotational ($\nabla \times \bar{\mathbf{M}} \neq 0$) and sources are accommodated ($\nabla \cdot \bar{\mathbf{M}} \neq 0$).
(ii) owing to the ordinary procedure discussed in Section 3, the substitutions of classical acoustic mode shapes are required in the right-hand side:

$$\hat{p} = \bar{p}\hat{\eta}_n \psi_n \; ; \quad \hat{M} = \frac{i}{\gamma k_n^2}\hat{\eta}_n \nabla \psi_n \tag{6.39}$$

where $\hat{\dot{\eta}}_n = i\bar{a}k_n \eta_n$.

Eventually the complex wavenumber, (6.11), is

$$
\begin{aligned}
k^2 = k_n^2 &+ \frac{\bar{a}^2}{\bar{p}E_n^2}\left\{ i\bar{p}\bar{a}k_n \oiint \left( \frac{\hat{\mathbf{M}}}{\hat{\eta}_{\mathbf{n}}} + \frac{1}{\gamma}\bar{\mathbf{M}}\gamma_n \right) \cdot \hat{n}\gamma_n dS \right. \\
&+ i(\gamma-1)\frac{k_n}{\bar{a}}\bar{p}\int \left( \nabla \cdot \bar{\mathbf{M}} \right) \psi_n^2 dV - i\frac{k_n}{\bar{a}}\int \frac{\hat{\mathcal{P}}}{\hat{\eta}_n}\psi_n dV \\
&\left. - \int \frac{\hat{\mathcal{F}}}{\hat{\eta}_n} \cdot \nabla \psi_n dV \right\}
\end{aligned}
\tag{6.40}
$$

It is important to understand that in the result unsteady gasdynamics (acoustics) and interactions between the acoustics and the mean flow are accounted for 'exactly' to $O(\bar{M}_r)$.

The real and imaginary parts of (6.40), written symbolically as equations (6.12) a,b and (6.14) a,b are sums of contributions from the various processes accounted for. For example, the formula for the growth constant appears in the form

$$\alpha = (\alpha)_{combustion} + (\alpha)_{mean\ flow/acoustics} + (\alpha)_{nozzle} + \cdots$$

Similar results can be derived for the case when the one-dimensional approximation is used. The required basis for the calculations is given by Culick (1998). The results for the frequency and growth constant are:

$$
\begin{aligned}
\omega = \omega_n &+ \frac{\bar{a}^2}{2\omega_\ell \bar{p}E_\ell^2}\left\{ -\bar{p}\bar{a}k_\ell \left[ \left( \frac{\hat{u}^{(i)}}{\hat{\eta}_\ell}\psi \right)S_c \right]_0^L \right. \\
&\left. + \bar{p}\bar{a}k_\ell \int_0^L \frac{1}{S_c}\int \left( \frac{\hat{u}_b^{(i)}}{\hat{\eta}_\ell} \right) dq\psi_\ell S_c dz \right\} + \text{ volumetric contributions (combustion)}
\end{aligned}
\tag{6.41}
$$

$$
\begin{aligned}
\alpha = &-\frac{\bar{a}^2}{2\omega_\ell \bar{p}E_\ell^2}\left\{ \bar{p}\bar{a}k_\ell \left[ \left( \frac{\hat{u}^{(i)}}{\hat{\eta}_\ell}\psi_\ell + \frac{1}{\gamma}\bar{u}\gamma_\ell^2 \right)S_c \right]_0^L \right. \\
&- \bar{p}\bar{a}k_\ell \int_0^L \frac{1}{S_c}\int \left( \frac{\hat{u}_b^{(i)}}{\hat{\eta}_\ell} + \frac{1}{\gamma}\bar{u}_b\psi_\ell \right) dq\psi_\ell S_c dz \\
&\left. + \frac{k_\ell \bar{p}^L}{\bar{a}}\int_0^L \frac{1}{k_\ell^2}\left( \frac{d\psi_\ell}{dz} \right)^2 \frac{1}{S_c}\int \bar{u}_b dq S_c dz \right\} + \text{ volumetric contributions (combustion)}
\end{aligned}
\tag{6.42}
$$

Two remarks on interpretation

(i) the first two terms in the formula for $\alpha$ represent the dynamical response of the enclosing surface and the net effect of linear interactions between the acoustic field and the mean flow.
(ii) the last term represents a dissipative process commonly called 'flow turning' due to inelastic acceleration of the incoming flow, initially normal to the surface, to the local axial velocity parallel to the surface. This process generates unsteady vorticity at the surface; the result shown here does not capture the entire contribution. See Flandro (1995) and Mulhotra (2001).

These results for linear stability have been applied extensively to problems of combustion instabilities in solid propellant rockets. Their validity has long been confirmed. However, their accuracy depends entirely on the accuracy of modeling processes rather than the gasdynamics shown explicitly in (6.40)–(6.42).

Due to the large uncertainties associated with modeling some processes, it is difficult—in fact impossible at this time—to make an entirely satisfactory comparison between theoretical results and measurements. Hence the best way to check theory is to compare results obtained here with results of numerical simulations, all for the same problem. Even this procedure is imperfect because different approximations must be made in the two approaches—it is impossible to solve the 'same' problem numerically and with the analysis given here.

Results of an example for a solid propellant rocket are shown in Figures 6.4–6.6. The calculations were carried out for nonlinear behavior. Figure 6.4 shows the development of the unstable motion into a stable limit cycle and Figure 6.5 is a comparison of the spectra of the waveforms in the limit cycle. The approximate analysis can be carried out only for a finite number of modes. As a consequence, although the frequencies are accurately predicted, the amplitudes have greater errors for the higher modes. Figure 6.6 shows one effect of truncating the modal expansion. For this example the effect is not large—the two-mode approximation seems quite adequate. That is not always true, a matter discussed in the following Section.
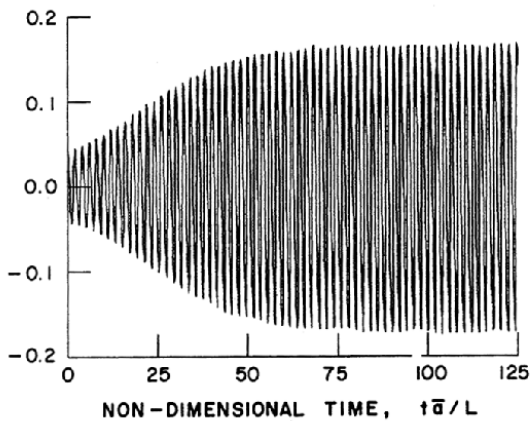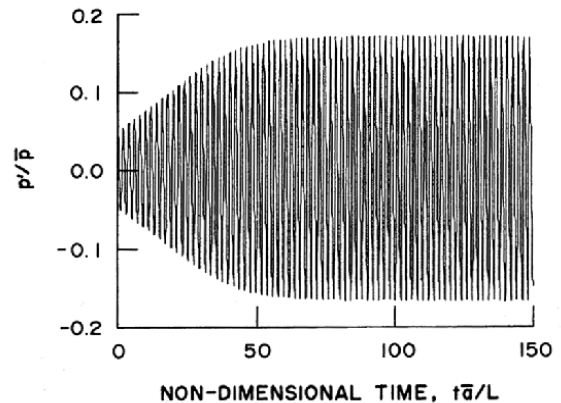


(a) Approximate Analysis     (b) Numerical Simulation

FIGURE 6.4. Growth of Unstable Motions According to (a) the Approximate Analysis; and (b) a Numerical Simulation

**Frequencies and amplitudes of acoustic pressures**

| Mode | Frequency, Hz 1 | 2 | 3 | 4 | 5 | Amplitude, $|p'/\bar{p}|$ 1 | 2 | 3 | 4 | 5 |
|---|---|---|---|---|---|---|---|---|---|---|
| Numerical | 926 | 1824 | 2698 | 3595 | 4491 | 0.151 | 0.042 | 0.0234 | 0.0203 | —— |
| Approximate | 895 | 1785 | 2683 | 3571 | 4449 | 0.151 | 0.0478 | 0.0280 | 0.0153 | 0.0188 |

(a)



(b)

FIGURE 6.5. Comparison of the Spectra for the Waveforms in Figure 6.4



FIGURE 6.6. Effect of Truncation in the Waveforms

# 7. NONLINEAR BEHAVIOR

It is linear behavior, especially linear stability, that is most easily understood and therefore has dominated discussions of combustion instabilities. Almost no attention has been paid to no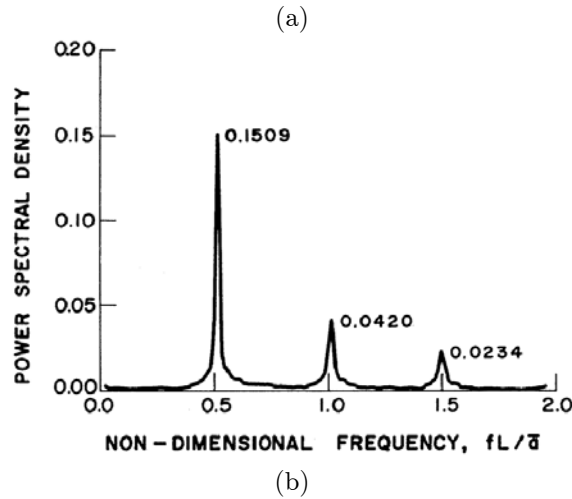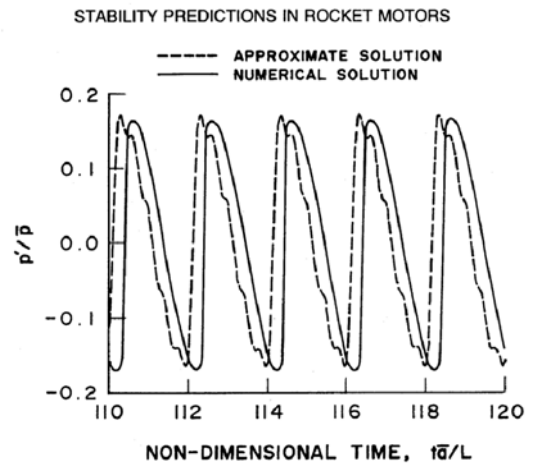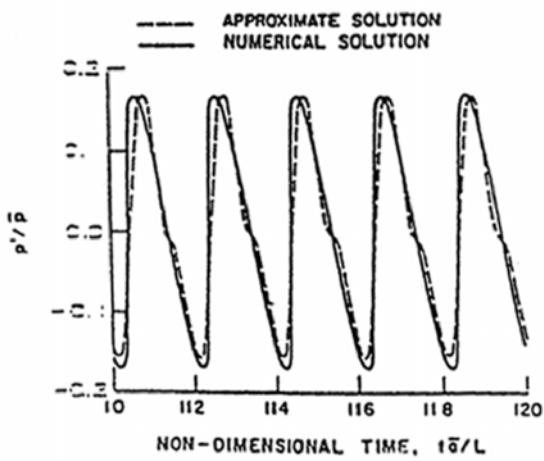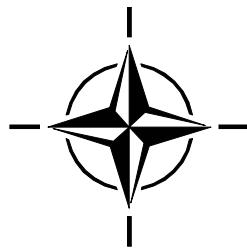nlinear behavior in works on control of combustion instabilities. One justification for that deficiency has been the view that if control of the oscillations works properly, it should stop the growth before the amplitude reaches a large value. There are several reasons why that reasoning is flawed:

- if the growth rates are unusually large the control system may not have a sufficiently large bandwidth to be effective;
- because combustion systems are intrinsically nonlinear design of a control system based only on linear behavior may produce a control system far from optimal;
- linear control demands actuation at the frequency of the oscillation to be controlled, while nonlinear control of particular types are effective at lower frequencies; an example is described in Section 7.
- observed nonlinear behavior contains much information about properties of the system in question and in the interests of understanding should not be ignored.

Existing examples of controlling combustion instabilities have almost totally ignored issues of nonlinear behavior. In no demonstration, either in the laboratory or full-scale, have the amplitudes of the oscillations been predicted or interpreted either before or after control has been exercised. Hence nothing has been learned about why the initially unstable motions reach the amplitudes they did, or, why the control system affected them in the observed way. In fact few attempts exist to determine quantitatively the stability of motions. Hence the subject of controlling the dynamics of combustion systems has largely been a matter of exercising the principles of control with little attention paid to the characteristics of the systems ('plants') being controlled. It seems that following this strategy is likely not the most fruitful way of achieving meaningful progress. Especially, this is not a sound approach to developing the basis for designing control systems. The current state of the art is that feedback control is designed and applied in *ad hoc* fashion for systems already built and exhibiting instabilities.

A central concern of a controls designer is construction of a 'reduced order' model of the system. What that really means in the present context is the need to convert the partial differential equations of conservation developed in Section 3, to a finite system of ordinary differential equations. The analysis developed in Section 3 and 4 accomplishes exactly that purpose. It is not the only approach possible (e.g. proper orthogonal decomposition has been examined briefly) but the method of modal expansion and spatial averaging has many favorable properties and has been proven to work well.

The main purposes of this section are to quote a few results displaying some aspects of the nonlinear behavior arising from gasdynamics; and to illustrate some consequences of truncating the modal expansion, that is, what might be the consequences of reducing the order of the model. Another important issue we will examine briefly is the application of time-averaging. As the calculations in Section 4 showed, the great advantage of time-averaging is that it replaces $N$ second order oscillator equation by $2N$ first order equations. That transformation enormously reduces the cost of obtaining solutions, aids theoretical work, and provides a simplified representation for application of feedback control. But as for truncation, the question arises: How accurate are the results and what are the limits of the validity of time-averaging?

Only the nonlinearities due to gasdynamics are treated in this section. The results must be viewed with that caveat, particularly because the forms of the nonlinearities are very special, if only because the dominant coupling acts to cause energy to flow from low to high frequency waves, the tendency which produces the familiar steepening of compressive disturbances into shock waves.

**7.1. The Two-Mode Approximation.** This is the simplest class of problems for which nonlinear mode coupling is accommodated. Each mode is characterized by two constants: $\alpha$ (energy gain or loss) and $\theta$ (frequency shift). The energy gain or loss may be nonlinear—that is, $\alpha$ could in principle depend on amplitude—but here both $\alpha$ and $\theta$ are taken to be constant, characterizing entirely the linear processes. As a result of several works

in the past few years, the two mode approximation is quite well understood (Awad and Culick, 1986; Paparizos and Culick, 1989; Yang and Culick 1990; Jahnke and Culick, 1994; Culick, 1994).
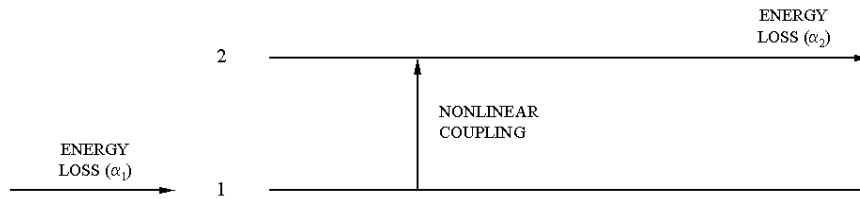


FIGURE 7.1. Energy Flow in the Two Mode Approximation

Only gasdynamic nonlinearities to second order are accounted for here. Their special form allows the convenient closed form solutions to the time-averaged equations, first found by Awad (1983). The results provide much basic understanding which is applicable to more complicated nonlinear problems. For example, contrary to one's expectation based on the behavior of shock waves, nonlinear behavior in the present context need not involve large amplitudes, and the pressure oscillation may appear to be a clean sinusoid, free of significant harmonic content. The basic reason is that here the two-mode system both gains and loses energy; each interaction with the environment is necessary. In the absence of the nonlinear modal coupling, or some other linear process, limit cycles cannot exist. Moreover, both stable and unstable limit cycles exist.

Truncation of the modal expansion to two modes introduces errors because the flow of energy to higher modes is blocked. The amplitude of the highest mode is therefore greater than the correct value in order to provide the higher linear rate of energy loss required to sustain a limit cycle. The example in Section 6.5.1 shows this effect.

It's an interesting feature of the two-mode approximation that nonlinear instability to stable limit cycles seems not to exist. Although no rigorous proof exists, experience with many examples has shown that conclusion to be quite generally true if only the acoustic (gasdynamics) nonlinearities are accounted for. 'Triggering' or pulsing to stable limit cycles does occur for special forms of nonlinear energy gain from the environment (i.e. extinction from the mean flow or supply from combustion processes).

If we ignore linear mode coupling and account for acoustic nonlinearities to second order, the oscillator equations can be put in the form

$$\frac{d^2\eta_n}{dt^2} + \omega_n^2\eta_n = \alpha_n\dot{\eta}_n + \theta_n\eta_n - \sum_{i=1}^{\infty}\sum_{j=1}^{\infty}\left\{A_{nij}\dot{\eta}_i\dot{\eta}_j + B_{nij}\eta_i\eta_j\right\} + F_n^{NL} \tag{7.1}$$

where $F_n^{NL}$ represents other nonlinear contributions. The coefficients $A_{nij}$, $B_{nij}$ are defined as integrals involving the basis functions $\psi_{nij}$. Hence their values are fixed primarily by the geometry of the chamber in question. See Culick (1976) for additional details of the derivation of (7.1). It is extremely important that the nonlinear gasdynamic terms involve no cross-products $\dot{\eta}_i\eta_j$ and also (not obvious here) no 'self-coupling', terms proportional to $\dot{\eta}_n^2$ or $\eta_n^2$. Those properties are the formal reasons that nonlinear instabilities do not exist if only these nonlinearities are included.

Equation (7.1) simplify considerably for longitudinal modes. Due to orthogonality and special properties of the $\cos k_n z$, the double sum becomes a single sum and (7.1) can be put in the form:

$$\frac{d^2\eta_n}{dt^2} + \omega_n^2\eta_n = \alpha_n\dot{\eta}_n + \theta_n\eta_n - \sum_{i=1}^{\infty}\left[C_{ni}^{(1)}\dot{\eta}_i\dot{\eta}_{n-i} + D_{ni}^{(1)}\eta_i\eta_{n-i}\right]$$
$$- \sum_{i=1}^{\infty}\left[C_{ni}^{(2)}\dot{\eta}_i\dot{\eta}_{n+i} + D_{ni}^{(2)}\eta_i\eta_{n+i}\right] + F_n^{NL} \tag{7.2}$$

The time-averaged forms of (7.2) are

$$\frac{dA_n}{dt} = \alpha_n A_n + \theta_n B_n + \frac{n\beta}{2}\sum^{i}[A_i(A_{n-i} - A_{i-n} - A_{i+n}) - B_i(B_{n-i} - B_{i-n} - B_{i+n})]$$

$$\frac{dB_n}{dt} = -\theta_n A_n + \alpha_n B_n + \frac{n\beta}{2}\sum^{i}[A_i(B_{n-i} - B_{i-n} - B_{i+n}) - B_i(A_{n-i} - A_{i-n} - A_{i+n})]$$

(7.3) a,b

where as in Section 3, $\eta_n = A_n \cos\omega_n t + B_n \sin\omega_n t$. For longitudinal modes, the frequencies are all integral multiples of the fundamental, a property that is crucial to the forms of (7.3) a,b. For example, for transverse modes in a cylindrical chamber, the nonlinear terms contain factors representing modulation.

For two modes, the four first order equations are

$$\frac{dA_1}{dt} = \alpha_1 A_1 + \theta_1 B_1 - \beta(A_1 A_2 - B_1 B_2)$$

$$\frac{dB_1}{dt} = \alpha_1 B_1 + \theta_1 A_1 - \beta(B_1 A_2 - A_1 B_2)$$

$$\frac{dA_2}{dt} = \alpha_2 A_2 + \theta_2 B_2 - \beta(A_1^2 - B_1^2)$$

$$\frac{dB_2}{dt} = \alpha_2 B_2 + \theta_2 A_2 - 2\beta B_1 A_1$$

(7.4) a,b,c,d

The great advantage of this system of equations is that some useful exact results can be found. One way to find them is to change independent variables to the amplitude and phases $(\Gamma_n, \phi_n)$ of the two modes by writing

$$\eta_1(t) = \Gamma_1(t)\sin(\omega_1 t + \phi_1)$$

$$\eta_2(t) = \Gamma_2(t)\sin(2\omega_1 t + \phi_2)$$

where $\Gamma_n = \sqrt{A_n^2 + B_n^2}$. The governing equations for $\Gamma_1, \Gamma_2$ and the effective relative phase $\psi = 2\phi_1 - \phi_2$ are

$$\frac{d\Gamma_1}{dt} = \alpha_1 \Gamma_1 - \beta\Gamma_1\Gamma_2\cos\psi$$

$$\frac{d\Gamma_2}{dt} = \alpha_2\Gamma_2 - \beta\Gamma_1^2\cos\psi$$

$$\frac{d\psi}{dt} = (\theta_1 - 2\theta_1) + \beta\left(2\Gamma_1 - \frac{\Gamma_1^2}{2}\right)\sin\psi$$

(7.5) a,b,c

where

$$\beta = \frac{\theta_2 - 2\theta_1}{2\alpha_1\alpha_2}$$

(7.6)

The problem of linear stability is solved directly:

$$\alpha_1, \alpha_2 < 0 \Longleftrightarrow \text{small amplitude motions are stable}$$

(7.7)

Nonlinear behavior in general poses two basic questions:

(i) What are the conditions for existence of limit cycles?
(ii) What are the conditions that the limit cycles are stable?

Stability of a limit cycle of course is a matter entirely separate from the linear stability of small amplitude motions. We are concerned here with a system executing a steady limit cycle. If the limit cycle in stable, then if slightly disturbed, the motion will eventually return to its initial form

### (a) Existence of Limit Cycles

In this time-averaged formulation, existence of limit cycles corresponds to existence of stationary or equilibrium points of the system (7.5) a,b,c:

$$\frac{d\Gamma}{dt} = \frac{d\Gamma_2}{dt} = \frac{d\psi}{dt} = 0 \Longleftrightarrow \text{transcendental algebraic equations}$$

The solutions are

$$\Gamma_{10} = \frac{1}{K}\sqrt{-\alpha_1\alpha_2(1+\beta^2)}$$

$$\Gamma_{20} = \frac{1}{K}\sqrt{\alpha_1^2(1+\beta^2)} \qquad \text{(7.8) a,b,c}$$

$$\psi_o = \tan^{-1}(-\beta)$$

where

$$K = \frac{\gamma+1}{2\gamma}\omega_1 \qquad\qquad\qquad (7.9)$$

For $\Gamma_{10}$ to be real, $-\alpha_1\alpha_2$ must be positive, implying that the constants $\alpha_1, \alpha_2$ must have opposite signs. The physical interpretation is that if the first mode is unstable, for example, $\alpha > 0$, then the second mode must be stable ($\alpha_2 < 0$): the rate of energy flow into the first mode must equal the rate of loss from the second mode in order that the amplitudes be constant in time. The transfer rate upwards due to coupling must have the same value. Similar reasoning explains the care when the second grade is unstable, requiring that the first mode to be stable.

### (b) *Stability of Limit Cycles*

To determine the stability of the limit cycles, the variables are written as $\Gamma_i = \Gamma_{i0} + \Gamma_i'$, $\quad \psi = \psi_o + \psi'$ and substituted in the governing equations (7.5) a,b,c. The linearized equations for the disturbances are then solved for characteristic value $\lambda$ in the assumed forms $\Gamma_i' = \Gamma_{i0}'e^{\lambda t}, \cdots$. For stability, an initial disturbance must decay. Applying that requirement produces regions of stability in the plane of the parameters $\beta_o = (\theta_2-2\theta_1)^2/(\alpha_2+2\alpha_1)^2$ and $\alpha_2/\alpha_1$, shown in Figure 7.2
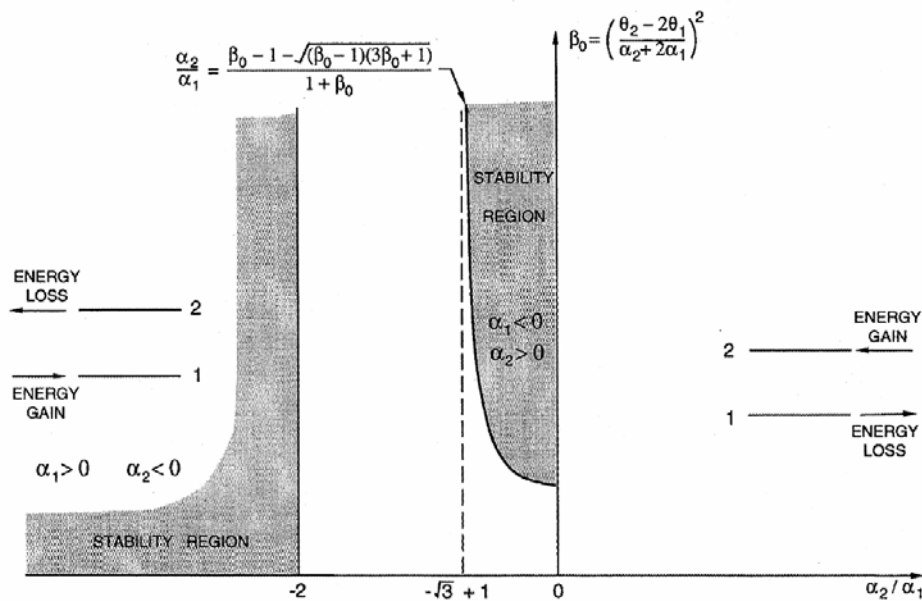


FIGURE 7.2. Regions of Stability for Two Modes, Time-Averaged Equations

There is presently no basis for understanding why stable limit cycles occur only for the special ranges of parameters shown in Figure 7.2. Moreover, it is impossible at this stage to understand the extent to which the shapes of the regions of stability depend on the use of time-averaged equations and on truncation to two modes. It is important for both practical and theoretical reasons to assess and quantify as far as possible the consequences of time-averaging and truncation. Considerable progress has been made in that direction by using a continuation method to solve the systems of oscillator equations. Some results are discussed in the following section.

Here it is useful to examine several special cases. Figure 7.3 shows that if the parameters are chosen so that the operating point lies with the range for stable limit cycles and the first mode is unstable, truncation may have relatively small effects. On the other hand, if the limit cycle is unstable within the two-mode approximation with an unstable first mode, it may become stable (with the same values of $\alpha_1, \alpha_2, \theta_1, \theta_2$) if more stable modes are accounted for.
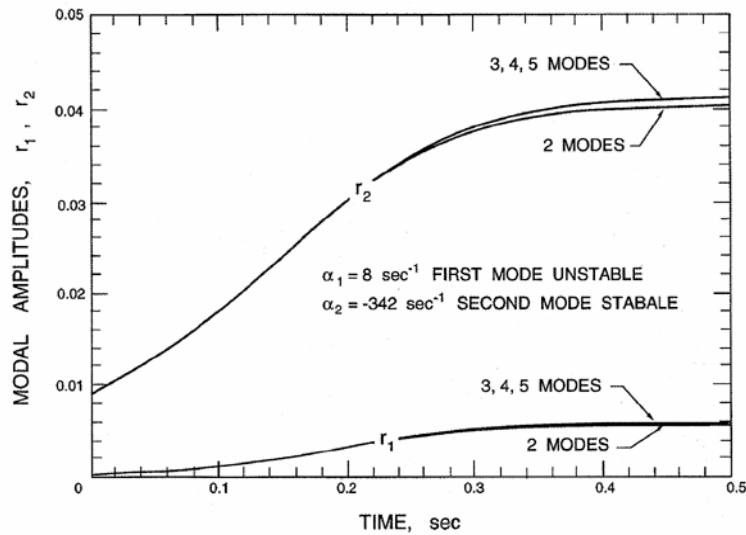


FIGURE 7.3. Effects of Truncation for a Stable Limit Cycle/First Mode Unstable
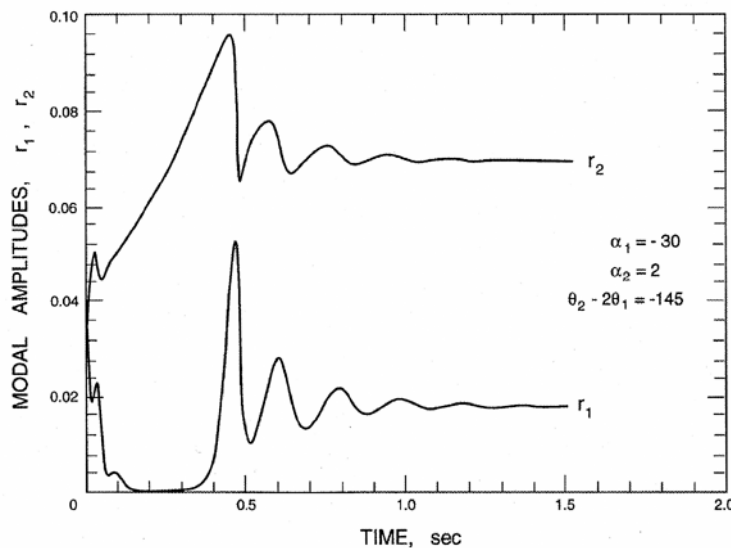


FIGURE 7.4. Development of a Stable Limit Cycle when the Second Mode is Unstable

Figure 7.4 is interesting for a quite different reason. In this case the second mode is unstable, and the motion evolves to a stable limit cycle. However, unlike the example in Figure 7.3, the amplitudes do not grow smoothly and monotonically to their values in the limit cycle. Their erratic behavior is due to the fact that with the second mode unstable, energy must flow from high frequency to low frequency. That is contrary to the direction of flow imposed naturally by the fluid mechanics (of the steepening of a compressive disturbance into a shock wave). The conflict between the natural action of the nonlinear coupling on the one hand and the flow of energy imposed by

energy exchange with the environment causes the amplitudes of the two modes to wander during the transient phase before finally reaching their ultimate values.

**7.2. Application of a Continuation Method.** Much of the work during the past decade at Caltech on chamber dynamics has been directed to understanding the extent to which nonlinear behavior can be explained on the basis of nonlinear gasdynamics. The reasoning is that first we know the model of gasdynamics—the Navier-Stokes equations for compressible flow—so we can do accurate analysis; and second, those features that cannot be explained must be due to other causes so, by elimination we have some guidelines for what we should seek in other processes. Experience has shown that 'other processes' is this context most probably means combustion.

To carry out this program with numerical simulations—after all, few exact results exist—would be a formidable task because of the number of characteristic parameters. The parameter space comprises those defining the geometry of a chamber and two parameters $(\alpha_n, \theta_n)$ characterizing linear behavior of each mode. The effect required to search the parameter space is much reduced by applying a continuation method. The procedure is an efficient system means of locating values of parameters for which the dynamical behavior suffers a qualitative change, i.e. bifurcation points. The simplest—almost trivial—example is the Hopf bifurcation point which arises when for a stable system one of the values $\alpha_n$ changes from a negative to a positive value; the system becomes linearly unstable and under suitable conditions the motion develops into a stable limit cycle. In fact, linear instability is not always such a simple matter. We have found cases with special sorts of nonlinear processes that a Hopf bifurcation may occur when the critical value of the critical $\alpha_n$ is non-zero.

The essential idea of a continuation method applied to limit cycles is illustrated in Figure 7.5 where the variables of the motion are $x(t)$ and $\mu$ is the parameter in question, the bifurcation parameter. A continuation method is a computational (numerical) scheme for following, in this case, the changes of a period solution—a limit cycle—as the values of one or more parameters are changed. A picture like Figure 7.5 is impossible to draw for more than three coordinates so the conventional display of information is a bifurcation diagram in which the amplitude of one variable in the limit cycle is plotted versus the parameters varied as the continuation method is applied. Figure 7.5 shows two examples, a Hopf bifurcation, also called a *supercritical bifurcation* and a *subcritical bifurcation* with a turning point. Those are the two types of bifurcation most common in the present context.
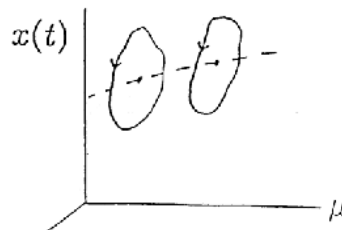


FIGURE 7.5. Schematic Illustration of the Continuation Method Applied to Limit Cycles



Supercritical bifurcation

Subcritical bifurcation with a turning point
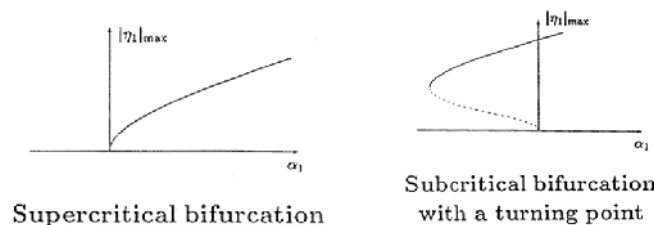
FIGURE 7.6. Two Examples of Bifurcation

Thus a bifurcation diagram is a locus of equilibrium point traced as the bifurcation parameter is changed. As a practical matter, application of a continuation method is more systematic and cheaper to use than use of numerical simulations. We have successfully used a continuation method (Doedel *et al.* 1991a,b; Doedel *et al.* 1997) to investigate four classes of problems:

(i) consequences of time-averaging
(ii) consequences of truncating the modal expansion
(iii) influences of the linear parameters $(\alpha_n, \theta_n)$ on nonlinear behavior
(iv) pulsed instabilities: the conditions for existence of stable limit cycles in a linearly stable system.

The problems (i) and (ii) are central to the matter of constructing reduced-order models. Hence it is important to emphasize that in our view, application of the continuation method to investigate the consequences of time-averaging and truncation is part of the procedure for establishing the validity of reduced order models within the framework of analysis based on modal expansion and spatial averaging.

The continuation method is a powerful means for investigating many nonlinear problems in the classic listed above. For more extensive discussions see Jahnke and Culick (1994); Burnley (1996); Burnley and Culick (1996); and Ananthkrishnan and Culick (2002). As an illustration we quote here some results for limit cycles for systems of longitudinal modes when only the gasdynamical nonlinearities are accounted for. We are interested in the consequences of truncation with time-averaging.

In Section 7.1 we cited a few results for the limiting case of two modes described by the four equations found with time-averaging. Figure 7.3 shows the special example of as effect of truncating the series expansion for the time-averaged system: increasing the number of modes apparently widens the region of stability. In fact, use of the continuation method has established the result that the existence for region of stability for limit cycles with two modes is due to truncation. When the first mode is unstable, stable limit cycles exist for all values of $\alpha$, if more than two modes are taken into account. That is true even if the original oscillator equations are used.

Figure 7.7 shows that if time-averaging is not used, there is a turning point in the bifurcation diagram. If
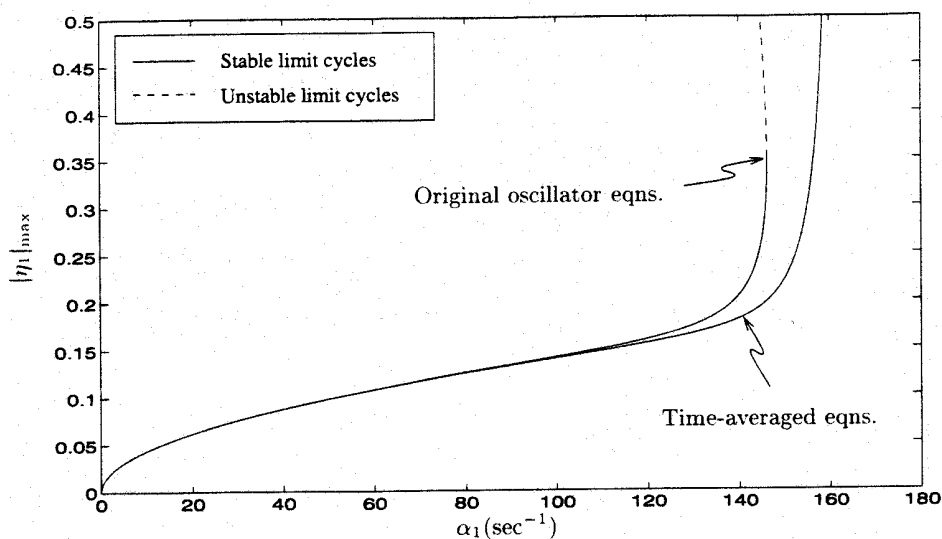


FIGURE 7.7. Effect of Time-Averaging for Two Modes

more than two modes are accounted for, the boundary of stability persists for the time-averaged equations but does not appear if more than two modes are included. Figure 7.8 is the result for the time-averaged equations and Figure 7.9 shows the case of 4 modes computed for the full oscillator equations.

It seems true that if the system is only slightly unstable, then the system of time-averaged equations for two-longitudinal modes is a good approximate model for investigating nonlinear behavior. However, if one is generally interested in producing reduced order models, the effects of truncation and time-averaging should be investigated. Applying a continuation method seems to be the best approach for doing so.
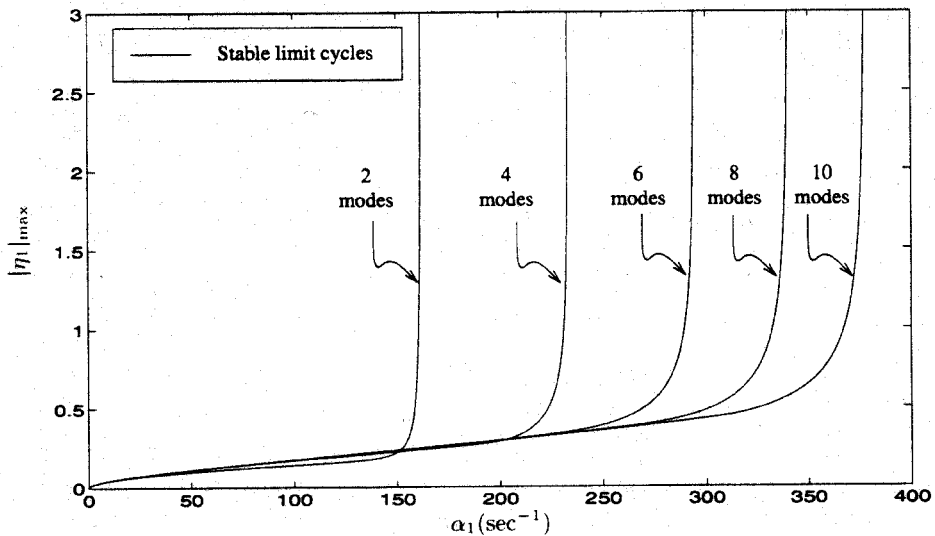
FIGURE 7.8. Stability Boundaries by Truncation of the Time-Averaged Equations
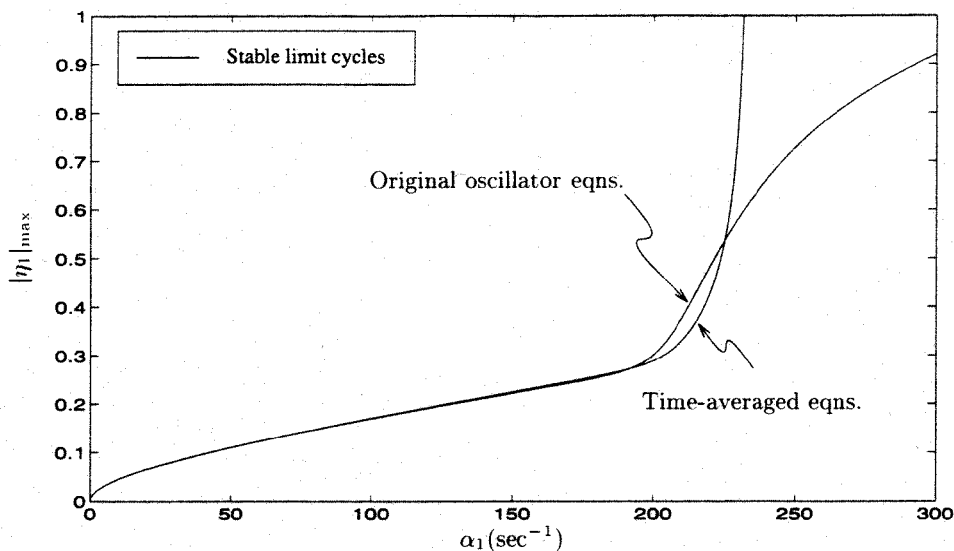


FIGURE 7.9. Maximum Amplitude of $\eta_1$ in The Limit Cycle: Four Modes, Comparison of Results for the Full Oscillator and the Time-Averaged Equations

**7.3. Hysteresis and Control of Combustion Instabilities.** The existence of hysteresis in the dynamical behavior of combustions is both an interesting phenomenon to investigation and a characteristic that has potentially important practical consequences. It seems that the first evidence for hysteresis in combustors was found by Russian researchers concerned with instabilities in liquid rockets (Natanzon *et al* 1993; Natanzon 1999). In that case, Natanzon and his co-workers proposed bifurcation of *steady states* of combustion, and the associated hysteresis, as a possible explanation for the random occurrences of combustion instabilities. The Russian workers were in a special situation affording them the opportunity to make such observations. The large Russian boosters were designed to use many (up to thirty-three) liquid rocket engines in a single stage. Hence large numbers of nominally identical engines were manufactured and tested for operational use. Sufficient data were obtained that statistical analysis of the behavior could be carried out. Hence a basis existed for identifying random behavior. The idea is the following.

In a liquid rocket many zones of recirculation are created at the injector where jets of liquid fuel and/or oxidizer enter the chamber. As an approximation, one may regard a recirculation zone as a chemical reactor whose behavior is known to be well-characterized by the temperature of the incoming gases entrained from the environment, and the average temperature within the zone. A fairly simple calculation based on consideration of energy and mass flows leads to the results sketched in Figure 7.10. The upper and lower branches of the
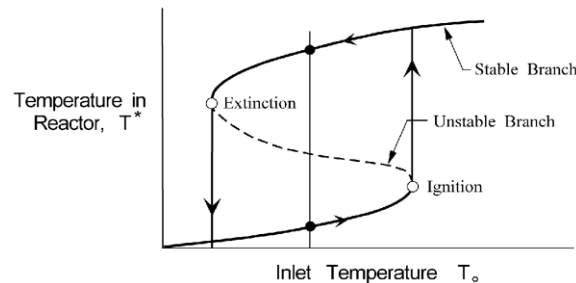


FIGURE 7.10. Hysteresis Loop for a Recirculated Zone Idealized as a Simple Chemical Reactor

hysteresis loop represent different branches of stable combustion. Those states have different influences on the state of combustion in the chamber. It was Natanzon's assertion that the state associated with the lower branch in Figure 7.10 (the cold recirculation zone) is more unstable and prone to lead to combustion instabilities. Which branch is reached depends on the history of the engine, starting from ignition or some other sort of abrupt transient. The final state of a recirculation zone therefore depends on random 'accidents' of history. Therefore random occurences or combustion instabilities may be observed. Figure 7.11 is a sketch of a possible recirculation zone and adjacent flow of a fuel or oxidizer jet, this model has been used as the basis for numerical calculations supporting Natanzon's proposal.
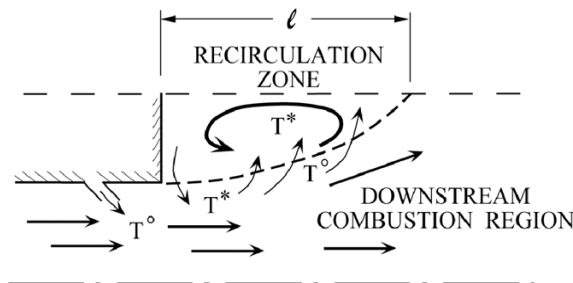


FIGURE 7.11. Sketch of a Recirculation Zone formed by a Jet of Fuel or Oxidizer

In the mid-1980's research with a dump combustor at Caltech revealed the presence of a different kind of hysteresis of dynamical states of combustion (Smith, 1985; Sterling, 1987). The combustor has been described in Section 1, Figure 1.3; Figure 6.2 shows the inlet region and the recirculation zone at the dump plane during steady combustion. The combustor showed combustion instabilities in the neighborhood of the stability boundary defined in the plane of flow rate and equivalence ratio. Figure 7.12(a). Figure 7.12(b) shows the hysteresis loop, observed as dependence of the level if pressure oscillation on equivalent ratio with the total flow rate held constant. This sort of behavior has been observed also in other dump combustors (J. Cohen, UTRC; and G. Richards, METC) as well as as in a flame-driven Rijke tube (Seywert, 2001) and in an electrically driven Rijke tube (Matveev, 2002).

More recent works (Knoop et al. 1996; Isella et al. 1996) have established the physical nature of the hysteresis in this case and have shown how active control can be used to extend the range of steady operation into the hysteretic region. High speed films have confirmed that the upper branch of the loop is associated with shedding of large vortices which, causing periodic combustion of entrained reactants sustain high amplitude pressure oscillations. The lower branch is associated with relatively quiet combustion in a shear layer shed from the lip at the inlet.
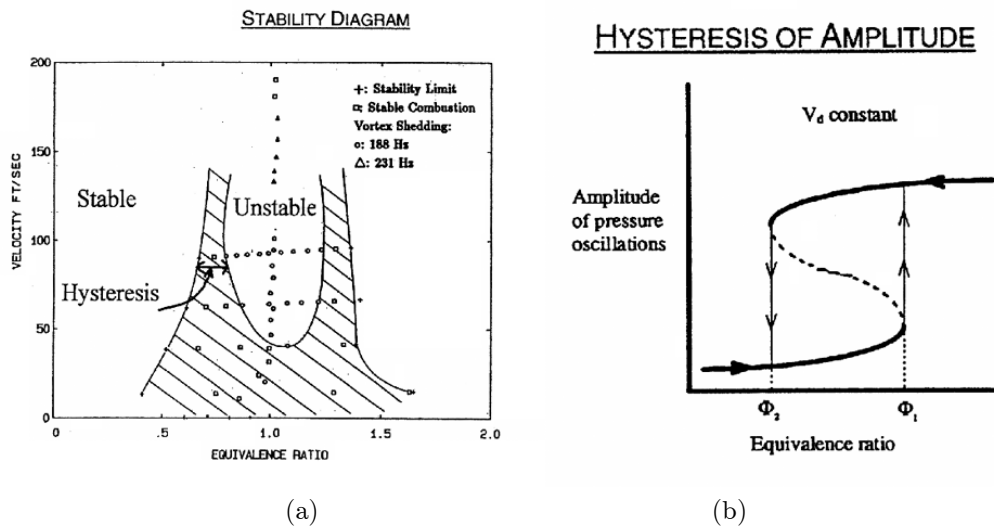
FIGURE 7.12. (a) Stability Boundary and (b) an Idealized Hysteresis Loop for the Caltech Dump Combustor

Familiar considerations of dynamical behavior suggest that it should be possible to achieve pulsed transitions between the two branches of stable dynamical states. Those processes were demonstrated by Knoop *et al* and Isella *et al* by injecting pulses of fuel at the inlet plane. Single pulses of fuel always cause transition from the upper to the lower branch. Thus with suitable sensing and actuation it is possible always to maintain the low level of oscillations (effectively 'noise') within the zone where hysteresis exists.

This is a form of nonlinear control. Although it has been demonstrated only for the range of equivalence ratio covering the zone of hysteresis, it is an important demonstration of active control at a frequency far less than the frequency of the oscillations. That is a significant characteristic because if the reduced bandwidth required of the control system, particularly the actuation.

**7.4. Representing Noise in Analysis of Combustor Dynamics.** Even a small laboratory combustor radiates considerable noise, generated by turbulent motions (often called 'combustion noise') within the chamber. See, for example, the spectrum reproduced earlier as Figure 1.4. The scaling laws are not known, but it is obvious to any bystander that a full-scale combustor of any sort is noisy indeed. Presently it is not well understood how important noise is to the behavior of combustion instabilities or to the application of feedback control. The purpose of this section is to introduce a means for investigating those matters within the framework developed in Sections 3 and 4.

There are three sorts of problems that will arise:

   (i) formal construction of noise (stochastic) sources in the framework of spatially averaged equations for unsteady motions in a combustor;

  (ii) modelling the noise sources;

 (iii) solving the stochastic differential equations.

The first step, as explained in Section 3.1, is to apply the principle of splitting small disturbances into the three basic modes of propagation: acoustic waves, vorticity waves, and entropy waves. All of the discussion so far in these lectures has been devoted to the acoustic field. Noise is associated with the random motions comprising mainly vorticity but also entropy (or temperature) waves in a combustion chamber. Our concern in the present context is directed chiefly to interactions of those motions with the acoustic field. The formal representation will be relatively simple and intuitively persuasive, but modelling the details remains to be accomplished. Numerical results require assumptions that cannot be justified *a priori.*

Following the principle of splitting, we write the flow variables as sums of the three contributions, one each corresponding to the three modes of motion:

$$p' = p'_a + p'_\Omega + p'_s$$
$$\mathbf{\Omega}' = \mathbf{\Omega}'_a + \mathbf{\Omega}'_\Omega + \mathbf{\Omega}'_s$$
$$s' = s'_a + s'_\Omega + s'_s$$
$$\mathbf{u}' = \mathbf{u}'_a + \mathbf{u}'_\Omega + \mathbf{u}'_s$$

(7.10) a,b,c,d

Subscripts $(\ \ )_a$, $(\ \ )_\Omega$, $(\ \ )_s$ denote acoustic, vortical and entropic contributions. Once again, the ordering procedure explained in Sections 3 and 4 allows us to derive meaningful results by considering only the first order components. Hence we assume that only the acoustic waves contain pressure fluctuation; only the waves of vorticity contain vorticity fluctuations; and only the entropy waves have fluctuations of entropy. The velocity field possesses contributions from all three modes.

The idea then is to substitute the assumed general forms of the variables and substitute in the primitive equations of motion expanded to third order in the fluctuations. Then form the nonlinear equation for the pressure and apply spatial averaging. This procedure was first reported by Culick *et al.* (1992) but in revised and corrected form by Burnley (1996) and Burnley and Culick (1999). Eventually one finds the oscillator equations,

$$\ddot{\eta}_n + \omega_n^2 \eta_n = F_n$$

by now $F_n$ contains stochastic sources. The 'general' form of $F_n$ is

$$-\frac{\bar{p}E_n^2}{\bar{a}^2}F_n = \bar{\rho}I_1 + \frac{1}{\bar{a}^2}I_2 + \bar{\rho}I_3 + \frac{1}{\bar{a}^2}I_4 + \bar{\rho}I_5$$
$$+ \oiint \left[\rho\frac{\partial \mathbf{u}'}{\partial t}\cdot\hat{u} + \bar{\rho}\frac{\partial \mathbf{u}'}{\partial t}\right]\cdot\hat{\mathbf{n}}\psi_n dS - \int \boldsymbol{\mathscr{F}}'\cdot\nabla\psi_n dV + \frac{1}{\bar{a}^2}\int\frac{\partial P'}{\partial t}\psi_n dV$$

where

$$I_1 = \int \left[\bar{\mathbf{u}}\cdot\nabla\mathbf{u}' + \mathbf{u}'\cdot\nabla\bar{\mathbf{u}}\right]\cdot\nabla\psi_n dV$$

and similar definitions for the remaining integrals $I_1$. See the references for details.

Then the unsteady velocity field is split according to (7.10) a,b,c,d. Eventually re-arrangement and application of the assumptions discussed above leads to the result

$$\ddot{\eta}_n + \omega_n^2\eta_n = 2\alpha_n\dot{\eta}_n + 2\omega_n\theta_n\eta_n - \sum_{i=1}^{\infty}\sum_{i=1}^{\infty}\left[A_{nij}\dot{\eta}_i\dot{\eta}_j + B_{nij}\eta_i\eta_j\right]$$
$$+ \sum\left[\xi_{ni}^v\dot{\eta}_i + \xi_{ni}\eta_i\right] + \Xi_n + \left(F_n^{NL}\right)_{other}$$

(7.11)

where the $\xi_{ni}^v$, $\xi_{ni}$ and $\Xi_n$ are stochastic sources defined as integrals over the vortical and entropic fluctuations of the velocity. See the references cited above for details.

No modeling based on experimental, theoretical or phenomenological grounds has been accomplished. Explicit results have been obtained by approximating the stochastic sources as white noise processes having properties chosen to be realistic, i.e. the results seem to be reasonably consistent with available measurements of actual behavior.

Two types of stochastic influences arise in (7.11):

(i) $\Xi_{ni}$, $\Xi_{ni}^v$ represent stochastic influences on the 'spring' or natural frequency of the $n^{th}$ mode and on the damping or growth rate. These are formally referred to as 'multiplicative noise sources' because they appear as factors multiplying the dependent variables, the displacement and velocity of the $n^{th}$ oscillator.

(ii) $\Xi_n$ represents a stochastic driving source causing excitation of the $n^{th}$ oscillator even in the absence of driving by combustion processes; the $\Xi_n$ are formally called 'additive noise sources'.

It is evident from the form of (7.11) that the random character of the stochastic sources will appear as random fluctuations imposed on the amplitudes $\eta_n(t)$ of the acoustic modes; exactly the sort of behavior found experimentally. Thus, Fourier synthesis of the pressure field, the modal expansion, continues to serve as a good approximate representation of the deterministic results can be obtained by retaining only a small number of terms.

Results were obtained first for the simplest, case of two modes, with noise sources only in the fundamental mode. Nonlinear gasdynamic coupling transfer stochastic behavior to the second mode. Computations have been carried out with a Monte-Carlo method to give probability density functions, with the equations written in the Stratonovich form of stochastic differential equations (Burnley, 1996). Figure 7.13 shows the pressure trace and spectrum for a simulation in which the first mode is unstable.
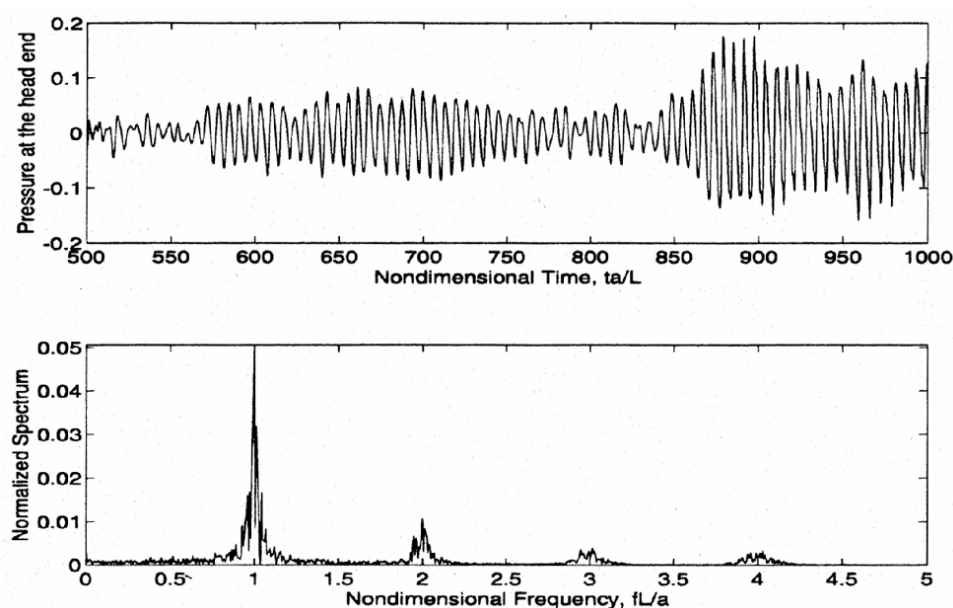


FIGURE 7.13. Pressure Trace and Spectrum for a Simulation with Noise; Four Modes Included, First Mode Unstable

This method of accounted for noise in a combustor seems to be very promising. However modeling the noise sources is in a primitive state, and comparisons of results with experimental observations can only be done qualitatively.

**7.5. System Identification for Combustor Dynamics with Noise.** Use of system identification in the field of combustor dynamics seems to have been developed first by Russian groups as part of their development of liquid rocket engines, beginning perhaps as early as the 1950's but certainly in the 1960's (Agarkov *et al.* 1993).

In several papers during the 1980's, Hessler (1979, 1980, 1982) and Duer and Hessler (1984), and more recently Hessler and Glick (1998) have asserted that the oscillations observed as combustion instabilities in solid rocket motors are *driven* rather than *self-excited.* The sources of the driving—i.e. the 'mechanisms'—are supposed to be either vortex shedding or noise. Hessler and co-workers conclude that the properties of the noise measured in a stable chamber can be used as the basis for infusing properties of the primary mechanism causing instabilities when they arise or more correctly, such data will provide quantitative information about the static stability margins—how close the dominant acoustic modes are to becoming unstable.

The basic idea is sound. When the mechanisms are interpreted as driving forces independent of the acoustic field, and they are assumed to be broad-band, then the acoustic modes are excited to amplitudes related directly to the amount of damping $(\alpha_n)$. Hence the idea is to process noisy records in such a fashion as to extract the values of the linear parameters $(\alpha_n, \theta_n)$. The proposed method can be tested using the oscillator equations with some sources derived in the preceding section.

Seywert and Culick (1999) have reported results of some numerical simulations carried out to check the idea just described. In particular, the main purpose was to determine the accuracy with which the experimental method would give the linear parameters. The procedure is straightforward. To be definite and to keep the computations within practical bounds, we consider a system of four modes, each containing noise sources which, as explained in Section 7.4, are assumed to be white noise. The amplitudes of the noise (rms values) are selected so that random amplitude fluctuations in the pressure spectrum have values in the ranges experimentally observed (Seywert and Culick).

Three types of problems arise, associated with the three types of noise sources: additive noise, $\Xi_n$; and two kinds of multiplicative noise, $\xi_n^v$ which affects mainly the growth and decay rates, and $\xi_n$ which causes random variations of the frequency. In all cases we are concerned here with discovering the ways in which noise affects the result of system identification. The idea is to select values of the $\alpha_n$, $\theta_n$ and carry out numerical simulations. The data are then processed to give values of the $\alpha_n$, $\theta_n$ which now have mean values and some uncertainties due to the presence of the noise. The questions to be answered are: How close are the mean values to the time values used as inputs? and How large are the uncertainties? These are important practical matters. If the method is effective, then data from hot firings of full-scale combustors could be used to infer the linear parameters characterizing the dynamics represented by several modes. Those parameters identify the poles of the response function of the chamber. Hence a relatively straightforward process would give the information required to proceed with designing a linear control system (see Section 2.5).

Actually there are two ways to get the information: process pressure records naturally occurring; or process the pressure record following an pulse. The method of pulsing has long been used as means of assessing the stability margin of liquid rockets (Harrje and Reardon, 1972). Both methods have been used for a stable system of four longitudinal modes having the parameters given in the table; the fundamental frequency is $900 \ s^{-1}$. Figure 7.14 shows a simulated pressure trace and Figure 7.15 shows its power spectrum and construction using Berg's method.[25]

| mode | 1 | 2 | 3 | 4 |
|------|------|------|------|------|
| $\alpha_n(s^{-1})$ | $-50$ | $-375$ | $-584$ | $-889$ |
| $\theta_n(s^{-1})$ | $12.9$ | $46.8$ | $-29$ | $-131$ |

TABLE 7.1. Values of the Linear Parameters
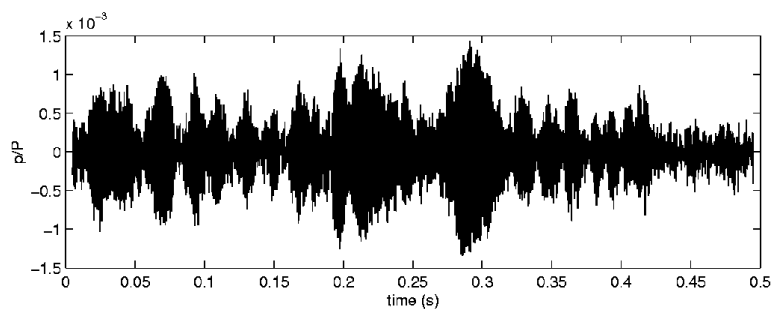


FIGURE 7.14. Simulated Pressure Trace with Noise; All Modes Stable

---

[25] Berg's method is a standard method of signal processing, widely available. We have used the software included in the Signal Processing Toolbox, and extension of MATLAB.

In Figure 7.17, a simulated response to a pulse is fitted by the superposition of four modes:

$$\frac{p'}{\bar{p}} = \sum_{i=1}^{4} A_i e^{\alpha_i t} \cos(\omega_i t + \phi_i)$$

The parameters $A_i$, $\alpha_i$, $\omega_i$, $\phi_i$ are fitted using a least squares method.
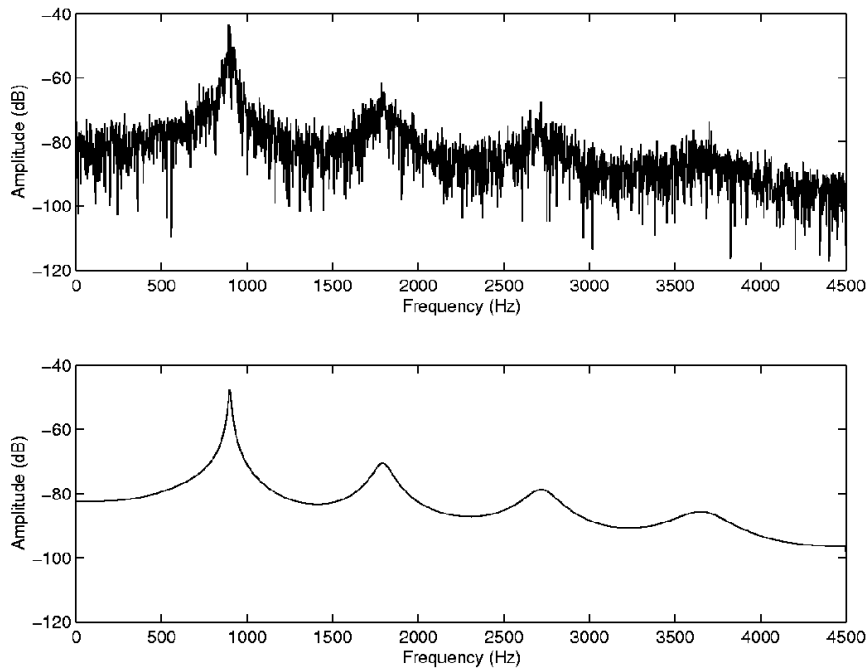


FIGURE 7.15. Application of Berg's Method: Power Spectrum of the Pressure Trace in Figure 7.14 and its Reconstruction
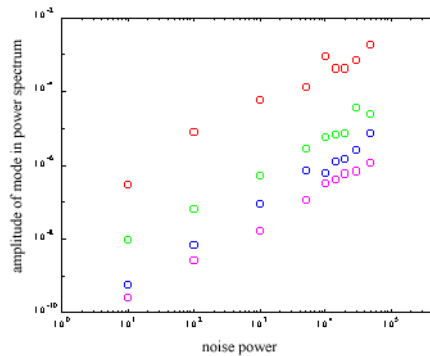


FIGURE 7.16. Dependence of the Peak Amplitudes of the Power Spectra for Four Modes, on Noise Power

Without good data for the noise in an actual combustor and no model, we assume white noise sources. Their amplitudes are chosen so that the average (rms) values of the simulated pressure records are reasonable Table 7.2 shows the relation between the rms value of the system response $(p'/\bar{p})$ and the noise power of $\Xi$. The 'noisepower' cannot be measured, being the height of the power spectral density of the noise. Figure 7.16 gives a more detailed picture, showing how the amplitudes of the spectra of the four modes increase with noise power.

We use the noise power as a parameter. Figure 7.18 shows an example of the sort of results one finds for multiplicative noise in the modal damping ($\xi_n^v \neq 0$; $\xi_n = 0$; $\Xi_n = 0$). The corresponding results of using the pulse method are given in Figure 7.19.

| Noise Power of $\Xi_n$ | rms Values of $p'/\bar{p}$ |
|:---:|:---:|
| $10^1$ | .005% |
| $10^3$ | .05% |
| $10^5$ | .5% |

TABLE 7.2. Relation Between the Noise Power of $\Xi_n$ and the rms Value of the Simulated Pressure Fluctuation
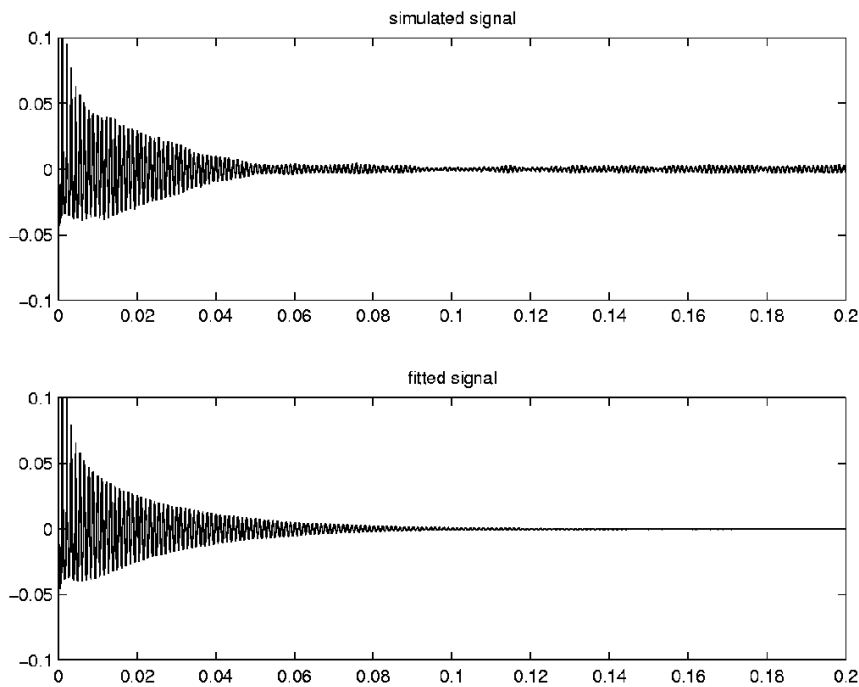


FIGURE 7.17. Reconstructed Pressure Trace for the Transient Response Excited by a 10% Pulse



| Noise | $\alpha_1$ | $\alpha_2$ | $\alpha_3$ | $\alpha_4$ |
|:---:|:---:|:---:|:---:|:---:|
| $10^1$ | -57±14 | -301±31 | -560±84 | -886±98 |
| $10^2$ | -51±13 | -307±52 | -576±75 | -903±126 |
| $10^3$ | -47±11 | -307±38 | -558±78 | -901±117 |
| $10^4$ | -56±16 | -300±51 | -591±88 | -883±150 |
| $10^5$ | -59±18 | -310±53 | -598±95 | -914±128 |
| $10^6$ | -53±15 | -310±46 | -564±84 | -905±172 |
| $10^7$ | -59±19 | -313±44 | -591±83 | -887±124 |
| correct | -50 | -325 | -584 | -889 |
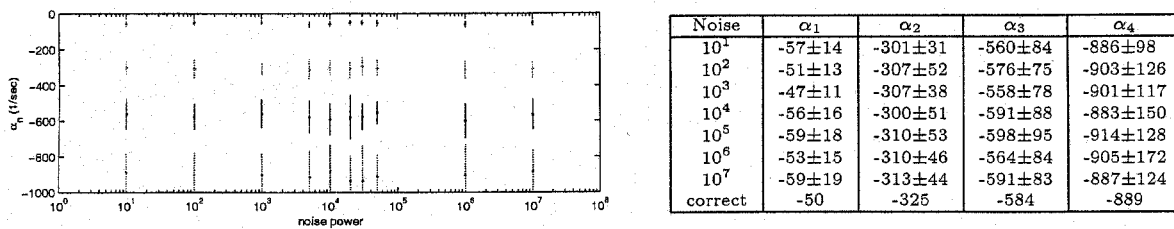
FIGURE 7.18. Values of Decay Rates (Modal Attenuation) Found with Berg's Method with Multiplicative ($\xi_n$) Noise

We conclude from these results that substantial errors may accompany system identification in the presence of realistic (we believe) noise. How significant the errors are depends the particular application at hand and in how small the stability margins are. For a weakly stable system, values of the margins determined in this way are suspect because of the finite uncertainties. The results would therefore not be useful as a basis for representing the combustor's response function.

| Noise | $\alpha_1$ | $\alpha_2$ | $\alpha_3$ | $\alpha_4$ |
|---|---|---|---|---|
| $10^1$ | $-50\pm2$ | $-323\pm6$ | $-584\pm9$ | $-889\pm35$ |
| $10^2$ | $-50\pm2$ | $-325\pm5$ | $-589\pm8$ | $-908\pm36$ |
| $10^3$ | $-50\pm2$ | $-322\pm4$ | $-587\pm10$ | $-891\pm44$ |
| $10^4$ | $-50\pm3$ | $-326\pm5$ | $-589\pm8$ | $-902\pm37$ |
| $10^5$ | $-49\pm3$ | $-326\pm4$ | $-586\pm12$ | $-895\pm35$ |
| $10^6$ | $-50\pm2$ | $-324\pm4$ | $-582\pm15$ | $-886\pm43$ |
| $10^7$ | $-49\pm3$ | $-327\pm4$ | $-583\pm11$ | $-877\pm51$ |
| correct | $-50$ | $-325$ | $-584$ | $-889$ |

FIGURE 7.19. Values of Decay Rates (Modal Attenuation) Found with the Method of Pulsing

It should be clear from the nature of the methods described here that the system must be stable (i.e. all modes must be stable) for this application. For example, if data (simulated) for a limit cycle are processed in this fashion, the inferred values of $\alpha_n$, $\theta_n$ have no apparent connection with the correct values.

# 8. PASSIVE CONTROL OF COMBUSTION INSTABILITIES

Given the irrefutable observational evidence that combustion instabilities will almost inevitably occur during development of new motors, the problem of treating them becomes crucially important. The goal must be to eliminate undesirable oscillation, but as a practical matter it may well be satisfactory to reduce their amplitudes to acceptable levels. The manufacturer and the customer must then be confident that the amplitudes will not grow unexpectedly at some later time.

Figure 1.6 suggests the intentions or goals of introducing passive control:

(i) Increase the losses of acoustic energy so they exceed the gains in the frequency range where the instability occurs;

(ii) Reduce the gains of acoustic energy below the losses; or

(iii) Shift the natural frequencies of the chamber modes so that none lie within the range of frequencies where the gains of acoustic energy exceed the losses.

The chief ways of achieving these goals in practice are:

(i) Increase the losses of acoustic energy:
   - modify the geometry including possibly, the shape of the nozzle entry section
   - add resonators, baffles or 'resonant rods'
   - introduce stability additives

(ii) Reduce the gains of acoustic energy:
   - eliminate geometrical causes of vortex shedding
   - change the composition of the propellant—notably the size distribution of oxidizer particles
   - introduce stability additives

(iii) Shift the natural frequencies of the chamber
   - change the geometry of the chamber
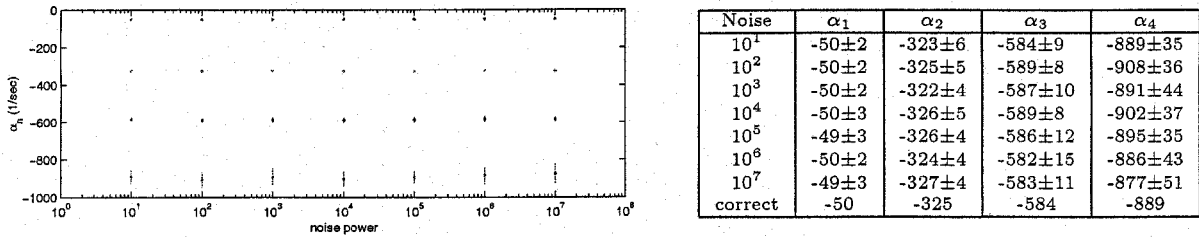
Of the various possibilities, the most commonly used now are changes of geometry, and introduction of stability additives.

Generally there are three reasons to revise the internal design: eliminate possible causes of vortex shedding; shift the frequencies of the normal modes; and increase the gains, or reduce the losses of acoustic energy. The last tactic rests on understanding the contributions to the growth/decay constant, as well as the way in which the shape of the grain changes with time during a firing. The results shown in Figure 8.1 illustrate the point.

It is particularly important to know as well as possible the relative importance of pressure and velocity coupling. That understanding requires knowing the acoustic mode shapes—easily acquired (or estimated if necessary)—and, more importantly, the response functions of the propellant for pressure and velocity coupling. We have emphasized in Section 2 that at the present time data for the pressure coupled response can be obtained only with difficulty and considerable uncertainty. There is no method for routinely determining the velocity coupled response.

The problem of relating changes of composition of a propellant to changes of its combustion dynamics remains essentially unsolved. Experience has provided some guidelines (influences of AP particle size distribution is perhaps the best example) but what is available has largely to do with the effects of quite significant changes of composition on the pressure-coupled response. The consequences of small changes of composition (which may be inadvertant and within manufacturing specifications) are simply not understood. The inability to obtain accurate experimental results is a serious obstacle to improving this situation.

To good approximation, the dynamics of velocity coupling are not understood. Qualitative ideas are available (see Section 2) but—again due to the lack of a good test method—the true mechanisms cannot be determined

and it is impossible to collect quantitative information. This remains, in the author's opinion, the most significant and difficult outstanding problem in this field.

In practice, much reliance has been placed on small changes of propellant composition, the use of 'stability additives.' Following the early use of resonance rods to provide stability in small motors, the favorable effects of stability additives were first investigated in the 1950s and 1960s (Summerfield 1960; Waesche 1999; Price 1971; Evans and Smith 1978). Much of the experience rests in proprietary company files, possibly under the heading "fairy dust."

Stability additives seem to have two main consequences: they may change the propellant response function (pressure or velocity coupling or both); and they certainly affect the properties of condensed combustion products that act to attenuate acoustic oscillations. As many as 80 different additives have been studied, but only a very small number have been widely used. The most common are aluminum oxide and zirconium oxide. Changing the properties of the primary metallic aluminum in the propellant may have substantial favorable consquences.

Changes in the response function may be due both to physical and chemical processes. What actually happens cannot be established unambiguously. In this situation, the collaboration of experimental tests (however crude); observation of the behavior of sub- and full-scale motors; spectulation; and theory, is extremely important. The continued elaboration of analyses of the sort discussed briefly in Section 2 is basic to this process, including calculation of linear and nonlinear dynamical behavior in motors.

For motors containing aluminum, the most significant damping process is the viscous interaction between condensed material and the surrounding gases under oscillatory conditions. The amount of attenuation is proportional to the amount of condensed material present but especially depends on the particle size distribution. Figure 8.1 shows the results of calculations of the attenuation. The main and extremely important point is that for a given frequency and particle loading (mass of particles per unit mass of gas/particle mixture) the maximum attenuation is strongly dependent on particle size. Hence in practice, means are sought to alter the combustion of the propellant and aluminum to generate particles of condensed aluminum oxide having size suitable for greatest damping of the instability at hand. In recent years this has been possibly the most widely used (or at least contemplated) strategy to treat instabilities in motors operating with metallized propellants and has often been successful. The strategy is of course less relevant to smokeless and low smoke systems. Hence the search for 'fairy dust.'
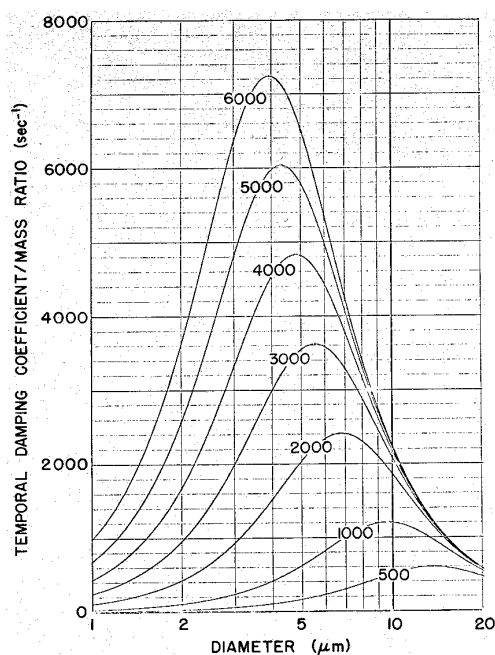


FIGURE 8.1. Attenuation of Acoustic Waves by Particles Suspended in a Gas.

## A. EQUATIONS OF MOTION

Combustion systems commonly contain condensed phases: liquid fuel or oxidizer and combustion products including soot and condensed metal oxides. Hence the equations of motion must account for two or three phases and at least one species in each. For investigating the dynamics of combustors, it is entirely adequate to represent each phase as its mass average over all member species. It is unnecessary to distinguish liquid and solid material and we assume a single species in the condensed phase, devoted by subscript ( )$_l$. For some applications it is appropriate to extend the representation slightly to accommodate distributions of particle sizes, not included in this appendix. There is some advantage to treating the gas phase as a multi-component reacting mixture. As the primitive conservation equations we therefore begin with the following set:

### A.1. General Equations of Motion. Conservation of Species

$$\frac{\partial \rho_i}{\partial t} + \nabla \cdot (\rho_i \mathbf{u}_i) = w_i + w_i^{(l)} + w_{ei} \tag{A.1}$$

**Global Conservation of Mass, Gas Phase**

$$\frac{\partial \rho_g}{\partial t} + \nabla \cdot (\rho_g \mathbf{u}_g) = w_g^{(l)} + w_{eg} \tag{A.2}$$

**Global Conservation of Mass, Condensed Phase**[26]

$$\frac{\partial \rho_l}{\partial t} + \nabla \cdot (\rho_l \mathbf{u}_l) = -w_g^{(l)} + w_{el} \tag{A.3}$$

**Global Conservation of Momentum**

$$\frac{\partial}{\partial t} \left( \sum^i \rho_i \mathbf{u}_i + \rho_l \mathbf{u}_l \right) + \nabla \cdot \left( \sum \rho_i \mathbf{u}_i \mathbf{u}_i + \rho_l \mathbf{u}_l \right) + \nabla p = \nabla \cdot \overset{\leftrightarrow}{\boldsymbol{\tau}}_v + \mathbf{m}_{eg} + \mathbf{m}_{el} \tag{A.4}$$

**Global Conservation of Energy**

$$\frac{\partial}{\partial t} \left( \sum \rho_i e_{oi} + \rho_l e_{ol} \right) + \nabla \cdot \left( \sum \rho_i \mathbf{u}_i e_{oi} + \rho_l \mathbf{u}_l e_{ol} \right) + \nabla \cdot \left( \sum p_i \mathbf{u}_i \right) = \nabla \cdot \left( \overset{\leftrightarrow}{\boldsymbol{\tau}}_v \cdot \mathbf{u}_g \right) - \nabla \cdot \mathbf{q} + Q_e \tag{A.5}$$

**Equation of State, Gas Phase**

$$p = \rho_g R_g T_g \tag{A.6}$$

For simplification, the above equations already contain some terms involving mass averaging over the species comprising the gas phase, namely the viscous tensor $\overset{\leftrightarrow}{\boldsymbol{\tau}}_v$; the vector $\mathbf{q}$ representing heat conduction; and the equation, of state (A.6). For more complete derivations of the equations for multicomponent mixtures, see for example Chapman and Cowling (1958); Hirschfelder, Curtis and Bird (19 ); Truesdell and Toupin (1960); and Williams (1985). Superscript ( )$^{(l)}$ means that the liquid phase is the source and subscript ( )$_e$ denotes an external source. It follows from repeated use of the Gibbs-Dalton law for mixtures of perfect gases that $p$ is the sum of partial pressures, $\rho_g$ is the sum of the densities and $R$ is the mass average of the individual gas species, so for the gas phase we have

$$p = \sum p_i$$
$$\rho_g = \sum \rho_i \tag{A.7} \text{ a,b,c}$$
$$R_g = \frac{1}{\rho_g} \sum \rho_i R_i$$

---

[26]Note that $\rho_l$ represents the mass of condensed material per unit volume of chamber, *not* the density of the material itself.

Subscript $(\ )_i$ identifies the $i^{th}$ gaseous species; and in all cases except $T_g$, $(\ )_g$ means a mass average over all gas species as, for example,

$$\mathbf{u}_g = \frac{1}{\rho_g} \sum \rho_i \mathbf{u}_i = \sum Y_i \mathbf{u}_i \tag{A.8}$$

where $Y_i = \rho_i / \rho_g$ is the mass concentration of the $i^{th}$ species.

Writing equations (A.1)–(A.5) explicitly with sums over species allows proper accounting of the influences of diffusion, and leads to the formula for energy released by chemical reactions written in the conventional fashion. Thus the basis for subsequently modeling is rigorously set. For analysis of unsteady motins in combustors it is perfectly adequate to reduce the general description for a multicomponent mixture to a model representing a single fluid having the mass-averaged properties of the actual mixture. Details of the procedure may be found elsewhere (Culick 1999). Only the results are germane here. The set of equations forming the basis for the theory and analysis we discuss in these lectures is:

$$\frac{D\rho}{Dt} = -\rho \nabla \cdot \mathbf{u} + \mathcal{W} \tag{A.9}$$

$$\rho \frac{D\mathbf{u}}{Dt} = -\nabla p + \boldsymbol{\mathcal{F}} \tag{A.10}$$

$$\rho \mathbf{C}_v \frac{DT}{Dt} = -p \nabla \cdot \mathbf{u} + \mathcal{Q} \tag{A.11}$$

$$\frac{Dp}{Dt} = -\boldsymbol{\gamma} p \nabla \cdot \mathbf{u} + \mathcal{P} \tag{A.12}$$

$$\frac{Ds}{Dt} = \frac{1}{T} \mathcal{S} \tag{A.13}$$

$$p = \mathbf{R} \rho T \tag{A.14}$$

For completeness we have also included the equation (A.13) for the entropy, obtained in familiar fashion by applying the combined. First and Second Laws of Thermodynamics to an element of fluid. That is, the relation $de = T ds - p dv$ can be written

$$\begin{aligned}
\frac{Ds}{Dt} &= \frac{1}{T} \left( \frac{De}{Dt} + p \frac{Dv}{Dt} \right) \\
&= \frac{1}{T} \left( \mathbf{C}_v \frac{DT}{Dt} + p \frac{Dv}{Dt} \right)
\end{aligned} \tag{A.15}$$

Substitution of (A.9) and (A.11) gives (A.13) with the source

$$\mathcal{S} = \mathcal{Q} - \frac{p}{\rho^2} \mathcal{W} \tag{A.16}$$

It is important to realize that this formulation contains all relevant physical processes, including those representing the actions of external influences associated, for example, with active control of combustor dynamics.

The source functions in (A.9)–(A.13) are

$$\mathcal{W} = w_e - \nabla \cdot (\rho_l \delta \mathbf{u}) \tag{A.17}$$

$$\boldsymbol{\mathcal{F}} = \nabla \cdot \overset{\leftrightarrow}{\boldsymbol{\tau}}_v + \mathbf{m}_e + \mathbf{m}_D - \boldsymbol{\sigma}_e - \delta \mathbf{u}_l w_g^{(l)} + \mathbf{F}_l + \delta \mathbf{F}_l \tag{A.18}$$

$$\mathcal{Q} = \overset{\leftrightarrow}{\boldsymbol{\tau}}_v \cdot \nabla \cdot \mathbf{u} - \nabla \cdot \mathbf{q} + Q^w + Q_e - (e_{og} w_{og} + e_{ol} w_l) + \chi_D + \sum h_i \nabla \cdot (\rho_g \mathbf{V}_i Y_i)$$
$$- \mathbf{u} \cdot (\mathbf{m} - \boldsymbol{\sigma}_e) + (\mathbf{u} \cdot \delta \mathbf{u}) w_g^{(l)} + \delta Q_l + \delta \mathbf{u} \cdot \mathbf{F}_l - \mathbf{u} \cdot (\boldsymbol{\mathcal{F}} - \mathbf{F}_l) \tag{A.19}$$

$$\mathcal{P} = \frac{\mathbf{R}}{\mathbf{C}_v}\mathcal{Q} + \mathbf{R}T\left[\mathcal{W} - \nabla \cdot (\rho_l \delta \mathbf{u})\right] \tag{A.20}$$

$$\mathcal{S} = \mathcal{Q} - \frac{p}{\rho^2}\mathcal{W} \tag{A.21}$$

The quantities $\delta(\ \ )$ represent differences between values for the gas and condensed phases. For example, $\delta T = T_l - T_g$ in the difference in temperature between the temperature $T_l$ of the condensed phase and that, $T_g$, of the gas phase.

**A.2. Expansions in Mean and Fluctuating Variables.** Following the steps suggested in Section 3.3 to produce equations (3.23)–(3.28) will give the expressions for the brackets defined there to simplify the appearance of the equations:

$$\{[\rho]\}_1 = \bar{\mathbf{M}} \cdot \nabla \rho' + \rho' \nabla \cdot \bar{\mathbf{M}} + \mathbf{M}' \cdot \nabla \bar{\rho} \tag{A.22}$$

$$\{\rho\}_2 = \nabla \cdot (\rho' \mathbf{M}') \tag{A.23}$$

$$\{[M]\}_1 = \bar{\rho}(\bar{\mathbf{M}} \cdot \nabla \mathbf{M}' + \mathbf{M}' \cdot \nabla \bar{\mathbf{M}} + \rho' \frac{\bar{D}\bar{\mathbf{M}}}{Dt} \tag{A.24}$$

$$\{M\}_2 = \rho' \frac{\partial \mathbf{M}'}{\partial t} + \bar{\rho}\mathbf{M}' \cdot \nabla \mathbf{M}' + \rho'\left(\bar{\mathbf{M}} \cdot \nabla \mathbf{M}' + \mathbf{M}' \cdot \nabla \bar{\mathbf{M}}\right) \tag{A.25}$$

$$\{M\}_3 = \rho' \mathbf{M}' \cdot \nabla \mathbf{M}' \tag{A.26}$$

$$\{[T]\}_1 = \bar{\rho}C_v\left(\bar{\mathbf{M}} \cdot \nabla T' + \mathbf{M}' \cdot \nabla \bar{T}\right) + C_v \rho' \frac{\bar{D}\bar{T}}{Dt} + p' \cdot \nabla \bar{\mathbf{M}} \tag{A.27}$$

$$\{T\}_2 = C_v \rho' \frac{\partial T'}{\partial t} + C_v \rho'\left(\bar{\mathbf{M}} \cdot \nabla T' + \mathbf{M}' \cdot \nabla \bar{T}\right) + C_v \bar{\rho}\mathbf{M}' \cdot \nabla T' + p' \nabla \cdot \mathbf{M}' \tag{A.28}$$

$$\{T\}_3 = C_v \rho' \mathbf{M}' \cdot \nabla T' \tag{A.29}$$

$$\{[p]\}_1 = \bar{\mathbf{M}} \cdot \nabla p' + \mathbf{M}' \cdot \nabla \bar{p} + \gamma p' \nabla \cdot \bar{\mathbf{M}} \tag{A.30}$$

$$\{p\}_2 = \mathbf{M}' \cdot \nabla p' + \gamma p' \nabla \cdot \mathbf{M}' \tag{A.31}$$

$$\{[s]\}_1 = \bar{\rho}\bar{T}\bar{\mathbf{M}} \cdot \nabla s' + \rho'\bar{T}\frac{\bar{D}\bar{s}}{Dt} + \bar{\rho}\left(\bar{T}\mathbf{M}' + T'\bar{\mathbf{M}}\right) \cdot \nabla \bar{s} \tag{A.32}$$

$$\{s\}_2 = \rho'\bar{T}\frac{\bar{D}s'}{Dt} + \rho'T'\frac{\bar{D}\bar{s}}{Dt} + \left(\rho'\bar{T} + \bar{\rho}T'\right)\mathbf{M}' \cdot \nabla \bar{s} + \bar{\rho}T'\frac{\partial s'}{\partial t} \tag{A.33}$$

$$\{s\}_3 = \left(\bar{\rho}T' + \rho'\bar{T}\right)\mathbf{M}' \cdot \nabla s' + \rho'T'\left(\mathbf{M}' \cdot \nabla \bar{s} + \bar{\mathbf{M}} \cdot \nabla s'\right) \tag{A.34}$$

$$\{s\}_4 = \rho'T'\mathbf{M}' \cdot \nabla s' \tag{A.35}$$

The subscript $\{\quad\}_n$ on the curly brackets means that the contained quantities are written to order $n$ in the fluctuations of flow variables. Similarly, the square brackets indicate that the terms are of first order in the Mach number of the mean flow. Higher order square brackets are not required, as explained in Section 3.3.1.

## B. THE EQUATIONS FOR ONE-DIMENSIONAL UNSTEADY MOTIONS

These are many problems for which the flow may be approximated as one-dimensional. Even when the approximation may not seem as accurate as we might like, it is always a good beginning. The desired results are usually obtained without real effect and often are inspiringly close to the truth. An elementary example is computation of the normal modes for a straight tube having discontinuities, Section 5.5.2. Here we are concerned with situations in which influences at the lateral boundary must be accounted for. The formulation of the general problem is then essentially the counterpart of the constitution of the one-dimensional equations for steady flow in ducts thoroughly discussed by Shapiro (1953).

Accounting for changes of area in the one-dimensional approximation is a straightforward matter; following the rules applied to derivations appearing in the three-dimensional equations:

$$
\begin{aligned}
\mathbf{u} \cdot \nabla(\quad) &\rightarrow u \frac{\partial}{\partial x}(\quad) \\
\nabla \cdot (\quad) &\rightarrow \frac{1}{S_c} \frac{\partial}{\partial x} S_c(\quad) \\
\nabla^2(\quad) &= \frac{1}{S_c} \frac{\partial}{\partial x} S_c \frac{\partial(\quad)}{\partial x}
\end{aligned}
\tag{B.1}
$$

where the axis of the duct lies along the x-direction and $S_c(x)$ is the distribution of the cross-section area.

More interesting are consequences of processes at the lateral boundary, particularly when there is flow through the surface. The most important applications arise in solid propellant rockets when burning propellant forms all or part of the lateral surface. Inflow of mass momentum and energy must be accounted for (Culick 1971, 1973; Culick and Yang 1992). The equations have the same form as the three-dimensional equations derived in Appendix A, equations (A.9)–(A.13) but the rule (B.1) applied and only the velocity component $u$ along axis of the duct taken to be non-zero:

**Conservation of Mass**

$$
\frac{D\rho}{dt} = -\rho \frac{1}{S_c} \frac{\partial}{\partial x} (S_c u) + \mathcal{W}_1 + \mathcal{W}_{1s}
\tag{B.2}
$$

**Conservation of Momentum**

$$
\rho \frac{Du}{Dt} = -\frac{\partial p}{\partial x} + \mathcal{F}_1 + \mathcal{F}_{1s}
\tag{B.3}
$$

**Conservation of Energy**

$$
\rho C_v \frac{DT}{Dt} = -p \frac{1}{S_c} \frac{\partial}{\partial x} (S_c u) + \mathcal{Q}_1 + \mathcal{Q}_{1s}
\tag{B.4}
$$

**Equation for the Pressure**

$$
\frac{Dp}{Dt} = -\gamma p \frac{1}{S_c} \frac{\partial}{\partial x} (S_c u) + \mathcal{P}_1 + \mathcal{P}_{1s}
\tag{B.5}
$$

**Equation for the Entropy**

$$
\frac{Ds}{Dt} = \frac{1}{T} (\mathcal{S}_1 + \mathcal{S}_{1s})
\tag{B.6}
$$

where

$$
\frac{D}{Dt} = \frac{\partial}{\partial t} + u \frac{\partial}{\partial x}
\tag{B.7}
$$

The source terms $\mathcal{W}_1$, $\mathcal{F}_1$, $\mathcal{Q}_1$, $\mathcal{P}_1$ and $\mathcal{S}_1$ are the one-dimensional forms of (A.17)–(A.21) written for the axial component of velocity only and with the rules (B.1) applied. In addition, sources of mass, momentum and energy associated with flow through the lateral boundary are represented by the symbols with subscript $(\quad)_s$ (Culick 1973, Culick and Yang 1995):

$$\mathcal{W}_{1s} = \frac{1}{S_c} \int m_s \, dq = \frac{1}{S_c} \int \left[ m_s^g + m_s^l \right] dq \tag{B.8}$$

$$\mathcal{F}_{1s} = \frac{1}{S_c} \int \left[ (u_s - u) m_s^g + (u_{ls} - u_l) m_s^l \right] dq \tag{B.9}$$

$$\mathcal{Q}_{1s} = \frac{1}{S_c} \int \left[ (h_{0s} - e_0) m_s^g + (e_{l0s} - u_{l0}) m_s^l + C_v T m_s^g \right] dq \tag{B.10}$$

$$\mathcal{P}_{1s} = \frac{R}{C_v} Q_{s1} \tag{B.11}$$

$$\mathcal{S}_{1s} = \frac{1}{p} Q_{1s} = \frac{p}{\rho} \mathcal{W}_{1s} \tag{B.12}$$

Superscripts ( )$^{(g)}$ and ( )$^{(l)}$ refer respectively to the gas and liquid phases and subscript ( )$_s$ denotes values at the surface. The mass fluxes at the surface, $m_s^{(g)}$ and $m_s^{(l)}$ are of course computed as values normal to the boundary and are positive for inward flow. Here $q$ stands for the parameter of the local section normal to the axis.

**B.1. Equations for Unsteady One-Dimensional Motions.** Forming the equations for the fluctuating motions within the one-dimensional approximation is done in exactly the same way as for the general equations, Appendix A. We need only apply the rules (B.1) and add to the inhomogeneous functions $h$ and $f$ the contributions from processes at the boundary. As for the general three-dimensional equations, we defer writing the fluctuations $\mathcal{W}_1'$, $\mathcal{F}_1'$, $\cdots$ until we consider specific problems.

The procedure introduced in Section 3.3.3 for forming the systems of equations for a hierarchy of problems applies equally to one-dimensional motions. As above, the equations are obtained from the three-dimensional equations by applying the rules (B.1): the results can be constructed when needed. However, the contributions from processes at the lateral boundary are special. Written to first order in the fluctuations and the Mach number of the mean flow; the dimensional forms of (B.8)–(B.12) are:

$$\mathcal{W}_{1s}' = \frac{1}{S_c} \int \left( m_s^2 \right)' dq \tag{B.13}$$

$$
\begin{aligned}
\mathcal{F}_{1s}' = {} & \frac{1}{S_c} \left( \bar{u}_s - \bar{u} \right) \int \left( m_s^g \right)' dq + \frac{1}{S_c} \left( \bar{u}_{ls} - \bar{u} \right) \int \left( m_s^l \right)' dq \\
& + \frac{1}{S_c} \left( u_s' - u' \right) \int \bar{m}_s^g \, dq + \frac{1}{S_c} \left( u_{ls}' - u_l' \right) \int \bar{m}_s^l \, dq
\end{aligned}
\tag{B.14}
$$

$$
\begin{aligned}
\mathcal{Q}_{1s}' = {} & \frac{1}{S_c} \left( \bar{h}_{0s} - e_0 \right) \int \left( m_s^g \right)' dq + \frac{1}{S_c} + \left( \bar{e}_{l0s} - \bar{e}_{l0} \right) \int \left( m_s^l \right)' dq + C_v \bar{T} \int \left( m_s^g \right)' dq \\
& + \frac{1}{S_c} \left( h_{0s}' - e_0' \right) \int \bar{m}_s^{g\,'} dq + \frac{1}{S_c} + \left( e_{l0s}' - e_{l0}' \right) \int \bar{m}_s^l + C_v T \int \left( m_s^g \right)' dq
\end{aligned}
\tag{B.15}
$$

$$\mathcal{P}_{1s}' = \frac{R}{C_v} Q_{1s}' \tag{B.16}$$

$$\mathcal{S}_{1s}' = \frac{1}{p} Q_{1s}' - \frac{p}{\rho} \mathcal{W}_{1s}' \tag{B.17}$$

# REFERENCES

Aaron, K. and Culick, F.E.C. (1984).

Akiba, R. and Tanno, M. (1959) "Low Frequency Instability in Solid Propellant Rocket Motors," *Proceedings of the 1st Symposium (International) on Rockets and Astronautics,* Tokyo, pp. 74–82.

Ananthkrishnan, N. and Culick, F.E.C. (2002) "Modeling and Dynamics of Nonlinear Acoustic Waves in a Combustion Chamber," $38^{th}$ AIAA/ASME/SAE/ASEE Joint Propulsion Conference & Exhibit, 7–10 Jul 2002, Indianapolis, Indiana, AIAA-2002-3592.

Anil Kumar, K.R. and Lakshmisha, K.N. (2000) "Nonlinear Intrinsic Instability of Solid Propellant Combustion Including Gas-Phase Thermal Inertia," *Comb. Sci. and Tech.,* Vol. 158, pp. 135–166.

Anil Kumar, K.R. and Lakshmisha, K.N. (2002) "Dynamic Combustion of Solid Propellants: Effects of Unsteady Condensed Phase Degradation Layer," *J. Prop and Power,* Vol. 15, No. 2, pp. 312–321.

Avalon, G., Casalis, G. and Grifford, J. (1998) "Flow Instabilities and Acoustic Resonance of Channels with Wall Injection," AIAA Paper No. 98–3218.

Avalon, G., Ugurtas, B. Grisch, F. and Bresson, F. (2000) "Numerical Computations and Visualization Tests of the Flow Inside a Cold Gas Simulation with Characterization of a Parietal Vortex Shedding," AIAA-2000-3387.

Awad, E. and Culick, F.E.C. (1986) "On the Existence and Stability of Limit Cycles for Longitudinal Acoustic Modes in a Combustion Chamber," *Combustion Science and Technology*, Vol. 46, pp. 195–222.

Awad, E. (1983) "Nonlinear Acoustic Instabilities in Combustion Chambers," Ph.D. Thesis, California Institute of Technology.

Barrére, M. and Bernard, J.J. (1962) "Combustion Instability of Solid Propellant with Time Delay Distribution," *8th Symposium (International) on Combustion,* William and Wilkins, pp. 886–894.

Baum, J.D. and Levine, J.N. (1982) "Numerical Techniques for Solving Nonlinear Instability Problems in Solid Rocket Motors," *AIAA Journal,* Vol. 20, No. 7, pp. 955–961.

Baum, J.D. and Levine, J.N. and Lovine, R.L. (1988) "Pulsed Instability in Rocket Motors: Comparison Between Predictions and Experiments," *Journal of Propulsion and Power,* Vol. 4, No. 4, pp. 308–316.

Beckstead, M.W., Ryan, N.W. and Baer, A.D. (1966) "Non-Acoustic Instability of Composite Propellant Combustion," *AIAA J.,* Vol. 4, No. 9, pp. 1622–1628.

Beckstead, M.W (1967) "Low Frequency Instability: A Comparison of Theory and Experiment," Paper 67-13, The Combustion Institute.

Beckstead, M.W. and Boggs, T.L. (1967) "The Effect of Oxidizer Particle Size on Non-acoustic Instability," *Fourth ICRPG Combustion Conference,* Stanford Research Institute.

Beckstead, M.W. and Culick, F.E.C. (1967) "A Comparison of Analysis and Experiment for the Response Function of a Burning Surface," *Fourth ICRPG Combustion Conference,* Stanford Research Institute; also Rept. NWCTP 4531, May 1968, U.S. Naval Weapons Center.

Beckstead, M.W. and Price, E.W. (1967) "Nonacoustic Combustion Instability," *AIAA J.,* Vol. 5, No. 11, pp. 1989–1996.

Beckstead, M.W., Mathes, H.B., Price, E.W. and Culick, F.E.C. (1969) "Combustion Instability of Solid Propellants," *12th Symposium (International) on Combustion,* pp. 203–211.

Beckstead, M.W. and Culick, F.E.C. (1971) "A Comparison of Analysis and Experiment for Solid Propellant Combustion Instability," *AIAA Journal,* Vol. 9, No. 1, pp. 147–154.

Beckstead, M.W., Derr, R.L. and Price, C.F. (1972) "A Model of Composite Solid Propellant Combustion Based on Multiple Flames," *AIAA Journal,* Vol. 8, pp. 2200–2207.

Beckstead, M.W., Richards, R.S. and Brewster, B.S. (1987) "Distributed Combustion Effects of Particle Damping," *AIAA J.,* Vol. 22, No. 3, pp. 383–387.

Beckstead, M.W. (1980) "Model for Double-Base Combustion," *AIAA J.,* Vol. 18, No. 8, pp. 980–985.

Beckstead, M.W. (1991) "A Review of Soviet Combustion and Combustion Instability Work on Solid Propellants," $28^{th}$ JANNAF Combustion Meeting, San Antonio, Texas.

Beckstead, M.W. and Erikson, W.W. (1996) "Solid Monopropellant Oscillatory Combustion Instabilities," Proceedings of the $2^{nd}$ International Conference on Combustion Conversion and Environmental Problems of Energetic Materails, St. Petersburg, Russia.

Beddini, R.A. (1998) "The Role of Turbulence Interactions in Solid Propellant Combustion Instability," $34^{th}$ AIAA/ASME/SAE/ASEE Joint Propulsion Conference, July 1998, AIAA Paper No. 98-3703.

Beddini, R.A. and Lee, Y. (1998) "The Treshold Condition of Propellant Velocity Response and its Relation to Local Turbulence Transition," $35^{th}$ JANNAF Combustion Meeting.

Bird, J.F., et al, (1960) "Effect of Solid Propellant Compressiblity on Combustion Instability," *J. Chem. Phys.,* Vol. 32, pp. 1423–1429.

Biron, D., Hébrard, P., Pauzin, S., and Laverdant, A. (1986) "Etude du couplage acoustique – instabilities aerodynamiques sur une acoustique," École Centrale de Lyon, Proceedings edited by Springer-Verlag.

Blomshield, F. and Mathes, H.B. (1993) "Pressure Oscillations in Post-Challenger Space Shuttle Redesigned Solid Rocket Motors," *J. Propulsion and Power*, Vol. 9, No. 2, pp. 217–221.

Brewster, Q. and Son, S.F. (1995) "Quasi-Steady Combustion Modeling of Homogeneous Solid Propellants," *Comb. and Flame,* Vol. 103, pp. 11–26.

Brewster, Q., Ward, M.J. and Son, S.F. (2000) "Simplified Combustion Modeling of Double Base Propellant: Gas Phase Chain Reaction vs. Thermal Decomposition," *Comb. Sci. and Tech.,* Vol. 159, pp. 1–30.

Brooks, K.P. and Beckstead, M.W. (1995) "The Dynamics of Aluminum Combustion," *J. Prop. and Power,* Vol. 11, No. 4, pp. 769–780.

Brown, R.S., Muzzy, R.J. and Steinle, M.E. (1967) "Effect of Surface Reactions on Acoustic Response of Solid Propellants," *AIAA J.,* Vol. 5, No. 9, p. 1718.

Brown, R.S., Dunlap, R., young, S.W. and Waugh, R.C. (1981) "Vortex Shedding as a Source of Acoustic Energy in Segmented Solid Rockets," *J. Spacecraft and Rockets*, Vol. 18, No. 4, pp. 312–319.

Brownlee, W.G. (1964) "Nonlinear Axial Combustion Instability in Solid Rocket Propellant Rocket Motors," *AIAA Journal,* Vol. 2, No. 2, pp. 275–284.

Burnley, V. (1996) "Nonlinear Combusiton Instabilities and Stochastic Sources," Ph.D. Thesis, Aeronautics, California Institute of Technology.

Burnley, V.S. and Culick, F.E.C. (1996) "Influence of Random Excitations on Acoustic Instabilities in Combustion Chambers," *AIAA Journal*, 38(8), 1403–1410.

Burnley, V.S. and Culick, F.E.C. (1997) "Comment on 'Triggering of Longitudinal Combustion Instabilities in Rocket Motors: Nonlinear Combustion Response'," *Journal of Propulsion and Power*, 16(1), 164–165.

Caltech MURI (2002) "Investigation of Novel Energetic Materials to Stabilize Rocket Motors," Final Report, ONR Contract No. N00014-95-1-1338, 1 October 1995 – 30 September 2001.

Cantrell, R.H., Hart, R.W. and McClure, F.T. (1964) "Linear Acoustic Gains and Losses in Solid Propellant Rocket Motors," *AIAA J.,* Vol. 2, No. 6, pp. 1100–1105.

Cantrell, R.H., McClure, F.T. and Hart, R.W. (1965) "Effects of Thermal Radiation on the Acoustic Response Function of Solid Propellants," *AIAA J.,* Vol. 3, No. 3, pp. 418–426.

Cantrell, R.H. and Hart, R.W. (1966) "Interaction Between Sound and Flow in Acoustic Cavities: Mass, Momentum, and Energy Transfer," *J. Acoust. Soc. Of America,* Vol. 36, pp. 697–706.

Cauty, F. (1999) "Solid-Propellant Combustion Response Function from Direct Measurement Methods: ONERA Experience," *J. Prop. and Power,* Vol. 15, No. 6, pp. 837–843.

Cardiff, E.H., Pinkham, J.D. and Micci, M.M. (1999) "Magnetic Flowmeter Measurement of a Pressure-Coupled Response of a Plateau Solid Propellant," *J. Prop. Power,* Vol. 15, No. 6, pp. 844–848.

Cheng, S.-I. (1954) "High Frequency Combustion Instability in Solid Propellant Rockets," *Jet Propulsion,* Pt. I, pp. 27–32, Pt. II, pp. 102–109.

Cheng, S.-I. (1955) "On 'Unstable Burning of Solid Propellants'," *Jet Propulsion,* Vol. 25, pp. 79–80.

Cheng, S.-I. (1959) "Combustion Instability in Solid Rockets Using Propellants with Suspended Metallic Powders," *1ˢᵗ Symposium (International) on Rockets and Astronautics,* Tokyo, pp. 62–70.

Cheng, S.-I. (1960) "Combustion Instability in Solid Rockets Using Propellants with Reactive Additives," *ARS Progress in Astronautics and Rocketry: Solid Propellant Rocket Research,* Vol. 1, edited by M. Summerfield, Academic Press, pp. 393–422.

Cheng, S.-I. (1962) "Unstable Combustion in Solid-Propellant Rocket Motors," *8ᵗʰ Symposium (International) on Combustion,* Williams and Wilkins, pp. 81–96.

Chu, B.-T. (1956) "Energy Transfer to Small Disturbances in a Viscous Heat Conductive Medium," Department of Aeronautics, Johns Hopkins University (no identifying number).

Chu, B.-T. and Kovasznay, L.S.G. (1957) "Non-linear Interactions in a Viscous Heat Conducting Compressible Gas," *J. Fluid Mech.,* Vol. 3, No. 5, pp. 494–512.

Clavin, P. and Lazini, D. (1992) "Theoretical Analysis of Oscillatory Burning of Homogeneous Solid Propellant Including Non-Steady Gas Phase Effects," *Comb. Sci. and Tech.,* Vol. 83, pp. 1–32.

Coates, R.L., Cohen, N.S. and Harvill, L.P. (1967) "An Interpretation of L\* Combustion Instability in Terms of Acoustic Instability Theory," *AIAA J.,* Vol. 5, No. 5, pp. 1097–2004.

Cohen, N.S. and Strand, L.D. (1982) "An Improved Model for the Combustion of AP Composite Propellants," *AIAA Journal,* Vol. 20, No. 12, pp. 1739–1746.

Cohen, N.S. and Strand, L.D. (1985) "Combustion Response to Compositional Fluctuations," *AIAA Journal,* Vol. 23, No. 5, pp. 760–767.

Cohen, N.S. and Strand, L.D. (1985) "Effect of AP Particle Size on Combustion Response to Crossflow," *AIAA Journal,* Vol. 23, No. 5, pp. 776–780.

Cohen, N.S., Shusser, M., Culick, F.E.C. and Beddini, R.A., (1999) "Combustion Modeling of AP Composite Propellants for Stability Analysis," *36ᵗʰ JANNAF Combustion Meeting.*

Cozzi, F., DeLuca, L.T. and Novozhilov, B.V. (1999) "Linear Stability and Pressure-Driven Response Function of Solid Propellants with Phase Transition," *J. Prop and Power,* Vol. 15, No. 6, pp. 806–875.

Crocco, L. and Cheng, S.-I. (1956) *Theory of Combustion Instability in Liquid-Propellant Rockets,* AGARDograph No. 8, Butterworths Scientific Publications, London.

Crocco, L., Grey, J. and Harrje, D.T. (1960) "Theory of Liquid Propellant Rocket Combustion Instability and Its Experimental Verification," *ARS J,* Vol. 30, No. 2, pp. 159–168.

Crocco, L. (1964) "Theoretical Studies on Liquid Propellant Rocket Instability," *10ᵗʰ Symposium (International) on Combustion,* The Combustion Institute, Pittsburgh, PA, pp. 1101–1128.

Culick F.E.C. (1961) "High Frequency Pressure Oscillations in Liquid Rockets," Sc.D. Thesis, M.I.T. Department of Aeronautics and Astronautics.

Culick F.E.C. (1963) "High Frequency Oscillations in Liquid-Propellant Rockets," *AIAA Journal,* Vol. 1, No. 5, pp. 1097–1104.

Culick, F.E.C. (1966) "Acoustic Oscillations in Solid Propellant Rocket Chambers," *Astronautica Acta,* Vol. 12, pp. 113–126.

Culick, F.E.C. (1967) "Calculation of the Admittance Function for a Burning Surface," *Astronautics Acta,* Vol. 13, No. 3, pp. 221–238.

Culick, F.E.C. (1967) "A Review of Calculations of the Admittance Function for a Burning Surface," *Combustion of Solid Propellants and Low Frequency Combustion Instability,* NOTS TP 4244, Naval Weapons Center, China Lake, CA, Appendix A.

Culick, F.E.C. (1968) "A Review of Calculations for Unsteady Burning of a Solid Propellant," *AIAA Journal,* Vol. 6, No. 12, pp. 2241–2255.

Culick, F.E.C. (1969) "An Elementary Calculation of the Combustion of a Solid Propellant," *Astronautics Acta,*.

Culick, F.E.C. (1969) "Some Problems in the Unsteady Burning of Solid Propellants," Naval Weapons Center Report NWC TP 4668.

Culick, F.E.C. and Dehovitz, G.L. (1969) "An Elementary Calculation for the Burning Rate of Composite Solid Propellants," *Comb. Sci. and Tech.,* Vol. 1, pp. 193–204.

Culick, F.E.C. (1970) "Stability of Longitudinal Oscillations with Pressure and Velocity Coupling in a Solid Propellant Rocket," *Comb. Sci. and Tech.,* Vol 2, No. 4, pp. 179–201.

Culick, F.E.C. (1971) "Nonlinear Growth and Limiting Amplitude of Acoustic Oscillations in Combustion Chambers," *Combustion Science and Technology,* Vol. 3, pp. 1–16.

Culick, F.E.C. (1976) "Nonlinear Behavior of Acoustic Waves in Combustion Chambers," Parts I and II, *Acta Astronautica,* Vol. 3, pp. 714–757.

Culick, F.E.C. and Magiawala, K. (1979) "Excitation of Acoustic Modes in a Chamber by Vortex Shedding," *J. Sound and Vibration,* Vol. 64, No. 3, pp. 455–457.

Culick, F.E.C. (1980) "Report of the JANNAF Workshop on Pressure Oscillations in Ramjets," $17^{th}$ JANNAF Combustion Meeting.

Culick, F.E.C. and Rogers, T. (1980) "Modeling Pressure Oscillations in Ramjets," $16^{th}$ AIAA/SAE/ASME Joint Propulsion Conference, Hartford, Connecticut, AIAA Paper 80-1192.

Culick, F.E.C. (1987) "A Note on Rayleigh's Criterion," *Combustion Science and Technology,* Vol. 56, pp. 159–166.

Culick, F.E.C. (1988) "Combustion Instabilities in Liquid-Fueled Propulsion Systems—An Overview," AGARD 72B Specialists' Meeting of the Propulsion and Energetics Panel AGARD CP 450.

Culick, F.E.C., Paparizos, L., Sterling, J. and Burnley, V.S. (1992) "Combustion Noise and Combustion Instabilities in Propulsion Systems," *Proceedings of the AGARD Conference on Combat Aircraft Noise,* AGARD CP512.

Culick, F.E.C. (1992) "Combustion Instabilities and Rayleigh's Criterion," *Modern Research Topics in Aerospace Propulsion*, (In honor of Corrado Casci), pp. 135–151.

Culick, F.E.C. and Yang, V. (1992) "Prediction of the Stability of Unsteady Motions in Solid Propellant Rocket Motors," *Nonsteady Burning and Combustion Stability of Solid Propellants,* edited by L. DeLuca, E.W. Price and M. Summerfield, Vol. 143, *Progress in Astronautics and Aeronautics,* AIAA, Washington, pp. 719–780.

Culick, F.E.C. (1994) "Some Recent Results for Nonlinear Acoustics in Combustion Chambers," *AIAA Journal,* Vol. 32, No. 1, pp. 146–169.

Culick, F.E.C. and Yang, V. (1995) "Overview of Combustion Instabilities in Liquid-Propellant Rocket Engines," First International Symposium on Liquid Rocket Engine Combustion Instability, The Pennsylvania State University, AIAA Progress Series, Vol. 169.

Culick, F.E.C. (1997) "A Note on Ordering Perturbations and the Insignificance of Linear Coupling in Combustion Instabilities," *Combustion Science and Technology*, Vol. 126, pp. 359–379.

Culick, F.E.C. Isella, G. and Seywert, C. (1998) "Influences of Combustion Dynamics on Linear and Nonlinear Unsteady Motions in Solid Propellant Rockets," AIAA-98-3704.

Culick, F.E.C. (1999) "Combustor Dynamics: Fundamentals, Acoustics and Control," A Short Course of Lectures.

Culick, F.E.C. (2002) "A Short Course of Lectures on Combustion Dynamics: Fundamentals, Acoustics and Control," accesible on the website http://www.its.caltech.edu/~culick.

DeLuca, L. (1990) "A Critical Review of Solid Rocket Propellant Transient Flame Models," *Pure and Applied Chem.,* Vol. 63, pp. 825–.

DeLuca, L. and Galfetti, L. (1991) "Combustion Modeling and Stability of Double-Based Propellants," *Modern Research Topics in Aerospace Propulsion,* Springer-Verlag, N.Y., pp. 109–134.

DeLuca, L. (1992) "Theory of Nonsteady Burning and Combustion Stability of Solid Propellants by Flame Models," *Combustion Stability of Solid-Propellant,* edited by L. DeLuca, E.W. Price and M. Summerfield, *Progress in Astronautics and Aeronautics,* Vol. 143, AIAA, Washington, pp. 519–600.

DeLuca, L., DiSilvestro, R. and Cozzi, F. (1995) "Intrinsic Combustion Instability of Solid Energetic Materials," *J. Prop and Power,* Vol. 11, No. 4, pp. 804–875.

Denison, M.R. and Baum, E. (1961) "A Simplified Model of Unstable Burning in Solid Propellants," *ARS Journal,* Vol. 31, No. 8, pp. 278–285.

Dickinson, L.A. (1962) "Command Initiation of Finite Wave Combustion Instabilities in Solid Propellant Rocket Engines," *ARS Journal*, April (pp. 643–644).

Dickinson, L.A. and Jackson, F. (1963) "Combustion in Solid Propellant Rocket Engines," Fifth AGARD Colloquium, High Temperature Phenomena.

Doedel, E.J., Champneys, A.R., Fairgrieve, T.F., Kuznetsov, Y.A., Sandstede, B., Wang, X. (1997) "AUTO 97: Continuation and Bifurcation Software for Ordinary Differential Equations," Concordia University, Montreal, Canada.

Doedel, E.J., Keller, H.B., Kernevez, J.P. (1991a) "Numerical Analysis and Control of Bifurcation Problems, (I) Bifurcation in Finite Dimensions," *International Journal of Bifurcation and Chaos*, Vol. 1, No. 3, pp. 493–520.

Doedel, E.J., Keller, H.B., Kernevez, J.P. (1991b) "Numerical Analysis and Control of Bifurcation Problems, (II) Bifurcation in Infinite Dimensions," *International Journal of Bifurcation and Chaos*, Vol. 1, No. 4, pp. 745–772.

Dotson, K.W., Koshigoe, S. and Pace, K.K. (1995) "Vortex Driven Pressure Oscillations in the Titan IV Solid Rocket Motor Upgrade," AIAA Paper No. 95-2732.

Duer, J. and Hessler, R. (1984) "Forced Oscillation Theory and Applications," $20^{th}$ AIAA/ASME/SAE/ASEE Joint Propulsion Conference, AIAA Paper No. 84-1356.

Dunlap, R. and Brown, R.S. (1981) "Exploratory Experiments on Acoustic Oscillations Driven by Periodic Vortex Shedding," *AIAA J.*, Vol. 19, No. 3, pp. 408–409.

Dunlap, R., Blackner, A.M., Waugh, R.C., Brown, R.S. and Willoughby, P.G. (1990) "Internal Flow Field Studies in a Simulated Cylindrical Port Rocket Chamber," *J. Prop. and Power,* Vol. 6, No. 6, pp. 690–704.

Dupays, J. and Vuillot, F. (1998) "Propagation of an Acoustic Wave in a Two-Phase Reactive Medium," AIAA Paper No. 98-3696.

Ernst, R.C. (1976) "A Combustion Model for Low Frequency Instability in Turbofan Augmentors," $12^{th}$ AIAA/SAE Propulsion Conference, AIAA Paper No. 76-680.

Evans, G.I. and Smith, P.K. (1978) "The Suppression of Combustion Instability in Smokeless Solid Propellant Rocket Motors," AIAA Paper 78-1568, *14$^{th}$ AIAA/SAE Joint Propulsion Conference.* Also see Paper #27, *AGARD Conference Proceedings* No. 259, *Solid Rocket Motor Technology*, National Technical Information Service (NTIS), Springfield, VA, July 1979.

Flandro, G.A. and Jacobs, H.R. (1974) "Vortex-Generated Sound in Cavities," AIAA Paper No. 73-1014, published in *Aeroacoustics: Jet and Combustion Noise*, AIAA Series *Progress in Astronautics and Aeronautics.* Vol. 37, pp. 521–533.

Flandro, G.A. (1986) "Vortex Driving Mechanism in Oscillatory Rocket Flows," *J. Propulsion and Power*, Vol. 2, No. 3, pp. 206–214.

Flandro, G.A. (1995) "Effects of Vorticity on Rocket Combustion Instability," *J. Propulsion and Power* Vol. 11, No. 4, pp. 607–625.

Friedly, J.C. and Petersen, E.E. (1966) "Influence of Combustion Parameters on Instability in Solid Propellant Motors," *AIAA J.,* Vol. 4, Pt. I: "Development of Model and Linear Analysis," pp. 1604–1609; Pt. II: "Nonlinear Analysis," pp. 1932–1937.

Geckler, E.D. (1955) "Unsolved Problems in Solid Propellant Combustion," *5$^{th}$ Symposium (International) on Combustion,* Reinhold, pp. 29–40.

Gostintsev, Yu.A., Pokhil, P.F. and Sukhanov, L.A. (1970) "Complete System of Equations for Nonsteady Processes at Propellant Burning in Semi-Closed Volume," *Dokl. AN SSSR,* Vol. 195, No. 1, pp. 137–140.

Grad, H. (1949) "Resonance Burning in Rocket Motors," *Communications on Pure Applied Mathematics,* Vol. 2, pp. 79–102.

Green, L., Jr. (1958) "Some Properties of Solid Propellant Burning," *Jet Propulsion,* Vol. 28, pp. 386–392.

Gusachenko, L.K., Zarko, V.E. and Rychkov, A.D. (1999) "Effect of Melting on Dynamic Combustion Behavior of Energetic Materials," *J. Prop. and Power,* Vol. 15, No. 6, pp. 876–822.

Hart, R.W. and McClure, F.T. (1959) "Combustion Instability: Acoustic Interaction with a Burning Propellant Surface," *J. Chem. Phys.,* Vol. 30, pp. 1501–1514.

Hart, R.W. and Cantrell, R.H. (1963) "Amplification and Attenuation of Sound by Burning Propellants," *AIAA J.,* Vol. 1, No. 2, pp. 398–404.

Hart, R.W. and McClure, F.T. (1965) "Theory of Acoustic Instability in Solid-Propellant Rocket Combustion," *10th (International) Symposium on Combustion,* The Combustion Institute, Pittsburgh, PA, pp. 1047–1065.

Hart, R.W., Farrell, R.A. and Cantrell, R.H. (1966) "Theoretical Study of a Solid Propellant Having a Heterogeneous Surface Reaction. I-Acoustic Response, Low and Intermediate Frequencies," *Comb. and Flame,* Vol. 10, pp. 367–380.

Hessler, R. (1979) "Studies of Motor Instability Problems," 16th JANNAF Combustion Sub-Committee Meeting.

Hessler, R. (1980) "Prediction of Finite Pressure Oscillations in Stable Rocket Motors," 17th JANNAF Combustion Sub-Committee Meeting.

Hessler, R. (1982) "Forced Oscillation Prediction," 19th JANNAF Combustion Sub-Committee Meeting.

Hessler, R. and Glick, R. (1998) "Application of Maximum Entropy Method to Passively Extract Motor Stability Information," Workshop 'Measurement of Thermophysical and Ballistic Properties of Energetic Material', Politecnico di Milano, Milan, Italy.

Hildebrand, F.B. (1952) *Methods of Applied Mathematics*, Prentice-Hall, Inc., New York.

Horton, M.D. (1961) "One-Dimensional Solid Propellant Oscillatory Burner," *ARS Journal,* Vol. 31, pp. 1596–1597.

Horton, M.D. (1962) "Acoustic Admittance of a Burning Solid Propellant Surface," *ARS Journal,* Vol. 32, No. 4, pp. 644–645.

Horton, M.D. and Price, E.W. (1963) "Dynamic Characteristics of Solid Propellant Combustion," *Ninth Symposium (International) on Combustion,* Academic Press, N.Y., pp. 303–310.

Horton, M.D. and Rice, D.W. (1964) "The Effect of Compositional Variables upon Oscillatory Combustion of Solid Rocket Propellants," *Comb. and Flame,* Vol. 8, pp. 21–28.

Ibiricu, M.W. and Williams, F.A. (1975) "Influence of Externally Applied Thermal Radiation on the Burning Rates of Homogeneous Solid Propellants," *Combustion and Flame,* Vol. 24, pp. 185–198.

Isella, G., Seywert, C., Culick, F.E.C. and Zukoski, E.E. (1996) "A Further Note on Active Control of Combustion Instabilities Based on Hysteresis," *Combustion Science and Technology*, Vol. 126, pp. 381–388.

Isella, G. and Culick, F.E.C. (2000) "Modeling Propellant Dynamics and Their Effects on the Global Dynamics of a Combustion Chamber," (in preparation).

Isella, G. and Culick F.E.C. (2000) "Modeling the Combustion Response Function with Surface and Gas Phase Dynamics," $38^{th}$ AIAA Aerospace Sciences Meeting, AIAA-2000-0310.

Isella, G.C. (2001) "Modeling and Simulation of Combustion Chambers and Propellant Dynamics and Issues in Active Control of Combustion Instabilities," Ph.D. Thesis, California Institute of Technology.

Istratov, A.G. and Librovich, V.B. (1964) "On the Stability of Propellant Combustion," *Zh. Prikl. Mekh. I Tekh. Fiz.,* No. 5, pp. 38–43.

Jahnke, C. and Culick, F.E.C. (1994) "An Application of Dynamical Systems Theory to Nonlinear Combustion Instabilities," *Journal of Propulsion and Power*, Vol. 10, No. 4, pp. 508–517.

King, M.K. (1979) "Erosive Burning of Composite Solid Propellants: Experimental and Modeling Studies," *J. Spacecraft and Rockets,* Vol. 16, No. 3, pp. 154–162.

King, M.K. (1980) "Composite Propellant Modeling," AIAA Paper No. 80-1124.

Knoop, P., Culick, F.E.C. and Zukoski, E.E. (1996) "Extension of the Stability of Motions in a Combustion Chamber by Nonlinear Active Control Based on Hysteresis," *Combustion Science and Technology*, Vol. 123, pp. 363–376.

Kochevets, S. Buckmaster, J. and Jackson, T.L. (2000) "Random Propellant Packs and the Flames They Support," AIAA-2000-3461.

Krier, H. et al. (1968) "Entropy Waves Produced in Oscillatory Combustion of Solid Propellants," *Third ICRPG/AIAA Solid Propulsion Conference,* Atlantic City, NJ.

Krier, H., T'ien, J.S., Sirignano, W.A. and Summerfield, M. (1968) "Non-Steady Burning Phenomena of Solid Propellants: Theory and Experiment," *AIAA J.,* Vol. 6, No. 2, pp. 278–285.

Krylov, N. and Bogoliubov, N. (1947) *Introduction to Nonlinear Mechanics*, Princeton University Press.

Kumar, R.N. (1973) "Condensed Phase Details in the in the Time-Independent Combustion of AP/Composite Propellants," *Comb. Sci. and Tech.,* Vol. 8, No. 2, pp. 133–148.

Kumar, R.N. and Culick, F.E.C. (1977) "Role of Condensed Phase Details in the Oscillatory Combustion of Composite Propellants," *Comb. Sci. and Tech.,* Vol. 15, No. 2, pp. 179–199.

Kuo, K.K., Gore, J.P. and Summerfield, M. (1984) "Transient Burning of Solid Propellants," *Fundamentals of Solid-Propellant Combustion,* edited by K.K. Kuo and M. Summerfield, *Progress in Astronautics and Aeronautics,* Vol. 90, AIAA, New York, pp. 599–659.

Landau, L.D. and Lifschitz, E.M. (1959) *Fluid Mechanics*, Addison-Wesley Publishing Co.

LeBreton, P., Guéry, J.-F., Vuillot, F., and Prévost, M. (1999) "Recent Advances in the Prediction of SRM Thrust Oscillations," *Premier Colloque Européen sur la Technologie des Lanceurs-Vibrations des Lanceurs*, Toulouse, France.

Lengellé, G. (1970) "Thermal Degradation Kinetics and Surface Pyrolyses of Vinyl Polymers," *AIAA J.,* Vol. 8, No. 11, pp. 1989–1996.

Lengellé, G., Kuentzmann, P. and Rendolet, C. (1974) "Response of a Solid Propellant to Pressure Oscillations," AIAA Paper No. 74-1209.

Levine, J.N. and Baum, J.D. (1983) "Modeling of Nonlinear Combustion Instability in Solid Propellant Rocket Motor," *19th Symposium (International) on Combustion,* pp. 769–776.

Levine, J.N. and Baum, J.D. (1983) "A Numerical Study of Nonlinear Instability Phenomena in Solid Rockets," *AIAA J.,* Vol. 21, No. 4 (pp. 557–564).

Levine, J.N. and Culick, F.E.C. (1972) "Numerical Analysis of Nonlinear Longitudinal Combustion Instability in Metalized Solid-Propellant Rocket Motors, Vol. 1 Analysis and Results," Ultrasystems, Inc., Report prepared for the Air Force Rocket Propulsion Laboratory, AFRPL TR–72–88.

Levine, J.N. and Culick, F.E.C. (1974) "Nonlinear Analysis of Solid Rocket Combustion Instability," Ultrasystems, Inc., Report prepared for the Air Force Rocket Propulsion Laboratory, AFRPL TR–74–45.

Lewis Laboratory Staff (1954) "Summary of Preliminary Investigations into the Characteristics of Combustion Screech in Ducted Burners," NACA-TR-1384.

Lord Rayleigh (1878) "The Explanation of Certain Acoustic Phenomena," *Royal Institution Proceedings*, VIII, pp. 536–542.

Lord Rayleigh (1945) *Theory of Sound*, Vol. 2, Dover, New York, Section 322g, pp. 232–234.

Louwers, J. and Gadiot, G.M.H.J.L. (1999) "Model for Nonlinear Transient Burning of Hydrazine Nitroformate," *J. Propulsion and Power,* Vol. 15, No. 6, pp. 778–782.

Lovine, R. L., Dudley, D. P., and Waugh, R. C. (1983) "Standardized Stability Prediction Method for Solid Rocket Motors," Vol. I, II and III. Aerojet Solid Propulsion Company. Report prepared for the Air Force Rocket Propulsion Laboratory, AFRPL-TR-76-32.

Lupuglazoff, N. and Vuillot, F. (1996) "Parietal Vortex-Shedding as a Cause of Instability for Long Solid Propellant Motors," AIAA Paper No. 96-0761.

Lupuglazoff, N. and Vuillot, F. (1998) "Numerical Simulations of Parietal Vortex Shedding Phenomena in a Cold Flow Set-Up," AIAA Paper No. 98-3220.

McClure, F.T., Hart, R.W. and Bird, J.F. (1960) "Acoustic Resonance in Solid Propellant Rockets," *J. Appl. Phys.,* Vol. 31, pp. 884–896.

McClure, F.T., Bird, J.F. and Hart, R.W. (1962) "Erosion Mechanism for Non-linear Instability in the Axial Modes of Solid Propellant Rocket Motors," *ARS J.,* Vol. 32, No. 3, pp. 374–378.

McManus, K., Poinsot, T. and Candel, S. (1993) "A Review of Active Control of Combustion Instabilities," *Progress in Energy and Combustion Science*, 19(1): 1–29.

Magiawala, K. and Culick, F. E. C. (1979) "Measurements of Energy Exchange Between Acoustic Fields and Non-Uniform Steady Fields," *Journal of Sound and Vibration*, Vol. 75, pp. 503–512.

Majdalani, J. (1999) "Vortical and Acoustic Mode Coupling Inside a Two-Dimensional Cavity with Transpiring Walls," *J. Acoust. Soc. of Amer.,* Vol. 106, No. 1, pp. 46–56.

Majdalani, J., Flandro, G.A. and Roh, T.-S. (2000) "Convergence of Two Analytical Flow Field Models Predicting a Destabilizing Agent in Rocket Combustion," *J. Prop. and Power,* Vol. 16, No. 3, pp. 492–497.

Malhotra, S. (2002) "On Combustion Instability," Ph.D. Thesis in preparation, California Institute of Technology.

Marble, F.E. and Rogers, D.E. (1956) "A Mechanism of High-Frequency Oscillation in Ramjet Combustors and Afterburners," *Jet Propulsion.*

Marble, F.E. and Wooten, D.C. (1970) "Sound Attenuation in a Condensing Vapor," *The Physics of Fluids*, Vol. 13, No. 12, pp. 2657–2664.

Marxman, G.A. and Wooldridge, C.E. (1968) "Effects of Surface Reactions on the Solid Propellant Response Function," *AIAA J.,* Vol. 6, No. 3, pp. 468–471.

Marxman, G.A. and Wooldridge, C.E. (1971) "Finite-Amplitude Axial Instability in Solid-Rocket Combustion," *12th Symposium (International) on Combustion,* pp. 115–127.

Mason, D.R., Folkman, S.L. and Behring, M.A. (1979) "Thrust Oscillations of the Space Shuttle Solid Rocket Boosters Motor During Static Tests," AIAA Paper No. 79-1138.

Mathes, B., Derr, R.L. and Culick, F.E.C. (1973).

Mathes, H.B. (1980) "Assesment of Chamber Pressure Oscialltions in the Shuttle Solid Rocket Booster Motors," AIAA Paper No. 80-1091.

Minch, M.M. and Kuo, K.K. (1995) "Characterization and Stability Behavior of Solid Propellants,"

Moore, F.K. and Maslen, S.H. (1954) "Transverse Oscillations in a Cylindrical Combustion Chamber," NACA-TN-3152.

Morse, P.M. (1936) *Vibration and Sound*, McGraw-Hill Book Co., New York.

Morse, P.M. and Feshbach, H. (1952) *Methods of Theoretical Physics*, McGraw-Hill Book Company.

Morse, P. and Ingard, L. (1968) *Theoretical Acoustics*, McGraw-Hill Book Co., New York.

Nachbar, W. and Green, L., Jr. (1959) "Analysis of a Simplified Model of Solid Propellant Resonant Burning," *J. Aerospace Sci.,* ol. 26, No. 8, pp. 518–526.

Nachbar, W. and Green, L., Jr. (1960) "Closure," *ARS J.,* Vol. 30, No. 6, pp. 576–577.

Natanzon, M.S. and Menshikova, O.M. (1992) "Bifurcation of Steady Combustion Regimes and Their Influence on the Onset of High-Frequency Oscillations in Combustion Chambers," *Physics of Combustion and Explosion*, Vol. 23, No. 4, pp. 10–18.

Natanzon, M. (1999) *Unsteady Combustion in Liquid Rocket Engines*, Electronic translation from the Russian edition (1984) with a revised Chapter 8 on Bifurcations; translation editor F.E.C. Culick.

Nickerson, G. R., Culick, F.E.C., and Dang, L.G. (1983) "Standard Stability Prediction Method for Solid Rocket Motors, Axial Mode Computer Program, User's Manual," Software and Engineering Associates (SEA), Inc. Report prepared for the Air Force Rocket Propulsion Laboratory, AFRPL-TR-83-01.

Nomoto, H. and Culick, F.E.C. (1982) "An Experimental Investigation of Pure Tone Generation by Vortex Shedding in a Duct," *J. Sound and Vibration*, Vol. 84, No. 2, pp. 247–252.

Novikov, S.S. and Ryazantzev, Yu.S. (1964) "On the Stability of Propellant Combustion," *Zh. Prikl. Mekh. I Tekh. Fiz.,* No. 1, pp. 57–61.

Novozhilov, B.V. (1965) "Burning of a Powder Under Harmonically Varying Pressures," *J. Appl. Mech. and Tech. Phys.,* Vol. 6, No. 6, pp. 141–144.

Novozhilov, B.V. (1965) "Condition of Stability of Steady-State Propellant Burning," *Zh. Prikl. Mekh. Tekh. Fiz.,* No. 4, pp. 157–160.

Novozhilov, B.V. (1965) "Propellant Burning at Harmonically Varying Pressure," *Zh. Prikl. Mekh. i Tekh. Fiz.,* No. 6, pp. 141–144.

Novozhilov, B.V. (1965) "Stability Criterion for Steady-State Burning of Powders," *J. Appl. Mech. and Tech. Phys.,* Vol. 6, No. 4, pp. 157–160.

Novozhilov, B.V. (1966) "Nonlinear Oscillations of Propellant Burning Rate," *Zhurnal Prikladnoi Mekhaniki I Tekhnicheskoi Fiziki,* No. 5, pp. 31–41.

Novozhilov, B.V. (1968) "Theory of Nonsteady Burning of Homogeneous Propellants," *Fizika Goreniya I Vzryva,* Vol. 4, No. 4, pp. 482–493.

Novozhilov, B.V. (1970) "Equation for Nonsteady Propellant Burning Rate," *Zh. Prikl. Mekh. i Tekh. Fiz.,* No. 4, pp. 73–78.

Novozhilov, B.V. (1973) "Nonstationary Combustion of Solid Rocket Fuels," Nauka, Moscow, Translation AFSC FTD-MD-24-317-74.

Novozhilov, B.V. (1992) "Second Harmonic Nonlinear Resonance in Propellant Combustion," *24th Symposium (International) on Combustion,* The Combustion Institute, Pittsburgh, PA, pp. 1939–1945.

Novozhilov, B.V. (1992) "Theory of Nonsteady Burning and Combustion Stability of Solid Propellants by the Zel'dovich-Novozhilov Method," *Nonsteady Burning and Combustion Stability of Solid Propellants,* DeLuca, L., Price, E.W. and Summerfield, M. (Editors), AIAA Progress Series, Vol. 14-3, pp. 601–641.

Novozhilov, B.V. (1993) "Acoustic Admittance of the Surface of Burning Condensed Matter," *Sov. J. Chem. Physics,* Vol. 10, No. 11, pp. 2363–2384.

Novozhilov, B.V., Kohno, M. Maruizumi, H., Shimada, T. (1996) "Solid Propellant Burning Rate Response Function of Higher Order," The Institute of Space and Astronautical Science, Report No. 661, Kanagawa, Japan.

Ofelein, J.C. and Yang, V. (1993) "Comprehensive Review of Liquid-Propellant Combustion Instabilities in F-1 Engines," *Journal of Propulsion and Power*, Vol. 9, pp. 637–677.

Paparizos, L. and Culick, F.E.C. (1989) "The Two-Mode Approximation to Nonlinear Acoustics in Combustion Chambers. I. Exact Solutions for Second Order Acoustics," *Combustion Science and Technology*, Vol. 65(1–3), pp. 39–66.

Perry, E.W. (1970) "Investigation of the T-Burner and its Role in Combustion Instability Studies," Ph.D. Thesis, California Institute of Technology.

Price, E.W. (1960) "Combustion Instability in Solid Propellant Rockets," *ARS J.,* Vol. 30, No. 6, pp. 574–576.

Price, E.W. (1965) "Experimental Solid Rocket Instability," *$10^{th}$ (International) Symposium on Combustion,* The Combustion Institute, Pittsburgh, PA, pp. 1067–1082.

Price, E.W. (1971) "Comments on Role of Aluminum in Suppressing Instability in Solid Propellant Rocket Motors," *AIAA J.*, Vol. 9, pp. 987–990.

Price, C.F., Boggs, T. and Derr, R.L. (1979) "The Steady-State Behavior of Ammonium Perchlorate and HMX," AIAA Paper No. 79-0164.

Putnam, A.A. (1971) *Combustion Driven Oscillations in Industry,* Elsevier, New York.

Raun, R.L. and Beckstead, M.W. (1993) "A Numerical Model for Temperature Gradient Effects on Rijke Burner Oscillations," *Combustion and Flame,* Vol. 94, No. 1/2, pp. 1–24.

Raun, R.L., Beckstead, M.W., Finlinson, J.C. and Brooks, K.P. (1993) "A Review of Rijke Tubes, Rijke Burners and Related Devices," *Prog. in Comb. Energy and Science,* Vol. 19, No. 4, pp. 313–364.

Roberts, A.K. and Brownlee, W.G. (1971) "Nonlinear Longitudinal Combustion Instability: Influence of Propellant Combustion," *AIAA Journal,* Vol. 9, No. 1, pp. 140–147.

Schultz, R., Green, L., Jr. and Penner, S. (1958) "Studies of the Decomposition Mechanism, Erosive Burning, Sonance and Resonance for Solid Composite Propellants," *3rd AGARD Colloquium on Combustion and Propulsion,* Pergamon Press, pp. 367–420.

Sehgal, R. and Strand, L. (1964) "A Theory of Low Frequency Combustion Instability in Solid Rocket Motors," *AIAA J.,* pp. 696–702.

Seywert, C. (2001) "Combustion Instabilities: Issues in Modeling and Control," Ph.D. Thesis, California Institute of Technology.

Seywert, C. and Culick, F.E.C. (1999) "Some Influences of Noise on Combustion Instabilities and Combustor Dynamics," $36^{th}$ JANNAF Combustion Conference.

Shapiro, A. (1953) *The Dynamics and Thermodynamics of Compressible Fluid Flow,* Ronald Press, N.Y.

Shusser, M., Cohen, N.S. and Culick, F.E.C. (2000) "Combustion Response of AP Composite Propellants," $37^{th}$ JANNAF Combustion Meeting, submitted to *AIAA J. Prop. and Power*.

Shusser, M., Culick, F.E.C. and Cohen, N.S. (2000) "Combustion Response of Ammonium Perchlorate," $36^{th}$ AIAA/ASME/SAE/ASEE Joint Propulsion Meeting, AIAA-2000-3694, accepted for publication in *AIAA Journal,* 2001.

Shusser M., Cohen N.S. (2001) "Effect of Variable Thermal Properties of the Solid Phase on Composite Solid Propellant Combustion," Caltech Internal Document CI01-04, submitted to *Astronautica Acta,* 2001.

Shusser, M. and Culick, F.E.C. (2001) "Analytical Solution for Composite Solid Propellant Response Function," $37^{th}$ AIAA Joint Propulsion Conference, Caltech Internal Document CI01-02, submitted to *AIAA Journal* 2001.

Shusser, M., Culick, F.E.C. and Cohen, N.S., (2001) "Pressure Exponent of a Composite Solid Propellant," Caltech Internal Document CI01-03, submitted to *AIAA Journal,* 2001.

Smith, A.F. (1960) "A Theory of Oscillatory Burning of Solid Propellants Assuming a Constant Surface Temperature," *ARS Progress in Astronautics and Rocketry: Solid Propellant Rocket Research,* Vol. I, edited by M. Summerfield, Academic Press, pp. 375–391.

Smith, D.A. and Zukoski, E.E. (1985) "Combustion Instability Sustained by Unsteady Vortex Combustion," $21^{st}$ AIAA/SAE/ASME/ASEE Joint Propulsion Conference, AIAA Paper No. 85-1248.

Smith, D.A. (1985) "An Experimental Study of Acoustically Excited, Vortex Driven Combustion Instability Within a Rearward Facing Step Combustor," Ph.D. Thesis, California Institute of Technology.

Smith, R.P. and Sprenger, D.F. (1954) "Combustion Instability in Solid Propellant Rockets," $4^{th}$ *Symposium (International) on Combustion,* Williams and Wilkins, pp. 893–906.

Sterling, J.D. (1987) "Longitudinal Mode Combustion Instabilities in Air Breathing Engines," Ph.D. Thesis, California Institute of Technology.

Sterling, J.D. (1993) "Nonlinear Analysis and Modelling of Combustion Instabilities in a Laboratory Combustor," *Combustion Science and Technology*, Vol. 89, pp. 167–179.

Sterling, J.D. and Zukoski, E.E. (1991) "Nonlinear Dynamics of Laboratory Combustor Pressure Oscillations," *Combustion Science and Technology*, Vol. 77, pp. 225–238.

Summerfield, M. (1951) "A Theory of Unstable Propulsion in Liquid-Propellant Rocket Systems," *Am. Rocket Soc. J.*, Vol. 21, No. 5, pp. 108–114.

Summerfield, M., editor (1960) *Solid Propellant Rocket Research*, Vol. 1 of the ARS (AIAA) Progress Series in Astronautics and Rocketry, Academic Press, New York.

Summerfield, M., Caveny, L.H. Battista, R.A., Kubota, N., Gostintsev, Yu.A., and Isoda, H. (1971) "Theory of Dynamic Extinguishment of Solid Propellants with Special Reference to Nonsteady Heat Feedback Law," *J. of Spacecraft and Rockets,* Vol. 8, No. 3, pp. 251–258.

Tennekes, H. and Lumley, J.L. (1972) *A First Course in Turbulence*, M.I.T. Press.

T'ien, J.S. (1972) "Oscillatory Burning of Solid Propellants Including Gas Phase Time Lag," *Comb. Sci, and Tech.,* Vol. 5, pp. 47–54.

Traineau, J.C., Prévost, M., Vuillot, F., LeBreton, P., Cuny, J., Preioni, N. and Bec, R. (1997) "A Sub-Scale Test Program to Assess the Vortex Shedding Driven Instabilities in Segmented Solid Rocket Motors," AIAA Paper No. 97-3247.

Truesdell, C. and Toupin, R. (1960) "The Classical Field Theories," *Handbuch des Physik*, Vol. III/1, Springer-Verlag, Berlin.

Tsien, H.S. (1952) "The Transfer Functions of Rocket Nozzles," *J. Am. Rocket Soc.*, Vol. 22, pp. 139–143.

Ugurtas, B., Avalon, G., Lupuglazoff, N. and Vuillot, F. (1999) "Numerical Computations of Hydrodynamic Instabilities Inside Channels with Wall Injection," AIAA Paper No. 99-2505.

Ugurtas, B., Avalon, G., Lupuglazoff, N., Vuillot, F. and Casalis, G. (2000) "Stability and Acoustic Resonance of Internal Flows Generated by Side Injection," *J. Propulsion and Power.*

UIUC MURI (2002) "Pressure-Coupled Response Function Measurements by Various Techniques for MURI Propellants," Final Report UILU-ENG-2002-4003, ONR Contract No. N00014-95-1-1339, September 1997 – September 2001.

Vuillot, F., Traineau, J.C., Prévost, M. and Lupoglazoff, N. (1993) "Experimental Validation of Stability Assesment Methods for Segmented Rocket Motors," AIAA Paper No. 93-1883.

Vuillot, F. (1995) "Vortex Shedding Phenomena in Solid Rocket Motors," *J. Propulsion and Power*, Vol. 11, No. 4, pp. 626–639.

Waesche, R.H.W., Wenograd, J. and Summerfield, M. (1961) "Research on Solid Propellant Combustion Instability," Aeronautical Engineering Rept. 564b, Princeton University.

Waesche, R.H.W., Wenograd, J. and Summerfield, M. (1961) "Entropy Wave Observations in Oscillatory Combustion of Solid Propellants: A Progress Report," Paper No. 64-154, AIAA.

Waesche, R.H.W. and Summerfield, M. (1961) "Solid Propellant Combustion Instability: Oscillatory Burning of Solid Rocket Propellants," Aerospace and Mechanical Sciences Rept. 751, Princeton University.

Waesche, R.H.W. (1999) "Mechanisms and Methods of Suppression of Oscillatory Burning by Metallic Additives," *AIAA J. Prop. & Power*, Vol. 15, Nov–Dec. 1999, pp. 919–922. Also see $35^{th}$ *JANNAF Combustion Meeting*, CPIA Pub. 680, Dec. 1998.

Ward, M.J., Son, S.F. and Brewster, M.Q. (1998) *Comb. and Flame,* Vol. 114, pp. 556–568.

Williams, F.A. (1962) "Response of a Burning Solid to Small Amplitude Pressure Oscillations," *Journal of Applied Physics,* Vol. 33, p. 3153.

Williams, F.A. (1973) "Quasi-Steady Flow Theory in Unsteady Burning of a Homogeneous Solid Propellant," *AIAA J.,* Vol. 11, No. 9, pp. 1328–1330.

Williams, F.A. (1985) *Combustion Theory,* Benjamin/Cummings, Menlo Park, CA.

Wood, W.A. (1963) "Oscillatory Burning of Solid Composite Propellants," $9^{th}$ *Symposium (International) on Combustion,* Academic Press, pp. 335–344.

Wooten, D.C. (1966) "The Attenuation and Dispersion Sound in a Condensing Medium," Part I of Ph.d. Thesis, California Institute of Technology.

Yang, V. and Culick, F.E.C. (1990) "On the Existence and Stability of Limit Cycles for Transverse Acoustic Oscillations in a Cylindrical Combustion Chamber I: Standing Modes," *Combustion Science and Technology*, Vol. 72, pp. 37–65.

Zabrowski, M.A. and Brewster, M.Q. (1996) "Theory of Unsteady Combustion of Solids: Investigation of Quasi-Steady Assumption," *J. Prop and Power,* Vol. 12, No. 3, pp. 564–573.

Zak, T. (1993) "An Investigation of the Reacting Vortex Structure Associated with Pulsed Combustion," Ph.D. Thesis, California Institute of Technology.

Zel'dovich, Ya. B. (1942) "On the Combustion Theory of Powder and Explosives," *J. Exp. and Theor. Phys.,* Vol. 12, No. 11, pp. 493–510.

Zel'dovich, Ya. B. (1942) "On the Theory of the Combustion of Powders and Explosives," *Zh. Eksp. Teor. Fiz.,* Vol. 12, No. 11–12, pp. 498–524.

Zel'dovich, Ya. B., Leipunskii, O.I. and Librovich, V.B. (1975) "Theory of Nonsteady Propellant Burning," Nauka, Moscow.

Zetterstrom, K.-A. and Sjöblom, B. (1985) "An Experimental Study of Side Dump Ramjet Combustors," *International Symposium on Airbreathing Engines*, Paper 85-7024.

Zinn, B.T. (1986) "Pulsating Combustion," in *Advanced Combustion Methods*, A.J. Weinberg (Ed.), Academic Press, London.

Zinn, B.T. and Lores, M.E. (1972) "Application of the Galerkin Method in the Solution of Nonlinear and Axial Combustion Instability Problems in Liquid Rockets" *Comb. Sci. and Tech.,* Vol. 4, No. 6, pp. 269.

Zinn, B.T. and Powell, E.A. (1970a) "Application of the Galerkin Method in the Solution of Combustion Instability Problems," *Proceedings of the $19^{th}$ International Astronautical Congress*, Vol. 3, pp. 59–73.

Zinn, B.T. and Powell, E.A. (1970b) "Nonlinear Combustion Instability in Liquid-Propellant Rocket Engines," *Thirteenth Symposium (International) on Combustion.*

# ATTACHMENT — AIAA-2002-3592
## N. Ananthkrishnan, Shardul Deo, F.E.C. Culick
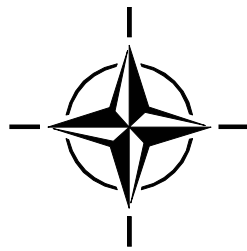
# Modeling and Dynamics of Nonlinear Acoustic Waves in a Combustion Chamber

N. Ananthkrishnan[*] and Shardul Deo[†]
*Indian Institute of Technology (Bombay), Mumbai 400076, India*
and
Fred E.C. Culick[‡]
*California Institute of Technology, Pasadena, CA 91125*

## Abstract

Future combustors designed for better efficiency and lower pollutant emission are expected to operate closer to their stability boundary, thereby increasing the risk of encountering combustion instability. Onset of combustion instability leads to limit cycle oscillations in the acoustical fluctuations that can often reach amplitudes large enough to cause severe damage. Active control strategies are, therefore, being considered to prevent combustion instabilities, but their development requires nonlinear models that can faithfully capture the combustor system dynamics. A framework for the approximate analysis of the nonlinear acoustics in a combustion chamber exists, which includes all relevant linear contributions and also second order gasdynamic nonlinearities. Nonlinear combustion effects in the form of pressure and velocity coupling models have also been incorporated into the analysis with the aim of capturing the phenomenon of triggered instability, where the acoustical fluctuations are linearly stable to small perturbations, but show a limit cycle behavior for larger perturbations. However, several questions such as those relating to 1) modal truncation of the equations for the acoustic dynamics, 2) absence of triggered limit cycles in the formulation with only second order gasdynamic nonlinearities, and 3) the form of the velocity coupling function, including the need for a threshold character, have not been satisfactorily resolved. In this paper, we address some of these questions on modeling and dynamics of acoustic waves in combustion chambers, using the approximate analysis, that have remained unanswered over the years.

## 1. Introduction

Combustion chambers operating under conditions that favor high efficiency and low pollutant emission are prone to suffer from combustion instabilities. These instabilities arise due to a coupling between the unsteady fluid motion and the combustion processes in the chamber. This interaction can be thought of as analogous to a positive feedback mechanism where fluctuations in the flow properties and in the combustion heat release drive each other in a regenerative manner. Amplitude dependent nonlinearities then cut in to limit the growth in the fluctuations. Thus, to an observer external to the chamber, combustion instabilities appear as self-excited limit cycle oscillations in the flow variables. It was shown by Chu and Kovasznay [1] that the fluctuations could be represented by a combination of acoustic, vortical, and entropic waves propagating in the combustion chamber. Traditionally, the term combustion instability has been used to refer to instabilities in the acoustical fluctuations. These acoustic oscillations can often reach amplitudes large enough to cause severe damage, and sometimes even complete failure. As a result, considerable effort has been made in the past to predict the onset of acoustic instabilities in combustion chambers. Solid propellant rocket motors have been known to exhibit two qualitatively different kinds of behavior at onset of combustion instability: 1) linear instability, where the acoustical fluctuations, in response to a small perturbation, build up to a limit cycle, and 2) nonlinear instability, where the acoustical fluctuations show a stable, damped response for small perturbations, but show a limit cycle response to larger perturbations. Nonlinear instability of this nature has been called pulsed or triggered instability [2, 3]. Both linear and nonlinear (triggered) instability have been observed in recent experiments on a gas turbine combustor as well [4].

Much of the early work on combustion instability dealt with the question of linear stability, assuming that the acoustic oscillations could be described in terms of the classical acoustic modes of the combustion chamber. The linear combustion instability problem appears to have been satisfactorily addressed, though work continues on the effects of the vorticity and entropy waves in the combustion chamber on the stability of the acoustic oscillations [5, 6]. It was, however, recognized early on that the dynamics of acoustic waves in combustion chambers was essentially nonlinear, and that it was necessary to be able to understand and model the nonlinear behavior of

---

[*]Assistant Professor, Department of Aerospace Engineering, Senior Member AIAA, akn@aero.iitb.ac.in
[†]Undergraduate Student, Department of Aerospace Engineering, deo@aero.iitb.ac.in
[‡]Richard L. and Dorothy M. Hayman Professor of Mechanical Engineering and Professor of Jet Propulsion, Fellow AIAA, fecfly@caltech.edu

these acoustic waves. The subject of nonlinear acoustics in combustion chambers began to be addressed by several researchers in the 1960's and 1970's. Most of these developments have been reviewed by Culick [**7, 8**], and are, therefore, not repeated here. The work by Culick [**9, 10**] during this period provided a general framework for the analysis of the nonlinear dynamics and stability of acoustic waves in combustion chambers. Under this framework, the partial differential equations of fluid conservation were approximated by a spatial averaging procedure to a set of ordinary differential equations for the amplitudes of the acoustic modes. The approximations in the analysis, and the derivation of the equations for the acoustic modes, have been described on several occasions [**7, 8**]. The equations for the modal amplitudes form a set of coupled, nonlinear differential equations that account for all relevant linear processes and include contributions from nonlinear gasdynamics to second order. On truncating the equations to a finite number of modes, the modal equations could be solved for the time evolution of the acoustic oscillations.

Culick and Yang [**11**] reported a numerically computed solution for the acoustic oscillations with a five-mode truncation of the approximate equations that was found to compare reasonably with a more exact numerical solution [**11**]. Conditions for the existence and stability of the limit cycle oscillations, and the qualitative dependence of the limit cycles on the system parameters, for the case of two longitudinal acoustic modes, were reported by Awad and Culick [**12**], and by Paparizos and Culick [**13**]. However, none of these studies were able to demonstrate triggered instability. It was felt, but not conclusively established, that the approximate analysis with nonlinear, second order gasdynamics alone was not capable of showing triggered instability. Extensions of the formulation to include third order gasdynamic nonlinearities and higher order interactions between the mean flow and the acoustics were equally unsuccessful in capturing triggered instability [**14**] in contrast to earlier results reported by Zinn [**15**]. The difference between the two conclusions remains unexplained. Nonlinear combustion models then remained the most attractive candidate to represent triggered instability within the framework of the approximate analysis. Unsteady combustion in solid propellant rockets had already been described in terms of pressure and velocity coupling models [**16**]. Numerical studies by Levine and Baum [**17**] with an ad hoc velocity coupling model showed that triggered instabilities could indeed be found when nonlinear combustion processes were accounted for. However, the form of the velocity coupling function was purely empirical and it was difficult to judge its validity or uniqueness. Also, it was not easy to arrive at qualitative conclusions regarding the conditions for onset of triggered instability from numerical simulations alone.

A significant step forward in the investigations came with the introduction of the methods of modern dynamical systems theory by Jahnke and Culick [**18**] to the analysis of nonlinear combustion instabilities. By using a continuation algorithm, it became possible to systematically and efficiently compute all steady state and limit cycle solutions over a range of parameter values. Stability of each steady state and limit cycle solution could be numerically established, and points of onset of instability could be identified with bifurcations. The qualitative behavior of the acoustic waves at onset of combustion instability then depends on the type of bifurcation, and on the nature of the limit cycles that emerge at the bifurcation point. This information is usually represented in the form of a plot of steady state values (peak amplitude in case of a limit cycle) against a suitable parameter in a bifurcation diagram. For longitudinal acoustic modes in a combustion chamber of uniform cross section, Jahnke and Culick [**18**] showed that results from a two-mode approximation were qualitatively dissimilar to those from a four- or six-mode approximation. However, they could draw no conclusion about the number of acoustic modes that need to be retained in their analysis, nor did their computations with second order gasdynamics alone display triggered limit cycles. Culick et al [**19**] extended the work in [**18**] by including the nonlinear combustion model of Levine and Baum [**17**] in addition to the second order gasdynamic nonlinearities. They confirmed that the nonlinear velocity coupling term in the Levine-Baum model did induce triggered limit cycles. However, their results with and without time-averaging showed significant discrepancies. Their studies also suggested that a four-mode approximation could satisfactorily capture the qualitative dynamics for the case of a first mode instability. Experiments by Ma et al [**20**] have suggested that the velocity coupling function has a threshold nature, i.e., there is a threshold value of the acoustic velocity below which the effects of nonlinear combustion are not felt. In a recent paper, using a four-mode truncation and an ad hoc threshold velocity coupling model, Burnley and Culick [**21**] have computed a bifurcation diagram which shows triggered limit cycles. Additional results are available in the thesis by Burnley [**22**].

Despite the impressive progress over the last three decades in modeling the nonlinear dynamics of acoustic waves in combustion chambers, many questions yet remain unanswered. For example, first of all, there is still no convincing argument for how many modes need to be retained in a truncated model of the coupled oscillator equations in order to predict the qualitative dynamics of the acoustic modes correctly. Secondly, though widely believed, it has never been definitely established that the approximate analysis with second order gasdynamics alone could not show triggered instability. Thirdly, the form of the velocity coupling function and, in particular, the need for a threshold character, has not been satisfactorily explained. These and such other questions have gained significance in the light of recent focus on active control of combustion instabilities [**23, 24**]. Rather than restrict operation to safe, stable regions at the cost of decreased performance, future combustors seeking higher performance will be operated closer to their stability boundary, thereby increasing the risk of encountering combustion instability. Active control strategies promise to provide a feasible solution to the problem of preventing instability in these combustors, but they are expected to depend heavily on nonlinear models that can successfully capture the qualitative features of the combustion system dynamics. The approximate formulation developed by Culick and his co-workers appears to provide a suitable framework for the development of active control laws for combustion instability, but there is a need to address questions such as those listed above before the Culick framework can be confidently applied to devise active combustion control strategies. Recent developments [**25, 26, 27**] in the use of bifurcation theory for the modeling of large-amplitude limit cycle oscillations have made it possible to seek answers to some questions on the qualitative dynamics of the acoustic waves at onset of combustion instability.

In the remainder of this paper, we first closely examine the coupled oscillator equations for the acoustic modal amplitudes. A careful study of the energy transfer between the acoustic modes provides a clue to the number of modes that need to be retained for a qualitatively correct analysis of the limit cycles at onset of combustion instability. The minimum order of the modal truncation for the first and second mode instability cases is determined, thereby resolving a longstanding issue in the modeling of acoustic waves in combustion chambers. Following this, two known mechanisms for triggered instability in coupled oscillator systems are briefly reviewed. With this knowledge, we then explain the lack of triggered limit cycles in the approximate formulation containing only second order gasdynamic nonlinearities. This is a result that, though widely believed in the past, has been theoretically established here for the first time. Finally, nonlinear combustion mechanisms for triggering are studied. Observations by Culick et al [**19**] that nonlinear pressure coupling does not lead to triggering are now explained. Velocity coupling models used in the past are evaluated and are found to display non-physical dynamical behavior. The need for a threshold velocity coupling function is critically examined and a new form of the velocity coupling function is derived that naturally shows a threshold character. The approach at all times is from the viewpoint of the qualitative theory of dynamical systems. However, numerical results are provided to illustrate the conclusions arrived at from the theory.

## 2. Coupled Oscillator Equations

The nonlinear dynamics of acoustic waves in a combustion chamber has been modeled by Culick [**10**] as a set of coupled second order oscillators, one for each acoustic mode. For the case of a combustion chamber of uniform cross section as considered in [**18, 19**], the modal natural frequencies can be assumed to be integral multiples of the primary acoustic mode frequency. Then, the coupled oscillator equations, with time non-dimensionalized by the primary mode frequency, can be written as follows:

$$\ddot{\eta}_n - 2\hat{\alpha}_n \dot{\eta}_n + n(n - 2\hat{\theta}_n)\eta_n = \quad -\sum_{i=1}^{n-1} \left( \hat{C}_{ni}^{(1)} \dot{\eta}_i \dot{\eta}_{n-i} + \hat{D}_{ni}^{(1)} \eta_i \eta_{n-i} \right)$$
$$-\sum_{i=1}^{\infty} \left( \hat{C}_{ni}^{(2)} \dot{\eta}_i \dot{\eta}_{n+i} + \hat{D}_{ni}^{(2)} \eta_i \eta_{n+i} \right) \quad (2.1)$$

where $\eta_n$ is the amplitude of the $n^{th}$ acoustic mode. Equation (2.1) includes linear contributions from combustion processes, gas-particle interactions, boundary conditions, and interactions between the steady and unsteady flow fields. Additionally, Eq. (2.1) also includes contributions from nonlinear gasdynamics to second order as given by the quadratic terms on the right hand side, where the coefficients $\hat{C}, \hat{D}$ are as follows:

$$\hat{C}_{ni}^{(1)} \quad = \quad \frac{-1}{2\gamma i(n-i)}[n^2 + i(n-i)(\gamma - 1)]$$

$$\hat{C}_{ni}^{(2)} = \frac{1}{\gamma i(n+i)}[n^2 - i(n+i)(\gamma - 1)]$$

$$\hat{D}_{ni}^{(1)} = \frac{\gamma - 1}{4\gamma}[n^2 - 2i(n-i)]$$

$$\hat{D}_{ni}^{(2)} = \frac{\gamma - 1}{2\gamma}[n^2 + 2i(n+i)]$$

The parameters $\hat{\alpha}_n$ and $\hat{\theta}_n$ in Eq. (2.1) are defined as

$$\hat{\alpha}_n = \alpha_n/\omega_1, \quad \hat{\theta}_n = \theta_n/\omega_1$$

where $\omega_1$ is the natural frequency of the first acoustic mode. For a cylindrical chamber of $L/D = 11.8$, the first mode frequency, $\omega_1$, is 5654.86 rad/s, and typical values for the linear growth rates, $\alpha_n$, and frequency shifts, $\theta_n$, are as given in Table 1. It can be seen from Table 1 that the modes are generally lightly damped and have only small frequency shifts, which means that the shifted modal frequencies remain appoximately integral multiples of the shifted primary mode frequency. It may also be noticed that the oscillators in Eq. (2.1) are linearly uncoupled, but are coupled through the nonlinear gasdynamic terms. In particular, it will be seen later that the quadratic terms on the right hand side of Eq. (2.1) with coefficients $\hat{C}^{(1)}$ and $\hat{D}^{(1)}$ ensure that the set of oscillators is resonantly coupled. For a set of resonantly coupled, lightly damped, nonlinear oscillators as in Eq. (2.1), it is not immediately obvious as to which modes affect the stability of a particular mode. Therefore, the question of how many higher order modes need to be retained for a correct solution of the $n^{th}$ mode instability problem is not easy to answer. Previous numerical results [**18, 19**] suggest that when too few modes are retained in an analysis, the qualitative predictions of the nonlinear dynamic behavior at instability may be incorrect. At the same time, inclusion of higher order modes beyond a point does not seem to have a significant influence on the quantitative accuracy. Both these observations are not surprising, but 'How few (modes) is too few?' is a question that has not received a satisfactory answer to date.

**Table 1. Data for parameters $\alpha_n$ and $\theta_n$.**

| Mode | 1 | 2 | 3 | 4 | 5 | 6 |
|---|---|---|---|---|---|---|
| $\alpha_n$, 1/s | Free | $-324.8$ | $-583.6$ | $-889.4$ | $-1262.7$ | $-1500.0$ |
| $\theta_n$, rad/s | 12.9 | 46.8 | $-29.3$ | $-131.0$ | $-280.0$ | $-300.0$ |

**2.1. Energy Transfer.** Looking at Eq. (2.1), it is clear that in the absence of the second order gasdynamic terms on the right hand side, the individual modes behave as uncoupled linear oscillators. The coupling, and hence the energy transfer, between the modes is entirely due to the nonlinear gasdynamics. The influence of the nonlinear terms in the energy transfer process is presented in a concise form in Table 2 for the first eight modes. Each entry in the second column of Table 2 represents a pair of nonlinear gasdynamic terms that transfer energy to a particular mode from a lower numbered mode, i.e., energy transfer up the mode numbers from lower to higher modes. The third column, on the other hand, lists the terms that cause reverse energy transfer, i.e., from higher mode numbers to the lower ones. For instance, in the row for mode number 2, a term '13' implies that the second mode is excited by terms of the form $\eta_1\eta_3$ and $\dot{\eta}_1\dot{\eta}_3$. The term '13' represents a reverse transfer of energy from the third mode to the second mode. It can be seen that terms with $\hat{C}^{(1)}$ and $\hat{D}^{(1)}$ as coefficients appear in the second column of Table 2, while the third column consists of terms with $\hat{C}^{(2)}$ and $\hat{D}^{(2)}$ as coefficients.

**Table 2. Inter-modal energy transfers.**

| Mode number | Energy transfer up the modes | Reverse energy transfer |
|---|---|---|
| 1 | | **12**, 23, 34, 45, 56, 67, 78 |
| 2 | 11 | 13, **24**, 35, 46, 57, 68 |
| 3 | 12, 21 | 14, 25, **36**, 47, 58 |
| 4 | 13, 22, 31 | 15, 26, 37, **48** |
| 5 | 14, 23, 32, 41 | 16, 27, 38 |
| 6 | 15, 24, 33, 42, 51 | 17, 28 |
| 7 | 16, 25, 34, 43, 52, 61 | 18 |
| 8 | 17, 26, 35, 44, 53, 62, 71 | |

A look down the second column of Table 2 shows that every term in the energy transfer up the modes acts as a near-resonant excitation. For instance, consider the first mode to be oscillating at its (shifted) natural frequency $\omega_1^s$, and recall that the (shifted) natural frequencies of the higher modes are approximately integral multiples of that of the first mode. Then, the terms '11' will excite the second mode at exactly $2\omega_1^s$, which is approximately equal to its (shifted) natural frequency. Likewise, terms like '12' and '21' will excite the third mode at a frequency $3\omega_1^s$, which will nearly resonate with its (shifted) natural frequency, and so on. Hence, the modes in Eq. (2.1) represent a set of resonantly coupled oscillators. In contrast, the reverse energy transfer terms in the third column of Table 2 typically excite the modes at frequencies much higher than their resonant frequency, and hence contribute little to the overall modal amplitudes, except for the terms in boldface. The boldface terms represent parametric excitations which can alter the dynamics of the modes, in contrast to the other terms which act as external forcings that can merely contribute to the modal amplitude at a particular frequency. When the boldfaced terms are taken to the left hand side of the respective oscillator equation in Eq. (2.1), they can be seen to alter the frequency and damping of the modes, and thus, they can change the qualitative dynamical behavior. This can be clearly seen, for example, by writing the dynamical equation for the first mode with the parametric excitations moved to the left hand side as follows:

$$\ddot{\eta}_1 + [-2\hat{\alpha}_1 + \hat{C}_{11}^{(2)}\dot{\eta}_2]\dot{\eta}_1 + [(1 - 2\hat{\theta}_1) + \hat{D}_{11}^{(2)}\eta_2]\eta_1 = \ [other\ RHS\ terms] \tag{2.2}$$

The term involving $\hat{C}_{11}^{(2)}$ represents a reverse transfer of energy from the second to the first mode that could potentially destabilize the first mode. The effect of the other boldface terms in Table 2 can be similarly interpreted as a change in the damping and frequency of the oscillator equation in which they appear.

**2.2. Modal Truncation.** We are now in a position to answer the question of how many modes need to be retained in an analysis to obtain qualitatively correct results for an $n^{th}$ mode instability. Consider the case where the first mode goes linearly unstable and begins oscillating at a frequency $\Omega$ (which may be slightly different from its shifted natural frequency $\omega_1^s$ due to nonlinear effects). Energy is then transferred to the second mode, which is resonantly excited by the terms '11' and set into oscillation at a frequency of $2\Omega$. A part of the energy from the second mode is reverse transferred to the first mode due to the boldfaced '12' terms in Table 2. Thus, the dynamics of the first mode is nonlinearly coupled to that of the second mode, and it is necessary to consider the first and second mode oscillators coupled together. However, since the parametric excitation terms '12' can significantly alter the dynamics of the first mode, it is important that they are correctly represented. When the third and higher modes are neglected, the second mode cannot transfer energy up the mode numbers as per the terms in the second column of Table 2. Instead, it is forced to reverse transfer part of this energy to the first mode, due to which the parametric excitations are larger than they ought to be, and the resulting dynamics may show large-amplitude limit cycles that are spurious. Such spurious limit cycles were observed, but could not be explained, in the two-mode continuation results of Jahnke and Culick [18], and, previously, in the two-mode analytical results reported by Awad and Culick [12], and by Paparizos and Culick [13]. Hence, the modal truncation should be such that all significant energy transfers up the modes are accommodated. This requires that all modes that directly receive energy from modes 1 and 2, individually or collectively, should be represented in the truncated set of equations. It is seen from Table 2 that direct energy transfer from modes 1 and 2 to the higher modes occurs through the terms '12' and '21' to the third mode, and through the term '22' to the fourth mode. All other energy transfers to the higher modes are indirect in the sense that they require the participation of the first/second mode and another higher mode. Thus, in a first mode instability, the third and fourth modes play an important role as energy sinks and must be included in the modal truncation, even though their direct influence on the dynamics of the first mode is not significant. In summary, the truncated set of equations for correct qualitative analysis of a first mode instability should contain at least four modes — the unstable mode (mode 1), the coupled modes (mode 2), and the energy sinks (modes 3 and 4). This argument can be easily extended to determine the minimum order of the modal truncation for analysis of an $n^{th}$ mode instability. For example, in case of a second mode instability, it can be shown that the modal truncation must retain at least the first eight modes.

Continuation results for first and second mode instability have been reported in [18, 19, 22], where upto sixteen modes have been retained. Examination of these results confirms that computations for first mode instability with a modal truncation that did not retain at least four modes were qualitatively incorrect. Similarly, second mode instability computations that retained fewer than eight modes are seen to be qualitatively inconsistent. In the

following sections of this paper, we shall examine the first mode instability problem with a four-mode truncation. In particular, we shall be interested in conditions under which triggered limit cycles occur.

### 3. Triggered Limit Cycles

The set of coupled acoustic oscillators in Eq. (2.1) can be seen to have an equilibrium state where each $\eta_n = 0$, i.e., none of the acoustic modes are excited. Since the oscillators are all linearly decoupled, the linear damping coefficient for each mode, $\hat{\alpha}_n$, determines whether or not that particular mode is linearly stable. When each $\hat{\alpha}_n$ is negative, then the equilibrium state of the set of acoustic oscillators is linearly stable. In that case, small perturbations from the equilibrium state damp out with time, and the system of oscillators tends to return to its equilibrium state. Combustion instability occurs when one of the modes gets undamped, i.e., the corresponding $\hat{\alpha}_n$ changes sign from negative to positive. For positive $\hat{\alpha}_n$, the equilibrium state is linearly unstable, and small perturbations in the acoustic mode amplitudes initially grow with time. Nonlinear effects then become important and the modal amplitudes eventually settle down to a periodic oscillation called a limit cycle. Thus, given a model for the nonlinear dynamics of the acoustic waves, such as that in Eq. (2.1), one needs to predict the amplitude and frequency of the limit cycle oscillations at onset of combustion instability. This is easily done by using a continuation and bifurcation software such as AUTO97 [**28**]. Consider the first mode instability problem with a four-mode truncation of the set of oscillators in Eq. (2.1), where the only nonlinear terms are due to second order gasdynamics. Equilibrium states and limit cycles for this case have been computed for varying values of first mode damping parameter $\hat{\alpha}_1$ using the data in Table 1. Results are obtained for the amplitudes of the first four modes and, in case of limit cycles, also the time period of the oscillation. Of these, the first mode amplitude is plotted in Fig. 1 (plots for the other modal amplitudes are qualitatively similar) over a range of values of the parameter $\hat{\alpha}_1$. Figure 1 shows that the zero-amplitude equilibrium is linearly stable for $\hat{\alpha}_1 < 0$ and becomes unstable for $\hat{\alpha}_1 > 0$, with onset of instability occuring at $\hat{\alpha}_1 = 0$. Stable limit cycles emerge at the critical point $\hat{\alpha}_1 = 0$, which is called a supercritical Hopf bifurcation point. For any negative value of $\hat{\alpha}_1$, the only stable solution is the zero-amplitude equilibrium, and the acoustic waves tend to damp out, no matter how large the initial perturbation. Thus, the coupled oscillator model with second order gasdynamics alone shows only linear instability.
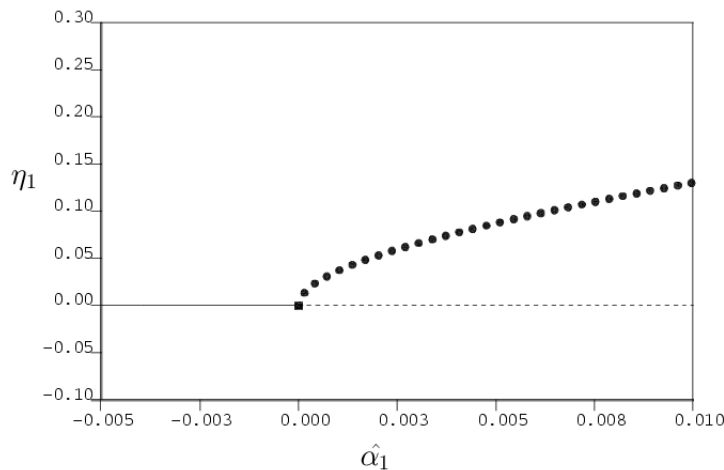


FIGURE 1. Stable limit cycles at a supercritical Hopf bifurcation for a first mode instability with second order gasdynamics alone (full line — stable equilibrium, dashed line — unstable equilibrium, filled circle — stable limit cycle, filled square — Hopf bifurcation).

Solid propellant rockets, as discussed earlier, have been known to show both linear and nonlinear or triggered instability. Examples of triggered instability are shown in the schematic bifurcation diagrams in Fig. 2, where $x$ is a variable and $\mu$ is a parameter. In each of the diagrams in Fig. 2, there is a range of values of the parameter $\mu$ for which a stable equilibrium state co-exists with a stable limit cycle. For any parameter value in this range, small perturbations in $x$ from the equilibrium state will tend to decay with time, but for larger perturbations,

the system may show stable limit cycle oscillations. That is, though the equilibrium state is linearly stable, the system could be pulsed or triggered into limit cycle behavior. These stable limit cycles are called triggered limit cycles. The triggered limit cycles in Fig. 2 are qualitatively different from the stable limit cycles in Fig. 1 in two respects: 1) Triggered limit cycles in Fig. 2 exist to the left of the Hopf bifurcation point that signifies onset of (linear) combustion instability, whereas the stable limit cycles in Fig. 1 occur only for parameter values to the right of the Hopf bifurcation. 2) Moving along the parameter axis from left to right, the triggered limit cycles in Fig. 2 begin abruptly with a finite non-zero amplitude at a fold bifurcation, as against the stable limit cycles in Fig. 1 whose amplitude starts from zero at the Hopf bifurcation point. Triggered limit cycles are, therefore, also called large-amplitude limit cycles in the literature [**25, 26, 27**]. The onset of triggered limit cycles at a fold bifurcation can be considered to be a nonlinear combustion instability phenomenon. Thus, with increasing values of the parameter $\mu$, the systems in Fig. 2 first show a nonlinear combustion instability at a fold bifurcation, and then a linear combustion instability at a Hopf bifurcation.
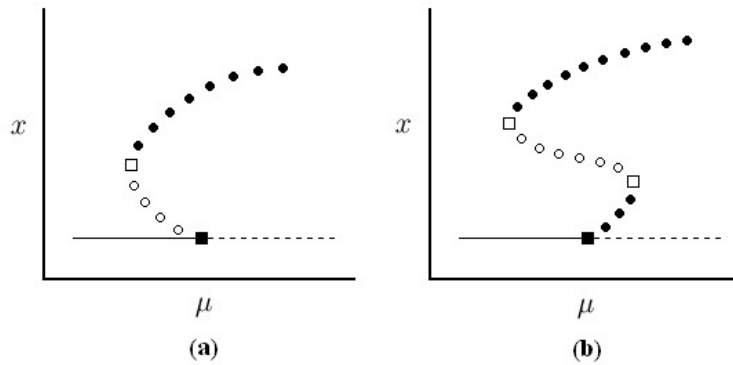


FIGURE 2. Triggered limit cycles at (a) subcritical Hopf bifurcation, and (b) supercritical Hopf bifurcation (full line — stable equilibrium, dashed line — unstable equilibrium, filled circle — stable limit cycle, empty circle — unstable limit cycle, filled square — Hopf bifurcation, empty square — fold bifurcation).

Triggered limit cycles can be a disquieting phenomenon due to the sudden increase in the amplitudes of the acoustic modes. Moreover, the phenomenon is worrisome because triggered instability could occur even when linearly stable operating conditions have been ensured. Hence, there is a need to develop models that can faithfully capture the qualitative dynamics of triggered limit cycles in combustion chambers. Unfortunately, the coupled acoustic oscillator model in Eq. (2.1), from past experience and as seen in Fig. 1, does not seem to accommodate triggered limit cycles, but this has never been definitely established. We can now explain the lack of triggered limit cycles in the oscillator model of Eq. (2.1) by comparing the influence of the second order gasdynamic nonlinearities with nonlinear terms that are known to cause triggering in coupled oscillator systems. There are two known mechanisms for generation of triggered limit cycles in systems of resonantly coupled oscillators.

1. Nonlinear damping terms of the form $|f(\eta_n)|\dot{\eta}_n$ or $|f(\dot{\eta}_n)|\dot{\eta}_n$ have been shown to produce triggered limit cycles with either subcritical or supercritical Hopf bifurcations, as sketched in Fig. 2 [**26**].
2. Parametric excitation terms of the form $c\dot{\eta}_{2n}\dot{\eta}_n$ or $c\eta_{2n}\dot{\eta}_n$ are also known to be able to create a subcritical Hopf bifurcation and triggered limit cycles, as pictured in Fig. 2(a), depending on the sign of the coefficient $c$, i.e., $c < 0$ for triggering, and $c > 0$ for non-triggering [**27**].

Examining the nonlinear terms in the equation for the first acoustic mode, which is reproduced below from Eq. (2.2),

$$\ddot{\eta}_1 + [-2\hat{\alpha}_1 + \hat{C}_{11}^{(2)}\dot{\eta}_2]\dot{\eta}_1 + [(1 - 2\hat{\theta}_1) + \hat{D}_{11}^{(2)}\eta_2]\eta_1 = [\text{other RHS terms}] \tag{3.3}$$

it can be observed that there are no nonlinear damping terms, but the second order gasdynamic term $\hat{C}_{11}^{(2)}\dot{\eta}_2\dot{\eta}_1$ does indeed act as a parametric excitation of the desired form as listed in 2. above. (The other parametric excitation term $\hat{D}_{11}^{(2)}\eta_2\eta_1$ is clearly not of the desired form.) However, on using the expressions following Eq. (2.1), the

coefficient $\hat{C}_{11}^{(2)}$ can be evaluated to be

$$\hat{C}_{11}^{(2)} = (3 - 2\gamma)/2\gamma$$

which is usually positive, where $\gamma$ is the ratio of specific heats. The term $\hat{C}_{11}^{(2)}\dot{\eta}_2\dot{\eta}_1$, thus, turns out to be a parametric excitation of the non-triggering type. It follows that second order gasdynamic nonlinearities, as they exist, are incapable of inducing triggered limit cycles. As an academic exercise, one may choose an arbitrary non-physical value of $\gamma$ that makes the coefficient $\hat{C}_{11}^{(2)}$ negative; then, triggered limit cycles can indeed be observed [**29**]. In summary, triggered limit cycles observed in solid propellant rockets cannot be explained by modeling the second order gasdynamic nonlinearities alone.

The most promising source for the triggering mechanism then appears to be nonlinear combustion. The approximate formulation of Eq. (2.1) already accounts for contributions from linear combustion processes. Nonlinear combustion phenomena can be included in the coupled oscillator system of Eq. (2.1) by introducing additional terms $F_n^{nc}$ representing pressure and velocity coupling effects. The modal equations for the set of coupled oscillators then appear as

$$\ddot{\eta}_n - 2\hat{\alpha}_n\dot{\eta}_n + n(n - 2\hat{\theta}_n)\eta_n = \quad -\sum_{i=1}^{n-1}\left(\hat{C}_{ni}^{(1)}\dot{\eta}_i\dot{\eta}_{n-i} + \hat{D}_{ni}^{(1)}\eta_i\eta_{n-i}\right)$$

$$-\sum_{i=1}^{\infty}\left(\hat{C}_{ni}^{(2)}\dot{\eta}_i\dot{\eta}_{n+i} + \hat{D}_{ni}^{(2)}\eta_i\eta_{n+i}\right) + F_n^{nc} \qquad (3.4)$$

where $\eta_n$ is again the amplitude of the $n^{th}$ acoustic mode. Culick et al [**19**] and Burnley [**22**] considered the nonlinear pressure coupling terms in the Levine-Baum model as a possible candidate for the creation of triggered limit cycles. They observed that the nonlinear pressure coupling terms did indeed cause triggering, but the required values of the coefficients of these terms turned out to be unrealistically large. Their observations can now be explained by noting that the nonlinear pressure coupling terms in the Levine-Baum model are in fact second order parametric excitation terms with a negative coefficient (see Eq. (33) of Culick et al [**19**]), and, hence, of the type that can cause triggering. Then, for a first mode instability problem with second order gasdynamics and nonlinear pressure coupling, the parametric excitation terms in the equation for the first acoustic mode appear as $(\hat{C}_{11}^{(2)} + C_1^{pc})\dot{\eta}_2\dot{\eta}_1$, where $C_1^{pc}$ is the coefficient of the pressure coupling term. Now, the combined coefficient $(\hat{C}_{11}^{(2)} + C_1^{pc})$ is required to be negative for triggering to occur, and although $C_1^{pc}$ is known to be negative, it clearly needs to be large enough to overcome the positive value due to $\hat{C}_{11}^{(2)}$. Unfortunately, for reasonable values of $C_1^{pc}$, the combined coefficient is still positive, and, as a result, the nonlinear pressure coupling model does not lead to triggering. This leaves us to consider velocity coupling models as a possible candidate to explain the occurrence of triggered instability.

## 4. Velocity Coupling Models

Levine and Baum [**17**] suggested a velocity coupling function of the form $F_n^{nc} = f(\dot{\eta}_n)\dot{\eta}_n$, with $f(\dot{\eta}_n) = C_n^{vc}|\dot{\eta}_n|$, to model the nonlinear combustion response to an acoustic velocity parallel to the burning surface. The equation for the first acoustic mode, with second order gasdynamics and the Levine-Baum velocity coupling model, is then of the form

$$\ddot{\eta}_1 + [-2\hat{\alpha}_1 + \hat{C}_{11}^{(2)}\dot{\eta}_2 + C_1^{vc}|\dot{\eta}_1|]\dot{\eta}_1 + [(1 - 2\hat{\theta}_1) + \hat{D}_{11}^{(2)}\eta_2]\eta_1 = \; [other\; RHS\; terms] \qquad (4.5)$$

The velocity coupling function in Eq. (4.5) represents a nonlinear damping mechanism, and can, therefore, be expected to create triggered limit cycles at onset of first mode combustion instability. This is confirmed by computing equilibrium points and limit cycles for a four-mode truncation of the coupled oscillator system Eq. (3.4) for the data in Table 1. The velocity coupling function in the equation for the first acoustic mode is taken as shown in Eq. (4.5) with $C_1^{vc} = 0.2$. Results for the first mode amplitude are plotted in Fig. 3 for varying values of the parameter $\hat{\alpha}_1$. Triggered limit cycles are clearly seen in Fig. 3 at a subcritical Hopf bifurcation, similar to that sketched in the schematic bifurcation diagram of Fig. 2(a). Thus, the Levine-Baum velocity coupling model along with the second order gasdynamic nonlinearities is adequate to capture triggered limit cycles in solid propellant combustion systems. However, from a qualitative point of view, the dynamics represented by the bifurcation diagram in Fig. 3 is not entirely satisfactory. This is because the stable triggered limit cycles terminate at some positive value of $\hat{\alpha}_1$ beyond which there are no stable equilibrium or limit cycle solutions. This implies that,

where there are no stable solutions, the slightest perturbation will cause the modal amplitudes to eventually grow to infinity. Such dynamical behavior is clearly non-physical and must be eliminated.
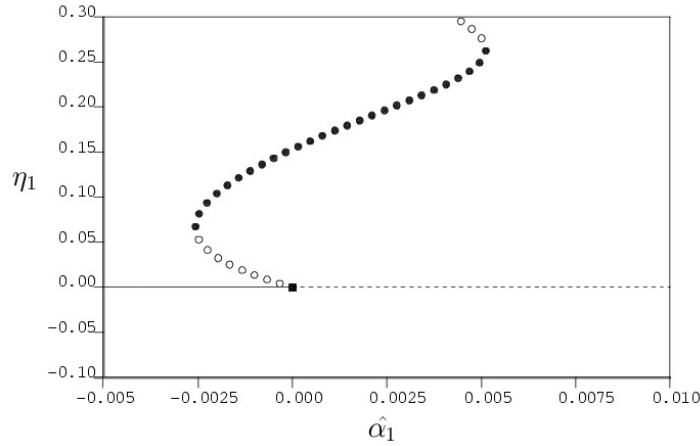


FIGURE 3. Triggered limit cycles at a subcritical Hopf bifurcation for a first mode instability with second order gasdynamics and the Levine-Baum velocity coupling function (full line — stable equilibrium, dashed line — unstable equilibrium, filled circle — stable limit cycle, empty circle — unstable limit cycle, filled square — Hopf bifurcation).

Levine and Baum [**17**] also suggested that threshold effects that had been observed experimentally be incorporated in the velocity coupling function. Burnley and Culick [**21**] modified the Levine-Baum velocity coupling function by introducing a dead zone to obtain an ad hoc velocity coupling function with a threshold, as follows:

$$
\begin{aligned}
f(\dot{\eta}_1) &= 0, & |\dot{\eta}_1| &< |\dot{\eta}_1^t| \\
f(\dot{\eta}_1) &= C_1^{vc}|\dot{\eta}_1 - \dot{\eta}_1^t|, & |\dot{\eta}_1| &\geq |\dot{\eta}_1^t|
\end{aligned}
\tag{4.6}
$$

where $\dot{\eta}_1^t$ is the threshold value of $\dot{\eta}_1$. Computation of equilibrium and limit cycle solutions is carried out as before, but with the Burnley-Culick velocity coupling function in Eq. (4.6) instead of the Levine-Baum model. The parameter $C_1^{vc}$ in Eq. (4.6) is retained unchanged, i.e., $C_1^{vc} = 0.2$, and a threshold value of $\dot{\eta}_1^t = 0.02$ is chosen. A plot of the first mode amplitude for this case with varying values of the parameter $\hat{\alpha}_1$ is shown in Fig. 4, where triggered limit cycles of the form sketched in Fig. 2(b) may be observed at a supercritical Hopf bifurcation. However, it is known that functions $f(\dot{\eta}_1)$ that are approximately quadratic in shape, e.g., the Levine-Baum function, show triggered limit cycles of the subcritical type, while those that are approximately quartic (fourth-order), like the Burnley-Culick function, show triggered limit cycles of the supercritical type [**26**]. It is not difficult to come up with velocity coupling models with no threshold, but with an approximately quartic function $f(\dot{\eta}_1)$, that also produce triggered limit cycles of the supercritical type as in Fig. 4 [**30**]. Thus, the change from subcritical triggering in Fig. 3 to supercritical triggering in Fig. 4 cannot be attributed to the threshold effect in the Burnley-Culick velocity coupling function. Besides, the non-physical dynamical behavior seen over a range of positive values of $\hat{\alpha}_1$ in Fig. 3 persists in Fig. 4 as well.

To resolve this issue, we go back to the bifurcation diagram of Fig. 3 and the Levine-Baum velocity coupling model. It is clear that the qualitative dynamics of triggered limit cycles at onset of first mode combustion instability at the subcritical Hopf bifurcation is adequately captured in Fig. 3. This means that the form of the Levine-Baum velocity coupling function is appropriate for small $\dot{\eta}_1$, i.e., near the region of onset of instability. The non-physical dynamics in Fig. 3 occurs for larger values of $\eta_1$ and $\dot{\eta}_1$, which implies that the form of the Levine-Baum velocity coupling model requires to be corrected for large $\dot{\eta}_1$, without affecting its shape in the neighborhood of $\dot{\eta}_1 = 0$. The lowest order correction term to the Levine-Baum function which meets these requirements is a quadratic term with value zero at $\dot{\eta}_1 = 0$, slope zero at $\dot{\eta}_1 = 0$, and a magnitude that subtracts from the value of the function for large $\dot{\eta}_1$. The new velocity coupling function, with such a quadratic term included, can be expressed as

$$
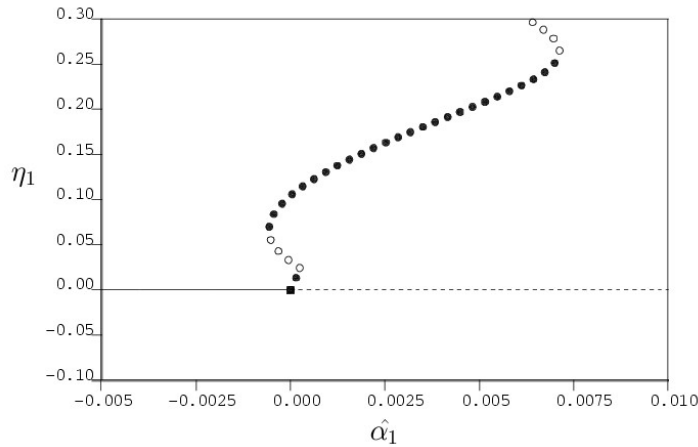f(\dot{\eta}_1) = C_1^{vc}|\dot{\eta}_1| - D_1^{vc}|\dot{\eta}_1|^2
\tag{4.7}
$$

FIGURE 4. Triggered limit cycles at a supercritical Hopf bifurcation for a first mode instability with second order gasdynamics and the Burnley-Culick threshold velocity coupling function (full line — stable equilibrium, dashed line — unstable equilibrium, filled circle — stable limit cycle, empty circle — unstable limit cycle, filled square — Hopf bifurcation).

For a particular choice of the coefficients, $C_1^{vc} = 0.2$ and $D_1^{vc} = 0.8$, the shape of the new velocity coupling function appears as plotted in Fig. 5. Surprisingly, the nonlinear function in Fig. 5 naturally shows a threshold character, but one that is quite different from the Burnley-Culick function. Computations are now carried out for equilibrium solutions and limit cycle amplitudes under identical conditions as was done for Fig. 3, but with the new velocity coupling function in Eq. (4.7) instead of the Levine-Baum model. Results for the first mode amplitude with varying parameter $\hat{\alpha}_1$ are shown in Fig. 6. As expected, the subcritical Hopf bifurcation in Fig. 6 is identical to that in Fig. 3, and the qualitative dynamics of the triggered limit cycles in the vicinity of the Hopf bifurcation point, i.e., for small $\eta_1$ and $\dot{\eta}_1$, remains unchanged. However, the stable limit cycles persist for all positive values of the parameter $\hat{\alpha}_1$, and the non-physical dynamical behavior in Fig. 3 is, therefore, eliminated in Fig. 6. Thus, the new velocity coupling function in Fig. 5 provides a satisfactory picture of the qualitative dynamics of the triggered limit cycles created at onset of combustion instability. In addition, the new velocity coupling function that is derived from dynamical considerations naturally satisfies the physical requirement of having a threshold character.
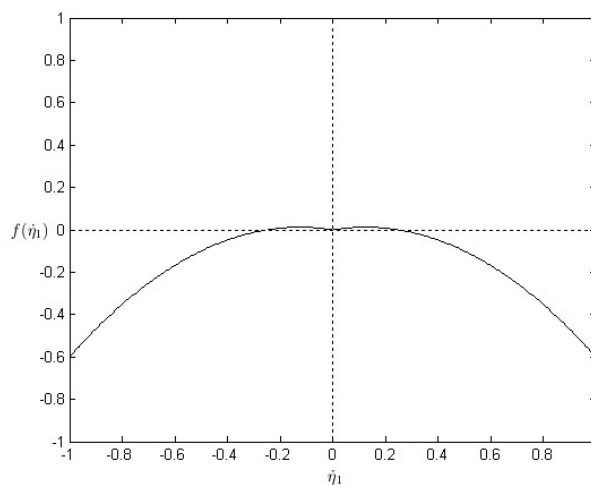


FIGURE 5. The form of the velocity coupling function obtained by correcting the Levine-Baum function with a suitable quadratic term.
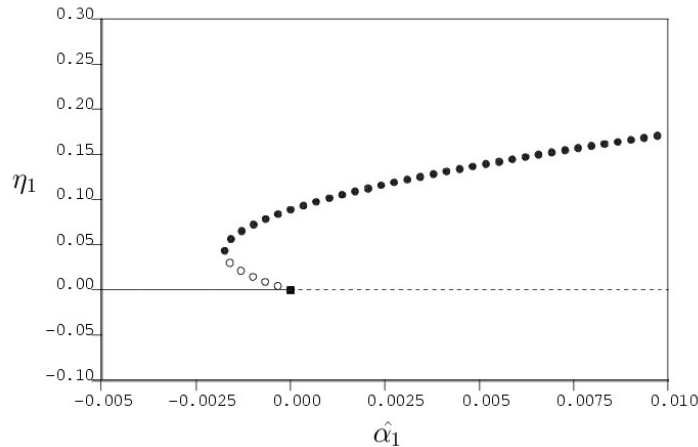
FIGURE 6. Triggered limit cycles at a subcritical Hopf bifurcation for a first mode instability with second order gasdynamics and the threshold velocity coupling function in Fig. 5 (full line — stable equilibrium, dashed line — unstable equilibrium, filled circle — stable limit cycle, empty circle — unstable limit cycle, filled square — Hopf bifurcation).

## 5. Conclusions

Several questions regarding the modeling and dynamics of acoustic waves in combustion chambers have been addressed in this paper using the approximate analysis originally developed by Culick. First among these is the question of modal truncation, i.e., how many modes need to be retained in a truncated model of the coupled oscillator equations in order to predict the qualitative dynamics of the acoustic waves correctly. Previous studies of first and second mode instabilities arbitrarily chose to retain between two and sixteen modes. We have now shown that a first mode instability requires a minimum of four modes in the modal truncation, while for a second mode instability, one needs to retain at least the first eight modes. Secondly, it has been widely believed from previous studies that the approximate analysis with only second order gasdynamic nonlinearities could not show triggered limit cycles. This has now been theoretically established by recognizing that second order gasdynamics does not contribute either nonlinear damping or parametric excitation terms in the form required to cause triggered limit cycles. Finally, nonlinear combustion mechanisms for triggering based on pressure and velocity coupling models have been studied. Results from a previous study which suggested that pressure coupling does not lead to triggering have now been explained. Velocity coupling models have been shown to induce triggered instability due to a nonlinear damping mechanism. Velocity coupling models used in the past have been examined, and a new velocity coupling function has been derived that captures the qualitative dynamics at onset of triggered instability. Interestingly, our velocity coupling function naturally shows a threshold nature unlike previous velocity coupling models that had an artificially imposed threshold character.

## 6. Acknowledgments
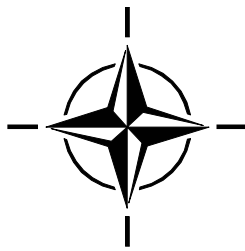
# Bibliography

[1] Chu, B.-T., and Kovasznay, L.S.G., "Nonlinear Interactions in a Viscous Heat-Conducting Compressible Gas," *Journal of Fluid Mechanics*, Vol. 3, No. 5, 1957, pp. 494-512.

[2] Baum, J.D., Levine, J.N., and Lovine, R.L., "Pulse Triggered Nonlinear Combustion Instability in Solid Rocket Motors," *AIAA Journal*, Vol. 22, No. 10, 1984, pp. 1413-1419.

[3] Baum, J.D., Levine, J.N., and Lovine, R.L., "Pulsed Instability in Rocket Motors: A Comparision Between Predictions and Experiments," *Journal of Propulsion and Power*, Vol. 4, No. 4, 1988, pp. 308-316.

[4] Lieuwen, T.C,, "Experimental Investigation of Limit Cycle Oscillations in an Unstable Gas Turbine Combustor," *Journal of Propulsion and Power*, Vol. 18, No. 1, 2002, pp. 61-67.

[5] Flandro, G.A., "Effects of Vorticity on Rocket Combustion Stability," *Journal of Propulsion and Power*, Vol. 11, No. 4, 1995, pp. 607-625.

[6] Garcia-Schafer, J.E., and Linan, A., "Longitudinal Acoustic Instabilities in Slender Solid Propellant Rockets: Linear Analysis," *Journal of Fluid Mechanics*, Vol. 437, 2001, pp. 229-254.

[7] Culick, F.E.C., "Some Recent Results for Nonlinear Acoustics in Combustion Chambers," *AIAA Journal*, Vol. 32, No. 1, 1994, pp. 146-169.

[8] Culick, F.E.C., "Combustion Instabilities in Propulsion Systems," *Unsteady Combustion*, F.E.C. Culick et al (eds.), Kluwer Academic Publishers, Netherlands, 1996, pp. 173-241.

[9] Culick, F.E.C., "Nonlinear Growth and Limiting Amplitude of Acoustic Oscillators in Combustion Chambers," *Combustion Science and Technology*, Vol. 3, No. 1, 1971, pp. 1-16.

[10] Culick, F.E.C., "Nonlinear Behavior of Acoustic Waves in Combustion Chambers, Parts I and II," *Acta Astronautica*, Vol. 3, 1976, pp. 714-757.

[11] Culick, F.E.C., and Yang, V., "Prediction of the Stability of Unsteady Motions in Solid Propellant Rocket Motors," *Nonsteady Burning and Combustion Stability of Solid Propellants*, L. de Luca, E.W. Price, and M. Summerfield (eds.), AIAA, Washington, 1992.

[12] Awad, E., and Culick, F.E.C., "On the Existence and Stability of Limit Cycles for Longitudinal Acoustic Modes in a Combustion Chamber," *Combustion Science and Technology*, Vol. 46, No. 6, 1986, pp. 195-222.

[13] Paparizos, L.G., and Culick, F.E.C., "The Two-Mode Approximation to Nonlinear Acoustics in Combustion Chambers, I. Exact Solution for Second Order Acoustics," *Combustion Science and Technology*, Vol 65, 1989, pp. 39-65.

[14] Yang, V., Kim, S.I., and Culick, F.E.C., "Triggering of Longitudinal Pressure Oscillations in Combustion Chambers, I: Nonlinear Gasdynamics," *Combustion Science and Technology*, Vol. 72, No. 5, 1990, pp. 183-214.

[15] Zinn, B.T., "A Theoretical Study of Nonlinear Combustion Instability in Liquid Propellant Rocket Engines," *AIAA Journal*, Vol. 6, No. 10, 1968, pp. 1966-1972.

[16] Culick, F.E.C., "Stability of Longitudinal Oscillations with Pressure and Velocity Coupling in a Solid Propellant Rocket," *Combustion Science and Technology*, Vol. 2, No. 4, 1970, pp. 179-201.

[17] Levine, J.N., and Baum, J.D., "A Numerical Study of Nonlinear Instability Phenomena in Solid Rocket Motors," *AIAA Journal*, Vol. 21, No. 4, 1983, pp. 557-564.

[18] Jahnke, C.C., and Culick, F.E.C., "Application of Dynamical Systems Theory to Nonlinear Combustion Instabilities," *Journal of Propulsion and Power*, Vol. 10, No. 4, 1994, pp. 508-517.

[19] Culick, F.E.C., Burnley, V., and Swenson, G., "Pulsed Instabilities in Solid Propellant Rockets," *Journal of Propulsion and Power*, Vol. 11, No. 4, 1995, pp. 657-665.

[20] Ma, Y., van Moorhem, W.K., and Shorthill, R.W., "Experimental Investigation of Velocity Coupling in Combustion Instability," *Journal of Propulsion and Power*, Vol. 7, No. 5, 1991, pp. 692-699.

[21] Burnley, V.S., and Culick, F.E.C., "Influence of Random Excitations on Acoustic Instabilities in Combustion Chambers," *AIAA Journal*, Vol. 38, No. 8, 2000, pp. 1403-1410.

[22] Burnley, V.S., "Nonlinear Combustion Instabilities and Stochastic Sources," Ph. D. Thesis, California Inst. of Technology, Pasadena, CA, 1996.

[23] Poinsot, T., Bourienne, F., Candel, S.H., and Esposito, E., "Suppression of Combustion Instabilities by Active Control," *Journal of Propulsion and Power*, Vol. 5, No. 1, 1989, pp. 14-20.

[24] McManus, K.R., Poinsot, T., and Candel, S.M., "A Review of Active Control of Combustion Instabilities," *Progress in Energy and Combustion Science*, Vol. 19, 1993, pp. 1-29.

[25] Ananthkrishnan, N., and Sudhakar, K., "Characterization of Periodic Motions in Aircraft Lateral Dynamics," *Journal of Guidance, Control, and Dynamics*, Vol. 19, No. 3, 1996, pp. 680-685.

[26] Ananthkrishnan, N., Sudhakar, K., Sudershan, S., and Agarwal, A., "Application of Secondary Bifurcations to Large Amplitude Limit Cycles in Mechanical Systems," *Journal of Sound and Vibration*, Vol. 215, No. 1, 1998, pp. 183-188.

[27] Ananthkrishnan, N., Sudershan, S., Sudhakar, K., and Verma, A., "Large Amplitude Limit Cycles in Resonantly Coupled Oscillators," *Journal of Sound and Vibration*, Vol. 231, No. 5, 2000, pp. 1377-1382.

[28] Doedel, E.J., Wang, X.J., Fairgrieve, T.F., Champneys, A.R., Kuznetsov, Y.A., and Sandstede, B., "AUTO97: Continuation and Bifurcation Software for Ordinary Differential Equations (with HomCont)," California Inst. of Technology, Pasadena, CA, 1998.

[29] Ananthkrishnan, N., "Qualitative Dynamics of Nonlinear Acoustic Waves in a Combustion Chamber, I: Modal Truncation and Triggering," Guggenheim Jet Propulsion Center Documents on Active Control of Combustion Instabilities, CI 00-03, California Inst. of Technology, Pasadena, CA, 2000.

[30] Ananthkrishnan, N., "Qualitative Dynamics of Nonlinear Acoustic Waves in a Combustion Chamber, III: Velocity Coupling Models," Guggenheim Jet Propulsion Center Documents on Active Control of Combustion Instabilities, CI 01-01, California Inst. of Technology, Pasadena, CA, 2001.

# REPORT DOCUMENTATION PAGE

| 1. Recipient's Reference | 2. Originator's References | 3. Further Reference | 4. Security Classification of Document |
|---|---|---|---|
| | RTO-EN-023 AC/323(AVT-096)TP/70 | ISBN 92-837-1103-3 | UNCLASSIFIED/ UNLIMITED |

| 5. Originator | Research and Technology Organisation North Atlantic Treaty Organisation BP 25, F-92201 Neuilly-sur-Seine Cedex, France |
|---|---|

| 6. Title | Internal Aerodynamics in Solid Rocket Propulsion |
|---|---|

**7. Presented at/Sponsored by**

The Applied Vehicle Technology Panel (AVT) and the von Kármán Institute for Fluid Dynamics (VKI), in support of a RTO/VKI Special Course presented on 27-31 May 2002 in Rhode-Saint-Genèse, Belgium.

| 8. Author(s)/Editor(s) | 9. Date |
|---|---|
| Multiple | January 2004 |

| 10. Author's/Editor's Address | 11. Pages |
|---|---|
| Multiple | 468 |

| 12. Distribution Statement | There are no restrictions on the distribution of this document. Information about the availability of this and other RTO unclassified publications is given on the back cover. |
|---|---|

**13. Keywords/Descriptors**

| | |
|---|---|
| Boosters for launch vehicles | Numerical modeling |
| Combustion instabilities | Performance |
| Combustion of metal particulates | Reduced costs |
| Combustion of solid propellants | Solid rocket |
| Flow/structural interactions | Space launchers |
| Internal aerodynamics | Tactical rockets |
| Internal flow dynamics | Two-phase flow |
| Military rockets | Vortex shedding |

**14. Abstract**

These RTO-AVT/VKI Special Course notes provide the state of the art in internal aerodynamics in solid rocket propulsion, in a way accessible to attendees coming from both academic and industrial areas. Two families of solid motors can be identified: tactical rockets and large boosters for launch vehicles. The military rockets are subjected to combustion instabilities while vortex shedding drives the instabilities in the large boosters. After an overview of the motor internal flow dynamics, combustion of solid propellants and metal particulates were presented. Numerical modeling of internal flow aerodynamic, two-phase flow and flow/structural interactions were addressed, before focusing on the motor flow and combustion instabilities.

**CENTRES DE DIFFUSION NATIONAUX**

**ALLEMAGNE**
Streitkräfteamt / Abteilung III
Fachinformationszentrum der
 Bundeswehr (FIZBw)
Friedrich-Ebert-Allee 34, D-53113 Bonn

**BELGIQUE**
Etat-Major de la Défense
Département d'Etat-Major Stratégie
ACOS-STRAT – Coord. RTO
Quartier Reine Elisabeth
Rue d'Evère, B-1140 Bruxelles

**CANADA**
DSIGRD2
Bibliothécaire des ressources du savoir
R et D pour la défense Canada
Ministère de la Défense nationale
305, rue Rideau, 9e étage
Ottawa, Ontario K1A 0K2

**DANEMARK**
Danish Defence Research Establishment
Ryvangs Allé 1, P.O. Box 2715
DK-2100 Copenhagen Ø

**ESPAGNE**
SDG TECEN / DGAM
C/ Arturo Soria 289
Madrid 28033

**ETATS-UNIS**
NASA Center for AeroSpace
 Information (CASI)
Parkway Center, 7121 Standard Drive
Hanover, MD 21076-1320

**FRANCE**
O.N.E.R.A. (ISP)
29, Avenue de la Division Leclerc
BP 72, 92322 Châtillon Cedex

**GRECE (Correspondant)**
Defence Industry & Research
 General Directorate, Research Directorate
Fakinos Base Camp, S.T.G. 1020
Holargos, Athens

**HONGRIE**
Department for Scientific Analysis
Institute of Military Technology
Ministry of Defence
H-1525 Budapest P O Box 26

**ISLANDE**
Director of Aviation
c/o Flugrad
Reykjavik

**ITALIE**
Centro di Documentazione
 Tecnico-Scientifica della Difesa
Via XX Settembre 123
00187 Roma

**LUXEMBOURG**
*Voir* Belgique

**NORVEGE**
Norwegian Defence Research Establishment
Attn: Biblioteket
P.O. Box 25, NO-2007 Kjeller

**PAYS-BAS**
Royal Netherlands Military
 Academy Library
P.O. Box 90.002
4800 PA Breda

**POLOGNE**
Armament Policy Department
218 Niepodleglosci Av.
00-911 Warsaw

**PORTUGAL**
Estado Maior da Força Aérea
SDFA – Centro de Documentação
Alfragide
P-2720 Amadora

**REPUBLIQUE TCHEQUE**
DIC Czech Republic-NATO RTO
VTÚL a PVO Praha
Mladoboleslavská ul.
Praha 9, 197 06
Česká republika

**ROYAUME-UNI**
Dstl Knowledge Services
Information Centre, Building 247
Dstl Porton Down
Salisbury
Wiltshire SP4 0JQ

**TURQUIE**
Milli Savunma Bakanlığı (MSB)
ARGE ve Teknoloji Dairesi Başkanlığı
06650 Bakanliklar – Ankara

**AGENCES DE VENTE**

**NASA Center for AeroSpace**
 **Information (CASI)**
Parkway Center, 7121 Standard Drive
Hanover, MD 21076-1320
ETATS-UNIS

**The British Library Document**
 **Supply Centre**
Boston Spa, Wetherby
West Yorkshire LS23 7BQ
ROYAUME-UNI

**Canada Institute for Scientific and**
 **Technical Information (CISTI)**
National Research Council
Acquisitions, Montreal Road, Building M-55
Ottawa K1A 0S2, CANADA

Les demandes de documents RTO ou AGARD doivent comporter la dénomination « RTO » ou « AGARD » selon le cas, suivie du numéro de série (par exemple AGARD-AG-315). Des informations analogues, telles que le titre et la date de publication sont souhaitables. Des références bibliographiques complètes ainsi que des résumés des publications RTO et AGARD figurent dans les journaux suivants :

**Scientific and Technical Aerospace Reports (STAR)**
STAR peut être consulté en ligne au localisateur de ressources uniformes (URL) suivant:
 http://www.sti.nasa.gov/Pubs/star/Star.html
STAR est édité par CASI dans le cadre du programme NASA d'information scientifique et technique (STI)
STI Program Office, MS 157A
NASA Langley Research Center
Hampton, Virginia 23681-0001
ETATS-UNIS

**Government Reports Announcements & Index (GRA&I)**
publié par le National Technical Information Service
Springfield
Virginia 2216
ETATS-UNIS
(accessible également en mode interactif dans la base de données bibliographiques en ligne du NTIS, et sur CD-ROM)

NORTH ATLANTIC TREATY ORGANISATION

RESEARCH AND TECHNOLOGY ORGANISATION

BP 25
F-92201 NEUILLY-SUR-SEINE CEDEX • FRANCE
Télécopie 0(1)55.61.22.99 • E-mail mailbox@rta.nato.int

**DISTRIBUTION OF UNCLASSIFIED**
**RTO PUBLICATIONS**

AGARD & RTO publications are sometimes available from the National Distribution Centres listed below. If you wish to receive all RTO reports, or just those relating to one or more specific RTO Panels, they may be willing to include you (or your Organisation) in their distribution.

RTO and AGARD reports may also be purchased from the Sales Agencies listed below.

Requests for RTO or AGARD documents should include the word 'RTO' or 'AGARD', as appropriate, followed by the serial number. Collateral information such as title and publication date is desirable.

If you wish to receive electronic notification of RTO reports as they are published, please visit our website (www.rta.nato.int) from where you can register for this service.

## NATIONAL DISTRIBUTION CENTRES

**BELGIUM**
Etat-Major de la Défense
Département d'Etat-Major Stratégie
ACOS-STRAT – Coord. RTO
Quartier Reine Elisabeth
Rue d'Evère
B-1140 Bruxelles

**CANADA**
DRDKIM2
Knowledge Resources Librarian
Defence R&D Canada
Department of National Defence
305 Rideau Street
9th Floor
Ottawa, Ontario K1A 0K2

**CZECH REPUBLIC**
DIC Czech Republic-NATO RTO
VTÚL a PVO Praha
Mladoboleslavská ul.
Praha 9, 197 06
Česká republika

**DENMARK**
Danish Defence Research
Establishment
Ryvangs Allé 1
P.O. Box 2715
DK-2100 Copenhagen Ø

**FRANCE**
O.N.E.R.A. (ISP)
29, Avenue de la Division Leclerc
BP 72
92322 Châtillon Cedex

**GERMANY**
Streitkräfteamt / Abteilung III
Fachinformationszentrum der
Bundeswehr (FIZBw)
Friedrich-Ebert-Allee 34
D-53113 Bonn

**GREECE (Point of Contact)**
Defence Industry & Research
General Directorate, Research Directorate
Fakinos Base Camp, S.T.G. 1020
Holargos, Athens

**HUNGARY**
Department for Scientific Analysis
Institute of Military Technology
Ministry of Defence
H-1525 Budapest P O Box 26

**ICELAND**
Director of Aviation
c/o Flugrad, Reykjavik

**ITALY**
Centro di Documentazione
Tecnico-Scientifica della Difesa
Via XX Settembre 123
00187 Roma

**LUXEMBOURG**
*See* Belgium

**NETHERLANDS**
Royal Netherlands Military
Academy Library
P.O. Box 90.002
4800 PA Breda

**NORWAY**
Norwegian Defence Research
Establishment
Attn: Biblioteket
P.O. Box 25, NO-2007 Kjeller

**POLAND**
Armament Policy Department
218 Niepodleglosci Av.
00-911 Warsaw

**PORTUGAL**
Estado Maior da Força Aérea
SDFA – Centro de Documentação
Alfragide, P-2720 Amadora

**SPAIN**
SDG TECEN / DGAM
C/ Arturo Soria 289
Madrid 28033

**TURKEY**
Milli Savunma Bakanlığı (MSB)
ARGE ve Teknoloji Dairesi Başkanlığı
06650 Bakanliklar – Ankara

**UNITED KINGDOM**
Dstl Knowledge Services
Information Centre, Building 247
Dstl Porton Down
Salisbury, Wiltshire SP4 0JQ

**UNITED STATES**
NASA Center for AeroSpace
Information (CASI)
Parkway Center, 7121 Standard Drive
Hanover, MD 21076-1320

## SALES AGENCIES

**NASA Center for AeroSpace**
**Information (CASI)**
Parkway Center
7121 Standard Drive
Hanover, MD 21076-1320
UNITED STATES

**The British Library Document**
**Supply Centre**
Boston Spa, Wetherby
West Yorkshire LS23 7BQ
UNITED KINGDOM

**Canada Institute for Scientific and**
**Technical Information (CISTI)**
National Research Council
Acquisitions
Montreal Road, Building M-55
Ottawa K1A 0S2, CANADA

Requests for RTO or AGARD documents should include the word 'RTO' or 'AGARD', as appropriate, followed by the serial number (for example AGARD-AG-315). Collateral information such as title and publication date is desirable. Full bibliographical references and abstracts of RTO and AGARD publications are given in the following journals:

**Scientific and Technical Aerospace Reports (STAR)**
STAR is available on-line at the following uniform
resource locator:
  http://www.sti.nasa.gov/Pubs/star/Star.html
STAR is published by CASI for the NASA Scientific
and Technical Information (STI) Program
STI Program Office, MS 157A
NASA Langley Research Center
Hampton, Virginia 23681-0001
UNITED STATES

**Government Reports Announcements & Index (GRA&I)**
published by the National Technical Information Service
Springfield
Virginia 2216
UNITED STATES
(also available online in the NTIS Bibliographic
Database or on CD-ROM)

ISBN 92-837-1103-3